

PROCEEDINGS OF THE 22<sup>ND</sup> EUROPEAN YOUNG GEOTECHNICAL ENGINEERS  
CONFERENCE, GOTHENBURG, SWEDEN, 26-29 AUGUST 2012

# EYGEC 2012

- setting the scene for future European geotechnical research

EDITED BY

Victoria Svahn & Tara Wood



**Svenska Geotekniska Föreningen**  
Swedish Geotechnical Society

Report 1:2012

EYGEC 2012

- setting the scene for future European geotechnical research

PROCEEDINGS OF THE 22<sup>ND</sup> EUROPEAN YOUNG GEOTECHNICAL ENGINEERS  
CONFERENCE, GOTHENBURG, SWEDEN, 26-29 AUGUST 2012

EDITED BY VICTORIA SVAHN & TARA WOOD

© SWEDISH GEOTECHNICAL SOCIETY, 2012

SGF Rapport 1:2012      ISBN 978-91-637-1435-1  
                                    ISSN 1103-7237  
                                    ISRN SGF-R-12/1-SE

Swedish Geotechnical Society  
c/o Arokad  
Plejadgatan 3  
SE-417 57 Göteborg  
Sweden  
E-mail: [info@sgf.net](mailto:info@sgf.net)

Printed by: Reproservice, Chalmers University of Technology, Gothenburg, Sweden, 2012  
Cover: The harbour of Gothenburg. Photo: Karin Holmgren



## TABLE OF CONTENTS

Preface	IX
History of EYGEC	XIII
Scientific and local organizing committee	XV
<b>Keynote lecture</b>	
Risk associated with geotechnical structures and Eurocode 7 <i>Vaniček, I.</i>	1
<b>Session 1 – Site investigations and laboratory testing</b>	
Internal erosion of three different geosynthetic clay liners tested over a perforated base pedestal <i>Ozhan, H.O. and Guler, E.</i>	9
Behaviour of foam glass aggregate under static loading <i>Steurer, A.</i>	15
Geotechnical investigations and solutions for Tourist centre near the town of Nin <i>Zubic, L. and Patrk, M.</i>	21
Important aspects in design of laminar soil container for 1-g shaking table tests <i>Cvetanovska J., Sesov V. and Edip, K.</i>	27
Modelling of horizontal soil deformations <i>te Boekhorst, C.W.J.</i>	33
Effects of loading rate and saturating fluid on chalk mechanical behavior <i>Johnsen, Ø., Cuisiat, F. and Grande L.</i>	39
The importance of preliminary investigations when working in areas blighted by historical mineworkings <i>O'Neill-Gwilliams, S.</i>	45
<b>Session 2 – Shallow and deep foundations</b>	
Comparative probabilistic analysis of bearing capacity formulae for shallow foundations using Monte-Carlo simulation <i>Koreta, O. and Myftaraga, E.</i>	51
Determination of 1200 mm working piles deformation parameters, using test of smaller diameter pile for the piled raft foundation of Capital Fort project <i>Parvanov, B.</i>	57

Comparison between results of static pile load testing, PDA results and calculated bearing capacities for pile design on the bridge over river Drava <i>Biščan, M. and Bolfan, L.</i>	63
Behavior of soil-structure interface under cyclic loading with large number of cycles <i>PRA-AI, S. and Boulon, M.</i>	69
Effect of creep on the stability of leaning towers <i>Marchi, M.</i>	75
The influence of the load eccentricity on the magnitude of the initial critical pressure of the foundation soil <i>Bejan, F.</i>	81
 <b>Session 3 – Deep excavations and retaining structures</b>	
Drawing up of a geotechnical dossier for the stabilization of historical quay walls along the river Scheldt in Antwerp <i>Vincke, L. and Haelterman, K.</i>	87
Seismic performance of caisson supported structures <i>Zafeirakos, A.</i>	93
Assessment of the technical condition of the retaining walls along the highway of the Black Sea coast of the areas of Tuapse and Big Sochi <i>Polishchuk, K.</i>	101
Ground vibrations due to pile and sheet pile driving – prediction models of today <i>Deckner, F., Viking, K. and Hintze, S.</i>	107
Change of shear strength in soft soil excavations <i>Yannie, J.</i>	113
Stiffness parameters for the foundation design of ‘The Landmark’ tower <i>Dewsbury, J.J.</i>	119
 <b>Session 4 – Tunnelling and underground structures</b>	
Cement free mortar for annular gap grouting in shield tunnelling with slurry face support <i>Thienert, C.</i>	125
Numerical simulation of tunnel construction in London Clay using three constitutive models <i>Santos, L.M.A., da Venda Oliveira, P.J. and de Almeida e Sousa, J.N.V.</i>	131

Influence of a core size on correlation between Schmidt rebound hardness and uniaxial compressive strength on Tertiary sedimentary rocks from Slovenia <i>Fabjan, T. and Vukadin, V.</i>	137
Backanalysis in tunnels using different minimization algorithms <i>de Santos, C., Ledesma, A. and Gens, A.</i>	143
Data analysis of cores and geophysical bore logs for systematic rock type interpretation <i>Johansson, S., Möller, H. and Friberg, O.</i>	149
Tunnel face stability under transient conditions: stand-up time in low permeability ground <i>Roberto Schürch, R. and Anagnostou, G.</i>	155
<b>Session 5 – Design parameters and modeling</b>	
Investigation of long-term creep deformations on soil strength <i>Kalos, A.</i>	161
Validation and verification of a practical constitutive model for predicting liquefaction in sands <i>Petalas, A., Galavi, V. and Brinkgreve, R.B.J.</i>	167
Concerning the vibrocreep issue <i>Aleksandrovykh, V.A.</i>	173
A simple numerical method to study buckling of flexible piles embedded in a multi-layered soil <i>Cuira, F.</i>	179
Basic study of the numerical analysis of jet grouting using smoothed particle hydrodynamics <i>Stefanova, B.</i>	185
3D-interaction of structure and subsoil for a new fly ash silo, Maasvlakte Rotterdam <i>Bekken, L.F.J. and Nohl, W.A.</i>	191
Smooth Particle Hydrodynamics (SPH) approach in simulating large penetration into soil <i>Danilewicz, A.</i>	197
Parallel computational framework for the solution of inverse problems in geotechnical engineering <i>Pekcan, O. and Seçkiner, S.</i>	203

### **Session 6 – Infrastructure projects**

Analyzing the displacements of a pile frame to determine its transverse load-bearing capacity <i>Tanev, T., Kerenchev, N., Manolov, A. and Dimitrov, H.</i>	209
Vintapperrampen: From detailed design to construction <i>Isgreen, T.V.</i>	215
Impact of the jack-up rig installation on the jacket platform piles Spudcan-soil-pile interaction analyses <i>Kellezi, L. and Sundararajan, S.</i>	221
Modeling of the effect of the embankment dimensions on the mechanical behavior of railway track <i>Kalliainen, A.</i>	227
Foundation design new Botlek lifting bridge <i>B. Rijnveld, B. and Jacobse, J.A.</i>	233

### **Session 7 – Ground improvement**

Lime-treatment of sand improved by bentonite addition <i>Mir Amid, H., Zine, N., Massart, T.J., Verbrugge, J-C. and François, B.</i>	239
Experimental study of fibre reinforced fly ash behavior <i>Čiháková, T.</i>	245
Improvement solutions for very compressible soils. Case study: Tulcea wastewater treatment plant <i>Burlacu, C.</i>	251
Influence of gravel density in clay reinforced with stone columns. Laboratory study <i>Miranda, M.</i>	257
Chemically enhanced drainage of clayey soils by means of guanidinium solutions: Experimental testing and numerical modeling <i>Minder, P., Plötze, M. and Puzrin, A.M.</i>	263

### **Session 8 – Slope stability and landslides**

The investigations and the monitoring of three landslides along Durres-Morine motorway <i>Kosho, A.</i>	269
Influence of non-local strain regularization on the evolution of shear bands <i>Schädlich, B. and Schweiger, H.F.</i>	275
Measuring of the horizontal stress in overconsolidated soils <i>Malát, R.</i>	281

Centrifuge tests to evaluate the Po river embankment seismic response <i>Giretti, D.</i>	287
Comprehensive geotechnical monitoring of the landslide processes and the retaining structures in the city of Sochi <i>Ryabukhin, A.</i>	293
The impact of seismic events to the intensity of 6 points or higher on the stress-strain state landslide dangerous slopes in clay neogenic age Carpathian region of Ukraine <i>Khavkin, K.</i>	297



## PREFACE

The hosting of the 22<sup>nd</sup> European Young Geotechnical Engineers Conference 2012 has proudly been undertaken by the Swedish Geotechnical Society (SGS). We formed an organization committee, led by the Vice President of the SGS – Mrs Victoria Svahn, who has done an incredible job in collaborating with the Swedish geotechnical elite both regarding co-members of the organization committee as well as the members of the scientific committee and keynote lecturers.

The aim of the conference is to be a social forum where young geotechnical engineers can meet and exchange ideas. It is also a possibility for us to show Sweden and give you some insight in what's going on here when it comes to infrastructure projects and geotechnical research.

As the President of the SGS I would like to thank all of you involved in this conference for your time and efforts in making this a memorable event for all participants. The keynote lecturers Prof Ivan Vaniček, Prof Stefan Larsson and Prof Minna Karstunen are thanked for their presentations on interesting topics. Also, many thanks to all authors for their contribution and making the conference possible.

The SGS would sincerely like to thank the scientific committee (who is also the session leaders of the conference) who has reviewed all published papers and helped achieve quality. For the proceedings the papers have been organized in the following sections:

- Site investigation and laboratory testing
- Shallow and deep foundations
- Deep excavations and retaining structures
- Tunnelling and underground structures
- Design parameters and modelling
- Infrastructure projects
- Ground improvement
- Slope stability and landslides

The SGS invites you to Gothenburg, situated on the west coast of Sweden. It's a strategic choice not only for the good communications but also because of the interesting geological situation with clay depths of up to 100 m, quick-clay areas and the birth place of the world wide famous geotechnical stabilization analysis method – the semi-circular analysis by Prof Fellenius.

With those words I would like again to welcome you to the 22<sup>nd</sup> EYGEC 2012! Please take the opportunity to find new international colleagues within the geotechnical field and learn a bit more about the other participant's work. Perhaps your expertise could be used in some of the large infrastructure projects going on right now in Sweden?

Yours sincerely,

*Stefan Aronsson - President of the Swedish Geotechnical Society*





## PREFACE

Dear young professional colleagues. You are attending the 22<sup>nd</sup> European Young Geotechnical Engineers Conference the tradition of which started at Copenhagen in 1987. From the last ones the meetings in Gyor – Hungary (2008), Brno-Czech Republic (2010) and Rotterdam – The Netherlands (2011) can be mentioned. From this long row only the last mentioned country, respectively the Netherlands National Society of the International Society on Soil Mechanics and Geotechnical Engineering, arranged this conference for the second time.

The main intention of the ISSMGE was and is to get young geotechnical engineers from all around Europe together. Certainly the main aim of these conferences is to present new scientific achievements at individual countries to show, which directions of the research are preferred there. Nevertheless of the same importance is the second face of such activities so called networking – to discuss in friendly, free atmosphere the problems in individual countries, starting from the academical and scientific ones and passing through political, cultural and sportive which are playing also important role for young engineers. These discussions, the exchange of own experiences are able only in chamber atmosphere; therefore the individual national societies should nominate basically two participants.

Therefore I believe that the meeting here in Goteborg will help you to find new friends, new ideas about possible future cooperation. The elder colleagues, firstly from Sweden, are here to help you to better understand broader implication of the scientific problems about which you will be speaking within your presentations.

Finally, I am wishing you enjoyable days in Goteborg and, I hope that the main aims of this meeting will be fulfilled and you will return safely back home with new ideas about your professional personal and or national developments.

Please note that next year the International Conference of the Young Geotechnical Engineers will be arranged in France, Paris just before the 18<sup>th</sup> International Conference on Soil Mechanics and Geotechnical Engineering, which will start on September 2<sup>nd</sup> 2013 to allow the young engineers to also attend this most important ISSMGE activity. Therefore the next 23<sup>rd</sup> EYGEC will be arranged as far as in 2014. The place was not fixed yet, so the national societies have still chance to apply for it and therefore you have below the history of all EYGEC.

*Ivan Vaniček - Vice-President ISSMGE for Europe (2009 – 2013)*



## HISTORY OF EYGEC

1 <sup>st</sup>	1987	Copenhagen	Denmark
2 <sup>nd</sup>	1988	Oxford	UK
3 <sup>rd</sup>	1989	Raubichi (Minsk)	Soviet Union (now Belorussia)
4 <sup>th</sup>	1990	Delft	The Netherlands
5 <sup>th</sup>	1991	Grenoble	France
6 <sup>th</sup>	1992	Lisbon	Portugal
7 <sup>th</sup>	1993	Boeblingen	Germany
8 <sup>th</sup>	1994	Stara Lesna	Slovakia
9 <sup>th</sup>	1995	Ghent	Belgium
10 <sup>th</sup>	1996	Izmir	Turkey
11 <sup>th</sup>	1997	Madrid	Spain
12 <sup>th</sup>	1998	Tallinn	Estonia
13 <sup>th</sup>	1999	Santorini	Greece
14 <sup>th</sup>	2001	Plovdiv	Bulgaria
15 <sup>th</sup>	2002	Dublin	Ireland
16 <sup>th</sup>	2004	Vienna	Austria
17 <sup>th</sup>	2006	Zagreb	Croatia
18 <sup>th</sup>	2007	Ancona	Italy
19 <sup>th</sup>	2008	Gyor	Hungary
20 <sup>th</sup>	2010	Brno	The Czech Republic
21 <sup>st</sup>	2011	Rotterdam	The Netherlands
22 <sup>nd</sup>	2012	Gothenburg	Sweden



## SCIENTIFIC AND LOCAL ORGANIZING COMMITTEES

### Scientific committee

Prof Claes Alén  
Adjunct Prof Lars-Olof Dahlström  
Associate Prof Leif Jendeby  
Prof Sven Knutsson  
Prof Stefan Larsson  
Associate Prof Sven Liedberg  
Doctoral student Mats Olsson  
MSc Yvonne Rogbeck  
Prof Göran Sällfors

Chalmers University of Technology  
NCC Construction  
Swedish Transport Administration  
Luleå University of Technology  
Royal Institute of Technology  
Skanska Sweden, Geotechnical Engineering  
Chalmers University of Technology, NCC  
Swedish Geotechnical Institute  
Chalmers University of Technology

### Local organizing committee

Chairman        Victoria Svahn  
Secretary       Tara Wood  
Members        Ulrika Isacson  
                      Henrik Möller

Vice President SGS, Swedish Geotechnical Institute  
NCC Construction  
WSP Sweden  
Tyréns



# Risk associated with geotechnical structures and Eurocode 7

I.Vaniček<sup>1</sup>

*Czech Technical University in Prague*

## ABSTRACT

The paper is focusing on the problem of the risk with which the design of geotechnical structures is associated with. Closer specification of this risk is defined, especially the risk connected with the limit state design approach recommended in Eurocode 7 – Geotechnical design. Dissimilarities of the Eurocode 7 from other Eurocodes are mentioned, which result from the fact, that the EC 7 is not only so called material code but also the code for interaction of nearly all structures with geological environment, in some cases also code for loading of other structures from surrounding soil or rock. Attention is also devoted to the recognition of this risk in the society generally as this fact has a great impact on the recognition of the geotechnical engineering profession.

Keywords: Risk, geotechnical structures, Eurocode 7, geological model, geotechnical model, calculation model, numerical model, risk sharing

## 1 INTRODUCTION

Most of the European countries accepted codes for the design of different structures during last few years. The Structural Eurocode programme comprises the following standards generally consisting of a number of Parts:

- EN 1990 Eurocode: Basis of Structural Design
- EN 1991 Eurocode 1: Actions on structures
- EN 1992 Eurocode 2: Design of concrete structures
- EN 1993 Eurocode 3: Design of steel structures
- EN 1994 Eurocode 4: Design of composite steel and concrete structures

- EN 1995 Eurocode 5: Design of timber structures
- EN 1996 Eurocode 6: Design of masonry structures
- EN 1997 Eurocode 7: Geotechnical design
- EN 1998 Eurocode 8: Design of structures for earthquake resistance
- EN 1999 Eurocode 9: Design of aluminium structures

The design of all structures is associated with following principles:

-Limit state design approach – which for geotechnical structures means that for each geotechnical design situation it shall be verified that no limit state is exceeded. EC 7 counts with

---

<sup>1</sup>Ivan Vaniček . Czech Technical University in Prague, Thákurova 7, Praha 6, 160 29, vaniceki@mat.fsv.cvut.cz

Ultimate Limit States (ULS) and with Serviceability Limit States (SLS). ULS are divided into limit states EQU – loss of equilibrium of the structure or the ground, STR – internal failure or excessive deformation of the structure or structural elements, GEO – failure or excessive deformation of the ground, in which the strength of soil or rock is significant in providing resistance, UPL – loss of equilibrium of the structure or the ground due to uplift by water pressure or other vertical actions and HYD – failures caused by hydraulic gradients as hydraulic heave, internal erosion and piping.

- Complexity of each design shall be identified together with the associated risks. For geotechnical design a distinction shall be made between 3 Geotechnical Categories.

The attention of this paper is focused in particular on the second principle.

## 2 SPECIAL POSITION OF EC 7 BETWEEN OTHER EUROCODES

The special position of Eurocode 7 between other Eurocodes is visible from the Fig. 1. Eurocodes No. 2,3,4,5,6, and 9 are so called material codes, whereas Eurocode No 7 – Geotechnical design is not only material code but also code for the interaction of nearly all other structures with subsoil. With the help of the EC 7 it is also possible to determine loading of structures from surrounding soil and rock, Bond and Harris (2008).

In addition the EC 7 is the only code for which CEN/TC250 accepted reality that the geotechnical design is unique and cannot be considered as the designs for other structures. Models generally used are different for different countries and so cannot be easily harmonized simply because geological conditions are different and create logical justification for local traditions – practice. Therefore CEN/TC250 accepted principle that EC 7 is devoted only to the basic principles of geotechnical design and should be supplemented by National standards (annexes), Frank (2002).

However the main variation between other Eurocodes and EC 7 can be found in different steps with which the design is associated. The safe design and execution of geotechnical structures is passing through the following steps, Vaniček (2011,a):

- a) Specification of **the geological model** which, on the one hand, represents a geometrical model of this environment, specifying the thickness and bedding of individual geological layers with quasi-homogeneous properties, their regularity, dislocation by different discontinuities, etc., and, on the other hand, gives them geological specification, however, not only for the area which is directly affected by new construction, but for a much larger area. As ground water is a natural part of the geological environment, the geological model must be supplemented by detailed information about ground water fully employing the achievements of hydrogeology.

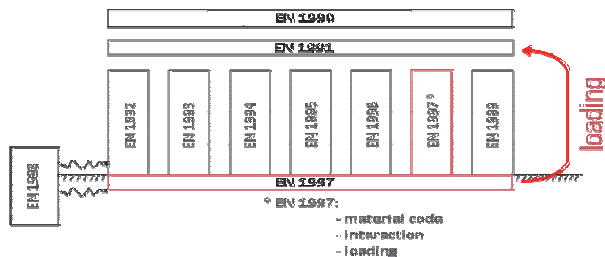


Figure 1. Layout of Eurocodes and the position of EC 7 Geotechnical design



b) Realization of laboratory and field tests on soils and rocks from which the geological environment is composed. Results of these tests or values obtained by theory, correlation or empiricism from these tests are so called derived values of geotechnical parameters.

c) Specification of the **geotechnical model** which specifies the mechanical and physical properties for individual quasi-homogeneous parts of the geological model, including discontinuities. In doing so these properties are obtained either from field investigation methods or from laboratory tests performed on samples obtained during site (ground) investigation. The properties are focused firstly on:

- Index properties – enabling the material classification;
- Deformation properties – e.g. modulus of deformation (Edef);
- Strength properties – e.g. shear parameters  $\phi$ ,  $c$ ;
- Filtration properties – e.g. coefficient of filtration (hydraulic conductivity)  $k$ .

However the allocated geotechnical parameters in the geotechnical model are not derived values but so called characteristic values. The selection of characteristic values for geotechnical parameters shall be based on the results and derived values from the laboratory and field tests, complemented by well-established experience. But what is more important is the fact that: "The characteristic value of a geotechnical parameter shall be selected as a cautious estimate of the value affecting the occurrence of the limit state". Therefore a great attention is devoted to the selection of these characteristic values in EC 7.

d) Selection of most appropriate calculation model, which may consist of any of the following:

- An analytical model;
- A semi-empirical model;

- A numerical model.

Note. According to EC 7 limit states can be verified not only with the help of calculation model, but also by

- Adoption of prescriptive measures;
- Experimental models and load tests;
- An observational method.
- Or by their combination

e) **Execution of the geotechnical structure.**

From this overview it is obvious that steps ad a) and b) are parts of Geotechnical investigation and the results are specified in the Ground investigation report. More details are given in Eurocode 7 Geotechnical design Part 2: Ground investigation and testing, known as EC 7-2. These steps are not typical for other structures, as they are mostly working with man made structural material (firstly steel, concrete). From this point of view it is important to stress that also the selection of the characteristic values of the geotechnical parameters by the designer is very sensitive process not typical for other structures. So it is evident that the design of geotechnical structures is associated with much higher risk than for other structures. One argument can be used for the support of this statement. During the design and execution of typical earth structure – embankment of transport infrastructure – the possibility to check the properties of soil in borrow pit is very limited, we can test roughly of 1 millionth of the whole volume of this borrow pit, (Vaniček, 2011,b). The quality of the realized embankment is also checked on very small part of this embankment (also roughly 1 millionth) and very often the controlled parameters are different than that used in the design – e.g. control is performed via dry density and moisture content, Vaniček,I., Vaniček,M. (2008). Therefore the uncertainties associated with geotechnical structures are much higher than for other structures, see Fig. 2.




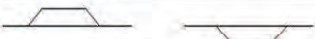
Steel Structures		3-5%	$E, \sigma_d, \sigma_t$
Concrete Structures		5-10%	
Timber Structures		10-20%	
Earth Structures	 Embankment (borrow pit) 1/1 000000 from the whole volume Indirect methods	cca 50%	$E_{def}, \varphi, c, k$

Figure 2. Uncertainties for different structures

### 3 RISK IN GEOTECHNICAL ENGINEERING

Risk in geotechnical engineering is directly connected with previously mentioned main phases of the design and performance of the geotechnical structures.

**Geological model** – the credibility of geological model depends on:

- Seriousness of the geological environment; its anisotropy, non homogeneity, irregularity of discontinuities; generally speaking, the more problematic this geological environment, the greater the risk connected with the design and performance is;
- Actual state of exploration of this geological environment; e.g. during earlier steps of site investigation and construction implementation;
- Extend of the ground investigation and its quality;
- Skill of the persons responsible for the site investigation interpretation.

This skill, according to Terzaghi (1959), is connected with a certain feeling for a geological environment and he called it as “capacity of judgment” and stated that “this capacity can be gained only by years of contact with field conditions”.

**Geotechnical model** – the credibility of geotechnical model depends not only on items mentioned for previous geological model, but also on other aspects as the number and precisions of field and laboratory tests, their evaluation and interpretation. It was mentioned previously that according to the recommendation of EU 7 “the characteristic value of a geotechnical parameter shall be selected as a cautious estimate of the value affecting the occurrence of the limit state.” EC 7 is highlighting again that we are not able to test all geological environments. “The zone of ground governing the behaviour of a geotechnical structure at a limit state is usually much larger than a test sample of the zone of ground affected in an in situ test. Consequently the value of the governing parameter is often the mean of a range of values covering a large surface of volume of the ground. The characteristic value

should be a cautious estimate of this mean value”.

When using standard tables of characteristic values related to soil investigation parameters – usually for geotechnical structures with lower risk – the characteristic value shall be selected again as a very cautious value.

For large geotechnical projects, where more tests are performed, the statistical methods of evaluation of the obtained results can be used. “If statistical methods are used, the characteristic value should be derived such that the calculated probability of a worse value governing the occurrence of the limit state under consideration is not greater than 5% “. In this respect “a cautious estimate of the mean value is a selection of the mean value of the limited set of geotechnical parameter value, with a confidence level of 95%; where local failure is concerned, a cautious estimate of the low value is a 5% fractile”.

**Calculation model** – selection of the most appropriate calculation model is also very sensitive problem. As young engineers often prefer numerical model based on FEM, few notes to this method and thereby to its credibility are mentioned:

- Precision of the subdivision of the solved environment (geotechnical model) into individual elements;
- Function expressing the change of properties within individual elements;
- Constitutive model – expressing the dependence of the deformation changes on stress changes;
- Final elements to model structural components;
- Finite elements to model interfaces;
- Boundary conditions.

Only few problems with constitutive models will be mentioned, expressing relation between strain changes on stress changes:

$$\Delta \varepsilon = E(\varepsilon, \sigma) \Delta \sigma \quad (1)$$

Fig. 3 is showing basic constitutive models used in geotechnical engineering. However, especially between young engineers, there is the tendency to apply even more sophisticated mod-

els. Therefore this tendency is connected with following questions: What is our ability to measure the parameters required for the quantification of the relation between stress changes and strain changes for complicated constitutive models with the help of field or laboratory methods? Are laboratory tested samples exactly describing the properties, which the in-situ obtained samples had?

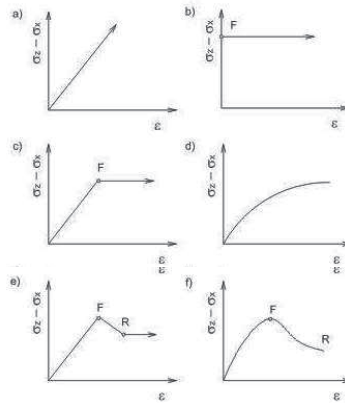


Fig. 3. Main constitutive models

**Execution of the geotechnical structure.**

Construction of civil engineering structures is in principle connected with high risk, which is in most cases evaluated by contractors with approach, which is now called – risk management.

Two typical problems are discussed below.

Firstly there are technological problems, e.g. for underground structures, the manner of rock breaking (excavation) is playing significant role. The selected technology can differently react to unexpected responses of the rock massif during the process of mining (excavation) and can have a different impact on the change of properties in the vicinity of the excavation perimeter.

Secondly it is problem of interaction with existing objects, which has different levels, from a purely technical up to legislative, juridical levels. Engineers, firstly geotechnical engineers, know very well that each change in stresses originates

changes in deformations. Therefore, when changes of stresses induced under new structures also influence the area under existing older structures, these stress changes induce changes in deformation as well. The problem is especially sensitive when the owner of the older structure agrees with the new structure only under the condition that “the new structure will not have any impact on the older one”. It is an obvious contradiction, however, it is very often accepted as this condition can be explained as a new one – the change does not cause “visible” deformations e.g. in the form of micro cracks on the façade of the older structure, Vaníček (2011,a). Very often all partners agree with this new, but unarticulated condition, and the design and structure construction is adapted to it. Therefore, this form of interaction is very sensitive for older historical structures which are more sensitive to small changes than new modern structures. Therefore, the passportization of an existing older structure before starting a new one is extremely important to be able to distinguish between older existing cracks and new cracks developed in the phase of the new structure construction.

#### 4 RISK AND PROBABILITY OF FAILURE

From the points mentioned above it is obvious that the risk associated with geotechnical structures design and performance is high and can be divided into 3 main parts:

- Risk associated with Geotechnical Investigation;
- Risk associated with Geotechnical Design – selection of characteristic values, firstly with characteristic values of the geotechnical parameters (but we cannot forget that EC 7 counts also with other characteristic values as actions and geometrical data) and secondly with selection of calculation model;
- Risk associated with structure performance.

During the education the main attention is devoted to the calculation model, however EC 7 advises:

“It should be considered that knowledge of the ground conditions depends on the extent and quality of the geotechnical investigations. Such knowledge and the control of workmanship are usually more significant to fulfilling the fundamental requirements than is precision in the calculation models and partial factors”.

Nevertheless the following summary to this discussion can be done:

- a) Limit state approach as based on the theory of probability counts with a certain risk of failure, it is its principle.
- b) Risk of failure is influenced by our level of understanding, depends on our ability to describe and to understand to the very complicated geological environments.
- c) Risk of failure is however also associated with our mistakes, sequent to our lack of education or lack of sufficient workmanship control.

Last point ad c) is usually under the control with the help of some regulations. In different countries these regulations can be different but in most cases are controlled by the Chamber of Civil engineers, specifying the conditions for persons examining geotechnical design and construction performance – e.g. authorization for geotechnical engineering which is usually needed for structures falling into Geotechnical Category 2 and 3.

Second point ad b) is associated with our level of knowledge, with the general effort of generations of our predecessors to understand to the geological environment as much as possible so that the final calculation model will represent its behaviour most authentically. Our effort in this direction should be focused on process of education, combining the theory with praxis. It is never ending process.

First point is associated with the fact that even if we will follow all recommendations of existing codes, in our case EC 7, there is a certain risk of failure. Therefore on this place there is rightful question, what probability of failure is accepted, can be defined and if yes by whom.

Up to now there is limited information on the

expected probability of failure, however roughly can be estimated as follows:

- 1:1 000 000 for the design and performance of spread foundations;
- 1:100 for large earth and rockfill dams – according to the evaluation of ICOLD for dams constructed between 1900 – 1975 – certainly this number is decreasing during last period;
- For shallow city tunnels this probability is even higher, even for last period.

From this it can be seen that there are a great differences. However e.g. probability of failure 1:10 000 ( $1 \cdot 10^{-4}$ ) means that in 9 999 cases the structure is safe, but can be also uneconomical – overdesigned. Therefore EC 7 up to a certain limit makes it possible to set up for individual European states this probability with the help of freedom with respect to the recommendation of the partial factor of safety. A certain possibility is also given via selection of characteristic values of the geotechnical parameters or via model factor. With respect to the model factor EC 7-1 in 2.4.7.1.(6) states that : “When calculating the design value of the resistance, ( $R_d$ ), or the design value of the effect of actions, ( $E_d$ ), model factors, ( $\gamma_{R,d}$ ) or ( $\gamma_{S,d}$ ) respectively, may be introduced to ensure that the results of the design calculation model are either accurate or err on the safe side”.

However for the precise decision how to set up these partial or model factors is not sufficient information. Therefore some countries decided to recommend these values after the recalculation of typical examples with the help of up to now used methods of design (usually counting with total value of factor of safety). Just to be sure that new approach is roughly in the range of expected values. It means that with time, after the evaluation of this probability of failure with time the partial factors and the recommendation for the selection of characteristic values can be altered. In some countries where the limit state approach was used before Eurocode acceptance – as is e.g. the case for the Czech Republic for the design of spread foundations, the situation is clearer. After the re-evaluation of experience with this approach we can say that we are still on the conservative side as really the probability of

failure is roughly 1:1 000 000, even if the initial idea was to count with the failure of failure roughly 1: 10 000.

## 5 CONCLUSION

At the end it is possible to summarize:

- Limit state approach accepted in Eurocodes counts with a certain probability of failure even if the all recommendations in the standards are taken into account.
- This probability of failure can be partly affected by the selection of partial factor of safety, namely partial factors for soil parameters  $\gamma_M$ , partial factors on actions  $\gamma_F$  or the effects of actions  $\gamma_E$  or the partial resistance factors  $\gamma_R$  – with respect to the design approach which in particular country was recommended.

Therefore the discussion to this probability of failure is so important between civil engineering communities, as on one side with very low probability of failure the design of structures should be so conservative, uneconomical, but on the other one each failure can lead to the decrease of the professional prestige.

The main problem probably is that the society in general demands no failures. Therefore it is necessary to speak about these problems also on the general level, just to explain that the approach with “zero” failures can be counter-productive for the society. During this discussion the following comparison can be used – medicine doctors are also “working” with very complicated environment (with human body) – however the risk of failure is fully recognized and accepted.

Nevertheless at present the following two ways can be recommended to decrease the probability of failure:

- to use more frequently the design approach using observational method of design – as simultaneously with construction our information about geological environment and its responses during construction are improving;
- to spread the risk between more partners

– first of all also on investor – as risk shearing can bring also some improvement, Cools (2011). If investor can invest more money into geotechnical investigation, can improve our knowledge about this environment and designer and contractors can use these information for the more optimistic design and for lowering the risk during construction performance.

## REFERENCES

- [1] A. Bond., A.Harris. *Decoding Eurocode 7*. Taylor and Francis, London, 2008, 598 p.
- [2] Cools, P.M.C.B.M.: The Geo-Impuls Programme reducing geotechnical failure in the Netherlands. In: *Proc. 3rd Int. Symposium on Geotechnical Safety and Risk*. Pp. 3-10. Munich, 2011, BAW, editors: Vogt, Schuppener, Straub and Brau, , pp. 191-197, 2011
- [3] EN 1997 Eurocode 7: Geotechnical design
- [4] R.Frank., Present state of development of Eurocode 7 – Geotechnical Design. In: *Proc. 3rd Conf. of the Croatian Society for SMFE „Geotechnics through Eurocode 7“*. Hvar, 2002, pp. 17- 29, 2002
- [5] K.Terzaghi. Soil Mechanics in Action. *Civil Engineering*: **69** (1959), pp.33-34.
- [6] I. Vaniček. Risk in geotechnical engineering and profession prestige. Introduction Lecture. In: *Proc. 3rd Int. Symposium on Geotechnical Safety and Risk*. Pp. 3-10. Munich, , BAW, editors: Vogt, Schuppener, Straub and Brau. , pp. 3-9.,2011a
- [7] I.Vaniček Present day position of Geotechnical Engineering. Keynote lecture. 21st EYGEC Rotterdam, 2011b.
- [8] I.Vaniček.,M.Vaniček., *Earth Structures in Transport, Water and Environmental Engineering*. Springer Science + Business Media B.V., 2008, 637 s.

# Internal erosion of three different geosynthetic clay liners tested over a perforated base pedestal

H. O. Ozhan<sup>1</sup>

*Istanbul Kemerburgaz University, Istanbul, Turkey*

E. Guler

*Bogazici University, Istanbul, Turkey*

## ABSTRACT

A geosynthetic clay liner (GCL) is a material composed of a thin layer of bentonite sandwiched between two layers of geotextiles. Geosynthetic clay liners are being investigated in regard to their hydraulic properties, chemical compatibility, gas migration, mechanical behaviour and durability. In this study, three different geosynthetic clay liners placed over base pedestals with different sized uniform circular voids (with diameters of 20 mm, 15 mm, 10 mm and 5 mm) were tested in flexible wall permeameter under high hydraulic heads of up to 50 m. All of the three different GCLs were produced in the laboratory without needle-punching the geotextile components through the bentonite component. Test results show that internal erosion of a GCL under high hydraulic head is directly related to the void diameter of the perforated base pedestal placed beneath the GCL. Internal erosion also depends on the engineering properties of the geotextile component that is in contact with the perforated base pedestal. The geotextile component (nonwoven versus woven) of a GCL that has a higher tensile strength showed better resistance against internal erosion. Mass per unit area and deformability of the geotextile that is in contact with the perforated base pedestal also influence the resistance of the GCL against internal erosion. However, the results show that the type of the bentonite (sodium versus calcium) does not have a significant effect on internal erosion.

Keywords: Internal erosion, geosynthetic clay liner, perforated base pedestal, permittivity

## 1 INTRODUCTION

Geosynthetic clay liners (GCLs) are preferred as environmental protection barriers in cover systems and base liners. Their main advantages are their low hydraulic conductivity, low cost and easiness of installation [1]. Generally, GCLs are used together with geomembranes at the bottom of landfills. However, in Turkey, GCLs are also often used alone as lining materials in fresh water reservoirs. In such applications, the soil beneath a GCL might be anything from clay to coarse-grained gravel. As the depth of water in those reservoirs increases, the pressure may push the GCL into the voids of the coarse gravel subgrade and in turn, causes the bentonite between the two geotextile layers to be extruded through the damaged geotextile. Because of this interaction, the permeability may significantly increase [2]. This is called internal erosion.

Hydraulic conductivity tests were performed on GCLs under high hydraulic gradients in order to evaluate the effect of subgrade type on internal erosion [3]. According to the test results, all of the GCL types placed over the gravel or geonet

subgrade experienced internal erosion under high hydraulic heads ranging from 8 m to 45 m except the GCL with a scrim-reinforced nonwoven geotextile. However, when sand subgrade was used, none of the GCL types did suffer from loss of bentonite under hydraulic heads of up to 80 m.

Results of the laboratory permeability tests [2] and [4] showed that an increase in particle size diameter of the material that was in contact with the GCL caused more bentonite to extrude out of the GCL. However, internal erosion was not observed during either research most likely due to very low hydraulic heads and short test periods.

Consolidated-drained direct shear tests were conducted on thin layers of sodium and calcium bentonites [5]. According to the test results, the shear strength of calcium bentonite was found to be approximately twice than that of sodium bentonite. Although the hydraulic conductivity of calcium bentonite was measured one order of magnitude higher than that of sodium bentonite when water was used as the hydration and permeation liquid, calcium bentonite had an advantage for applications in which shear strength was crucial. It was also shown that the hydraulic con-

---

<sup>1</sup> H. O. Ozhan. Asst. Prof., Istanbul Kemerburgaz University / Istanbul-Turkey, hakkiozhan@hotmail.com

ductivity of both granular and powdered sodium bentonite permeated with water was the same [5]. Having the same hydraulic conductivity makes it logical to compare the performance of the GCL with granular bentonite to the performance of the GCL with powdered bentonite against internal erosion.

The objective of the current research is to investigate the parameters that affect internal erosion of geosynthetic clay liners that are used as lining materials in fresh water lagoons under high hydraulic heads. In order to better understand the effect of various parameters, a base pedestal with circular voids was used instead of natural gravel particles.

## 2 MATERIALS

Three different GCL samples were tested. All specimens were assembled in the laboratory without needle-punching the geotextile and bentonite components. The first GCL is designated as GCL-A and it consisted of a natural, granular sodium bentonite between a woven slit-film polypropylene geotextile ( $108 \text{ g/m}^2$ ) and a nonwoven needlepunched polypropylene geotextile ( $203 \text{ g/m}^2$ ). For the second GCL (GCL-B), calcium bentonite was sandwiched between the same woven (W1) and nonwoven geotextiles (N1) as used in GCL-A. The third GCL (GCL-C) was also assembled in the laboratory by using the same granular sodium bentonite between the same nonwoven geotextile as used in GCL-A and a woven geotextile (W2) with a relatively higher tensile strength than the one used in GCL-A. The engineering properties of the geotextile components used are listed in Table 1.

Table 1. Engineering properties of the geotextile components

Property	Value (N1)	Value (W1)	Value (W2)
Mass per Unit Area ( $\text{g/m}^2$ )	203	108	210
Tensile Strength ( $\text{kN/m}$ )	15.4	12.2	44
Elongation (%)	45	10	15
Static Puncture Resistance (N)	490	310	5600

The bentonite used in GCL-A and GCL-B was a natural, granular, high-swelling Wyoming sodium bentonite. The geotechnical properties of

the granular sodium bentonite are as follows: Swell Index=28 ml/2g;  $w_{LL}$ =344%;  $w_{PL}$ =36%. However, the bentonite used in GCL-C was a powdered calcium bentonite. The geotechnical properties of the calcium bentonite are as follows: Swell Index=20 ml/2g;  $w_{LL}$ =141%;  $w_{PL}$ =41%.

### 2.1 Specimen preparation

The same amount of bentonite was placed between geotextiles. The bentonite was wetted homogeneously to create a bonding of the geotextiles to the bentonite. Details of specimen preparation for GCL specimens are described in [6]. For the powdered calcium, deionized water was sprayed on the bentonite homogeneously and when the dispersed calcium bentonite platelets began to flocculate, the wetted bentonite was placed on the nonwoven geotextile [6].

### 2.2 Base pedestal used beneath GCL

Irregular subgrades such as natural gravel would make the evaluation of the effect of the void size difficult. Therefore, in order to simulate the natural subgrade, a new type of pedestal was devised. The base pedestal was a Plexiglas that had circular voids in it. To make the evaluation of different void sizes on the permeability of GCLs easier, spherical particles were considered and the maximum size of circular void in between these particles was predicted. In reality, the void was obviously not circular but by approximation, the void could be taken as a circle. As a result, when uniform gravel with particle diameter of 50 mm was considered, the maximum void diameter was estimated to be 20 mm. Similarly, for a uniform grain size of 37.5 mm, 25 mm and 12.5 mm, the maximum void diameter was 15 mm, 10 mm and 5 mm, respectively. Therefore, four Plexiglas bases with diameters of 100 mm and thicknesses of 10 mm were prepared each with 20 mm, 15 mm, 10 mm and 5 mm holes as shown in Figure 1.

All of the test configurations are shown in Table 2.



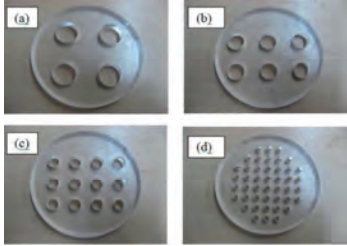


Figure 1. Perforated base pedestal with: (a) 20 mm, (b) 15 mm (c) 10 mm and (d) 5 mm diameter holes.

Table 2. Combinations of parameters of GCL

Specimen Name	GCL Type	Void Size of Base Pedestal (cm)	Geotextile Type in contact with Base Pedestal
GCL-A-NW-D2	GCL-A	2	Nonwoven
GCL-A-W-D2	GCL-A	2	Woven
GCL-A-NW-D1.5	GCL-A	1.5	Nonwoven
GCL-A-W-D1.5	GCL-A	1.5	Woven
GCL-A-NW-D1	GCL-A	1	Nonwoven
GCL-A-W-D1	GCL-A	1	Woven
GCL-A-NW-D0.5	GCL-A	0.5	Nonwoven
GCL-A-W-D0.5	GCL-A	0.5	Woven
GCL-B-NW-D2	GCL-B	2	Nonwoven
GCL-B-W-D2	GCL-B	2	Woven
GCL-B-NW-D1.5	GCL-B	1.5	Nonwoven
GCL-B-W-D1.5	GCL-B	1.5	Woven
GCL-B-NW-D1	GCL-B	1	Nonwoven
GCL-B-W-D1	GCL-B	1	Woven
GCL-B-W-D0.5	GCL-B	0.5	Woven
GCL-C-W-D2	GCL-C	2	Woven
GCL-C-W-D1.5	GCL-C	1.5	Woven
GCL-C-W-D1	GCL-C	1	Woven

### 3 TEST PROCEDURE

After specimen preparation, constant head flexible-wall permeability tests were conducted as outlined in [7]. In order to prevent clogging, a polypropylene needlepunched nonwoven geotextile was placed between the perforated base pedestal and the bottom cap of the permeameter cell.

The hydraulic head was kept constant during the permeation stage of the test. When there was not a drastic increase in permittivity of the GCL specimen, the hydraulic head was increased and the

same procedure was followed till internal erosion occurred or till 50 m of hydraulic head was maintained without a significant increase in permeability. The GCL specimen was permeated from top to bottom in order to simulate the internal erosion phenomenon. When the flow became steady, the head was increased to 5 m by 1 m increments in every 10 minutes. Permeation was continued under a constant head for approximately 12 days. Duration of 12 days was chosen because a considerable amount of increase in permittivity was obtained approximately within 12 days for all tested GCL specimens that experienced internal erosion [6].

### 4 TEST RESULTS AND DISCUSSION

Test results show that when internal erosion occurred, the increase in permittivity usually began at least 100 hours after the hydraulic head had been applied. For instance, according to the results of GCL-A-W-D1.5, when a hydraulic head of 15 m was applied, permittivity began to increase after about 130 hours as shown in Figure 2. The rate of the increase of permittivity remained small for approximately another 40-45 hours. Then, a sudden and much higher increase in permittivity was measured within less than an hour. This sudden increase was almost two orders of magnitude. The test continued for 177 hours and within this duration, approximately three and a half orders of magnitude of increase in permittivity was measured and almost two orders of magnitude of this increase took place in the last one hour.

Lower rates of increase measured on the GCLs can be interpreted as a sign that internal erosion had started. By facing high hydraulic head, the lower geotextile component began to deform and after a while, some bentonite particles began to migrate out of the lower geotextile which caused an increase, usually up to one order of magnitude in permittivity. As time passed, the lower geotextile could not resist high hydraulic heads which caused more bentonite particles to extrude out. Finally, a very high increase, up to three orders of magnitude in permit-

tivity was measured for all of the GCLs which experienced hydraulic failure. During the last stages of internal erosion, a high amount of bentonite extrusion was observed.

In some permeability tests, even under hydraulic heads equal to 50 m, no internal erosion was observed within 12 days. GCL-C-W-D2 is a specimen that did not experience internal erosion under a 50 m hydraulic head. According to the permeability test results, low permittivity was measured even at the end of the test under a 50 m hydraulic head. The permittivity of GCL-C-W-D2 decreased from  $8.19 \times 10^{-11}$  to  $2.05 \times 10^{-11}$  1/s from the beginning to the end of the test and no increase in permittivity was observed at any stage of the test.

As shown in Figure 3, eight GCL-A specimens were tested. For six combinations, the specimens experienced internal erosion. Internal erosion occurred in the following cases: GCL-A-W-D2 under 10 m hydraulic head, GCL-A-W-D1.5 under 15 m head, GCL-A-NW-D2 under 20 m head, GCL-A-W-D1 under 30 m head, GCL-A-NW-D1.5 under 35 m head and GCL-A-NW-D1 under 50 m hydraulic head. However, the permittivities of the two GCL-A specimens which were tested over the perforated base pedestal with 0.5 cm diameter did not increase for 300 hours even when the hydraulic head was 50 m. The values that are given in parentheses in Figure 3, 4 and 5 are the maximum hydraulic heads. All of the GCL specimens tested in this study are listed in Table 2 with different designations by taking the GCL type, the geotextile component that was in contact with the perforated base pedestal and the void size of the perforated base pedestal into account. These designations are also shown in Figure 3, 4 and 5.

As shown in Figure 4, seven GCL-B specimens were tested. For six combinations, the specimens experienced internal erosion. Internal erosion occurred in the following cases: GCL-B-W-D2 under 5 m hydraulic head, GCL-B-W-D1.5 under 15 m head, GCL-B-NW-D2 under 20 m head, GCL-B-W-D1 under 25 m head, GCL-B-NW-D1.5 under 35 m head and GCL-B-NW-D1 under 50 m hydraulic head. However, the permittivity of GCL-B-W-D0.5 which was tested over the perforated base pedestal with 0.5 cm void di-

ameter did not increase for 280 hours even when the hydraulic head was 50 m.

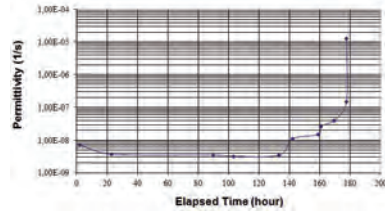


Figure 2. Change of Permittivity with time (GCL-A-W-D1.5; Hydraulic head 15 m).

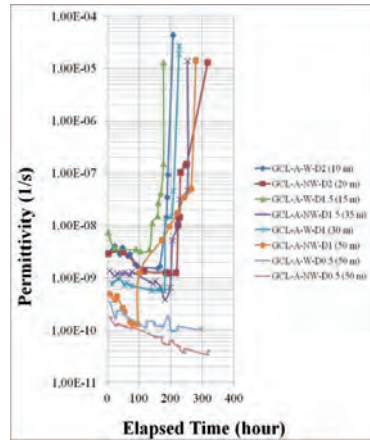


Figure 3. Permittivity - Elapsed Time Graph for GCL-A.

However, all of the three GCL-C specimens did not experience internal erosion even under hydraulic head of 50 m. Permittivity of the specimens decreased approximately half order of magnitude within almost 250 hours as shown in Figure 5.

The surfaces of the GCL specimen facing the voids on the perforated base pedestal formed a crest as shown in Figure 6. The other surfaces where the GCL specimen was in contact with the solid parts of the perforated base pedestal remained flat. High increase in permittivity of

GCL-A-NW-D1.5 was due to the high amount of bentonite migration from the openings caused by the damaged fibres of the crest zones on the nonwoven geotextile as shown in Figure 6.

The thickness of the crests on GCL-C-W-D2 was not as high as that of the other GCL specimens which experienced internal erosion. When the deformation was low, the openings of the crest zones remained small which prevented high amount of bentonite extrusion. The slit film tapes on the woven geotextile (W2) were not damaged due to the high tensile strength of the woven geotextile (W2).

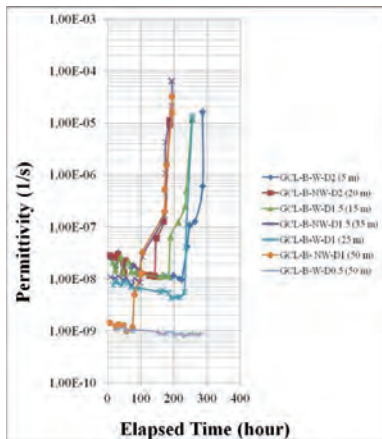


Figure 4. Permittivity - Elapsed Time Graph for GCL-B.

As the void size got larger, the thickness and area of the crest zone also got larger. As a result, higher amount of bentonite could migrate from the openings and damaged regions on the crest zones and internal erosion could occur on the GCLs under lower hydraulic heads. GCL specimens tested over the perforated base pedestal having voids of 5 mm diameter did not experience internal erosion even under a 50 m hydraulic head. This indicates that internal erosion becomes less critical as the grain size of the natural soil and as a consequence also the void size, decreases.

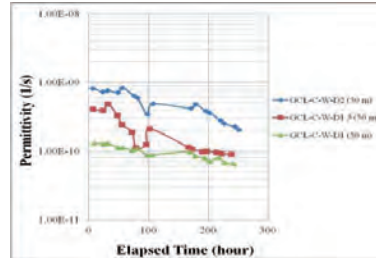


Figure 5. Permittivity - Elapsed Time Graph for GCL-C.

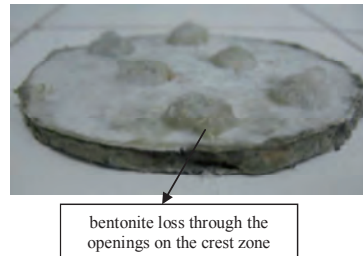


Figure 6. GCL-A-NW-D1.5 after the permeability test.

Performance of GCL-A specimens against internal erosion was almost the same as that of GCL-B specimens. GCL-A and GCL-B specimens experienced internal erosion under the same hydraulic head when the specimens were tested with their nonwoven geotextile component over the perforated base pedestals. Furthermore, the performance of the woven geotextile component of GCL-A was just slightly better than that of GCL-B against internal erosion.

These results show that bentonite type (sodium versus calcium) does not influence internal erosion of a GCL specimen so much. However, hydraulic conductivity of calcium bentonite was found to be higher than that of sodium bentonite [5] where the effect of high hydraulic heads was not taken into account.

Among all of the three types of GCLs used in this study, GCL-C showed the best performance against internal erosion. GCL-C specimen did not experience internal erosion even with its woven geotextile component tested over the perfo-

rated base pedestal with 20 mm void diameter under 50 m hydraulic head. The main reason for the resistance of GCL-C specimens against internal erosion was the high tensile strength of the woven geotextile component (W2). The wide-width tensile strength of W2 was higher than three and a half times of that of W1 and almost three times of that of N1. Very high tensile strength of W2 prevented the formation of defects on the slit film tapes.

The nonwoven geotextile component (N1) performed better against internal erosion than the woven geotextile component (W1) of all of the GCL-A and GCL-B specimens. One of the main reasons for the better performance of the nonwoven geotextile (N1) against internal erosion than the woven geotextile (W1) was the capability of nonwoven geotextiles to deform extensively before failure. Because of the higher rigidity, some of the slit film tapes on the crest zones of the woven geotextile component were damaged much more easily than those on the nonwoven geotextile component. Higher mass per unit area and tensile strength of the nonwoven geotextile (N1) than those of the woven geotextile (W1) were also the other parameters that caused the better performance of N1 against internal erosion.

### 3 CONCLUSION

In this study, laboratory permeability tests were performed to represent the field conditions when a GCL was used as a lining material in fresh water reservoirs. The following conclusions are reached as a result of the permeability tests:

The diameter of the voids of the perforated base pedestal plays a significant role on internal erosion. As the void size increased, internal erosion occurred at lower hydraulic heads. For the test configurations chosen and GCL specimens used in this research, no internal erosion occurred for the base pedestal that had a void diameter size of 5 mm. According to this result, it is advised to use GCLs placed over gravels not coarser than 5 mm for the conditions where the GCLs were facing high hydraulic heads up to 50 m.

The type of bentonite (sodium versus calcium)

used in the GCLs did not play a significant role in terms of internal erosion under high hydraulic heads. Performance of the GCLs with sodium bentonite against internal erosion was almost the same as that of the GCLs with calcium bentonite.

Engineering properties of the geotextile components play a significant role on internal erosion. The GCL with the woven geotextile (W2) facing the perforated base pedestal behaved the best in terms of internal erosion. This is estimated to be due to the very high tensile strength of W2. However, the performance of the nonwoven geotextile component (N1) was better than that of the woven geotextile (W1) against internal erosion. This result is estimated to be due to the capacity of the nonwoven geotextile to deform extensively before failure. This conclusion is based on the observation that when the woven geotextile (W1) was facing the perforated base pedestal, the slit film tapes were damaged much more easily which caused high amount of bentonite extrusion.

### REFERENCES

- [1] A. Bouazza, *Geosynthetic Clay Liners, Geotextiles & Geomembranes* 20 (2002), 3-17.
- [2] H. Y. Shan, & R. H. Chen, Effect of Gravel Subgrade on Hydraulic Performance of Geosynthetic Clay Liner, *Geotextiles & Geomembranes* 21 (2003), 339-354.
- [3] R. K. Rowe, & C. Orsini, Effect of GCL and Subgrade Type on Internal Erosion in GCLs under High Gradients, *Geotextiles & Geomembranes* 21 (2003), 1-24.
- [4] P. J. Fox, P. D. J. De Battista, & D. G. Mast, Hydraulic Performance of Geosynthetic Clay Liners under Gravel Cover Soils, *Geotextiles & Geomembranes* 18 (2000), 179-201.
- [5] M. H. Gleason, D. E. Daniel, & G. R. Eykholt, Calcium and Sodium Bentonite for Hydraulic Containment Applications, *J. of Geotech. & Geoen. Eng. ASCE* (1997), 438-445.
- [6] H. O. Ozhan, Internal Erosion of Geosynthetic Clay Liners under High Hydraulic Heads, Ph. D. Thesis, Bogazici University, Istanbul, Turkey, 2011.
- [7] ASTM D 5084, Standard Test Method for Measurement of Hydraulic Conductivity of Saturated Porous Materials Using a Flexible Wall Permeameter, American Soc. for Test. & Mat., West Conshohocken, Pennsylvania, USA, 2003.

# Behavior of foam glass aggregate under static loads

A. Steurer<sup>1</sup>

*Vienna University of Technology, Institute of Geotechnics, Karlsplatz 13/220-2, A-1040 Wien, Austria,  
armin.steurer@tuwien.ac.at*

## ABSTRACT

Foam glass aggregate is produced in a controlled production process. Due to its low density and thermal conductivity foam glass aggregate offers a broad variety of applications. Based on extensive laboratory tests foam glass aggregate is investigated in the scope of a joint research project performed at Vienna University of Technology and University of Innsbruck. The mechanical properties of single grains are investigated by uniaxial compression tests on cut foam glass prisms. The uniaxial compression test shows both a linear-elastic and a plastic behavior in the stress-strain relationship. A large-scale laboratory test was developed for the determination of the load-deformation behavior of foam glass aggregates taking into account the grain size distribution and the conditions during the compaction process in field. Deformation modulus can be directly derived while for the determination of the stiffness modulus the theory of the elastic-isotropic half space needs to be addressed. The time dependent load-deformation behavior of foam glass aggregate is determined from confined compression tests in an oedometer. Further confined compression tests with foam glass aggregate samples with different grain properties are investigated.

Keywords: Foam glass aggregate, uniaxial compression test, confined compression tests

## 1 INTRODUCTION

Foam glass aggregate is characterized by high porosity within the grains. This is reflected in a low density and low thermal conductivity. Due to these specific properties the material offers a wide variety of applications. Foam glass aggregate is mainly used as fill material under slabs, frost insulation material, and for light embankments especially for roads and highways.

In a funded joint scientific research project foam glass aggregate is investigated at Vienna University of Technology and University of Innsbruck.

Based on extensive laboratory testing stiffness, time-dependent settlement behavior, shear strength, bearing capacity, frost resistance, as well as permeability of foam glass aggregate layers with different boundary conditions is analyzed.

This paper describes different types of compression tests for the determination of the load-deformation behavior of foam glass aggregate under static loading.

---

<sup>1</sup> Corresponding Author. Affiliation, Contact address, e-mail

## 2 PRODUCTION PROCESS AND GENERAL PROPERTIES OF FOAM GLASS AGGREGATE

Foam glass aggregate is produced in a defined recycling process of waste glass material. In the first step of the production process waste glass is milled to glass powder. Furthermore, the powder is mixed with a foaming agent. The glass powder-foaming agent mix is heated in an oven up to 1000°C. Due to this temperature the glass powder foams up to foam glass. In the end of the production line the hot foam glass is taken out of the oven and cools down to ambient air-temperature. The fast cooling process induces tensile stresses in the sheets that easily let the foam glass break into foam glass aggregates.

The pores inside a single grain are closed. This is shown in a very low water absorption of about 11 vol.%.  
 The density of foam glass aggregate depends on the grain density, the degree of compaction, and the degree of water content. An overview of the range of the various densities taking into account different boundary conditions is given in Table 1.

Table 1. Density of foam glass aggregate

Boundary condition	Density [kg/m <sup>3</sup> ]
Dry, loose	150 - 210
Dry, degree of compaction 25 % <sup>1)</sup>	190 - 260
Wet <sup>2)</sup> , degree of compaction 25 % <sup>1)</sup>	270 - 365

<sup>1)</sup> Reduction of the volume of 25 %

<sup>2)</sup> At a maximum of water absorption

## 3 LABORATORY TESTS TO DETERMINE THE PROPERTIES OF SINGLE GRAINS

The following properties of single grains have been determined:

- Grain density
- Uniaxial compressive strength

Both properties are tested on cut prismatic foam glass grains. The measurements of the square prisms are approximately 15 mm in the edge length of the cross-section and comprise a height of about 35 mm. Thus, the proportion factor of the samples H/D (height / coextensive diameter) is about 2 [-].

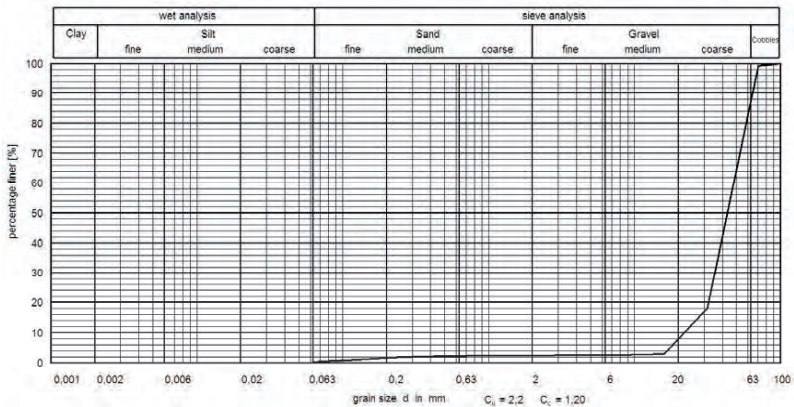


Figure 1. Grain size distribution of foam glass aggregate.

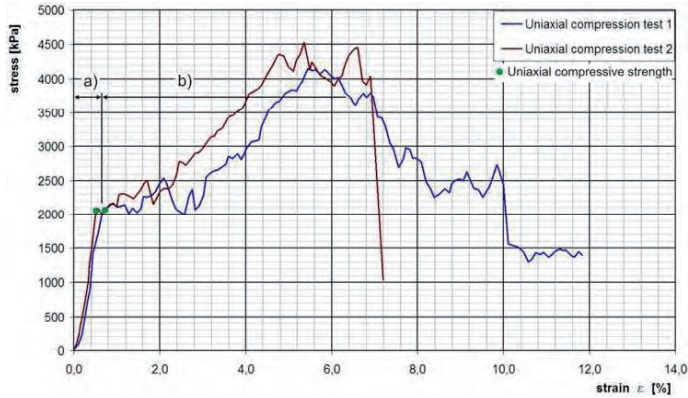


Figure 2. Load-deformation behavior of two foam glass prisms from uniaxial test: phase a) Linear elastic load deformation behavior, phase b) plastic load-deformation behavior.

### 3.1 Grain density $\rho_s$

The grain density was determined on foam glass prisms based on the particular measurements and weight of each sample and results in a range of 0,202 – 0,433 g/cm<sup>3</sup>.

### 3.2 Uniaxial compressive strength

The uniaxial compressions tests have been performed on foam glass prisms with a feed rate  $H/100$  per minute [mm/minute]. Figure 2 shows two typical load-deformation behaviors of foam glass prisms. In the first phase a) a linear elastic behavior of the sample-material can be observed. In this phase no crushing of the foam glass grains occurs. The uniaxial compression test shows a horizontal load level with plastic deformations in combination with stress-rearrangement next to the linear elastic phase. The foam glass sample material is obviously hardening in the plastic range b) up to the fracture. The uniaxial compressive strength is defined by the change of the linear elastic to the plastic behavior. Figure 3 shows the correlation between the grain density and the uniaxial compressive strength.

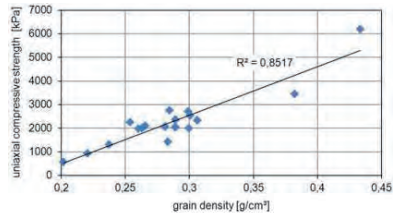


Figure 3. Correlation between grain density and uniaxial compressive strength.

## 4 EXPLORATION TO DETERMINE THE LOAD-DEFORMATION OF FOAM GLASS AGGREGATE

### 4.1 Large-scale compression tests

At the University of Innsbruck large-scale compression tests with samples in a test box measuring 3.80 m x 0.70 m and a depth of 0.60 m have been conducted to determine the load deformation behavior and ground failure mechanisms as well. The load is applied by a rectangular load plate.



Five types of foam glass aggregate from three manufacturers with varied degrees of compaction were tested.

The compaction process of the material in the test box is achieved with a vibration plate. The boundary conditions in the laboratory are more or less same as in field.

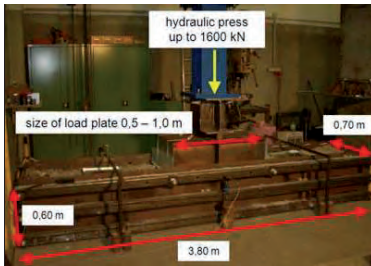


Figure 4. Test set-up of the large-scale compression test in the laboratory of the University of Innsbruck and the geometry of load plate and test box. [1]

The large-scale compression test is performed with a constant load increasing rate of 2 kN per second for initial loading as well as for reloading. The loading is done in cycles with a load increase of 100 kPa per step. In the first load cycle the foam glass aggregate sample is pressurized up to 100 kPa followed by a reloading with a minimum pressure of 10 kPa. The second load cycle has a defined maximum load of 200 kPa. The compression test is finished after eight load cycles respectively at a maximum load level of 800 kPa. One test takes about 20 minutes.

The strain of the foam glass aggregate body in transverse direction (cross to the length of the test box) is comparable to the strain of the samples of the confined compression test [chapter 4.2]. Due to the development of strains in longitudinal direction of the material in the test box the stiffness modulus cannot be derived directly.

The calculation of the stiffness modulus is based on the theory of elastic isotropic half space given in Formula (1).

$$E_s = \frac{2 \cdot b \cdot \Delta q}{\pi \cdot \Delta z} \cdot \frac{(1-\nu)^2}{(1-2 \cdot \nu)} \cdot \left[ 2 \ln \cot \frac{\beta}{2} - \frac{1}{1-\nu} \cdot \cos \beta \right] \quad (1)$$

- $E_s$  stiffness modulus [MPa]
- $2 \cdot b$  width of load plate [m]
- $\Delta q$  stress [MPa]
- $\Delta z$  settlements in vertical direction [m]
- $\nu$  Poisson ratio [-]
- $\beta$   $\arctan(b/z)$  [°]
- $z$  height of sample [m]

Actually the exact Poisson ratio of foam glass aggregate is unknown.

Figure 5 illustrates exemplarily the progress and the value of the stiffness modulus of foam glass aggregate samples at initial loading with different ratios of compaction between 10 % and 25 % of volume reduction with a chosen Poisson ratio of 0.46.

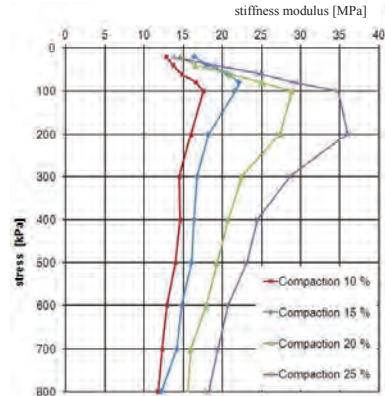


Figure 5. Exemplary depiction of the modulus of stiffness at initial loading with a Poisson ratio of 0.46.

The measurements of the load plate and the test box go conform with the grain size distribution of foam glass aggregate. The compaction in our experiment is selected to reproduce the compaction in field. Due to the high costs of the large-scale compression tests it is not possible to



perform long term tests. For the determination of time dependent load-deformation behavior compression tests in small scale are carried out.

#### 4.2 Confined compression tests

Confined compression tests in a large oedometer have been performed at Vienna University of Technology. The oedometer comprises a diameter of 250 mm. The compaction of the sample material is carried out with a proctor hammer. The loading procedure is done similar to the loading of the large-scale tests in the test box. Consequently, the comparability between the results of the large-scale tests and the confined tests is given. Figure 6 shows a comparison of the stiffness modulus with compacted foam glass aggregate samples examined in large-scale and confined compression tests (25% volume reduction by compaction).

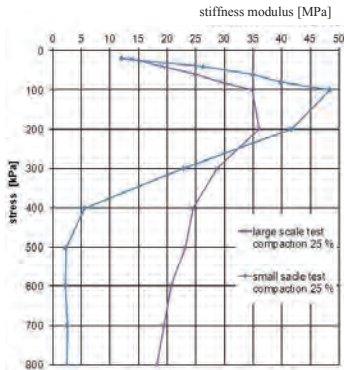


Figure 6. Comparison of the stiffness modulus between confined and large-scale compression tests with sample material with the same ratio of compaction.

The curves in Figure 6 show a similar trend of the progress of the stiffness modulus. Yet their levels are different. The distinct values of the modulus result from various test conditions, mainly from the different size of the oedometer (confined compression test) and the test box (large-scale compression test).

#### 4.2.1 Long-term confined compression tests

Long-term confined compression tests have been carried out over a period of three to five days per test run to evaluate the time-dependent settlement behavior of foam glass aggregate.

The tests are performed in the oedometer with a diameter of 250 mm in accordance with the confined compression tests [chapter 4.2].

Two initial test load applications are investigated:

- loading steps of 20 kPa from 2 kPa to 100 kPa
- loading steps of 100 kPa from 100 kPa to 800 kPa

Every load step is finished when the strain rate is smaller than 0.05% per hour.

The stiffness modulus and the creep value were determined at every load step.

In Figure 7 the results of long-term tests are illustrated by using foam glass aggregate samples with different uniaxial strength and different grain density as well as different porosity. The illustrated curves showing the development of the stiffness modulus were determined with foam glass aggregate compacted to a volume reduction of 25%.

The analysis of the long-term confined compression test results indicates that the maximum stiffness modulus is obtained between 30 MPa and 43 MPa and is nearly independent of the grain density. Material containing fine pores (violet curve) shows high stiffness at higher pressure loads and significant creeping occurs only at higher load steps as well.

A correlation between low creep values and high stiffness modulus is evident.

The extrapolation of the time dependent load-deformation behavior from the long-term confined compression test to the large-scale compression test is given by the comparison of the stiffness modulus between confined and large-scale compression tests [Figure 6]

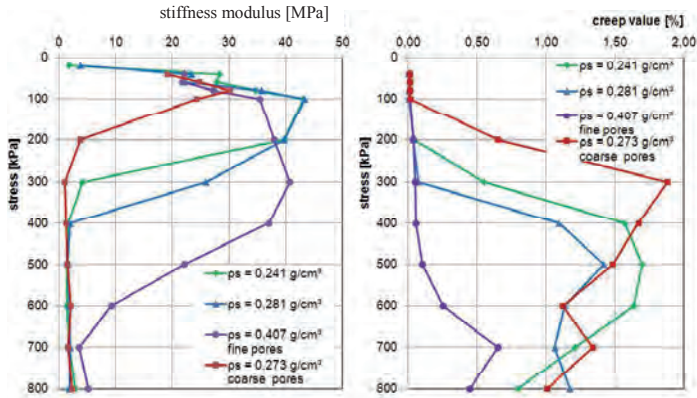


Figure 7. Stiffness modulus and creep value of foam glass aggregate samples as a result of long-term confined compression tests with different grain properties.



Figure 8. Two different types of foam glass aggregate prisms left fine pores, right coarse pores.

## 5 CONCLUSIONS

In the scope of a funded research project to determine the mechanical properties of foam glass aggregate, laboratory tests have been performed both with single grains and the aggregate. Uniaxial compression tests on single grains disclose a linear-elastic and a plastic range of the material behavior. The intersection of the linear-elastic to the plastic deformation in the stress-strain curve defines the uniaxial compressive strength, which correlates with the grain density.

For the investigation of the load-deformation behavior of foam glass aggregates under static loads different kinds of compression tests have been performed. As expected, the load defor-

mation behavior and stiffness modulus are similar.

Furthermore, the time-dependent deformations of the foam glass aggregates strongly depend on the applied load, the density of the material, the degree of compaction, and the porosity of the grains.

Finally, the tests showed that the stiffness modulus does not depend on the uniaxial compressive strength.

## ACKNOWLEDGEMENT

This research project is funded by the Federal Ministry for Transport, Innovation and Technology and is implemented as a part of the program "Haus der Zukunft plus".

The author would like to thank the whole project group for the close collaboration.

## REFERENCES

- [1] A. Andreatta, A. Steurer, J. Feix, D. Adam, Experimentelle Untersuchungen zur Tragfähigkeit von Glasschaumgranulat, *Schriftenreihe der Österreichischen Vereinigung für Beton- und Bautechnik Heft 70* (2011), 5–10.

# Geotechnical investigations and solutions for Tourist centre near the town of Nin

L. Zubcic <sup>1</sup>, M. Patrk <sup>2</sup>

*Geotehnicki studio d.o.o., Branch office Zadar*

## ABSTRACT

Complex geotechnical investigations were conducted as a part of design of future tourist centre near the town of Nin, Croatia. The centre consists of four groups of buildings spreading on the area of about 120 000 square meters. Future buildings are situated partly on a plateau and partly on the slope between plateau and the sea coast. The terrain is intersected with lots of prominences and depressions caused by erosive acting of streaming, seeping and ground water. Investigations were conducted in three phases. With the obtained data from the investigations a stratification of soil is defined as well as its physical-mechanical characteristics. After calculations of bearing capacity, settlement and slope stability had been conducted, solutions regarding foundation, ground water and slope stability were chosen. Solutions include lowering ground water level, founding parts of buildings on piles, protection of two excavation pits, filling of depression zones and building retaining walls at several positions.

Keywords: Geotechnical investigations, ground water, erosion, drainage, piles, excavation pit protection, fill, retaining walls

## 1 INTRODUCTION

The location of planned construction is characterised with specific morphology, hydrological and hydrogeological processes. It consists of a plateau about 15 meters above the sea level and slope between the plateau and the sea coast. Result of hydrogeological processes is vast amount of mud with medicinal characteristics that is found along the coast near the location and is one of the reasons the tourist centre is planned. Program of investigation works was based on geotechnical investigation regulations, technical data

regarding construction works and detailed preliminary terrain prospection.

## 2 INVESTIGATIONS

Investigations were carried out in three phases and consisted of field investigation works and laboratory tests. Field investigations included installation of permanent measuring equipment for monitoring of ground water level.

<sup>1</sup> MCE, Geotehnicki studio d.o.o. Branch office Zadar, N. Tesle 12b, Zadar, Croatia, geotehnicki.studio@zd.t-com.hr

<sup>2</sup> MCE, Geotehnicki studio d.o.o. Branch office Zadar, N. Tesle 12b, Zadar, Croatia, geotehnicki.studio@zd.t-com.hr

## 2.1 Field investigations

First phase of field investigations consisted of engineering geological and hydrogeological mapping of the location. Based on these investigations three engineering geological soil complexes were determined:

- quaternary sediments on the plateau,
- unstable slope between the plateau and the sea coast, formed by multiple collapsing of sediments down the slope and
- clayey alluvial sediments at the bottom of the slope.

Hydrogeological mapping indicated complex hydrogeological processes that triggered recent appearances in terrain morphology.



Picture 1. Example of erosive acting of water on the location



Picture 2. Example of suffosive acting of ground water on the location

In order to determine detailed characteristics of main soil complexes a program of investigations was assembled for second and third phase.

### 2.1.1 Geophysical investigations

Two profiles of geoelectric tomography were carried out. Depth of investigations was 30 m, and they determined the thickness and geophysical characteristics of primary quaternary sediments.

### 2.1.2 Geotechnical investigations – boring, dynamic probing and trial pits

Boring was carried out with continuous coring and standard dynamic penetration testing on 21 locations. During the boring representative undisturbed samples of soil were taken for laboratory determination of basic and physical-mechanical characteristics. Core was classified according to the AC classification method.

Dynamic probing was carried out by DPH method (Deep Probing Heavy) on 24 locations.

Le Franc soil permeability tests were carried out in the borings that were in areas of sandy/silty soil.

In all together 17 trial pits uniaxial compressive strength using pocket penetrometer and undrained shear strength using pocket vane were measured.

### 2.1.3 Permanent measuring equipment

Due to specificity of location regarding ground water and its influence on soil characteristics and slope stability, Casagrande piezometers were installed in seven boreholes in order to monitor ground water level. To obtain precise data on ground water level it was measured twice a month during one year's time.

There was no significant variance of ground water level during the monitoring.

## 2.2 Laboratory tests

Representative samples of soil were tested in a registered geotechnical laboratory according to Croatian norms. In order to determine basic characteristics of soil following tests were carried

ried out: unit weight determination, natural water content, Atterberg's plasticity limits and granulometric composition. In order to determine physical-mechanical characteristics of soil following tests were carried out: direct shear, determining residual parameters of strength and stiffness in oedometer, Proctor's test and CBR test.

### 3 GEOTECHNICAL SOIL MODEL

Based on all the obtained data from the investigations and laboratory tests, a geotechnical model consisting of five dominant layers was formed: Layer 1 – coarse granular sand uniformly to poorly granulated (SU/SP) – top layer in the plateau zone.

Layer 2 – smaller grain size sand uniformly to poorly granulated, often with silty particles (SU/SP/ML) – regularly bored below layer 1 – characterized by presence of ground water and significantly reduced stiffness.

Layer 3 – silts with interlayers of coarsely granulated sand, organic materials or gravelly and partly calcified interlayers (ML/SFc) – layer below layer 2 – characterised by fair stiffness.

Layer 4 – high plasticity clay (CH) – bottom layer at the most part of the location – characterised by good stiffness.

Layer 5 – limestone – bottom layer on a smaller part of the location – it has minor influence on future construction so its characteristics were irrelevant.

In the following table estimated characteristics of soil layers are presented:

Table 1. Physical-mechanical characteristics of soil layers

	Layer 1 (SU/SP)	Layer 2 (SU/SP/ML)
$\gamma$ (kN/m <sup>3</sup> )	19	19
$c$ (kN/m <sup>2</sup> )	0	0
$\phi$ (°)	30	28
$M_v$ (kN/m <sup>2</sup> )	7	2,5 – 3,5
	Layer 3 (ML/SFc)	Layer 4 (CH)
$\gamma$ (kN/m <sup>3</sup> )	18	18
$c$ (kN/m <sup>2</sup> )	10	20
$\phi$ (°)	22	17
$M_v$ (kN/m <sup>2</sup> )	9	13

## 4 CALCULATIONS

Using obtained data on soil and ground water, calculations of bearing capacity, settlements of soil and slope stability were carried out.

### 4.1 Bearing capacity and settlement

Bearing capacity calculations were carried out by soil failure criteria [1]. According to architectural design, foundation was planned to be built by strip foundations.

Input data for calculations were physical-mechanical characteristics of soil (see Table 1), foundation width ranging from 0,5 m to 1,0 m and foundation depth of 1,0 m.

Settlement calculations were carried out using computer program based on [2] and [3]. Results of the calculations are displayed in the following table:

Table 2. Results of bearing capacity and settlement calculations

Soil	Foundation width / depth (m)	Bearing capacity (kN/m <sup>2</sup> )	Settlement (cm)
Layer 1	0,5–1,0 / 1,0	192	2,1 – 3,3
Layer 2	0,5–1,0 / 1,0	163	2,4 – 3,5
Layer 2 (slope)	0,5–1,0 / 1,0	165	4,4 – 6,4
Layer 3	0,5–1,0 / 1,0	165	2,1 – 3,2
Layer 4	0,5–1,0 / 1,0	173	1,3 – 2,7

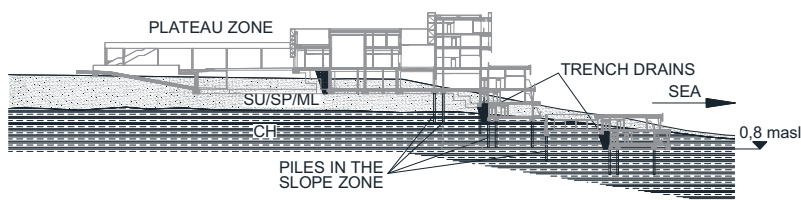
### 4.2 Slope stability

Slope stability calculations were carried out using computer program SLOPE/W (Calgary, Canada), based on Bishop, Janbu and Spencer methods. Purpose of the calculations was to estimate critical slip surfaces with associated safety factor, with various ground water levels and loads from future structures.

## 5 GEOTECHNICAL CONCLUSIONS AND SOLUTIONS

According to the results of investigations and calculations these conclusions were made:

- streaming, seeping and ground water acting decrease soil characteristics and slope stability,
  - settlements and differential settlements on the transition from the plateau to the coast are too large scale for proposed shallow strip foundations.
- With these conclusions and defined architectural features of future buildings the following geotechnical solutions were chosen:
- construction of drainage system in order to lower ground water level and thus ensure the stability of the slopes,
  - parts of buildings located on the transition from the plateau to the coast will be founded on bored reinforced concrete piles,
  - protection of two excavation pits that need to be carried out due to architectural solution of the building,
  - filling depression zones underneath future bottom levels of foundations,
  - construction of retaining walls at several positions.



Picture 3. Characteristic cross section through the main building showing soil layers, piles and trench drains

### 5.1 Drainage system

A system of trench drains was designed for lowering ground water level. Input data for designing of trench drains were:

- hydrological calculations,
- characteristics of ground surface (infiltration of precipitation),
- soil permeability estimated by field and laboratory tests,
- hydraulic calculations,
- experience.

Each of four groups of buildings has its own drainage system which surrounds the buildings from three sides and at some places intersects them. Total length of drainage system is 1860 m.

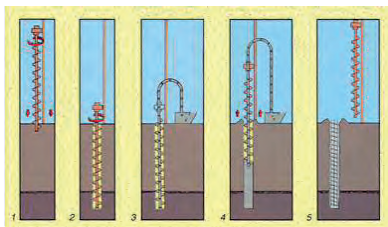
Direction of ground water flow is towards the sea coast. Water collected in trench drains flows into system of water absorption trench and absorption wells situated between the buildings and the sea coast.

### 5.2 Bored piles

Piles were designed to be positioned in the bottom layer of stiff high plasticity clay. Bearing capacity of the piles was calculated according to DIN 1054-2005 standards. Designed diameter of the piles is 40 cm and the length is 6 – 13 m depending on distance between the pile head and layer of high plasticity clay.

Due to large number of piles (901 pieces) and unstable boreholes in upper sandy layers, construction has to be relatively quick and the stability of the boreholes must not be an issue. Chosen method for pile construction is CFA (Continuous

Flight Auger). Stages of construction by this method are presented in the following picture:



Picture 4. CFA pile construction stages: 1,2 – augering; 3,4 – concrete casting and auger extraction; 5 – steel cage insertion

Three static pile load tests are included in the main design.

### 5.3 Protection of excavation pits

Architectural solution of centre's main building includes construction of two corridors that "slice" through the soil perpendicular to the slope. Construction of the corridors includes protection of excavation pits. Maximum depth of the pits is 13,0 m.

Protection construction consists of pile walls at the sides of the corridors secured by steel pipe struts. All 189 piles for pit protection are 40 cm in diameter and 9,5 – 16 m in length. Chosen method for their construction is CFA.

### 5.4 Fill and retaining walls

A lot of earthworks are included in future building. Before and during construction about 450 000 cubic meters of excavation should be carried out. At the location of centre's main building there's a large depression zone in the terrain. Designed foundation bottoms lie above the ground in the depression zone so the filling of about 7000 cubic meters is required. Most of the filling material will be sand from the excavation which will be built in in layers about 30 cm thick

with constant compaction.

Due to cascade forms of buildings and terrain configuration, a part of geotechnical works is also building of retaining walls at several positions, up to 9,2 m of height.

## 6 CONCLUSIONS

Large scale of planned building, as well as diversity of architectural forms required lots of geotechnical investigations and solutions. Specific morphological, geological and hydrogeological properties of the location made it a demanding task.

Main conclusion of the investigations was that streaming, seeping and ground water decreases soil characteristics and reduces the stability of the slope on which a part of the building was planned. To overcome these problems, a system of trench drains around future buildings was designed in order to eliminate negative influence of water on soil and foundations. Parts of buildings in the zones of soil with decreased characteristics will be founded on piles. A part of geotechnical design is filling of a depression zone.

Other solutions regard more the architectural design other than geotechnical specificities of the location and include protection of two excavation pits and building of several retaining walls.

## REFERENCES

- [1] Brinch Hansen (1970) with supplements by Meyerhof (1951), Vesic (1973) and Spangler and Handy (1982): Soil failure criteria
- [2] N. Janbu: "Settlement calculations based on the tangent modulus concept", Technical university of Norway, Trondheim (1967)
- [3] E. N. Fox: "The mean elastic settlement of a uniformly loaded area at a depth below the ground surface", Proceedings of the Second international conference on soil mechanics and foundation engineering, Rotterdam (1948).





# Important aspects in design of laminar soil container for 1-g shaking table tests

Julijana Cvetanovska<sup>1</sup>, Vlatko Sesov and Kemal Edip  
*Institute of earthquake engineering and engineering seismology-IZIIS,  
University Ss. Cyril and Methodius, Skopje, Macedonia*

## ABSTRACT

Earthquake geotechnical studies can involve different methodologies and approaches such as dynamic soil element tests, reduced scaled models, numerical and analytical models and full scaled field tests. If done properly, scaled model tests can be advantageous for seismic studies due to their ability to give more realistic information about ground acceleration amplification, change in pore pressures in the soil medium, nonlinear behavior of soil, occurrence of failure, and soil structure interaction phenomena. This paper describes the important aspects in design, fabrication and commissioning of a single axis laminar shear box for use in seismic geotechnical studies. A laminar box is a container which allows 'free' horizontal movement of soil model and it is placed on a shaking table platform to simulate wave propagation during earthquakes through a soil layer of finite thickness. The laminar box described in this paper is designed to be used for investigation of the liquefaction phenomena of saturated sand profile on the shaking table test in the Institute of Earthquake Engineering and Engineering Seismology – IZIIS, Skopje, Macedonia. The numerical analysis and preliminary calculations conducted to study the performance of the laminar box in order to fulfill the design criteria are also taken into consideration. Also, important aspects for the experimental setup of liquefaction studies, characterization of investigated sand, model preparation, and soil properties are explained.

Keywords: 1-G seismic shaking testing, laminar box, liquefaction

## 1 INTRODUCTION

Earthquake geotechnical studies can involve different methodologies and approaches such as dynamic soil element tests, reduced-scale model tests, numerical and analytical models and full-scale field tests. If done properly, scaled model tests can be advantageous for seismic studies because of their ability to give economic and realistic information about ground amplification,

change in pore water pressure, soil non-linearity, and occurrence of failure and soil structure interaction [1]. Model tests are essential when the prototype behaviour is complex and difficult to understand. In model testing, usually the boundary conditions of a prototype problem are reproduced in a small-scale model. Model tests are used to understand the effects of different parameters and the process leading to failure of prototype at a real time. The model tests can be

---

<sup>1</sup> IZIIS-Skopje, Salvadore Aljende 73, 1000 Skopje, Macedonia, jule@pluto.iziis.ukim.edu.mk

divided into two categories, namely, those performed under gravitational field (generally called shaking table tests) and those performed under higher gravitational field (centrifuge tests). Both shaking table and centrifuge model tests have certain advantages and limitations. Shaking table tests have the advantage of well controlled large amplitude, multi-axis input motions and easier experimental measurements and their use is justified if the purpose of the test is to validate the numerical model or to understand the basic failure mechanisms [2]. In the case of geotechnical structures, an additional issue is related to the presence of a container which will set the boundary conditions of the soil.

Lately, the rising of damages caused by earthquakes is increasing due to the population growth. That is the reason why the development of earthquake geotechnical engineering which include understanding ground behavior during shaking, effects of earthquake on geotechnical facilities, site amplification studies, liquefaction phenomena etc., have shown tremendous progress.

This paper describes the important aspects in the process of design and commissioning of laminar box for shaking table studies on liquefaction phenomena. The laminar box is designed and is planned to be set in the laboratory for dynamic testing of soils at the Institute for earthquake engineering and engineering seismology IZiIS in Skopje, Macedonia. The laminar box is planned to be used for experimental testing on fully saturated cohesionless soil in order to investigate the liquefaction phenomena and cyclic behavior of cohesionless soil in earthquake conditions.

## 2 1-G SHAKING TABLE TESTS

The fundamental problem with 1-g physical models of seismic behavior of structures is to provide the correspondence between the model and the prototype. A number of works have been carried out to understand the failure mechanism and behavior of earth structures using shaking table tests. Shaking table research has provided valuable insight into liquefaction, post-earthquake settlement, foundation response and

lateral earth pressure problems. For the models used in shaking tables, soil can be placed, compacted and instrumented relatively easily. Though higher gravitational stresses cannot be produced in a shaking table test, the contractive behaviour associated with high normal stresses at significant depths can be simulated by placing soil very loosely during model preparations.

In order to reproduce actual earthquake data, a six degree of freedom shaking table is essential. It is a very complex electro-hydraulic system which is very expensive and requires high maintenance and operational costs. However, when the response and failure mechanisms of earth structures like embankment, retaining wall, quay wall are of importance, single horizontal translational degree of freedom are sufficient. In the following paragraph the characteristics of the shaking table in IZiIS are described.

### 2.1 The shaking table in IZiIS

The shaking table in IZiIS is one of the first installed vibrations platform in Europe. One interesting fact that in its life time many structures have been investigated, yet no geotechnical structure with proper boundary conditions have been tested. The study presented in this paper is a part of a research proposal in order to investigate the liquefaction phenomena and cyclic behavior of cohesionless soil in laminar box described in this paper.



Figure 1. The shaking table in IZiIS

The shaking table (fig.1 and fig. 2) has the following characteristics:

- Size 5.0m x 5.0m

- Mass 330 kN
- Maximum model mass 400 kN with height of 6.0m
- Frequency range 0-80 Hz
- Maximum Acceleration horizontal 0.70g

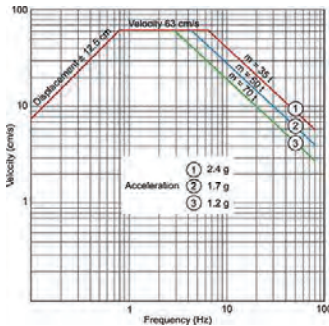


Figure 2. Dynamic characteristics of the shaking table in IZIIS

### 3 THE LAMINAR BOX

The geotechnical model cannot be directly mounted on shaking table due to the requirements of confinement. An ideal container should be large, flexible, massless and transparent. However, it is impossible to provide all the essential features. During the last decade many laminar boxes are being developed across the globe to suit field conditions better. Table 1 presents some of the existing laminar boxes around different research centers in the world.

In this paper the issues regarding the design of the laminar box in IZIIS are described as well some important aspects for the detailed experimental setup are mentioned.

The geometrical shape of the cross section may be square or circle. Due to symmetry, the circle cross section is more suitable. However, constructing a container having square cross section is easier from the manufacturing point of view. Effects of the corners on the measuring points

can be decreased by installing the measuring devices into center cross section of the container.

Table 1. Some laminar boxes designs (modified after Turan et al.(2009) [1])

Author	Dimensions (W x L x H) [mm <sup>3</sup> ]
Gibson	350x900x470
Prasad et al.	500x1000x1000
Meymand	2280x2130x2130
Ueng and Chang	1888x1888x1520
Van Laak et al.	254x457x254
Pamuk et al.	355x710x355
Shen et al.	584x500x500
Takanashi et al.	200x450x325
A.T. Carvalho et al.	750x2000x1750
Jafazaderh F.	1000x1000x1000
Wienbroer et al.	600x800x2100

#### 3.1 General pattern of the laminar box designed in IZIIS

According to the capacity of the shaking table, the models weighing up to 40 tons can be tested on the shaking table. Thus the square cross section with 2 x 1 m dimensions in plan and 1.5 m in height is defined.

For flexibility in the walls of the container a laminar system is applied, since in this system, the shear stiffness of the walls is limited to the friction between the layers and the influence of rubber membrane inside the box. So this kind, so called laminar shear box; at the time of liquefaction, has the least undesirable effect in the real behavior of the model [3].

#### 3.2 Design criteria of the container

The ideal container is one that gives a seismic response of the soil model identical to that obtained in the prototype, i.e. the semi-infinite soil layer 1D response under vertically propagating shear waves. The boundary conditions created by the model container walls have to be considered carefully, otherwise the field conditions cannot be simulated properly.

The presence of rigid and smooth end walls in the case of a ground model introduce three serious boundary effects compared with a semi-infinite soil layer in the prototype: deformation incompatibility, stress dissimilarity and input excitation pattern dissimilarity (Fig. 3).

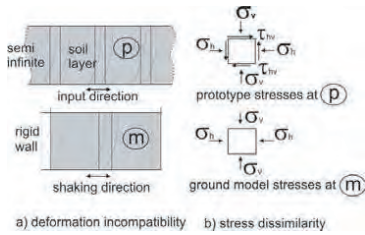


Figure 3. Effects of rigid boundary end walls (after A.T. Carvalho et al., 2010) [4].

The present laminar box is designed according the following criteria:

- Layers and the membrane inside should have minimum stiffness to horizontal shear.
- The laminar box should have mass much smaller than the soil material which is built inside it
- It retains water and air without leakage.
- It offers little resistance to vertical settlement of soil.
- Height of each layer is small which increased the flexibility for the deformation of soil inside.
- It is fairly large to better simulate field behaviour.
- It possesses capability to increase confining pressure.
- It maintains its horizontal cross section during shaking.
- It develops shear stress on the interface between soil and vertical wall equal to that on the horizontal plane.
- It provides good contact between the bearings and groove.
- It allows free movement of soil along the transverse cross section.
- It possesses provision for instrumentation.
- It is strong and stable against all the dynamic forces and moments.
- To provide stiff connection to the shaking table

### 3.3 Description of the components of the container

The 3 dimensional layout of the designed container is shown in Figure 4. The container consists of the following main components:

- Aluminum layers and ball bearings;
- Base plate with the saturation and drainage system in the floor;
- The upper and the side guides;
- Internal membrane used as a cut-off and keeping the moving bearings away from dust.

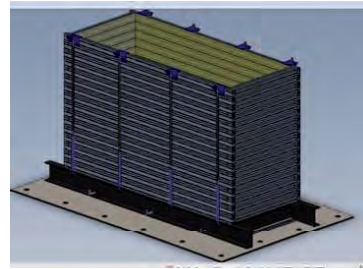


Figure 4. 3-d view of the laminar box designed in IZIIS

#### 3.3.1 The layers and the mechanism of motion

Each layer is a square ring which is composed of hollow aluminum profiles with  $40 \times 80 \text{ mm}^2$  section (Fig. 5). The whole system is composed of 12 layers-rings with height of 1.5 m. (Figure 7 and 8) In order to minimize the friction between the layers, transfer ball bearings have been used so that the two dimensional motion in the horizontal plane is possible. These balls are designed in a way that they can be simply as possible and without any additional devices to provide maximum sliding of rings with minimum friction. This makes the balls act as a column between the lower and upper hollow aluminum sections and prevents the surface from being deformed, by the point contact stress between the ball bearing and the surface of the aluminum profile. In order to make the distribution uniform, 12 rotating ball bearing are used in each layer and the gap between the 2 adjacent layers is 3 mm.



Figure 5. Perspective view of the laminar ring

### 3.3.2 Base plate and saturation and drainage systems

The lowest layer has been fixed on a steel base with  $2.1 \times 1.5 \times 0.01$  m in dimensions. In order to allow saturation of the soil model, the base has been designed with double bottom plates (one is perforated) and system of small pipes (Fig. 6). The bottom plate of the model is covered with porous stone. In this way, not only saturation and drainage of the samples is facilitated but this improves the contact between the soil and the steel plate of the container which makes better shear stress transition.

For hydraulic cut-off system and the protection of the ball bearings, the inside of the container is covered by a 2 mm thick rubber membrane.

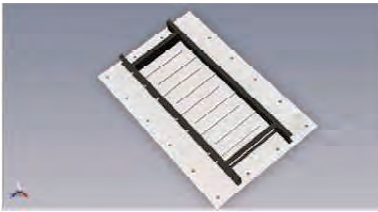


Figure 6. View of the base plate with the saturation system

### 3.3.3 The upper and side guides

In the four sides of the box 4 steel columns have been installed, so as to prevent the frames from the oversize deformations while conducting the test. Also, in order to prevent the layers from getting separated at the time of vibration, a horizontal steel cross has been installed above the col-

umns tangent to the ball bearings of the uppermost layer.



Figure 7. Cross section of the laminar box

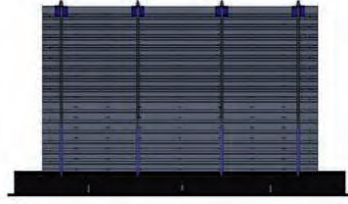


Figure 8. Longitudinal section of the laminar box

### 3.4 Calibration of the laminar box

Main factors which may influence the performance of a laminar box can be classified as follows:

- Inertia effect
- Friction effect
- Membrane effect
- Wall effect

These effects are planned to be investigated in this study performing static calibration tests as described in [2].

## 4 EXPERIMENTAL SETUP AND PLAN FOR LIQUEFACTION STUDIES

The designed laminar box is going to be used in order to investigate the liquefaction phenomena and cyclic response of cohesionless soils.

A number of works have been carried out to understand the failure mechanisms and behaviour of earth structures using shaking table tests. Various authors carried out shaking table tests in order to investigate the dynamic behavior of soils [2] [6]. The use of element tests, *in situ* soil investigation, case histories, including shaking table tests are essential to understand and develop the failure mechanism during liquefaction. For the research presented in this paper the following further activities are planned to be done:

- Characterization and definition for dynamic parameters of representative sand type by series of triaxial and simple shear tests
- Analysis of the similitude laws for scaling of the model for testing and the prototype [7]
- Design of sieve with the dimensions of the laminar box for installing the sand into the laminar box by method of raining
- Obtain the necessary measurement equipment for the acceleration, displacement and pore water pressure.
- Numerical analysis of the behavior of the empty box and verification by dynamic tests on the shaking table
- Simulation of the experimental setup with nonlinear material model and infinite boundary elements [5].

## 5 CONCLUSIONS AND RECOMMENDATIONS

Model testing under 1-G environment in earthquake geotechnical engineering has become an integral part of research. Detail design procedure and description of the components of the laminar shear container which will be installed in IZIIS have been presented in this paper. The laminar box is a part of investigation study on the liquefaction phenomena and cyclic behavior of cohesionless soil. The study is ongoing and further plans for the experimental setup are also described. Use of laminar box will improve the efficiency of testing and simulating the real ground conditions. Amplification, liquefaction and cyclic mobility phenomenon, excess pore

water pressure generation and dissipation rates can be performed using such facilities.

## ACKNOWLEDGEMENT

The research and the design is supported by the European FP7 Project UREDITEME REGPOT-2008-1 (Upgrading of research equipment for dynamic testing of large scale models), grant no. 230099.

## REFERENCES

- [1] Alper Turan, Sean D. Hinchberger, et al., Design and commissioning of a laminar soil container for use on small shaking tables, *Soil Dynamics and Earthquake Engineering* **29**: (2009) 404-414.
- [2] S. K. Prasad, I. Towhata, G. P. Chandradhara and P. Nanjundaswamy. Shaking table tests in earthquake geotechnical engineering. *Current science, special section: geotechnics and earthquake hazards* (2004) **87**(10)
- [3] Jafarzadeh, f. Design and evaluation concepts of laminar shear box for 1g shaking table tests. *13th world conference on earthquake engineering (2004) Paper No. 1391*. Vancouver, B.C., Canada.
- [4] A.T. Carvalho, J. Bilé Serra, et al. Design of experimental setup for 1 g seismic load tests on anchored retaining walls. *Physical Modelling in Geotechnics – Springman, Laue & Seward (eds) L.* © 2010 Taylor & Francis Group, ISBN 978-0-415-59288-8.
- [5] K. Edip, M. Garevski, et al. Numerical simulation of wave propagation in soil media. *21st European Young Geotechnical Engineers Conference Rotterdam, the Netherlands.(2011)*
- [6] V. Sesov. Dynamic behavior of potentially nonstable layers and application of a model for decreasing the seismic risk of liquefaction occurrence. PhD Thesis (2003). University Ss. Cyril and Methodius-Skopje, Macedonia
- [7] S. Iai. Similitude for shaking table tests on soil-structure-fluid model in 1g gravitational field. (1989) *Soils and Foundations* **29**(1): 105-118.

# Modelling of horizontal soil deformations

C.W.J. te Boekhorst<sup>1</sup>  
*Volker InfraDesign*

## ABSTRACT

In the daily geotechnical practice it still appears to be difficult to predict horizontal soil deformations with a satisfying degree of accuracy. Large deviations between predictions and measured values are possible. This can be problematic in the design of foundations where horizontal soil deformations are frequently a governing constraint. A plausible explanation why the conventional models perform poorly is that important soil properties such as consolidation, creep and anisotropy are often neglected. This paper elaborates on a number of soil models which do account for these important soil features. Two of the considered models are isotropic, which are the Modified Cam Clay (MCC) model and the Soft Soil Creep (SSC) model. The other models that have been analyzed with special interest are the S-Clay1 model and the Anisotropic Creep (AC) model. Both models use a rotational hardening rule to account for anisotropy. These models can be implemented as a user-defined model in the finite element program Plaxis. The performance of considered models is analyzed with the in-situ measurements of a road embankment constructed on a soft soil deposit. The results show that the predictions made with the anisotropic models nicely fit the in-situ measurements, while conventional isotropic models consistently overestimate the amount of horizontal soil deformation. As a result, a more reliable and economical design is possible when an anisotropic soil model is used.

Keywords: anisotropy, consolidation, constitutive behaviour, creep, deformation, embankment, numerical modelling, soft soils

## 1 INTRODUCTION

The predictability of horizontal soil deformations resulting from an embankment construction on normally consolidated and lightly overconsolidated soft soils is subject of discussion. Adjacent structures such as piled foundations, sewage pipes or electricity cables can be adversely affected by these horizontal soil movements.

The analytical models Loof and Van IJsseldijk are the traditional models for predicting horizontal soil deformations in the Netherlands, these models assume undrained linear elastic soil be-

haviour. Another model that is frequently used in the daily geotechnical practise is the model of Bourgens and Mieussens that is based on the empirical relations of Tavenas [1]. A popular soil model that is often used in Plaxis to simulate horizontal deformations is the Hardening Soil model. The cases in literature show that the relative error between measured and predicted horizontal soil deformation with these models generally varies between 50% and 100% even if the vertical deformations are matched [2,3].

The introduction of the Design & Construct contract and the shorter construction times calls

---

<sup>1</sup> C.W.J. (Coen) te Boekhorst, MSc. Volker InfraDesign bv, Korenmolenlaan 2 3447GG Woerden, The Netherlands, M +31 (0)6 5168 8002, E cteboekhorst@volkerinfraDesign.nl

for an update of the standard models for predicting horizontal deformations. The models that have been analyzed with special interest are the S-Clay1 model and the AC model. These models can be implemented as a user-defined model in Plaxis. Both models use a rotational hardening rule to account for anisotropy. It is important to emphasize that these anisotropic models only need two additional input parameters and do not require any non-standard laboratory testing.

In section 2 a brief description is given about the anisotropic models. The next section shows the comparison between the predictions of the models with the in-situ measurements of a road embankment in Uithoorn, the Netherlands. This road embankment is constructed on highly compressible layers of clay and peat. Finally, some conclusions are drawn.

## 2 ANISOTROPIC MODELS

### 2.1 S-Clay1 model

The S-Clay1 model is an extension of the conventional critical state model. This model is introduced by Wheeler and co-workers in 2003 [4]. The extension includes a rotational hardening rule that accounts for anisotropy in soft soils, which causes the yield contour to be sheared. Unlike many anisotropic elastoplastic models that are published previously, the suggested rotational hardening rule of this model includes dependence on the plastic volumetric strain increments as well as plastic shear strain increments. This is in contrast to many other anisotropic models, incorporating only plastic volumetric strain increments in the rotational hardening rule.

The rotational hardening rule of S-Clay1 has been validated by a number of case studies. Figure 1 shows the result of the simulated yield curve with the measured yield points for Bothkennar clay [4]. The figure shows that the yield points are nicely described by the simulated yield curve. However, the accuracy is highly dependent on the ratio  $q/p'$  [5]. If the ratio is high, indicating that the soil is close to the critical state line, the post-yield volumetric strains can be sig-

nificantly underestimated. It is believed that the underestimation of the plastic strains is the result of destructuration (i.e. change of soil structure).

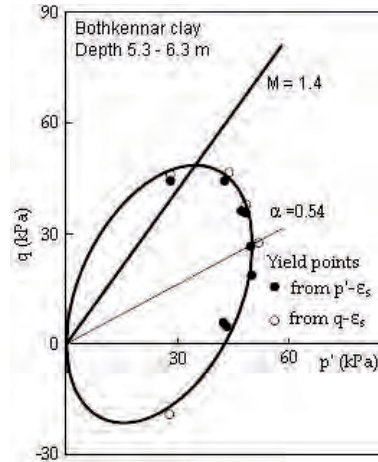


Figure 1. Initial yield curve for Bothkennar clay.

For lower  $q/p'$  ratios the post-yield strains are reasonably well predicted by the S-Clay1 model. This indicates that the effect of destructuration is most pronounced when the soil is close to failure. In addition, the amount of destructuration during shearing is also dependent on the sensitivity of the soil [6]. As a rule of thumb, if the sensitivity index  $S_i$  of a soil is smaller than 10 and if it is not close to critical state the destructuration can be ignored. In the Netherlands destructuration is mostly not relevant because Dutch soils have a small sensitivity and during construction of an embankment on a soft subsoil the soft soil layers are generally not subjected to loading conditions close to critical state ( $FoS > 1.1$ ).

The S-Clay1 model is a model that is developed for normally and lightly overconsolidated clays. It is kept as simple as possible. It considers only plastic anisotropy, because plastic deformations are likely to be dominating in normally and lightly overconsolidated clays. Also no attempt has been made to model non-linearity for small



strain stiffness. Again, this is in the interest of simplicity, and is justified by the fact that non-linearity is mainly important for heavily over-consolidated clays.

In comparison to the MCC model, S-Clay1 requires two additional parameters ( $\beta$  and  $\mu$ ) that are required to describe rotational hardening. The soil constant  $\beta$  controls the relative effectiveness of the plastic shear strains and plastic volumetric strains in rotating the yield curve. The value of parameter  $\beta$  can be estimated from the  $K_0$  condition. Formula 1 shows the analytical solution proposed by Wheeler [6].

$$\beta = \frac{3}{8} \cdot \frac{4M^2 - 4 \cdot (q_0/p_0)^2 - 3 \cdot (q_0/p_0)}{(q_0/p_0)^2 - M^2 + 2 \cdot (q_0/p_0)} \quad (1)$$

The model parameter  $\mu$  controls the rate at which  $\alpha$  progresses towards the critical state line. Unfortunately, there is no direct method at hand to determine the value of this parameter. The only solution is to perform model simulations with different values of  $\mu$ , and then compare these simulations with the observed behaviour to select the most appropriate  $\mu$  value. In practice this procedure is mostly not feasible. As a first indication it is sufficient to use a  $\mu$  value between  $10/\lambda$  to  $15/\lambda$  [7,8].

## 2.2 Anisotropic Creep model

The Anisotropic Creep (AC) model is an extension of the isotropic viscoplastic Soft Soil Creep model. This model is developed a few years ago by Leonie and co-workers [9,10]. It accounts for anisotropy during viscoplastic straining. To incorporate the anisotropy a rotational hardening rule has been used, which is nearly similar to the one implemented in the S-Clay1 model. This means that the predictions with the S-Clay1 model should be identical to the AC model at very small creep strain rates.

A visualization of the anisotropic creep ellipses is presented in figure 2 [9]. The biggest rotated ellipse defines the normal consolidation surface (NCS). The intersection of the vertical tangent to the ellipse with the  $p'$  axis is the isotropic effective preconsolidation pressure  $p'_{pc}$ . The other ellipse represents the current stress

surface (CSS), on this surface the actual effective stress  $\sigma'_{ij}$  can be found. The intersection of this ellipse with the horizontal axis is the equivalent mean stress  $p'_{eq}$ . When the sheared ellipses of the CSS and the NCS are overlapping the soil is in a normal consolidated state.

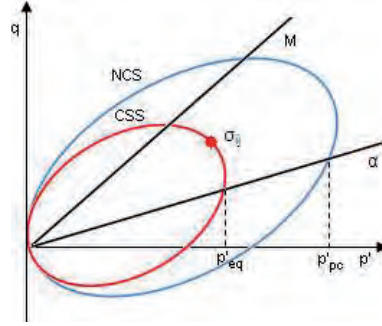


Figure 2. Anisotropic creep ellipses in  $p'$  and  $q$  space in tri-axial stress space.

The evolution of the shearing of the ellipse is governed by the rotational hardening. Formula 2 shows the rotational hardening rule that is incorporated in the AC model.

$$\partial\alpha = \omega \cdot \left[ \left( \frac{3q}{4p'} - \alpha \right) \cdot \partial\epsilon_r^c + \omega_d \cdot \left( \frac{q}{3p'} - \alpha \right) \cdot \partial\epsilon_v^c \right] \quad (2)$$

The soil constants  $\omega$  and  $\omega_d$  control the rotation rate of the ellipse. Both parameters are related to basic soil parameters, and do not require any calibration. The shear rotation parameter  $\omega_d$  is equivalent to the parameter  $\beta$  in S-Clay1 (see formula 1), whereas parameter  $\omega$  controls the absolute rate in which the NCS rotates with viscoplastic straining. Parameter  $\omega$  can be determined from formula 3 [10].

$$\omega = \frac{1}{\lambda^2} \cdot \ln \frac{10M^2 - 2\alpha_0\omega_d}{M^2 - 2\alpha_0\omega_d} \quad (3)$$

It is important to state that  $\omega$  is closely related to  $\mu$  in the S-Clay1 model, so their order of mag-

nitude should be about similar. If  $\omega$  is set to zero the NCS remains in its initial rotated state.

The AC model uses an extended version of the overstress theory of Perzyna [11]. According to the classical overstress theory the total strain rate is composed of an elastic and viscoplastic strain rate component. The main difference with the extended version is that creep strains can also develop in the initially overconsolidated state. This results in a smooth transition between the mainly elastic region and the viscoplastic region, which is more realistic for natural soils than an abrupt kink that is normally simulated with the classical overstress models.

### 3 N201 ROAD EMBANKMENT

The existing N201 road runs straight through Uithoorn, which is a small city 20 km south of Amsterdam. During rush hour this motorway is often heavily congested. Apart from the drivers who face daily delays, the traffic also causes a lot of hindrance to local residents. For this reason, a few years ago the province of Noord-Holland decided to construct a bypass around Uithoorn. The construction works for this new road started in the spring of 2011.

The road embankment for this bypass is built on a highly compressible soil deposit. From surface level it starts with a 3.5 m thick layer of fibrous peat (FP), which is underlain by an organic clay (OC) layer with a thickness of about 4.0 m. Beneath the organic clay layer there is a thin layer of amorphous peat (AP). The amorphous peat layer is overlying the Pleistocene sand. This dense sand deposit continues at least till 30 m below surface level. The water table is generally 0.5 m below the ground surface.

The considered embankment is built without vertical drainage, and constructed in subsequent stages of 1.0 m. The waiting period between the construction stages was about four weeks. The slope of the embankment was 2v:3h. To reduce the amount of settlement the subsoil under the embankment is improved by replacing the fibrous peat with sandy material.

During the construction of the embankment the settlements are recorded with a large number

of settlement plates. At locations where the embankment passes dwellings and greenhouses at close distances several inclinometers are installed to monitor the development of the horizontal soil deformations. The majority of these buildings are founded on slender prestressed concrete piles, which are known to be sensitive for horizontal movements in the subsoil.

At the considered cross section inclinometers are placed at the toe, 5 m outside the toe and 10 m outside the toe of the embankment. The applied inclinometers consist of steel profiles with a cross section of 45x45x2 mm and a length of 0.5 m which are stacked upon each other. The horizontal soil deformations have been measured every two weeks with MEMS (Micro-Electro-Mechanical System) inclinometer equipment. At the time of writing field data of almost a year is available for comparison.

The horizontal soil deformations are predicted with the finite element program Plaxis 2D version 2011. The soil models that have been used are MCC, SSC, S-Clay1 and AC. Table 1 shows the model parameters for the compressible soil layers. Note that for the sand layers a simple Mohr Coulomb model is applied.

Table 1. Model parameters for the compressible soil layers.

Parameter	Unit	FP	OC	AP
$\gamma_{sat}$	kN/m <sup>3</sup>	10.0	14.0	11.0
$\phi'_{cv}$	°	31.0	24.0	28.0
$c'$	kN/m <sup>2</sup>	1.0	1.0	1.0
POP	kN/m <sup>2</sup>	10.0	15.0	25.0
$k_v$	m/s	1.2 E-08	5.8 E-09	8.6 E-09
$K_0^{NC}$	-	0.48	0.59	0.53
$\lambda$	-	1.17	0.39	0.61
$\kappa$	-	0.29	0.16	0.15
$\lambda^*$	-	0.20	0.13	0.15
$\kappa^*$	-	0.05	0.05	0.04
$\mu^*$	-	0.02	0.01	0.01
$\mu$ (or $\omega$ )	-	10.7	32.1	20.5
$\beta$ (or $\omega_b$ )	-	1.2	0.8	1.0

The critical state value of the effective friction angle  $\phi'_{cv}$  and the effective cohesion  $c'$  are both estimated from single stage CU triaxial tests. It is important to stress that  $\phi'_{cv}$  is determined at 5% strain to prevent an overestimation of  $K_0^{NC}$ . The measured  $c'$  values at this strain level were prac-

tically zero, however to avoid numerical issues in Plaxis a practical value of  $1.0 \text{ kN/m}^2$  has been adopted. The  $K_0^{NC}$  value is based on Jaky's formula  $(1 - \sin \phi'_{cv})$ . The measured  $\phi'_{cv}$  values are significantly higher in peat, and consequently this results in lower  $K_0^{NC}$  values. Note that this difference can be mainly attributed to fibre structure of peat. The stiffness parameters and POP values are determined from standard oedometer tests. Note that the rotational hardening parameter  $\mu$  is estimated from the empirical correlation  $12.5/\lambda$  and  $\beta$  is derived from formula 1.

Table 2 presents the predicted and measured maximum horizontal soil deformation directly after the first construction stage at the toe ( $x=0$ ), 5 m outside the toe ( $x=5$ ) and 10 m outside the toe ( $x=10$ ) of the embankment. It also presents the settlement at the centre of the embankment.

Table 2. Maximum horizontal soil deformation at different sections directly after 1<sup>st</sup> construction stage (unit = m).

Model	$u_{h,max}$ $x=0$	$u_{h,max}$ $x=5$	$u_{h,max}$ $x=10$	$u_y$ centre
MCC	0.15	0.10	0.07	0.16
SSC	0.14	0.08	0.06	0.18
S-Clay1	0.10	0.05	0.03	0.21
AC	0.13	0.08	0.05	0.23
In-situ	0.11	0.06	0.03	0.20

From this table it becomes clear that the magnitude of the horizontal soil deformation sharply decreases with distance outside the toe. It also shows that the relative differences between the models are significant. However, the difference between the elastoplastic and viscoplastic models is small, which can be explained due to the fact that creep is not dominant at the beginning of the construction process. From table 2 it appears that the incorporation of plastic anisotropy increases the predicted settlement.

In figures 3 and 4 the predicted and measured horizontal deformation profiles are presented at the toe and 10 m outside the toe of the embankment for 225 days after the 2<sup>nd</sup> construction stage. The maximum horizontal deformation at the toe is found at NAP -5 m, while 10 m outside the toe of the embankment the maximum horizontal deformation is found at surface level. This is predominantly the result of the different stress

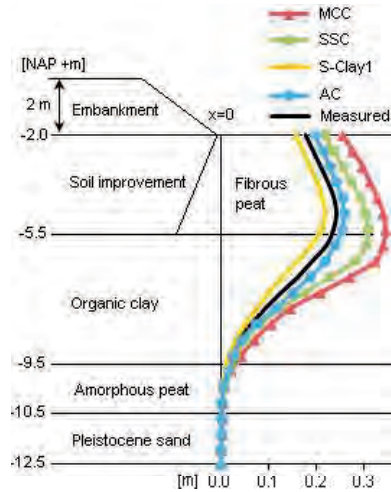


Figure 3. Horizontal deformation profiles at the toe of the embankment – 225 days after 2<sup>nd</sup> construction stage.

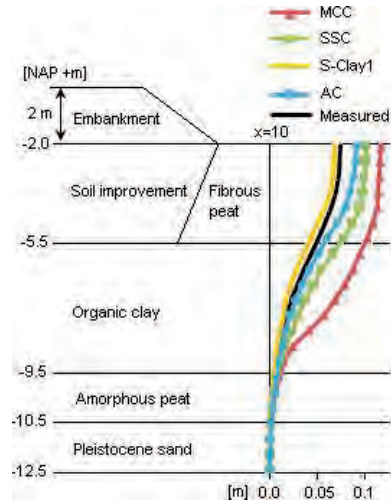


Figure 4. Horizontal deformation profiles 10 m outside toe of the embankment – 225 days after 2<sup>nd</sup> construction stage.

conditions under the embankment. Under the toe the stress condition is similar to a direct shear test, while the stress condition 10 m outside the toe is more like a triaxial extension test.

The horizontal soil deformations are significantly overestimated with the MCC model. This is mainly the result of the associative flow rule in combination with an isotropic yield contour. The back-calculated  $K_0^{NC}$  values in Plaxis are considerably larger than the ones presented in table 1. Similar findings are reported for an embankment on Boston blue clay [12,13].

The  $K_0^{NC}$  value is an input parameter in the SSC model. This parameter has a direct relation with the slope of the critical state line M. Figures 3 and 4 show that this alternative definition of M leads to a smaller amount of horizontal deformation compared to the MCC model. Note that due to the absence of vertical drainage the creep strains are not dominant 225 days after construction. However, 10.000 days after construction the SSC model predicts more horizontal deformation at the toe (0.43m) than the MCC model (0.38m).

The S-Clay1 and AC model result in good matches with the measurements. This indicates that anisotropy plays at least an important role during the early stage of consolidation. In this case the permeability of the soft soil layers is very low and no drainage has been installed, it could take years before a creep model yield better results. At the time of writing the long-term deformations could not be validated.

## CONCLUSIONS

After a description of the S-Clay1 and AC model the field data of an embankment constructed on a soft soil deposit is used to assess performance of four soil models in Plaxis 2D. The results show that isotropic models consistently overestimate the horizontal soil deformation. The anisotropic models produce much better fits at the cost of just two extra input parameters. It is therefore worthwhile to use an anisotropic model because the prediction is lower and closer to reality. As a result a more reliable and economical design is possible when an anisotropic model is used.

## ACKNOWLEDGEMENTS

The author is grateful to the Combinatie Amstelhoeck for offering me the possibility to investigate the field data of the N201 road project. I also would like to thank the reviewers René Thijssen of Volker InfraDesign and François Mathijssen of Royal Boskalis Westminster for their constructive comments.

## REFERENCES

- [1] F. Tavenas et al., Lateral displacements in clay foundations under embankments, *Canadian Geotechnical Journal* **16** (1979), 532-550.
- [2] P.H. Mestak, Momis: a database for the numerical modelling of embankments on soft soils and the comparison between computational results and in situ measurements, *Bulletin des Laboratoires des Ponts et Chaussées* **232** (2001), 45-59.
- [3] C.W.J. te Boekhorst, Modelling horizontal soil deformations – validation of the state of the art models with in-situ measurements, MSc thesis, Delft University of Technology, 2010.
- [4] S.J. Wheeler et al., An anisotropic elastoplastic model for soft clays, *Canadian Geotechnical Journal* **40** (2003), 403-418.
- [5] H. Krenn et al., Influence of anisotropy and destructuration on an embankment on soft clay, Proceedings of the International Workshop on Geotechnics of Soft Soils, Noordwijkerhout, 2003.
- [6] M. Karstunen and M. Koskinen, Anisotropy and destructuration of Murro clay, In Advances in Geotechnical Engineering: The Skempton Memorial Conference, London, 2004.
- [7] R. Zentar et al., Comparison of two approaches for modelling anisotropy of soft clays, Proceedings of the 8<sup>th</sup> NUMOG, Rome, 2002.
- [8] M. Karstunen and M. Koskinen, Plastic anisotropy of soft reconstituted clays, *Canadian Geotechnical Journal* **45** (2008), 314-328.
- [9] M. Leonie et al., Anisotropic creep model for soft soils, *Géotechnique* **15** (2008), 215-226.
- [10] M. Leonie et al., Validation of anisotropic creep model for soft soils, *Geotechnics of Soft Soils*, Taylor and Francis Group, London, 2009.
- [11] P. Perzyna, The constitutive equations for rate sensitive plastic materials, *Quarterly of Applied Mechanics* **20** (1963), 321-332.
- [12] H.P. Neher et al., An evaluation of soft soil models based on trial embankments, University of Stuttgart, Stuttgart, 2001.
- [13] Ladd, C.C. et al., Stress-deformation behaviour of an embankment on Boston blue clay, ASCE Geotechnical Special Publication No. 40 (1994), 1730-1759.

# Effects of loading rate and saturating fluid on chalk mechanical behavior

Ø. Johnsen\*, F. Cuisiat, and L. Grande  
*Norwegian Geotechnical Institute, Oslo, Norway*

## ABSTRACT

The mechanical response of reservoir chalk subjected to distinct pore fluid type and saturation and varied loading rate under hydrostatic and uni-axial ( $K_0$ ) conditions was studied in the laboratory. High pressure triaxial loading cells developed at the Norwegian Geotechnical Institute were used to reproduce in situ conditions and enable precise and independent control of pore pressure and external load exerted radially and axially onto the sample. Brine saturated and partially gas saturated chalk samples were tested under hydrostatic and uniaxial ( $K_0$ ) conditions to investigate the onset of yield (pore collapse) and the time dependent behavior of chalk at various loading rates, from usual laboratory conditions to loading rates 100 times slower (0.01 MPa/hour). In this context, chalk demonstrates a complex behavior, strongly dependent on porosity, the type of pore fluid and the degree of saturation, as well as the applied loading rate. The results confirm the well known rate dependent (isochat) behavior of chalk within the strain rates investigated. The experiments provide valuable data as a basis to the development and validation of constitutive models to predict the behavior of hydrocarbon reservoirs in chalk formation under representative in situ conditions.

Keywords: Geomechanics, chalk, experiment, tri-ax, load rate, fluid saturation, porosity, modeling

## 1. INTRODUCTION

Many oil and gas fields in the North Sea are found in very porous overpressured chalk formations which compact significantly during the lifetime of the field. Reservoir compaction, leading to sea bed settlement (subsidence) results in reduced air gap for the platforms, as experienced at Valhall or Ekofisk, and well casing failures [1]. Compaction, on the other hand, contributes significantly to the recovery mechanism, up to 50-60 % for Valhall in some areas of the field [2]. Reservoir compaction is not solely the result of the changes in effective stresses, but also due to water weakening of the chalk during massive seawater injection. The underlying mechanisms behind water weakening are not fully understood, but are well studied in the literature. Several factors have been proposed such as suction

or capillary effects [3], dissolution, precipitation, or chemical ionic substitution at the chalk surface [4]-[6].

Field observations and laboratory experiments have shown that the behavior of reservoir chalk is also time-dependent, exhibiting pronounced creep deformations under constant load at high stresses, or strain rate dependent elastic limit [7]. Models for the time dependent behavior of chalk are proposed by [8],[9]. Since laboratory experiments are carried out at load or strain rates much faster than experienced in the field, procedures have been developed to extrapolate the observed laboratory behavior to field depletion rate. Using a rate-type compaction model proposed by de Waal [8], Andersen et al. [9] suggested a procedure to predict compaction curves at the field depletion rate. The extrapolation assumes nevertheless that the same rate dependency is valid in the range of strain rates of practical interest (i.e. from laboratory rates to field rates), which can be

\* oistein.johnsen@ngi.no

debated. Omdal et al. [10] for instance, did not observe significant difference in chalk behavior during pore pressure depletion tests under uniaxial strain conditions with very low rates (0.02 - 0.0007 MPa/min).

In this paper, we report on a series of laboratory experiments to characterize the time-dependent behavior of a reservoir chalk. Due to strict constraints on the maximum subsidence that could be tolerated during field exploitation, an experimental program was started to estimate reservoir compaction and associated subsidence due to gas production, as well as after production stopped. Unfortunately, the experimental program was limited by the amount, quality, and lack of orientation of reservoir cores available for testing. Thus, data from open literature was used as far as possible to supplement the study. The experimental program was defined around three main controlling factors: chalk porosity, nature of saturating fluid, and load rate

## 2. TEST BACKGROUND AND PROTOCOL

### 2.1. Reservoir conditions

Table 1: Initial stress conditions for laboratory experiments.

Stress / Pore pressure	Value (MPa)
Total vertical stress $\sigma_V$	22.5
Initial total horizontal stress $\sigma_H$	18.0
Initial octahedral stress $\sigma_{oct}$	19.5
Initial Reservoir Pressure $P_o$	13.5
Initial effective vertical stress $\sigma'_V$	9.0
Initial eff. horizontal stress $\sigma'_H$	4.5
Initial eff. octahedral stress $\sigma'_{oct}$	6.0

Table 2: Brine composition.

Salt	Concentration (g/l)
NaCl	58
KCl	-
CaCl <sub>2</sub> , 6 H <sub>2</sub> O	55.6
MgCl <sub>2</sub> , 6 H <sub>2</sub> O	8.5

The total vertical stress is the maximum principal stress, and equals the weight of the overburden. The horizontal stress is unknown. Previous testing assumed a ratio between total horizontal and

vertical stresses  $K$  of 0.8. The initial stress conditions are given in Table 1 and reservoir brine composition is tabulated in Table 2. The formation is ~30% brine saturated.

### 2.2. Sample selection and preparation

10 samples were selected from 1134m to 1309m depth originating from the same field in (Upper Cretaceous), but two different wells. One of the wells has a deviation of 27° from vertical direction, and since the plugs were drilled out parallel (vertical plugs) or normal (horizontal plugs) to the core axis, the plugs were not fully representative of the in-situ vertical and horizontal direction. The porosity of the readymade core plugs could be separated into three porosity classes (~31%, ~34%, and ~36-37%). Final selection was made upon a criterion of maximum uniformity, i.e. absence of intrusions and no visible fissures, based on CT scan imagery.

The selected samples were dried at 60°C over two days to minimize the water content before weighing in. It is crucial for the planned testing that the applied heat during drying does not exceed 70°C. This is due to the fact that chalk (calcite and carbonate minerals) is susceptible to micro-fracturing at higher temperatures.

Edges were trimmed to remove flaws. The test specimens were sprayed with a latex resin to produce an impermeable rubber membrane around the specimen to ensure isolation of the pore fluid from the confining cell fluid during testing. Pins for mounting deformation sensors were glued onto the specimen. All the test specimens were mounted with metal filter disks at top and bottom.

### 2.3. Partial saturation

The chalk water weakening effect is a well known phenomenon both for oil-water [11]-[13]. Gas-water experiments, although not as numerous, indicate a similar response as for the oil-water system: a radical increase of (plastic) deformation by pore collapse up to 15% water saturation, and only small mechanical weakening is observed beyond 15%. Since the *in situ* water

saturation is documented of minimum 30%, a full water weakening effect is assumed to be promoted, suggesting little difference in mechanical response beyond the critical saturation threshold, 100% saturation.

In the lack of a defined saturation threshold for the gas-water system it has great value to assess possible implications of this assumption, by performing laboratory tests at 100% and 30% water/brine saturation, where 30% is representative of reservoir conditions.

We apply a dilution/evaporation technique [14] to achieve and mimic the ~30% reservoir saturation: The plug was dried completely at 60°C over two days, before it was gradually immersed and flooded along its axial direction in a vacuum chamber. When fully immersed it was left to soak for approximately 2 hours. Then the specimen was put to evaporate inside a closed and controlled environment cabinet, i.e. the humidity was kept at constant 60%, until it reached target weight. At this point the brine concentration matched the prescribed one in Table 2.

The validity of the method was cross checked by using a micro-focus industrial CT-scanner. For each degree of saturation; dry, fully saturated, and partial saturation a scan was performed giving a complete 3D grey level representation of the solid matrix and the pore content proportional with the density. The axial profile shows uniform distribution along the sample. No attempts have been made to similarly quantify saturation laterally.

#### 2.4. Experimental setup

The NGI experimental triaxial apparatus setup and procedures are thoroughly presented in detail in by Berre [15].

#### 2.5. Test protocol

Uniaxial strain condition with pore pressure decrease is usually representative as an analogue for reservoir and deformation associated with field production by depletion, given boundary conditions of a small horizontal to lateral extension ratio. The formation is roughly 4-5km in di-

ameter and limited to a thickness of 40-50 m, including the gas, transition, and water zones. A uniaxial laboratory model would then hold for most of the reservoir, except close to the reservoir boundaries, given that the test specimens are oriented with bedding perpendicular to principal load axis (i.e. drilled vertically).

However, testing procedures were limited by the accessible chalk samples and their properties, i.e. number of samples, their drilled direction (axis near parallel or vertical with respect to bedding), and their physical dimensions. Uniaxial depletion testing (CAUST) [15] was performed with the accessible vertical plugs, while in the case of horizontally drilled plugs, an isotropic testing procedure is more meaningful in terms of studying fluid and load rate effects on the mechanical behavior and elastic-plastic transition.

Four samples were tested specifically with the combined effect of strain rate and saturating fluid in mind. One convenient approach to assess the rate effects and associated material compaction rate and stiffness is to sequentially vary the applied loading rate [16], [17]. The following typical protocol for isotropic compression tests is established (see examples in Figure 1):

- (i) The sample was built into the triaxial cell and saturated with the specified brine solution at low effective hydrostatic stress of 0.5 MPa.
- (ii) Pore pressure and cell pressure was increased to *in situ* stresses at a normal load rate = 1MPa/hour.
- (iii) Further increased cell pressure using 1MPa/h while maintaining constant pore pressure, close to but below the estimated and expected pore collapse, then adjusted load rate to 0.01 MPa/h. Load at a low load rate of 0.01 MPa/hour beyond pore collapse, until steady state was accomplished. Steady state is defined as when the strain grows linearly with respect to the applied mean stress, i.e. opposed to phases when the strain rate accelerates during pore collapse.
- (iv) Sequentially vary the loading rate (0.01, 0.1, 1 and 10 MPa/h were used). Creep (0 MPa/h) was also added for few of the tests.



### 3. RESULTS AND DISCUSSION

#### 3.1. Load rate dependency

Consulting the literature the onset of pore collapse was estimated based on porosity and rate prior to start of test sequence, and the first rate alternation between elastic load phases was dictated by this value.

See Figure 1 for an overview of load phases and rates. The onset of plastic regime is identified as departure from the preceding linear elastic behavior, which at 0.01 MPa/h load rate is approximately (a)  $P_c \approx 16$  MPa (b)  $P_c \approx 15$  MPa.

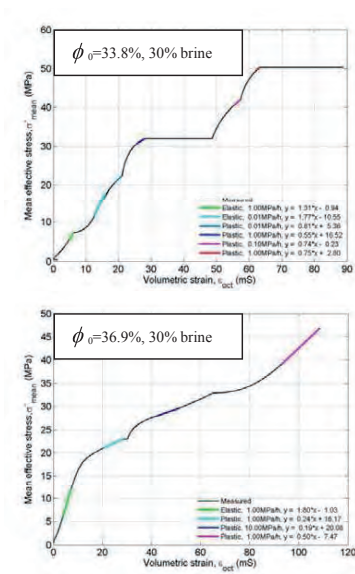


Figure 1. Stress-strain diagram for test two tests covering load rates from 0 MPa/h (creep phase) to 10 MPa/h for fully and partially saturated samples.

Establishment of steady state was allowed for before changing load rate. In the plastic regime the load rate was alternated as specified in Figure

1. From these load phases one may assess the rate dependent material stiffness by considering the slope  $\sigma'_{mean}/\epsilon_{oct}$ . The slope is found by linear fit of a given stress segment and given in the respective figures. The stiffness depends on the stress level and amount of plastic hardening.

Experiments show the plastic region at 0.01 MPa/h exhibit a stiffer behavior than loading than both 0.1MPa/h and 1.0 MPa/h, through direct comparison of slopes. At 0.1MPa/h and 1.0 MPa/h the behavior the stiffness compares while 10% shows a relatively softer behavior. Difference in stiffness for the plastic domain is inversely proportional to loading rate.

A creep period was included preceding the 1 MPa/h plastic regime in (a). Resuming loading after this period of creep deformation demonstrates strain hardening, i.e. by comparing slopes at same rates before and after (slope 0.55 and 0.75 respectively). Load phases also indicate presence of strain hardening following an S-curve as demonstrated in Figure 2.

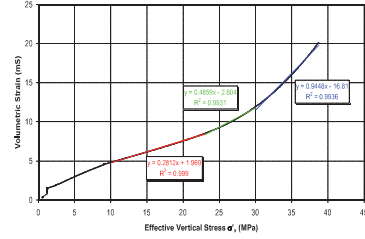


Figure 2. Volumetric strain versus effective vertical stress during testing on brine saturated 31% porosity chalk . Three distinguishable regimes, characterized by different stiffness behaviour, are highlighted: Elastic (red), plastic post pore collapse (~23 MPa), and stiffer plastic behaviour due to strain hardening (blue).

The load rate dependency is estimated using the RTCM model [8] linking pressure points on the curve ( $p_1$  and  $p_2$ ) and the associated load rates ( $\dot{p}_1$  and  $\dot{p}_2$ ) through the exponent

$$b = \ln\left(\frac{P_2}{P_1}\right) / \ln\left(\frac{\dot{P}_2}{\dot{P}_1}\right) \quad (1)$$



An average value of 0.055 agrees with the open literature [2], [8], [16]. The  $b$ -parameter allows for extrapolating laboratory yield stresses and incurred deformation to field through relevant load rates, i.e. for known depletion rates.

### 3.2. Elastic-plastic transition

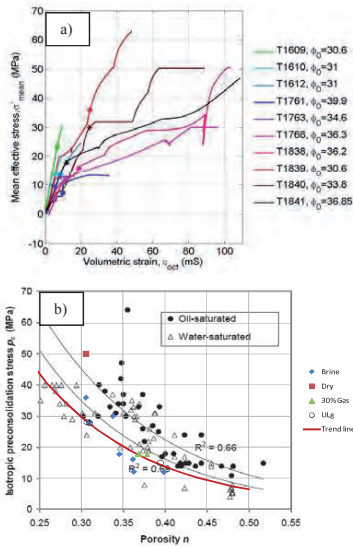


Figure 3. Pore collapse for an assembly of isotropic and  $K_0$  tests at equivalent load rate of 1 MPa/h load rate (a) compared with literature on oil-saturated and water-saturated (b) [11],[16]. Trend line of our experiments (in red).

The transition from elastic to plastic behavior occurs to a large extent by collapse of the porous structures within the chalk when exceeding a given stress level defined by the porosity dependent yield envelope following the cam clay model. This stress level is lower the higher the porosity. The onset of plastic yield by pore collapse is inversely related to the chalk porosity – increasing porosity effectively shifts the failure envelope to lower stress levels [16].

It is also governed by the interstitial fluid, i.e. the skeleton is significantly weakened by introduction of water [11],[18]-[20].

Elastic-plastic transition or pore collapse onset,  $p_c$ , identified at different load rates are translated to a common 1 MPa/h reference and compared with the open literature in Figure 3 with agreeable precision with the yield pressure trend line

$$p_c = 346.5 e^{-7.7 n} \quad (2)$$

### 3.3. Time dependent deformation

Under constant isotropic loading, the RTCM model [8] gives the following creep strains and rates as function of time as:

$$\epsilon_v^t = C_c \ln \left[ 1 + \frac{t}{\tau} \right] \rightarrow \dot{\epsilon}_v^t = \frac{C_c}{t + \tau} \quad (3)$$

$C_c = bc_{b,0} p$  and  $\tau = bc_{b,0} p / \dot{\epsilon}_{v0}$ , where  $\dot{\epsilon}_{v0}$  being the volumetric strain rate at the start of creep loading at time  $t=0$ ,  $p$  isotropic pressure,  $b$  friction parameter relating strain/stress rates, and  $c_{b,0}$  bulk compressibility at creep onset.

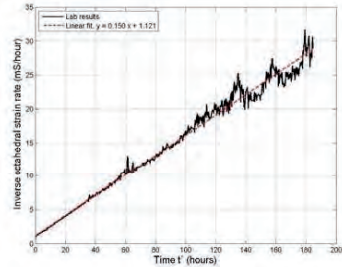


Figure 4. Example of time dependent deformation visualized as the inverse octahedral strain rate vs time  $t'$  during creep phase. The  $b$ -parameter is inferred from the slope  $1/C_c$  and the offset  $\tau/C_c$ .

The  $b$ -parameter is directly inferred by curve fitting, exemplified in Figure 4 giving the slope  $1/C_c$  and the offset  $\tau/C_c$ . Given the stress level used for the creep phase and the bulk compressibility prior to creep, one can back calculate  $b$

from  $C_c$ . The typical  $b$  parameter obtained ranges from 0.4 to 0.65 and are in fair agreement with the estimations based on the load phases and compares well with chalk literature [8], [16].

#### 4. CONCLUSIONS

The mechanical response of reservoir chalk subjected to distinct pore fluid type and saturation and varied loading rate under hydrostatic and uni-axial compaction was studied using high pressure triaxial loading cells to reproduce in situ stresses. Onset of plastic yield and time dependent behavior proves sensitive to a complex set of control parameters; porosity, load rate, type of pore fluid, and saturation. The results are compared with, and agree well with the trend lines drawn from the open literature.

#### REFERENCES

- [1] N.B. Nagel, Compaction and subsidence issues within the petroleum industry: from Wilmington to Ekofisk and Beyond, *Phys. Chem. Earth (A)*, Vol. 26, No 1-2, pp. 3-14, 2001
- [2] T.G. Kristiansen, B. Plischke, History matched full field geomechanics model of the Valhall Field including water weakening and re-pressurisation. SPE Europec/EAGE Annual Conference and Exhibition held in Barcelona, Spain, 14-17 June 2010.
- [3] V. De Gennaro and J.M. Pereira. Viscoplastic modeling of unsaturated geomaterials. In Proc. 12<sup>th</sup> International Conference of International Association for Computer Methods and Advances in Geomechanics (IACMAG), Goa, India, 2232-2241, 2008.
- [4] R. Hellmann, P.J.N. Renders, J.P. Gratier, and R. Guiguet, Experimental pressure solution compaction of chalk in aqueous solutions Part I. Deformation behavior and chemistry. In *Water-Rock Interactions, Ore Deposits, and Environmental Geochemistry, A Tribute to David A. Crerar*, eds. R. Hellmann and S.A. Wood, The Geochemical Society, Special publication No. 7, 129–152, 2002.
- [5] T. Heggheim, M.V. Madland, R. Risnes, and T. Austad, A chemical induced enhanced weakening of chalk by seawater. *Journal of Petroleum Science and Engineering*, 46 (3):171–184, 2005.
- [6] R.I. Korsnes, M.V. Madland, and T. Austad, Impact of brine composition on the mechanical strength of chalk at high temperature. In *Eurock, Proceedings of the International Symposium of the International Society for Rock Mechanics*, 133–140. Taylor & Francis/Balkema, Belgium, 2006
- [7] G. Priol, V.D. Gennaro, P. Delage, and T. Servant, Experimental Investigation on the Time Dependent Behaviour of a Multiphase Chalk. In *Experimental Unsaturated Soil Mechanics*, volume 112, Part III of Springer Proceedings in Physics, 161–167, Springer Berlin Heidelberg, 2007.
- [8] J.A. de Waal, On the rate type compaction behavior of sandstone reservoir rock. Ph.D. thesis, Technische Hogeschool, Delft, The Netherlands, 1986.
- [9] M.A. Andersen, N. Foged, H.F. Pedersen, The rate-type compaction of a weak North Sea chalk. *Rock Mechanics, Tillerson & Waversik* (eds), 1992 Balkema, Rotterdam ISBN 90 5410 045 1, 1992
- [10] E. Omdal, M.V. Madland, T.G. Kristiansen, N.B. Nagel, R.I. Korsnes, A. Hiorh, Deformation behavior of chalk studied close to in situ reservoir conditions. *Rock Mechanics and Rock Engineering*, DOI 10.1007/s00603-010-0087-4, 2010.
- [11] R. Risnes, M.V. Madland, M. Hole, and N.K. Kwabiah, Water weakening of chalk: Mechanical effects of water-glycol mixtures. *Journal of Petroleum Science and Engineering* 48:21–36, 2005.
- [12] M.V. Madland, Water weakening of chalk: A mechanistic study. Dr. Ing. Thesis, University of Stavanger, ISBN: 82-7644-257-9, JCR, 2005
- [13] F. Collin, Y. J. Cui, C. Schroeder, and R. Charlier, Mechanical behaviour of Lixhe chalk partly saturated by oil and water: experiment and modeling, *International Journal for Numerical and Analytical Methods in Geomechanics*. 26:897–924 (DOI: 10.1002/nag.229), 2002.
- [14] N. Springer, U. Korsbech, and H.K. Waage, SCA2003-38: Resistivity index measurement without the porous plate: A desaturation technique based on evaporation produces uniform water saturation profiles and more reliable results for tight North Sea chalk. In *International Symposium of the Society of Core Analysts*, Pau, France, 21-24 September 2003.
- [15] T. Berre, Triaxial testing of soft rock, *Geotechnical Testing Journal*, Vol. 34, No. 1, 2011.
- [16] R. J. Hickman, Formulation and Implementation of a Constitutive Model for Soft Rock. PhD Thesis, Virginia Polytechnic Institute, September 2004.
- [17] R.M.M. Smits, J.A. de Waal, and J.F.C. van Kooten, Prediction of Abrupt Reservoir Compaction and Surface Subsidence Caused by Pore Collapse in Carbonates. In *SPE Formation Evaluation*, June 1988, 340-346, 1988.
- [18] R. Risnes and C.N. Kristensen, Triaxial Testing on High Porosity Chalk with Different Saturating fluids. In Proc. 5<sup>th</sup> North Sea Chalk Symp., Reims, France, 1996
- [19] T. Heggheim, M.V. Madland, R. Risnes, T. Austad, A chemical induced enhanced weakening of chalk by seawater. *Journal of Petroleum Science and Engineering* 46:171-184, 2005.
- [20] R.I. Korsnes, M.V. Madland, and T. Austad. Impact of brine composition on the mechanical strength of chalk at high temperature. In *EUROCK 2006*, eds. Van Cotthem, Charlier, Thimus & Tshibangu, 133-140, 2006.

# The importance of preliminary investigations when working in areas blighted by historical mineworkings

Scott O'Neill-Gwilliams<sup>(1)</sup>  
*URS Infrastructure & Environment Limited*

## Abstract

Throughout the Industrial revolution and to the mid-latter part of the last century mining formed a major part of the United Kingdom's industrial output.

The legacy of this rich history now poses significant challenges and hazards for the development of land previously used during these industrial processes.

This paper discusses the methods and tools available to the practising geotechnical engineer/geologist in searching for, and identifying, abandoned workings and the risks associated with them. In particular issues related to coal workings are discussed. The paper gives specific reference through the use of an example to where the poor application of these tools resulted in significant additional cost to an engineering project.

Coal workings, abandoned, mine shafts, legacy, pillar and stall, roadways, crownhole, grout, site investigation, ground investigation

## 1. INTRODUCTION

The impact of the legacy of the industrial revolution in the United Kingdom (UK) continues to cause hindrance to development.

Coal has been mined in the UK since Roman times, but the advent of the Industrial Revolution led to mines being progressively driven to deeper depths and working larger areas. From initial bell pits which may have worked only a small area from the access to large pillar and stall workings which may have worked seams of coal many meters thick.

In the United Kingdom from the mid 19<sup>th</sup> Century entire communities built up around easily available sources of coal, fireclays and other economic resources.

Now, decades later many of these towns have no evidence of this rich history visible at the surface beyond made ground deposits and the occasional spoil mound. However many of the worked horizons are within a few metres of the current ground level and are easily within influencing

distance of proposed developments posing a significant risk during both construction and the life of the proposed development.

While in many areas long wall mining or similar methods resulted in subsidence occurring relatively contemporaneously with the mining activities. In other locations mines remain 'open' especially where roadways and accesses were well engineered and supported by pillars of the worked material, often the case in coal mines, or by wooden supports or props. These supports can fail at any time through a combination of spalling, increased loading or through simply rotting away. In addition to the risk posed from workings themselves, mine entries can present an equal danger. Whilst ordinarily many of these man-made geo-hazards remain ignored, they can become of particular importance when redevelopment of mining areas is proposed.

While this paper primarily discusses the author's experiences of mining related problems in the UK the issues noted can be applied to any country where historical mining has occurred. For example Sweden has a rich history of

metalliferous mining dating back over one thousand years.

## 2. INITIAL REVIEW

The most important first step for the geo engineering professional is to undertake a desk based study or review. This study should draw together as many of the available resources of information regarding the site as possible. Best practice guidelines and regulations require the practicing engineer to gather this information together prior to any works commencing on site. This data should be summarised and presented in a concise format to allow the target audience (potentially not qualified engineering professionals) to understand and make use of the information contained within.

In areas of suspected previous historical mineworkings it is vital that a full ground model is developed at desk study stage to allow any hazards to be further investigated as soon as possible to allow input into design and costing schedules. Initial evidence for historical working may come from a site walkover/inspection, geology plans, or aerial photographs.

In the UK the Coal Authority, hold a repository of thousands of abandonment plans that cover large areas of the British Isles. Many of these plans were prepared when workings ceased, and were prepared by the mine operators. This resource is invaluable to the engineering professional when creating initial ground models. However, there are a number of important issues which should be considered when referring to any historical plans, briefly these include;

- The scale of the plans – historical plans will often require electronic enlargement or reduction to enable them to be overlaid with modern base-maps. It is important that this is completed correctly in order to avoid confusion regarding the extent of suspected workings.
- The accuracy of the plans – The original surveys were undertaken without any modern mapping equipment and therefore the accuracy of any plans should be considered suspect until proven by other means.
- Do the plans show the full extent of the workings? Historically it was common practice for workings to be revisited by the

same mine operator or even subsequent owners in order to 'rob' coal from pillars and workings. Resulting in plans under representing the worked areas.

The geo-professional must be able to obtain and understand these plans and use them in conjunction with modern day mapping, GIS systems etc. Often this will require the assistance of CAD and GIS specialists.

However, as a word of warning it is important to be aware that in the UK the recording of mine workings only became obligatory in 1872. When not working in the UK the details of any similar regulations should be sought. There are numerous instances of unrecorded workings and mine entrances being found on site during investigation and construction works. Therefore it is of paramount importance that when working in an area of known productive coal (or other mineable minerals) consideration should be given to the possibility of locating the unknown and unrecorded (Figure 1).



Figure 1 Shallow test shaft located during an earthworks operation near Tefford, UK. Note: the capping of overlying made ground and the shallow depth the shaft was taken to.

In addition to mining abandonment plans other historical documents should be consulted in order to aid in the creation of an understanding of the history of the site. Such other documents may include Parish plans, third party land searches and review of local archives. Local historical societies should also be considered as a rich source of information.

## 3. INVESTIGATION TECHNIQUES

Planning on-site investigation works in areas of historical mining requires careful consideration

and forethought. In seams which have been completely mined out there may be very little trace of the original strata.

Where support has been removed or has collapsed it is not uncommon that a combination of bed separation of the strata directly overlying the removed material, and void migration, can result in confusion regarding the positioning of the encountered strata in the geological sequence. Due to the thickness of known strata having been reduced due to working.

There are a number of methods of investigation available these range from non-intrusive geophysics a through to intrusive drilling works. The merits of these techniques are largely dependant on the ground conditions prevalent across the area of interest (Table 1).

Method	Advantages	Disadvantages
Surface geophysics	Relatively quick and easy to undertake.  Relatively this is a low cost option.	Interpretation can be difficult.  Can be hindered by thick (>3m) overlying deposits. This can be particularly troublesome in areas of previous high-industrialisation for example the Midlands area of the UK.
Subsurface geophysics	Can be used to locate mineshafts in close proximity.  Depending on ease of access, for the equipment, may be a low cost option.	Requires boreholes or known (safe) mineshaft to already be present to allow technique to be used.  In large open voids it may possible
Cameras/ echo sounding	Can be used in large open voids in competent strata. For example limestone or metalliferous ore workings	Again requires an initial method of gaining access to the workings.  Relatively specialist equipment
Rotary Drilling (Open Hole)	Relatively low cost when compared to cored drilling.  Can provide very good indication of the presence of voids or disturbed ground.	Interpretation of geological sequence can be very suspect due to the poor quality of arisings.  Requires constant return of drilling fluid – where fluid is lost in broken or disturbed ground the casing may have to be advanced. Resulting in increased difficulty and cost.  Interpretation is largely based on the skill and descriptions provided by the Lead Driller.  Requires permission to use as a technique (in the UK)
Rotary Drilling (Cored Hole)	Provides clear visual indication of encountered strata.	Can be very expensive as depth increases.  Expensive if used at numerous locations within a small site.  Requires permission to use as a technique (in the UK)
Excavation	Cheap and straightforward intrusive method,	Depth limited by the size of the equipment used.  Requires permission to use as a technique (in the UK)
Cable Tool Drilling	Cheap and straightforward intrusive method,	Limited to shallow depth only.

Table 1 Summary of popular techniques used to investigate for the presence of mine entries and mine workings on site.

It should be noted that as with many aspects of geotechnical engineering the costs of any research, investigation and treatment of abandoned mineworkings is not insignificant. Desk studies can often cost upward of £3000.00 (GBP) depending on the site and the complexity of the proposed development. Even for sites that require significant treatment works the end result can often be that the site appears to be in a very similar condition when compared to how it appeared prior to the works being undertaken. It is therefore the role of the professional to adequately explain to the client the risks inherent to the site and to concisely explain the reasons for the required investigation and works and the benefit they will provide.

As a consequence of the need to reduce costs the professional will often find that interpretation of the presence of workings is based on minimal information. Therefore, the importance of a well prepared desk study to build into the ground model created during the ground investigation phase should not be underestimated.

The end result of the desk and site based researches should be the preparation of a risk assessment. The risk assessment should include reference to the proposed end use of the site, including loadings, foundation selection, retaining structures and any other feature that may be being proposed.

#### 4. TREATMENT

Where investigation, interpretation and risk assessments conclude that treatment is required it is often undertaken using bulk infilling techniques, end tipped stone, or through the use of a rotary drilling rig which drills a primary grid of boreholes – usually on 6m grid spacing. These holes are injected with a pressurised grout. Grouts can be mixed using a variety of materials but are often a low strength combination of sand or Pulverised fuel ash (PFA) and Ordinary Portland Cement (OPC).

Where grout takings are considered excessive – based on the depth of the borehole and the anticipated volume of worked ground secondary

and even tertiary drilling may be undertaken on progressively smaller grid spacing.

In areas where workings are known to dip steeply (i.e. beyond sub horizontal) or in areas where grout takes are considered high. It may be prudent to inject a ‘grout curtain’ around the perimeter of the site to prevent loss outside the zone of influence. This curtain would be formed from a more viscous grout mix, often including coarse gravels. The curtain has a steeper angle of repose and is injected at closely spaced intervals (1-2.5m centres) and creates a barrier beyond which the more fluid grouts cannot escape.

#### 5. MINESHAFTS

Mineshafts can often pose their own very unique problems which may be completely disconnected from any issues relating to workings at depth. There are thousands of shafts across the British Isles in a number of geological materials. In areas where competent rock is close to the surface the workings themselves may not prove a risk to the public. For example in Cornwall, in the South West of the UK, where shafts associated with Tin Mines can be found within a few inches of the surface and therefore require treatment. However the worked veins they are often associated with may have tens of meters of hard igneous rock cover therefore effectively protecting the surface from the danger of collapse. In other areas the depth of made ground and superficial deposits may result in large excavation being required to expose the top of shafts to allow treatment works to be undertaken. Alternatively the shafts may be underlain by prohibitive thickness of superficial materials that would require a much larger excavation than is physically possible within the confines of the site boundary. In these cases it is not unusual for the shaft to be infilled and then protected by creating a bulb of grout over the mouth of the shaft. Although not an ideal solution this method has been adopted for use across many parts of the UK.

In filling of the shaft itself is often undertaken using bulk infill, such as stone, where the shaft is open. In cases where the shaft cannot easily be accessed then it is usually drilled to the base to

prove the depth – using a platform mounted drilling rig for safety, followed by the injection of a grout.

## 6. CASE STUDY

In one particular example the author was called to a new highway scheme in the UK where a drilling and grouting programme had already been completed. However, following high rainfall crownholes (depressions caused by collapse at depth) appeared across the site at formation level. The site records provided by the contractor who had undertaken the treatment works identified a number of sub-horizontal coal seams at shallow (<50m) beneath the base of the excavation works.

Upon further investigation it became apparent that the desk study information had pre-dated the construction of the scheme by nearly a decade and had not been updated in the intervening period.

Mining abandonment plans obtained from the Coal Authority identified several worked horizons occurring at the levels suggested by the drilling records. Review of the historical borehole logs, undertaken some ten years previously, showed that they also encountered the worked horizons but recorded solid coal. Hindsight suggests that the historical boreholes had, in the most part, encountered pillars and areas outside of the worked zone.



Figure 2. Coal being extracted from a seam exposed in an earthworks cut.

The earthworks for the scheme involved a deep cut operation which at points exposed open supported roadways and galleries which were in the majority of case sufficiently to large enough to suggest that minimal spalling or roof failure had occurred following cessation of mining operations. Many of the roadways were supported by wooden props which were up to 300mm in diameter and appeared to be in very good condition (Figures 2 and 3).



Figure 3. Coal being extracted from a seam exposed in an earthworks cut.

The desk study information was updated and a new site model created. The model was then successfully used to create a new treatment scheme including a number of primary and secondary drilling grids and the use of a grout curtain to prevent the migration of grout offsite.

Whilst the revised works were successful, the resultant delay to the project while they were undertaken and the increased costs associated with the works themselves led to an overall increase in the cost of the project. While the cost was unavoidable as the risk required additional treatment it was an additional cost to the project.

## 7. SUMMARY

In areas where historical mineworkings are suspected special care and attention must be given. The importance of a fully conceptualised ground model should not be ignored. This is of particular importance in areas where historical

mineworkings are proven by investigation to have actually taken place. Failure to fully understand the ground model will likely result in delay and increased costs and possibly in the worst case situation take a design past it's Ultimate Limit State i.e., in the case of a structure cause failure or collapse or for a highway this may be a unacceptable amount of differential settlement.

#### REFERENCES

1. EARL, B. 'Cornish Mining', Bradford and Barton, 1968.
2. CIRIA Special Publication 32, 'Construction Over Abandoned Mine Workings', 1984.
3. RAYBOULD, T.J. 'The Economic Emergence of the Black Country', David and Charles, 1973.
4. WARDELL, K. and WOOD, J.C. 'Ground instability arising from old shallow mine workings'. – Proceedings of the Midland Soil Mechanics and Foundations Society, 7, 1965.

Invest in Sweden website:

<http://www.investsweden.se/world/Industries/Mining-minerals-metals/>



# Comparative probabilistic analysis of bearing capacity formulae for shallow foundations using Monte-Carlo simulation

Olsi Koreta<sup>1</sup>

*PLUS Communication, Department of Deployment, Section of Design and Construction*

Erdi Myftaraga

*POLIS University, Faculty of Architecture and Design, Department of Human and Applied Sciences*

## ABSTRACT

In order to calculate the bearing capacity of shallow foundations different formulae are used, most of which are based on Terzaghi's formulation. This formula has been used for a long period and is still broadly in use, but during years several changes are made to take into account various factors. The bearing capacity that results from the application of these formulae ( $q_{ult}$ ) is divided by a safety factor (mostly based on previous experience) and the obtained allowable bearing capacity ( $q_{adm}$ ) is used to define the foundation dimensions. In order to consider the uncertainties of the soil properties ( $\phi$ ,  $c$  and  $\gamma$ ) is necessary to make a probabilistic analysis of the bearing capacity. Using this analysis is possible to give a more accurate judgment about the use of the safety factor for different reliability levels. In this paper, a comparison between the deterministic and probabilistic calculations of the bearing capacity, using Monte Carlo simulation, is done. This comparison is done in the context of a formula used broadly in Albania, which is used to calculate the soil bearing capacity  $R$ . This formula differs from Terzaghi's formula in some aspects and has an incorporated safety factor.

Keywords: Shallow foundations, bearing capacity, factor of safety, soil uncertainties, coefficient of variation, Monte-Carlo simulation

## 1 INTRODUCTION

Calculating the bearing capacity of a shallow foundation (footing) may be considered as one of the fundamental and basic applications in geotechnical engineering. Despite this, this exercise often is surrounded by multiple insecurities and uncertainties, and often the results are somewhat contradictory. The causes for such result instabilities can be found in various aspects of the pro-

cess of calculation itself. Possibly, the most influential causes can be the use of many different calculation models and formulae. Combined this with the large amount of available calculations methods, with different codes and standards, with soil spatial variation and randomness, with subjective engineering judgment, with model uncertainties, and with soil parameter uncertainties, can lead us to different values of the bearing capacity (calculated for the same situation). This is

---

<sup>1</sup> Olsi Koreta. PLUS Communication Sh.A., Dept. of Deployment, Sect. of Design and Construction, Tirana, str.Deshmoret e 4 shkurtit, New building, 2<sup>nd</sup> floor, 1000, [olsi\\_koreta@yahoo.com](mailto:olsi_koreta@yahoo.com)

of course an awkward situation, since is not easy to decide which value to choose. Unavoidably the process may result in less than perfect design, some may not be reliable and some overly conservative and costly [1].

One of the factors that create variation on the results is the used value of the factor of safety FS, which is based on previous experience and usually ranging from 2.5 to 4 [1]. The application of FS usually leads to conservative design and this is mainly addressed to the fact that (through regulation and tradition) the same value of FS is often applied to conditions that involve widely varying degrees of uncertainty [2]. Probably, the best way to consider properly the amount of uncertainties involved on a specific case is the reliability analysis, which provides the possibility to quantify the level of uncertainty and to make a more rational decision regarding the chosen value of bearing capacity. In this paper is intended to be done a reliability analysis of the bearing capacity of shallow foundations, using different calculation formulae, with the aim to define which would be the most rational value of the FS, applied for the required level of safety.

This initiative has been encouraged from the fact that often the reliability concepts can be applied in simple ways, without more data, time, or effort than are commonly available in geotechnical engineering practice [2]. The evaluations of reliability, combined with adequate safety factors, can be seen as a more acceptable way of engineering judgment and design.

## 2 BEARING CAPACITY EQUATIONS FOR SHALLOW FOUNDATIONS

In 1943 Terzaghi was the first to present a comprehensive theory for evaluating the bearing capacity of shallow rough foundations [3], according to the previous work of Prandtl. Terzaghi's equation has been and remains the most widely used formula for this purpose. Several parts of the equation have been modified during years to take into account various factors (foundation shape, depth of embedment, and load inclination). Since these changes have been made from different authors and in a wide time span, we see

now that the evaluated value of the bearing capacity depends largely on the form of the equation used (which on the other hand depends from the engineer's country and his education). In our analysis we are considering various shapes of calculating bearing capacity, such as: the ones based on Terzaghi's equation, the proposed equation in Eurocode 7 and the soil bearing capacity R equation known in Albania.

### 2.1 Terzaghi's equation of bearing capacity

This equation (also known as the triple N formula) calculates the ultimate bearing capacity for continuous foundation as below [3]

$$q_u = c \cdot N_c + q \cdot N_q + 0.5 \cdot \gamma \cdot B \cdot N_\gamma \quad (1)$$

Where  $c$  = cohesion of soil,  $\gamma$  = unit weight of soil,  $q = \gamma D_f$  = surcharge of the soil above the foundation, ( $N_c$ ,  $N_q$  and  $N_\gamma$ ) = nondimensional bearing capacity factors depending on soil friction angle ( $\phi$ ), and  $B$  = width of the foundation. The allowable bearing capacity ( $q_{all}$ ) can be calculated by dividing  $q_u$  with an adequate factor of safety

$$q_{all} = \frac{q_u}{FS} \quad (2)$$

In Equation (1) we are not considering the correcting factors for foundation shape, depth of embedment and load inclination.

Regarding the bearing capacity factors, many proposed formulations, from several authors, exist and are currently in use. The ones used in our calculations are summarized in Table 1 [4].

### 2.2 Calculating bearing capacity – R

In Albania a widely used formula for the calculation of bearing capacity is [5]

$$R^n = (A \cdot b + B \cdot H) \cdot \gamma + D \cdot c \quad (3)$$

Where  $R^n$  = normative bearing capacity of soil (in accordance with  $q_u$ ),  $b$  = width of foundation,  $\gamma$  = unit weight of soil,  $c$  = cohesion of soil,  $H$  =

depth of embedment, (A, B and D) = coefficients depending on soil friction angle (in accordance with  $N_c$ ,  $N_q$  and  $N_\gamma$ ). The formulae used to calculate the three coefficients are

$$\begin{aligned}
 A &= 0.25 \cdot \frac{\pi}{\cot \varphi + \varphi - \frac{\pi}{2}} \\
 B &= 1 + \frac{\pi}{\cot \varphi + \varphi - \frac{\pi}{2}} \\
 D &= \frac{\pi}{\left( \cot \varphi + \varphi - \frac{\pi}{2} \right) \cdot t_{\frac{\pi}{2}} \varphi}
 \end{aligned}
 \tag{4}$$

The value of  $R^n$  is equivalent with the critical pressure that causes local sliding surfaces till the depth of

$$z \leq 0.25 \cdot b \tag{5}$$

At the end we find the calculating bearing capacity as

$$R = R^n \frac{m_1 \cdot m_2}{k} \tag{6}$$

Where R = calculating bearing capacity (in accordance with  $q_{all}$ ),  $m_1$  = coefficient of working conditions of the foundation (depending on soil type; range 1.1-1.4),  $m_2$  = coefficient of working conditions of both foundation and structure (depending on soil type, structure rigidity and dimensions; range 1.0-1.4), and k = coefficient of reliability (depending on the reliability of soil resisting parameters; range 1.0-1.4).

Table 1. Bearing capacity factors from different authors

Author	$N_\gamma$	$N_c$	$N_q$
Terzaghi	$\frac{\tan \varphi}{2} \left( \frac{K_{q\varphi}}{\cos^2 \varphi} - 1 \right)$	$(N_q - 1) \cdot \cot \varphi$	$\frac{a^2}{2 \cos^2 \left[ \left( \frac{\pi}{4} + \frac{\varphi}{2} \right) \right]}$ $a = \exp \left[ \left( \frac{3\pi}{4} - \frac{\varphi}{2} \right) \tan \varphi \right]$
Meyerhof	$(N_q - 1) \cdot \tan(1.4\varphi)$	$(N_q - 1) \cdot \cot \varphi$	$\tan^2 \left( \frac{\pi}{4} + \frac{\varphi}{2} \right) \exp(\pi \cdot \tan \varphi)$
Hansen	$1.5(N_q - 1) \cdot \tan \varphi$	$(N_q - 1) \cdot \cot \varphi$	$\tan^2 \left( \frac{\pi}{4} + \frac{\varphi}{2} \right) \exp(\pi \cdot \tan \varphi)$
Vesic	$2(N_q + 1) \cdot \tan \varphi$	$(N_q - 1) \cdot \cot \varphi$	$\tan^2 \left( \frac{\pi}{4} + \frac{\varphi}{2} \right) \exp(\pi \cdot \tan \varphi)$
Eurocode 7	$2(N_q - 1) \cdot \tan \varphi$	$(N_q - 1) \cdot \cot \varphi$	$\tan^2 \left( \frac{\pi}{4} + \frac{\varphi}{2} \right) \exp(\pi \cdot \tan \varphi)$

### 3 UNCERTAINTIES IN SOIL PARAMETERS

One of the most crucial aspects in every geotechnical design application is the evaluation of soil or rock properties. In the case of determining the bearing capacity for a shallow foundation, the used soil parameters are: the friction angle ( $\varphi$ ), the cohesion (c), and the unit weight ( $\gamma$ ). In order to perform a probabilistic analysis, the first step

consists in quantifying the respective uncertainties related to the above parameters. There are three primary sources of geotechnical properties uncertainties [6]: inherent variabilities (depending on site conditions), measurement uncertainties (depending on equipment and procedural control), and transformation uncertainties (depending on the quality of the correlation model). We are considering here that the parameters used in the calculations are determined through laboratory testing. Many previous publications, from several authors, express the range of the coefficient of variation (COV) for most of soil properties. We have collected the ones related to the pa-

rameters in our interest, and the data are presented in Table 2 [2] [7] [6] [8]. Due to the very specific and often unknown circumstances of determining the COV and due to the wide range of

values for the same parameter, in our calculations it has been considered to use the complete range of COV.

Table 2. Values of coefficient of variation (COV) for used geotechnical properties

Soil property	Coefficient of variation [%]	Source
Unit weight $\gamma$	3-7	Harr (1984),Kulhawy (1992)
	3	Harr (1987)
Friction angle ( $\phi$ )	2-13	Harr (1984),Kulhawy (1992)
	12-56 (clays)	Lee et al. (1983)
	5-15 (sands)	Phoon & Kulhawy (1999a), Lee et al. (1983)
	6-20	Phoon & Kulhawy (1999b)
	9	Lumb (1966)
	40 (clays)	Kotzias et al. (1993)
	16 (alluvial)	Wolff (1996)
	2-5 (sands)	Lacasse & Nadim (1996)
	5-20 (tailings)	Baecher (1983)
	10 (sand)	LD25 Rehab Report (1992)
Cohesion (c) or undrained shear strength ( $s_u$ )	40	Harr (1987)
	13-40	Harr (1984),Kulhawy (1992), Lacasse & Nadim (1997), Duncan
	20-50 (clays)	Lee et al. (1983)
	25-30 (sands)	Lee et al. (1983)
	5-20 (clay, triaxial)	Lacasse & Nadim (1996), Lumb (1974)
	10-30 (clayey silt)	Lacasse & Nadim (1996), Lumb (1974)
	7-40	Phoon & Kulhawy (1996b)

## 4 CALCULATION EXAMPLE AND PROCEDURE

### 4.1 Example used

To compare the bearing capacity from different formulae, we are studying the case of a shallow strip foundation, carrying a linear uniformly distributed load (e.g. the foundation under a wall). The foundation width is  $B=2\text{m}$  (Fig.1) and it is positioned 1.5 below the ground level ( $D_f$ ). To consider the influence of the soil type (sandy and clayey soils), two type of soils are taken into account: soil 1 (unit weight  $\gamma=17.5\text{kN/m}^3$ , friction angle  $\phi=25^\circ$ , and cohesion  $c=10\text{kN/m}^2$ ) and soil 2 (unit weight  $\gamma=18\text{kN/m}^3$ , friction angle  $\phi=5^\circ$ , and cohesion  $c=30\text{kN/m}^2$ ).

### 4.2 Calculation procedure

The first step of the calculations consists in evaluating the deterministic ultimate bearing capacity ( $q_u$ ) for the above example using R formula, and Terzaghi's equation (using the bearing capacity factors from several authors listed in Table.1). In order to compare this formulae from the probabilistic point of view we have used the Monte Carlo simulation method, implemented in an excel spreadsheet. Soil friction angle and cohesion are considered as random variables, meanwhile the unit weight of the soil is considered as a deterministic value, since its coefficient of variation (COV) is well fewer than 10% [9]. For the friction angle the range of the COV (%) is 0 to 15 (3, 6, 9, 12, and 15), and for the cohesion the range of COV (%) is 0 to 40 (10, 20, 30, and 40). The mean values of  $\phi$  and  $c$  are the values mentioned in the given example. The influence of the variation of  $\phi$  and  $c$  is considered separately, taking one parameter as random variable and the other as a deterministic value, and vice versa.

With the mean and the COV of  $\phi$  (and then  $c$ ), we can calculate the standard deviation  $s_\phi$  (and  $s_c$ ). Using the Excel function *NORMINV(RAND(),mean,standard\_dev)* we generate random values of the parameter (random variable), which are consistent with the mean and standard deviation. The generated random values of  $\phi$  (and  $c$ ) are used as input data to gain the histogram of the ultimate bearing capacity. In this procedure are used 10 000 iterations. The histogram enables to calculate the mean and standard deviation of  $q_u$  and  $R$ . Using the Excel function *NORMINV(probability,mean,standard\_dev)* we can calculate the bearing capacity for the desired/required level of reliability (e.g. 90%, 95%). Also, for each level of reliability is possible to calculate a factor of safety (FS), with which the deterministic value should be divided to gain the corresponding bearing capacity.

## 5 RESULTS

In Figures 1 and 2 are shown the results of deterministic calculations of bearing capacities using all the available formulae (described above). As is clear,  $R$  value is much lower than  $q_u$  (for all formulae).  $R$  is conceived as a value to be used directly in the calculation of foundation dimensions, without using any safety factor. On the other hand,  $q_u$  is supposed to be divided by a safety factor, in the range 2.5 to 4.

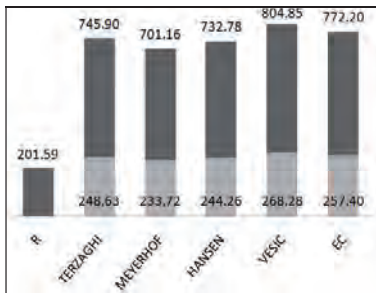


Figure 1. Deterministic bearing capacities for soil 1.

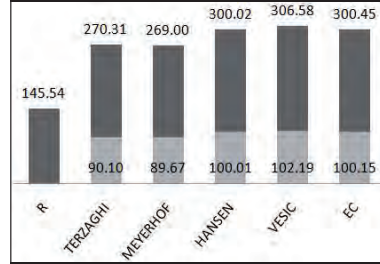


Figure 2. Deterministic bearing capacities for soil 2.

In fact,  $q_{all}$  values ( $q_u/FS$ ) for  $FS=3$ , are very similar with  $R$  value. This statement is in accordance to deterministic calculations. To take into account parameter uncertainties, we can refer to the graphs in Figures 3 and 4.

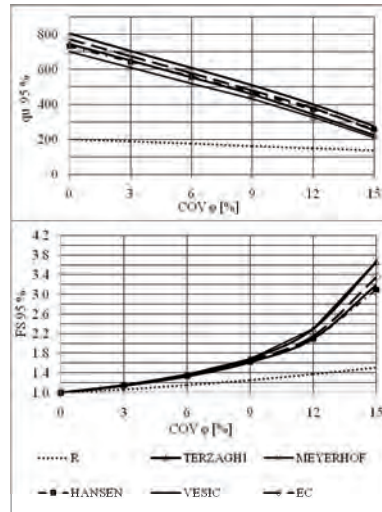


Figure 3. Relationship between  $q_u$  and FS with the COV of friction angle (soil 1), for 95% reliability.

Fig.3 shows the variation of  $q_u$  and FS with the COV of friction angle, for 95% reliability. From the first graph we can infer that with the

increasing of COV we have a decrease of the bearing capacity, in order to maintain the same level of reliability. We have also calculated a needed FS, with which the deterministic bearing capacity must be divided (second graph). FS increases with the increase of COV. An interesting result is that R is less affected by the increase of COV of friction angle.

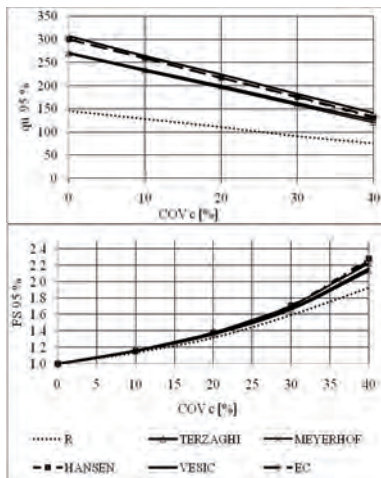


Figure 4. Relationship between  $q_u$  and FS with the COV of cohesion (soil 2), for 95% reliability.

The same analysis is done for the COV of cohesion (Fig.4). For formulae that calculate  $q_u$ , the effect of  $COV_c$  has a similar tendency as for  $COV_\phi$ . The values of R are also affected by  $COV_c$ , at the same rate (second graph).

## 6 CONCLUSIONS

Although only two soils have been considered in the calculations, some valuable conclusions could be highlighted. It seems clear and more reasonable to use a FS according to the level of uncertainty of soil parameters, instead of a fixed value taken from previous experience. The value of FS should reflect the level of uncertainties in-

involved, in order to have a more rational design. The application of a FS > 2.5 may result in conservative design, when we have small COV of soil properties.

The normal design practice in Albania implies the direct use of R in calculations, without using any safety or partial factor. Anyway, for large values of COV (for  $\phi$  and  $c$ ), the application of a FS may result necessary. This FS seems smaller than the one used for  $q_u$  and is mostly affected from the cohesion value.

## ACKNOWLEDGEMENT

The authors are grateful to the Organizing Committee for the opportunity to make this presentation. The special thanks go to Luljeta Bozo for the support provided in the preparation of the paper.

## REFERENCES

- [1] B.H. Fellenius, Bearing capacity of footings and piles-A delusion?, *DFI Annual Meeting*, October 14-16 (1999), Dearborn, Michigan.
- [2] J.M. Duncan, Factors of safety and reliability in geotechnical engineering, *Journal of Geotechnical and Environmental Engineering*, Vol. 126 No. 4, (2000).
- [3] Braja M. Das, *Principles of foundation engineering*, sixth edition, Thomson Canada Limited, Toronto, Ontario, Canada, 2007.
- [4] J.E. Bowles, *Foundation analysis and design*, McGraw-Hill, New York, 1996.
- [5] L. Bozo, *Gjeoteknika 1 - Mekanika e dherave*, Tirana, Albania, 2005.
- [6] K.K. Phoon, Towards reliability-based design for geotechnical engineering, *Special lecture for Korean Geotechnical Society*, Seoul, 9 July 2004.
- [7] G.B. Baecher and J.T. Christian, *Reliability and statistics in geotechnical engineering*, John Wiley & Sons Ltd, England, 2003.
- [8] U.S. Army Corps of Engineers, Reliability Analysis and risk assessment for seepage and slope stability failure modes for embankment dams, ETL 1110-2-561, 31 January 2006.
- [9] F.H. Kulhawy, K.K. Phoon and W.A. Prakoso, Uncertainty in basic properties of geomaterials, *GeoEng 2000*, Melbourne, Australia, 19-24 November 2000.

# Determination of 1200 mm working piles deformation parameters, using test of smaller diameter pile for the piled raft foundation of Capital Fort project

B. Parvanov<sup>1</sup>  
*Strukto Ltd, Sofia, Bulgaria*

## ABSTRACT

Capital Fort mixed used development comprises a 30-storey, 126 m high office tower and an 8-storey, 35 m high, L-shaped office building, unified with a two storey deep basement. Foundation structure is a raft with a variable thickness under both buildings and bored piles under the high-rise. Deformation and strength characteristics of the soil, received from the geological survey, are used for a preliminary analysis of the combined piled raft foundation. Deformation modules are defined using the results from the standard penetration test. Single pile test is performed for determination of the geotechnical parameters used for refinement of soil analytical model. Working piles are 28 m deep and have a diameter of 1200 mm. Pile with smaller diameter (600 mm) is used for the test. The depth of the tested pile is the same as the working ones. Casing and concrete grade C25/30 are used for the construction of the pile. Anchoring system comprises four working piles. Hydraulic loading system with 8000 kN capacity is used. Measuring system monitors the settlement of the pile head and comprises three dial gauges with 0.01 mm precision, placed at 120 degrees in plan. The pile is loaded in 11 steps of 700 kN each, up to 7700 kN, realizing 30.5 mm settlement. Results from the test and a comparison with the analytical results from the preliminary adopted parameters are presented in the article.

Keywords: Piled raft foundation, pile test, high-rise building, numerical modeling

## 1 INTRODUCTION

The Combined Piled Raft Foundation is a comparatively new design concept, developed mainly in the last twenty years.

Load bearing elements of the pile raft are piles, raft and soil. There is complex soil-structure interaction between the foundation elements, defined in [1] as:

- soil-pile interaction
- pile-pile interaction

- soil-raft interaction
- pile-raft interaction

Due to the interaction effects, the load bearing behavior of the pile as a part of the piled raft is quite different from the comparable single pile. Despite of the principal difference, single pile test is often used in the verification of the piled raft numerical model. Back analysis of the single pile tunes the soil deformation parameters which afterwards are used in the large sophisticated model of the building foundation.

---

<sup>1</sup> Boris Parvanov. Strukto Ltd, 74A Hristo Smimenski Blvd, 1164 Sofia, Bulgaria, bparvanov@strukto-bg.com

In the project presented below, the main advantage of the piled raft foundation is the ability to reduce the differential settlements. This is achieved by concentrating the piles under the eccentrically loaded area of the raft. This allows the raft to be designed as a single structure, eliminating the settlement joint between the areas with different loading.

## 2 PROJECT DESCRIPTION

Capital Fort is a mixed used development, located in Sofia, Bulgaria. When completed, it will be the highest building in Bulgaria with its 126 m.

The site is with almost rectangular shape, 150 m long and 90 m wide. The project comprises two buildings – high-rise block A and low-rise block B (Figure 1).



Figure 1. Capital Fort 3D montage

Reinforced concrete cast on site is the main structural material used for the construction of the buildings. Block A is a 30-storey office tower that rises to a height of 126 m above the ground surface. Lateral stability of the superstructure is provided by a central core and two perimeter frames. Post tensioned flat plate is used for the floor system.

Block B is an 8-storey, 35 m high, L-shaped office building. Three cores, located at the corners, carry the lateral loading from earthquake and wind. The typical floor system consists of band beam slabs.

Both buildings sit on two storeys, 9.5 to 11 m deep basement.

The Client requires advanced vertical transportation in the high-rise, thus twelve extremely fast lifts are located in the central core. Maximum horizontal displacement at the top of the shafts is limited to 2.5 cm. It results in maximum tilt of around 1/4000 which is an unusually strict requirement.

Another very important issue is that low-rise building should be finished much faster than the high-rise (Figure 2). In this way almost the whole settlement of the high-rise transforms to a differential settlement between the buildings.



Figure 2. Pile construction beneath the high-rise footprint and raft construction in the low-rise area

Considering the severe service requirements and the construction sequence, piled raft foundation is adopted in the design. Foundation structure is a raft with a variable thickness and large diameter bored piles under the high-rise. Raft thickness is 2.5 m beneath block A and 1.2 m for the rest of the building. 129 piles with diameter 1200 mm and 28 m deep are concentrated beneath the high-rise footprint.



### 3 SOIL CONDITIONS

The site is located in the south-east part of the Sofia Pliocene Basin. The main feature of the region is the alternating layers of clays, sandy clays, sands and gravels. Soil layers beneath the raft are listed below (Figure 3).

- Sand – medium, grey-brown to grey-green, SPT value  $N_{30}=40-50$ ;
- Clay 1 - stiff, grey-brown to grey-green, SPT value  $N_{30}=48-50$ ;
- Clay 2 – stiff, dark-grey to grey-green, SPT value  $N_{30}=55$ . This clay layer goes down to the bottom of the 60 m deep boreholes. Thin intercalations of sand are found in the Clay 2 layer;

Underground water level is found 16 m under the raft bottom surface.

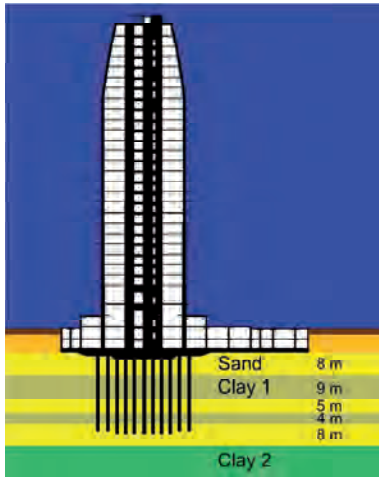


Figure 3. Soil layers and section through the high-rise

Seismicity in Sofia is high with a maximum ground acceleration  $a_{g,max}=2.65 \text{ m/s}^2$ .

### 4 PILE TEST

Loading system with maximum capacity of 8 MN was available at the time of the pile test.

Preliminary design of the working piles, 1200 mm diameter, showed that loading of only 8 MN couldn't achieve large settlement and is not suitable for producing adequate single pile load-settlement curve. Furthermore, the pile bearing capacity is not the major concern in piled raft foundation design. Due to the complex pile-raft-soil interactions there is no distinguished capacity of the pile within the group. Monitored piled rafts around the world shows piles working with a load much higher than the ultimate bearing capacity, received from the single pile load tests.

Considering the limited loading system capacity and the behavior of the pile within the piled raft, it was decided to test a pile with smaller diameter.

#### 4.1 Test Pile Description

The test pile is reinforced concrete bored pile with 600 mm diameter. It is constructed using the same technology, material and depth as the working piles. Casing is used for the whole depth of the pile excavation.

Concrete cube with 1.15 m side length is constructed at the top of the circular pile in order to provide enough space for the loading jacks (Figure 4).

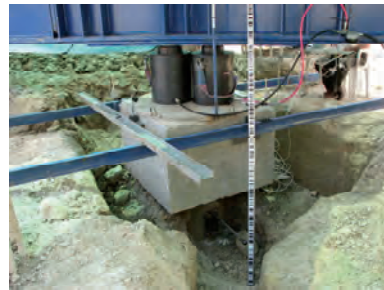


Figure 4. Concrete cap at the pile top with loading jacks and measurement devices

The section of the test pile is designed for maximum load of 7000 kN with concrete grade C25/30 and reinforcement percentage  $\mu=2.6\%$  of B500 steel. Test is performed 30 days after concreting of the pile.

#### 4.2 Loading System

The loading system consists of two hydraulic “Europress” jacks with 300 mm stroke diameter and a hydraulic pump. Loading force is controlled by pressure manometer.

#### 4.3 Anchoring system

The anchoring system comprises four working piles with 1200 mm diameter and two crossed, 900 mm high steel beams (Figure 5). A bell-like element is connected to the beams and welded for the anchor piles reinforcing bars.



Figure 5. Anchoring system – tension working piles and crossed steel beams

#### 4.4 Measuring system

The measuring system consists of three dial gauges with 0.01 mm precision. They measure the settlement at the concrete cube sides. The gauges form an equilateral triangle, which center lies in the center of the test pile (Figure 6).

Electronic level with 0.1 mm precision is situated outside the test area and is used as a control measurement. It monitors the settlement of the

test pile body, beneath the concrete cap and the upward movement of the anchor piles.

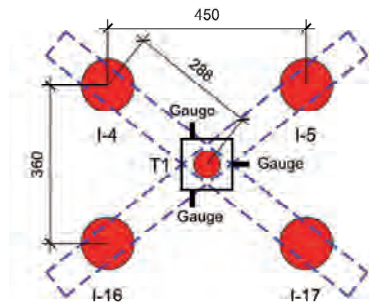


Figure 6. Test configuration – position of the elements and dimensions – test pile (T1), anchor piles (I-4, I-5, I-16, I-17)

#### 4.5 Test procedure

The loading procedure adopted conforms to the provisions of [2].

The static loading force is increased in 11 steps to the final force  $Q_{max}=7700$  kN. All load increments are of equal magnitude of 700 kN.

A time interval of one hour is used for each load step. During the one hour steps the pile displacements are recorded at 0, 2, 5, 10, 15, 20, 25, 30, 40, 50 and 60 min. Next step of the loading begins only if the displacement of the pile head is less than 0.1 mm / 20 min.

#### 4.6 Test results

Each one of the loading steps is realized within the one hour period without considerable creep. Settlement at the final load is 30.5 mm. The difference between the average settlement of the gauges and the electronic level is 1.5 mm. Load – settlement test curve is presented in Figure 7.

Some cracks are observed at the pile surface just beneath the pile cap (Figure 8). The reason is that the test pile reinforced concrete section is overloaded with 10% from the calculated compression resistance.

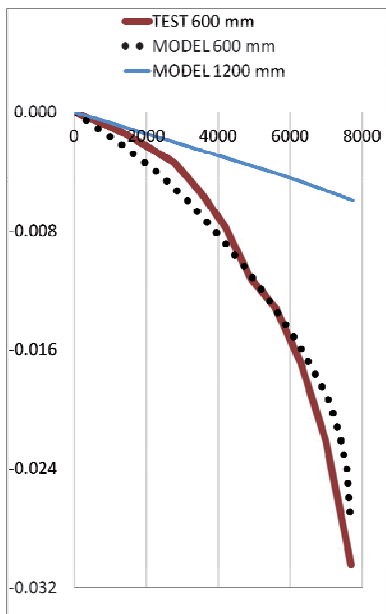


Figure 7. Load-settlement curve from pile test and numerical model



Figure 8. Cracks in the test pile located beneath the pile cap

## 5 NUMREICAL MODELING

Spatial finite element model is used for back analysis of the single pile test (Figure 9). Four anchor piles (1200 mm diameter), together with the test pile (600 mm diameter) are simulated. Additionally, load test of 1200 mm diameter pile is simulated by adding a group of five working piles.

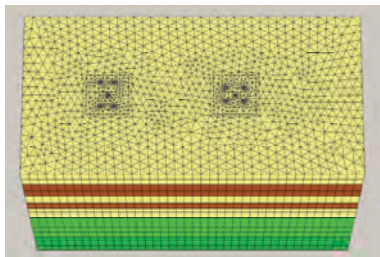


Figure 9. Finite element model for back analysis of the pile test.

As a first estimate the soil elastic modulus based on the work of Decourt [3], [4] are assumed. SPT values are used for definition of the deformation characteristics of the soil.

Mohr-Coulomb elastic-plastic model is used. Due to the constant average stiffness in each soil layer, Mohr-Coulomb model computations are fast and suitable for engineering practice.

More rigorous soil models are available in the advanced software codes as Plaxis, Flac 3D, Ansys, etc. They all could be useful for better modeling of the single pile test, but often can't handle large models of the whole building foundation.

Comparison of the load-settlement curve of the pile test and finite element model can be seen at Figure 7. Even the first choice soil parameters set gives quite close results. The final settlement computed is 27.6 mm for the 600 mm pile.

Calculated load-settlement curve of the modeled working pile (1200 mm diameter) is also

shown in Figure 7. The settlement at  $Q_{\max}=7700$  kN is around 6 mm.

## 6 CONCLUSIONS

In the presented project, piles in the piled raft are used primary to reduce the differential settlements and to avoid the excessive tilt of the high-rise tower. It was very important to find an appropriate way to prove the numerical soil model in order to compute the real settlements of the foundation.

Results from the load test and numerical model shows that:

- Load-settlement curves are quite close and soil model can be used for design purposes.
- Determination of soil deformation modules based on SPT is adequate and rather accurate. It can be implemented very efficiently together with simple Mohr-Coulomb soil model in the design of large scale foundations. This results in very fast computation time and gives the opportunity to investigate different foundation variants.
- Back analysis of the load test with 600 mm pile makes it possible to determine the load-settlement curve of the larger working pile. These results are further used in the next analysis – settlement analysis of the building foundation and structural analysis of the whole structure.
- Observed cracks at the pile surface shows that further improvement in the numerical model should account for the stiffness degradation of the concrete pile section.

Piled raft foundation of Capital Fort Project is monitored by three instrumented piles and three pressure cells. Settlements are monitored by geodetic net with more than 15 points. Results from the monitoring, together with more comprehen-

sive analysis of the foundation will be presented after the building is completed. Concrete shell of the low-rise block B was finished in the middle of August 2011, while the high-rise block A has 12 finished stories in the middle of May 2012 (Figure 10).



Figure 10. Construction progress at the middle of May 2012

## ACKNOWLEDGEMENT

The author is grateful to Prof. George Ilov from the University of Architecture, Civil Engineering and Geodesy, Sofia for the priceless advices during the design phase of the project.

Thanks also to the management of Capital Fort for understanding the value of the experimental work and to Bauer AG and Strukto Ltd teams for the patience and support during the tests.

## REFERENCES

- [1] J.A. Hemsley, *Design applications of raft foundations*, Thomas Telford Ltd, London, 2000.
- [2] ISO/TC 182/SC 1, *Draft international standard ISO/DIS 22477-1*, International Organization for Standardization, 2005.
- [3] L.Decourt, SPT-State of the art report, Proc. 12 ICSMFE (1989), Rio de Janeiro.
- [4] L. Decourt, Prediction of load settlement relationship for foundations on the basis of SPT, Ciclo De Conf. Int. "Leonardo Zeevert" (1995), UNAM, Mexico, 85-104.

# Comparison between results of static pile load testing, PDA results and calculated bearing capacities for pile design on the bridge over river Drava

M. Biščan<sup>1</sup>  
*Institut IGH*

L. Bolfan  
*Institut IGH*

## ABSTRACT

On the Corridor Vc in the Republic of Croatia, bridge over the river Drava has been designed. The Corridor Vc is a part of the TEM network infrastructure of Southeastern Europe, passing from Budapest (Hungary), through Osijek (Croatia), Sarajevo (B&H), up to the Port of Ploče (Croatia). Bridge over the river Drava is 2485 m long. The bridge is designed like cable-stayed bridge, with 100 +220 +100 long spans, and concrete semi-prefabricated structure on the river banks (approximately 35 m long spans). The heights of the pylons are 75 m. All piers are placed on  $\Phi 150$  cm, 19, 22, 25 and 30 m long bored piles, in layers of uniform graduated loose to medium dense sands. In the design stage four static pile load tests have been performed. PDA tests were performed on same piles. Additional 40 PDA tests will be performed on piles in the construction of the bridge. Comparison between results of static pile load tests with PDA results and comparison with the calculated bearing capacities will be shown in this paper (Reese and O'Neill -  $\beta$  method, calculation of pile bearing capacities from CPTU tests).

Keywords: Static pile load tests, PDA tests,  $\beta$  method, Measuring

## 1 INTRODUCTION

The bridge over the river Drava is part of the International Pan-European road corridor Vc and one of the most important part of the TEM / TER Project. The route of the highway is part of a European network E73, which connects northern Europe with the Adriatic, passing Budapest (Hungary), via Osijek (Croatia), Sarajevo (B & H) to the port of Ploče (Croatia).

The bridge is designed like cable-stayed bridge and concrete semi-prefabricated structure on the river banks (approximately 35.0 m long spans). The length of the bridge is 2485,0 m.

Structure of the main span is suspended steel-concrete composite box (100.0 +220.0 +100.0 m long spans). Main span consists of composite steel beams, reinforced concrete pylons and cables. A reinforced concrete pylon is A shaped with height of 75.0 m. All piers are placed on a reinforced concrete,  $\Phi 150,0$  cm, 19, 22, 25 and 30 m long bored piles.

According to reference [1], relating to the determination of bearing capacity of piles, the four characteristic sites are chosen for static and dynamic pile load tests. In reference [2] the four test locations are defined as trial fields (two on each side of the river bank). Tests on the test field P1 (pier S19) and test field P2 (Pylon S1g) were conducted by Institut IGH, Department of

---

<sup>1</sup> M. Biščan, Institut IGH, Croatia, Zagreb, Janka Rakuše 1, marko.biscan@igh.hr

Geotechnical Engineering. The procedures and test results will be presented in this paper.

## 2 GEOTECHNICAL PROPERTIES OF SOIL

The soil profile is as follows:

- Up to a maximum depth of 2,8 m, 4,0 m in places, extending from the surface, layers of clay and silt, low and high plasticity, mainly medium stiff to stiff consistency, gray-brown colored
- To the testing depth, around 35 m, soil layers are uniformly graded and medium-grained sand, with silt mixtures (SW, SU, SU / SM), loose to medium density, gray colored. The percentage of clay and silt particles is generally about 10-25%.
- CPTU cone resistances and the SPT blow counts (N60) generally increase with depth.
- On individual boreholes and CPTU probes the low plasticity silt layer, medium stiff to stiff consistency ( $c_u = 60 \rightarrow 150$  kPa from CPTU tests,  $N_{kt} = 20$ ) at a depth of about 15,5, and about 21,0 to 24,0 m.
- SPT:  $N_{60} = 3-25$ .
- The groundwater level at the time of testing was registered at a depth of 3-5 m. There may be substantial changes in groundwater levels (and ground flooding) during the year, that are related to the water level of the river Drava.

## 3 PILE BEARING CAPACITY ASSESSMENT BY CALCULATION

Bearing capacity of test piles will be determined using two different methods:

- $\beta$  method, according to Reese et al [6].
- Directly from the results of CPTU tests - Bustamante and Gianselli method [7]

Length of the test piles was 20,0 m in the ground with a diameter of 80,0 cm. Test piles have smaller dimensions from the piles in the bridge structure, because the static pile load testing of a greater pile length and diameter require a unreasonable test structure and measurement

equipment for that magnitude of load application.

Table 1 Results of pile bearing capacity assessment

Calculation method	Pile bearing capacity (kN)					
	Test field P1 (S19)			Test field P2 (pylon S1g)		
	Qs	Qb	Qult	Qs	Qb	Qult
$\beta$ method	3101	577	3678	3101	577	3678
Bustamante and Gianselli method	2828	3400	6238	1884	3100	4984

From the results of pile bearing assessment it is clear that different calculation method give very different values of pile bearing capacity. Besides the big differences in the total pile bearing capacity there is a great difference between pile shaft and base resistances.  $\beta$  method is an empirical method developed on interpretation of a numerous static pile load tests in similar geotechnical conditions and is of recent date, and as such is taken as representative. The second method gives unrealistic high pile base resistance.

It is concluded that the maximum expected bearing capacity is  $Q_{max} = 5000$  kN.

## 4 STATIC PILE LOAD TESTING

### 4.1 Equipment used for testing

#### 4.1.1 Apparatus for applying loads

Load is transferred from the main steel beams to the secondary beam, and further through the anchor piles into the ground. Apparatus for the pile load test consists of:

- Four anchor piles 16,0 m long with 80,0 cm diameter, spaced at 4,3 m from axis, (spaced at 3,8 D from the test pile - minimum spacing required by reference [3] is 3,5 D).
- Geotechnical prestressed anchors  $9 \times \Phi 0,62'' = 9 \times 150 = 1350$  mm<sup>2</sup>, embedded in tension piles. The fixed anchor length is 8,5 m long and is extending nearly to the pile base. Free anchor length is stretching to the

peak of the secondary beams where the anchor is prestressed at force  $P_0 = 1375$  kN

- Steel beams for applied load transfer to the tensile piles. The structure is consisted of a main beam 5,6 m long, and two secondary beams 5,6 m long. These beams are together placed in a horizontal H position in which the secondary beams are in H vertical and main beams H horizontal position.

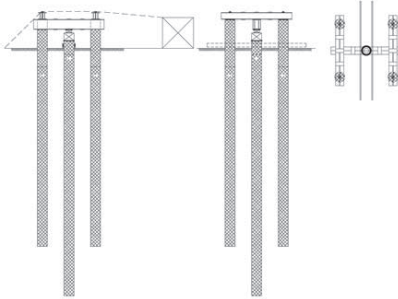


Figure 1 Schematic set-up of apparatus for applying loads

#### 4.1.2 Hydraulic jack

Axial compressive force is applied to the pile using the hydraulic jack capacity of 8000 kN. Center of compressive force is achieved using a spherical joint at the top of the piston press.

#### 4.1.3 Measurement equipment and instrumentation

Loads at pile head are measured by a load cell of 10000 kN capacity, mounted directly above the hydraulic jack. Pile head displacements were measured using 4 digital strain gauges over aluminum reference beam 8 m long. Measurement accuracy was 0.001 mm.



Figure 2 Apparatus for static pile load testing.

#### 4.2 Load step sequence

Static pile load testing was conducted in accordance with reference [3]. The maximum pile load ( $Q_L = 5000$  kN) is defined according to the pile bearing capacity calculated in reference [2]. The adopted collapse criterion is to realize the vertical pile displacement at magnitude of 10% of pile diameter ( $\approx 8$  cm). Pile is loaded in two stages (see Figure 3). The unloading steps serve to show the elastic and plastic components of the pile head displacement. A load of 500 kN is a "datum load" - the start of measurement. In the first phase the pile was loaded up to 50% of final test loading - up to 2500 kN. In this way any downtime and contact system adjustments was eliminated. In the second phase the pile was loaded to the maximum test load.

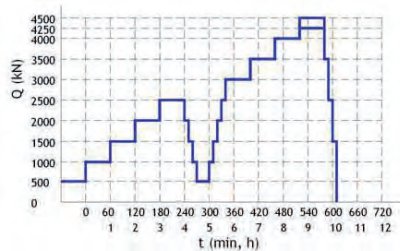


Figure 3 Load step sequence – two-cycle loading



#### 4.3 Review and interpretation of test results

The measurement results will be displayed for interpretation in the form of equivalent diagrams:

- Relation between load and displacement of the pile head after displacement stabilization - Figure 4.
- Increase of pile head displacement under constant load (creep) as a time function Figure 6 and 7.
- Presentation of creep under constant load - relation between load and displacement in the same increment of time - Figure 5.

During the test the creep was controlled (increase of displacement at constant load) of the pile in the last 30 minutes of each increment. The creep load,  $Q_c$ , is defined as the intersection of two lines which represent average values of  $\Delta S_{i,30}$ . Based on the test result interpretation the critical creep load was determined for test pile.

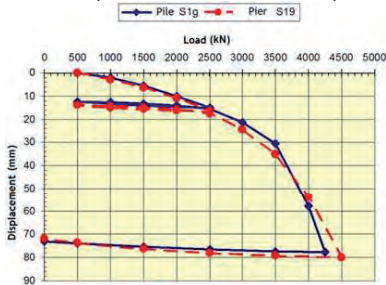


Figure 4 Load-displacement diagram for pile head

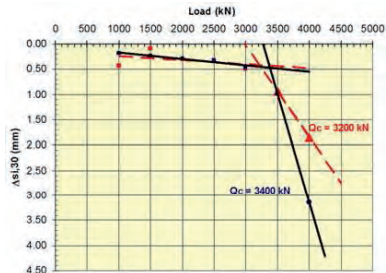


Figure 5 Creep load ( $Q_c$ ) determination

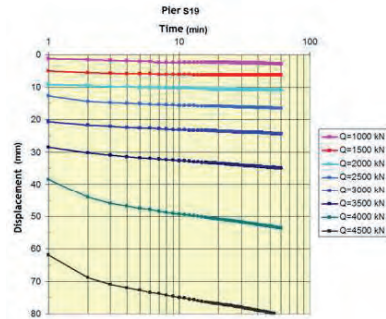


Figure 6 Pile head displacement under constant load, test field P1 (pier S19)

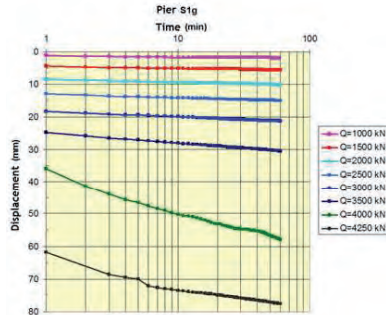


Figure 7 Pile head displacement under constant load, test field P2 (pylon S1g)

As a criterion for determining the pile bearing capacity from the measured load-displacement diagram (Figure 4) the load that gives displacement more than 10% of pile diameter (8 cm) was adopted.

Table 2 Results of static pile load testing

Test field	Pier	Maximum test loading = pile bearing capacity	Creep load $Q_c$ (kN)
		Qult (kN)	
P1	S19	4500	3200
P2	S1g - pylon	4250	3400



From the diagram shape (Figure 4 and 5) we can conclude that the piles had expected load-displacement behavior during the test. Although piles haven't expressed the collapse load from the load-displacement curve shape (Figure 4) it is clearly showed that the displacements progressively increase at small load increase (nonlinearity). Also the creep of pile at the maximum load increment was very high and it was not possible to sustain the constant load.

## 5 DYNAMIC PILE LOAD TESTING (PDA)

Dynamic pile load testing procedure, accompanied by an instrument, "Pile Driving Analyzer" (PDA), was analyzed with computer program "CAPWAP" and used to determine the static bearing capacity of piles.

### 5.1 Energy input system

For energy input for performance of dynamic load test, we used a special designed structure with the 12 tons weight. Maximum free fall of weight is 3 meters, Figure 8.

### 5.2 Test sequence

On pile on which the test was carried out the sensors for measuring strain and acceleration were attached, mounted axially symmetrically on each side, approx. 1,2 m under the pile head, parallel to the pile axis. Two acceleration gauges, and four strain gauges were used. For each pile three weight blows were recorded. Permanent pile displacement after each blow was geodetically measured and had a value of 1-4 mm per blow.



Figure 8 Dynamic pile load testing on the test field P2

### 5.3 Analysis and test results

After dynamic load test derived analogue load and displacement data are digitized for computer analysis of the IBM-PC computer program CAPWAP (CAPWAP® - GRL Engineers, Inc. Copyright©1997-2006 Pile Dynamics, Inc. USA), which base is wave equation. Pile and ground model we represent with one of the measured curves, and with iterations (changing pile and ground models) we look for the best overlap of the measured and calculated curves. When we achieve a satisfactory overlap of the curves, soil properties of model and ultimate bearing capacity of tested pile are known. Gradual loading so obtained pile and ground model (computer simulation of static pile load test) we get graphically display of the load-displacement for the tested pile (Figure 9 and 10). The end result is the ultimate bearing capacity of test pile.

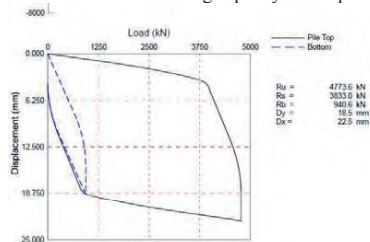


Figure 9 Load-displacement diagram for pile head on test field P1

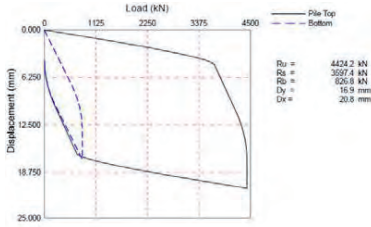


Figure 10 Load-displacement diagram for pile head on test field P2

Table 3 Results of dynamic pile load testing

Test field	Ru (kN)		Rb (kN)
	Total bearing capacity	Rs (kN) Shaft resistance	
P1	4773	3833	940
P2	4424	3597	827

## 6 CONCLUSION

By comparing the pile bearing capacities of the static and dynamic pile load testing, excellent matching is observed. The PDA test gives about 5% higher values. It can also be observed that the ratio of shaft and pile base resistance calculated and from PDA test is very similar ( $Q_b/Q_{tot} \approx 15\%$ ,  $R_b/R_u \approx 18\%$ ). PDA results are encouraging and suggest that the relatively expensive and complicated static test can be replaced with a larger number of PDA tests that can be done quickly and easily. During the test, piles had expected load-displacement behavior. The tested pile bearing capacities,  $Q_{ult}$ , are 21% and 15% higher than the calculated values,  $Q_{tot}$ . Deviations of calculated pile bearing capacities from tested values of 20% in the geotechnical practice are considered excellent.

Table 4 Results of calculated, static and dynamic pile tested bearing capacities

Pier	Pile bearing capacity assessment ( $\beta$ method) Qult (kN)	Static test bearing capacity (kN)	Static test creep load (kN)	Dynamic test bearing capacity (kN)
		Qc	Qc	Ru
S19	3678	4 500	3 200	4773
S1g - pylon	3678	4 250	3 400	4424

## ACKNOWLEDGEMENT

The authors are grateful to colleagues in geotechnical design department of Institute IGH especially Mr. Krešimir Bolanča who was designer of this project and provided measured data and constructive discussions.

## REFERENCES

- [1] EN 1997-1:2004
- [2] Main geotechnical design of bridge over river Drava, ZOP: A05-1/2-GP/0, design number: 74000-733-2011, map G-12-1, march 2011. designer: Krešimir Bolanča, Msc Eng (C.E.)
- [3] Suggested method ISSMGE, Subcommittee on Field and Laboratory Testing: „Axial Pile Loading Test-Part 1: Static Loading“, Geotechnical Testing Journal, GTJODJ, Vol. 8, No 2, June 1985, pp.79-90.
- [4] Structure design and program for pile loading test – baranjska side, design number.: 74000-799-2011, July 2011., designer: Krešimir Bolanča, Msc Eng (C.E.)
- [5] ASTM D 4945-96 – Standard Test Method for High-Strain Dynamic Testing of Piles.
- [6] Reese, L.C., Isenhower, W.M., Wang, S.T. 2006. Analysis and design of shallow and deep foundations. John Wiley&Sons, N.Y. USA
- [7] M. Bustamante & L. Ganeselli, Pile bearing capacity prediction by means of static penetrometer CPT, Proceedings of the Second European Symposium on Penetration Testing / Amsterdam / May 1982.

# Behavior of soil-structure interface under cyclic loading with large number of cycles

Suriyavut PRA-AI<sup>1</sup>, Marc Boulon

*Laboratoire 3S-R, Universités de Grenoble BP 53 38041 Grenoble cedex 9 France*

## ABSTRACT

The aim of this paper is to present a series of cyclic direct shear tests on sand (Fontainebleau)/rough material interfaces under constant normal load (CNL) and constant normal stiffness (CNS) conditions. These tests simulate the situation along the shaft of piles subjected to a large number of cycles due to environmental or anthropic loadings. These cycles (typically  $10^4$ ) which are small (10 and 20 kPa in terms of shear stress) as the service loads are not supposed to produce an early rupture. It is demonstrated that the influence of interface behavior depends on the sand compaction, initial normal stress, normal stiffness and the position of the "center of cycles" in the stress plane. The existence of dilative or contractive behavior is exhibited according to the characteristic state developed by Luong (1980). For future numerical simulations by the FEM these tests will be interpreted and formulated in a visco-plastic framework, the number of cycles being a fictitious time. This work belongs to the National French Project SOLCYP.

Keywords: Direct shear tests, granular soil-structure interface, cyclic loading, mean cyclic path, large number of small cycles, characteristic state

## 1 INTRODUCTION

The action of cyclic loadings on foundations, including piles and micro piles, remains a subject to study, or at least to improve, in geotechnical field. We often talk about this degradation of shaft friction, although we know that the friction coefficient of soil-structure interface varies little. This degradation mechanism should actually be related to variations in normal stress pile-soil,

even for a small number of cycles (Boulon and Foray, 1986). The problem of soil subjected to cyclic loading has been the subject of numerous publications. One of the most recent studies (Wichtmann, 2005) is mentioned. Soil-structure interfaces have so far been well studied in the laboratory for a few cycles, typically  $10^2$  (Desai et al, 1985; Al-Douri and Poulos, 1991; Tabucanon et al, 1995; Fakharian and Evgin, 1997; Mortara et al, 2002). Modeling cyclic loading is

---

<sup>1</sup> Corresponding Author. Laboratoire 3S-R, Universités de Grenoble, BP 53 38401 Grenoble cedex 9 France  
e-mail: suriyavut.pra\_ai@hmg.inpg.fr

also plentiful enough for soil-structure interfaces (Desai and Nagaraj, 1988; Aubry et al, 1990; Boulon and Jarzebowski, 1991; Shahrouz and Rezaie, 2002; Mortara et al, 2002). But cyclic loading on soil-structure interfaces and model pile tests have been relatively little studied in the laboratory and in situ for large numbers of cycles, because of the cumbersome testing (Boulon and Puech, 1984).

The study presented here provides some of experimental results from a series of direct shear tests of sand and rough structure in the SOLCYP (ANR and National Program) project. It is about large number of small cycles corresponding to, for example, loads in the vicinity of offshore pile foundations or wind turbines.

## 2 EXPERIMENTAL DEVICE

The test machine is a modified Casagrande shear box as shown in Figure 1. The first modification consisted in replacing  $\frac{1}{2}$  lower half box by a rough metallic plate (2). The generating engine (1) is employed to apply the normal load and normal displacement on the interface. The operation of this generating engine is controlled by a computer to impose a constant normal stress or constant stiffness conditions. It consists in controlling the variations of the normal stress  $\sigma_n$  to normal relative displacement  $[u]$  according to the relation;

$$C = \Delta\sigma_n - k\Delta[u] = 0 \quad (1)$$

Possible paths of direct shear according to value of  $k$  are :

- Case I.  $k = 0$  ; constant normal stress
- Case II.  $k = \infty$  ; constant volume
- Case III.  $k > 0$  ; constant normal stiffness

The measured and recorded variables are the stress vector applied to the interface (normal,  $\sigma_n$  ( $>0$  in compression) and shear,  $\tau$  components, resolution 0.5 kPa) and the relative displacement vector on soil-structure (components normal  $[u]$  ( $>0$  dilating) and tangential  $[w]$ ).

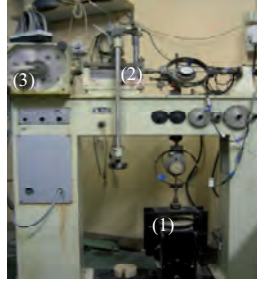


Figure 1. Dispositif experimental

The motor-reducer (3) generating the shear stress is also controlled by computer system. In the case of cyclic tests, two thresholds (high and low, adjustable) shear stress are prescribed, causing a reversal of shear direction when they are reached. The selected speed of shearing is of 0.5 mm/minute (pseudo-static range). During shearing, the set (1) where  $k$  is the imposed normal stiffness is applied with a precision of 0.1 kPa. This makes it possible to follow the path of direct shear the most general. The  $\frac{1}{2}$  box containing the soil has a diameter of 6 cm.

## 3 MATERIALS

One material, standard Fontainebleau sand, is used in this study. The important physical characteristics are summarized in Table 1. This sand was tested for density index  $I_D = 30\%$  (loose state) and  $I_D = 90\%$  (dense state).

The rough plates used in this study were made by gluing on a steel plate 1 cm thick layer of 0.2 mm from a mixture of araldite and Fontainebleau sand (30 g of araldite per 100 g of sand), this method then represents a high roughness.

Table 1. Physical characteristics of the Fontainebleau sand

$d_{50}$ (mm)	$\gamma_d^{\max}$ ( $\text{kN/m}^3$ )	$\gamma_d^{\min}$ ( $\text{kN/m}^3$ )	$e_{\max}$	$e_{\min}$	$C_u$ ( $d_{60}/d_{10}$ )
0.23	16.856	13.916	0.868	0.542	1.72

#### 4 EXPECTED RESULTS

In order to formulate the results of this test campaign in a visco-plastic constitutive model in which the number of cycles is a fictitious time, and the mean path during cycles interests us more than the detail of each cycle. We set all the tests at  $N = 10^4$  cycles, at least if the failure is not reached before this objective. Moreover, as indicated above, the cycles are carried out between two shear stress thresholds. The data aimed in these dry tests, i.e. completely drained tests, are the mean cyclic or irreversible relative displacements as well as the interface stiffness modification, and finally the interface resistance modification during the cycles. The interface variables are defined (Figure 2) as:

- $\delta_p$  and  $\delta_{crit}$  respectively the peak and critical friction angle (resistance),  $\eta_p$  and  $\eta_{crit}$  the corresponding stress ratio ( $\eta = \tau/\sigma_n$ );
- $\delta_{car}$  ( $0 < \delta_{car} < \delta_{crit} < \delta_p$ ) the characteristic angle of soil-structure interface (separating cyclic contracting and dilating domains);
- $\sigma_{n\,cm}$  and  $\tau_{cm}$  respectively the level of mean cyclic normal and shear stress,  $\eta_{cm}$  the corresponding stress ratio;

$$\eta_{cm} = \tau_{cm} / \sigma_{n\,cm} = \tan(\delta_{cm}) \quad (2)$$

- $\Delta\tau_c$  the amplitude of the cycles in terms of shear stress, the amplitude of stress ratio;

$$\Delta\eta_c = \Delta\tau_c / \sigma_{n\,cm} \quad (3)$$

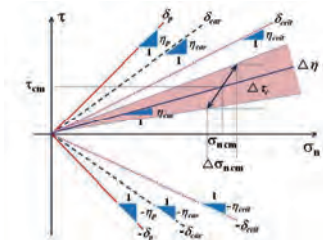


Figure 2. Characterization of the implemented cycles

The expected results are: mean cyclic tangential  $[w]_{cm}$  (4) and mean cyclic normal  $[u]_{cm}$  (5) relative displacement, the normal  $k_n$  (6) and tangential  $k_t$  (7) stiffness of the interface, the inter-

face resistance  $\delta_i$  (8), and additionally the granulometry of the interface zone

$$[w]_{cm} = [w]_{cm}(I_D, \sigma_{n\,cm}, \eta_{cm}, \Delta\eta, N) \quad (4)$$

$$[u]_{cm} = [u]_{cm}(I_D, \sigma_{n\,cm}, \eta_{cm}, \Delta\eta, N) \quad (5)$$

$$k_n = k_n(I_D, \sigma_{n\,cm}, \eta_{cm}, \Delta\eta, N) \quad (6)$$

$$k_t = k_t(I_D, \sigma_{n\,cm}, \eta_{cm}, \Delta\eta, N) \quad (7)$$

$$\delta_p = \delta_p(I_D, \sigma_{n\,cm}, \eta_{cm}, \Delta\eta, N) \quad (8)$$

#### 5 OPERATING MODE AND EXPERIMENTAL BIAS

The operating mode follows from the data requirements outlined in the previous paragraph, but induces experimental bias inherent in the direct shear test, because testing is never ideal, and therefore not fully compliant with the wishes of the operator.

##### 5.1 Operating mode

Taking into account the collection of expected information (§ 4), the test procedure consists of 5 consecutive phases:

- Phase 1: monotonic compression since the neutral state until  $\sigma_{n\,cm}$ .
- Phase 2: monotonic shearing until  $\tau_{cm}$ .
- Phase 3:  $N$  cycles of small amplitude of controlled shear stress  $\Delta\tau_c$ .
- Phase 4: one cycle of shear to failure in order to characterize the change of interface resistance ( $\delta_p$ ) due to cycles.
- Phase 5: discharge in normal stress until  $\sigma_n = 0$ .

##### 5.2 Experimental bias

The rough plates (paragraph 3) have roughness amplitude of about 0.2 mm. So that the upper half shear box does not rub directly on the rough plate, a spacing of 0.3 mm created by a pair of brass foil was arranged between the plate and the  $\frac{1}{2}$  box during the construction of the sand sample to the desired density. A continuous measurement of the level of the box was also recorded for all purposes by using LVDT. Thus a certain "loss of sand" took place during the test between

the 1/2 box and the rough plate, equivalent to contraction interference. This loss of material, very small, was measured at end of test. But this loss also occurred during phase 4. Consequently, tests without phase 4 were carried out to specifically isolate the loss due to the cycles. Correction  $[u]_{cm}$  is systematically applied to unrefined results.

## 6 TEST RESULTS

A test program conceived according to the philosophy of the experimental design has been decided, and encouraging preliminary results already exist.

### 6.1 Testing program

These tests are classified into two groups for two purposes: identification, CNL (constant normal stress) tests, (Table 2) and validation of constitutive law, CNS (constant normal stiffness) tests, (Table 3). All tests are planned to  $10^4$  cycles, unless early termination occurs ( $\eta_{cm}$  close to  $\eta_p$ ).

Table 2. Tests for identification<sup>2</sup>, CNL path, parameters

$I_D$	$\sigma_{n,cm}$ (kPa)	$\eta_{cm}$	$\Delta\tau_c$ (kPa)
30%	60	0 (L)	10, 20
90%	120	1/2 $\eta_p$ (M)	10, 20
	310	$\approx 9/10 \eta_p$ (H)	10, 20

Table 3. Tests for validation, CNS path, parameters

$I_D$	Path	$\sigma_{n,cm}$ (kPa) $\eta_{cm}$	$\Delta\tau_c$ (kPa)
30%	1000(kN/mm)	100, 1/2 $\eta_p$	10, 20
90%		100, 2/3 $\eta_p$	10, 20
	2000(kN/mm)	100, 1/2 $\eta_p$	10
		100, 2/3 $\eta_p$	10
	5000(kN/mm)	100, 1/2 $\eta_p$	10, 20
		100, 2/3 $\eta_p$	10, 20

<sup>2</sup> Test code: No1 XY No2; where No1 =  $\Delta\tau$  (kPa), X = L (loose) or D (dense), Y = L (low) or M (medium) or H (high) value of  $\eta_{cm}$ , No2 = level of normal stress (kPa).

### 6.2 Summary of results

For CNL tests, when subjected to the cyclic loading, the structure of sand-structure interface varies as a result of the progressive densification due to cycles. Figures 3 and 4 show respectively the typical results of mean cyclic normal  $[u]_{cm}$  and tangential  $[w]_{cm}$  relative displacements, in dependence on the number of cycles, for two distinct levels of initial normal stress,  $\sigma_{n,cm}$  (60 and 300 kPa), and 3 levels of stress ratio,  $\eta_{cm}$  or  $\delta_{cm}$  (0, 1/2 $\eta_p$ , 9/10 $\eta_p$ ) on both densities ( $I_D = 30\%$  and 90%), with a cyclic amplitude ( $\Delta\tau$ ) of 10 and 20 kPa.

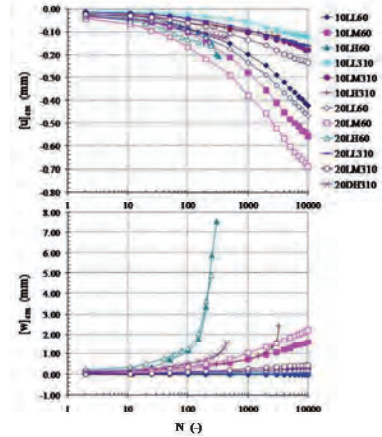


Figure 3. Evolution of  $[u]_{cm}$  and  $[w]_{cm}$  depending on the number of cycles (N), CNL,  $I_D = 30\%$ ,  $\Delta\tau = 10$  and 20 kPa

For loose sand as for dense sand, an exponential acceleration of  $[w]_{cm}$  when  $\eta_{cm}$  tends towards  $\eta_p$  can be observed. The interface is always contractive at low density. On the other hand, for high density, the existence of the characteristic state developed by Luong (1980) (separating the contractive and dilative behavior) was obvious. A dilative behavior occurred at  $\eta_{cm} = 9/10\eta_p$  in the domain between  $\eta_{car}$  and  $\eta_p$ . The rate of  $[u]_{cm}$  and  $[w]_{cm}$  increased with increasing the cyclic amplitude. The interface underwent the gradual contraction with an increasing function of cyclic

amplitude ( $\Delta\tau$ ) within the range of  $\eta_{cm} < \eta_{car}$ . In case of  $\eta_{cm}$  close to  $\eta_p$ , the number of cycles for reaching the failure decreased with increasing the cyclic amplitude.

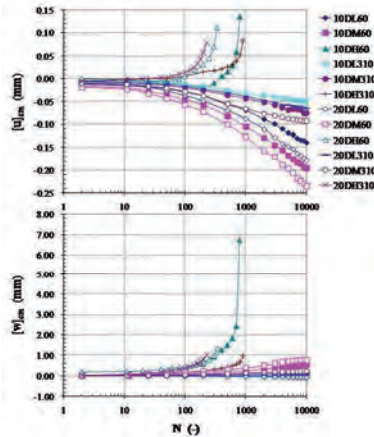


Figure 4. Evolution of  $[u]_{cm}$  and  $[w]_{cm}$  depending on the number of cycles ( $N$ ), CNS,  $I_D = 90\%$ ,  $\Delta\tau = 10$  and  $20$  kPa

An important feature of this study is to observe the behavior of interface in cyclic CNS condition. The constant normal stiffness is one of the factors influencing the behavior of interfaces. This series was carried out from  $\sigma_{n\ cm0} = 100$  kPa. The main effect observed in this series is a significant degradation of normal stress as a result of more progressive contraction accompanied with  $N$  leading to the critical state easily. Figure 5 shows the effect of the normal stiffness leading to the degradation of normal stress on dense sand. It can also be observed that a great number of cycles, in this case  $N = 4858$  for  $k = 2000$  kPa/mm and  $30 < \tau_{cm} < 40$  kPa, are necessary to reach the critical condition. Table 4 shows the influence of  $k$ ,  $\eta_{cm}$  and  $\Delta\tau$  on the number of cycles for reaching the critical state.

While the mean shear stress was kept constant during cyclic loading under CNS condition, the normal stress decreased as a function of  $N$  and  $[w]$  then the stress state evolved towards the

critical line. An increase of  $\eta_{cm}$  resulted in less number of cycles for reaching the critical condition. This is due to the stress state of high  $\eta_{cm}$  which is close to  $\eta_{crit}$  at the beginning of cyclic loading moves towards critical state earlier than that of low  $\eta_{cm}$ .

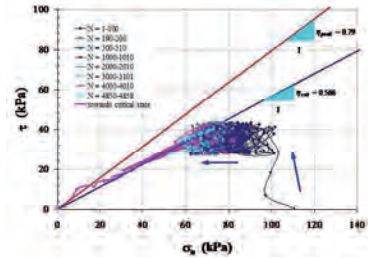


Figure 5. Stress path in  $\tau$ - $\sigma_n$  plane, CNS,  $k = 2000$  kPa/mm,  $\sigma_{n\ cm0} = 100$  kPa,  $I_D = 90\%$ ,  $\Delta\tau = 10$  kPa,  $30 < \tau_{cm} < 40$  kPa

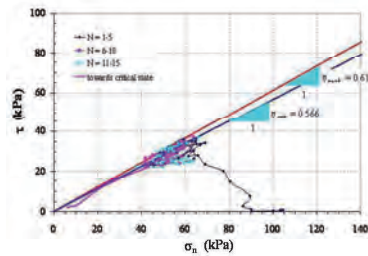


Figure 6. Stress path in  $\tau$ - $\sigma_n$  plane, CNS,  $k = 1000$  kPa/mm,  $\sigma_{n\ cm0} = 100$  kPa,  $I_D = 30\%$ ,  $\Delta\tau = 10$  kPa,  $25 < \tau_{cm} < 35$  kPa

This degradation of normal stress was very significant on loose sand as represented by Figure 6 and 7. Obviously at high value of  $k$ , in this case  $k = 5000$  kPa/mm, and the amplitude of cycle  $\Delta\tau = 10$  kPa ( $5 < \tau_{cm} < 25$  kPa), the mean normal stress dropped rapidly during the first cycles (from 100 to 50 kPa) and the stress state therefore reached the critical condition with only two cycles (Figure 7).

Table 4. Number of cycles ( $N_{crit}$ ) and  $\sigma_{n,crit}$  for reaching the critical state in cyclic CNS tests,  $\sigma_{n,crit} = 100$  kPa

$I_D$ (%)	$k$ (kPa/mm)	$\eta_{cm}$ (-)	$\Delta\tau$ (kPa)	$\sigma_{n,crit}$ (kPa)	$N_{crit}$
90	1000	0.30	10	70	11970
		0.50	10	98	3990
	2000	0.30	20	77	3630
		0.50	10	92	2550
	5000	0.30	10	65	1660
		0.30	20	70	1175
30	1000	0.30	10	57	15
		0.30	20	55	2
	2000	0.20	10	36	5
		0.15	10	24	6
	5000	0.15	10	24	6
		0.15	20	37	2

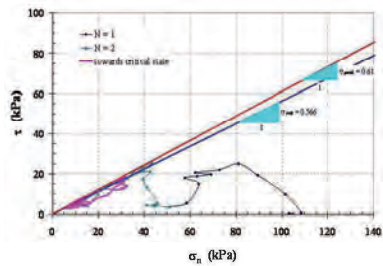


Figure 7. Stress path in  $\tau$ - $\sigma_n$  plane, CNS,  $k = 5000$  kPa/mm,  $\sigma_{n,crit} = 100$  kPa,  $I_D = 30\%$ ,  $\Delta\tau = 10$  kPa,  $S < \tau_{cm} < 25$  kPa

## 7 DISCUSSION AND CONCLUSION

This article presents some results of a series of consistent cyclic direct shear tests granular soil (Fontainebleau sand)-structure (metal), and the beginning of their interpretation, to model the behavior of cyclically loaded piles in very large numbers of cycles. Contraction and dilation phases have been well identified, depending on the position of the cycle in terms of stress. It remains to formulate all of these properties.

## ACKNOWLEDGEMENT

This research is conducted within the framework of the ANR SOLCYP, driven by IREX. The au-

thors warmly thank to the persons in charge of this action for their support.

## REFERENCES

- [1] Al-Douri R. H. and Poulos H. G., Static and cyclic shear tests on carbonate sands, *ASTM GTJ* **15(2)** (1991), 138-157.
- [2] Aubry D., Modaressi A. and Modaressi H., A constitutive model for cyclic behaviour of interfaces with variable dilatancy, *Computers and Geotechnics*. **9(1-2)** (1990), 47-58.
- [3] Boulon M. and Puech A., Simulation numérique du comportement des pieux sous chargement axial cyclique, *Revue Française de Géotechnique* **26** (1984), 7-20.
- [4] Boulon M. and Foray P., Physical and numerical simulations of lateral shaft friction along offshore piles in sand, *3<sup>rd</sup> Int. Conf. On Numerical Methods in offshore piling, Nantes* (1986), 127-147.
- [5] Boulon M. and Jarzabowski A., Rate type and elastoplastic approaches for soil-structure interface behaviour: a comparison, *Proc. 7<sup>th</sup> Int. Conf. IACMAG, Cairns, Australia* (1991), 305-310.
- [6] Desai C. S., Drumm E. C. and Zaman M. M., Cyclic testing and modeling of interfaces, *ASCE JGE* **111(6)** (1985), 793-815.
- [7] Desai C. S. and Nagaraj B. K., Modeling for cyclic normal and shear behavior of interfaces, *ASCE JGE* **114(7)** (1988), 1198-1217.
- [8] Fakharian K. and Evgin E., Cyclic simple shear behaviour of sand-steel interfaces under constant normal stiffness condition, *ASCE JGGE* **123(12)** (1997), 1096-1105.
- [9] Mortara G., Boulon M. and Ghionna V. (2002), A 2-D constitutive model for cyclic interface behaviour, *International Journal for Numerical and Analytical Methods in Geomechanics* **26** (2002), 1071-1096.
- [10] Luong MP, Stress-strain aspects of cohesionless soils under cyclic and transient loading, *International Symposium on Soils under Cyclic and Transient Loading, Swansea, 7-11 January, Pande GN, Zienkiewicz OC (eds) 1980*; 315-324.
- [11] Shahrouf I. and Rezaie F., An elastoplastic constitutive relation for soil-structure interface under cyclic loading, *Computers and Geotechnics* **52(1)** (2002), 41-50.
- [12] Tabucanan J. T., Airey D. W. and Poulos H. G., Pile skin friction in sand from constant normal stiffness tests, *ASTM GTJ* **18(3)** (1995), 350-364.
- [13] Wichtmann T, *Explicit accumulation model for non cohesive soils under cyclic loading*, Dissertation, Ruhr Universität Bochum, Allemagne 2005, 274 pages.



# Effect of creep on the stability of leaning towers

Michela Marchi<sup>1</sup>

*University of Bologna, Bologna, Italy*

## ABSTRACT

Safety assessment of historical towers is an important challenge in the preservation of the national and worldwide artistic heritage. This paper illustrates a novel unified methodology developed to evaluate the key phenomena governing the geotechnically related collapse of towers: bearing capacity failure, due to lack of strength of the supporting soil, instability of equilibrium, due to lack of foundation stiffness and a rotational creep process. The analysis, introduced in the framework of a strain-hardening plasticity model for shallow footings, shows that rotational creep is the main cause of the progressive deterioration of stability for real towers. The proposed analytical process is applied to the history of the Santo Stefano bell tower in Venice. This example demonstrates not only the potential of the proposed methodology but also the importance of past rotational records for the prediction of the eventual response of such a tower.

Keywords: bearing capacity, creep, footings/foundations; soil/structure interaction, stability, towers

## 1 INTRODUCTION

It is rather common whilst travelling or simply walking around a town, especially an Italian one, to notice an ancient tower and not infrequently the inclination of the structure may appear to be dangerous. A considerable number of structural configurations (Figure 1) have arisen as a consequence of the great variety of purposes served by them (bell towers, civic towers, chimneys, watch towers in city walls, etc.). In many cases they became distinctive features of their historical centers (e.g. Pisa, Bologna, Venezia, etc.), so that evaluation of the overall safety of historical tow-

ers is an important challenge in the preservation of the national and worldwide artistic heritage. In the analysis of such towers both structural and foundation behaviors are areas where our understanding needs to be improved.



Figure 1. Bologna, full of towers (by G. Rivani-La Mercanzia-1954 [1]).

<sup>1</sup> DICAM - University of Bologna, Viale Risorgimento 2 - 40136 BOLOGNA – ITALY, e-mail: michela.marchi@unibo.it

The role of geotechnical engineering in this framework is relevant, not only for the definition of possible failure mechanisms of tower foundations, but also for prediction of the creep (tilting) rate of the structure. In fact, progressive increase of tilting can produce high compressive stresses in the masonry, and consequent structural failure (Heyman [2], Federico *et al.* [3]). Ancient towers, in the presence of weakened and disconnected masonry, can also suffer catastrophic failure even with very little tilting, as attested by the sudden collapse of many masonry towers (e.g. San Marco bell tower in Venice, in 1902 [4]). This hazard is not considered in the paper, although it emphasizes the fundamental importance of the tilting rate prediction for the long-term safety of towers.

## 2 FAILURE MECHANISMS OF LEANING TOWERS

### 2.1 Theoretical framework: the macroelement models for shallow foundations

Historical tower foundations are usually shallow. Strain-hardening plasticity models – developed in relation to the overall soil – footing system (i.e. the so-called ‘macro-element’ models) enable us to define the strength and stiffness of such foundations, starting from a vertical load – penetration curve ([5]-[7]). The two major, geotechnically related, failure modes of tower foundations are: (a) bearing capacity failure, due to lack of strength of the supporting soil; and (b) instability of equilibrium, due to lack of foundation stiffness. Marchi *et al.* [8] suggested tackling both these hazards, usually treated separately, in a unified way, using such models.

The long-term process that may lead towers into such failure conditions is, essentially, the foundation creep (rotational in particular). The inclusion of creep phenomena into these model formulations was introduced for the first time by Marchi *et al.* [8], specifically in relation to the study of leaning towers. The general methodology is presented in the following sections.

### 2.2 Stability of equilibrium

The stability of equilibrium, a soil– structure interaction problem, can be tackled in different ways, depending on the model assumed for the connection between soil and structure: elastic models (Habib & Puyo [9], Hambly [10], Lancellotta [11]), have been progressively extended to elasto-plastic support, which enables irreversible and non-linear soil behaviour to be considered (Desideri & Viggiani [12], Federico *et al.* [3] and Marchi *et al.* [8]). In stability of equilibrium analyses the tower is usually represented by a uniform rigid bar, resting on a support at which the deformability of the system is concentrated). The problem is sketched in Figure 2, where  $W$  is the weight of the tower,  $h$  the height of the centre of gravity,  $\theta$  the rotation from the vertical position and  $\theta_0$  the initial imperfection of the structure. The equilibrium condition imposes the external moment ( $M_e = W \cdot h \sin \theta$ , for small rotations  $\approx W \cdot h \cdot \theta$ ) equal to the resisting moment ( $M_r$ , also called rotational stiffness of the tower) generated by the foundation:

$$W \cdot h \cdot \theta = M_r \quad (1)$$

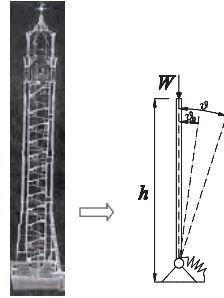


Figure 2. Modelling of a real tower as rigid bar column with flexible support:  $\theta$  is the total rotation and  $\theta_0$  the initial inclination of the column from vertical position.

The resisting moment  $M_r$ , a function of the rotation of the tower relative to the initial tilt  $\Delta\theta = (\theta - \theta_0)$ , can be established using strain-hardening plasticity models for shallow founda-

tions. Such models provide consistent predictions of the displacements generated by vertical, horizontal and moment loads applied to a shallow foundation using the vertical load – penetration curve as the basic hardening function.

The stability analysis, assuming an elastoplastic – and consequently load-path dependent – soil model, is best presented in the  $M - \theta$  plane. Plotting  $M_e$  and  $M_r$  together, as first suggested by Cheney *et al.* [13], Equation (1) is satisfied when the line ( $M_e$ ) intersects the curve ( $M_r$ ), defining the stable and unstable equilibrium conditions (respectively point  $E_0$  and point  $E_1$  in Figure 3). The definition of the critical equilibrium condition then depends on the way the creep phenomena are modelled.

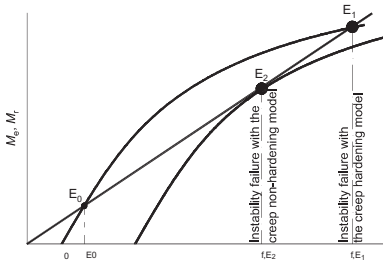


Figure 3. Stability of equilibrium failure prediction via conventional non-hardening and hardening rotational creep models for a tower (from Marchi *et al.* [8]).

### 2.2.1 Effect of creep on the stability of towers

Stability failure can be assessed, following Cheney *et al.* [13] via a non-hardening creep model. In this simplified creep interpretation, the shape of the  $M_r$  curve is not affected by creep deformation and it merely translates along the  $\theta$  axis (progressive tilting due to creep is analogous to an increase of initial rotation  $\theta_0$ ). Instability failure occurs at  $E_2$  when  $M_r$  and  $M_e$  paths become tangent. Assuming an hardening model, such as the one integrated directly into the ‘macro-element’ models by Marchi *et al.* [8], the relevant rotational stiffness to be considered for equilibrium of the tower is the rotational unload–reload stiffness of the soil – foundation system. The predicted value of  $\theta$  at which the tower col-

lapses, the critical equilibrium condition, is shown by point  $E_1$  in Figure 3. Since the creep rate will accelerate rapidly as failure is approached, the time ratio increase in the lifetime of the tower deduced from the alternative analyses will be much less than the rotation ratio shown in Figure 3.

### 2.3 Bearing capacity

It is well known that bearing-capacity of foundations subjected to combined loads can be predicted by means of interaction diagrams [14]. This approach generated a number of strain-hardening plasticity models ([15], [5], [6]), formulated in terms of force resultants ( $V$ ,  $M/2R$ ,  $H$ ), and corresponding displacements of the footing ( $w$ ,  $\theta$ ,  $u$ ). Where  $R$  is the radius of the foundation,  $V$ ,  $H$  and  $M$  are the vertical, horizontal and moment load components,  $w$  and  $u$  the vertical and horizontal displacements and  $\theta$  the rotation of the foundation. For a simple bearing capacity analysis, knowledge of the failure envelope (existing only for brittle bearing capacity failure) is sufficient to define the failure load conditions. The bearing capacity prediction for the relevant load path of a tower ( $V=W$ , with  $W$  tower weight, and increasing  $M$ ) is shown in Figure 4. If punching failure is expected, this is the most likely outcome for ancient towers in long term conditions, no specific failure envelope exists and stability of equilibrium failure is the only possible collapse mechanism of the foundation.

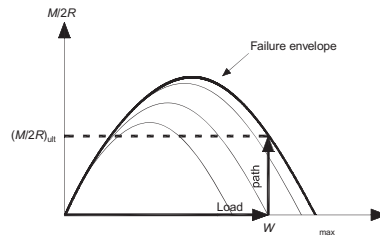


Figure 4. Bearing capacity analysis for a tower foundation subjected to its typical load path (from Marchi *et al.* [8]).

## 2.4 Combination of failure modes

The ultimate moment ( $M_{ult}$  in Figure 5) of the foundation, in the case of brittle bearing capacity failure, locates in the  $M - \theta$  plane the critical value of rotation ( $\theta$ ) at which bearing capacity failure will occur (point B in Figure 5). Combining the bearing capacity and stability of equilibrium failure predictions in this way, the most probable failure mechanism is identified. If punching failure is expected, then the tower will not collapse until the stability failure point E (defined by a non-hardening creep model - Figure 5) is reached.

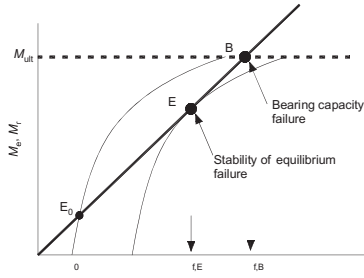


Figure 5. Stability of equilibrium against brittle bearing capacity failure in the  $M - \theta$  plane.

## 3 CREEP RATE PREDICTION OF LEANING TOWERS

Creep is the main cause of the progressive deterioration of stability for real towers.

A rotational creep function (introduced by Marchi *et al* [8]), governing the rate at which post-construction rotation increases (triggered by  $\theta_0$ ), is:

$$\theta(t) = \left[ \ln \left( 1 + \frac{t}{t_0} \right) - c \ln \left( 1 - \frac{t-t_2}{t_1} \right) U(t-t_2) \right] + \theta_0 \quad (2)$$

where  $\theta_0$  is the initial imperfection of the structure,  $t_0$  a time-scaling factor with the same units as  $t$ ,  $c$  a parameter to be determined by the field

data and  $t_1$  predicts the tower collapse at  $t_3 = (t_1 + t_2)$ .  $U(t-t_2)$  is a 'unit step function', equal to 0 for  $(t-t_2) < 0$  and 1 for  $(t-t_2) \geq 0$ . In addition,  $t_2$  is the time at which tilt and the consequent moment load increase rapidly to failure (also called "tertiary creep"). It is reasonable to assume that such a process could start when the inclination of the tower becomes large enough for the unloaded edge of its base to begin to lose contact with the ground, nominally, for a squared base, when the load eccentricity becomes one third of its breadth. After this point is reached, the effective area of the foundation will reduce progressively with increasing rotation. The form of Equation (2) is illustrated in Figure 6 for  $t_0 = 1$  year,  $t_1 = 300$  years,  $t_2 = 700$  years (hence  $t_3 = 1000$  years),  $c = 1$  and  $\theta_0 = 1^\circ$ .

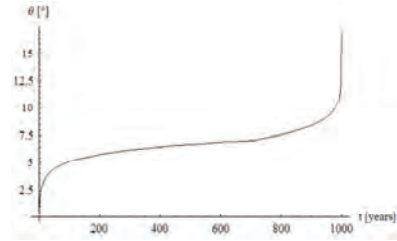


Figure 6. Trend of Equation 2 for generic parameters.

## 4 THE SANTO STEFANO BELL TOWER IN VENICE

The Santo Stefano bell tower (Figure 7), in Venice, is an interesting case study because of the considerable rotation it has undergone over the centuries. Construction of the tower began in 1450. When it had reached a height of 27 m work stopped, due to the evident rotation. Work recommenced nearly 100 years later, in about 1550. The vertical axis of the bell tower is not straight because the masonry walls were built vertically in the second stage of construction, in an attempt to correct the lean. The height of the building from its foundations to the belfry is c.62 m and the foundation has an external width of 9 m. The first record of leaning, dated 1774, was

measured as horizontal displacement of 0.8 m at the level of the belfry towards the east side, along which a little canal (“Rio Malatin”) flows. Later on, in 1900, the rate of such movement was 7 mm per year, which led to a deviation from vertical of up to 1.7 m, also measured at the level of the belfry. After the collapse of the San Marco bell tower, in 1902, a strengthening intervention with buttresses on piles (shown in Figure 7) was carried out [16]. The aim of the following analysis is to predict what would have happened if the intervention had not been done.

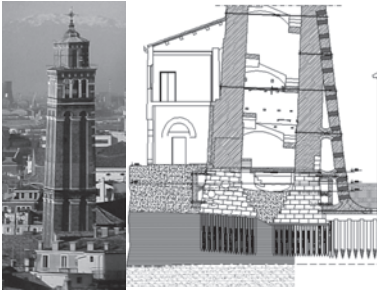


Figure 7. Picture of the Santo Stefano Bell Tower and schematic section of the tower foundation with buttresses built in 1903.

#### 4.1 Stability and strength analysis

The strain hardening plastic soil model described in Marchi [17] has been applied to the Santo Stefano bell tower. The general tower properties required in order to develop the analysis are: weight of the tower,  $W = 35$  MN; foundation width,  $2R = 9$  m; height of the centre of gravity,  $h = 25$  m; foundation embedment,  $d = 2.7$  m; and depth of the water table below ground level,  $h_w = 1$  m. The mean soil properties are: effective shear strength angle,  $\phi' = 27^\circ$  and saturated soil unit weight,  $\gamma_{\text{sat}} = 20$  kN/m<sup>3</sup>; the parameter  $V_{\text{max}} = 68$  MN, defining the plastic potential  $g$  in [17], can be estimated as the long-term, vertical, central load-bearing capacity of the foundation. The input hardening law, which predicts the vertical plastic displacement under a vertical central load, derived using oedometer data, is:

$$V_0 = 109(1 - e^{-0.5v_p}) \quad (3)$$

The complete output of such model provides the  $M$ - $\theta$  curve and the vertical settlement of the foundation for the specific load path, characterized by the application of the weight of the tower (at constant null moment) followed by moment increments ( $\delta M = W \cdot h \cdot \delta \theta$ ) under constant vertical load  $V=W$ . The long-term footing response of the Santo Stefano bell tower is a punching behaviour, thus excluding the possibility that bearing capacity failure might occur first.

The basic stability of equilibrium diagram of the tower, incorporating the calculated  $M$ - $\theta$  curve (assuming  $\theta_0 = 0.1^\circ$ ) and the  $M_e$  line, is shown in Figure 8. The known rotation of the tower before the beginning of stabilisation work in 1903 was about  $2.2^\circ$ , which corresponds to an external moment of about 36 MN m, and establishes point C in Figure 8. Excluding the effect of any remedial measures, a stability failure by way of the conventional non-hardening creep model suggested by Cheney *et al.* [13] (i.e. tangency of the  $M$ - $\theta$  curve to the external moment line at point  $E_2$ ) is then predicted to occur with  $\theta$  about  $2.6^\circ$ , which correspond to the tower rotation at present. On the other hand, the stability analysis by way of the creep-hardening model establishes the stability failure point ( $E_1$ ) at about  $3.9^\circ$ .

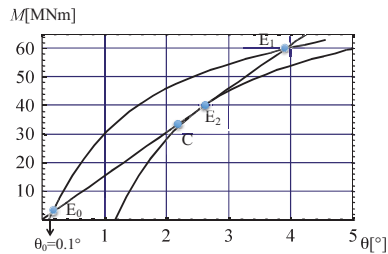


Figure 8. Stability analysis of Santo Stefano bell tower via conventional and creep-hardening models.

#### 4.2 Creep rate analysis

In order to develop a creep rate analysis of the tower (for its situation before the intervention) using Equation (2) historical rotation data have

been collected. The record of the inclination is shown by points in Figure 9 (rotation in 2002 is only a reference value and is not considered in the calibration of the model). The thick line shows the inclination predicted by Equation (2) using  $t_0 = 21$  years,  $t_1 = 75$  years,  $t_2 = 525$  years (hence  $t_3 = 600$  years),  $c = 0,15$  and  $\theta_0 = 0.1^\circ$ . The  $t=0$  datum was set at 1750 and the onset of tertiary creep was assumed to occur in 2275, in fact, at  $\theta \approx 3.4^\circ$  the tower will be about to lose contact with the ground.

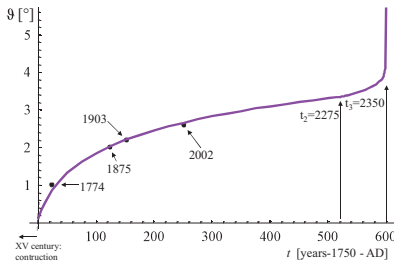


Figure 9. Santo Stefano bell tower field data compared with creep-hardening model prediction.

## 5 CONCLUSIONS

This paper describes how the two major, geotechnically related, collapse mechanisms of tower foundations - bearing capacity, due to lack of soil strength, and instability of equilibrium, due to lack of soil stiffness, and a rotational creep process can be effectively included in the framework of a strain-hardening plasticity model for shallow footings. Such an analysis has been presented in the paper for the case history of the Santo Stefano bell tower in Venice. The analysis shows that before the strengthening intervention of 1903 the tower was starting to approach a stability of equilibrium failure.

It is important to note that rotational creep analysis has to be calibrated using historical rotation measurements for each specific tower. For many towers the lack of records of tilting is a big impediment to any analysis. Installation of modern monitoring systems for tilt-rate recording is

of primary importance for risk assessment of such structures. Unfortunately, such records need to be made over a long period of time before they become useful.

## REFERENCES

- [1] F. Giordano, *La torre Garisenda*, Costa Editore, Bologna, 2000 (In Italian).
- [2] J. Heyman, (1992). Leaning Towers. *Meccanica*, 27(3), 153–159.
- [3] F. Federico, S. Ferlisi & R. Jappelli (2001). Safety evolution of masonry leaning towers on deformable soils. Proc. 15th Int. Conf. Soil Mech. Geotech. Engng, Istanbul 1, 679 – 682.
- [4] A. Croce (1985). Old monuments and cities: research and preservation. AGI: geotechnical engineering in Italy: an overview, Published on the occasion of ISSMFE Golden Jubilee.
- [5] G. Gottardi, G.T. Houlsby & R. Butterfield (1999). The plastic response of circular footings on sand under general planar loading. *Géotechnique*, 49(4), 453-470.
- [6] G.T. Houlsby, M.J. Cassidy (2002). A plasticity model for the behaviour of footing on sand under combined loading. *Géotechnique*, 52(2), 117-129.
- [7] M.F. Randolph, M.J. Cassidy, S. Gourvenec & C. Erbrich (2005). Challenges of offshore geotechnical engineering. Proc. XVI Int. Conf. Soil Mech. Geotech. Eng., ICSMGE, Osaka, Japan, vol. 1, 123-176.
- [8] M. Marchi, R. Butterfield, G. Gottardi, & R. Lancellotta (2011). Stability and strength analysis of leaning towers. *Géotechnique*, 61(12), 1069–1079.
- [9] P. Habib & A. Puyo (1970). Stabilité des fondations des constructions de grande hauteur. Ann. ITBTP 275, 117–124 (in French).
- [10] E. C. Hambly (1985). Soil buckling and the leaning instability of tall structures. *The Structural Engineer* 63A(3), 77–85.
- [11] R. Lancellotta (1993). Stability of a rigid column with non-linear restraint. *Géotechnique* 43(2), 331–332.
- [12] A. Desideri & C. Viggiani (1994). Some remarks on the stability of towers. Proceedings of the symposium on developments in geotechnical engineering, Bangkok, 457–468.
- [13] J. Cheney, A. Abghari, & B. L. Kutter (1991). Stability of leaning towers. *J. Geotech. Geoenviron. Engng ASCE* 117(2), 297-318.
- [14] G. Gottardi & R. Butterfield (1993). On the bearing capacity of surface footings on sand under general planar load. *Soils and Foundations*, 33(3), 68-79.
- [15] R. Nova & L. Montrasio (1991). Settlements of shallow foundations on sand. *Géotechnique* 41(2), 243–256.
- [16] M. Marchi, R. Butterfield, G. Gottardi, & A. Zervos (2008). On the stability of Santo Stefano bell tower in Venice. ICOF, Dundee, Scotland, UK, IHS BRE Press, vol. 2, 1581–1592.
- [17] M. Marchi (2008). *Stability and strength analysis of leaning towers*. PhD thesis, University of Parma, Italy.

# The influence of the load eccentricity on the magnitude of the initial critical pressure of the foundation soil

Florin BEJAN<sup>1</sup>

*Department of Roads, Railways, Bridges and Foundations, Faculty of Civil Engineering and Building Services, Technical University "Gheorghe Asachi" Iasi, Romania*

## ABSTRACT

Using the finite element method and Stanciu's algorithm, the influence of the eccentricity of the load on the value of the initial critical pressure ( $p_{cr.in}$ ) was analyzed. The Mohr-Coulomb elastic - perfectly plastic model and the Hardening Soil nonlinear elastic-plastic model were used for determining the initial critical pressure values for a series of virtual foundations subjected to loads with variable eccentricities ( $e_r=0$ ; B/24; B/12; B/8; B/6). These values were used to establish relations for the computation of the correction factors of the initial critical force ( $e_f$ ) and pressure ( $e_p$ ). Unlike the technical regulations which use a single empirical correction factor ( $m = 1.2$ ) the results enable the determination of the initial critical pressure, with values differentiated according to the value of the relative load eccentricity.

Keywords: foundations, bearing capacity, initial critical pressure, load eccentricity, finite element method

## 1 INTRODUCTION

Shallow foundation design must be done in such a way that limit states are prevented. According to EN 1990 and EN 1997 a foundation subjected to different actions must comply with requirements of the Ultimate Limit States (ULS) and of the Serviceability Limit States (SLS). For SLSs it is necessary to calculate the foundation settlements.

For this it is necessary to calculate the stress distribution in soil due to transmission of loads by foundations. Solutions recommended by Annex F are based on the elasticity theory. According to F2, section (4) of Annex F the methods based on elasticity theory should be used only if

the stresses in the ground are such that no significant yielding occurs and if the stress-strain behavior of the ground may be considered to be linear. Therefore the initial critical pressure is a limiting pressure for a certain development of plastic zones at which the solutions of elasticity theory may be applicable [1] [2]. This acceptable pressure can be determined using the Pigeau (1921) - Puzirevski (1929) - Ghersevanov (1930) - Fröhlich's (1934) theory ( $p_{acc}=p_{cr.in}$ ) [1][2][3].

These relationships are valid for strip foundations subjected to vertical centric loads. In reality, at the foundations level appear bending moments that are induced by the horizontal loads (earth pressure, wind pressure, seismic forces, hydrostatic pressure, etc.). In this case some

<sup>1</sup> Florin Bejan, Eng. PhD student, Technical University "Gheorghe Asachi" Iasi, Faculty of Civil Engineering and Building Services, Department of Roads, Railways, Bridges and Foundations, 43 D. Mangeron, +40.232.278.683. Email: [bejanflorin85@yahoo.com](mailto:bejanflorin85@yahoo.com)

technical regulations [4] [5] propose the multiplication of the initial critical pressure with a dimensionless coefficient with the value of 1.2.

Prof. A. Stanciu established an original algorithm (Hooke model) that determined numerically the initial critical pressure coefficients for foundations subjected by eccentric inclined loads [6]. This algorithm does not consider the influence of the coexistence of elastic and plastic zones within the soil over the stress state.

The yielding under the footing (Fig. 1) begins at low values of the load and it is dependent on the type of soil and also the foundation depth. For foundations located on sand the yielding begins when the load is applied. Finite element method (FEM) can be used to determine with significant accuracy the development of plastic zones in the soil for a certain value of the load. However, FEM is an elaborated and sophisticated method which requires time and experience. Therefore, FEM may not be accessible to all practicing engineers. Moreover, for small or medium geotechnical works FEM is not a good economically choice. It is thus necessary for calculating precise relationships available to all engineers and practitioners.

## 2 CLASSICAL APPROACH FOR THE DETERMINATION OF THE INITIAL CRITICAL PRESSURE

Determination of the initial critical pressure for the plane problem using the relations (1) established by Pigeau – Puzirevski – Ghersevanov – Fröhlich considers that the maximum depth of the plastic zone development ( $z_{max}$ ) to be equal to 0, i.e. to exclude the development of plastic zones under the footing [1][2][3].

$$P_{cr.in.} = \frac{\pi \left( \gamma \cdot D_f + \frac{c}{\tan \varphi} \right)}{\cot \varphi + \varphi - \frac{\pi}{2}} + \gamma \cdot D_f \quad (1)$$

where,  $\gamma$  – weighted value of the soil unit weight,  $D_f$  – the foundation depth;  $\varphi$  – the internal friction angle and  $c$  – the cohesion of the soil.

Because equation (1) is not influenced by the value of the foundation width (B), although this

influences the initial critical pressure, different authors have considered different maximum depths of the plastic zone development. Thus Maslov admits a development of the plastic zones up to a maximum depth  $z_{max}=B \cdot \tan \varphi$  and Iaropolski to  $z_{max}=0,5 \cdot B \cdot \cot(45-\varphi/2)$  (Fig. 1) [3].

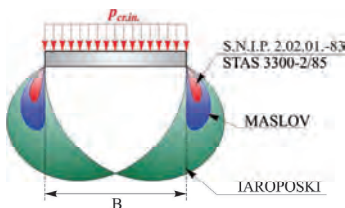


Figure 1. Development of the plastic zones according to different authors

The Romanian [4] and the Russian [5] technical regulations consider a development of the plastic zones up to a maximum depth  $z_{max}=B/4$ , resulting:

$$P_{cr.in.} = m_1 \cdot (\gamma \cdot B \cdot N_1 + q \cdot N_2 + c \cdot N_3) \quad (2)$$

where,  $m_1$  – the coefficient of working conditions;  $q$  – the overload at the footing level and laterally displayed from it ( $q=\gamma \cdot D_f$ ),  $N_1$ ,  $N_2$  and  $N_3$  – are the initial critical pressure coefficients:

$$N_1 = 0.25 \cdot \pi / \left( \cot \varphi - \frac{\pi}{2} + \varphi \right) \quad (3)$$

$$N_2 = 1 + \pi / \left( \cot \varphi - \frac{\pi}{2} + \varphi \right) \quad (4)$$

$$N_3 = \pi \cdot \cot \varphi / \left( \cot \varphi - \frac{\pi}{2} + \varphi \right) \quad (5)$$

## 3 DEFINITION OF THE PROBLEM

In this study it was analyzed the computation of the initial critical pressure of the foundation soil as a homogeneous medium under a strip foundation with width B, for eccentric vertical loading (Fig. 2). It is considered that the unit weight of the earth is  $\gamma$ , the footing is rough, the depth of foundation is  $D_f$  and the force (F) is applied with the eccentricity e.



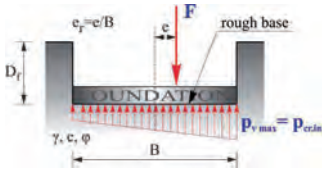


Figure 2. Strip foundation subjected to eccentric vertical load

When a load is applied eccentrically the pressure on the footing, for a linear distribution, acquires a vertical trapezoidal distribution with maximum and minimum values which are determined by relations (Fig. 2):

$$p_{vmax} = \frac{1+6 \cdot e_r}{B} \cdot F; p_{vmin} = \frac{1-6 \cdot e_r}{B} \cdot F \quad (6)$$

In this case the initial critical pressure is defined as the maximum vertical pressure corresponding to a development of plastic zone to a depth  $z_{max}=B/4$ . Also the initial critical force ( $F_{cr.in.}$ ) it is defined to be the force  $F$  which determines the development of plastic zone to a depth  $z_{max}=B/4$ .

### 3.1 Numerical modeling

To study the evolution of the plastic zone depth under eccentric loading it was used the Plaxis2D numerical analysis software. The soil was modeled using the Mohr-Coulomb linear elastic-perfectly plastic constitutive model (MC) and the Hardening Soil nonlinear elastic-plastic constitutive model (HS). In both cases it was used the same model with a triangular mesh of 15 nodes elements (Fig. 3). The action of the soil above the footing level is represented by the overload  $q = \gamma \cdot D_f$ . The force  $F$  on the foundation soil was taken into account by the effect of the trapezoidal distribution of pressure applied directly to the soil.

In the case of the MC model the value of Young modulus does not affect the initial pressure value. Also the Poisson's ratio ( $\nu=0.499$ ) it was chosen to simulate the undrained condition.

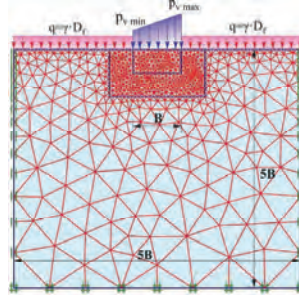


Figure 3. Half-plan under inclined loading meshed with triangular finite elements

The Hardening Soil model [7] is an advanced model of soil yielding which is based on the hyperbolic model but with some changes: primarily through the use of the theory of plasticity instead of the theory of elasticity, secondly by including the dilatancy angle of the soil ( $\psi$ ) and thirdly by including a yielding cap [8].

The basic parameters used by the HS model are the parameters corresponding to the Mohr-Coulomb model ( $c$ ,  $\phi$ , and  $\psi$ ) and in addition are used:  $E_{50}^{ref}$  the secant modulus at 50% of the failure stress and at effective reference pressure of  $p^{ref}$ ;  $E_{oed}^{ref}$  the constrained modulus at  $p^{ref}$ ;  $E_{ur}^{ref}$  the un/reloading modulus at  $p^{ref}$ ;  $\nu_{ur}$  the Poisson's ratio for un/reloading and  $m$  the power for stress-level dependency of stiffness (Fig. 4).

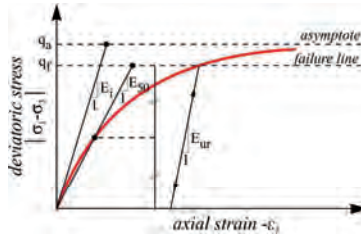


Figure 4. The hyperbolic stress strain curve for standard drained triaxial tests

### 3.2 Calibration of soil parameters

To study the influence of the stiffness parameters on the value of the initial critical pressure it was conducted a series of tests in which different parameters were varied in turn (Table 1). The characteristics of the foundation and of the soil are:  $B=1.30$  m;  $D_f=2.00$  m;  $\gamma=18.70$  kN/m<sup>3</sup>;  $\varphi=20^\circ$ ;  $c=21$  kPa. The reference stiffness parameters considered are:

$$E_{\text{ocd}}^{\text{ref}}=E_{50}^{\text{ref}}=13000 \text{ kN/m}^2; E_{\text{ur}}^{\text{ref}}=39000 \text{ kN/m}^2; \\ m=0.50; \nu_{\text{ur}}=0.20; p_{\text{ref}}=100; K_0=0.658.$$

Table 1. Variation of the soil deformability characteristics

Case	Parameter variation
FEM 1	Reference parameters
FEM 2	=FEM1, but $\nu_{\text{ur}}=0.30$
FEM 3	=FEM1, but $E_{50}^{\text{ref}}, E_{\text{ocd}}^{\text{ref}}, E_{\text{ur}}^{\text{ref}}$ increased by 20%
FEM 4	=FEM1, but $E_{\text{ur}}^{\text{ref}}$ reduced by 20%
FEM 5	=FEM1, but $E_{50}^{\text{ref}}$ increased by cu 10 %
FEM 6	=FEM1, but $E_{\text{ocd}}^{\text{ref}}$ increased by cu 10 %
FEM 7	=FEM1, but $E_{\text{ocd}}^{\text{ref}}$ increased by cu 20 %

By increasing the Poisson's ratio for un/reloading (FEM 2) the initial critical pressure decrease from 334 kPa (for  $\nu_{\text{ur}} = 0.20$ ) to 329 kPa (for  $\nu_{\text{ur}} = 0.30$ ). Proportional increase of the modulus of rigidity by 20% does not cause changes in the initial critical pressure value (FEM 3). If the value of the un/reloading modulus decreases by 20% (FEM 4), but the ratio between secant modulus and the oedometric modulus is constant, the initial critical pressure does not change.

A change is observed when the ratio between the secant modulus and the oedometric modulus is modified (Fig. 5). Thus a ratio of 1.10 (FEM 5) corresponds to a critical value of initial pressure of 323 kPa, a ratio of 0.91 (FEM 6) corresponds to the value of 344 kPa and a ratio of 0.83 (FEM 7) corresponds to the value of 357 kPa.

The results presented show that the parameters that define the deformability of the soil for Hardening Soil model has a very little influence on the initial critical pressure value. So for all

performed analysis were used the reference stiffness parameters (FEM 1).

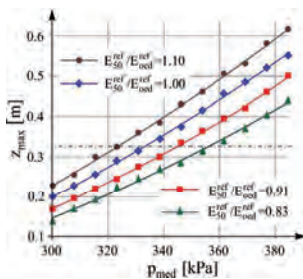


Figure 5. Variation of the maximum depth of the plastic zone development  $z_{\text{max}}$  depending on the value applied pressure  $p_{\text{med}}$  and the  $E_{50}^{\text{ref}} / E_{\text{ocd}}^{\text{ref}}$  ratio

## 4 THE INFLUENCE OF THE ECCENTRICITY OF THE LOAD ON THE MAGNITUDE OF THE INITIAL CRITICAL PRESSURE

For the determination of the initial critical pressure coefficients Stanciu's algorithm was used [6]. Therefore three strip foundations were chosen (Table 2) with different sizes located on soils with the same internal friction angle.

Table 2. Characteristics of the soil and of the foundation analyzed

Foundation name	$\gamma$ [kN/m <sup>3</sup> ]	$c$ [kPa]	$B$ [m]	$q$ [kN/m <sup>2</sup> ]
F1	18.70	21	1.30	37.40
F2	19.00	22	3.50	28.50
F3	15.80	16	6.00	35.55

Writing the equation (2) for each case it results a compatible determined system of three equations with three unknowns :

$$\begin{cases} \gamma_1 \cdot B_1 \cdot N_1 + q_1 \cdot N_2 + c_1 \cdot N_3 = p_{\text{cr.in.1}} \\ \gamma_2 \cdot B_2 \cdot N_1 + q_2 \cdot N_2 + c_2 \cdot N_3 = p_{\text{cr.in.2}} \\ \gamma_3 \cdot B_3 \cdot N_1 + q_3 \cdot N_2 + c_3 \cdot N_3 = p_{\text{cr.in.3}} \end{cases} \quad (7)$$

The values of the initial critical pressures were determined using the Plaxis software through an

$p-z_{\max}$  iteration (Fig. 5) both for MC model and the HS model. The values of the initial critical pressure coefficients for a given internal angle friction are obtained by solving the system of equations (7). Using the same procedure, the values of the initial critical pressure coefficients for each case results by changing the internal friction angle ( $\varphi=5^\circ, 10^\circ, 15^\circ, 20^\circ, 25^\circ, 30^\circ$ ) and the relative load eccentricities ( $e_r=0, 1/24, 1/12, 1/8, 1/6$ ).

#### 4.1 The correction coefficients of the initial critical pressure and force for Hooke model

The values of the initial critical pressure coefficients determined by Prof. A. Stanciu for foundations subjected to eccentric loads are represented in Fig. 6 [3] [6].

Based on these coefficients two correction factors of the initial critical pressure ( $e_p$ ) and force ( $e_f$ ) were proposed.

$$e_p = p_{cr.in}(e_r \neq 0) / p_{cr.in}(e_r = 0) \quad (8)$$

$$e_f = F_{cr.in}(e_r \neq 0) / F_{cr.in}(e_r = 0) \quad (9)$$

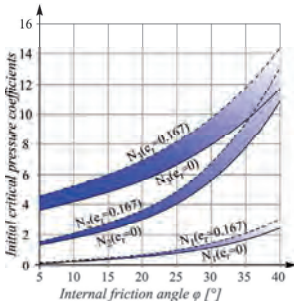


Figure 6. The initial critical pressure coefficients depending on the internal friction angle and the relative load eccentricity for Hooke model

It was noted that these factors depend only on the relative load eccentricity ( $e_r$ ). The expressions of these coefficients were obtained using the method of the least squares.

$$e_p = 1 - 3.22 \cdot e_r + 6.21 \cdot e_r^2 - 5.67 \cdot e_r^3 \quad (10)$$

$$e_f = 1 + 2.76 \cdot e_r - 12.02 \cdot e_r^2 + 21.21 \cdot e_r^3 \quad (11)$$

The  $e_p$  correction factor has values lower than one and the initial critical pressure increases by increasing the load eccentricity. The  $e_f$  correction coefficient has sub-unitary values and the initial critical force decreases by increasing the load eccentricity.

#### 4.2 The influence of the eccentricity on the magnitude of the initial critical pressure for MC model

Studies have shown that the values of the initial critical pressure determined by MC model differ slightly from those determined with Hooke model. In Figure 7 the values of the correction factors of the initial critical pressure  $e_p$  are represented for MC model.

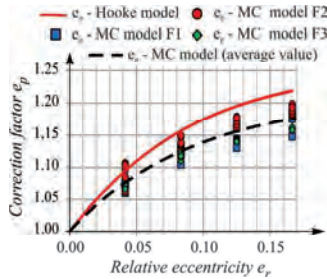


Figure 7. Variation of the correction factor  $e_p$  according to the relative load eccentricity for MC model

The average values of the correction factor  $e_p$  determined with MC model are lower than those determined with the H model.

#### 4.3 The influence of the eccentricity on the magnitude of the initial critical pressure for HS model

By using the HS model new values of the coefficients  $N_1, N_2$  and  $N_3$  were determined, leading to initial critical pressure values closer to reality, without the need for a coefficient of working conditions as when using the Hooke or Mohr-Coulomb models.

The values of the initial critical pressure determined with the HS model exceed those determined with the Hooke model (up to 75%). How-

ever, there are not significant differences in the value of the correction factors  $e_p$  (Fig. 8).

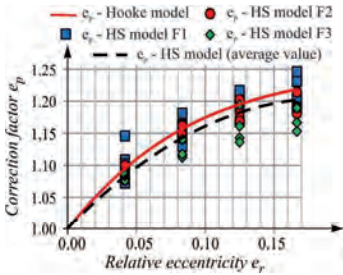


Figure 8. Variation of the correction factor  $e_p$  according to the relative load eccentricity for HS model

Differences between the minimum and maximum correction factors for both the  $e_p$  and  $e_F$  for the MC and HS models are small which allows the consideration of average values (Fig. 9)

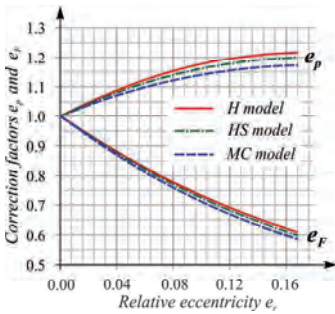


Figure 9. The correction factors  $e_p$  and  $e_F$  according to the relative load eccentricity and the constitutive model

Equations describing the variation of the  $e_p$  and  $e_F$  factors by relative eccentricity are:

$$MC \begin{cases} e_p = -0.190 \cdot e_r^2 + 2.468 \cdot e_r + 1 \\ e_F = -6.316 \cdot e_r^2 - 3.154 \cdot e_r + 1 \end{cases} \quad (12)$$

$$HS \begin{cases} e_p = -0.366 \cdot e_r^2 + 2.368 \cdot e_r + 1 \\ e_F = -3.059 \cdot e_r^2 - 3.271 \cdot e_r + 1 \end{cases} \quad (13)$$

## 5 CONCLUSIONS

In this paper it was analyzed the influence of the load eccentricity on the value of the initial critical pressure for three constitutive models: the Hooke (H) linear elastic model, the Mohr-Coulomb (MC) linear elastic-perfectly plastic model and the Hardening Soil (HS) nonlinear elastic-plastic model. Based on these analyzes, relationships for calculating the correction factors of the initial critical pressure/force have been proposed depending on the relative load eccentricity.

## ACKNOWLEDGEMENT

This paper was realized with the financial support of POSDRU CUANTUMDOC "DOCTORAL STUDIES FOR EUROPEAN PERFORMANCES IN RESEARCH AND INNOVATION" ID79407 project funded by the European Social Fund and Romanian Government.

## REFERENCES

- [1] J. Verdeyen, R. Victor and J. Nuyens, Applications de la mecanique des sols I, Dunod, Paris, 1971.
- [2] N Tsyvovich, Soil Mechanics (translated from Russian by V Afanasyev), Mir Publishers, Moscow, 1976.
- [3] A. Stanciu, I. Lungu, Fundații 1 – Fizica și mecanica pământurilor, Editura Tehnică, București, 2006.
- [4] STAS 3300/2-85, Foundation ground – Foundation analysis for shallow foundations (in Romanian), București, 1985.
- [5] S.N.I.P. 2.02.01-83, Osnovanie zdanii i sooruzenii, Moskva, 1983.
- [6] A. Stanciu, Le calcul de la pression critique initiale d'une fondation superficielle, Revue Francaise de Geotechnique, no. 67 (1994), 33-54.
- [7] T. Shanz, P.A. Vermeer and P.G. Bonnier, The hardening soil model: Formulation and verification, Computers and Geotechnics – 10 years of PLAXIS, Balkema, Rotterdam (1999).
- [8] A. Stanciu, I. Lungu and F. Bejan, Computation of the initial critical pressure based on the Hardening Soil criterion for the foundation soil: Proceedings of the international conference DEDUCON - Sustainable development in civil engineering, Iasi (2011).

# Drawing up of a geotechnical dossier for the stabilization of historical quay walls along the river Scheldt in Antwerp

Leen Vincke, Koen Haelterman  
*Geotechnics Division Flemish Government, Belgium*

[Leen.vincke@mow.vlaanderen.be](mailto:Leen.vincke@mow.vlaanderen.be)  
[Koen.haelterman@mow.vlaanderen.be](mailto:Koen.haelterman@mow.vlaanderen.be)

Reinhilde Van Hooydonck, Koen Segher  
*Waterwegen en Zeekanaal NV, Belgium*

## ABSTRACT

Within the context of the Scheldt Quays Masterplan, the stabilization of the dilapidated historical quay walls was put to study. For drawing up the geotechnical dossier all available geological and geotechnical information along the quay wall section was collected; beneficial use could be made of the Regional Database of the subsoil of Flanders (DOV). Based on this inventarisation an extensive program of in situ tests and complementary monitoring and laboratory tests was elaborated.

Analysis of the investigation data resulted in a characterisation of the soil layering and corresponding soil parameters. The schematic geotechnical profile consists of an upper layer of fill material, overlaying a dense tertiary sand layer (Berchem Formation) and the very stiff overconsolidated Boom clay.

The foundation level of the quay wall is situated just above or in the Boom clay. The excavation works for the foundation resulted therefore in a stress relief of the upper part of the clay layer. Quite rapidly after construction important horizontal deformations of the quay wall as a whole appeared. Due to this movements, design of stabilized walls should be performed on basis of residual shear strength parameters derived from direct shear tests.

To determine the water pressure distribution along the quay wall open standpipes (in the sand layers) and closed piezometers (in the Boom clay) were continually monitored and tidal variations were noted. Furthermore a long time CPTU dissipation test was performed in the Boom clay.

The extensive geotechnical design resulted in an economic and sustainable design for the stabilized quay walls.

Keywords: geotechnical investigation, Boom clay, monitoring, residual shear strength, dissipation test

## 1 INTRODUCTION

The historical quay walls along the river Scheldt in Antwerp were built late 19<sup>th</sup> century and consist of gravity walls in brickwork construction built upon steel caissons filled with concrete. Figure 1 shows a cross section of the wall.

Quite rapidly after construction important horizontal deformations of the quay wall as a whole appeared (as a result being referred to as the walking quay walls). Prop boxes placed at the toe of the gravity wall were intended to resolve

the stability problems, but didn't prove to be satisfactory.

The Scheldt Quays Masterplan generates an overall vision for the future use of these quays, also resolving specific questions of mobility and parking, with respect for the historical heritage. Within this context the stabilization of the dilapidated historical quay walls was put to study.

The total trajectory of the quay walls has a length of about 5,5 km and is divided into 6 different zones. This paper gives a description of the in situ and laboratory testing and monitoring

program for determination of the geotechnical design conditions for the stabilization study. This paper will further focus on zone 4 (Figure 2).

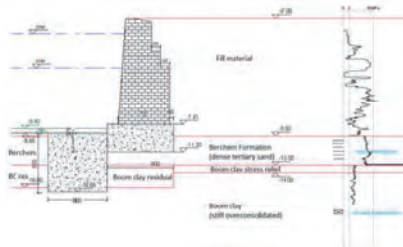


Figure 1. Cross section quay wall.



Figure 2. Trajectory quay walls- zone 4.

## 2 AVAILABLE GEOLOGICAL AND GEOTECHNICAL INFORMATION

For drawing up the geotechnical dossier all available geological and geotechnical information along the quay wall section was collected.



Figure 3. DOV-output zone 4

Beneficial use could be made of the Regional Database of the subsoil of Flanders (DOV). Figure 3 shows the DOV-output of zone 4 with all available cone penetration tests (CPT) and borings. Based on this inventarisation an extensive program of in situ tests and complementary monitoring and laboratory tests was performed [1].

## 3 GEOTECHNICAL INVESTIGATION

### 3.1 Field testing

Electrical CPT's were performed every 50m along the quay wall trajectory. Figure 4 shows a typical CPT plot. The upper layer consists of fill material (refill during the construction of the wall), overlaying a dense tertiary glauconite sand layer (Berchem Formation) and the very stiff overconsolidated Boom clay.

CPT's were also performed in cross sections perpendicular to the quay wall to determine the expanse of the fill.



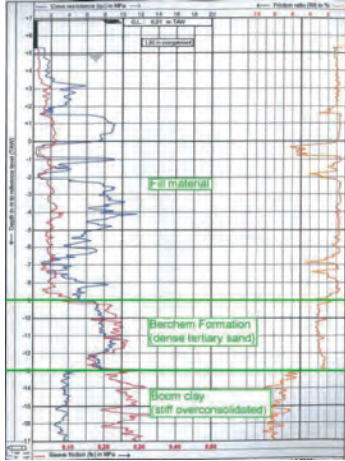


Figure 4. CPT soil profile.

The foundation level of the quay wall is situated just above or in the Boom clay (see also figure 1). The excavation works for the foundation resulted therefore in a stress relief of the upper part of the clay layer. Furthermore, due to the instability problems, the design of the stabilization should be performed on basis of residual shear strength parameters of the Boom clay. Therefore borings with discontinuous sampling were performed and undisturbed samples were taken for laboratory testing.

To determine the water pressure distribution along the quay wall, open standpipes were placed in the sand layers and closed piezometers in the Boom clay. Tidal variations became clear.

Also a long time CPTU dissipation test was performed in the Boom clay.

The results are discussed further in this paper.

### 3.2 Laboratory testing

The laboratory investigation program on the undisturbed samples focused on the determina-

tion of the geotechnical parameters of the Boom clay.

The standard laboratory tests (soil identification tests, oedometer tests, CU and UU triaxial tests) were performed on all samples.

For the Boom clay samples, additional direct shear tests, Bender element tests and falling head permeability tests were performed.

## 4 EVALUATION GEOTECHNICAL DATA

### 4.1 Geotechnical parameters Boom clay

#### 4.1.1 Shear strength

For deriving the peak values of the shear strength characteristics of the Boom clay, CU-triaxial tests were performed as follows: after applying a back-pressure of 100 kPa (for saturation), isotropic consolidation is performed with consolidation stresses calculated on the basis of a geological overburden of 90m sediment. Consolidation stresses of 1/2, 1 and 2 times the spherical effective stress are applied. Then vertical stresses are applied until failure. In figure 5 an example of a stress path is given.

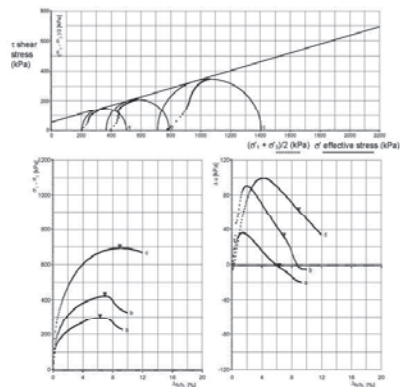


Figure 5. CU-triaxial test Boom clay.

A statistical regression analysis is performed on the CU-triaxial tests (at 95% confidence for the mean value). Figure 6 shows the p-q data plot of the Boom clay samples of zone 4 at maximum deviatoric stress. Only the samples in the relevant stress area were considered.

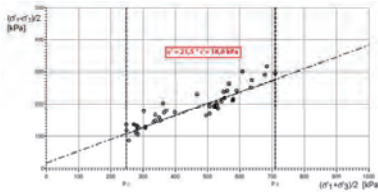


Figure 6. Regression analysis peak Boom clay

The upper part of the clay layer was subjected to a stress relief due to the excavation works for the foundation of the quay wall. In the CPT profiles, this stress relief is indicated by the lower cone resistances in the upper first meter of the Boom clay. Due to the limited thickness of this upper layer not enough samples were available to perform a regression analysis. Therefore, a rule of thumb was used to set the shear strength parameters, namely a halving of the cohesion value with unchanging shearing angle.

To determine the residual shear strength parameters, direct shear tests were performed. Figure 7 shows a typical graph. Residual shear stress was derived at a horizontal displacement of 7 mm (where the curve stays flat behind the peak in all direct shear tests).

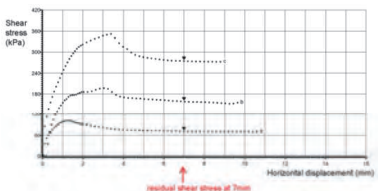


Figure 7. Direct shear test Boom clay.

In figure 8 the residual shear stress was plotted against the vertical confining stress. The value  $\phi' = 15^\circ$  proposed by De Beer seems to be a good assumption for the friction angle of residual Boom clay [2]. Because of the large number of tests, a mean value is acceptable.

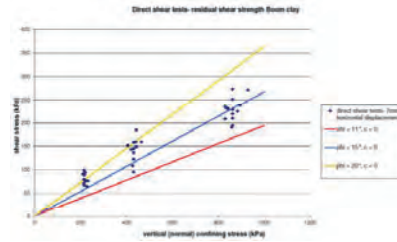


Figure 8. Shear strength parameters Boom clay.

#### 4.1.2 Stiffness moduli

The small strain shear modulus  $G_0$  was derived from Bender element tests. In figure 9  $G_0$  is plotted against the confining stress.



Figure 9.  $G_0$ -values from Bender element tests Boom clay.

The oedometer modulus  $E_{\text{ced}}$  was derived from the consolidation tests. In figure 10 the results are plotted against the depth (mTAW). Via the Poisson's ratio  $\nu$ , the Young's modulus can be calculated. In the finite element calculations (Plaxis) the following values were used:

$$E_{\text{ref}} = 9000 \text{ kN/m}^2 ; E_{\text{inc}} = 400 \text{ kN/m}^2/\text{m}$$



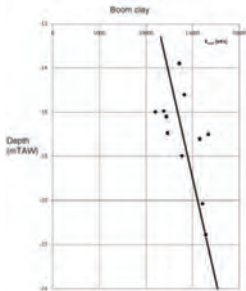


Figure 10.  $E_{0ed}$  from compression test Boom clay.

#### 4.2 Waterpressure distribution

The waterpressure distribution around the quay wall is depending on the tidal variations in the river Scheldt. Because of the importance of importing the right water pressures in the calculations of the stabilization design, an extensive monitoring program was executed.

In the boreholes, performed just behind the quay wall, closed piezometers were installed in the Boom clay.

In different boreholes open standpipes were placed, equipped with divers (data logger for automatic continuous measurement of water pressure). Open standpipes were placed in the tertiary sand layer and in the upper fill material. A diver data logger on the riverside of the quay wall was to monitor the water level in the river Scheldt at the same location.

Figure 11 shows the diurnal variation of measured water levels.

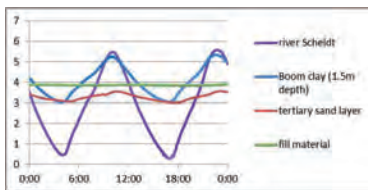


Figure 11. Measured water levels (just behind the quay wall).

The following conclusions can be drawn concerning the water levels just behind the quay wall:

- The phreatic level in the fill material shows little variations due to the tide in the river Scheldt
- The tidal variations in the tertiary sand layer amount to about 1m max
- The closed piezometers in the Boom clay show tidal variations up to 2m.

Furthermore a long time CPTU dissipation test was performed (just behind the quay wall) at different depths in the Boom clay. Figure 12 shows pore pressure against time in the Boom clay. The river level was also plotted in the graph and we can conclude that there is no time delay between high tide and rise in the pore water pressure of the Boom clay. The tidal variations are like an overburden for the nearly impermeable Boom clay. Due to the short time span, all tidal variations are transferred to the pore water pressure.

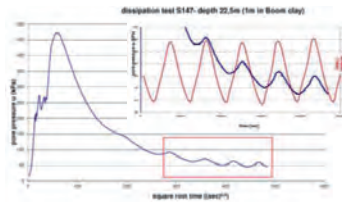


Figure 12. Long term CPTU dissipation test Boom clay.

To determine the water pressure distribution in front of and under the quay wall, a fully coupled stress/pore pressure analysis using Sigma/w-modeling was performed and the calculated water levels behind the quay wall were checked with the measured values [3]. Figure 13 shows the calculated water level. A good correspondence was found (compare to figure 11).

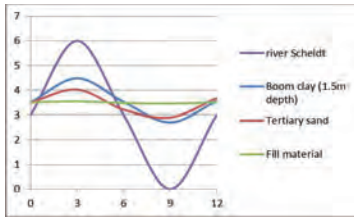


Figure 13. Calculated water levels just behind the quay wall.

Thanks to the monitoring and the Sigma/W-modeling, a clear understanding of the water pressure distribution in the different soil layers was obtained. Figure 14 and 15 show the distribution at high water, respectively low water level.

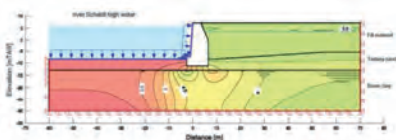


Figure 14. Sigma/W model high water.

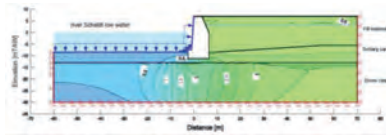


Figure 15. Sigma/W model low water.

## 5 STABILIZATION DESIGN

The stabilization calculations are finished for zone 4. Stabilization of the quay walls will be accomplished by injection of the cavities in the masonry, placing cross screens underneath the foundation caisson by VHP-grouting and drilling grout anchors (see figure 16).

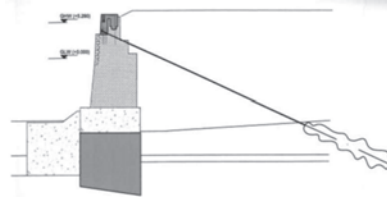


Figure 16. Stabilization design.

The stabilisation of a first section of the quay walls will start soon.

## 6 CONCLUSIONS

An extensive geotechnical investigation program (which includes in situ tests, laboratory tests and monitoring) was elaborated with emphasis on the geotechnical parameters of the Boom clay and the water pressure distribution around the quay wall.

This resulted in an economic and sustainable design for the stabilized quay walls.

## ACKNOWLEDGEMENT

Our acknowledgements go to the Geotechnical Consultant SBE and Technum- Tractebel Engineering for their input in evaluating the geotechnical tests and for calculating the stabilization design.

## REFERENCES

- [1] Geotechnics division Flemish Government, *several reports on geotechnical testing and monitoring*.
- [2] De Beer E., Shear strength characteristics of the Boom clay, *Proceedings of the Geotechnical Conference Oslo 1967*, Vol. 1.
- [3] Feremans G. & Laemont A. 2010 *Rekennota D1-004-C Verificatieberekeningen technische deelstudie stabilisering kaaimuren en ontwerp bijkomende waterkering voor de Scheldekaaien te Antwerpen*, 2010.

# Seismic Performance of Caisson Supported Structures

A. Zafeirakos<sup>1</sup>

National Technical University of Athens, Greece

## ABSTRACT

A numerical study of a 3D nonlinear soil-foundation-structure system is performed under the prism of a new "capacity design" principle, in which soil "failure" mechanisms are deliberately mobilized to protect the superstructure. For caisson supported systems this involves material and geometric nonlinearities such as soil inelasticity, separation (gapping) between the caisson and the soil, slippage at the soil-caisson interface, base uplifting, and perhaps even loss of soil strength (e.g. due to development of excess pore water pressures). To investigate the effectiveness of such an approach, simple structures of varying deck mass, simulating heavily or lightly loaded structures founded through similar rigid cubic caissons on a 2-layer soil stratum are used as examples. Two alternatives are compared: one complying with conventional capacity design, with over-designed foundation so that the soil is marginally plastified (the plastic hinge on the column); the second design follows the new approach in which the foundation is under-designed, thereby "inviting" the plastic "hinge" below ground surface. The comparison is performed through Incremental Dynamic Analysis (IDA), where the alternatives are subjected to several ground motion records, each scaled to multiple levels of intensity. IDA curves are produced for a variety of intensity and damage parameters describing both the maximum and the residual response of the system. The results emphasize the beneficial role of foundation nonlinearities on reducing the seismic demands of the superstructure.

Keywords: Caisson foundations, Dynamic soil-structure interaction, Soil and interface nonlinearities, Incremental Dynamic Analysis (IDA), Engineering Demand Parameters (EDP)

## 1 INTRODUCTION

The seismic design of structures is based on capacity design approaches, where the structural response is presumed ductile. The concept of ductility design for foundation elements is still new in earthquake engineering practice. In essence, the capacity design methodology explicitly considers the problem of determining the failure mechanism of structural members and

ensures that regions of inelastic deformation are carefully detailed to provide adequate structural ductility, without transforming the structure into a mechanism. Elastic response of the foundation is usually ensured by increasing the structural strength of the foundation so that plastic hinging occurs in the superstructure instead of the foundation. The possibility of *soil yielding*, denoting the non-linear inelastic soil response without necessarily resulting in bearing-capacity failure,

---

<sup>1</sup> National Technical University of Athens, School of Civil Engineering, Geotechnical Dept., 9, Iroon Polytechniou str., 157 80 Zografou, Athens, Greece. azafeirakos@yahoo.com

is forbidden in existing regulations, codes and specifications. In simple geotechnical terms, the designer must ensure that the foundation system will not even reach a number of “thresholds” that would conventionally imply failure. For the case of deep caisson foundations, this indicates that passive and shear failure along the sides and the base is prohibited, introducing appropriate “overstrength” factors plus factors of safety larger than 1 against each “failure” mode, as in static design. Although such a restriction may, at first, appear reasonable (the inspection and rehabilitation of foundation damage after a strong earthquake is not a trivial task), it may lead to *unconservative* oversimplifications, especially in strong earthquake loading where geometric nonlinearities and soil inelasticity are usually unavoidable (separation (gapping) between the caisson shaft and the soil, slippage at the soil-caisson shaft interface, base uplifting). Therefore neglecting such phenomena prohibits the exploitation of strongly non-linear energy dissipating mechanisms in defense of the superstructure in case of occurrence of ground motions larger than design. In fact, recent research on surface foundations suggests that soil compliance and subsequent soil–foundation plastic yielding may be beneficial, and should be considered in the analysis and perhaps allowed in the design [e.g. 2, 3, 4].

In this framework, the present study aims to investigate the effectiveness of the new capacity design (compared to conventional capacity design) of caisson supported structures, through 3-D *Incremental Dynamic Analysis* (7). IDA is a powerful tool to assess the global and local capacity of structures, by subjecting the soil-structural model to several ground motion records, each scaled to multiple levels of intensity, providing thus useful inputs for applications of performance-based evaluation. The comparison is performed between structures founded on similar caissons, while varying the mass and the height of the superstructure. In total, the response of four (4) idealized configurations is studied: (a) two corresponding to a conventionally and an un-conventionally designed foundation resulting from a “heavy” superstructure (safety factor for static loading  $FS_V = 2.5$ ), and (b) two corre-

sponding to a conventionally and an un-conventionally designed caisson resulting from a “light” superstructure (safety factor for static loading  $FS_V = 5$ ).

## 2 PROBLEM DEFINITION AND ANALYSIS METHODOLOGY

### 2.1 Problem definition

The studied problem is portrayed in Figure 1: A mass-and-column structure is founded through a rigid cubic caisson of side  $h = 10$  m in a 20 m thick 2-layer cohesive soil stratum. The soil is considered to be undrained with  $S_u = 65$  kPa at the upper 6 m and  $S_u = 130$  kPa at the lower 14 m. The mass-and-column superstructures are modeled as SDOF oscillators. The mass of the deck,  $m$ , is given parametrically the values of 5400 and 2700 Mg, corresponding to a static factor of safety  $FS_V = 2.5$  (“heavy” superstructure) and  $FS_V = 5$  (“light” superstructure) respectively. The alternative design approaches, conventional and un-conventional for each case of  $FS_V$ , are represented by two different column heights. In total, a set of four structural configurations are analysed.

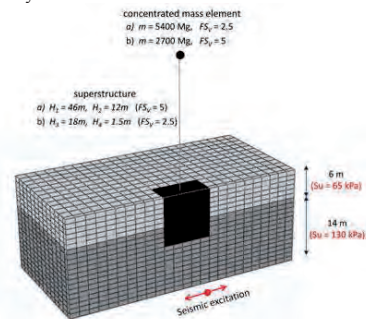


Figure 1. Overview of the 3D Finite Element model used in the analysis.

The height of the superstructure is calculated from static pushover analysis, so that it deliber-

ately matches a "target" critical (yielding) acceleration ( $\mathbf{a}_{c,f}$ ) associated with bearing capacity of the foundation. Structural yielding is then either prevented (un-conventional design) or pursued (conventional design) by designing the superstructure for a critical acceleration ratio  $\frac{\mathbf{a}_{c,f}}{\mathbf{a}_{c, \text{str}}} < 1$

or  $\frac{\mathbf{a}_{c,f}}{\mathbf{a}_{c, \text{str}}} > 1$  respectively, where  $\mathbf{a}_{c, \text{str}}$  is the critical-at yield-spectral acceleration of the superstructure.

Since the superstructure is modeled as SDOF oscillator, the horizontal force at the top of the caisson is related to the overturning moment at failure according to:  $M = m \cdot \mathbf{a}_{c, \text{str}} \cdot H$ . To compare the seismic performance of the two alternative design schemes on a 'fair' basis, the critical acceleration ratio,  $\mathbf{r}_{\text{max}}$ , defined as:

$$\mathbf{r}_{\text{max}} = \frac{\max\{\mathbf{a}_{c,f}, \mathbf{a}_{c, \text{str}}\}}{\min\{\mathbf{a}_{c,f}, \mathbf{a}_{c, \text{str}}\}} \quad (1)$$

is kept constant for all cases considered, and deliberately set equal to 2.67. Assuming  $\mathbf{a}_{c,f} = 0.3 \text{ g}$  for the un-conventional design, condition (1) leads to  $\mathbf{a}_{c, \text{str}} = 0.8 \text{ g}$ . Likewise, assuming  $\mathbf{a}_{c,f} = 0.8 \text{ g}$  for the conventional design, condition (1) leads to  $\mathbf{a}_{c, \text{str}} = 0.3 \text{ g}$ . The four model configurations are summarized in Table 1:

## 2.2 Numerical and constitutive modeling

The problem is analysed with the use of the finite element code ABAQUS. Both caisson and soil are modeled with 3D 8-noded solid elements, assuming elastic behavior for the former and nonlinear for the latter. The superstructure is modeled with 3D nonlinear Timoshenko beam elements. The caisson is connected to the soil with special contact surfaces, allowing for realistic simulation of the possible detachment and sliding at the soil-caisson interfaces. The soil stratum reaches 10 m deeper than the caisson base, thus having a negligible influence on the response. To ensure uniform stress distribution at the head of the caisson, the nodes of the associated elements are tied through appropriate kinematic constraints. For the total stress analysis under undrained conditions, soil behavior is

modeled through a nonlinear constitutive model (5) which is a slight modification of a model incorporated in ABAQUS. It uses the Von Mises failure criterion with yield stress  $\sigma_y$  related to the undrained shear strength  $S_u$  as

$$\sigma_y = \sqrt{3} S_u \quad (2)$$

along with a nonlinear kinematic and isotropic hardening law, and an associative plastic flow rule. The model parameters are calibrated to fit published  $G-\gamma$  curves of the literature. Rayleigh damping, representing material damping, is taken equal to 5% between the eigenfrequency of the soil deposit and the dominant frequency of the earthquake ground motion. Appropriate kinematic constraints are imposed to the lateral edges of the model, allowing it to move as the free-field (6).

The nonlinear behavior of the superstructures is described by a simple hyperbolic backbone curve in moment ( $M$ )–curvature ( $k$ ) space, defined as:

$$k = \frac{M_y}{EI} \left( \frac{M}{M_y - M} \right) \quad (3)$$

where  $EI$  the initial structural bending stiffness, calculated from the geometric characteristics of each cross section and the elastic properties of the reinforced concrete, and  $M_y$  the ultimate strength associated with the critical acceleration ( $\mathbf{a}_{c, \text{str}}$ ).

Table 1. Summary of the model configurations used in the analyses

	<b>m</b> (Mg)	<b>H</b> (m)	<b>ac</b> : critical spectral acceleration	Design paradigm
model 1	2700	46	0.3g (foundation) 0.8g (superstructure)	under- designed foundation
model 2	2700	12	0.8g (foundation) 0.3g (superstructure)	over- designed foundation
model 3	5400	18	0.3g (foundation) 0.8g (superstructure)	under- designed foundation
model 4	5400	1.5	0.8g (foundation) 0.3g (superstructure)	over- designed foundation

### 3 INCREMENTAL DYNAMIC ANALYSIS

Incremental Dynamic Analysis (IDA) is a powerful analysis method that offers thorough seismic demand and capacity prediction capability [7]. It involves a series of nonlinear dynamic analyses time-history analyses under suitable scaling, aiming at covering the entire range of response, from elasticity to collapse., selecting proper Engineering Demand Parameters (EDPs) to characterize the structural response and an Intensity Measure (IM) to represent the seismic intensity. The output of an IDA is an IDA curve, i.e. a plot of a selected IM versus a selected EDP. Similarly, an IDA curve set is a collection of IDA curves of the same structural model under different records that have been parameterized on the same IM.

#### 3.1 Intensity measure and Earthquake Demand Parameters

Different options are available for the IM to be used in the IDA curves. In this paper, however, a single IM is used, and in particular the PGA calculated at the free-field (top of soil profile). Though the PGA is not the most representative IM, it is preferred among others due to the inherent difficulty in determining a priori the IM at the surface for a given input acceleration time history. Without any doubt, the PGA is the most suitable IM to be approximately estimated through 1-D deconvolution analysis.

Selecting an EDP is application-specific. In this paper two EDPs are considered, which are known to relate well to structural performance and global dynamic instability:

- The maximum ductility demand of the soil–caisson–structure system:  $\max\{\mu_s\}$ , defined as the ratio of the maximum displacement of the system  $\mathbf{u}_{\max}$ , imposed by an earthquake, to the yield displacement  $\mathbf{u}_y$ , which is a soil–caisson–structure system property:

$$\mu_s = \frac{u_{\max}^{\text{mass}} - \left[ u_{\max}^{\text{structure base}} + \theta \cdot H \right]}{u_y} \quad (4)$$

where  $\theta$  is the caisson rotation and  $H$  the structure height. The yield displacement  $\mathbf{u}_y$  is assessed through static push-over analyses of the alternatives, according to the N2 method of Eurocode 8 [1].

- The maximum caisson rotation,  $\theta_{\max}$

#### 3.2 Record suite

An ensemble of 10 records has been chosen as base excitation. The selected records, presented in Figure 2, cover a wide range of seismic motions, ranging from medium intensity (e.g. Kalamata, Aegion) to relatively stronger (e.g. Lefkada-2003, Imperial Valley), and to very strong accelerograms characterized by forward-rupture directivity effects, or large number of significant cycles, or fling-step effects (e.g. Takatori, JMA, TCU).

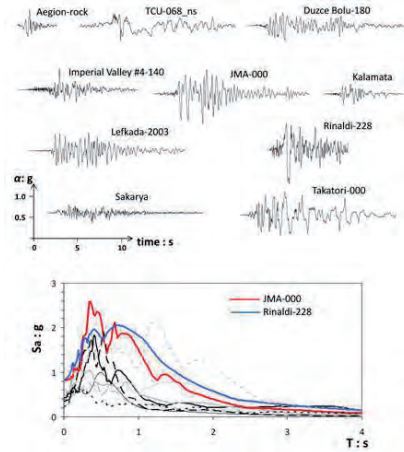


Figure 2. Real earthquake records used for analysis of the design alternatives, along with their elastic spectra.

In this work, the seismic records are appropriately scaled so that 5 ascending target PGA values of free-field motion, namely 0.1 g, 0.2 g, 0.3 g, 0.4 g and 0.6 g, are calculated at the top of the soil profile through 1-D deconvolution analysis.

Obviously, since IDA involves nonlinear wave propagation, the actual computed PGA from each scaled record will differ from the targeted one. The reason for examining PGA values smaller than 0.6 g lies in the shear strength of the soil. Stronger signals would produce intense soil yielding which, in turn, would either significantly attenuate the transmitted seismic waves or even leading to bearing capacity failure.

#### 4 ANALYSIS RESULTS AND DISCUSSION

The comparison of the performance of the design alternatives through the IDA curves generated from the analysis results is presented in Figures 3 – 5 for the two most representative cases: *model 1*, lightly loaded *under*-designed foundation and *model 4*, heavily loaded over-designed foundation. The IDA curves for the systems' maximum displacement ductility demand ( $\mu$ ), associated with structural distress, are portrayed in Figure 3. Undoubtedly, the most advantageous design alternative concerning structural demand is the *under*-designed lightly loaded *model 1*, exhibiting ductility demands  $\mu \leq 0.45$  for most of the seismic motions, while the heavily loaded over-designed *model 4* exhibits  $\mu \geq 3.0$ : a clear evidence of beneficial effect from mobilizing substantial geometric nonlinearities.

Figure 4 presents the IDA curves for maximum caisson rotation,  $\theta_{max}$ . The performance of the two alternative design schemes does not seem to deviate from any rational intuitive expectation: the *under*-designed system demonstrates substantially larger rotations than the over-designed counterpart, as a result of the intense caisson-soil interface separation and gapping. Notice the tremendous demand imposed by the large velocity pulse (2.6 m/s) of huge duration (6.3 s) of the TCU-068 record on the *under*-designed alternative, causing global instability and system failure of the lightly loaded *model 1* at PGA = 7 m/s<sup>2</sup>. Nevertheless, it is remarkable that with the exception of the performance under the TCU record at high PGA levels, these alternative can avoid collapse sustaining rather toler-

able rotations and displacements. Furthermore, it should be stated at this point that in the conventional design the developed drift is mainly due to flexural distortion, leading to a subsequent increase in structural distress, whereas in the *unconventional* design the drift is mainly due to foundation rotation, causing less seismic loading to the superstructure.

To elaborate on the results from IDA, Figure 5 illustrates the comparison in terms of contours of plastic shear strain magnitude in the soil at the end of the shaking, for the case of JMA-000, scaled at free-field PGA = 0.4 g. Observe the extended soil plastification (material nonlinearities) dominating the response of the conventionally designed *model 4*. In stark contrast, the unconventionally designed *model 1* suffers rather extended "plastic hinging" in the form of mobilization of passive-type soil failure in front and back of the caisson accompanied by gap formation and sliding in the sides and base (geometric nonlinearities).

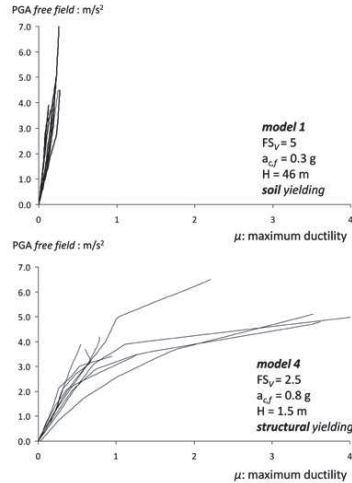


Figure 3. IDA curves of EDP:  $\mu$  (maximum ductility) for *model 1* and *model 4*.

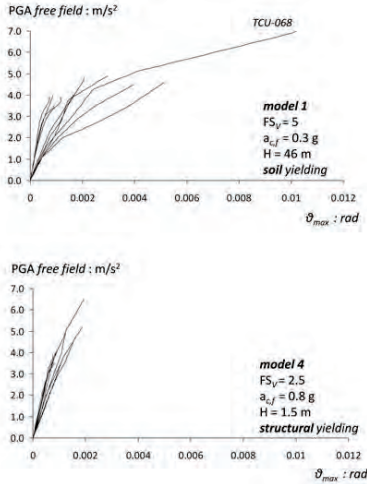


Figure 4. IDA curves of EDP:  $\theta_{max}$  (maximum caisson rotation) for *model 1* and *model 4*.

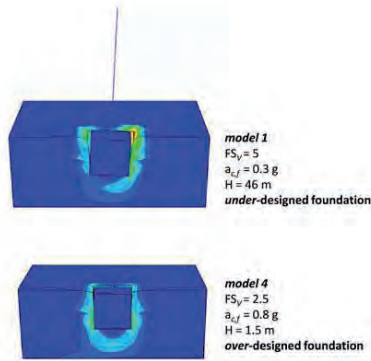


Figure 5. Contours of plastic shear strain magnitude in the soil (PEMAG) at the end of shaking for *model 1* and *model 4*. Record: JMA-000, scaled at free-field PGA = 0.4 g (deformation scale factor = 20).

The stress-strain response of the soil for the two representative cases (*model 1*, lightly loaded

*under-designed* foundation and *model 4*, heavily loaded over-designed foundation) is illustrated in Figure 6, in terms of shear stress-strain loops calculated at the caisson-soil interface near the surface.

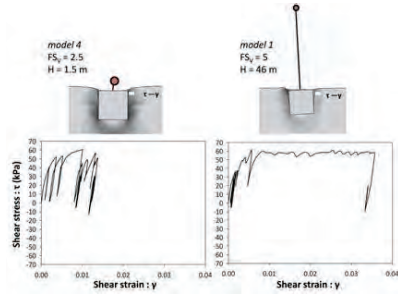


Figure 6. Shear stress-strain loops calculated at the caisson-soil interface near the surface, for the heavily loaded *model 4* and the lightly loaded *model 1*. Record: JMA-000, scaled at free-field PGA = 0.4 g.

The larger shear strains computed in *model 1* reflect the mobilization of extensive geometric nonlinearities (gapping between the caisson and the surrounding soil) as compared to the strong material nonlinearities developed in the soil by the heavily loaded *model 4*. Observe that the ultimate shear strength does not exceed the undrained shear strength ( $S_u = 65$  kPa) in both cases.

## 5 CONCLUSIONS

The present study is the first attempt to explore the nonlinear soil-foundation-structure interaction (SFSI) effects during the earthquake loading of caisson foundations. Within this framework, the efficacy of the capacity design "philosophies", the conventional (without allowing for nonlinear SFSI effects) and the *unconventional* (allowing for SFSI effects), in reducing the seismic structural demand of the supported structures was compared. SDOF structures of varying deck mass, simulating heavily or lightly loaded structures founded through similar rigid cubic caissons on a 2-layer soil stratum are used as ex-



amples. The investigation is performed considering soil and structural inelasticity through 3D finite element incremental dynamic analysis (IDA).

From the numerical results, it was observed that the response of "heavy" structures is determined by excessive material (soil) inelasticity, whereas intense caisson–soil interface separation and gapping prevails in the response of "light" structures. Furthermore, the results highlight the effectiveness of interface nonlinearities in dissipating the seismic energy and the favorable performance of the *under*-designed foundation–structure systems with high static safety factor compared to the conventionally designed heavy structures in both static and dynamic terms, providing a low-cost solution with high seismic isolation potential.

#### ACKNOWLEDGEMENT

This research has been co-financed by the European Union (European Social Fund – ESF) and Greek national funds through the Operational Program "Education and Lifelong Learning" of the National Strategic Reference Framework (NSRF)—Research Funding Program: Heracleitus II. Investing in knowledge society through the European Social Fund.

The invaluable contribution of Dr Nikos Gerolymos, Lecturer NTUA, Dr Vasileios Drosos, Post-Doctoral researcher NTUA and Dr George Gazetas, Professor NTUA is also acknowledged.

#### REFERENCES

- [1] EC8, Eurocode8, *Design of structures for earthquake resistance*, European Committee for Standardisation: Brussels, Belgium, The European Standard EN 1998-1, 2004.
- [2] R. Figini, R. Paolucci, C.T. Chatzigogos, A macro-element model for non-linear soil–shallow foundation–structure interaction under seismic loads: theoretical development and experimental validation on large scale tests, *Earthquake Engineering & Structural Dynamics* **41** (2012), 475–493.
- [3] S. Gajan, B.L. Kutter, J.D. Phalen, T.C. Hutchinson, G.R. Martin, Centrifuge modeling of load-deformation behavior of rocking shallow foundations, *Soil Dyn Earthquake Eng* **25** (2005), 773–783.
- [4] G. Gazetas, M. Apostolou, I. Anastasopoulos, Seismic Uplifting of Foundations on Soft Soil, with Examples from Adapazari (Izmit 1999, Earthquake), *BGA Int Conf on Found Innov. Observations, Design & Practice*, Univ of Dundee, Scotland, Sept 25 2003:37–50.
- [5] N. Gerolymos, G. Gazetas, Static and dynamic response of massive caisson foundations with soil and interface nonlinearities—validation and results, *Soil Dyn Earthquake Eng* **26** (2006), 377–94.
- [6] A. Giannakou, N. Gerolymos, G. Gazetas, T. Tazoh, I. Anastasopoulos, Seismic behavior of batter piles: Elastic response, *J Geotech Eng, ASCE* **136** (2010), 1187–1199.
- [7] D. Vamvatsikos, C.A. Cornell, Incremental dynamic analysis, *Earthquake Engineering and Structural Dynamics* **31** (2002), 491–514.



# Assessment of the Technical Condition of the Retaining Walls along the Highway of the Black Sea Coast of the Areas of Tuapse and Big Sochi

K. Polishchuk<sup>1</sup>

*“NTS GeoProjekt”, Russia, Krasnodar,*

*Kuban State Agrarian University, Russia, Krasnodar*

## ABSTRACT

The results of an investigation of the retaining walls along A-147 federal-aid highway Dzhubga – Sochi are considered in the article; their technical condition is estimated. Was found the main causes of the deformations of the structures and a reduction of their load-carrying ability and to trace the most complicated sections of the highway, which require capital expenditures. The data being obtained serve as a basic material for an elaboration of the engineering measures aimed at a restoration, a reconstruction and repair of the retaining walls.

Keywords: retaining walls, highway, inspection

## 1 INTRODUCTION

Frequently, construction of the highways under the complicated geotechnical conditions causes the necessity to strengthen the vertical slopes, which are dug in soil or appear on the embankments. In order to solve such problems, various types of the retaining walls are widely used [1]. At present (in the year of 2012), in connection with the forthcoming Olympic Games in the city of Sochi, the reconstruction and the restoration of the highways of the Black sea coast become topical. In this article, the items connected with the assessment of the condition of the retaining

walls, which provide safe conditions of the operation of A-147 federal-aid highway Dzhubga – Sochi, are considered<sup>2</sup>.

## 2 GEOTECHNICAL CONDITIONS

The soil conditions of the section being considered are described as the complicated ones [2]. When the geotechnical situation on the Black Sea coast is analysed, it is possible to state that there are sections of development of the landslide and slough processes of various types and intensity [3]. According to E. Voznesensky [3],

---

<sup>1</sup> K. Polishchuk: “NTS GeoProjekt”, Kuban State Agrarian University, Russia, Krasnodar, [ksenya\\_8@mail.ru](mailto:ksenya_8@mail.ru)

<sup>2</sup> The following employees of the limited company “NTS GeoProjekt” participated in the work on inspection of the retaining walls: D. Pleshakov, A. Bychikhin, N. Lyubarsky, A. Semenets, V. Lesnoy et al. The work was performed under the scientific supervision of Doctor of Technical Sciences, Prof. S. Matsiy

the route being considered can be divided into 6 segments conditionally. Such division has been made taking into consideration the peculiarities of the geological structure, the area relief of its sections and the degree of affection by the landslide processes.

### 3 METHOD OF ASSESSMENT OF THE CONDITION OF THE RETAINING WALLS ACCORDING TO THE SYMPTOMS

In order to assess the condition of the retaining walls, their visual inspection at the section of the alignment of the highway from 9 to the 214 kilometre was carried out in summer of the year of 2011. The inspection results showed that 783 retaining walls of various constructional decisions have been constructed along the highway since the year of 1940 till the year of 2011. The majority of them are the massive retaining walls [4], which have been erected on the foundation of the shallow contour interval. It has been found that the retaining walls of the medium height of 1 to 5 m prevail along the highway being considered; the majority of them are the upper ones (56%).

Most of the walls were made of rubble and rubble concrete; they are 45% of their total number. The portions of the walls made of monolithic concrete and precast concrete and reinforced concrete at the section being considered are practically equal and are 22% and 24%, respectively. The walls made of prefabricated monolithic (combined) material form the smallest share: 9% all in all.

In order to assess the technical condition of the retaining walls, it has become necessary to ascertain a category of this condition according to the symptoms and to match the prediction of its time variations.

According to Construction Regulations 13-102-2003 [6], at present there exist 5 categories of technical condition of the construction: intact condition, serviceable condition, limitedly serviceable condition, inadmissible condition and alert condition. But just now there is no clear algorithm concerning reliability evaluation and ac-

cident probability. The task has been solved according to the expert judgment method<sup>3</sup>. A determination of the retaining wall serviceableness for operation, repair periods as well as the necessity of the use of the tool survey techniques was the long-run objective.

In order to determine a category of the technical condition of a structure depending on the damages, an index of its relative safety  $J$  is used [5]:

$$J = 1 - \varepsilon \quad (1)$$

where  $\varepsilon$  – is a value of the total physical wear of the structure. The value  $\varepsilon$  is determined according to the following formula:

$$\varepsilon = (\alpha_1 \varepsilon_1 + \alpha_2 \varepsilon_2 + \dots + \alpha_i \varepsilon_i) / (\alpha_1 + \alpha_2 + \dots + \alpha_i) \quad (2)$$

where  $\varepsilon_1, \varepsilon_2, \dots, \varepsilon_i$  and  $\alpha_1, \alpha_2, \dots, \alpha_i$  – are the values of the damages and the factors of significance of the separate elements of the structure, respectively.

The factors of significance of the elements  $\alpha$  are established proceeding from the possible consequences of their destruction. The value of damage of the separate structural element is established according to the results of the visual inspection: when there are no damages and defects,  $\varepsilon = 0$ ; when a total destruction takes place,  $\varepsilon = 1$ . If it is impossible to assess the condition of an element (a pile, an anchor, etc.) during the visual inspection, it is recommended to set a damage value  $\varepsilon$  proportionally to design service life.

Relative safety of the structure during its operation is determined according to the following formula:

$$J = \gamma / \gamma_0 \quad (3)$$

where  $\gamma, \gamma_0$  are the actual safety factor and the generalized safety factor (taking into consideration the damages being available), respectively.

<sup>3</sup>The method was developed together with S. Matsiy, Doctor of Technical Sciences, Prof., and N. Lyubarsky, Candidate of Technical Sciences

The generalized (total) safety factor  $\gamma_0$  is calculated according to the construction norms in the following way:

$$\gamma_0 = \gamma_m * \gamma_c * \gamma_f * \gamma_n \quad (4)$$

where  $\gamma_m$ ,  $\gamma_c$ ,  $\gamma_f$ ,  $\gamma_n$  are partial safety for materials, partial safety for loads, partial safety for operating conditions and partial safety for purpose, respectively.

The value  $\gamma_0$  is 1.5 to 2.0. At the time of destruction, the actual safety factor  $\gamma$  is equal to 1; the corresponding value of relative safety J, which is calculated according to the formula (3), is 0.65 to 0.50.

When the category of the technical condition is inspected, it is recommended to take into account a level of responsibility of the highway being protected: less responsible structures can be permitted to be operated even if they have large damages. It is connected with the fact that an event becomes dangerous when it can result in the unfavourable consequences being connected with vital activity of people. The recommended values of relative safety of the retaining walls on the highways of various categories are given in Table 1.

The technical assessment makes it possible to determine strength and strain properties of the retaining wall at the time of the inspection. In order to make a conclusion concerning further operating regime, it is necessary to know their time variations taking into consideration the damage accumulation. As the investigation results show [5], a change of load-carrying ability of the retaining structure during its operation can be described with the help of the exponential law. When the structure property change within a certain time interval is assessed, it is possible to get a wear constant:

$$\lambda = -\ln J / t_\phi \quad (5)$$

where  $t_\phi$  is time, which has passed from the beginning of operation, expressed in years.

The permissible useful life of the structure  $t_a$  since the date of its beginning till complete overhaul (in years) is determined according to the following formula:

$$t_a = -\ln J / \lambda \quad (6)$$

According to the results of such calculations, time safety of the retaining structure was assessed quantitatively; the terms and a sequence of reparative work carrying out were established. Repair types (the measures being required), which depend on the category of the technical condition of the retaining walls, are given in Table 1.

Table 1. The category of the technical condition of the retaining walls depending on the value of relative safety of the structure J and the category of the highway being protected

Category of the technical condition of the retaining wall	Measures being required	J, % depending on the highway category		
		I	II-III	IV-V
Intact condition	Repair work is unnecessary	100-96	100-91	100-86
Serviceable condition	Normal operation is provided by maintenance and permanent repair	95-81	90-76	85-71
Restrictedly serviceable condition	Complete overhaul of separate elements of the structure	80-71	75-66	70-61
Impermissible condition	Complete overhaul of the whole structure with restoration, structure strengthening or replacement of all faulty components	70-66	65-61	60-56
Accident condition	Temporary fastening arrangement, restoration or reconstruction of the whole structure	≤ 65	≤ 60	≤ 55

#### 4 AN EXAMPLE. REQUIRED TO DETERMINE THE CATEGORY OF TECHNICAL CONDITION OF THE RETAINING WALL EMPLOYING A PILE FOUNDATION

During the planned inspection of the retaining walls along A-147 highway Dzhubga – Sochi of

the 2nd class, it was necessary to determine a technical condition of the lower retaining wall. The construction is made of reinforced concrete and employs a pile foundation (Figure 1). Nearly 10 years have passed since putting the construction into operation.

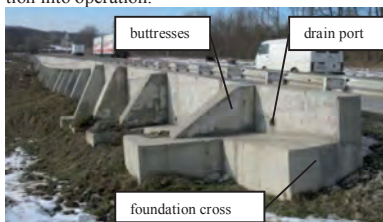


Figure 1. Lower retaining wall at the section of A-147 highway Dzhubga – Sochi

According to visual inspection of the construction, no significant displacements were found; its various elements had the following values of damages:

- the reinforced wall: there are solitary chips of the protective layer without a denudation of reinforcing steel;  $\varepsilon = 0 \dots 0.25$ , an average value of the damage is  $\varepsilon_1 = 0.15$ ;

- drain system: the drain ports are partially blocked and weedy;  $\varepsilon = 0.1 \dots 0.25$ , an average value of the damage is  $\varepsilon_2 = 0.2$ ;

- the reinforced concrete foundation cross: there are solitary hair crackings in some parts;  $\varepsilon = 0 \dots 0.05$ , an average value of the damage is  $\varepsilon_3 = 0.05$ ;

- the pile foundation: as it is impossible to get an access to the element, an average value of the damage is defined taking into consideration a design service life (50 years) being equal to  $\varepsilon_4 = 0.1$ .

The present construction is characterized by the reinforcement with the help of the buttresses and the absence of a lining panel (the foundation cross is arranged on the same level as the road-bed of the highway). Taking it into consideration, the significance coefficient was accepted as  $\alpha_1 = 0.20$ . The rest coefficients are accepted:  $\alpha_2 = 0.15$  for the drain system,  $\alpha_3 = 0.20$  for the foundation cross and  $\alpha_4 = 0.45$  for the pile foundation.

According to the formula (2), we find a value of the general physical wear of the construction:

$$\varepsilon = (\alpha_1 \varepsilon_1 + \alpha_2 \varepsilon_2 + \dots + \alpha_4 \varepsilon_4) / (\alpha_1 + \alpha_2 + \dots + \alpha_4) = (0.15 * 0.15 + 0.2 * 0.2 + 0.2 * 0.05 + 0.45 * 0.1) / (0.15 + 0.2 + 0.2 + 0.45) = 0.118 / 1 = 0.118$$

According to the formula (1), we determine a relative reliability of the construction:

$$J = 1 - \varepsilon = 1 - 0.118 = 0.882$$

According to Table 1, the technical condition of the construction, which protects the highway of the 2nd class, can be subsumed as belonging to the "serviceable" category. For safe operation, routine maintenance is enough (Table 1). Let us calculate a constant of wear according to the formula (5) if the useful life at the time of the inspection is  $t_\phi = 10$  years:

$$\lambda = -\ln J / t_\phi = -\ln 0.882 / 10 = 0.012$$

According to the formula (6), we determine the overhaul term from the operation start. As the overhaul was performed at the time when the construction passed into the impermissible condition, it corresponds to  $J = 0.65$  for the highway of the 2nd class (Table 1):

$$t_a = -\ln J / \lambda = -\ln 0.65 / 0.012 = 36 \text{ year,}$$

it means that it is necessary to perform the overhaul only in  $t = t_a - t_\phi = 36 - 10 = 26$  year. If no overhaul is performed, the construction will pass into the alert condition ( $J = 0.6$ ) in 45 years from the operation start, respectively (Figure 2). A difference between the design service life (50 years) and an occurrence of the alert condition is 5 years only; it means that the operating regime of the retaining construction corresponds to the design one with a small acceleration of physical wear.

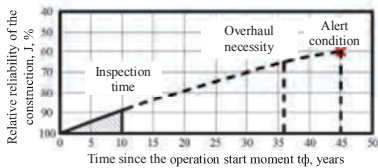


Figure 2. Diagram of a predicted change of the technical condition of the retaining wall being inspected

## 5 ANALYSIS OF THE RETAINING WALL INSPECTION RESULTS

An analysis of the received materials has shown that all walls being considered are proportioned in the following ratio depending on the category of the technical condition: 79% of the retaining walls are in the serviceable condition, 16% are in the restrictedly serviceable condition and 5% are in the impermissible and accident condition (Table 2, Figure 3).

Table 2. The categories of the technical condition of the retaining walls (June-August, 2011)

Technical condition of the retaining wall	Number of the walls, pieces	Per cent of the total number of the walls, %
Intact condition	0	0
Serviceable condition	621	79
Restrictedly serviceable condition	122	16
Impermissible and Accident condition	40	5
Total	783	100



Figure 3. Upper retaining wall in Adler district (the 196th km) in the accident technical condition

Besides, in order to assess the technical condition of the walls the flood installations were inspected: drainage systems, the upper conduits and the lower ones along the structures.

An analysis of the results has shown that the majority of the retaining walls has no flood installations; if such flood installations are available, they are littered and do not operate (Table 3).

Table 3. Water removal measures in the retaining walls

Flood installation type	Available		Unavailable	
	Number of walls, pieces	Per cent of total number of walls, %	Number of walls, pieces	Per cent of total number of walls, %
Upper conduits	48	7	649	93
Lower conduits	255	37	442	63
Drainage	165	24	532	76

In order to ascertain a highway section with the largest number of the retaining walls, their specific concentration per kilometre along the road in each district has been calculated. It has been found that the largest number of the structures is situated in Khostinsky district (Table 4, column 7): 60% of each kilometre is protected with the help of the walls. If the findings are matched with the geotechnical conditions, it is possible to state that the highway at this part is the most complicated one and requires closer attention and more investments than other parts. The minimal concentration of the retaining walls has been registered in Tuapsinsky district and Central district: 20% in each district. When the number of the retaining structures was assessed, it was found that the walls constitute 35%

The indices concerning the structure technical condition assessment show that out of the whole extension of the retaining walls being 74 kilometres, 18.5 kilometres are presented by the structures, which are in the impermissible condition, accident condition

and the restrictedly serviceable technical condition. It is 25% of the whole extension of the highway. The retaining structures of Lazarevsky district and Adlersky district are in the worst technical condition: 32% out of the whole extension of the walls require repair work.

Table 4. Calculation of the quantitative indices according to the results of the retaining wall inspection

District	High way section extension, km	Length of the walls at the high way section, km	Length of the walls in accident/restrictedly serviceable technical condition, km	Number of the retaining walls per km of the highway within the limits of one district, %	Per cent of length of the walls in accident/restrictedly serviceable technical condition out of total length of all walls along the highway, %
1	2	5	6	7	8
Tuapsinsky	81	16	0.2 / 2.5	20	0.3 / 3.4
Lazarevsky	89	33	2 / 8.8	40	2.7 / 12
Central	11	2	0 / 0.2	20	0 / 0.3
Khostinsky	16	10	0.2 / 2.2	60	0.2 / 3
Adlersky	17	7	1 / 1.3	40	1.4 / 1.8
Bypass	12	6	0 / 0.1	50	0 / 0.1
Total	214	74	3.4 / 15.1		4.6 / 20.6

When the causes of deformation of the retaining walls and a reduction of their load-carrying ability are assessed, it is possible to state that physical wear exerts a great influence upon the retaining wall destruction. The walls are erected long ago; it is necessary to increase their stiffness and rigidity. Besides, practically all structures have no flood installations in the form of conduits and drainage systems. It results in an accumulation of water along the structure base and, consequently, in its soaking and materi-

al destruction. For the retaining walls, which are in the accident technical condition, urgent measures should be taken in order to strengthen them; in some parts, it is necessary to replace the existing structure by the new ones. It is the most topical question as far as the lower retaining walls are concerned (46 walls are in the restrictedly serviceable condition and 21 walls are in the accident condition), because a load-carrying ability failure is closely connected with rigidity of the air faces along the highway.

Thus, the work being performed has made it possible to assess the technical condition of the retaining walls for the elaboration of the engineering measures connected with their restoration, reconstruction and repair.

## REFERENCES

- [1] ODM 218.3.008-2011. *Recommendation concerning monitoring and inspection of retaining walls and holding structures in the landslide sections of highways*. M.: Federal state unitary enterprise Informator, 2011. 47 pages.
- [2] Building Code 11-105-97. *Geotechnical surveys for construction. Part I. General rules of work*. M.: Federal state unitary enterprise CPP, 1997.
- [3] General explanatory note, topic: "Diagnostics of landslide sections, retaining walls and holding structures in the sections of A-147 federal-aid highways Dzhubga - Sochi - border of the Republic of Abkhazia, A-149 Adler-Krasnaya Polyana, bypass of the city of Sochi" (volume 1). Book 2. *Sections of downslope processes development. (Part 1. Condition of the slopes in the sections of A-147 federal-aid highway Dzhubga - Sochi - border of the Republic of Abkhazia)*. The Head of work is E. Voznesensky. - Krasnodar: limited company "SochiTicizProject", the Moscow State University named after Lomonosov, Geological Faculty, 2011. 80 pages.
- [4] Reference manual to construction norms and regulations 2.09.03-85. *Industrial enterprise construction. Designing of the retaining walls and the walls of the cellars*. M.: Stroyizdat, 1990.
- [5] Dobromyslov A.N. *Diagnostics of the damages of buildings and engineering structures: reference manual*. M.: publishing house ACB, 2006. 256 pages.
- [6] Construction Regulations 13-102-2003. *Regulations of the inspection of the bearing building structures of the buildings and the constructions/Gosstroy of Russia*. M.: TSITP of Gosstroy of Russia, 2004.



# Ground vibrations due to pile and sheet pile driving – prediction models of today

F. Deckner<sup>1</sup>

*Royal Institute of Technology/NCC Engineering*

K. Viking

*Norconsult*

S. Hintze

*NCC R&D/Royal Institute of Technology*

## ABSTRACT

As part of a construction work pile and sheet pile driving unavoidably generates vibrations. As of today construction works are often located in urban areas and along with society's increasing concern of environmental impact the need for vibration prediction prior to construction is of immediate interest. This study presents a review of the prediction models existing today. For prediction of ground vibrations from pile and sheet pile driving there are roughly three different types of models; empirical models, theoretical models and engineering models. A prediction model should be reliable in all cases where it is meant to be used. It is also important that it is relatively easy to use and that the input data is easily obtained. This study concludes that, as of today, there is a lack of such a model. Today's models either lack in reliability or require great amounts of input data, knowledge and skills as well as time and money. The findings within this study constitute the initial part of an on-going research project at the division of Soil- and Rock Mechanics at the Royal Institute of Technology in cooperation with the Development Fund of the Swedish Construction Industry and NCC Construction Sweden.

Keywords: Ground vibrations, pile driving, vibration prediction, pile, sheet pile, prediction model

## 1 INTRODUCTION

Construction work and especially the driving of piles and sheet pile has for a long time been one of the most important sources for vibrations in urban areas. The induced vibrations can have a negative impact on the surroundings. As a consequence of society's increased concern of environmental impact and the fact that construction projects more often are located in urban areas

and close to existing structures, vibration assessment and prediction has become of immediate interest.

The prediction of the vibration level in a construction project can have important economic and technical consequences. Unnecessarily conservative estimations will increase costs, may limit the choice of construction methods and delay the project. If, on the other hand, the vibration level is underestimated, it might lead to

---

<sup>1</sup> Corresponding Author. NCC Engineering, Vallgatan 3, 17080 Solna, fanny.deckner@ncc.se

damaged structures, disturbed occupants and suspension of the construction work.

Today an estimation of expected vibration level is usually based upon experience or field test measurements. This study presents a review of the existing prediction models for vibrations caused by pile and sheet pile driving and is part of an on-going research project aiming for better prediction and understanding of ground vibrations induced by pile and sheet pile driving.

## 2 BASIC THEORY

In order to estimate the effect of pile/sheet pile driving it is necessary to consider the entire vibration transfer process from the source to the damage object. The process is divided into three main parts; vibration source, wave propagation in soil and damage object (Figure 1). Vibrations are generated by the driving equipment (impact or vibratory) and are transmitted through the pile cap and further into the pile. There is an interaction between the soil and the pile shaft and pile toe, leading to vibrations being transmitted into the ground. From thereon vibrations propagate through soil and eventually interact with possible damage objects.

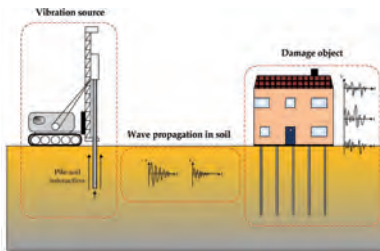


Figure 1. Schematic illustration of the vibration transfer during pile driving.

At the pile-soil interface vibrations from the pile are transmitted to the soil as different waves and wave fronts (Figure 2). At the pile toe spherical wave fronts of both P- and S-waves are created. From the shaft a conical wave front is cre-

ated consisting of S-waves. As the wave fronts reach the ground surface part of the vibration energy is transferred to surface (R-)waves.

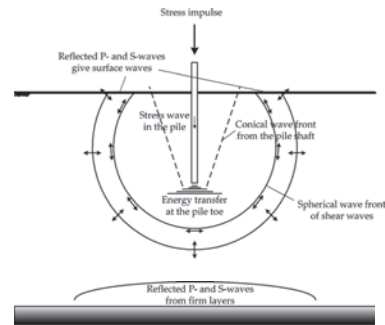


Figure 2. Schematic representation of different wave types generated at pile driving, modified after [1].

As waves propagate through the soil attenuation takes place in the form of geometrical and material damping. Geometrical damping is caused by the energy spreading over an increasing soil volume, and material damping is due to internal friction and hysteresis. The total attenuation of vibrations propagating in soil is usually approximated by the following relationship:

$$A_2 = A_1 \left( \frac{r_2}{r_1} \right)^{-n} e^{-\alpha(r_2 - r_1)} \quad (1)$$

where

$A_1, A_2$  = vibration amplitude at distance  $r_1$  respectively  $r_2$  from the source

$\alpha$  = absorption coefficient ( $m^{-1}$ ) depending on soil material and vibration frequency

$n = 1/2$  for surface waves, 1 for body waves, 2 for body waves along the surface

## 3 CURRENT PREDICTION MODELS

The magnitude of induced vibrations in a specific project can be measured fairly well in the field

but the prediction of its magnitude prior to driving is very insecure. Several examples can be found in literature stating that as of today there is little guidance to be found regarding how practising engineers can make a prediction of the vibrations during a pile or sheet pile driving work (e.g. [2], [3], [4], [5], [6], [7] and [8]).

The existing prediction models are in this study divided into three different categories depending on their approach:

- Empirical models – based on empirical knowledge from former measurements and experience of piling works
- Theoretical models – based on theoretical knowledge usually consisting of numerical models
- Engineering models – a mix of empirical, theoretical and engineering knowledge (sometimes also called mixed-approach models)

### 3.1 Empirical models

Even if there are no generally accepted methods for predicting vibrations during pile- and sheet pile driving, there exist a lot of measurements and empirical knowledge.

In 1967 Wiss [9] discovered that the vibration magnitude due to pile driving varied with the amount of energy transmitted to the soil, the soil properties and the distance from the source. Wiss [9] then concluded that the particle velocity varied with the square root of the energy of the hammer. Attewell & Farmer [1] proposed that, for practical estimates of vibrations due to pile driving, the vibration intensity attenuates directly with distance from the pile and that the geotechnical character of the ground can be ignored. Hence, in 1973 Attewell & Farmer [1] presented one of the first empirical prediction models where they suggest that the vertical peak particle velocity,  $v$ , is given according to the general formula:

$$v = k \left( \frac{\sqrt{W_0}}{r} \right)^x \quad (2)$$

where

$k$  = empirically determined constant (-)

$W_0$  = input energy (hammer energy) (J)

$r$  = horizontal distance between pile and monitoring point (m)

$x$  = empirically determined index (-)

From field measurements [1] claimed that the results correlate quite well with setting  $k = 1$  and  $x = 1$ , however, they suggested that  $k = 1.5$  is used for practical conservative prediction of ground vibrations due to pile driving. The energy based relationship in Eq. (2) has since been developed by various researchers proposing values for  $k$  and  $x$  ([10], [11], [2], [12], [13] and [14]).

Attewell et al. ([11] and [15]) found that a quadratic regression curve was a better fit to measurements of ground vibrations due to pile driving than the former used linear regression curve in Eq. (2). The developed model proposes the following equation for the prediction of vibration velocity due to pile driving:

$$\log v = k + m \log \left( \frac{\sqrt{W_0}}{r} \right) + n \log^2 \left( \frac{\sqrt{W_0}}{r} \right) \quad (3)$$

where

$k$ ,  $m$  and  $n$  = constants of proportionality (-)

Constants  $k$ ,  $m$  and  $n$  are functions of the soil conditions at the site of pile driving and the driving method. Suggested values for the constants are published in [15].

Svinkin [16] presented a development of the energy based relationship founded on determination of the vibration velocity at the pile head, and from that computed the ground vibrations. In Eq. (2)  $x$  is set as 1 and  $k$  is equal to the pile vibration at the pile head,  $v_p$ .

### 3.2 Theoretical models

Theoretical models use a different approach for the prediction of vibrations than the one used in empirical models. Theoretical models are usually based on numerical or analytical modelling using different computer programs. Davis [8] listed several numerical methods which can be

used for prediction of ground vibrations, the most common are:

- Finite Difference Time-Domain Method (FDM)
- Finite Element Method (FEM)
- Boundary Element Method (BEM)

FDM can take layering and anisotropy of the soil into account; however, there is uncertainty in the loss of energy due to material damping. Another drawback of the FDM is that it requires high levels of mathematical skills from the user [8]. FEM is commonly used for the modelling of problems in soil and rock materials. There are a number of commercial computer programs based on FEM (Plaxis being the most common among geotechnical engineers). BEM is somewhat more limited in its use than FEM and FDM due to its need for reformulation of the partial differential equations. To overcome the limitations with BEM the soil immediately next to the source can be modelled with FEM while the rest of the propagation path can be modelled using a coupled BEM model. For the modelling of ground vibration problems with infinite domains BEM is considered to be better than FEM regarding efficiency, accuracy and user friendliness [8].

Theoretical models often consist of sub-models for the pile, the soil and sometimes also for damage objects. The sub-models are modelled separately and thereafter connected to make the prediction [17]. Several of the existing prediction models mix different numerical methods in their prediction models (e.g. [3] and [18]).

Table 1. Theoretical models for prediction of vibrations due to pile and sheet pile driving, modified after [19].

Researcher	Numerical method
Holeyman (1993)	Radial discrete model
Waarts & Bielefeld (1994)	Stress wave simulation and FEM
Ramshaw et al. (2000)	Finite and infinite element method
Liyanapathirana et al. (2001)	FEM
Mahutka & Grabe (2006)	FEM (Abaqus)
Rocher-Lacoste & Semblat (2007)	FEM (Cesar-LCPC)
Masoumi et al. (2007)	FEM and BEM
Whenham (2011)	FEM (Plaxis)

Whenham [19] has listed several publications where numerical methods have been used to predict the vibrations induced by pile driving. From that list modifications and additions have been made resulting in Table 1.

### 3.3 Engineering models

Engineering models mix different approaches in the same model to make a prediction. Jongmans [4] presented an engineering model that aims towards reconstructing the whole vibration signal generated during pile driving. The model consists of two parts; the first part is based on the use of geophysical prospecting to represent the response of the site (Green's function) and the other part is an equivalent source function idealising energy transmission from pile toe to soil.

A model presented by Svinkin [21] uses the concept of the impulse response function to model the soil behaviour. The impulse response function is determined by setting up an experiment in which known magnitudes of impact are applied on the site of interest. Once the impulse response function is known the dynamic loads for pile driving are computed by wave equation analysis. Duhamel's integral is then used to find the predicted vibrations.

In 2008 Massarsch & Fellenius [20] introduced a model for estimating vibrations from impact pile driving. The method includes the force applied to the pile head, the dynamic stresses in the pile and the dynamic resistance along the pile toe and pile shaft.

## 4 COMMENTS ON CURRENT PREDICTION MODELS

### 4.1 Empirical models

Hope & Hiller [22] draw the conclusion that prediction models not taking soil conditions into consideration are less accurate than prediction models taking soil conditions into account. Several others ([21], [23] and [20]) are critical towards empirical relationships for estimation of ground vibration as they do not take soil conditions into account in an adequate way. According

to [4] it is likely that soil conditions affect not only the vibration magnitude but also its frequency content and wave form. Hope & Hiller [22] and Massarsch & Fellenius [20] showed that the empirical approach is too crude for reliable analysis of ground vibrations and that some of the relationships assumed in these empirical models are invalid.

However, according to [11] and [24] it is quite reasonable that ground vibrations due to pile driving can be estimated by the use of empirical methods. They stated that empirical methods are the most sensible and suitable for use on site. In [23] it is also reasoned that empirical models have their limitations, nevertheless, they are easy to apply and thus valuable for piling practitioners.

#### 4.2 Theoretical models

Athanasopoulos & Pelekis [23] believed that theoretical models are capable of modelling the whole vibration problem and producing predicted vibration levels. Svinkin [21] stated that analytical prediction models usually give good agreement between predicted and measured vibrations for a certain site. However, designing the models takes a lot of time and knowledge in order to get the calculations right. A theoretical model is in most cases strongly influenced by the user and his/her expertise and knowledge, which affects the predicted vibrations [17]. Making reliable predictions also requires detailed input data that in many cases needs to be estimated.

#### 4.3 Engineering models

The advantage of Jongmans' model is that it takes the site characteristics into account [4]. The model presented by Massarsch & Fellenius [20] also considers soil conditions in the form of soil resistance. And Svinkin [21] stated that the advantage of the impulse response function is that it reflects real soil behaviour without the need for investigations of the soil properties.

The engineering models presented in section 3.3 all include soil conditions in one way or another; however, they lack validation in the form of comparison to vibration levels measured in the field.

#### 4.4 Reliability of prediction models

One of the main conclusions in the study of [17] was that the uncertainty in vibration prediction generally is quite large; however, using sophisticated FEM-models reduced the uncertainty compared to expert judgement. Another conclusion was that the user of the prediction model has a huge influence on the outcome of the prediction.

Hope & Hiller [22] presented a review of the prediction models available at that time, focusing on vibrations from impact pile driving. They showed that the accuracy of the existing prediction models were limited. Most prediction models presented considerably over-estimated the vibration magnitudes at distances less than 11 m from the pile. In [19] predicted vibrations from the Attewell et al. model ([11] and [15]) were compared with measured results showing that the model over-predicted the actual vibrations with a factor of 2 to 10. Nevertheless, most prediction models are intentionally conservative.

In order to highlight the complexity of the problem and the difficulty in prediction, a relative comparison between the Attewell & Farmer-model (Eq. 2) and the Attewell et al.-model (Eq. 3) has been conducted within this study. The comparison showed that when using the same input data ( $W_0 = 5000$  J and  $r = 15$  m) predicted vibration levels were 7.1 mm/s respectively 3.4 mm/s. The other models all require the assumption of large amounts of different input data making a relative comparison insignificant.

## 5 CONCLUSIONS

A prediction model should be reliable in all cases where it is meant to be used. It is also important that it is relatively easy to use, the mathematical operations should not take days to execute and the input data should be readily available. This study shows that, as of today, such a model is lacking. Current empirical models have the advantage that they are easy to use and require relatively small amounts of input data, however, they cannot be considered reliable as they tend to highly overestimate the vibration level. Today's theoretical prediction models seem to be some-

what more reliable, but instead they require great amounts of input data, knowledge and skills as well as time and money. The engineering models lack validation in order to be considered reliable; however, they seem to have the potential of producing a prediction model satisfying the above criteria.

A prediction model simple enough to be used by practising geotechnical engineers yet sophisticated enough to reliably predict vibrations will hopefully be available in the future. In order to get there further research clarifying how to better quantify the vibration actually transferred from the pile to the soil and also how to better incorporate soil conditions into a prediction model is required.

#### ACKNOWLEDGEMENT

The support of the Development Fund of the Swedish Construction Industry, the Royal Institute of Technology and NCC Construction Sweden AB is gratefully acknowledged.

#### REFERENCES

- [1] P.B. Attewell & I.W. Farmer. Attenuation of ground vibrations from pile driving. *Ground Engineering*, Vol. 3(7), pp. 26-29 (1973).
- [2] P.J. Whyley & R.W. Sarsby. Ground borne vibration from piling. *Ground Engineering*, Vol. 25(4), pp. 32-37 (1992).
- [3] P.H. Waarts & M.W. Bielefeld. Prediction and Control of Vibrations due to Pile Driving and Sheet Pile Vibrations. Proc. 5th Int. Conf. & Ex. Piling and Deep Foundations, Bruges, pp 2.11.1-2.11.6 (1994).
- [4] D. Jongmans. Prediction of ground vibration caused by pile driving: A new methodology. *Engineering Geology*, Vol. 42(1), pp. 25-36 (1996).
- [5] S. Hintze, S. Liedberg, R. Massarsch, M. Hanson, H. Elvhammar, B. Lundahl & S-E. Rehman. *Omgivningsspåverkan vid päl- och spontslagning. Pålkommissionen rapport 95*, Linköping, 1997.
- [6] K.R. Massarsch. *Vibrations Caused by Pile Driving. Deep foundations, summer 2004 and fall 2004 (two parts)* (2004).
- [7] C.K. Madhewaran, R. Sundaravivelu, A. Boomnathan & K. Natarajan. Response of Ground during Pile Driving. *IE (I) Journal-CV*, Vol. 86, pp. 22-27 (2005).
- [8] D. Davis. A Review of Prediction Methods for Ground-Borne Noise due to Construction Activities. Proc. 20th Int. Cong. on Acoustics, Sydney (2010).
- [9] J.F. Wiss. Damage Effects of Pile Driving Vibration. Highway Research Board Record 155, pp 14-20 (1967).
- [10] J.F. Wiss. Construction Vibrations: State-of-the-Art. *Journal of Geotechnical Engineering Division*, Vol. 107(GT2), pp. 167-181 (1981).
- [11] P.B. Attewell, A.R. Selby & L. O'Donnell. Estimation of ground vibration from driven piling based on statistical analyses of recorded data. *Geotechnical and Geological Engineering*, Vol. 10 (1), pp. 41-59 (1992).
- [12] G. Nilsson. *Markvibrationer vid påslagning*. Master thesis Nr 3:89, Royal Institute of Technology, Stockholm, 1989.
- [13] W.S. Heckman & D.J. Hagerty. Vibrations Associated with Pile Driving. *Journal of the Construction Division*, Vol. 104(CO4), pp 385-394 (1978).
- [14] J.M. Head & F.M. Jardine. *Ground-borne vibrations arising from piling*. CIRIA Technical Note 142, CIRIA, London, 1992.
- [15] P.B. Attewell, A.R. Selby & L. O'Donnell. Tables and graphs for the estimation of ground vibration from driven piling operations. *Geotechnical and Geological Engineering*, Vol. 10(1), pp. 61-87 (1992).
- [16] M.R. Svinkin. Soil and structure vibrations from construction and industrial sources. Proc. 6th Int. Conf. Case Histories in Geotechnical Engineering, Arlington (2008).
- [17] P.H. Waarts & M.S. de Wit. Does more sophisticated modelling reduce model uncertainty? A case study on vibration predictions. *HERON*, Vol. 49(2), pp. 119-137 (2004).
- [18] H.R. Masoumi, G. Degrande & G. Lombaert. Prediction of free field vibrations due to pile driving using a dynamic soil-structure interaction formulation. *Soil Dynamics and Earthquake Engineering*, Vol. 27(2), pp. 126-143 (2007).
- [19] V. Whenham. *Power Transfer and Vibrator-Pile-Soil Interactions within the framework of vibratory pile driving*. Doctoral Thesis, University of Louvain, Belgium, 2011.
- [20] K.R. Massarsch & B.H. Fellenius. *Ground Vibrations Induced by Impact Pile Driving*. Proc. 6th Int. Conf. Case Histories in Geotechnical Engineering, Arlington (2008).
- [21] M.R. Svinkin. Overcoming soil uncertainty in prediction of construction and industrial vibrations. Uncertainty in the geologic environment: from theory to practice, ASCE, *Geotechnical Special Edition No. 58*, pp. 1178-1194 (1996).
- [22] V.S. Hope & D.M. Hiller. The prediction of ground-borne vibration from percussive piling. *Canadian Geotechnical Journal*, Vol. 37(3), pp. 700-711 (2000).
- [23] G.A. Athanasopoulos & P.C. Pelekis. Ground vibrations from sheetpile driving in urban environment: measurements, analysis and effects on buildings and occupants. *Soil Dynamics and Earthquake Engineering*, Elsevier, Vol. 19(5), pp. 371-387 (2000).
- [24] D.M. Hiller & V.S. Hope. Groundborne vibration generated by mechanized construction activities. *Geotechnical Engineering*, Vol. 131(4), pp. 223-232 (1998).

# Change of shear strength in soft soil excavations

Yannie, Jorge<sup>1</sup>

*Chalmers University of Technology, Gothenburg, Sweden.*

## ABSTRACT

Sweden's approach in the execution of excavations in soft soils has become a tradition among practitioners. It has been proved that the methods used work and that successful excavations have been performed. However, questions arise when studying in detail the theory behind the design procedures as given in the Swedish Handbook for sheet pile walls (in Swedish "Sponhandboken") [1].

One important aspect to consider is the approach utilized to assess the shear strength of the soil being excavated. In practice, the soil is considered to have isotropic characteristics and the shear strength is generally based on the consolidated direct simple shear (CDSS). In addition, the value is fixed in time and is only varying with depth. However, in reality this is not the case, since the soil is anisotropic in its behavior and its properties change with time (i.e. consolidation). The above situation is counter-balanced in practice when using a traditional design approach; for example, by using partial factors which allow for uncertainties from both theory and practice.

Nowadays the trend is to use numerical models for calculations. These can account for factors like soil behavior, soil-structure interaction and construction time. Furthermore, if properly used, realistic results can be obtained in a geo-structural matter. On the other hand limit equilibrium, stress field and semi-empirical methods can be unrealistic predicting soil behavior and not always take into account the latter mentioned factors. This can translate into unsafe failure mechanisms in the soil mass and load effects in the supporting structure. A wise design is necessary to balance the economics and safety of the geo-structure.

This paper will discuss about the factors which influence changes in shear strength in an excavation in slightly over-consolidated clays in Gothenburg, Sweden. Focus will lie predominantly on the decrease in shear strength caused by unloading at the bottom of the excavation. Examples are given for a single strutted excavation.

Keywords : sheet pile walls, shear strength, clay, soft soil, passive earth pressure, unloading, swelling, stress path, stress state, decrease in shear strength, undrained, drained, partially drained

---

<sup>1</sup> [jorge.yannie@chalmers.se](mailto:jorge.yannie@chalmers.se), Civil and Environmental Engineering, Chalmers.

## 1 INTRODUCTION

The current design approach in Sweden for excavations in clay supported by flexible structures, namely sheet-pile walls, is based on the stress field method. Furthermore, it is considered that the soil behaves isotropic and time effects are neglected (total stress analysis for undrained conditions) [1]. However, this is not the case in reality, where the soil behaves anisotropic and consolidation takes place [2]. In addition, soil parameters are usually obtained from in-situ tests or pre-investigation tests in the laboratory, accounting for a different stress state from that of the excavation.

Nowadays developments in numerical modeling and machinery provide us with the capacity of dealing with more complex geotechnical projects. This translates to larger open excavations and for longer time periods located in complex areas (e.g. urban areas), therefore requiring a better understanding of the soil-structure system behavior.

Numerical models and new design approaches have been developed to capture the above mentioned behavior [3–5]. These are implemented in Finite Element (FE) programs and provide results that approach to the reality.

## 2 DISTURBING FACTORS IN AN EXCAVATION

The stability of an excavation in soft soil depends highly in the construction methods and the soil properties, specially the shear strength. The latter plays an important role within the acting earth pressures. Moreover the soil is affected by several factors like the installation of the sheet-pile wall, ground improvements with piles and particularly with the unloading of the soil mass [6]. The response of the soil to these is observed with the increase or decreases in the excess pore water pressure (and deformation); changing the stress state from in-situ conditions [7]. As a result the shear strength will be affected and could deviate from that considered in an ideal scenario. This must be taken into account in the pre-investigation and design phases.

From the above factors, focus is set in the unloading of the soil mass at the middle of the excavation bottom (see Figure 1). In this area the wall effects are small and vertical unloading is dominant [4].

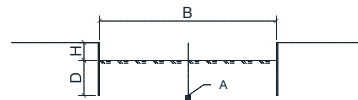


Figure 1. Excavation outline.

## 3 SHEAR STRENGTH PROPERTIES

The west coast of Sweden, namely Västra Götaland, is characterized by having large extensions of deep deposits of clay. Soil deposition in this area can be considered one dimensional, and thus anisotropic. A common soil profile in urban areas will be that of a top filling layer followed by a deep layer of homogeneous clay. The top part of the clay layer is in general lightly overconsolidated, decreasing gradually until an almost constant OCR value (the latter influenced by creep effects) [8].

An empirical relation that considers initial anisotropic undrained shear strength for Swedish clay is shown in Equation (1) [8].

$$c_u^{ani} = a \cdot \sigma_c' \cdot OCR^{-(1-b)} \quad (1)$$

This is related to the stress history of the soil, the current stress state, the loading conditions and soil intrinsic properties. This equation is limited to a certain range of OCRs, thus very large OCR values might give deviated results. An example with typical parameters for overconsolidated ( $OCR=1.3$ ,  $w_L=80\%$ ) Gothenburg clay is shown in Table 1.



Table 1. Empirical anisotropy [8].

	Factors	Example
b	0.70-0.90	0.80
	<i>Active</i> : $a \approx 0.33$	$c_u^A \approx \frac{1}{3} \cdot \sigma_c'$
a	<i>DSS</i> : $a \approx 0.125 + 0.205 \cdot \frac{w_L}{1.17}$	$c_u^{DSS} \approx \frac{1}{4} \cdot \sigma_c'$
	<i>Passive</i> : $a \approx 0.055 + 0.205 \cdot \frac{w_L}{1.17}$	$c_u^P \approx \frac{1}{5} \cdot \sigma_c'$

With the help of this equation, a good approximation of the anisotropic behavior could be incorporated in FE or traditional calculations. Note, however that the equation is limited by a certain stress range (limited OCR).

#### 4 STRESS PATH AND CONSOLIDATION

The stress paths in an excavation are unique for every point; however they show similar trends for different zones within the involved excavation area. It is important to consider the initial stress conditions of the soil before any work [7]. Soil deformation is stress path dependent and, the shear strength is depending on several factors as mentioned above, and one of this is the current stress state in the soil [4].

In the center of the excavation, the vertical unloading is the dominating case, with a reduction of the vertical stresses and an increase in the overconsolidated ratio (OCR). The latter situation can be simulated in a oedometer unloading test and the shear strength could be obtained from the traditional extension triaxial test, with the unloading of the axial stress and constant cell pressure.

Knowing the stress paths during the excavation can help to track the mobilization of shear strength, the maximum value expected and, based on the stress rotation, the expected type of failure (e.g. active or passive).

##### 4.1 Predicting the change in pore pressure

In order to estimate the changes in stresses and find the steady state conditions, knowledge of the pore water pressure is required. As discussed in

Kempfert, Gebreselassie [4] and stated by Janbu [9] among others, also the short term undrained strength of clays is governed by the effective stress state. The pore water pressure can be affected by several factors like volumetric (swelling) and shear deformations (dilation or contraction). However, the problem arises when estimating the change in excess pore water pressure, since it is hard to approximate it precisely. The latter is an obstacle for obtaining a proper stress state just after the excavation. In addition it is difficult to predict the stress path to steady state. Persson [10] suggested that the change in pore water pressure could be estimated by the change in mean total stresses.

The regain of a steady state pore pressure after the excavation can occur in a short time that is usually within the construction period, as discussed in Kempfert, Gebreselassie [4] and observed by Persson [10] (see section below). Therefore one must consider the changes in the stress state at the bottom of the pit and the subsequent variation of the shear strength. However, one should concentrate in the steady state condition since this state will be the critical one.

##### 4.2 Consolidation

Questions arise of when to consider a short undrained or long drained condition. These can be regarded from multiple situations, for example, at the active, passive or center area of the excavation, and with loading or unloading of the soil mass.

For the unloading case in the middle of the excavation, the excess negative pore water pressure will dissipate simultaneously with the swelling of the soil, creating a new stress state. This drained transition is important since the soil will experience changes in effective stresses, and consequently new stability and deformation properties.

From the steady state the soil will experience an undrained behavior if reloaded above its pre-consolidation pressure. On the other hand, a partially drained or drained behavior is expected if loaded below it.

Following Vermeer and Meier [11] suggestion of applying the one dimension classical consoli-

dition theory, typical Gothenburg clay parameters are used to roughly estimate the time for undrained (degree of consolidation  $U \leq 10\%$ ) and drained ( $U \geq 90\%$ ) conditions. The soil parameters are given for a 10 meters depth point, below a 3.5 meters excavation. Here the drainage path is considered as the length of embedment of the wall; draining at the excavation bottom only.

Both loading (above pre-consolidation) and unloading cases are presented in Figure 2 and Figure 3. It is observed that the dissipation of excess pore water pressure occurs rather fast in the unloading case, as discussed in the previous section.

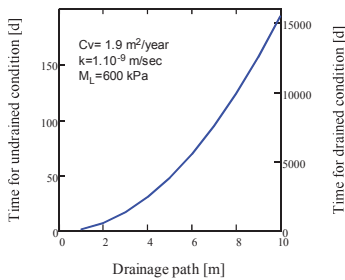


Figure 2. Loading; normally consolidated clay.

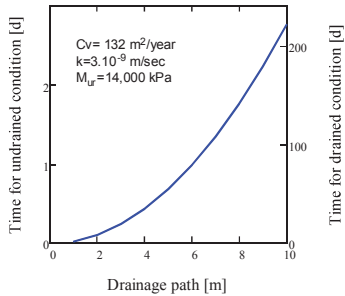


Figure 3. Unloading; overconsolidated clay.

## 5 THEORETICAL EXAMPLE

In order to illustrate the discussed above, an example of a typical excavation in clay ( $\gamma_{\text{clay}}=16 \text{ kN/m}^3$ ) was used with focus on the center of the pit (point A in Figure 1). The assumed geometry of the excavation was 3.5 meters deep and 40 meters wide with a large length ( $L \gg B$ ; plane strain). The water table was located at the ground surface and a fill layer of 0.5 meters was considered ( $\gamma_{\text{fill}}=19 \text{ kN/m}^3$ ,  $\phi=32^\circ$ ). At the excavation pit, the pore water pressure was assumed to reach a steady state increasing linearly from the bottom to a depth of 25 meters as discussed by Persson [10], see Figure 4. From this, the new stress state was calculated along with the change in shear strength.

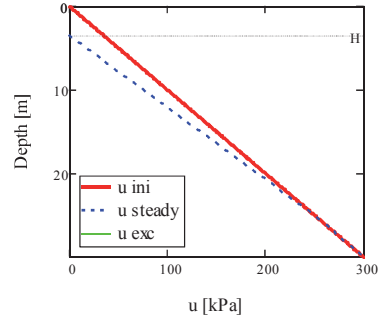


Figure 4. Pore water pressure before the excavation (hydrostatic), after and at steady state.

Initial conditions on the field and after the excavation are shown in Figure 5 and Figure 6. One can see the drop in effective stresses from the excavation point to the steady state and hence a higher OCR.



If one would design the sheet pile wall with the current guidelines; without taking into account the initial anisotropy and the drained (steady state) condition, one would obtain the earth pressures shown in Figure 9. For this, the penetration depth obtained was of 8.70 meters below the excavation bottom. On the other hand, considering the drop of shear strength for the area nearby the wall; as the average value between the initial condition and the unloaded state and, the same penetration depth, the total safety factor applied to the shear strength must be reduced by 7% (from 1.58 to 1.47) to keep the guideline design as valid.

In general, the difference is not very large; however for deeper excavations it is expected that the effect will be greater.

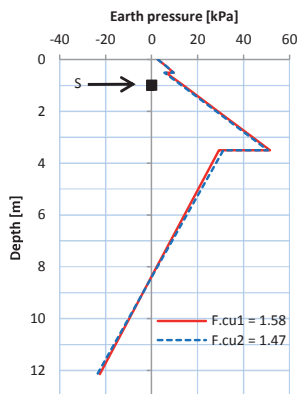


Figure 9. Design earth pressures. The strut force for case 1 was  $S=119$  kN/m and for case 2  $S=120$  kN/m.

## 7 CONCLUSION

All in all, more detailed design approaches are suggested to be implemented nowadays. Calculation using the FE method could provide more details of the excavation and soil behavior; accounting for other factors that are overlooked with analytical calculations.

Drained conditions should be considered in the transition from in-situ conditions to the steady state after the excavation. From the new steady state conditions, partially drained or undrained properties must be considered for the loading of the excavation bottom according to the construction time and method.

From the theoretical example it was observed that the calculated safety can be less in reality if one would consider a more detailed behavior of the soil. The global safety of the wall will still be enough for this particular construction; however the safety margin will be smaller.

## ACKNOWLEDGEMENT

I will like to thanks Chalmers and my colleagues of the Geotechnical and Structure division. Special thanks to my supervisors Claes Alén and Anders Kullingsjö.

## REFERENCES

- [1] A. Ryner, A. Fredriksson, and H. Stille, *Spont-handboken - för konstruktion och utformning av sponter*. 1996, p. 154.
- [2] D. M. Wood, *Soil Behaviour and Critical State Soil Mechanics*. 1990, p. 462.
- [3] M. D. Potts and L. Zdravkovic, *Finite element analysis in geotechnical engineering - theory*. 1999, p. 440.
- [4] H.-G. Kempfert and B. Gebreselassie, *Excavations and Foundations in Soft Soils*. 2006, p. 576.
- [5] A. Kullingsjö, "Effects of deep excavations in soft clay on the immediate surroundings," Chalmers University of Technology, 2007.
- [6] H. Tanaka, "Behavior of a braced excavation in soft clay and the undrained shear strength for passive earth pressure," 1994.
- [7] R. Finno, "Saturated clay response during braced cut construction," *Journal of geotechnical engineering*, vol. 115, no. 8, pp. 1065-1084, 1989.
- [8] R. Larsson, G. Sällfors, P.-E. Bengtsson, C. Alén, U. Bergdahl, and L. Eriksson, "Skjuvhållfasthet - utvärdering i kohesionsjord," 2007.
- [9] N. Morgenstern, G. E. Blight, N. Janbu, and D. Resendiz, "Slopes and excavations," in *No. 9 - International Conference on Soil Mechanics and Foundation Engineering = Comptes Rendus du Congrès International de Mécanique des Sols et des Travaux de Fondations*, 1977, pp. 547-604.
- [10] J. Persson, "The Unloading Modulus of Soft Clay: A field and laboratory study," Chalmers University of Technology, 2004.
- [11] P. A. Vermeer and C. P. Meier, "Standsicherheit und verformungen bei tiefen baugruben in bindigen boeden," pp. 133-148, 1998.

# Stiffness parameters for the foundation design of ‘The Landmark’ tower

J.J. Dewsbury<sup>1</sup>  
*Buro Happold Ltd./University of Southampton*

## ABSTRACT

This paper reviews the selection of stiffness parameters used for the foundation design of ‘The Landmark’ tower, by comparing the results from numerical modelling with monitored settlement data. In doing so the role of single pile load tests in determining the stiffness parameters for design is assessed.

Keywords: Piled raft, stiffness parameters, Young’s modulus, geophysics, pressuremeter, weak rock, mudstone, gypsum.

## 1 INTRODUCTION

‘The Landmark’ is a 330m tower on the Corniche in Abu Dhabi. It consists of five storeys of basement and 72 storeys above ground. ‘The Landmark’ is supported on a pile assisted raft consisting of 34 piles, each 14m long with a diameter of 1.5m. This paper initially details the geology, engineering properties, and the design parameters used for ‘The Landmark’. Stiffness profiles are then back-figured from two single pile load tests using a numerical model. The stiffness profiles back-figured from the pile load tests were used in a numerical model of the piled raft to ascertain if they provided a good prediction of the monitored piled raft settlement. Finally, a stiffness profile that best matched the monitored settlement of the piled raft was determined. Settlement data that the numerical model could

be matched to was available from extensometers in the soil, and survey points on top of the raft.

## 2 GEOLOGY AND STRATIGRAPHY

The geological succession of the region consists of sand deposits overlying weak calcareous sandstone and calcarenite. This overlies interbedded weak mudstone, siltstone and very stiff gypsum bands. The original ground level at the site was +2.5mADD. The bearing level of the piled raft is at approximately -21mADD, consequently, the piles and raft are mainly situated in mudstone.

The mudstone is generally weak with bands of weak to moderately weak gypsum. The layers correlated across the borehole sections indicated that the stratigraphy is generally consistent and horizontal. No cavities were encountered in the mudstone and fracturing within the rock was generally sub-horizontal, tight, and with no evidence of infilling or weathering. The mudstone

---

<sup>1</sup>Jonathan Dewsbury, Buro Happold Ltd, Camdem Mill, Lower Bristol Road, Bath, UK, BA2 3DQ, Jonathan.Dewsbury@BuroHappold.com

was proven to 100m depth. Below approximately 50m depth (~47.5mADD) the mudstone was interbedded with calcareous sandstone bands.

Unconfined compressive strength (UCS) tests on mudstone samples recovered from high quality coring ranged between 0.53MPa to 4.8MPa, bulk density varied between 1900 kg/m<sup>3</sup> and 2100kg/m<sup>3</sup>. The gypsum bands are stronger than the mudstone with unconfined compressive strength varying between 5.7MPa and 14.5MPa, and bulk density between 2000 kg/m<sup>3</sup> and 2200 kg/m<sup>3</sup>. The ground water was at 0mADD, indicating that dewatering within the basement footprint would be necessary during construction of the temporary diaphragm walls.

### 3 ENGINEERING PROPERTIES

Young's modulus estimated from downhole geophysics, pressuremeters (High Pressure Dilatometer), and laboratory UCS tests (instrumented with strain gauges) are compared in Figure 1. The stiffness determined from the UCS tests is the secant Young's modulus at 50% of the maximum shear stress. The Young's modulus estimated from the downhole geophysics used the average velocity through the strata, ignored the effect of refraction at material boundary layers, and assumed the material was isotropic [1]. The modulus estimated from the pressuremeter data is the unload/reload modulus. The initial modulus from the pressuremeter was assumed to be accompanied by disturbance, and to give a low estimate of the true *in situ* stiffness.

If the small strain values obtained from the geophysics are reduced by a factor of five to account for the strain level, good agreement with the values of Young's modulus obtained from the pressuremeters could be achieved.

The Young's modulus derived from the UCS tests (which is likely to have positive bias as only the strongest samples would have survived coring) are marginally smaller than those determined from the pressuremeter data. This may be because of sample disturbance during retrieval and handling, although, the agreement between UCS and pressuremeter data does improve with depth.

Both the UCS tests and the pressuremeter indicate a zone of high compressibility around -20mADD (Figure 1). It was hypothesised that the zone of high compressibility was caused by drilling as stress relaxation and potential softening of the mudstone can occur due to availability of moisture. However, this could not be confirmed and therefore an allowance for a weaker zone was made in design.

Figure 2 compares the strength from the UCS tests and those derived from the pressuremeter tests assuming a Tresca failure criterion. The estimate of the strength from the pressuremeter is generally closer to the higher values of strength predicted by the UCS tests. It is usual for strength estimated from the pressuremeter to be higher than that predicted from laboratory testing [2]. The pressuremeter proved useful in identifying the stiff gypsum layers. As shown in Figure 2, there is good correlation between the material identified as gypsum in the UCS tests, and the strength at similar depths predicted from the pressuremeter data.

### 4 SINGLE PILE LOAD TESTS

Working pile load tests were conducted on two piles (CP8 and CP19). Both load tests were conducted before the basement was excavated, using a bi-directional jack operated from the ground surface (~7mADD). For CP8 the jack was positioned 3m from the pile toe, whereas for CP19 the jack was positioned 1m from the pile toe (Figure 3). The location of the jacks was chosen to separate the base and shaft response of the pile. Load was applied incrementally up to a value of 18.3MN and to 16.2MN in each direction for CP8 and CP19 respectively. Movement was measured against a reference frame, using extensometers installed at the top and bottom of the hydraulic jack assembly.

The working load tests were back analysed using a 3D numerical model in the finite element software Abaqus CAE 6.7-1. A linear elastic constitutive model with a Tresca failure criterion was adopted for the weak rock. ' $K_0$ ' was assumed to be unity and the initial *in situ* vertical stress profile was created based on each of the

material's densities multiplied by the gravitational force.

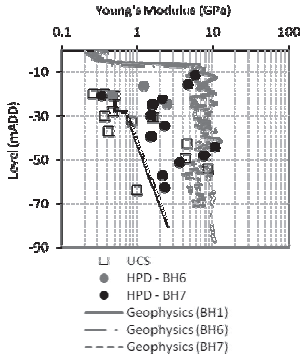


Figure 1: Variation of Young's modulus with elevation

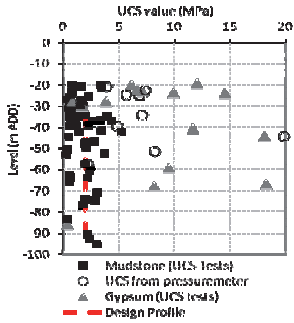


Figure 2: Variation of unconfined compressive strength with elevation

Three different stiffness profiles were used along the shaft of the pile in the numerical model. All three profiles assumed a constant value of stiffness along the pile shaft that was based on the magnitude of stiffness predicted by the UCS data, the pressuremeter, and the geophysics data. The borehole records indicated two stiff gypsum bands along the length of the pile. These were considered to be of significance and were included in the numerical model. They were taken to occur at -19.15mADD and -22.4mADD (Figure

2) with a thickness of 0.25m and 1.2m respectively. In the original design gypsum bands were not modelled. The adopted stiffness values for the materials along the pile shaft are shown in Table 1.

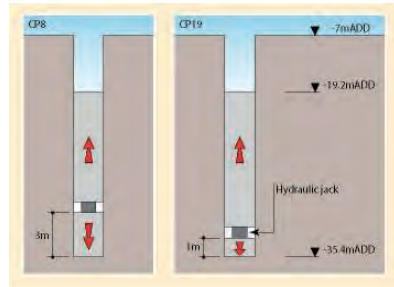


Figure 3: Illustration of pile load tests

As shown in Figure 4 and 5, for load test CP8 and CP19 respectively, the shaft response of both piles was very stiff and non-linear. The first two load steps of CP8 (Figure 4) agreed with the numerical model using the geophysics data, then on increased loading the pressuremeter data, and finally for the last three load steps, with the UCS data. This result indicates the inability of a linear elastic constitutive model to match the full pile shaft response. It was decided that using a stiffness profile based on the pressuremeter data in the numerical model would provide the best estimate of pile shaft displacement, for the majority of load steps. The recorded displacement after the first load step of CP19 (Figure 5), matched the predictions from the numerical model using the stiffness profile based on the pressuremeter the best. On increased loading, the stiffness profile based on the UCS data matched better. Thus, it was decided that a numerical model with a stiffness profile based on the UCS data would provide the best estimate of shaft displacement for the most load steps of CP19.

Base response of pile load tests CP8 and CP19 are shown in Figure 6. The response of CP8 is stiffer than that of CP19, because it tested a larger portion of pile below the hydraulic load cell. To match the base response of both load tests it was necessary to reduce the Young's modulus of

the soil directly surrounding the base. For CP8 and CP19, the Young's modulus in the numerical model for soil directly surrounding the pile base, was reduced to 0.4GPa and 0.1GPa respectively. This represented a decrease by a factor of 2.5 and 10 from that assumed in the design for load test CP8 and CP19 respectively.

Table 1. Magnitude of stiffness assumed for back-analysis of shaft load test

Ref.	Young's Modulus (GPa)			UCS (MPa)	$\nu$	$\rho$ (kg/m <sup>3</sup> )
	UCS	HPD	Geo-physics			
Mudstone	0.7	1.0	5.0	1.0	0.23	2040
Gypsum	5.0	5.0	10	8.0	0.24	2240
Concrete	35	35	35	n/a	0.15	2450

The site investigation data indicated that the mudstone was susceptible to softening if subjected to stress relaxation and moisture. If during construction, there was a delay in pouring the concrete, or the drilling fluid was not completely removed, the mudstone may have softened. This would explain the soft pile bases indicated by both pile load tests. The final adopted stiffness profiles for each load test are compared to the site investigation data in Figure 7.

## 5 PILED RAFT

The stiffness profiles back-figured from the pile load tests (Figure 7) were used in the 3D numerical model of the piled raft. The results of the numerical analysis were compared to the monitored settlement of the piled raft after the completion of floor 36, 52, and 72 (the top).

Figure 8 compares the settlement predicted from the numerical model when using the parameters derived from load test CP19, and those recorded by the extensometers just beneath the raft. The locations of the extensometers are shown by the inset in Figure 8. The settlement from the numerical model is taken from the centre of the slab at the ground/slab interface. It will be noted that the use of the parameters derived from CP19 over predicted the settlement (27mm) when compared to the monitored data (22mm).

To match the monitored settlement after the construction of the 72<sup>nd</sup> floor, it was necessary to adopt stiffness values similar to those estimated from the pressuremeter. This meant a profile of stiffness twice that assumed in design. The prediction from the numerical model using the back-figured stiffness profile, and the monitored settlement for all three construction stages are shown in Figure 8. Interestingly, the back-figured stiffness profile was the same magnitude of stiffness back-figured from load test CP8. For this reason, the prediction from the numerical model using the stiffness back-figured from load test CP8 is not plotted in Figure 8. The back-figured stiffness profile is compared to the site investigation data, and the original design profile in Figure 9. The numerical model indicated 13mm differential settlement and 6mm heave, compared with a monitored differential of 16mm, and a heave of 5mm.

## 6 DISCUSSION

Back analysis of the piled raft suggests that the moduli derived from the unload/reload cycle of the pressuremeter test provides a good estimate of the *in situ* stiffness for piled rafts in weak rock. Similar evidence has been presented for the loading of barrettes in soft calcareous rock in Dubai [3].

The stiffness derived from the pressuremeter data was about twice that assumed in design. However, it should be remembered that the pressuremeter provides a measurement of horizontal shear stiffness. Adopting the stiffness derived from the pressuremeter assumes that the material is inherently isotropic. Most soils and weak rock can be expected to display stiffness anisotropy [4].

Comparison of the numerical model and the single pile load tests shows that the linear elastic constitutive model adopted in these analyses may not be optimal. Both pile load tests indicated non-linear shaft behaviour after very small displacements, with CP8 indicating yield at around 0.1% of the pile diameter. Therefore, future analysis may benefit from adopting a non-linear elastic perfectly plastic constitutive model.



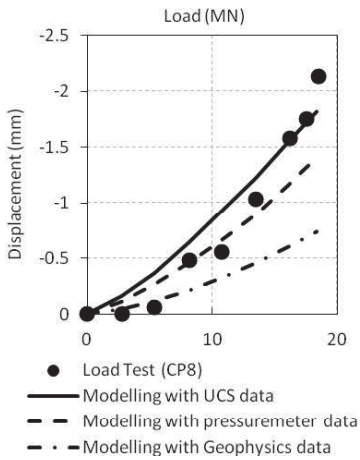


Figure 4: Comparison of shaft response from load test CP8 and numerical modeling

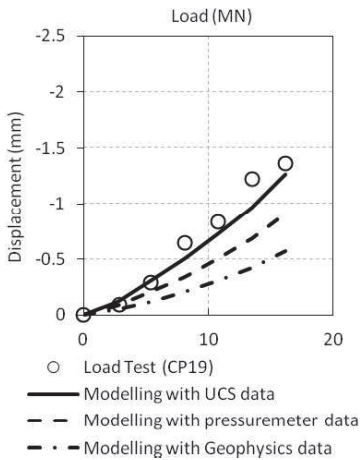


Figure 5: Comparison of shaft response from load test CP19 and numerical modeling

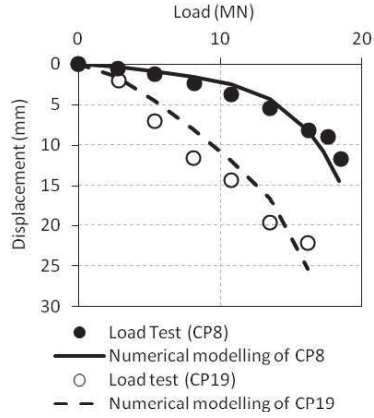


Figure 6: Comparison of base response from load tests and numerical modeling

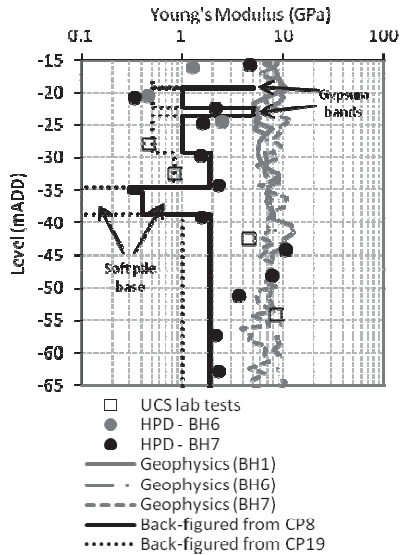


Figure 7: Comparison of SI data and stiffness profiles back-figured from pile load tests

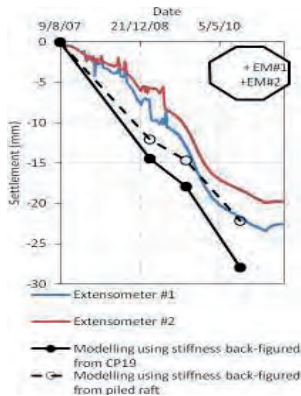


Figure 8: Comparison of monitored settlement and predictions from numerical modelling of piled raft. (Settlement taken from centre of raft at raft/ground interface).

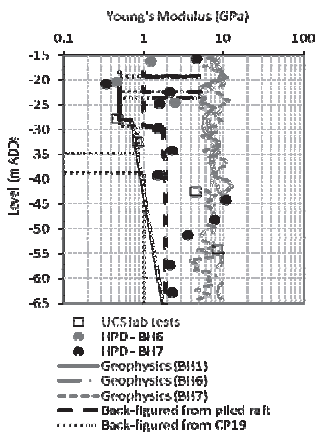


Figure 9: Comparison of back analysed stiffness profile, design profile and SI data

The stiffness back-figured from the pile load test CP19 was about half that back-figured from the monitored piled raft settlement, whilst the stiffness back-figured from CP8 was about the

same magnitude. Both load tests indicated soft pile bases, although the inclusion of soft pile bases in the numerical model was not critical to achieving a match with the monitored settlement.

## 7 CONCLUSIONS

This case study has shown that:

- The use of a stiffness profile derived from the pressuremeter data in the numerical model provides the best match with settlement of a piled raft in weak rock.
- The use of a linear elastic perfectly plastic constitutive model was not appropriate for modelling a single pile load settlement response in weak rock.
- The shaft response from pile load tests can be used to obtain estimates of ground stiffness for use in piled raft settlement analyses, but the results need to be compared with data from other sources before it can be used with confidence.
- The pile base response from load tests cannot be relied upon to estimate ground stiffness due to the potential for softening during pile construction.

## ACKNOWLEDGEMENTS

EPSRC, University of Southampton, Buro Happold, Prof. Chris Clayton, Peter Scott, and Andy Websper.

## REFERENCES

- [1] G.M. Pinches, and R.P. Thompson, Crosshole and downhole seismic surveys in the UK Trias and Lisa, *Engineering Geology Special Publications* (Geological Society), 6 (1990), 299-307
- [2] B.G. Clarke, *Pressuremeters in geotechnical design*, Blackie Academic and Professional, Glasgow, 1995.
- [3] C.M. Haberfield, D.R. Paul, M.C. Ervin & G. Chapman, Cyclic loading of barrettes in soft calcareous rock using Osterberg cells. In: *S. Gourvenec and D. White eds. Frontiers in Offshore Geotechnics II*, Taylor and Francis, Perth, 2011.
- [4] C.R.I. Clayton, Stiffness at small strain: research and practice, *Geotechnique*, 61,1, (2011), 5-37.

# Cement free mortar for annular gap grouting in shield tunnelling with slurry face support

Chr. Thienert<sup>1</sup>

Research Association for Underground Transportation Facilities – STUVA –

## ABSTRACT

For the decoupling of logistic dependences on a tunnel boring machine (TBM) annular gap grout mortar that is totally free of cement represents an interesting alternative. In addition, in soils with sufficient water permeability such grout mortar can provide stiff bedding to the segmental lining possibly earlier than conventional cement based grout mortar. For the development of shear strength and stiffness, grout mortar mixing water has to be expelled into the surrounding ground so that a drainage process occurs. In the present paper it is indicated which influences has slurry at the excavation reveal in tunnel drives with slurry face support on this process. Furthermore, it is illustrated how the grout mortar drainage process that gives properties similar to soil to the first pumpable grout mortar can be calculated depending on ground properties. In the result it is demonstrated that cement-free annular gap grout mortar is surely applicable in soils with  $k_f > 1,0 \cdot 10^{-5}$  m/s. In addition, several ground-mechanical properties of this innovative building material are presented.

Keywords: Shield tunnelling, Hydraulic face support, Slurry, Bentonite suspension, Supporting liquid, Thixotropy, Cement-free grout mortar, Grout, Mortar, Annular gap grouting, Tail void grouting, Drained grout mortar, Shear strength, Stiffness

## 1 INTRODUCTION

### 1.1 Annular gap grouting

In the course of annular gap grouting in mechanised shield tunnelling in granular soil, the annular gap with a width of approx. 8 to 18 cm for traffic tunnels is grouted according to state-of-the-art technology mostly with conventional cement mortar, see Fig. 1. Alternatively two-component material, i.e. cement bentonite suspension with accelerator addition at the end of the grout injection lines is often used.

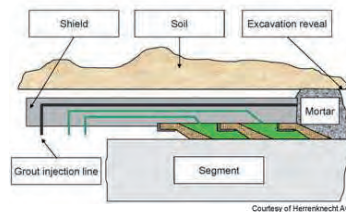


Figure 1. Annular gap grouting through the shield tail.

<sup>1</sup> Dr.-Ing. Chr. Thienert, Research Association for Underground Transportation Facilities – STUVA – Mathias-Brueggen-Str. 41, 50827 Cologne (Germany), c.thienert@stuva.de

The use of conventional cement mortar implies the disadvantage that this material starts setting already in the grout feed system due to hydration during longer tunnel drive shutdown periods. This can lead to feared blockages which must be removed time-consuming before resumption of the tunnel drive.

Although meanwhile as established regarded two components grouting material reduces the described logistic dependence extensively, however, it is rather expensive especially due to the application of solidification accelerators. Cement-free grout mortar with a robust mixture design and good stability qualities is cost-neutral or even slightly cheaper than cement grout mortar. In addition, it possesses similar logistic advantages like two components grout.

### 1.2 Cement-free annular gap fill

Depending on ground permeability an additional consumption of grout mortar, compared with the theoretical target volume, can be registered with all mentioned materials for annular gap grouting. This can be explained by the fact that filtrate water is expelled from the grout mortar into the pore volume of the surrounding ground as a result of pressure difference between injection pressure  $p_0$  and ground pore water pressure  $p_w$ . Firstly, the expelling of filtrate water causes a loss of flow ability of the grout and, finally, leads to a purely physically caused solidification.

The idea behind cement-free grout mortar is to use this solidification effect deliberately so that in the final state, in a ground-mechanical sense, a drained material is present which fills the annular gap. The solid state form can be reached (in the case of presence of sufficient ground permeabil-

ity) mostly quicker than with cement grout mortar whose chemical solidification generally only begins after several hours. This is also to avoid damages to the segmental lining an important advantage because in that way an early stiff bedding performance can be ensured.

## 2 INFLUENCES OF SLURRY

In order to use reliably cement-free annular gap grout mortar, it is essential to have some knowledge of the boundary conditions which influence the drainage process for the development of shear strength and stiffness. Besides the building material-technological grout mixture design, particularly the interaction with the surrounding ground, i.e. the arising flow resistance of filtrate water, is of importance, see Fig. 2. This has

- First to penetrate at the radial excavation reveal an interface of filtered slurry (bentonite membrane) and/or to displace stagnated slurry (bentonite suspension).
- Afterwards it must get into the pore space of the surrounding ground.

For reasons of simplicity, it is subsequently assumed that the permeability of the surrounding ground is much higher than those of the bentonite membrane. This can be taken as given for a  $k_F$  value according to DIN 18130  $k_F \geq 1,0 \cdot 10^{-5}$  m/s (so for at least water-permeable ground for the purposes of the norm). At the same time, these soils represent the typical operational area of a TBM with slurry face support. The effective support pressure  $\Delta p$ , that holds the ground grains, arises from slurry pressure in the excavation chamber  $p_{Susp}$  less pore water pressure  $p_w$  in the ground:

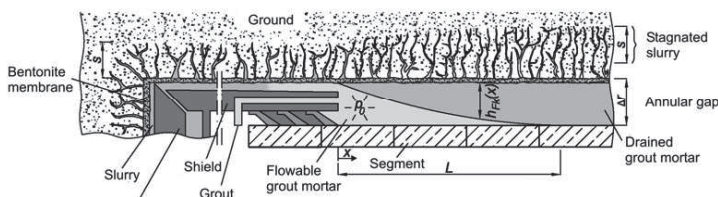


Figure 2. Draining of mortar in the annular gap in the course of shield tunneling with slurry face support.

$$\Delta p = p_{Susp} - p_w \quad (1)$$

Approximately it can be assumed that in the annular gap the same pressure boundary conditions are present like at the tunnel face.

### 2.1 Face support pressure transmission by means of a bentonite membrane

According to the assumptions in DIN 4126 a bentonite membrane – a so called filter cake – is formed for support pressure transmission in fine-grained grounds with a grain diameter of  $d_{10} \leq 0,2$  mm. This means that the effective support pressure  $\Delta p$  is transferred with normal stresses on the ground grain structure by a high pressure gradient in a thin low water-permeable layer of the thickness  $h_{Bent}$  with a coefficient of permeability  $k_{F,Bent}$ :  $\Delta p = \Delta p_{Bent}$ , see Fig. 3a).

The flow process of filtrate water from the grout mortar within this bentonite membrane can be grasped with the help of the common approach according to Darcy about the value  $k_{F,Bent}$  of this layer. The flow resistance  $R_{Bent}$  is bigger, the greater the appropriate membrane layer thickness  $h_{Bent}$  is:

$$R_{Bent} = h_{Bent} / k_{F,Bent} \quad (2)$$

The effective drainage pressure  $\overline{\Delta p_0}$ , which causes solidification of the grout mortar, arises by presence of a bentonite membrane from the pressure difference between injection pressure  $p_0$  and pore water pressure in the ground  $p_w$ :

$$\overline{\Delta p_0} = p_0 - p_w \quad (3)$$

### 2.2 Face support pressure transmission by means of static shear stresses

In grounds with a grain diameter of  $d_{10} > 0,2$  mm a stagnant penetration of slurry to the extent  $s$  can be assumed according to DIN 4126. In this area the effective support pressure  $\Delta p$  is transferred by means of static shear stresses as a result of the slurry yield point  $\tau_F$ :

$\Delta p = \Delta p_{Stag}$ . With regard to the expelling of grout mortar filtrate water into the surrounding ground, this pressure amount acts as an additional static counter-pressure to the pore water pressure  $p_w$ . However, no bentonite membrane has formed, therefore  $R_{Bent} = 0$ .

As a result of thixotropic hardening, in the time span between initial penetration of slurry into the pore space of the ground and having an effective annular gap grouting process under a pressure  $p_0$  – which is connected to a further shifting of the stagnated plug of slurry of the length  $s$  – the value  $\Delta p_{Stag}$  rises on  $\overline{\Delta p_{Stag}}$ . Depending on the bentonite sort, its dosage and duration of thixotropic hardening the relation amounts to  $\overline{\Delta p_{Stag}} / \Delta p_{Stag} \approx 1,5 \dots 2,5$ . This corresponds to the quotient of static yield point  $\tau_{F,stat}$  and calculative yield point  $\tau_F$  according to DIN 4126. Consequently, for the drainage process of grout mortar which is injected with a pressure  $p_0$  only a reduced effective drainage pressure  $\overline{\Delta p_0}$  is available, see also Fig. 3b):

$$\overline{\Delta p_0} = p_0 - (\overline{\Delta p_{Stag}} + p_w) \quad (4)$$

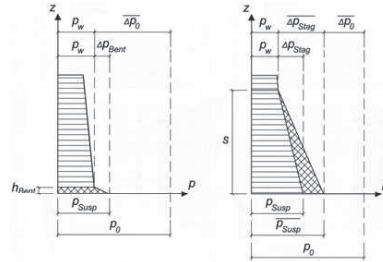


Figure 3. Pressure conditions at the roof excavation reveal  
a) Bentonite membrane, b) Stagnation of slurry

### 2.3 Hybrid form of pressure transmission

According to recent findings, both described mechanisms can be active proportionately depending on ground and slurry properties so that a hybrid form of support pressure transmission is present, see [1]. This applies, in particular, to re-

generated slurries from which with building site-common equipment (vibrating screens and hydro cyclones) not all silty and sandy grain fractions can be separated.

### 3 DRAINAGE PROCESS

According to [2] the time-dependent grout mortar drainage process can be described mathematically with the help of a filtration equation known from industrial processes. The layer from drained mortar material  $h_{Fk}$  (see also  $h_{Fk}(x)$  in Fig. 2) steadily growing with the time can be considered as a filter cake and the expelled grout mortar mixing water as filtrate (water). After the necessary drainage time  $t_{erf}$  the process has finished and the annular gap is filled completely with drained mortar material, i.e.  $h_{Fk} = \Delta r$ .

The approach presented in the above mentioned publication was valid originally only for the presence of a bentonite membrane with a flow resistance  $R_{Bent}$  as described in section 2.1. As in the case of support pressure transmission by means of static shear stresses (see section 2.2) – linked with a stagnant penetration  $s$  as a result of slurry yield point  $\tau_F$  – only the pressure amount  $\Delta p_0$  according to equation 4 has changed, it is also possible to take into account this mechanism. The result is a modified filtration equation, see Eqn. 5. Furthermore, in that way also a hybrid form of support pressure transmission as mentioned in section 2.3 can be taken into account.

$$h_{Fk} = \Delta r = \sqrt{2 \cdot \frac{1 - a_v}{a_v} \cdot \frac{\Delta p_0}{\gamma_w} \cdot k_{F,Fk} \cdot t_{erf} + \frac{(k_{F,Fk} \cdot R_{Bent})^2 - k_{F,Fk} \cdot R_{Bent}}{k_{F,Fk} \cdot R_{Bent}}} \quad (5)$$

With: $h_{Fk}$	Height of mortar filter cake
$\Delta r$	Annular gap width
$a_v$	Volume loss as a result of drainage
$\Delta p_0$	Eff. drainage pressure (acc. to Eqn. 3 or 4)
$\gamma_w$	Specific weight of pore water
$k_{F,Fk}$	Permeability of mortar filter cake
$t_{erf}$	Necessary drainage duration
$R_{Bent}$	Membrane resistance (acc. to Eqn. 2)

#### 3.1 Example calculation

With the help of an exemplary traffic tunnel it shall be indicated which duration the drainage process of cement-free grout mortar takes up in practice. In the course of this, a section of the annular gap is regarded in the area of the tunnel roof. The following assumptions are made, see also Fig. 4:

- Excavation diameter:  $D = 9,00$  m
- Overburden:  $1,5 \cdot D = 13,5$  m
- Depth of groundwater table: 2 m
- Annular gap width:  $\Delta r = 15$  cm
- At least permeable soil:  $k_F \geq 1,0 \cdot 10^{-5}$  m/s
- Specific weights:  $\gamma / \gamma' = 21,0 / 12,0$  kN/m<sup>3</sup>
- Eff. face support pressure:  $\Delta p = 50$  kN/m<sup>2</sup>

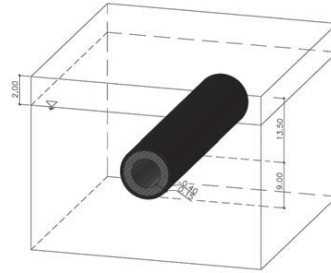


Figure 4. Tunnel of example

The grouting pressure  $p_0$  in the area of the tunnel roof is usually so adjusted that it corresponds just to the overlaying ground and ground water pressure. For the above example there is:  $p_0 = 2,00 \cdot 21,0 + 11,5 \cdot (12,0 + 10,0) = 295$  kN/m<sup>2</sup>.

With regard to the properties of the grout mortar, values of experience are estimated which can be determined through simple lab tests (e.g. filter press set-up according to DIN 4127), see [1]. Regarding the drainage process, above all, the permeability of the growing mortar filter cake  $k_{F,Fk}$  and the volume loss as a result of drainage  $a_v$  are of importance. The drainage process takes up a longer duration if the mortar filter cake permeability is low and a lot of mortar mix-

ing water must flow into the surrounding ground. Typical values are:

- Permeability of grout mortar filter cake:  
 $k_{F,Fk} = 2,5 \cdot 10^{-8}$  m/s
- Volume loss as a result of drainage:  
 $a_v = 10$  %

### 3.1.1 Bentonite membrane

On the basis of experience values a current flow resistance of the bentonite membrane of  $R_{Bent} = 3,0 \cdot 10^7$  s is assumed. This value arises according to equation 2 for a layer thickness of  $h_{Bent} = 3$  mm with a coefficient of water permeability of  $k_{F,Bent} = 1,0 \cdot 10^{-10}$  m/s. The latter value can be derived, for example, also on the building site by evaluating of the tunnel drive associated slurry protocol (filter press set-up).

In the case of support pressure transmission by means of a bentonite membrane, the effective drainage pressure  $\overline{\Delta p_0}$  corresponds after equation 3 to the grouting pressure  $p_0$  less ground water pressure  $p_w$ . Therefore there is  $\overline{\Delta p_0} = 295 - 115 = 180$  kN/m<sup>2</sup>. Insertion of the values and dissolving of equation 5 after  $t_{erf}$  delivers the necessary drainage duration:

$$0,15 = \sqrt{2 \cdot \frac{1-0,1}{0,1} \cdot \frac{180}{10} \cdot 2,5 \cdot 10^{-8} \cdot t_{erf} + \frac{(2,5 \cdot 10^{-8} \cdot 3,0 \cdot 10^7)^2}{-2,5 \cdot 10^{-8} \cdot 3,0 \cdot 10^7}}$$

$$\Rightarrow t_{erf} = 30.600 \text{ s} = 8,5 \text{ h}$$

### 3.1.2 Static shear stresses

Provided that the effective face support pressure  $\Delta p$  is transmitted by means of static shear stresses as a result of the slurry yield point  $\tau_F$  the effective drainage pressure  $\overline{\Delta p_0}$  decreases (according to the implementation in section 2.2) over the amount  $p_w$ . Nevertheless, no low water-permeable bentonite membrane exists which must be passed by mortar filtrate water, i.e.  $R_{Bent} = 0$ .

In the present calculation example thixotropic hardening is considered by the factor

$\overline{\Delta p_{Stag}} / \Delta p_{Stag} = \tau_{F,stat} / \tau_F = 2,0$ . The effective drainage pressure  $\overline{\Delta p_0}$  according to equation 4 for this tunnel with an effective face support pressure  $\Delta p = \Delta p_{Stag} = 50$  kN/m<sup>2</sup> amounts to:  $\overline{\Delta p_0} = 295 - (2,0 \cdot 50 + 115) = 80$  kN/m<sup>2</sup>. Insertion of the values and dissolving of equation 5 after  $t_{erf}$  delivers the necessary drainage process duration again:

$$0,15 = \sqrt{2 \cdot \frac{1-0,1}{0,1} \cdot \frac{80}{10} \cdot 2,5 \cdot 10^{-8} \cdot t_{erf}}$$

$$\Rightarrow t_{erf} = 6.300 \text{ s} = 1,8 \text{ h}$$

### 3.2 Limitations of application

A comparison of the calculated values indicates that grounds in which (solely) a support pressure transmission occurs by means of static shear stresses are the optimum range of application for cement-free grout mortar. These are generally at least high water-permeable gravelly sands with  $k_F \geq 5 \cdot 10^{-3}$  m/s. But also in "only" water-permeable soil conditions (in terms of DIN 18130 with  $k_F \geq 1 \cdot 10^{-5}$  m/s (and with it to negligible flow resistance in the surrounding ground in the course of the mortar drainage process) a complete grout mortar draining in the annular gap occurs already within a few tunnel driving cycles. Consequently, here can be spoken of a possible range of application. To sum up, these conclusions are shown in Fig. 5.

Nevertheless, condition for the validity of the time spans  $t_{erf}$  calculated above is that of optimum manner the grouting pressure  $p_0$  in the annular gap will maintain on a high level also during tunnel drive interruptions. For this

- In particular it has to be guaranteed that the grouting pumps are not switched off before the end of the actual driving process and
- Besides, single manual – or automatically steered – pump strokes must be executed during shutdown periods.

Provided that the listed demands are fulfilled, cement-free grout mortar is already after the assembling and grouting of a few segmental lining rings no longer flowable but in a state form simi-

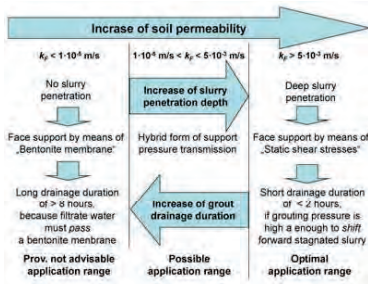


Figure 5: Application ranges of cement-free grout mortar

lar to ground. In consequence, damages on the segmental lining elements due to spalling of concrete, which are to be registered in general already from 5 to 10 rings after leaving the shield tail of the TBM, can be avoided in suitable ground conditions (i.e. in at least water-permeable grounds in terms of DIN 18130-1 with  $k_F \geq 1 \cdot 10^{-5}$  m/s) more effectively than with a conventional cement grout mortar whose hardening only begins after several hours.

#### 4 PROPERTIES OF DRAINED MORTAR

The characteristic ground-mechanical property of drained mortar material with regard to lining bedding behavior is the stiffness or the consistency. The latter should be at least "stiff" or better "semi-solid". In the course of this, the effective drainage pressure level  $\overline{\Delta p_0}$  plays a crucial role because of non-linearity in stress strain behaviour. Hence, many parameters cannot be specified generally but have to be referred to the effective stress  $\sigma'$  in the annular gap:  $\sigma' = \overline{\Delta p_0}$ .

Based on a passed lab testing program the following ground-mechanical properties of a more exactly examined cement-free mortar of reference with a high flour grain content for securing pumpability as well as a good grain gradation by the fine sand area up to the used largest grain diameter from  $d_{\max} = 6$  mm can be specified:

- Values of the stiffness module  $E_S$  (measured in a large-scale oedometer with a diameter of 20 cm and one-sided drainage

possibility) are to be achieved which amount about to the 100-fold of the effective stress level  $\sigma'$ :  $E_S \approx 100 \cdot \sigma'$ .

- In consolidated and drained (CD) triaxial compression tests an angle of internal friction of  $\varphi' = 40^\circ$  was determined. Besides, on account of the flour grain portion a low cohesion of  $c' \approx 10$  kN/m<sup>2</sup> was registered.

#### 5 RESUME

In sufficient water-permeable grounds with  $k_F \geq 1 \cdot 10^{-5}$  m/s grout mortar for annular gap grouting that is totally free of cement and with optimized mixing design with regard to quick draining performance (and coefficient of water permeability  $k_F$  of the grout mortar filter cake of approx.  $k_F \geq 2,5 \cdot 10^{-8}$  m/s) is earlier able to provide to the segmental tunnel lining elements stiff bedding than conventional cement grout mortar whose hardening only begins after several hours. In consequence, besides the decoupling of logistical dependences on a TBM this type of grout mortar has the strong advantage of contributing to avoid damages on the segmental lining.

Hence, it is suggested to rethink about the demand for a high unconfined compression strength  $q_u$  of the annular gap material at the age of one day in the range  $q_u = 0,5 \dots 1,0$  MN/m<sup>2</sup> or the general specification „according to the qualities of the surrounding ground“ that can up to now often be found in calls for bids. Instead it is recommended, basing on the present paper, to require short drainage duration in the course of the usage of cement-free grout mortar.

#### REFERENCES

- [1] Chr. Thienert, *Zementfreie Mörtel für die Ringspaltverpressung beim Schildvortrieb mit flüssigkeitsgestützter Ortsbrust. (Cement free mortar for annular gap grouting in shield tunnelling with hydraulic face support)*, Report No. 31, Geotechnical Institute of the University of Wuppertal, Editor: M. Pulsfort, ISBN: 978-3-8440-0167-9, Shaker-Verlag Aachen, 2011
- [2] A.M. Talmon, A. Bezuijen, *Simulating the consolidation of TBM grout at Noordplaspolder*, *Tunnelling and Underground Space Technology* 24 (2009), 493-499



# Numerical simulation of tunnel construction in London Clay using three constitutive models

Luis Manuel Araújo Santos<sup>1</sup>

*Coimbra Institute of Engineering, Coimbra, Portugal*

Paulo José da Venda Oliveira, Jorge Nuno Veiga de Almeida e Sousa

*University of Coimbra, Coimbra, Portugal*

## ABSTRACT

This paper presents the results of numerical simulations of the extension of the Jubilee Line of the London Underground system (UK) at St. James' Park. The analyses were carried out using the Finite Element software UCGeoCode, developed at the University of Coimbra, Portugal, employing three distinct constitutive relationships: elasto-perfectly plastic Mohr-Coulomb, Modified Cam-Clay and the MIT-E3 model. The parameters for each of these constitutive laws are presented, while the impact of the different models in the obtained results is evaluated by comparing the simulated behaviour with field monitoring data. It is demonstrated that, even though the more sophisticated models reproduce most features of soil behaviour observed in laboratory testing, the agreement between the numerical results and field data does not improve substantially. At least, the introduction of a non-realistic  $K_0$  in the calculation is discussed.

Keywords: numerical simulation, tunnel, MIT-E3, London Clay, Jubilee Line

## 1 INTRODUCTION

The increasing use and complexity of underground construction works have resulted in the development of sophisticated techniques aimed at characterising the stress and strain states of the surrounding soil. Among these procedures, the Finite Element Method has been extensively employed in such studies.

One of the most fundamental aspects of a numerical analysis using this method is the chosen constitutive law. Indeed, with the objective of reproducing soil behaviour with a greater degree

of accuracy, several material models have been proposed with distinct levels of complexity. In this paper, the MIT-E3 bounding surface plasticity model, which has been shown to be particularly suited for simulating the stress-strain response of saturated, over-consolidated clays ( $OCR < 8$ ), is employed in the numerical analysis of tunnel construction and its performance is compared to that of simpler constitutive relationships, such as elasto-perfectly plastic Mohr-Coulomb and Modified Cam-Clay models.

---

<sup>1</sup> Corresponding Author. Coimbra Institute of Engineering, Rua Pedro Nunes – Quinta da Nora, 3030-199 Coimbra, Portugal, lmsantos@isec.pt

## 2 CASE STUDY

### 2.1 Initial conditions

The extension works of the Jubilee Line of the London Underground system took place between 1993 and 1999 and connected Green Park to Stratford, totalling a length of 16km, 12.4 of which are underground [1] The excavation works have been carried out with different types of tunnelling machines, depending on the soil characteristics. Two 4.85m diameter twin tunnels have been constructed, one for each running direction. During the construction, extensive field monitoring was carried out, providing a wide range of field data and allowing detailed numerical studies to be performed, such as the one presented in this paper.

For this analysis, the instrumented section located at St. James' Park has been chosen, between Green Park and Westminster underground stations. In this area, the underground line construction took place under "Greenfield" conditions, allowing the study the effects on the surrounding soil due only to the excavation of the tunnels.

### 2.2 Local geology and section geometry

Underneath St. James' Park, the two twin tunnels were dug in London Clay. The westbound tunnel (WB) was the first to cross the monitored section and, roughly 250 days after, the eastbound tunnel (EB) crossed the section [2]. 21.5m separate the vertical axis of the westbound and eastbound tunnels and their horizontal axis are, respectively, at a depth of 31.0m and 20.5m, as shown in Fig. 1 [3].

Fig. 1 also summarises the geological conditions. Above the London Clay formation, there is a 4.9m thick layer of Thames River Terrace Gravel, topped by a 4.1m thick layer of made ground over alluvium. The water table is located between the last two soil layers and, according to the field data, the piezometric pressure distribution is near-hydrostatic [1].

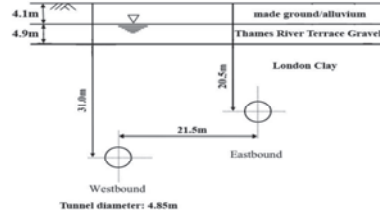


Figure 1. Soil Profile (adapted from Addenbrooke et al. [4]).

## 3 DETAILS OF NUMERICAL ANALYSES

The 2D-analyses were carried out using the finite element (FE) mesh presented in Fig 2. Similar meshes have been used in previous works, such as Addenbrooke et al. [4] and Burland et al. [3]. In the present article, the FE mesh is constituted by 1010 eight-noded quadrilateral finite elements. The bottom and the two lateral boundaries were considered impermeable, while a pore water pressure of 0.0 kPa was assumed for the interface between the made ground/alluvium and Thames River Terrace Gravel.

The existing soils at St. James' Park were simulated using different constitutive models. However, given that the present article focuses on the behaviour of London Clay, the response of the remaining materials was modelled employing identical parameters and constitutive laws to those presented on the aforementioned works. Thus, the behaviour of the made ground/alluvium was predicted by an isotropic linear elastic law, while the behaviour of the Thames River Terrace Gravel was assumed as elastic-perfectly plastic with a Mohr-Coulomb failure criterion.

Regarding the tunnel lining, isotropic linear elastic model was used, characterised by  $E' = 28\text{GPa}$ ,  $\nu' = 0.15$  and  $\gamma = 24\text{kN/m}^3$ , as it has been proposed by Addenbrooke et al. [4]. Drainage through the tunnels was considered.

In particular, the present study concerns only the results due to the excavation of the first tunnel (WB), since its construction was not influenced by any existing structures.

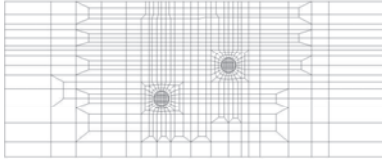


Figure 2. Adopted Finite Element Mesh.

#### 4 CONSTITUTIVE MODELS USED TO DEFINE LONDON CLAY

Three different constitutive relationships were used to simulate the behaviour of London Clay due to the excavation of the WB tunnel: elasto-perfectly plastic Mohr-Coulomb, Modified Cam-Clay and MIT-E3 model. The values of the respective parameters are discussed below, given particular emphasis to the calibration of the latter.

In order to improve the accuracy of the numerical simulations, the London Clay was further subdivided into 4 layers, with different  $K_0$  values and, consequently, distinct OCRs. For the first 15m of London Clay, the  $K_0$  values decreased from 1.5 to 1.0, remaining constant for deeper levels. The bulk unit weight for London Clay was  $20\text{kN/m}^3$ .

Finally, anisotropic permeability was used, characterised by  $k_h = 2.8 \times 10^{-11}$  m/s and  $k_v = 1.1 \times 10^{-11}$  m/s, which is consistent with the test results and the anisotropy ratio presented by Chandler et al. [5].

##### 4.1 Mohr-Coulomb (MC)

The first model used in the numerical simulation of London Clay was the elasto-perfectly plastic Mohr-Coulomb model, which is perhaps the most popular constitutive model in geomechanics. The strength parameters assumed were the average of the values presented by Burland et al. [3], i.e.  $c' = 6\text{kPa}$  and  $\phi' = 26^\circ$ . The adopted elastic parameters were  $\nu' = 0.288$  and  $E' = 40\text{MPa}$ . Unlike previous works, the latter value was assumed constant with depth.

##### 4.2 Modified Cam-Clay (MMC)

The Modified Cam-Clay model, along with de Cam-Clay model, were the first critical state models describing the behaviour of clays. As it is well known, its formulation is based on four critical state parameters, which are determined by common laboratorial testes.

The Critical State parameters for London Clay have been widely discussed in previous works. In this paper, the values firstly proposed by Schofield and Wroth [6] were used:  $\lambda = 0.161$ ,  $\Gamma = 2.759$ ,  $\kappa = 0.062$  and  $M = 0.888$ . The finite element software automatically defined the specific volume for  $p' = 1\text{kPa}$  on the virgin compression line (VCL).

##### 4.3 MIT-E3

The MIT-E3 model was developed in order to represent the behaviour of overconsolidated saturated clays (OCR up to 8) under cyclic loading, since the behaviour of these clays obeys a normalized behaviour [7]. According to these authors, the model comprises three components: (1) an elastoplastic model for normally consolidated clays, which describes anisotropic properties and strain-softening behaviour; (2) equations for the small strain nonlinearity and hysteretic stress-strain response due to unload-reload cycles; and (3) bounding surface plasticity for irrecoverable, anisotropic and path-dependent behaviour of overconsolidated clays. In fact, the development of this constitutive relationship was originally intended as a form of reproducing several features of soil behaviour registered in laboratory tests, which could not be adequately simulated by the numerical model used so far, such as the Modified Cam-Clay model [7].

The formulation of the MIT-E3 model is beyond the scope of this paper. Indeed, this paper focuses solely on the presentation and discussion of the adopted parameters employed by the abovementioned constitutive relationship. Additionally, further information on the procedure followed for the implementation of the MIT-E3 model into UCGeoCode – the Finite Element software developed at the University of Coimbra, Portugal – can be found in Venda Oliveira [8].

The MIT-E3 model is controlled by fifteen parameters, eight of which lack physical meaning and are, therefore, indirectly estimated by comparing experimental and numerical results. The other seven parameters are physical soil properties and are determined from laboratory tests or by correlation with other geotechnical parameters. The input parameters for the model and their physical meaning are summarised in Table 1.

Table 1. Input parameters for MIT-E3 model.

Parameter	Whittle [9]	Santos [10]
$K_0^{NC}$	0.62	0.62
$\phi'_{TC}$	22.5	22.5
$\phi'_{TE}$	22.5	22.5
$e_0$	1.21	1.21
$\lambda$	0.172	0.172
$\kappa_0$	0.001	0.001
$2G/K$	0.99	0.99
$Sr$	3.90	3.90
$c$	0.80	0.80
$w$	0.20	0.03
$\gamma$	0.50	0.50
$C$	65	50
$n$	1.50	1.50
$h$	0.10	0.10
$\psi_0$	100	100

The various studies that have been performed on London Clay by several authors in different locations have allowed an accurate estimation of the fifteen parameters. Among these, the experimental works conducted by Fourie [11], Jardine [12] and, more recently, Gasparre [13] are highlighted, due to their valuable contribution to the characterisation of this material. Additionally, the input parameters for this model proposed by Whittle [10] for London Clay are shown in Table 1, together with the results of the present calibration procedure.

As it is shown on Table 1, the calibration of the MIT-E3 model has provided identical parameters to those proposed by Whittle [9], except for the constants  $C$  and  $w$ . The value for parameter  $C$  proposed in this paper, is smaller than that presented by Whittle [9]. Fig. 3 shows that, for high levels of volumetric extension, the numerical results with  $C = 65$ , deviates from the laboratory

data. Conversely, by using 50 for this constant, an accurate reproduction of the laboratory curve for values of volumetric extension up to 7% is obtained.

Concerning the constant  $w$ , the soil response simulated using the value suggested by Whittle [9] is considerable less stiff than that observed in laboratory tests. Conversely, for small strains, the numerical results obtained with  $w = 0.03$  agree better with the measured values, as is shown in Fig. 4.

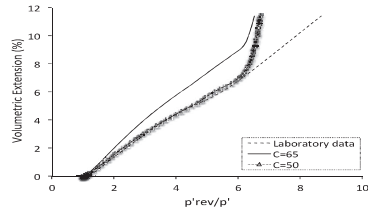


Figure 3. Calibration of Parameter  $C$

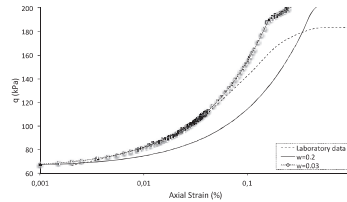


Figure 4. Calibration of parameter  $w$ .

## 5 RESULTS FROM NUMERICAL ANALYSES

The numerical prediction of ground movement due to tunnelling was controlled by the volume loss of the Westbound Tunnel. According to Nyren [1], the volume loss measured by the field instrumentation was 3.2%. For each model, a specific percentage of unloading has been defined in order to obtain a volume loss close to the real one. For both Modified Cam-Clay and Mohr-Coulomb models, a percentage of unloading-

ing of 60% was used, resulting in volume losses of 3.11% and 3.15%, respectively. The numerical analysis with the MIT-E3 model required a slightly larger percentage of unloading (66.5%) to reach a volume loss of 3.17%. A second calculation was performed with the MIT-E3 model. In this numerical analysis, hereinafter referred to as MIT-E3(ZR), it was used a reduced  $K_0$  of 0.5 in London Clay around the tunnel, instead of the real value, as it has been proposed by Adenbrooke [14]. This last simulation has used a percentage of unloading of 32%, reaching a volume loss of 3.25%.

### 5.1 Short-term results

The surface settlement profiles for the numerical analyses carried out, as well as the field data, are presented in Fig. 5(a). The numerical results of the MCC and MC models are very similar. The settlement profiles are clearly too wide, predicting only a maximum displacement of 7mm, while 18mm were registered by the field instrumentation. Conversely, the analysis with the MIT-E3 model has resulted in a deeper and narrower settlement trough. However, despite the clear improvement of the numerical simulation when using this model, the maximum vertical displacement above the westbound tunnel is about half of that measured in the field, while the reproduced settlement profile is flatter and wider. The conjunction of the MIT-E3 model with a reduced  $K_0$  around the tunnel provides the better results. The maximum vertical displacement is 2mm smaller than the measured by the instrumentation and the shape of the obtained subsidence trough is very similar to the real.

In terms of the soil response in depth, it can be seen in Fig. 5(b) that, with the exception of the analysis MIT-E3(ZR), which reproduces correctly the evolution in depth of the maximum settlement, the remaining numerical analyses are unable to reproduce the maximum observed vertical displacement. Indeed, with the exception of the soil immediately above the tunnel crown, the evolution of this component of deformation above the tunnel axis is practically parallel to that measured in the field. For the area closer to the tunnel, probably due to a larger influence of

the simulated plastic behaviour, the rate of variation of vertical displacements is higher than that observed “in situ”.

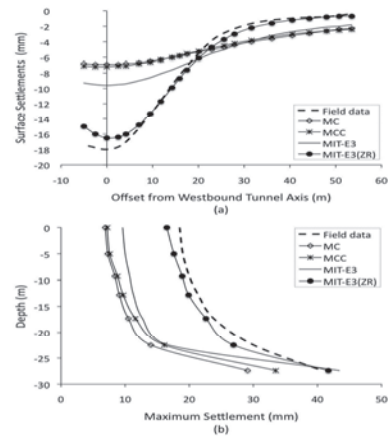


Figure 5. Short-term results: (a) Surface settlement profile of the westbound tunnel; (b) Variation in depth of the maximum settlement above the tunnel WB.

### 5.2 Long-term results

As previously mentioned, 250 days separated the construction of the two tunnels. During this period, the vertical displacements have increased due to the consolidation process. The data collected by the field instrumentation are plotted in Fig. 6, together with the results of the numerical analyses for this period.

Independently of the constitutive model employed to simulate the behaviour of London Clay, Fig. 6 clearly shows that the computed evolutions of the maximum settlement at the surface exhibit a similar trend to that defined by the field data. In all the illustrated cases, between the end of the construction of the westbound tunnel and the beginning of the excavation of the eastbound tunnel, the vertical displacement increases by about 30% of its initial value.

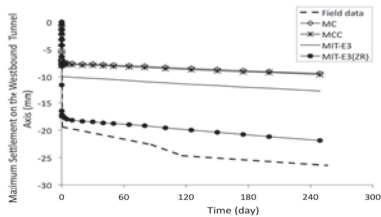


Figure 6. Evolution of the maximum surface settlement.

## 6 CONCLUSIONS

The new set of parameters for the MIT-E3 model presented in this work allows a better adjustment of the numerical simulations of tests conducted on London Clay. However, despite reproducing accurately the stress-strain response measured in laboratory tests, the performed numerical analysis using this model was unable to replicate the ground movements observed at St. James' Park, due to tunnel excavation. Both the maximum vertical settlement and the surface settlement profile obtained don't match the field data, which shows a stiffer behaviour of the modelled material than the real one.

Nevertheless, when compared to the performance of the two other constitutive relationships presented in this paper (Mohr Coulomb and Modified Cam-Clay), it was shown that the use of the MIT-E3 model leads to a better agreement with the displacements registered in the field in the short term. A way to obtain better results in numerical analyses with the MIT-E3, is considering a non-realistic low value of  $K_0$  around the tunnel. But, as the London Clay formation is an overconsolidated clay, this solution has neither theoretical nor experimental support.

Lastly, regarding the evolution with time of the surface settlement resulting from ground consolidation, the three constitutive relationships studied in this paper led to similar trends.

## ACKNOWLEDGEMENT

This article would not have been possible without the detailed field data made available by Dr. Jamie Standing of Imperial College London, London. His support is greatly acknowledged.

## REFERENCES

- [1] Nyren, R. J, *Measurements above twin tunnels in London in London Clay*, Ph. D. Dissertation, Imperial College of Science, Technology and Medicine, London, 1998.
- [2] Burland, J. B., Standing, J. R., Jardine, F. M, *Building Response to Tunnelling: case studies from construction of the Jubilee Line Extension, London. Volume 2: Case Studies*, Thomas Telford Ltd, London, 2001.
- [3] Burland, J. B., Standing, J. R., Jardine, F. M, *Building Response to Tunnelling: case studies from construction of the Jubilee Line Extension, London. Volume 1: Projects and Methods*, Thomas Telford Ltd, London, 2001.
- [4] Addenbrooke, T. I., Potts, D. M., Puzrin, A. M. The influence of pre-failure soil stiffness on the numerical analysis of tunnel construction. *Géotechnique* 47, No 3 (1997), 693-712.
- [5] Chandler, R. J., Leroueil, S., Trenter, N. A. Measurements of the permeability of London Clay using a self-boring permeameter. *Géotechnique* 40, No 1 (1990), 113-124.
- [6] Schofield, A. & Wroth, P, *Critical State Soil Mechanics*, McGraw-Hill, London, 1968
- [7] Whittle, A. J. & Kavvasdas, M. J, Formulation of MIT-E3 model for overconsolidated clays. *Journal of Geotechnical Engineering* 120, No 1 (1994), 173-198.
- [8] Venda Oliveira, P. J. 2000, *Embankment in soft clays – numerical analyses* (in Portuguese), Ph. D. Dissertation, University of Coimbra, Coimbra, 2000.
- [9] Whittle, A. J, Evaluation of a constitutive model for overconsolidated clays, *Géotechnique* 43, No 2 (1993), 289-313.
- [10] Santos, L. M. A, *The importance of constitutive laws to model tunnels in soils* (in Portuguese), MSc Dissertation, University of Porto, Porto, 2009.
- [11] Fourie, A. B, *The behaviour of retaining walls in stiff clay*, Ph. D. Dissertation, Imperial College of Science, Technology and Medicine, London, 1984.
- [12] Jardine, R. J, *Investigation of pile – soil behaviour with special reference to the foundations of offshore structures*, Ph. D. Dissertation, Imperial College of Science, Technology and Medicine, London, 1985.
- [13] Gasparre, A, *Advanced laboratory characterisation of London Clay*, Ph. D. Dissertation, Imperial College of Science, Technology and Medicine, London, 2005.
- [14] Addenbrooke, T. I. *Numerical analysis of tunnelling in stiff clay*, Ph. D. Dissertation, Imperial College of Science, Technology and Medicine, London, 1996.

# Influence of a core size on correlation between Schmidt rebound hardness and uniaxial compressive strength on Tertiary sedimentary rocks from Slovenia

Teja Fabjan<sup>1</sup>  
*IRGO Consulting*

Vladimir Vukadin  
*IRGO – Institute for Mining, Geotechnology and Environment*

## ABSTRACT

Tertiary sedimentary rocks discussed in this paper cover a significant part of Slovenian territory and are often encountered in geotechnical construction. During geotechnical site investigation Schmidt hammer test is frequently employed because it is quick and non-destructive method, which provides continuous information over entire length of core. However, Schmidt rebound hardness has no direct geotechnical meaning, unless is correlated with uniaxial compressive strength.

As shown by many researchers [7, 10, 12, 16] Schmidt rebound hardness is depended on specimen diameter and lithology. For this purpose influence of drill cores size on Schmidt rebound hardness was investigated to predict strength-size relationship. Measurements were carried out on six types of Tertiary rock including marl, siltstone, sandstone, their combination (flysch), porous sandstone and limestone. The collected data were analyzed and empirical correlations between uniaxial compressive strength and Schmidt rebound hardness was obtained for different rock types.

Keywords: Schmidt hammer, Schmidt rebound hardness, uniaxial compressive strength, core diameter

## 1 INTRODUCTION

Schmidt hammer test is often used during geotechnical site investigation. It was developed in late 1940s for testing concrete hardness [1] and was later used to determine hardness of rock [2]. Since then it has been widely used, because it is a quick, usually non-destructive and inexpensive method. It could be used in the laboratory or in the field. Result of the testing is a Schmidt hammer rebound hardness number/value ( $Hr$ ).

However, Schmidt hammer rebound value has no direct geotechnical meaning, unless it is cor-

related with uniaxial compressive strength (UCS). In last few decades many researchers have developed correlations with Schmidt hammer rebound values mainly for estimating UCS and Young modulus ( $E$ ) for different rock types. Developed correlations can be divided into three categories:

- Linear correlation: Deere and Miller [3] based on basalt, diabase, dolomite, gneiss, limestone, marble, quartzite, rock salt, sandstone, schist, siltstone and tuff; O'Rourke [4] based on sandstone, siltstone, limestone and anhydrite; Sachpazis [5]

<sup>1</sup> Teja Fabjan. IRGO Consulting, Slovenčeva 93, 1000 Ljubljana, Slovenia, teja.fabjan@irgo.si

based on 33 different carbonates; Tuglur and Zarif [6] based on granitic rocks; Shalabi et al. [7] based on dolomite, rock shale, marble, deopside, anhydrite and limestone; and Cobanoglu and Clik [8] based on sandstone, limestone and cement mortar;

- Exponential correlation: Xu et al. [9] based on Mica-schist; Katz et al. [10] based on marble, limestone, granite, sandstone, chalk and syenite; Yilmaz and Sendir [11] based on gypsum rock; and Aydin and Basu [12] based on granitic rocks;
- Power correlation: Derman and Irfan [13] based on granitic rocks; Gökçeoğlu [14] based on marl; Yasar and Erdogan [15] base on limestone, sandstone, marble and basalt; Yagiz [16] based on travertine limestone, schist and dolomitic limestone; and Kilic & Teymen [17] based on 19 rock types.

Some of the researchers [3, 7, 15, 16] also developed correlations between UCS or Schmidt hammer rebound value and unit weight ( $\gamma$ ) or water content ( $w$ ).

In this paper, influence of a core size on correlation between Schmidt hammer rebound values and UCS is presented on several Tertiary sedimentary rocks from Slovenia. In addition, the influence of unit weight and water content is also investigated.

## 2 RESEARCH AREA AND MATERIALS

In this study, six different rock types are compared from three different sites in Slovenia. The Draženci – Gruškovje site (site A) is located in the eastern part of Slovenia and the other two sites Divača – Koper (site B) and Jagodje – Lucija (site C), are located in SW Slovenia, as is shown on Figure 1. All the data were collected during geotechnical investigations for highway and railway projects that are currently under way. Particular site spans over area of several kilometers in length.

On all three sites only Tertiary sedimentary rocks were encountered: rocks of Miocene age at site A (sandstone, porous sandstone and silt-

stone) and rocks of Eocene age at sites B and C (limestone, marl, siltstone, sandstone and flysch). Flysch (sequence) represents rocks with variable combinations of marl, siltstone or/and sandstone.

Altogether 103 measurements were taken from specimens at site A, 189 from site B and 43 specimens from site C. The detailed information about tests and measurements is given later.



Figure 1. Location of study sites: A) highway Draženci - Gruškovje (red point), B) railway Divača - Koper (yellow point) and C) highway Jagodje-Lucija (blue point).

## 3 METHODS AND TESTING PROCEDURES

For purpose of this study, the measurements of Schmidt hammer rebound values and UCS were carried out. The Schmidt rebound hardness was executed in accordance with ISRM suggested methods [18] and ASTM standard [19] using Matest concrete test hammer, model C380, with 2.207 J spring impact energy. The Schmidt hammer was used in the laboratory and in the field on cylindrical specimens taken from boreholes with diameter ranging from 43.7 to 101 mm. Measurements were never taken on outcrops or rock cuts. The Schmidt hammer was held in downward position on fresh specimens, which were placed in a 26 kg V-steel base. No additional correction curves provided by manufacturer were applied for downward position.



UCS tests were following ASTM standard [20] using the 1140 kN SBEL compression machine on cylindrical specimens with diameter ranging from 47.5 to 101 mm.

In addition to Schmidt hammer rebound values and UCS, measurements of water content and unit weight were carried out on specimens tested in laboratory. The total number of tests on different rock types is shown in Table 1.

Table 1. Number of measurements for each rock type and investigated sites.

Site	Rock type	No. of UCS	No. of $H_r$	No. of $\gamma$	No. of $w$
A	sandstone	37	26	37	36
	porous sandstone	7	5	7	7
	siltstone	59	29	59	58
B	limestone	127	68	127	66
	sandstone	39	0	39	0
	siltstone	1	0	1	1
	marl	3	2	3	2
	flysch*	19	0	19	0
C	sandstone	7	7	7	7
	siltstone	1	1	1	1
	marl	2	2	2	2
	flysch*	33	33	33	3
	<b>Total</b>	<b>335</b>	<b>173</b>	<b>335</b>	<b>183</b>

\*flysch represents a specimen variable combinations of marl, siltstone or/and sandstone.

#### 4 RESULTS AND ANALYSIS

As can be seen from Table 1, total of 173 Schmidt hammer rebound values were made on different rock types on different core diameters from all three sites. Results from all measurements are presented on Figure 2. A significant scatter of results can be observed when all results are compared. Detailed analysis has shown that there is no significant difference between the same rock types from different site, so all the data from the same lithology is treated together regardless of their origin.

The best correlation was observed for limestone ( $R^2 = 0.72$ ); somewhat lower correlation for siltstone ( $R^2 = 0.49$ ), while the data for sandstone and flysch correlates very poorly ( $R^2 < 0.20$ ). The scatter observed on flysch is expected because of different combinations of sandstone, siltstone and marl components.

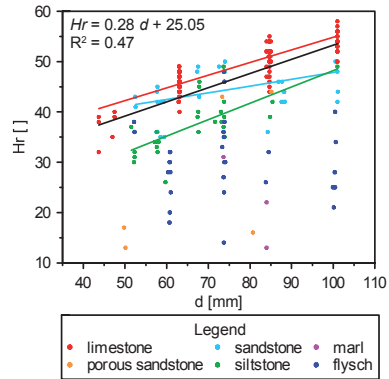


Figure 2. Correlation between Schmidt hammer rebound values  $H_r$  and specimen diameter  $d$ .

It is harder to explain the weak correlation observed in sandstone. It can probably be attributed to varying contents of calcareous and quartz components. Data for porous sandstone and marl are also shown on Figure 2, but without correlations because of the small number of measurements.

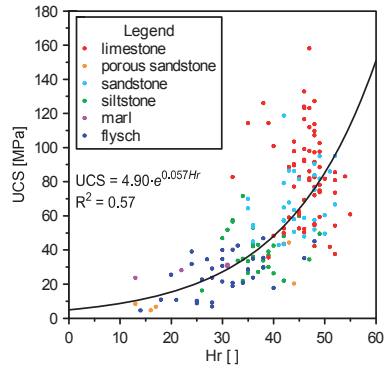


Figure 3. Correlation between UCS and Schmidt hammer rebound values  $H_r$  based on rock lithology.

The correlation between UCS and Schmidt hammer rebound values for all rock types is shown on Figure 3. Again larger scatter can be observed, and the exponential correlation has low correlation coefficient ( $R^2 = 0.57$ ).

The same data are shown again on Figure 4, however, this time they are interpreted regarding on specimen diameter ( $d$ ). Significantly improved correlations can be observed and correlation coefficient is increasing from smallest diameter ( $R^2 = 0.57$ ) towards largest diameter ( $R^2 = 0.81$ ) regardless of the rock type. It was discovered that a correlation curves of wider diameter sizes are moving down on the graph.

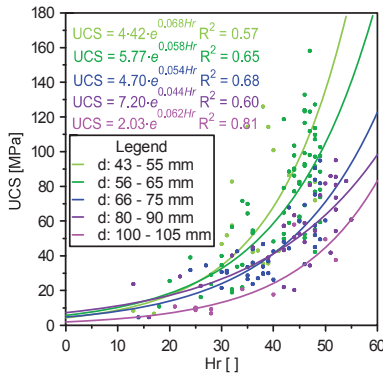


Figure 4. Correlation between UCS and Schmidt hammer rebound values  $Hr$  based on specimen diameter (core).

Despite weak correlation coefficient for exponential curve between UCS and Schmidt hammer rebound values, we can see on Figure 5 that the correlation from this study falls within range of exponential and power empirical equations derived by other researchers [3-17].

However, for the same Schmidt hammer rebound value empirical correlations developed by different researchers could give up to 5 times different values of UCS. This implies that these empirical correlations are not general in nature and have to be used with great care. Computed UCS values should be treated as an approximate

estimation appropriate only for general determination.

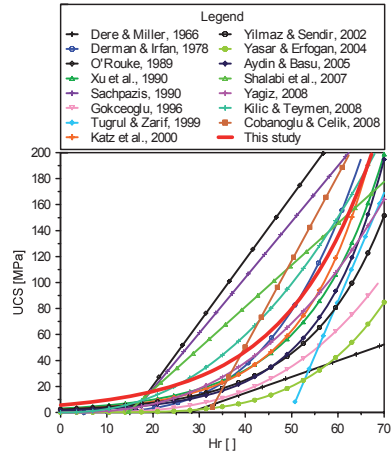


Figure 5. Comparison between developed correlations between UCS- $Hr$  from this and other studies [3, 7, 12, 15, 16].

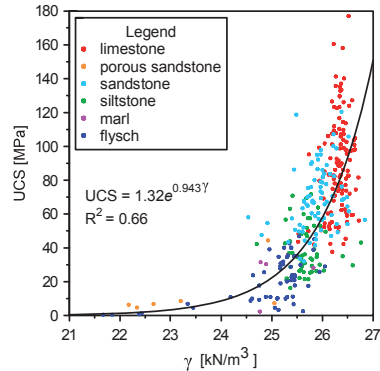


Figure 6. Correlation between UCS and unit weight  $\gamma$ .

The following two figures (Figure 6 and Figure 7) show correlation between unit weight and UCS, and Schmidt hammer rebound values.

In both cases we can clearly see that UCS and Schmidt hammer rebound values are increasing with increasing unit weight, which is expected and was also reported by other studies [3, 7, 15, 16].

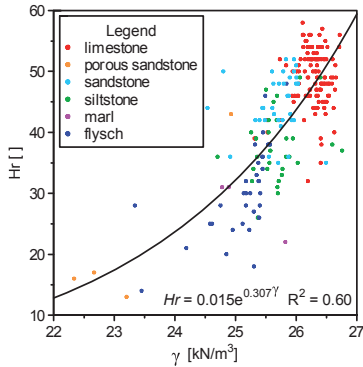


Figure 7. Correlation between Schmidt hammer rebound values  $Hr$  and unit weight  $\gamma$ .

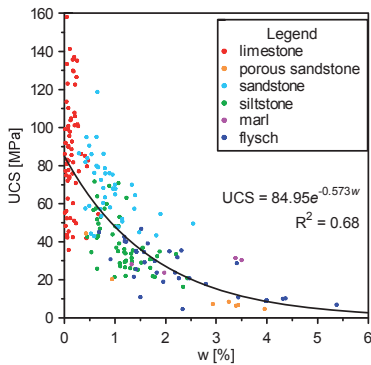


Figure 8. Correlation between UCS and water content  $w$ .

In the final two figures (Figure 8 and Figure 9) show correlation between water content and UCS, and Schmidt hammer rebound values. A decrease of UCS and Schmidt hammer rebound values with increasing water content is clearly

seen. On Figure 9 data points fall closer to the fitted curve at high Schmidt hammer rebound values, but become more scattered at lower values. This suggests the ability to estimate water content of rocks using Schmidt hammer test is the best at the high Schmidt hammer rebound values, and less reliable at lower values.

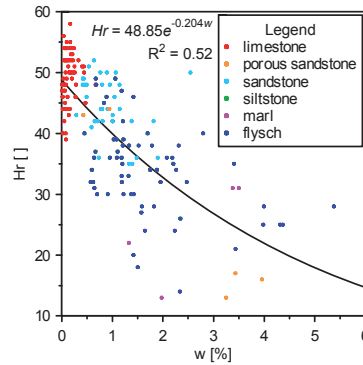


Figure 9. Correlation between Schmidt hammer rebound values  $Hr$  and water content  $w$ .

## CONCLUSIONS

In this paper a core size diameter influence on Schmidt hammer rebound values and the correlation with UCS was investigated on Tertiary sedimentary rocks from Slovenia. Specimens were collected from three different locations and based on the presented data the following conclusions can be made:

- The core size diameter strongly influences on Schmidt hammer rebound values. By increasing core diameter also is observed the rising of Schmidt hammer rebound value (Figure 2).
- Weak correlation coefficient ( $R^2 = 0.57$ ) and large data scatter show that results obtained with Schmidt hammer tests have to be analyzed carefully when a correlation with UCS is sought (Figure 3).

- When core size diameter is taken into account much better results with higher correlation coefficient ( $R^2 = 0.57 - 0.81$ ) can be obtained as was shown on Figure 4.
- With increasing unit weight UCS and Schmidt hammer rebound values are also increasing (Figure 6 and Figure 7).
- With increasing water content UCS and Schmidt hammer rebound values are decreasing (Figure 8 and Figure 9).

Even though a large scatter was observed presented correlation falls within range obtained by other researchers. Low correlation coefficients can be attributed to relatively small number of investigated specimens. With further investigations additional data will be added and presumably better correlation will be obtained.

A large scatter of proposed empirical correlation presented in Figure 5, implies that this correlations are not general. They have to be used and interpreted in light of analyzed rock type, site location, core diameter and measurement procedure. In this light the proposed correlation can currently be used only for approximate estimate of UCS at the investigated locations in Slovenia.

#### ACKNOWLEDGEMENT

Laboratory work was conducted at the Institute for Mining, Geotechnology and Environment (IRGO). Many thanks to Maja Rojšek, Zdene Omejec and Brane Merhar for help, advices and support.

#### REFERENCES

- [1] E. Schmidt, A non-destructive concrete tester, *Concrete* **59** (1951), 34-35.
- [2] ISRM, Suggested methods for the quantitative description of discontinuities in rock masses, *Int. J. Rock Mech. Min. Sci. & Geomech. Abstr.* **15** (1978), 319-368.
- [3] D.U. Deere, R.P. Miller, Engineering classification and index properties for intact rocks, *Air Force weapons Lab. No. AFNL-TR* (1966), 65-116.
- [4] J.E. O'Rourke, Rock index properties for geoengineering in underground development, *Min. Eng.* **41** (1989), 106-110.
- [5] C.I. Sachpazis, Correlating Schmidt hardness with compressive strength and Young's modulus of carbonate rocks, *Bull. Int. Assoc. Eng. Geol.* **42** (1990), 75-83.
- [6] A. Tugrul, I.H. Zarif, Correlation of mineralogical and textural characteristics with engineering properties of selected granitic rocks from Turkey, *Eng. Geol.* **51** (1999), 303-317.
- [7] F. Shalabi, E.J. Cording, O.H. Al-Hattamleh, Estimation of rock engineering properties using hardness tests, *Eng. Geol.* **90** (2007), 138-147.
- [8] I. Cobanoglu, S.B. Celik, Estimation of uniaxial compressive strength from point load strength, Schmidt hardness and P-wave velocity, *Bull. Eng. Geol. Environ.* **67** (2008), 491-498.
- [9] S. Xu, P. Grasso, A. Mahtab, *Use of Schmidt hammer for estimating mechanical properties of weak rock*, Proc. 6<sup>th</sup> International IAEG Congress, Balkema, Rotterdam, 1990.
- [10] O. Katz, Z. Reches, J.C. Roegiers, Evaluation of mechanical rock properties using a Schmidt Hammer, *Int. J. Rock Mech. Min. Sci.* **37** (2000), 723-728.
- [11] I. Yilmaz, H. Sendir, Correlation of Schmidt hardness with unconfined compressive strength and Young's modulus in gypsum from Sivas (Turkey), *Eng. Geol.* **66** (2002), 211-219.
- [12] A. Aydin, A. Basu, The Schmidt hammer in rock material characterization, *Eng. Geol.* **81** (2005), 1-14.
- [13] W.R. Derman, T.Y. Irfan, *Assessment of the degree of weathering in granite using petrographic and physical index tests*. Proc. Int. Symp. on Deterioration and Protection of Stone Monuments, Unesco, Paris, 1978.
- [14] C. Gökçeoğlu, Schmidt sertlik çekici kullanılarak tahmin edilen tek eksenli basınç dayanımı verilerinin güvenilirliği üzerine bir değerlendirme, *Jeol. Mühendis.* **48** (1996), 78-81.
- [15] I. Yasar, Y. Erdogan, Estimation of rock physio-mechanical properties using hardness methods, *Eng. Geol.* **71** (2004), 281-288.
- [16] S. Yagiz, Predicting uniaxial compressive strength, modulus of elasticity and index properties of rocks using the Schmidt hammer, *Bull. Eng. Geol. Environ.* **68** (2009), 55-63.
- [17] A. Kılıç, A. Teymen, Determination of mechanical properties of rocks using simple methods, *Bull. Eng. Geol. Environ.* **67** (2008), 237-244.
- [18] ISRM, Suggested methods for determining hardness and abrasiveness of rocks, *Int. J. Rock Mech. Min. Sci.* **15** (1978), 89-97.
- [19] ASTM, Standard test method for determination of rock hardness by rebound hammer method (D 5873-00), 2000.
- [20] ASTM, Standard test method for unconfined compressive strength of intact rock core specimens (ASTM D2938-95), 1995.

# Backanalysis in tunnels using different minimization algorithms

C. de Santos, A. Ledesma, A. Gens  
*Technical University of Catalunya - UPC, Barcelona, SPAIN*

## ABSTRACT

The paper describes a procedure to perform backanalysis of tunnel excavation problems in an automatic manner. The measured displacements are compared with the calculated ones obtained from a Finite Element Analysis, forming the objective function. The parameters that best represent the measured data are those that minimize the objective function and a suitable minimization algorithm is required. In this paper a genetic algorithm and a gradient based method are described. The Finite Element code Plaxis has been used as a tool for the direct analysis. The parameters to identify are the coefficient of lateral earth pressure ( $K_0$ ) and the reference Young's modulus for unloading and reloading ( $E_{ur}^{ref}$ ), to the reference pressure ( $p^{ref}$ ). The "Hardening soil model" from Plaxis has been the constitutive model selected to simulate the soil behavior. The geometry considered is a synthetic case involving the excavation of a circular tunnel. The paper shows the advantages and disadvantages of each optimization algorithm in the context of this tunnel excavation problem.

Keywords: Backanalysis, Genetic Algorithm, Tunnel

## 1 INTRODUCTION

Nowadays the use of commercial software based on finite element method (FEM) has become very popular in geotechnical engineering. Moreover, these programs continuously incorporate more sophisticated constitutive models to simulate soil behavior and consequently, more parameters are required to define them. Often some parameters (especially in sophisticated constitutive models) do not have a real geotechnical

meaning as they just come from a mathematical expression, which makes them difficult to identify.

Traditionally soil parameters have been obtained from laboratory tests. However, in many cases samples in a laboratory test do not represent the whole soil environment. In addition to that, sample extraction by itself causes some disturbance and changes on the soil properties are difficult to quantify. In order to avoid those problems some researchers have been working on

backanalysis trying to identify soil parameters using in situ instrumentation data. The estimation of soil and rock parameters based on field instrumentation data is a common procedure in Geomechanics [1]. From a mathematical point of view, the identification of parameters results in a minimization problem. Examples of backanalysis in the context of tunnel excavation problems are described in Ledesma et al [2], Ledesma and Romero [3], and Gens et al [4], among others. In those works, a maximum likelihood approach is presented to estimate the required parameters and the gradient method is used as optimization algorithm. The main difficulty when estimating parameters is that several combinations of them may give similar results in terms of measurement variables and therefore the solution is not unique. Because of that, part of the research in this field has been devoted to the improvement of the optimization process itself. A recent example of identification in Geomechanical problems using genetic algorithms has been presented by Levasseur et al [6].

This paper describes the identification of some of the most relevant soil parameters in a tunnel construction as the coefficient of lateral earth pressure ( $K_0$ ) and the reference Young's modulus for unloading and reloading ( $E_{ur}^{ref}$ ), corresponding to the reference pressure ( $p^{ref}$ ). The Hardening Soil Model defined by Schanz et al [7] has been chosen as the constitutive model and a synthetic case has been used to represent the tunnel construction using the commercial geotechnical program Plaxis. Two different backanalysis techniques have been used. One of them is based on a genetic algorithm and the other one is based on the gradient method.

## 2 BACKANALYSIS PROCEDURE

It is assumed that a fixed and deterministic model relates a set of variables  $\mathbf{x}$  and a set of parameters  $\mathbf{p}$ . Some of the variables  $\mathbf{x}$  are measured and form the vector of measurements  $\mathbf{x}^*$ . The best parameters are those that minimize the difference between measured variables and computed variables. A simple procedure to establish that, is defining the so called "objective function",  $F$ :

$$F = \sum_{i=1}^m (x_i^* - x_i)^2 \quad (1)$$

where  $m$  is the number of measurements, i.e. soil displacements.  $F$  represents the error between the measurements and the same variables computed with the model. In this case, the objective function is based on the least squares criterion. Expression (1) can be generalized when measurements are not independent or have different errors [2]. Note that  $F$  is a function of the parameters, as  $\mathbf{x} = M(\mathbf{p})$ , where  $M$  represents the model. Minimizing  $F$  will provide with the set of parameters that best simulate the measurements obtained.

It should be pointed out that  $F$  depends in a nonlinear manner on the parameters. The model  $M$  is usually represented by a Finite Element procedure, maybe with a nonlinear constitutive law. Even when a linear law is used, the objective function,  $F$ , is nonlinear with respect to the parameters  $\mathbf{p}$ . That makes difficult to find the minimum of  $F$ . When only one or two parameters are identified, a simple inspection of the values of  $F$  may be enough to estimate the minimum. This has been the case in the example described in this paper. Moreover, the plot of the objective function is useful to understand the sensitivity of measurements to the parameters considered in the analysis. However, if more than two parameters are involved, then it is more convenient to use any minimization algorithm available.

In general it is necessary to choose between methods that only need evaluations of the function and methods that also require computations of the derivative of that function. Algorithms using the derivative of the objective function are expected to be more powerful than those using only the values of the function itself, but they may be generally more time consuming. A combination of both approaches can be also a good strategy in complex problems.

## 2.1 Genetic algorithm

A genetic algorithm is an optimization method inspired by Darwin's theory of evolution and proposed by Holland [8] and subsequently by Goldberg [9]. Genetic algorithm has been used in many different fields to optimize all kind of functions from the beginning but it wasn't applied in geotechnics until Levasseur et al [6]. The algorithm is a stochastic global search technique, which does not need to evaluate derivatives and it works evaluating a cloud of possible solutions and selecting the best ones for the next iteration (generation). Crossover and mutation are the operators in charge of driving the search. Crossover is the one which exploits the areas with good potential solutions (individual) and mutation is the one which explores new areas where good potential solutions could be. The objective function is used to evaluate how good an individual is. This method does not guarantee that the optimum solution is found, but it can find relatively close solutions to the optimum, especially in problems with a large number of parameters.

## 2.2 Gradient method

The gradient approach is based on the Gauss-Newton method, described in [2]. Starting from an initial set of parameters, the next set is computed in this manner:

$$\begin{aligned} \mathbf{p}_{k+1} &= \mathbf{p}_k + \Delta \mathbf{p}_k \\ \Delta \mathbf{p}_k &= (\mathbf{A}^T \mathbf{A})^{-1} \mathbf{A}^T \Delta \mathbf{x} \\ \Delta \mathbf{x} &= (\mathbf{x}^* - \mathbf{x}) \end{aligned} \quad (2)$$

where  $\mathbf{A}$  is the sensitivity matrix, defined as

$$\mathbf{A} = \partial \mathbf{x} / \partial \mathbf{p} \quad (3)$$

Note that in general these derivatives must be computed using a finite difference approximation. This is the procedure considered in this paper: starting from a set of parameters and the corresponding computed displacements, one of the parameters is slightly incremented keeping the rest constant. The new displacements are computed and the change in displacements is divided by the increment of the parameter, obtaining a first order approximation to the derivative. The

determination of the appropriate increment of the parameter must be analyzed previously for each type of model.

## 3 SYNTHETIC CASE

A synthetic case has been chosen to study the behaviour and the performance of the backanalysis procedure using two different optimization techniques. The aim of using a synthetic case is because of its simplicity helps to focus the study on the understanding of the different techniques rather than the final parameter values.

### 3.1 Description

The case study is a symmetric circular tunnel 20 m deep and 10 m diameter. The model is 80 meter wide and 40 meter high. The hardening soil model in undrained condition has been used as constitutive model. The parameters are shown in table 1. The rest of parameters used in the model are the default program parameters.

Table 1. Soil parameters (Hardening Soil Model).[10]

Parameter	Value
$\gamma_{unsat}$	19 [kN/m <sup>3</sup> ]
$\gamma_{sat}$	21 [kN/m <sup>3</sup> ]
Permeability	0.026 [m/day]
$E_{50}^{ref}$	25000 [kN/m <sup>2</sup> ]
$E_{ed}^{ref}$	20000 [kN/m <sup>2</sup> ]
$E_{ur}^{ref}$	50000 - 350000 [kN/m <sup>2</sup> ]
$c_{ref}$	10 [kN/m <sup>2</sup> ]
$\phi$	28 [°]
$R_{inter}$	0.6
$K_0$	0.4 - 2

Three different stage constructions have been defined to simulate the tunnel excavation.

- Phase 1: Tunnel excavation using the Plaxis method  $\Sigma M_{Stage}$  to simulate a volume loss close to 0.5% ( $\Sigma M_{Stage} = 0.2$ ).
- Phase 2: Tunnel construction activating the lining. See table 2 for lining properties.
- Phase 3: Dissipation of all the excess of water pressure caused by the tunnel construction process.

Table 2. Lining tunnel parameters.  $d$  is thickness,  $w$  is the lining weight. EA, EI are stiffness parameters [10]

Parameter	Value
EA	1.125E7 [kN/m]
EI	1.898E5 [kNm <sup>2</sup> /m]
$d$	0.45 [m]
$w$	11.250 [kN/m/m]
$v$	0.2

### 3.2 Measurements

Ten points with vertical displacement information have been chosen as in situ instrumentation data. The locations of these points try to simulate an extensometer 2 meters away from the tunnel side (see figure 1).

The measurements used in this case have been extracted from a direct calculation using the Plaxis model with  $E_{ur}^{ref}=75000\text{kN/m}^2$  and  $K_0=1.5$ . Final displacements after all phases have been considered in the backanalyses.

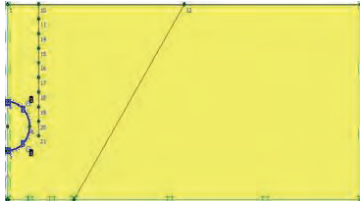


Figure 1. Plaxis geometry model.

### 3.3 Identification of parameters

To identify  $E_{ur}^{ref}$  and  $K_0$  three backanalysis procedures have been conducted. The first one used genetic algorithm and the two others used the gradient method with different starting points.

The parameters controlling the genetic algorithm performance have been defined following the recommendations proposed by De Jong [11] and Grefenstette [12]. A calibration process tuning the genetic algorithm parameter has been performed as well. Table 3 presents the parameters employed.

Table 3. Genetic algorithm parameters. Pc: Probability to apply crossover, Pm: Probability to apply mutation and GAP: Overlapping.

Parameter	Value
Population Size	51
Pc	0.95
Pm	0.01
GAP	1
Selection Strategy	Elitist

The search space has been defined as the all possible combinations of  $E_{ur}^{ref}$  and  $K_0$  for the following values:

- $E_{ur}^{ref} \text{ minimum} = 50000 \text{ kN/m}^2$
- $E_{ur}^{ref} \text{ maximum} = 350000 \text{ kN/m}^2$
- Step Size ( $E_{ur}^{ref}$ ) = 1000 kN/m<sup>2</sup>
- $K_0 \text{ minimum} = 0.4$
- $K_0 \text{ maximum} = 2$
- Step Size ( $K_0$ ) = 0.01

The search space contains around 50000 possible solutions and one of them corresponds to the solution (the parameters that have been used to generate the “measured” displacements). As it can be observed, the accuracy of the final result depends on the search space definition. A very refined search space can give us a very good solution, but it has an expensive computational cost. To visualize the search space, the objective function has been depicted in figure 2.

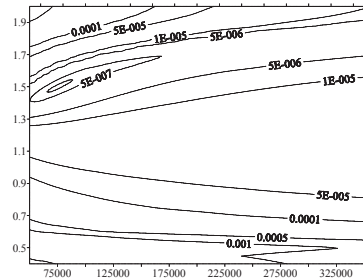


Figure 2. Search space.  $K_0$  is represented in the vertical axis and  $E_{ur}^{ref}$  [kN/m<sup>2</sup>] in the horizontal one. The optimum is located in  $K_0 = 1.5$  and  $E_{ur}^{ref} = 75000\text{kN/m}^2$ .

As only two parameters are identified, it is possible to plot contours of  $F$  and to locate the minimum by visual inspection. Thus, the evolu-



tion of the identification algorithms can be depicted as well.

The results using genetic algorithm are shown in figures 3 and 4 where the first one represents the initial population in the search space and the other one represents the population in the last generation. The algorithm has reached the optimum ( $E_{ur}^{ref}=75000\text{kN/m}^2$  and  $K_0=1.5$ ) after five generations and after evaluating 158 possible solutions.

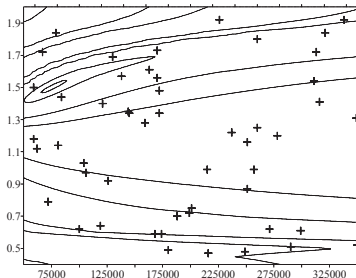


Figure 3. Genetic algorithm. Initial population.  $K_0$  is represented in the vertical axis and  $E_{ur}^{ref}$  [ $\text{kN/m}^2$ ] in the horizontal one.

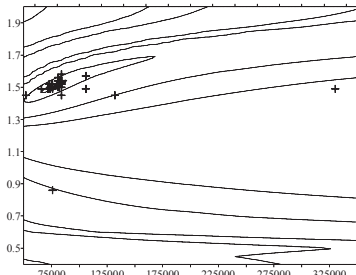


Figure 4. Genetic algorithm. Final population.  $K_0$  is represented in the vertical axis and  $E_{ur}^{ref}$  [ $\text{kN/m}^2$ ] in the horizontal one.

To identify the parameters using the gradient method two different starting points have been chosen.

- Starting Point 1:  $E_{ur}^{ref} = 325000\text{kN/m}^2$   
 $K_0 = 0.4$

- Starting Point 2:  $E_{ur}^{ref} = 325000\text{kN/m}^2$   
 $K_0 = 0.6$

Using the starting point 1 the method gets stuck into a local minimum. Therefore, no solution has been obtained using the initial point 1. The starting point 2 has been chosen out of the area where the local minimum is located in order to avoid that. The problem is that, usually, it is very difficult to decide in advance where a good starting point is and the performance highly depends on this initial point on the search space. Figure 5 shows how the method drives the search to get the optimum.

After seven iterations using the starting point 2 the method has reached the optimum ( $E_u^{ref}=75000\text{kN/m}^2$  and  $K_0=1.5$ ) and it just needed to evaluate 19 times the Plaxis model.

Table 4 presents a summary of both types of approaches with respect to this example. Note that the gradient method is very efficient in terms of number of calculations employed, but it may fail sometimes depending on the initial point adopted. On the contrary, the genetic algorithm may require many analyses, but it is easy to get a solution close enough to the real one, if the search space is well explored.

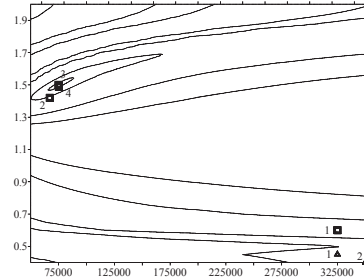


Figure 5. Gradient method. ( $\blacktriangle$ ) Iteration using the starting point 1. ( $\blacksquare$ ) Iteration using the starting point 2.

Table 4. Summary of results.

Genetic Algorithm	Gradient Method (starting point 2)
Parameter estimated	Parameter estimated
$E_{ur}^{ref} = 75000 \text{ kN/m}^2$	$E_{ur}^{ref} = 75000 \text{ kN/m}^2$
$K_0 = 1.5$	$K_0 = 1.5$
Number of calculations	Number of calculations
158	19

#### 4 CONCLUSIONS

The paper presents a methodology to perform backanalysis of geotechnical problems in an automatic manner. Measurements obtained from field instrumentation are used as input data to identify the best set of parameters by minimizing an objective function. This function depends on the differences between the measured values and the computed ones using a defined model.

The objective function is nonlinear with respect to the parameters, even when a linear elastic constitutive law is used. There are several options to compute the minimum of that function. Two procedures are considered in this work: a gradient method, which requires to compute derivatives of the objective function, and a genetic algorithm which only needs to evaluate the function for some particular values of the parameters. A synthetic example, based on a tunnel excavation problem, has been used to show the capabilities of both approaches. A set of 10 displacements computed using a set of parameters of the hardening soil model have been adopted as "measurements". Two parameters have been identified,  $K_0$  and  $E_{ur}^{ref}$ , from those "measured" displacements. On the one hand, the gradient method resulted efficient but very sensitive to the initial point assumed for the iterative process (in one case there was not convergence). On the other hand, the genetic algorithm always reached the minimum, although required a large number of computations of the direct case. Therefore an improved strategy for future developments would be to combine both procedures to find the minimum of the objective function.

#### REFERENCES

- [1] Gioda, G., Sakurai, S. Back analysis procedures for the interpretation of field measurements in Geomechanics. Int. J. for Numerical Analyt. Methods Geomech. (1987), 11:555-583.
- [2] Ledesma, A., Gens, A., Alonso, E.E., Estimation of parameters in Geotechnical Backanalysis – I. Maximum Likelihood Approach. Computers and Geotechnics (1996), 18:1-27.
- [3] Ledesma, A., Romero, E., Systematic backanalysis in tunnel excavation problems as a monitoring technique. Proc. 14<sup>th</sup> Int. Conf. Soil Mech. Found. Engng. Hamburg, Balkema, 3, p.1425-1428, 1997.
- [4] Gens, A., Ledesma, A., Alonso, E.E., Back analysis using prior information – Application to the staged excavation of a cavern in rock. Numerical Methods in Geomechanics, Swoboda ed., Innsbruck, Balkema, (1988), p. 2009-2016.
- [5] Gens, A., Ledesma, A., Alonso, E.E., Estimation of parameters in Geotechnical Backanalysis – II. Application to a tunnel excavation problem. Computers and Geotechnics (1996), 18:29-46.
- [6] Levasseur, S., Malécot, Y., Boulon, M., Flavigny, E., Soil parameter identification using a genetic algorithm. Int. J. for Num. Analyt. Methods Geomechanics (2008), 32(2):189-213.
- [7] Schanz, T., Vermeer, P.A., and Bonnier, P.G., Formulation and verification of the hardening soil model. In Beyond 2000 in Computational Geotechnics, R.B.J. Brinkgreve ed., Balkema, Rotterdam, (1999), p. 281-290.
- [8] Holland, J.H., "Adaptive in Natural and Artificial Systems". The University of Michigan, (1975)
- [9] Goldberg, D.E., "Genetic Algorithms in Search, Optimization and Machine Learning". Adison Wesley Publishing Company, (1989)
- [10] R.B.J. Brinkgreve & W. Broere. PLAXIS 2D MANU-AL (version 9.0), 2008
- [11] De Jong, K., Analysis of the behavior of a class of genetic adaptive systems. Ph.D. dissertation. Dept. Comput. Commun. Sci., Univ. Michigan, Ann Arbor, (1975)
- [12] Grefenstette, J., Optimization of control parameters for genetic algorithms. IEEE Trans. Syst., Man, Cybern., (1986), vol. 16, no. 1, p. 122-128.

# Data analysis of cores and geophysical bore logs for systematic rock type interpretation

S. Johansson<sup>1</sup>  
*Tyréns AB*

H. Möller, O. Friberg  
*Tyréns AB*

## ABSTRACT

The bedrock in the area of Södertunneln in Helsingborg consists of a complicated stratigraphy of mainly mudstone, sandstone and intermediate rock types. During the project, 13 core drillings were carried out, visually examined and classified and logged with different geophysical methods. In addition, 27 hammer borings were carried out and logged, but not classified. A statistical analysis aiming to find relationships between rock type and the resistivity, conductivity and gamma logs respectively were made using five of the 13 core drilled bore holes. The results were used to develop a model which interprets the rock stratigraphy based on the response of the geophysical core logs in the hammer bore holes. The model was validated against independent data using the eight remaining core drilled bore holes. The result of the validation showed that the model prediction of rock stratigraphy is satisfying. The modeled rock stratigraphy in the 27 hammer bore holes was used together with the results from the core drilled bore holes, to provide a more detailed picture of the geology in the investigation area. The aim of this paper is to describe the data analysis associated with the development of the model.

Keywords: Borehole logging, statistics, modeling, data analysis

## 1 INTRODUCTION

Södertunneln is a rail tunnel that was planned to extend south of Helsingborg, Sweden at around 15 meters depth below the ground surface. Extensive amounts of geological and geotechnical data from the site was visualized in 3D (ArcScene) during the project, among other reasons to act as a tool for an integrated interpretation taking all different disciplines into account.

In order to define the rock stratigraphy, 13 cores were drilled for visual examination. However, the bedrock in the area of Södertunneln consists of a complicated stratigraphy of mainly mudstone, sandstone and intermediate rock types, complicated by vertically displaced fault zones. This makes the original horizontal extension of respective rock type very irregular and difficult to follow between the core drilled boreholes. Figure 1 show a picture from ArcScene where the rock stratigraphy in the 13 cored boreholes has been visualized beneath the city of Helsingborg.

---

<sup>1</sup> Sara Johansson, Tyréns AB, Isbergs gata 15, 205 19 Malmö, Sweden, sara.johansson@tyrens.se

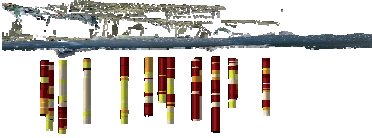


Figure 1. Rock stratigraphy in core boreholes visualized in ArcScene.

In addition to the core drillings, also 27 hammer drillings were carried out. Geophysical logging was performed in both the core boreholes and the hammer boreholes.

A data analysis was performed in order to search for relationships between rock types and logged geophysical data in the core boreholes. The aim of this paper is to describe the methods and ideas of the data analysis, which eventually led to the development of a model that was used to systematically predict rock stratigraphy in the hammer boreholes, based on the geophysical logs.

## 2 MATERIALS: DESCRIPTION OF DATA

### 2.1 Visual examination of cores

The geological classification of the cores was made by SGU (Sweden's Geological Investigation) through visual examinations. The results are qualitative and based on the experience of the geologist. The rock types found in all 13 cores were divided into main- and sub groups with respect to both geological bedding and relative ratios of sand/silt versus clay, see table 1.

The main groups Heterolite clay and Heterolite sand/silt were described as "laminated fine grained sand/silt-stone and claystone", with domination of clay- and sand/silt layers respectively. Sandstone clay was described as "sandstone with thin layers of clay, most often fine grained "soiled" sandstone", and Sandstone sand/silt was referred to as "fine to medium grained sandstone

with occasional thin layers of clay". The main group Claystone 1A consisted mainly of clay but with a varied amount of sand/silt layers.

Table 1. Rock types from the visual examination and classification.

Main group	Sub group	Sand/silt (%)	Clay (%)
Claystone 1A	1A	10	90
Heterolite clay 2C	2Ca	20	80
	2Cb	30	70
	2Cc	40	60
Heterolite sand/silt 2S	2Sa	80	20
	2Sb	70	30
	2Sc	60	40
Sandstone clay 3C	3Ca	80	20
	3Cb	70	30
	3Cc	60	40
Sandstone sand/silt 3S	3Sa	80	20



Figure 2. Cores during visual examination. Top: Heterolite clay. Bottom: Sandstone sand/silt.

Besides these five main groups, also irregular or so called "disturbed" rock types consisting of a mix of clay- and sandstone occurred, as well as coal and coal-rich claystones. These rock types together made up 3.2% of the bedrock in the classified cores. The most common rock type in the cores was Heterolite clay, which corresponded to approximately 40%.

Some laboratory tests, such as triaxial shear strength tests, were performed on different rock types in the cores. However, no relationships between the mechanical characteristics and rock types were found. These characteristics are beyond the scope of this paper and are not further mentioned.

## 2.2 Geophysical data from bore logs

The borehole logging was performed by the Danish geotechnical institute (GEO) with recording systems from Robertson Geologging Ltd [1]. The geophysical parameters logged in each borehole were gamma, conductivity and resistivity. Data was recorded at each centimeter of the boreholes.

The gamma radiation in counts per second (cps) was detected in a caliper probe by scintillation on a crystal of sodium iodide (NaI) [2]. The photons detected by the gamma log originate from decay of naturally occurring potassium, uranium and thorium [3]. The steel casing in the upper part of the boreholes only have a small influence on the detected gamma emission [2].

The guard resistivity probe measures the resistivity of the formation with a high vertical resolution. An alternating current is sent through an electrode in the center of the probe, creating a disc-shaped measure volume in the bedrock. The height of the measurement volume is 1cm in the vertical direction and the radius is 1m in the horizontal direction. The measurements must be performed in a liquid-filled borehole and are not suitable in the steel casing [2].

The focused induction probe measures conductivity by electromagnetic induction. A magnetic field is set up in the rock by coils in the probe, and the electric field generated from the induced current and secondary magnetic field is measured. In contradiction to the guard resistivity probe, the focused induction probe can be used in both dry and water-filled boreholes. It is however not possible to use the instrument inside the steel casing [2].

## 3 METHODS

### 3.1 Hypotheses

The overall relationships that were expected between rock stratigraphy and geophysical data could be summarized in the following hypotheses:

- 1) Gamma decrease with increasing ratio of sand/silt versus clay in the bedrock
- 2) Conductivity decrease with increasing ratio of sand/silt versus clay in the bedrock
- 3) Resistivity increase with increasing ratio of sand/silt versus clay in the bedrock

The theory behind hypothesis 1 was that potassium and thorium contents are high in natural clay (see for example [3]). Hypothesis 2 and 3 originated in accepted knowledge of electrical resistivity values of earth materials (see for example [4]). Conductivity is the reciprocal of resistivity.

### 3.2 Statistical methods

The hypotheses listed above are no new found relationships between geological material and geophysical properties. However, some consideration and decisions must be involved to obtain useable significant relationships.

The aim of the statistical data analysis was to obtain an understanding of the data and to derive empirical equations to build the model upon. Therefore, only five of the boreholes were used for the statistical analysis, while the remaining eight were left for an evaluation of the model against independent data. The boreholes selected for the statistical analysis/model development and the validation respectively were geographically evenly distributed over the investigation area.

One consideration during the statistical analysis was an appropriate method to group the rock types. While the hypotheses are related to the relative amount of clay, silt and sand in the bedrock, there are no substantiated reasons to believe that geological bedding have a major impact on the logged geophysical data. Several of the rock types in table 1 have the same approximate amount of sand/silt relative to clay. For example, a section of the rock consisting of on average 80% sand/silt could be defined as Heterolite sand/silt, Sandstone clay or Sandstone sand/silt, depending on the geological bedding (see table 1). Equivalently, rocks with 70% or 60% sand/silt could belong to either Heterolite sand/silt or Sandstone clay [5].

It was decided that all data values of gamma, resistivity and conductivity from the five core boreholes should be sorted into the corresponding sub groups listed in table 1. The values corresponding to the rock types “disturbed” or “coal” were removed from the data set. These rock types were rarely present, and were also inhomogeneous groups that were not expected to show any consistent response to any of the geophysical parameters.

The statistical methods selected were, in addition to a general statistical description, test for significant differences between groups (One-Sample Kolmogorov-Smirnov Test for normal distribution, Oneway ANOVA and Post Hoc Bonferroni Test) as well as regression analysis to determine if significant relationships existed.

For the regression analysis, the rock sub groups were ordered according to increasing relative amount of sand/silt on a numeric scale from 1 to 11. The rock types with equal relative amounts of sand/silt were internally ordered with respect to the geological bedding. For example, Heterolite sand/silt 2Sa with 80% sand/silt were assigned the value 9, while Sandstone clay 3Ca (also 80% sand/silt) were assigned the value 10 and Sandstone sand/silt 3Sa (80% sand/silt) the value 11. The reason for this order lies in the fact that the geological descriptions (as well as the nomenclature), despite the same average amount of sand/silt, indicate a decreasing importance of the imbedded clay in the same order. The regression analysis was used to determine if significant relationships between geophysical data and rock types existed, and in that case how the relationships looked and to which degree they could explain the variations in the geophysical data (for details on statistical methods, see for example [6]).

### 3.3 Results of statistical analysis

Figure 3 shows how the total amount of data values used in the statistical analysis was distributed between the different sub groups. The consequence of this was that the characteristic mean values of the groups with a lower number of data values generally became more uncertain. Sub

group 3Cc was not present in any of the five cores.

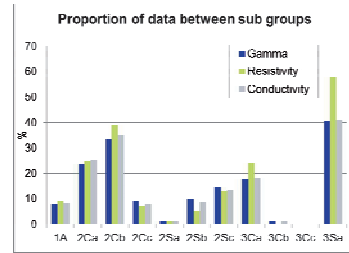


Figure 3. Logged data in statistical analysis, distributed between the rock sub groups.

The result of the regression analysis showed that there was a significant linear relationship between gamma and rock type, while significant both logarithmic and exponential relationships were found between conductivity/resistivity and rock type. Figure 4 shows the mean values and standard deviations of gamma and conductivity, and linear and logarithmic trend lines respectively through the mean values.

With the ANOVA test, significant differences of mean values in gamma were found between most groups, however with a few exceptions. For example, the mutual differences between the mean values of sub group 3Cb (70% sand/silt), 2Sa (80% sand/silt) and 3Ca (80%) were not statistically significant. The low amount of data in the statistical analysis for two of these sub groups, illustrated in figure 3, can probably at least partly explain this uncertainty.

Mutual significant differences of mean values in conductivity were found between the clayey sub groups 1A, 2Ca, 2Cb and 2Cc as well as Heterolite 2Sc, while there were no significant differences between most of the sandier sub groups. The reason is in this case probably that the relationship between rock type (increasing amount of sand/silt) and conductivity is logarithmic/exponential. For mean values in resistivity, the ANOVA results showed significant differences between most groups, with the

exception of mutual similarity between some nearby sub groups, such as e.g. 2Cb and 2Cc.

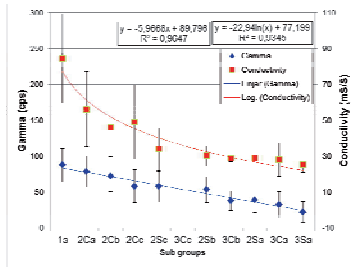


Figure 4. Mean values and standard deviations of conductivity/gamma versus rock types with trend lines.

A large part of the variation within the groups (illustrated in figure 4 as standard deviation bars) is probably explained by the fact that the rock types are categorized from an estimated value of relative sand/silt and clay amounts, rounded off to 10% intervals (see table 1). The internal variation in the rock groups is also the reason that the degree of explanation for the regression curves are approximately 55% for gamma, 53% for conductivity and 40% for resistivity (with some variation depending on the type of regression curve). However, the degree of explanation for correlation of mean values and rock types is convincing, as can be seen in figure 4.

### 3.4 Model development

A mathematical model based on the results from the statistical analysis was constructed in Matlab. The logged data values were imported into the model and transformed to interpreted rock stratigraphy, via the derived empirical equations and comparisons between the responses of the different logs. The model was adjusted until the results fitted the geological classification of the cores, through careful studies of the nature of the data. For example, probability was incorporated to a certain degree, since different rock types were better represented by different geophysical logs. For example, the logarithmic/exponential relationship between conductivi-

ty and rock group means that clayey rock groups are more reliably detected by conductivity than sandy rock groups, since the difference between the mean values is larger among the clayey than the sandy rock groups. The relationship between gamma and rock type is linear, which means that the interpretation is equally reliable for all rock groups.

Since the model is based on a statistical analysis of geophysical data from the boreholes, it can be defined as a functional descriptive model that can only be applied to data from a limited geographical area. A statistical model means that empirical equations are derived from a statistical analysis performed on the measured data, which can later be used to predict one of the parameters of the equations. The term functional descriptive model means that the model is used to describe observations within the current conditions, without explaining the underlying processes (for more information on modeling, see for example [7]).

### 3.5 Model validation

Independent data that had not been incorporated when the model was developed was used for the validation of the model. Each data value in the modeled cores was compared to the geological classification at the same level. The total quantitative result for all eight validation cores was that on average 60% of the model interpretations were in the right rock main group and 20% are in the wrong main group but with an uncertainty of max 10% in sand/silt ratio (see table 1). 20% of the model interpretations had larger errors compared to the geological classification. More importantly, the model predicted rock stratigraphy for the independent data equally as well as for the data that the model was developed from.

A quantitative validation of this type of model is difficult to interpret, since the data used for the validation (visual examination and classification) is qualitative. It is therefore probable that one obtains less satisfying results of a quantitative validation than what would be the case if the indata for the model and validation data had been of the same data type. However, this does not automatically mean that the model results are wrong.

Considering these circumstances, the correlation between visual examination and model interpretation is relatively high.

#### 4 RESULTS & DISCUSSION

Since the validation was considered to prove the suitability of the model to be used on independent data, the model was applied to the logged geophysical data in the 27 hammer boreholes. The result, visualized in ArcScene together with the 13 visually classified cores, is shown in figure 5.

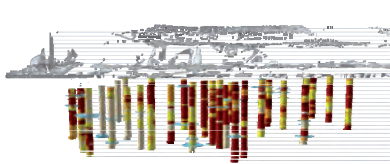


Figure 5. Rock stratigraphy in core and hammer boreholes, ArcScene.

The modeled hammer boreholes helped to provide a better understanding of the large scale geological pattern in the investigation area. For example, a sandier (white) section to the left in figure 5 and a more clayey (red) section in the middle could be stressed.

Generally, two different patterns that influence the quantitative validation could be observed visually. A large part of the on average 20% incorrect data values corresponded to thin layers on the borders between different rock types. The other type of often occurring incorrect model interpretations was found in the upper levels of the core. At levels around 8-10m, incorrect interpretations that originates from the gamma and conductivity data were seen in some of the cores. The reason is probably that the logging of the geophysical parameters has begun in the metal pipe, or that the geophysical data has been influenced by other factors, e.g. that the walls of the bore hole have collapsed in upper part of the bedrock (the latter was observed at some of the cores during the drilling and visual examination, Mikael Erlström personal commu-

nication). A further investigation of the reasons for the larger misinterpretations of the model at these depths, as well as a deeper review of the level of uncertainties in the indata and geological control analyses of the cores are means to further increase the quality and reliability of the model.

#### 5 CONCLUSIONS

An important conclusion of the current study is that much knowledge about the study site can be gained from the already collected data, if careful data analyses are made. New approaches and visualization techniques can facilitate the assessment of the geology in large-scale projects. The results presented here provided a cost-efficient alternative to more core drillings and visual examinations of cores.

#### ACKNOWLEDGEMENT

Acknowledgements to my collaborators at Tyréns, especially Henrik Möller, Mats Svensson and Olof Friberg, and to Mikael Erlström at SGU for giving conversations and feedback.

#### REFERENCES

- [1] GEO. Danish geotechnical institute, *Helsingborg. Södertunneln. Geophysical Logging in Hammer Borings. Cored Borings and Soil/Rock Probing*s, Factual report. GEO project no 32976, Report 4, 2010-11-19, 2010.
- [2] Robertson Geologging Ltd, <http://www.geologging.com/english/products/probes/probes.htm>, 2012-02-13, 2012.
- [3] Raddadi, M.C., Vanneau, A. A., Poupeaub, G., Carri-Schaffhauser, E., Arnaud, H. and Riverad, A., *Interpretation of gamma-ray logs: The distribution of uranium in carbonate platform*, Comptes Rendus Geoscience Volume 337 16 (2005), 1457–1461.
- [4] Sharma, P., *Environmental and engineering geophysics*, Cambridge University Press, Cambridge, 1997.
- [5] Mikael Erlström, *Personal communication*, SGU (Sveriges geologiska undersökning) / Department of Geology, Lund University
- [6] Rogerson, P. *Statistical methods for geography*. A student's guide. Los Angeles: SAGE 2010, 2010
- [7] Smith, J. & Smith, P., *Environmental modeling an introduction*, Oxford University Press, Oxford, 2007.



# Tunnel face stability under transient conditions: stand-up time in low permeability ground

Roberto Schürch<sup>1</sup>  
Georg Anagnostou  
ETH Zurich, Switzerland

## ABSTRACT

A tunnel face collapse with crater formation at the surface is the most serious hazard in shallow tunneling. The stability of the tunnel face is often time-dependent. In shallow tunnelling through water bearing ground, the time-dependency can almost always be traced back to consolidation, i.e. to the stress changes and deformations associated with the transient seepage flow process that is triggered by the drainage action of the tunnel. Undrained conditions and steady state (or drained) conditions mark the beginning and the end, respectively, of the process. The present paper deals with the face stability of shallow tunnels under transient conditions, i.e. under conditions which lie somewhere between these two extremes. The main topic is the stand-up time during standstills in low permeability ground. The short-term behaviour ("undrained conditions") is more favourable than the long-term one ("drained conditions"): the deformations increase with time; the tunnel face may be stable initially and fail only after some time. The calculations are carried out with a three dimensional finite element model considering a full hydraulic-mechanical coupling.

Keywords: Tunnelling, transient conditions, numerical modelling, failure criterion, stand-up time.

## 1 INTRODUCTION

We investigate the issue of the time-dependency of tunnel face stability assuming that all time effects are due to the consolidation process of the ground. More specifically, we analyse a common geotechnical situation for which the unsupported tunnel face remains stable in the short-term (undrained conditions), but collapses under drained conditions. The paper focuses on the transient conditions between these two extremes. The top-

ic is important for medium permeability soils such as the glacial deposits which are widely present in Central Europe.

Traditionally, face stability assessment is based upon a kinematic approach to the failure mechanism [1, 5]. However, these methods are not applicable to transient problems, because the ground response to tunnelling is governed inherently by the interaction between seepage flow and soil *deformation*. Face collapse under transient conditions can therefore be investigated only

---

<sup>1</sup> Roberto Schürch, ETH Zurich, Switzerland, roberto.schuerch@igt.baug.ethz.ch

by a fully coupled hydraulic-mechanical analysis. Due to the complexity of the problem, few works have addressed this topic: [6] investigated the stability of the unsupported face during ongoing tunnel excavation, while [8] showed the face reinforcement required as a function of the consolidation time. There is also relatively little research work on the similar problems of delayed failure of slopes and excavations [7, 9, 12].

## 2 COMPUTATIONAL MODEL

The numerical analysis is carried out using the finite element program Abaqus [4]. Figure 1 shows the geometry of the numerical model. The ground is discretized with 8-node brick elements (C3D8P). The element size varies from 0.5 m (close to the tunnel face) to 6 m (at the model boundary).

The water table is taken equal to the elevation of the ground surface. No-flow conditions are imposed at the tunnel wall (impervious lining) and at the symmetry plane. The hydraulic potential is taken equal to the elevation at the tunnel face (seepage face under atmospheric pressure) and equal to the initial value at the far field boundaries (no draw-down of the water table). The tunnel lining is simulated in a simplified way by fixing the nodal displacements of the excavation contour.

The initial stress field corresponds to the overburden pressure at each elevation and assumes a coefficient of lateral pressure  $K_0 = 0.7$ . The ground is modelled as isotropic, linearly elastic and perfectly plastic according to the Mohr-Coulomb yield criterion. Non dilatant plastic behaviour is assumed (UMAT subroutine according to [3]). Table 1 resumes the geotechnical parameters considered in the analysis.

Table 1. Assumed material constants of the ground

$\gamma$ [kN/m <sup>3</sup> ]	8
$E$ [MPa]	20
$\nu$ [-]	0.3
$\phi'$ [°]	30
$\psi'$ [°]	0
$c'$ [kPa]	15
$k=k_x, k_z=k_y$ [m/s]	$10^{-7}$

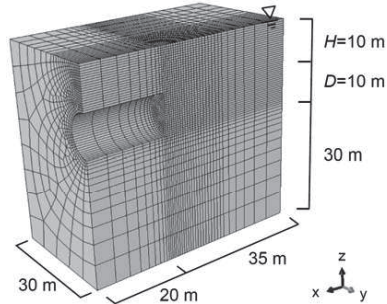


Figure 1. Numerical model.

## 3 UNDRAINED TUNNEL FACE STABILITY

Undrained stability is investigated by reducing the total support pressure  $\sigma_n$  from its initial value  $\sigma_{n0}$  to zero stepwise in very short (relative to the permeability) time intervals.

Figure 2 shows the contour of the plastic zone and the displacement vectors at the two points A and B after complete unloading of the tunnel face (dashed lines). It can be seen that the plastic zone remains localized in front of the tunnel face. Figure 3 shows the displacements at points A and B of Figure 2 for different values of normalized total support pressure (defined as the ratio of the total support pressure to the initial total stress normal to the face). The displacements occur mainly in the vicinity of the face (surface settlement is very small) and reach a finite value even if the tunnel face is completely unsupported, thus indicating stable face conditions.

The prediction of stable undrained conditions agrees with the results obtained by applying the kinematic approach [5] assuming a uniform undrained shear strength corresponding to the mean effective stress at the tunnel axis elevation (i.e.,  $c_u = c' \cos \phi' + \sin \phi' \sigma'_{zz} (1+2K_0)/3 = 73$  kPa [2]).

#### 4 DRAINED TUNNEL FACE STABILITY

In the first step of the numerical analysis (step i), the pore pressure at the tunnel face is reduced from its initial value to zero, while the effective support pressure is kept equal to its initial value  $\sigma'_{n0}$ . Figure 3 shows that displacements occur in this step due to the steady state seepage forces and effective stress changes developing in the ground ahead of the face.

Subsequently we reduce the effective support pressure of the face stepwise taking account of the steady state pore pressure field. Figure 3 shows the displacements at points A and B over the normalized effective face support pressure  $\sigma'_n/\sigma'_{n0}$ .

With decreasing effective support pressure  $\sigma'_n$ , the displacements increase and the plastic zone ahead of the face becomes larger (see solid lines ii and iii of Figure 2). In contrast to the undrained conditions, the displacement of the face (point A) does not reach a finite value, but increases asymptotically to infinity when the support pressure  $\sigma'_n$  approaches a critical value of about 50%  $\sigma'_{n0}$  (unloading step iv). This indicates that the system has reached its ultimate state. Re-distribution of the effective stresses is no longer possible and the face becomes unstable (cf. [10]). A comparative calculation based upon [1] gives a critical support pressure very close to the numerical one ( $\sigma'_n/\sigma'_{n0} = 55\%$ ). Figure 2 shows that at collapse the plastic zone does not reach the ground surface. Similar localized failures were obtained by [10] with an FEM calculation assuming dry ground with a high friction angle and tension cut-off. Investigations are continuing as to whether the localization of the failure in our case is numerically determined or whether the soil around the tunnel face stabilizes due to arching.

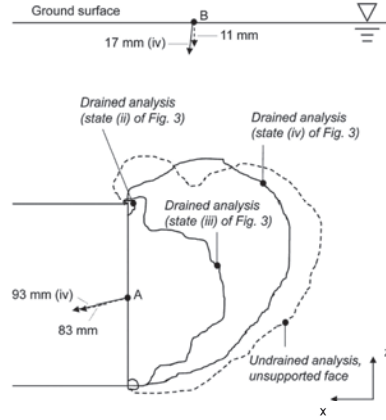


Figure 2. Contour of the plastic zone and displacement vectors (not scaled) of the points A and B.

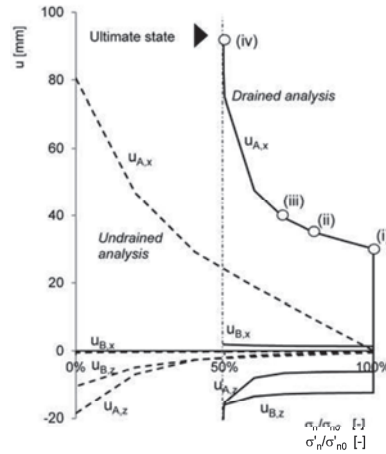


Figure 3. Displacement of points A and B as a function of the normalized total face support pressure (undrained analysis, dashed lines) or the normalized effective face support pressure (drained analysis, solid lines).

## 5 TUNNEL FACE STABILITY UNDER TRANSIENT CONDITIONS

The results of Sections 3 and 4 show that an unsupported tunnel face will be stable under undrained conditions (time  $t_0^+$ ), but fails under drained conditions. So a question arises as to the evolution of face stability over time and, more specifically, the stand-up time of the tunnel face.

At the ultimate state, re-distribution of the stresses in the ground is no longer possible, and so the effective stresses remain constant while the displacements continue to increase. A constant effective stress field means that the elastic volumetric strains also remain constant. As the assumed plastic behaviour is non-dilatant, the volumetric strains are equal to elastic ones and, consequently, they also remain constant at collapse. For these reasons, the ultimate state of the model can be identified by observing the time-development of the displacements, the volumetric strains and the effective stresses at certain control points (e.g. points A, C and D in Fig. 4). Figure 5a shows the displacement evolution over time. The displacements increase rapidly after 2 hours and become infinitely large after 2.8 hours. Note that displacements larger than 1 m violate the small strain and small displacement assumptions and are included in the diagram only for the sake of completeness.

The rapid evolution of the displacements indicates that the system is approaching the ultimate state. From Figure 5b, it seems that the volumetric strains trend to a constant value at 2.4 hours. Figure 6 indicates that the effective stresses in a distance of 0.25 m ahead of the face (point A) decrease over the time due to the swelling process (dissipation of the short-term pore water suction), and trend to a constant value after 2.4 hours. All of these observations support the statement that the system reaches collapse after about 2.4 hours. Figure 4 shows the evolution of the plastic zone and and of some displacement vectors over time. The kinematics of failure agree well with the known wedge and prism mechanism used in limit equilibrium analyses (e.g. [1]).



Figure 4. Contour of the plastic zone and displacement vectors (not scaled) of points A, B, C and D at  $t=t_c=2.4$  h (ultimate state).

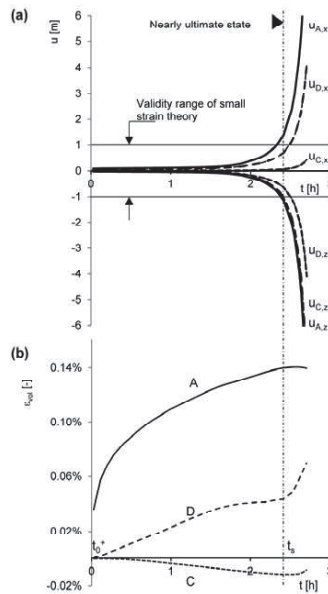


Figure 5. (a) Evolution of the displacements ( $u_x, u_z$ ) and of (b) the volumetric strain ( $\epsilon_{v(i)}$ ) at points A, C and D over time. The dashed vertical line crossing the time axis at  $t=t_c=2.4$  h corresponds to the near ultimate state.

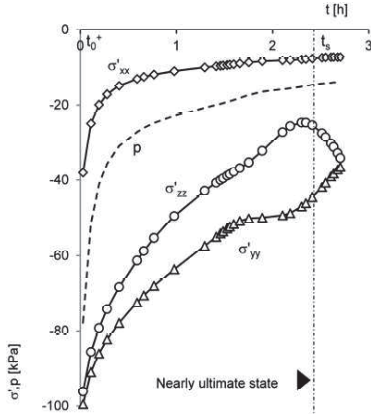


Figure 6. Evolution of the effective stresses ( $\sigma'_{xx}$ ,  $\sigma'_{yy}$ ,  $\sigma'_{zz}$ ) and of the pore pressure ( $p$ ) at point A over time. The dashed vertical line crossing the time axis at  $t=t_s=2.4$  h indicates the near ultimate state.

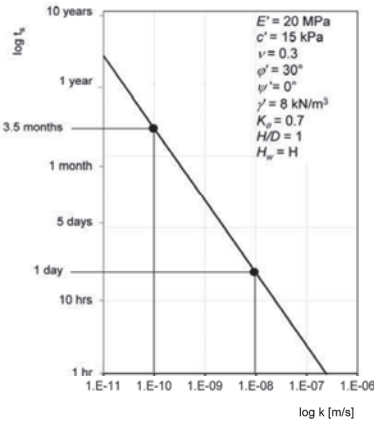


Figure 7. Stand-up time  $t_s$  of the tunnel face as a function of the ground permeability  $k$ .

The stand-up time, which amounts to about 2.4 hours in the example discussed, depends essentially on the permeability  $k$  of the ground. More

specifically, for dimensional reasons, it increases linearly with the inverse value of  $k$  and may amount to a few hours or several months (Fig. 7). A pronounced time-dependency can be observed for permeabilities between  $10^{-10}$  m/s and  $10^{-8}$  m/s. At higher permeabilities, the face fails practically immediately, while at lower permeabilities the face is stable for all practically relevant standstill periods.

## 6 NUMERICAL STABILITY ISSUES

Although both the extent of the plastic zone and the magnitude of the displacements consistently indicate that the system approaches the ultimate state at about 2.4 hours, it should be noted that the quality of the numerical solution decreases close to collapse.

So for example, at times  $> 2.4$  hrs, the volumetric strains at points C and D increase suddenly instead of remaining constant. The same problem is observed in the time-development of the effective stresses, which do not reach a constant value. (According to Figure 6, the horizontal effective stress  $\sigma'_{yy}$  and the vertical stress  $\sigma'_{zz}$  decrease and increase, respectively.)

Figure 8 presents additional evidence of numerical stability problems. The diagrams show the distribution of the pore pressure  $p$  and of the axial effective stress  $\sigma'_{xx}$  along the tunnel axis ahead of the face at certain time points. Under undrained conditions (time  $t_0^{un}$ ), negative excess pore pressures (suctions) develop in the ground up to a distance of 5 m ahead of the tunnel face, but dissipate during the subsequent consolidation process. As can be seen from the continuity equation

$$-k \cdot \partial \partial \Phi = \dot{\epsilon}_{vol}^{pl} = 0, \quad (1)$$

the pore pressure distribution at the limit state should be identical with the steady state distribution in the case of non-dilatant plastic behaviour. Figure 8a shows, however, that the numerical solution does not fulfil this condition. The distribution of the hydraulic potential close to ultimate state is clearly different from the expected,

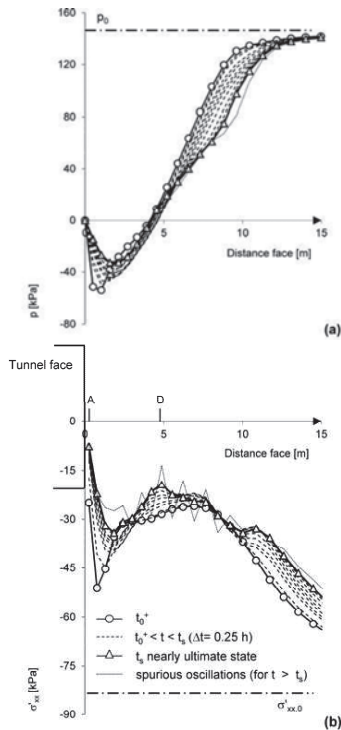


Figure 8. Distribution, (a), of the pore pressure  $p$  and, (b), of the axial effective stress  $\sigma'_{xx}$  along the horizontal axis ahead of the tunnel face at different time points.

steady-state distribution. The reason is that for a time longer than 2.4 hours, spurious oscillations appear in the effective stresses (Fig. 8b). These oscillations do not have any physical meaning but confirm the occurrence of numerical problems.

## 7 CONCLUSION

The assessment of tunnel face stability under transient conditions is important for shallow tun-

nels excavated in medium-permeability water-bearing ground. Due to the numerical complexity and computational cost of the problem, there is little work in the literature dealing with this issue. The results of the present paper show that transient, hydraulic-mechanical coupled analyses provide useful indications as to the loss of stability over time and the stand-up of the tunnel face. The numerical analyses performed, however, show that numerical accuracy and stability problems both occur at the limit state. The nature and importance of these problems are under investigation.

## REFERENCES

- [1] Anagnostou G, Kovári K, The face stability of slurry-shield driven tunnels. *Tunn Undergr Space Technol* **9** (1994), 65–174.
- [2] Broms BB, Bennermark H, Stability of vertical openings. *Journal of the Soil Mechanics and Foundations Division* **93** (1967), 71–94.
- [3] Clausen J, Damkilde L, Andersen L, An efficient return algorithm for non-associated Mohr-Coulomb plasticity. *Proceedings of the Tenth International Conference on Civil, Structural and Environmental Engineering Computing*, B. H. V. Topping Ed., Civil-Comp Press, Stirling, United Kingdom, 2005.
- [4] Dassault Systèmes, Abaqus 6.10, Theory Manual (2010).
- [5] Davis EH, Gunn MJ, Mair RJ, Seneviratne HN, The stability of shallow tunnels and underground openings in cohesive material. *Géotechnique* **30** (1980), 397–416.
- [6] Höfle R, Fillibeck J, Vogt N, Time depending stability of tunnel face. *Proceedings of the 35th IFA-ATIS General Assembly*, Budapest, 2009.
- [7] Holt DA, Griffiths DV, Transient analysis of excavations in soil. *Computers and Geotechnics* **13** (1992), 159–174.
- [8] Ng CWW, Lee GTK, A three-dimensional parametric study of the use of soil nails for stabilizing tunnel faces. *Computers and Geotechnics* **29** (2002), 673–697.
- [9] Potts DM, Kovacevic N, Vaughan PR Delayed collapse of cut slopes in stiff clay. *Géotechnique* **47** (1997), 953–982.
- [10] Ruse NM, *Räumliche Betrachtung der Standsicherheit der Ortsbrust beim Tunnelvortrieb*. Mitteilung 51 Universität Stuttgart, Institut für Geotechnik, 2004.
- [11] Ströhle PM, Vermeer PA, Tunnel face stability with groundwater flow. *Proceedings of the 7th European Conference on Numerical Methods in Geotechnical Engineering*, Trondheim, 2010.
- [12] Vaughan PR, Walbancke HJ, Pore pressure changes and the delayed failure of cutting slopes in overconsolidated clay. *Géotechnique* **23** (1973), 531–539.

# Investigation of long-term creep deformations on soil strength

A. Kalos<sup>1</sup>

*National Technical University of Athens, Greece*

## ABSTRACT

Clays under high shear stress levels can exhibit significant loss of long-term shear strength which can even cause delayed creep-induced failure. While volumetric creep (often called secondary compression) tends to increase the shear strength, deviatoric creep has deleterious effects on shear strength which often prevail in the overall soil behaviour. The paper presents an incremental elastoplastic-viscoplastic constitutive model based on the overstress theory for natural clays possessing structure. The model combines structure/strength degradation due to plastic shear strains and strength envelope degradation due to creep shear strains. The elastoplastic-viscoplastic constitutive model incorporates a Structure Strength Envelope along with an Intrinsic Compressibility Framework, to account for structural degradation associated with plastic strain evolution. On the other hand, strength envelope degradation is realized through the evolution of the inclination of the critical state line in strength space to a residual state. Model predictions tested in triaxial shearing mode reveals that the model can predict tertiary creep behaviour, i.e., long-term creep-induced failure under high shear stress levels. The model is implemented in the commercial F.E. Code ABAQUS and used in the bearing capacity of surface foundations.

Keywords: constitutive relations, elastoplasticity-viscoplasticity, tertiary creep, soil structure, strength degradation, clays, finite elements

## 1 INTRODUCTION

The mechanical behaviour of clayey soils is inhibited by the rate of deformation either induced or imposed [1]. In landslides, pile penetration and offshore foundation wave loading the rate governs the overall mechanical behaviour associated with strength and deformation characteristics. Constitutive relations have been widely employed to represent the viscoplastic characteristics associated with creep. The elastoviscoplastic constitutive models are based on (1) the overstress theory [2, 3], (2) the non-stationary flow surface theory [4, 5] and (3) other general

time dependent formulations that elude the purpose of this paper [6].

The focal point of the present paper is the development and application of a generalized time-dependent constitutive model for cohesive soils able to predict the rheological transformations undertaken during tertiary creep. The model is founded on the concept of bounding surface plasticity, in the generalized stress space, and the critical state soil mechanics principles implemented within the framework of a generalized creep theory. The general overstress theory employed is not limited to boundary and loading conditions, inherently associated with rheologi-

---

<sup>1</sup> National Technical University of Athens, School of Civil Engineering, Geotechnical Dept., 9, Iroon Polytechniou str., 157 80 Zografou, Athens, Greece. [alkalos83@gmail.com](mailto:alkalos83@gmail.com)

cal models, but can describe all possible stress paths and boundary conditions.

## 2 CREEP CHARACTERISTICS

Creep is a term employed to account for the time evolving deformations under constant loading conditions i.e. in oedometer or triaxial tests. The modes of creep however, activated in the two experiments are entirely different. In the oedometer tests the volumetric deformation measured is the keystone leading to a decrease in void ratio and increase of soil strength (Fig1). On the other hand, undrained triaxial specimens imposed to relatively high stress levels tend to fail in tertiary creep portrayed in Fig2. It is evident that in the triaxial tests the deviatoric term of creep reveals its deleterious effect on the overall mechanical behaviour.

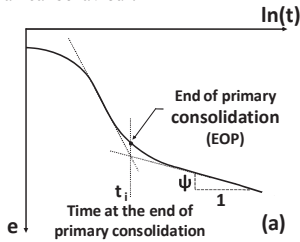


Figure 1. Definition of the secondary compression coefficient  $\psi$  for an oedometer test.

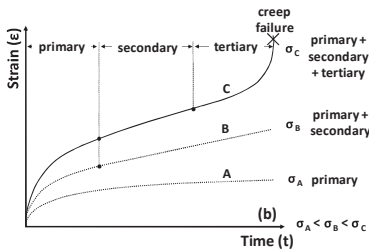


Figure 2. Definition of creep stages for triaxial creep tests at different stress levels.

The general creep theory based on overstress needs to account for instantaneous alterations of

the volumetric and deviatoric creep components of strain. Thus, the overstress formulation employed herein has undertaken modification to allow for simultaneous evolution of both components.

The standard logarithm creep rate was selected for the prediction of the volumetric creep component while the Singh & Mitchell expression [7] was employed to express the evolution of the deviatoric creep strain rate.

The elastoplasticity-viscoplasticity theory however, requires the incremental form of the rate formulated in terms of stress and strain rather than stress and time. Since, all mechanical parameters already defined in conventional elastoplasticity are described fully by the state of stress and strain characteristics it stands to reasoning that the time-dependent formulations should be defined in similar trend. The volumetric can be expressed as follows:

$$\dot{\epsilon}^t = \frac{\psi}{(1+e)t_0} \exp\left[-\frac{(1+e)}{\psi} \epsilon^t\right] \quad | \quad t \geq t_0 \quad (1)$$

$$\dot{\epsilon}_q^t = \frac{B}{\left[1 + \frac{(1-m)}{B \cdot t_0} \epsilon_q^t\right]^{\frac{m}{1-m}}} \quad \left. \begin{array}{l} m \neq 1 \\ t \geq t_0 \end{array} \right\} \quad (2)$$

The secondary compression coefficient  $\psi$ , void ratio  $e$  and reference time  $t_0$  are employed in the expression above. In the definition of the deviatoric creep strain rate above the shear stress

level  $\bar{D} = \frac{q}{q_F}$  is employed in the formation of

another quantity  $B = 2A \cdot \sinh(\bar{\alpha} \bar{D})$ . Where  $A, \bar{\alpha}, \bar{D}, m$  are the Singh-Mitchell coefficients.

Although the volumetric portion of creep is evident even in the elastic region, the deviatoric component takes place only at the plastic state. Thus, the viscous nucleus in the case of volumetric creep coincides with the isotropic axis, since the envelopes employed are oriented along the



octahedral axis (**Fig3**). Conversely, the viscous nucleus associated with the deviatoric component of creep is identical to the structure strength envelope (*SSE*).

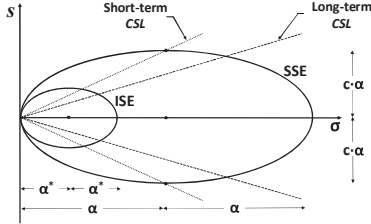


Figure 3. Characteristic surfaces of the proposed model.

In order for expressions (1) and (2) to be employed in the elastoplasticity-viscoplasticity the creep strain rate components need to be redefined in the generalized stress space.

### 3 THE PROPOSED MODEL

In this section, the author shall attempt to elaborate on the bounding two-surface elastoplastic-viscoelastoplastic formulation which incorporates the Critical State concepts into the Structured Soils behavioural framework (**Fig3**). Assuming that the infinitesimal strain increments  $d\boldsymbol{\varepsilon}$  can be decomposed in an elastic  $d\boldsymbol{\varepsilon}^e$  and an inelastic portion  $d\boldsymbol{\varepsilon}^i$ , consisted of the plastic  $d\boldsymbol{\varepsilon}^p$  and rheological components:

$$d\boldsymbol{\varepsilon} = d\boldsymbol{\varepsilon}^e + d\boldsymbol{\varepsilon}^i = d\boldsymbol{\varepsilon}^e + d\boldsymbol{\varepsilon}^p + \boldsymbol{\varepsilon}^i \cdot dt \quad (3)$$

#### 3.1 Characteristic Surfaces

The proposed model adopts the Structure Strength Envelope (*SSE*) and one reference surface corresponding to the Intrinsic Strength Envelope (*ISE*) [8, 9]. The *ISE* corresponds to the intrinsic soil properties denoted with a star symbol:

$$F^* = \frac{1}{c^2} \mathbf{s}^* : \mathbf{s}^* + (\sigma^* - \alpha^*)^2 - (\alpha^*)^2 \quad (4)$$

The size of the *SSE* denoted  $\alpha$  is characteristic of the magnitude of the soil structure and is described by an isotropic hardening rule. The *SSE*'s mathematical formulation is described below:

$$F = \frac{1}{c^2} \mathbf{s} : \mathbf{s} + (\sigma - \alpha)^2 - \alpha^2 \quad (5)$$

Where the stress tensor has been decomposed in the isotropic component denoted  $\sigma = p$  and the stress tensor deviator  $\mathbf{s}$ . In this version of the model the Plastic Yield Envelope is assumed to coincide with the *SSE*.

In the general case an incrementally linear non-associative flow rule is employed for the computation of the plastic strains [8, 9].

#### 3.2 Isotropic Hardening

An isotropic hardening rule has been employed in the constitutive mathematical formulation as to control the size of the *SSE*:

$$d\alpha = \frac{1+e}{\lambda - \kappa} \alpha^i \cdot d\boldsymbol{\varepsilon}^i - (\alpha - \alpha^*) A_q^p \cdot d\boldsymbol{\varepsilon}_q^p \quad (6)$$

Thus, the size of the *SSE* is inextricably associated to the intrinsic characteristic surface *ISE*. It is evident that in the expression above there is no component for the volumetric component due to structure/strength degradation. The measured value of secondary compression coefficient comprises the net effect of the structure/strength degradation, due to volumetric plastic strain, and volumetric creep. In other words, the effect of volumetric plastic strain on the degradation of the *SSE* has already been incorporated in the definition of the volumetric creep component.

The parameter  $A_q^p$  employed is associated to the deviatoric creep strain modulus as follows:

$$A_q^p = \zeta_q^p \cdot \exp(-\eta_q^p \cdot \boldsymbol{\varepsilon}_q^p) + \theta_q^p \quad (7)$$

The constants  $\zeta_q^p, \eta_q^p, \theta_q^p$  comprise the parameters associated to the destructuring process [8,

9]. Aiming to capture the rheological transformations undertaken in the tertiary creep process we initially attempted to capture the delayed failure through structure/strength degradation. However, keeping in mind that the deviatoric component of creep accumulates only once the plastic state has been achieved and the volumetric component continuously increases the size of the SSE it stands to reasoning that the state of stress returns to the elastic region with evolving time.

In order to resolve the aforementioned issue and ultimately capture the failure in tertiary creep we employed the inclination of the critical state line (CSL) is the stress space denoted  $c$  in expression (5) as a hardening variable. The inclination of the CSL is representative of rapid rates of induced strain. On the other hand, ageing is a rheological phenomenon evolving through time. In this end, the need to employ a limiting value of the CSL for quasi-static loading  $c_{cs}$ . Incrementally the rate of inclination of the CSL transitioning from rapid to long-term loading conditions can be defined as:

$$\dot{c} = -(c - c_{cs}) a \cdot \dot{\epsilon}'_q \quad (8)$$

Instead of the creep strain to produce plastic stress we here state that considerable plastic deformation needs to take place for the soil to fail in tertiary creep. This can be justified by the fact that deviatoric creep strain can only be accumulated once the plastic state has been achieved. Parameter  $a$  controls the tempo at which failure in tertiary creep is attained. Assuming that creep experimental data leading to tertiary failure are available parameter  $a$  can be calibrated via trial and error analyses.

#### 4 FINITE ELEMENT RESULTS

In this section, results will be presented on tri-axial drained specimens along with a bearing capacity problem of a 2m wide footing. Since creep is a time dependent phenomenon revealing its deleterious effects on shear strength after the consolidation equilibrium has been attained, it

stands to reasoning that the results to be presented here below should assume drained rather than undrained boundary conditions.

##### 4.1 Triaxial Test Results

In **Fig4** the effect of structure is evident on shear strength. Regardless that the overall behaviour might portray significant alterations from the elastoplastic response predicted by the Modified Cam-Clay (MCC) the specimen tends to fail at the same level of shear stress.

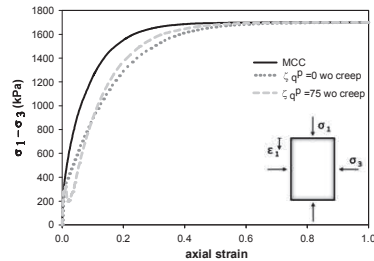


Figure 4. Effect of structure on shear strength at drained tri-axial specimens without creep.

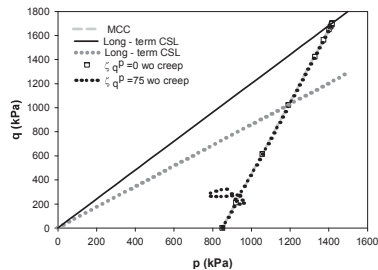


Figure 5. Tri-axial stress paths at drained conditions without creep.

Although the **Fig4** is informative in terms of shear strength it fails to provide a clear portrait of the stress paths. **Fig5** provides a visual representation of the triaxial stress path at drained conditions in the  $p$ - $q$  space.

Numerical analyses have been conducted for two different shear stress levels. In one case the specimen is stressed at a point lying above the

quasi-static CSL. Assuming that the inclination of the CSL is allowed to evolve then eventually the specimen will fail in tertiary creep (Fig6).

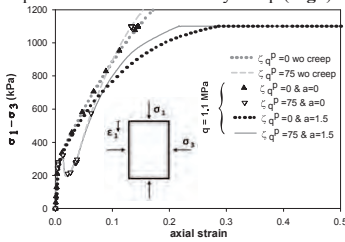


Figure 6. Shear strength experienced at high levels of shear stress with creep.

On the other hand, if the stress point lays underneath the threshold of the short-term CSL (Fig7) the specimen will not fail.

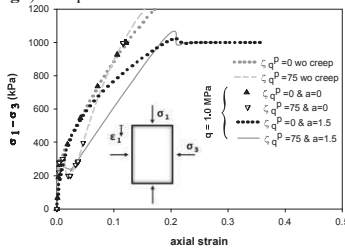


Figure 7. Shear strength experienced at low levels of shear stress with creep.

It is evident that even for high levels of loading the effect of structure degradation does not produce failure.

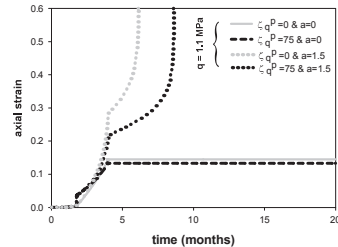


Figure 8. Axial strain as a function of time at high shear stress levels with creep.

On the other hand, strength envelope degradation towards its residual state has revealed the deleterious effect on shear strength. Regardless whether structure/strength degradation is evident or not, the evolution of the SSE inclination tends to cause creep-induced failure. In Fig8 the axial strain is portrayed as a function of time.

#### 4.2 Bearing Capacity of Surface Foundations

The bearing capacity of a 2m wide footing overlaying a clayey deposit under drained conditions has been examined. The soil medium portrays a punching failure mechanism rather than distinct failure lines which become evident only at undrained conditions, as can be seen from Fig9.

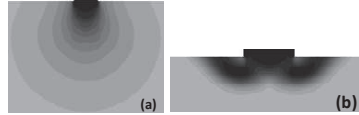


Figure 9. Displacement contour plots for (a) drained and (b) undrained boundary conditions without creep.

The effect of structure and structure/strength degradation is evident on shear strength in Fig10.

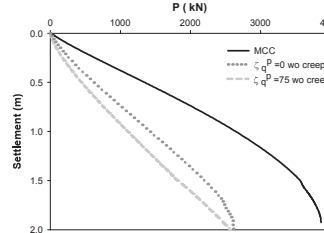


Figure 10. Effect of structure on shear strength at drained tri-axial specimens without creep.

For imposed displacement equal to the width of the footing the soil reaction is significantly less than the one obtained from an elastoplastic analysis without an ISE surface.

Numerical analyses have been conducted for two different levels of imposed loading. The loads selected (0.5 & 1MN) appear to be nowhere near the bearing capacity. In Fig11 settlement is given as a function of soil reaction for the case of  $P=0.5MN$ .

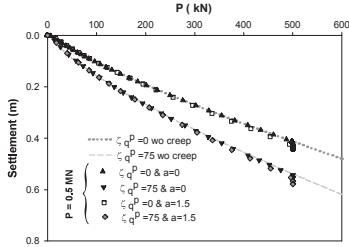


Figure 11. Soil reaction as a function of settlement,  $P=1/2$  MN.

On the other hand, once the level of imposed loading doubles in value the footing tends to fail in creep as can be seen in Fig 12.

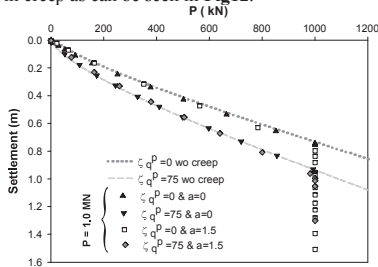


Figure 12. Soil reaction as a function of settlement,  $P=1$  MN.

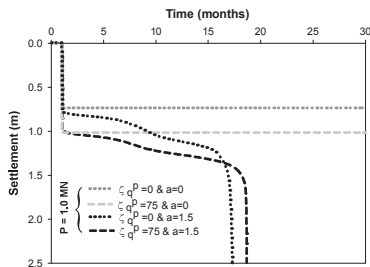


Figure 13. Settlement as a function of time,  $P=1$  MN.

Even for high levels of loading the effect of structure/strength degradation does not produce failure. On the other hand, degradation of the strength envelope revealed the deleterious effect of creep on shear strength, as can be seen from Fig 13.

## 5 CONCLUSIONS

A new elastoplastic-viscoplastic constitutive model has been developed based on the concepts of bounding surface plasticity and critical state soil mechanics principles incorporated within the framework of the overstress theory. Although structure/strength degradation has been shown not to result in tertiary creep, delayed failure can be realized through degradation of the CSL in the stress space to a residual state. Model predictions tested in triaxial shearing mode revealed that the model can predict tertiary creep behaviour at high shear stress levels. The model is implemented in the commercial F.E. Code ABAQUS and was further employed in the bearing capacity of a surface footing reproducing similar results.

## REFERENCES

- [1] Sorensen, K. K., B. A. Baudet, and B. Simpson (2007), Influence of Structure on the Time-Dependent Behaviour of a Stiff Sedimentary Clay., *Geotechnique*, 57(1), 113–124.
- [2] Perzyna, P. (1966), Fundamental Problems in Viscoplasticity., *Advances in Applied Mechanics*, 9, 244–377.
- [3] Debernardi, D., and G. Barla (2009), New Viscoplastic Model for Design Analysis of Tunnels in Squeezing Conditions, *Rock Mechanics and Rock Engineering*, 42(2), 259–288.
- [4] Dragon, A., and Z. Mroz (1979), A model for plastic creep of rock-like materials accounting for the kinetics of fracture., *International Journal of Rock Mechanics and Mining Sciences & Geomechanics Abstracts*, 16(4), 253–259.
- [5] Sekiguchi, H. (1984), Theory of undrained creep rupture of normally consolidated clay based on elastoviscoplasticity., *Soils and Foundations*, 24(1), 129–147.
- [6] Kaliakin, V. N., and Y. F. Dafalias (1990a), Theoretical Aspects of the Elastoplastic-Viscoplastic Bounding Surface Model for Cohesive Soils, *Soils and Foundations*, 30(3), 14.
- [7] Mitchell, J. K., R. G. Campanella, and A. Singh (1968), Soil Creep as a Rate Process, *Soil Mechanics and Foundation Division, Proceeding of the American Society of Civil Engineers*, 64(SM1), 231–253.
- [8] Kavvasas, M. J., and A. Amorosi (2000), A Constitutive Model for Structured Soils, *Geotechnique*, 50(3), 263–274.
- [9] Kavvasas, M. J., and G. Belokas (2001), An anisotropic elastoplastic constitutive model for natural soils., paper presented at 10th International Conference on Computer Methods and Advances in Geomechanics., Tucson, Arizona.

# Validation and verification of a practical constitutive model for predicting liquefaction in sands

A. Petalas,<sup>1</sup>

*Plaxis bv, Delft, The Netherlands*

V. Galavi

*Plaxis bv, Delft, The Netherlands*

R.B.J Brinkgreve

*Delft University of Technology & Plaxis bv, Delft, The Netherlands*

## ABSTRACT

The numerical modeling of soil liquefaction induced by dynamic loading is a very complicated task. In this paper the validation, and verification of the UBC3D-PLM model which is implemented in PLAXIS as a user defined soil model is presented. After a short introduction, the key features of the UBC3D-PLM are presented. New features implemented by the authors are highlighted. Namely, the Lode angle dependency of the plastic potential function, a soil densification rule for higher accuracy in the predicted pore pressure evolution, a second yield surface to ensure a smooth transition into the liquefied state and finally a post liquefaction factor to model the post-liquefaction behaviour. The predicted behaviour of loose Syncrude sand under undrained triaxial loading and undrained simple shearing is presented and is compared with experimental data. The influence of the proposed features is thoroughly discussed. The results from modeling various cyclic simple shear tests on Fraser Sand are also presented and compared with experimental data. It is concluded that the densification rule plays a major role for the liquefaction prediction and the model is able to predict with high accuracy the pore pressure evolution as shown in the experimental results. Finally, the proposed model is validated in a finite element scheme. A dynamic centrifuge test is modeled with the dynamic module of PLAXIS 2D and the results are compared with published experimental data.

Keywords: Liquefaction, sands, constitutive model, validation, verification

## 1. INTRODUCTION

The UBC3D-PLM is a simple but powerful constitutive model for liquefaction prediction. The use of numerical modelling techniques in earthquake engineering practice is a challenge which forms the framework for the development of simple but adequately accurate constitutive models for soil liquefaction.

UBC stands for University British Columbia where the original 2D formulation derived by Puebla et al. [1] and Beaty et al. [2], 3D stands for the 3-dimensional extension which was de-

veloped and implemented by Tsegaye [3] as a User Defined Model in PLAXIS and PLM stands for Plaxis Liquefaction Model.

The UBC3D-PLM model uses the Mohr-Coulomb yield condition in a 3-D principal stress space. Moreover, a modified non-associated plastic potential function based on Drucker-Prager criterion is used, in order to maintain the assumption of stress-strain coaxiality in the deviatoric plane for a stress path beginning from the isotropic line Tsegaye [3].

In the proposed reformulated version of UCB3D-PLM a correction is made in the equation of the plastic multiplier which governs the constitutive relationship between the stresses and

---

<sup>1</sup> PLAXIS B.V., Delftechpark 53, 2628 XJ Delft, The Netherlands, ap@plaxis.com

strains and higher accuracy is succeeded during monotonic loading. Moreover, the plastic potential function is modified in order to account the Lode angle dependency, i.e., the modification of the slope of the Drucker-Prager equation due to the different loading stress paths. Furthermore, a soil densification rule is added to predict more realistic evolution of excess pore pressures during cyclic loading. This allows the increase of the pore pressures with a decreasing rate during shearing. Finally, a post-liquefaction factor introduced in order to model the soil stiffness during the liquefied state.

The main characteristics of the model are presented in the following sections.

## 2. KEY FEATURES OF THE UBC3D-PLM

### 2.1 Yield surface

The UBC3D-PLM model uses the well-known Mohr-Coulomb yield function generalized in 3-D principal stress space [1]. The formulation of the surface is give in Equation [1].

$$f_m = \frac{\sigma'_{max} - \sigma'_{min}}{2} - \left( \frac{\sigma'_{max} + \sigma'_{min}}{2} + c' \cot \varphi'_p \right) \sin \varphi'_m \quad (1)$$

where:

$\sigma'_{max}$  and  $\sigma'_{min}$  are the maximum and minimum principal stresses respectively,  
 $c'$  is the cohesion of the soil,  
 $\varphi'_p$  is the peak friction angle of the soil,  
 $\varphi'_m$  is the mobilized friction angle during hardening.

### 2.2 Elastic behaviour

The elastic behaviour which occurs within the yield surface is governed by a stress dependent non-linear rule defined by Puebla et al. [1]. The bulk modulus ( $K$ ) and the elastic shear modulus ( $G$ ) are stress dependent and are given by the following equations:

$$K = K_B^e P_A \left( \frac{p}{P_{ref}} \right)^{me} \quad (2)$$

$$G = K_G^e P_A \left( \frac{p}{P_{ref}} \right)^{ne} \quad (3)$$

In these equations  $K_B^e$  and  $K_G^e$  are the bulk and the shear moduli numbers respectively, at a reference stress level. The factors  $me$  and  $ne$  are parameters to define the rate of stress dependency of stiffness. In the literature, the reference stress level ( $P_{ref}$ ) is commonly taken as the atmospheric pressure ( $P_A = 100 \text{ kPa}$ ). Pure elastic behaviour is predicted by the model during the unloading process.

### 2.3 Elasto-plastic behaviour

The reformulated UBC3D-PLM consists of two yield surfaces (primary and secondary) and its formulation is based on both isotropic and kinematic hardening. The hardening rule as introduced by Puebla et al. [1] and implemented by Tsegaye [3] is presented by Equation [5].

$$d\sin \varphi_m = 1.5 K_G^p \left( \frac{p}{P_A} \right)^{np} \frac{P_A}{p} \left( 1 - \frac{\sin \varphi_m}{\sin \varphi_p} R_f \right)^2 d\lambda \quad (4)$$

$K_G^p$  is the plastic shear modulus which is entered as an input parameter,  $d\lambda$  is the plastic multiplier and  $R_f$  is the failure ratio  $n_f / n_{ult}$ , ranging from 0.5 to 1.0, based on the Duncan-Chang model.  $n_f$  is the stress ratio  $q/p$  at and  $n_{ult}$  is the ultimate stress ratio.

### 2.4 Plastic potential function

A non-associated flow based on the Drucker-Prager plastic potential function formulated in 3-D space (Equation [8]).  $a$  is the slope of the Drucker-Prager surface and is computed as shown in Equation [7]. This slope is Lode angle dependent ( $\theta$ ) which is given in Equation [6]. The Lode angle dependency of the plastic potential function gives more accurate plastic strains for different stress paths.

$$\theta = \tan^{-1} \left[ \frac{1}{\sqrt{3}} \left( 2 \frac{\sigma'_{23} - \sigma'_{33}}{\sigma'_{11} - \sigma'_{33}} - 1 \right) \right] \quad (5)$$

$$a = \frac{\sqrt{3} \sin \psi_{mob}}{\cos \theta + \frac{\sin \theta \sin \theta}{\sqrt{3}}} \quad (6)$$

$$g = p' - a(p' + c' \cot \phi'_p) \quad (7)$$

The influence of the Lode angle on the computed slope of the Drucker-Prager surface is presented in Figure 1. The linear flow rule of the UBC3D-PLM (Section 2.5) is used in order to compute the mobilized dilatancy angle, starting with a mobilized friction angle equal to 0 and reaching a value which equals the sinus of the constant volume friction angle ( $\sin \phi_{cv}$ ). The constant volume friction angle for this arbitrary soil equals  $33^\circ$ .

It can be concluded that the influence of the stress path followed during loading, i.e., the Lode angle in the 3-D generalized space, can be significant, especially between the triaxial compression path and triaxial extension path.

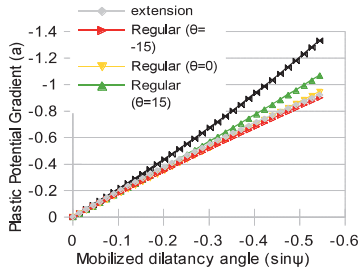


Figure 1: Influence of the Lode angle ( $\theta^\circ$ ) on the calculated slope of the Drucker-Prager plastic potential. Comparison of the different stress paths with triaxial compression (Black line).

## 2.5 Flow rule

In the UBC3D-PLM model the flow rule of the original UBCSAND model is used, which is de-

rived from energy considerations by Puebla et al. [1]. The flow rule in the model is based on the stress-dilatancy theory developed by Rowe [4], linearised and simplified according to energy considerations. The relationship is given as follows:

$$de_v^p = \sin \psi_m dy^p \quad (8)$$

$$\sin \psi_m = \sin \phi_m - \sin \phi_{cv} \quad (9)$$

Where,  $de_v^p$  is the plastic volumetric strain increment and  $\phi_{cv}$  is the constant volume friction angle.

## 2.6 Cyclic mobility and stress reversal

Based on the mobilized friction angle an unloading-reloading criterion is defined in the model as follows:

$$\sin \phi_m^e < \phi_m^0 \quad (\text{Unloading; elastic behaviour})$$

$$\sin \phi_m^e > \phi_m^0 \quad (\text{Loading or reloading; elastoplastic behaviour})$$

Where,  $(\phi_m^0)$  is the initial and  $(\phi_m^e)$  is the current mobilized friction angle. During unloading, pure elastic behaviour is predicted until the stress point reaches the  $p'$  axis.

A soil densification rule was introduced by the authors in order to have higher accuracy in the predicted evolution of the excess pore pressures following Beaty et al. [5]. A secondary yield surface was also introduced in the model for the secondary loading in order to ensure a smooth transition into the liquefied state of the soil.

The secondary yield surface generates less plastic strains compared to the primary yield surface. An isotropic hardening rule is used for the primary yield surface, while a simplified kinematic hardening rule is used for the secondary surface.

The plastic shear number  $K_c^p$  during primary loading is identical with the one entered as input parameter. However, during secondary loading it increases as a function of the number of cycles in order to capture the effect of soil densification (Equation 11). This leads to an increase of the

excess pore pressure during undrained cyclic loading until the liquefied state is approached. The rate of generation of excess pore pressure decreases by increasing number of cycles.

$$K_G^{p'} = K_G^p \left( 4 + \frac{n_{cross}}{2} \right) hard\ fac_{hard} \quad (10)$$

Where,  $n_{cross}$  is the number of times that the stress path touches the  $p'$  axis from the beginning of the test,  $hard$  is a factor to correct the densification rule for loose soils [6] and  $fac_{hard}$  is a multiplier which is a user input parameter for calibration.

The densification rule is fully valid for symmetric loading cycles, i.e., for the case that shearing starts from the isotropic stress state.

Finally, a post-liquefaction factor is introduced which controls the plastic shear number  $K_G^p$  when the soil is in the liquefied state (Equation [12]). If it is less than one the post-liquefaction behaviour of the soil is approximated.

$$K_G^p = K_G^p fac_{post} \quad (11)$$

### 3. VALIDATION OF THE UBC3D-PLM IN ELEMENT TESTS

#### 3.1 Validation of the UBC3D-PLM in monotonic loading

Table 1. UBC3D input parameters for all the validation tests.

Parameter	Syncrude S. (TxC, DSS)	Fraser S. (Cyclic DSS)	Centri- fuge
$\phi_p$ (°)	33.7	33.8	34
$\phi_{cv}$ (°)	33	33	31
$K_B^e$	300	607	721
$K_G^e$	300	867	1031
$K_G^p$ (TxC)	310	-	-
$K_G^p$ (DSS)	98.3	266	700
$me=ne$	0.5	0.5	0.5
$np$	0.5	0.4	0.4
$R_f$	0.95	0.81	0.74
$N_{I_{60}}$	8	8	14
$fac_{hard}$	1	1	0.7
$fac_{post}$	0	0.6	0

The validation of the UBC3D-PLM in monotonic loading is presented in this section. The behaviour of loose Syncrude sand is modelled with UBC3D-PLM and the numerical results are compared with experimental data as well as numerical results (original UBCSAND) both published by Puebla et al. [1].

The input parameters for modelling the undrained triaxial test (TxC) and the undrained direct simple shear test (DSS) on loose Syncrude sand are given in Table 1. The results are presented in Figures 2 and 3. The results of the UBC3D-PLM are in a good agreement with the experimental and numerical results of the original UBCSAND as published by Puebla et al. [1].

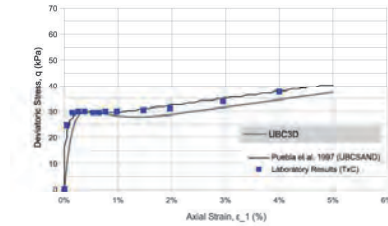


Figure 2 Numerical modeling of loose Syncrude sand under undrained triaxial compression.

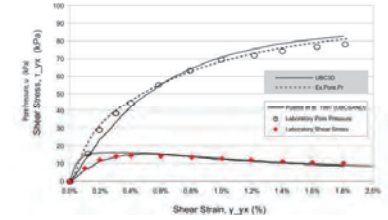


Figure 3 Numerical modeling of loose Syncrude sand under undrained simple shearing (DSS). Prediction of the excess pore pressure evolution with the UBC3D-PLM (dashed line) and comparison both with the 2D UBCSAND and experimental data.



### 3.2 Validation of the UBC3D-PLM in cyclic loading

The behaviour of loose Fraser sand under undrained cyclic direct simple shear (DSS) is modeled and the numerical results are compared with experimental data as published by Sriskandakumar [6]. The relative density ( $RD$ ) of the tested sand is 40%.

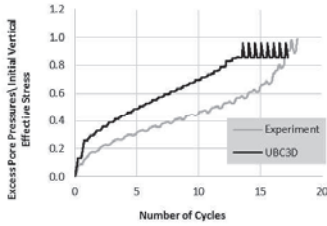


Figure 4 Evolution of excess pore pressures during undrained simple shearing (DSS) on Fraser sand ( $RD=40\%$ ).  $CSR=0.08$ .  $\sigma_v=100$  kPa.

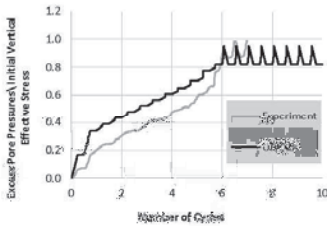


Figure 5 Evolution of excess pore pressures during undrained simple shearing (DSS) on Fraser sand ( $RD=40\%$ ).  $CSR=0.1$ .  $\sigma_v=100$  kPa.

In Figures 4, 5 and 6 the evolution of excess pore pressure in three stress controlled DSS tests are presented. The applied Cyclic Shear Stress ratio ( $CSR$ ) equals 0.08, 0.1 and 0.12 respectively. The vertical applied stress is 100 kPa in all cases. The earth pressure coefficient,  $K_0$  factor is assumed to be 1 for simplification.

Even though modeling the onset of liquefaction in the framework of classical plasticity is very complicated, the UBC3D-PLM constitutive model is in close agreement with the experimental results. The densification rule added in this formulation decreases the rate that the excess pore pressures are developing after the first full cycle. This mechanism gives higher accuracy.

In Figure 7 the influence of the post liquefaction factor  $fac_{post}$  can be seen. By setting this factor to 0.6 the maximum shear strain is more realistic for sands being in liquefied state.

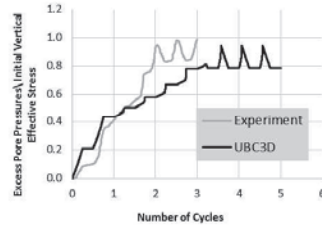


Figure 6 Evolution of excess pore pressures during undrained simple shearing (DSS) on Fraser sand ( $RD=40\%$ ).  $CSR=0.12$ .  $\sigma_v=100$  kPa.

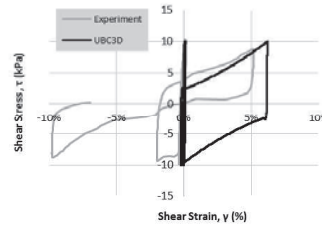


Figure 7 Evolution of shear strains during undrained simple shearing (DSS) Fraser sand ( $RD=40\%$ ).  $CSR=0.1$ .  $\sigma_v=100$  kPa.

#### 4. VALIDATION OF THE UBC3D-PLM IN A FINITE ELEMENT SCHEME

A dynamic centrifuge is modeled with PLAXIS 2D dynamics in order to validate the UBC3D-PLM in a boundary value problem. The numerical results are compared with the experimental results published by Byrne et al. [7].

The depth of the sand in the model is 38.1 m on prototype scale. The width does not have a major influence in numerical modeling and a 1D soil response is predicted. The total time of the input acceleration is 33 seconds. 50 loading cycles are modeled with constant amplitude of acceleration equal to  $1.96 \text{ m/s}^2$ .

The results of the predicted evolution of excess pore pressure are presented in Figure 9. At 13.1 meters depth the numerical prediction is in a close agreement with the experimental result. The model can predict the onset of liquefaction with adequate accuracy for this depth. However, in the two higher depths, i.e., at 24.8 and 30.8 meters, the model shows inaccuracy during the first loading cycles. However, the onset of liquefaction can be modeled with an adequate accuracy.

It is concluded from this research that the absence of a stress densification feature in the model leads to a rapid evolution of the pore pressures in the first loading cycles. The effective confining pressure does not influence the behaviour of the current model. Moreover, the  $K_\theta$  factor is assumed 0.5 in this test. This leads to inaccuracy of the densification rule, which is fully valid for stress paths starting from the isotropic line.

#### 5. CONCLUSIONS

The formulation of the UBC3D-PLM as well as the new features implemented by the authors is presented in this paper. The model is a simple but powerful in modeling the onset of liquefaction in sands. It is concluded that after the improvements presented in this paper the model can predict with adequate accuracy the onset of liquefaction. Finally, the aspect of stress densification as well as the anisotropic consolidation

( $K_\theta \neq 1$ ) should be further investigated for a future reformulation

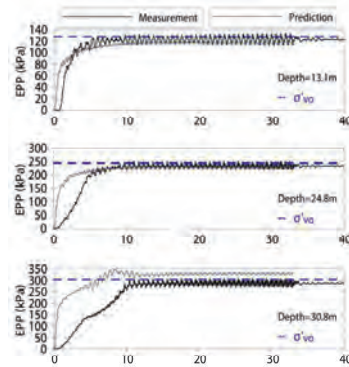


Figure 8 Comparison of the predicted evolution of excess pore pressure by the UBC3D with the experimental results published by Byrne et al. [6].

#### REFERENCES

- [1] H. Puebla, M. Byrne, and P.Philips. Analysis of canlex liquefaction embankments prototype and centrifuge models. *Canadian Geotechnical Journal* (1997), 34:641-651.
- [2] M. Beaty, and P. Byrne, An effective stress model for predicting liquefaction behaviour of sand, *Geotechnical Earthquake Engineering and Soil Dynamics III, ASCE geotechnical special publication No. 75* (1998), 1:766-777.
- [3] A. Tsegaye, *Plaxis liquefaction model, PLAXIS knowledge base*, 2011.
- [4] P.W. Rowe, The stress-dilatancy relation for static equilibrium of an assembly of particle in contact. *Proc. R. Soc.* (1962), 269A:500-527.
- [5] S. Srisakandakumar, *Cyclic loading response of fraser sand for validation of numerical models simulating centrifuge tests*. The University of British Columbia, Master thesis, 2004.
- [6] M.H. Beaty, and P.M. Byrne, *UBCSAND constitutive model version 904aR*, Itasca, page 69, 2011.
- [7] P.M. Byrne, S.S. Park, M.Beaty, M.Sharp, L. Gonzales, and T. Abdoun, *Numerical modeling of dynamic centrifuge tests*, 13<sup>th</sup> world conference in Earthquake engineering, 2004.

# Concerning the Vibrocreep Issue

V.A. Aleksandrovych  
KNAME, 12 Revolutsia st., Kharkiv, Ukraine

## ABSTRACT

Weak decaying settlement of foundations under dynamic load has been analyzed in the paper. Dynamic loads imposed on foundations cause uneven foundations settlement of adjacent building and structures and cause their damage. Uneven foundation settlements of adjacent machines involved in the same technological process cause its disfunction. The deformation of basement soil under dynamic loads has been referred to as soil vibrocreep. The existing theories concerning soil vibrocreep have been reviewed in the paper presented. Two main approaches are known: the first is based on the energy balance equation, while the second on the hereditary creep theory. The approximate convergence of experimental and theoretical data, obtained by means of hereditary creep theory, has been found out. The technique of forecasting machinery foundations settlement has been described. The laboratory facility and the computer software have been developed to implement it. The conclusions have been confirmed by the results of the researches conducted and the technique reliability have been suggested.

Keywords: vibrocreep, soil, foundation.

## 1 THE ANALYSIS OF FOUNDATIONS SETTLEMENT UNDER DYNAMIC LOADS

The dynamic loads caused by machinery operation can lead to weak decaying machinery foundations settlements which can often be quite substantial and uneven.

According to N.M. Gersevanov, under static loads three phases of foundation soil should be distinguished: soil consolidating, initial shears developing and damaging. The available observational and experimental data obtained while facilities were being subjected to dynamic loads indicate that similar three phases could be moni-

tored when foundation is under both static and dynamic loads [1].

The fact is known when the dynamic load caused by a hammer foundation led to the destruction of a three-floored building meant for the forge shop amenity rooms. The vibration amplitude amounted to 1mm, while vibration frequency was 15Hz. The building damaged was located on the distance of 6m from the hammer foundation and it had a strip rubble concrete foundation exerting the pressure of 0.2MPa to the soil. The foundation bed was composed of water-saturated fine sand. Obviously, the building collapsed because its foundation was exposed to different dynamic pressure at different foundation points. Therefore, significant uneven

settlements were formed, at first damaging the foundation and then the walls of the whole building. The frame of the forging workshop building was damaged as well. Uneven footings settlements under the columns located at different distances from the dynamic load source caused damaging the node points of the building frame and induced big cracks in walls.

There have been known some accidents with turbounits precast foundations with beds composed of medium and fine water-saturated sand. The character turbounits foundations settlement before launching them into operation did not differ from the foundations settlement of other constructions built on the same site. After the turbounits had been put into operation significant uneven foundation settlements of turbounits, mills and neighbouring workshop columns arised and led to shaftings misalignment. The turbounite vibration amplitude did not exceed  $8\mu\text{m}$ . The vibration effect on water-saturated sands became the origin of uneven settlements. It is significant that when turbounits and mills were out of operation during repairing work, settling process was not observed.

Machinery vibration effect can even cause the pile foundations settlement. Uneven settlement of turbounits and condensation rooms platform pillars foundations can be considered as another example. Fine-grained water-saturated sand of average density is the foundation bed. The turbounits vibration amplitude does not exceed  $5\mu\text{m}$  while the platform foundations one is up to  $3.5\mu\text{m}$ .

The uneven foundation settlement was observed in the accident at the ore beneficiation workshop where many ore grinding mills and breaking machines exposed significant dynamic loads to the ground base were installed. The fine and medium sand of average density with the deformation modulus of  $E=23\text{Mpa}$  was the foundation bed. The static pressure on the foundations bed was  $0.4\text{Mpa}$ . The maximum calculated settlement under the indicated static pressure must not exceed  $60\text{mm}$ . But it has already reached the value of  $300\text{mm}$  and the process is still progressing. The columns

vibration amplitudes measured did not exceed  $20\mu\text{m}$  at frequency  $5\text{-}7\text{Hz}$ .

The observational data are available as to the settlements on the areas occupied by several dozens of city buldings which average annual settlement has increased several times over the last 100 years as the vibration background caused by city transport has been increasing. It is proved by the fact that the average annual settlement affected the buildings located in  $30\text{m}$  radius from the traffic axis and has never been observed in other places.

Therefore, in most cases the lasting foundation settlements being the result of dynamic loads occur where the foundation beds are fine and pulverescent water-saturated sand and are not observed on the clays beds.

## 2 THEORETICAL BACKGROUNDS TO FORECAST FOUNDATION SETTLEMENT UNDER DYNAMIC LOADS

Until the present time there have been used two basic approaches (described in [2] and [3]) to the explanation of the origin of weak decaying foundation settlement under the dynamic loads. The phenomenon foundation settlement under the dynamic loads has been named soil vibrocreep. Both approaches are based on the principle of superposition, which implies that the resulting settlement value is the sumation of the settlement under the static load  $S_{st}$  and the vibrocreep settlement  $S(t)$ .

$$S = S_{st} + S(t) \quad (1)$$

The approach presented in paper [2] was based on the balance equation of the vibration exciter energy and the energy absorbed by the foundation bed. The finite equation reflecting the settlement progressing with time was as follows:

$$S(t) = (Dt)^{0.5}, \quad (2)$$

where  $D$  is the vibrocreep coefficient.

The approach described in paper [3] is considered to be the first attempt to apply the hereditary creep theory to estimate the additional settlement resulted from vibrocreep. In this case the equa-

tion reflecting the settlement progressing with time can be presented in the following way:

$$S(t) = S_{st} \frac{\delta}{\alpha} t^\alpha, \quad (3)$$

where  $\alpha$  and  $\delta$  are some coefficients.

Abel kernel application built in this approach as a creep kernel the approach also results in the exponential increase of the settlement with time as well as in the first approach. As  $S_{st}$ ,  $\alpha$  and  $\delta$  are constants we obtain the expression similar to (2), with the only difference that the exponent  $\alpha$  is not assigned initially (0.5 in the first approach) but determined as other coefficients.

Nevertheless, as the experiments conducted proved, the description of vibrocreep settlement progress with time by exponential law is not always reliable.

### 3 EXPERIMENTAL RESEARCH OF VIBROCREEP

Both approaches mentioned above imply the vibrostamp experimental tests in compliance with the technique specified in [4]. Tests can be performed by either of the schemes in accordance with the technique.

In the first scheme after the vibrostamp has subjected to the static load, and some settlement stabilization  $S_{st}$  has been achieved, the vibro stamp is subjected to the dynamic load. In the second scheme the vibrostamp is subjected to different stepwise changing static loads under the constant vibration amplitude. The duration of static phases is determined by current standards while the duration of dynamic ones by the relative stabilization achievement under the settlement rate of 0.02mm/h over the period of 4-8hrs.

A large-scale container was constructed at Kharkiv National Academy of Municipal Economy to conduct the tests and vibrostamp installation was designed on its basis for the laboratory testing (fig. 1).



Fig.1 Facility overview

The container measured 1.8x1.8x1.8m is equipped with a telfer to provide easier installation assembly. The container design allows soil water saturation or draining if necessary, as well as the watermark monitoring.

The vibrostamp (fig. 2) is a three-dimensional frame with the vibrator mounted on its bottom plate. The stamp measured 200x400mm is rigidly attached underneath. The hydraulic jack, mounted on the vibrostamp upper plate, abutting against the thrust beam, creates the required static pressure the stamp is subjected to. The upper and bottom plates are jointed with posts with spiral springs in the top parts to provide vibro insulation.



Fig.2 Vibrostamp

The stamp settlement is estimated by two deflectometers “6-PAO” rigidly mounted on the benchmark container.

The vibrostamp vibration frequency and amplitude are assigned by the vibrator rotary speed regulation and the parameters of unbalance at-

tached to its shaft, and controlled by the vibration measuring equipment consisting of “D21A” mechanical motion transducer, “VIP-2” vibrometer, and “Oscill” digital oscillograph. The deflectometer readings as well as the vibration parameters obtained by means of vibro measuring equipment are displayed on a PC screen.

The experiment operator sets the vibration parameters, controls their constancy and logs the data obtained for further processing.

According to our experimental research, the settlement progressing with time can be observed as follows:

1) at the initial stage the character of settling process is approximated by the exponential function, that is conformed to the conclusions made in papers [2] and [3];

2) when the testing period exceeds the indicator  $t > 24-30$ hrs, the settlement progress becomes of the explicit logarithmical character, that is well conformed to fundamental paper conclusions [5] (if the experiment is conducted under the constant static pressure  $P_{st}$ , the vibration amplitude  $a$  and harmonic vibration frequency  $f$ ).

Taking into consideration the facts mentioned above, “Graph” software was developed to analyze the settlement vibrocreep progressing by time on the basis of the experimental data obtained. “Graph” allows to define and to take into account all settling process peculiarities mentioned above, and to specify the final dynamic stage at which the vibration parameters cause sustained settling.

The basic tasks of the analysis are as follows:

- to log the experiment results;
- to construct the curve of settlement progress with time;
- to distinguish separate stages of settlement process;
- to determine the optimal approximation function for each settlement stage;
- to determine the approximation function parameters at the specified stage;
- to construct the approximation curve for each stage;
- to forecast the settlement at specified time span;

- to prepare the final report on the results of the experiment conducted.

The experimental results with the following initial data are given below as an example of the experiment and further log data processing:

- soil conditions: medium sand, the density  $\rho=1.96t/m^3$ , the skeleton density  $\rho_d=1.62t/m^3$ , moisture  $w=0.21$ , the voids ratio  $e=0.64$ , the angle of internal friction  $\varphi=33^0$ , the relative cohesion  $c=3kPa$  ; the deformation modulus  $E=38MPa$ .

- the static pressure  $P_{st}=0.25MPa$ ;
- the vibration frequency  $f=10Hz$ .

The aim of the test is to forecast the machinery settlement while it is in operation on the given basement soil under the indicated vibration parameters.

The tasks:

- to determine the vibration amplitude which causes the sustained settling;
- to derivate the equation of settling progress with time for the experiment phases amplitudes;
- to forecast the settlement in the specified time span.

The experiment was conducted in accordance with using the first test scheme [4]. The data obtained were fixed in the program log (fig. 3). The curve of settling progress with time (fig. 4) has been constructed according to the log data and the equations reflecting the process at each stage have been derived.

№	Time (min)	Time spent (min)	Manometer (kPa)	Left	Right	Temp. (°C)	Amplitude (mm)
150	15:00	0,25	1,25	2046	7961	9,719	10
151	15:45	0,25	1,25	2046	7959	9,725	10
152	16:00	0,25	1,25	2050	7956	9,747	10
153	16:15	0,25	1,25	2052	7953	9,725	10
154	16:30	0,25	1,25	2055	7951	9,702	10
155	16:45	0,25	1,25	2055	7948	9,747	10
156	17:00	0,25	1,25	2058	7945	9,835	10

Fig.3 Fragment of the experiment log.

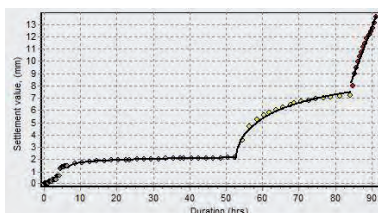


Fig. 4 The curve of settlement progress with time:

- ◇ static phase;
- ◇ dynamic phase,  $a = 5 \mu\text{m}$ ;
- ◇ dynamic phase,  $a = 10 \mu\text{m}$ ;
- ◇ dynamic phase,  $a = 15 \mu\text{m}$ ;
- ◆ experimental data;
- approximating curve.

The following equations describing settling process have been derived:

$$1. a = 5 \mu\text{m} \quad \begin{cases} S = 1.58 t^{0.08} + 1.44, t < 23.25 \\ S = 0.15 \ln(t) + 1.58, t \geq 23.25 \end{cases} \quad (4)$$

The approximation reliability  $R2=0.990$

$$2. a = 10 \mu\text{m} \quad \begin{cases} S = 4.08 t^{0.18} + 2.16, t < 15.97 \\ S = 0.97 \ln(t) + 3.96, t \geq 15.97 \end{cases} \quad (5)$$

The approximation reliability  $R2=0.995$

$$3. a = 15 \mu\text{m} \quad S = 0.77 t + 8.48 \quad (6)$$

The approximation reliability  $R2=0.986$

At the third dynamic stage ( $a = 15 \mu\text{m}$ ) the program derived the approximation equation as a straight-line equation (6), that indicates that under the given parameters the settling progressing under constant speed, i.e. becomes sustained. Therefore, if the machinery under investigation generates the forced vibrations with the amplitude  $a < 15 \mu\text{m}$  while in operation, the program will forecast the settlement in the specified time span (considering the settlement from static load). The forecasted settlement value is compared with the maximum allowed value indicated in the foundation design requirements specification for the given machinery. But if the amplitude  $a \geq 15 \mu\text{m}$ , the foundation bearing surface

should be increased (decreasing  $P_{st}$ ) and the tests should be replicated.

## CONCLUSIONS

The examples of the buildings and structures damaged, mentioned in the first chapter, as well as the machinery dysfunction have proved the importance of the issue under consideration.

The research conducted has confirmed the possibility of applying the hereditary creep theory to determine the vibrocreep settlement value with some amendments compared to the previous scientific studies. These amendments have been implemented due to the development of the laboratory facility and the "Graph" program which have been designed to forecast the vibrocreep settlement value for a long-term period on the basis of the comparatively short-term data obtained in the vibrostamp tests conducted.

Long-duration ( $t > 100$ hrs) tests, with data approximation reliability  $R2=0.98-0.99$  confirms the reliability of the technique developed.

## ACKNOWLEDGEMENT

I would like to express my gratitude to all those who gave me the assistance to complete this paper.

My special gratitude to my research supervisor Prof. Dr. V.G. Taranov for researching and writing the paper all-round aid and A.V. Aleksandrovych for technical support in experimental facility construction.

## REFERENCES

- [1] O.A. Savinov, *Modern Designs of Machinery Foundations and Their Calculation*, Leningrad, 1979
- [2] V.Ya. Khain, *Theoretical Analysis of Sustained Foundation Settlements under Static and Dynamic Loads, Dynamics of Subgrades and Structures*, (1977), 206-209.

- [3] O.R. Phillipov, Experimental Studies of Stamps Settlements on Water-Saturated Soil Under Vibrations, *Dynamics of Subgrades and Structures*, (1977), 198-201
- [4] V.G. Taranov et al., *Recommendations to Conducting Field Tests in Turbounits Foundations Subgrades Vibrostability*, Moscow, 1986.
- [5] Yu.N. Rabotnov, *Elements of Hereditary Solid Mechanics*, Moscow, 1977.



# A simple numerical method to study buckling of flexible piles embedded in a multi-layered soil

Fahd Cuiira<sup>1</sup>  
TERRASOL

## ABSTRACT

A numerical method has been implemented for the buckling analysis of flexible piles, allowing direct computation of the critical buckling load of any pile with known rigidity and shape, embedded in a multilayered soil. The method consists of coupling beam finite elements for the pile with a heterogeneous distribution of continuous springs for soil. This enables to write the 2<sup>nd</sup> order static equilibrium of the pile as a simple matrix system whose eigenvalues are the critical buckling loads, and eigenvectors are the characteristic buckling mechanisms. Results illustrate how the critical buckling load is significantly increased by introducing lateral soil reaction. It is also shown that a pure buckling analysis has practically no impact on flexible piles design even in very poor soil conditions. Moreover, the method enables easily to compute 2<sup>nd</sup> order amplification of displacements and bending forces. Thus, a complete buckling analysis shows that for a pile with an initial deflection, 2<sup>nd</sup> order effects lead rigorously to a bending failure long before reaching the theoretical value of the critical buckling load.

Keywords: buckling, 2<sup>nd</sup> order effects, flexible piles, numerical modeling, geotechnical tools, soil-pile interaction

## 1 INTRODUCTION

The design of deep foundation requires studying several failures mechanisms: bearing capacity, lateral reaction, bending moments... For the case of a flexible pile axially loaded such as mini/micro-piles or long inclusions, an other mechanism may be considered: failure by buckling. Geotechnical engineers know that except the case of a form flaw, the buckling analysis has generally no significant impact on the design of an embedded pile even in very poor soil conditions. Nevertheless, we have to prove it by checking the critical buckling load taking into account lateral soil reaction. Moreover, when the computing of critical buckling load becomes

possible by analytical approaches for some simple cases or by performing numerical processing in large displacement, it remains necessary to consider the 2<sup>nd</sup> order effect related to a possible initial form flaw or to a first lateral loading (service or parasitic...). The 2<sup>nd</sup> order effects could be in some case very penalizing even for a loading level much lower than the one of critical buckling load.

## 2 REFERENCE TO SOME EXISTING APPROACHES

Several analytical solutions are proposed in existing bibliography with regard to pile buckling. All are based on the Winkler model: the pile is

---

<sup>1</sup> Fahd Cuiira, TERRASOL, 46 quai de la Râpée, Paris, France, [f.cuiira@terrasol.com](mailto:f.cuiira@terrasol.com)

simulated by an elastic beam model and soil is introduced by means of a constant or depth-dependant reaction modulus. We can cite the works of Mandel [1] and Hetenyi [2], regarding piles embedded in homogeneous soil profile; Davission [3], assuming a soil modulus linearly increasing with depth, and Souche [4], considering a partially embedded pile. All of the solutions above are given in graphical form due to the complexity of the analytical expressions which are used to calculate the critical load. Even though those solutions are well adapted to simple configurations, they are proved inefficient when applied to cases of multi-layered stratum and pile geometry imperfections. Furthermore, no indication on pre-buckling behavior (evolution of bending forces due to 2nd order effects) is given when using these methods. Analysis of such phenomena demands generally an updated mesh numerical modeling considering large deflection theories, which are not always adapted to practical geotechnical applications.

### 3 PILE UNDER LATERAL LOADING

#### 3.1 Bending behavior of an isolated pile

Consider the case of an isolated flexible pile embedded in a multilayered soil and laterally loaded by forces, either imparted at its head or at any point along the shaft. The bending behavior of the pile can be approached by a simple beams model according to the general equation below:

$$EI \frac{d^4 y}{dx^4} = q(x) - r(x) \quad (1)$$

Where:

- x : local co-ordinate along the pile
- y(x): lateral displacement of the pile
- EI: bending stiffness of the pile
- r(x): lateral soil reaction
- q(x): density of lateral loading on the pile (other than the lateral soil reaction)

Solving the equation (1) can be based on a simple finite element formulation, using, for example, beam elements with two nodes and four degrees of freedom (Kirchhoff model, [5]). Thus, the equation (1) can be written as an equivalent matrix system:

$$\mathbf{K}^e \cdot \mathbf{y} = \mathbf{F}^{ext} - \mathbf{R}^s \quad (2)$$

Where

- $\mathbf{K}^e$  : pile stiffness matrix
- $\mathbf{F}^{ext}$  : lateral loading vector
- $\mathbf{R}^s$  : soil reaction vector
- $\mathbf{y}$  : equivalent displacement vector consisting of the displacement and the rotation at each node.

#### 3.2 Modeling of soil reaction

The soil response can be simulated basing on a distribution of elastoplastic springs. Thus, as shown in the figure 1, springs behavior can be characterized by a bi-linear reaction curve relating the lateral displacement of the pile to soil reaction.

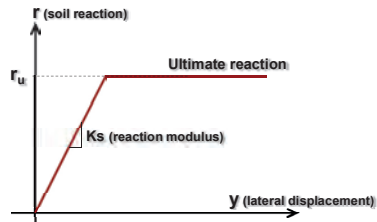


Figure 1 : Typical soil reaction curve

Theoretically [6], the reaction modulus denoted “Ks” (expressed in kN/m<sup>2</sup>) can be directly related to the soil shear modulus G by the relation: Ks ~ 4 x G. French practice consists in estimating the value of Ks and the ultimate reaction “ru” (expressed in kN/m) by correlation with Pressurimeter test results.

Using the matrix formulation presented previously, the soil reaction vector can be written as follows:

$$\mathbf{R}^s = \mathbf{K}^s \cdot \mathbf{y} + \mathbf{C}^e \quad (3)$$

Where,

$\mathbf{K}^s$ : soil stiffness matrix corresponding to the “elastic” part of the reaction curve

$\mathbf{C}^e$ : plastic reaction vector corresponding to the “plastic” part of the reaction curve

### 3.3 Solution

Combining equations (2) and (3) leads to the following global matrix system, to be completed by boundary conditions:

$$\left( \mathbf{K}^s + \mathbf{K}^e \right) \cdot \mathbf{y} = \mathbf{F}^{\text{ext}} - \mathbf{C}^e \quad (4)$$

Given the elastoplastic behavior of soil response, the resolution of the system above requires an iterative analysis where  $\mathbf{K}^s$  and  $\mathbf{C}^e$  are evolving until convergence.

## 4 CALCULATION OF CRITICAL BUCKLING LOADS

### 4.1 Generalities

The buckling failure is an elastic instability form which results in generation of a non-zero deflection under axial loading (figure 2).

This phenomenon occurs for definite values of the axial load called critical buckling loads. Each of these load values is related to a specific buckling mechanism. Generally, a buckling analysis consists of estimating the lowest value of critical buckling loads, and checking that it remains larger than the service axial load, with sufficient safety.

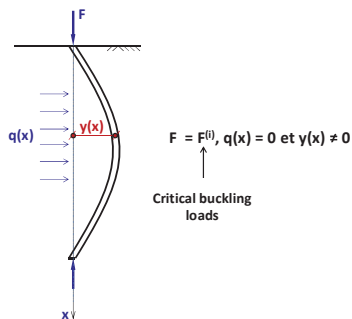


Figure 2 : Definition of the buckling phenomenon

Actually, there is an obvious analogy between buckling as an elastic instability form and the “resonance” phenomenon as a dynamic instability form which occurs for definite values of the loading frequency (Eigen frequencies). The presented approach here is based on this analogy and allows evaluating critical buckling loads by applying the eigenvalues method to the matrix formulation obtained previously.

### 4.2 Governing equations

Consider the case of a flexible pile under an axial load “F”. No lateral loading is applied to the pile. The axial force is assumed to be constant along the pile: we neglect dissipation of axial loading by lateral friction, which constitutes a pessimistic assumption. Thus, the 2<sup>nd</sup> order equilibrium of the pile can be written as follows:

$$EI \frac{d^4 y}{dx^4} + F \frac{d^2 y}{dx^2} = q(x) - r(x) \quad (5)$$

Applying the matrix formulation presented previously (§3.3), the equation (5) can be expressed in an equivalent matrix system:

$$\left( \mathbf{K}^s + \mathbf{K}^e \right) \cdot \mathbf{y} = \mathbf{F} \cdot \mathbf{M} \cdot \mathbf{y} \quad (6)$$

Where “M” represents a “transfer” matrix related to the 2<sup>nd</sup> order effects. The other terms are those already introduced in equation (4).

By definition, F is a critical buckling load if and only if the equation 6 (and consequently, the equation 5) admits a non-zero solution y. Mathematically, this means that F is an eigenvalue of the matrix system (6). Thus, seeking out eigenvalues and eigenvectors of this matrix system leads respectively to the critical buckling loads and the corresponding failure mechanisms.

#### 4.3 Practical application

To apply the presented method, we have to define, in addition to possible boundary conditions, the bending stiffness of the pile and the soil reaction curve for each model layer. The method has been implemented as a numerical program which sets up the matrix system and computes its eigenvalues and eigenvectors. In particular, the lowest eigenvalue is not other than the critical buckling load to be used for the buckling analysis.

The following figures (3) and (4) show the case of a micro-pile embedded in a multilayered soil (five layers). Three situations are considered depending on the value of the shear modulus assumed for the soft clay soil:  $G = 0$  MPa (no lateral reaction in this layer),  $G \sim 0,5$  MPa and  $G \sim 1$  MPa. This condition has a significant effect on the potential buckling mechanism and therefore on the value of critical buckling load  $F_{cr}$  : we have respectively  $F_{cr} = 850, 3400$  and  $4600$  kN for the three studied situations.

Results illustrate how the critical buckling load is significantly increased by introducing lateral soil reaction. In practice, a pure buckling analysis has no impact on flexible pile design even in very poor soil conditions.

Note that for simple cases where usual analytical approach can be used, as the case of piles embedded in a homogenous soil [1] or the case of piles partially embedded [4], the developed method leads exactly to the same results.

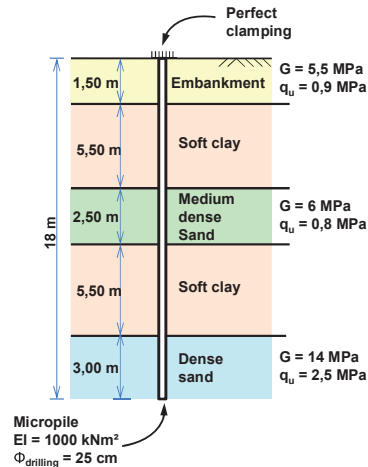


Figure 3 : Practical application, calculation of critical buckling loads.

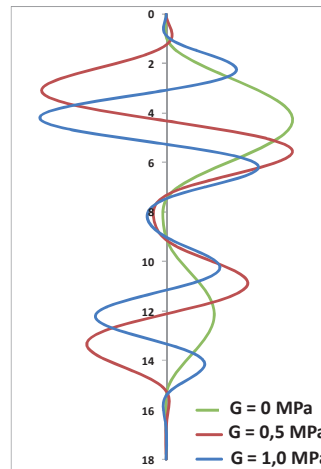


Figure 4 : Practical application, critical buckling mechanisms obtained for studied situations.

## 5 PILE WITH INITIAL DEFLECTION

### 5.1 Governing equations

Consider now the case of a flexible pile with an initial deflection denoted “ $y_0$ ”, which may be representative, either of a first lateral loading or of a form flaw. Then, as shown in the figure 5, the pile is subject to the application of an axial force  $F$ , leading, by 2<sup>nd</sup> order effect, to an additional deflection denoted “ $y$ ”.

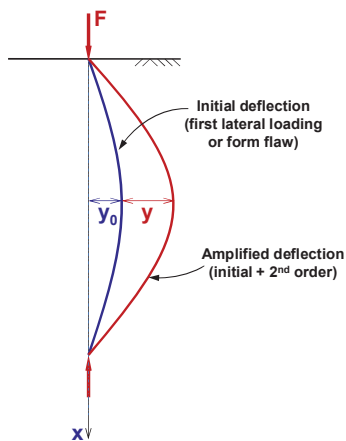


Figure 5 : Consideration of 2<sup>nd</sup> order effects

In these conditions, the 2<sup>nd</sup> order equilibrium of the pile can be written as follows:

$$EI \frac{d^4 y}{dx^4} + Ks \cdot y + F \frac{d^2}{dx^2} (y + y_0) = 0 \quad (7)$$

Basing on the matrix formulation presented previously, the equation (7) can be put in a homogeneous matrix form:

$$\left( \mathbf{K}^s + \mathbf{K}^e \right) \mathbf{y} = F \cdot \mathbf{M} \cdot (\mathbf{y} + \mathbf{y}_0) \quad (8)$$

In the case there is no initial deflection ( $y_0 = 0$ ), we have:

$$\left( \mathbf{K}^s + \mathbf{K}^e \right) \mathbf{y} = F \cdot \mathbf{M} \cdot \mathbf{y} \quad (9)$$

Which is exactly the same system (6), whose eigenvalues are the buckling loads  $F^{(i)}$ , and its eigenvectors are the related buckling mechanisms  $\mathbf{y}^{(i)}$ :

$$\left( \mathbf{K}^s + \mathbf{K}^e \right) \mathbf{y}^{(i)} = F^{(i)} \cdot \mathbf{M} \cdot \mathbf{y}^{(i)} \quad (10)$$

The matrix forming the system (10) are symmetric and positive-definite. Then, the eigenvectors of this system constitute an orthogonal basis. In particular,  $\mathbf{y}$  and  $\mathbf{y}_0$  can be written as a linear combination of those vectors:

$$\mathbf{y} = \sum_{i=1}^n \alpha^{(i)} \mathbf{y}^{(i)} \quad \mathbf{y}_0 = \sum_{i=1}^n \alpha_0^{(i)} \mathbf{y}^{(i)} \quad (11)$$

By projecting and substituting in (8), we obtain:

$$\mathbf{y} + \mathbf{y}_0 = \sum_{i=1}^n \phi^{(i)} \alpha_0^{(i)} \mathbf{y}^{(i)} \quad \phi^{(i)} = \frac{F^{(i)}}{F^{(i)} - F} \quad (12)$$

Where “ $\mathbf{y} + \mathbf{y}_0$ ” constitutes the amplified displacement and  $\phi^{(i)}$  are the apparent amplification factors due to 2<sup>nd</sup> order effects. Note that when  $F$  tends to one of critical buckling loads  $F^{(i)}$ , corresponding amplification factor  $\phi^{(i)}$  tends to infinity. This means that 2<sup>nd</sup> order effects lead to bending failure long before reaching the critical buckling load [7]. Moreover, notice that the presented approach is comparable to the modal analysis which consists in evaluating forced dynamic response by projecting onto eigen modes.

### 5.2 Practical application

The following figure illustrates the case of a mini-pile ( $\Phi < 60$  cm) embedded in a three-layer soil. The initial deflection of the pile corresponds to a first lateral loading  $T_0$  applied to its head. The pile is also subject to the application of an

axial force  $F$  which does not exceed the buckling critical load. Basing on the presented method, we can estimate displacements and bending moments taking into account 2<sup>nd</sup> order effects (figure 7).

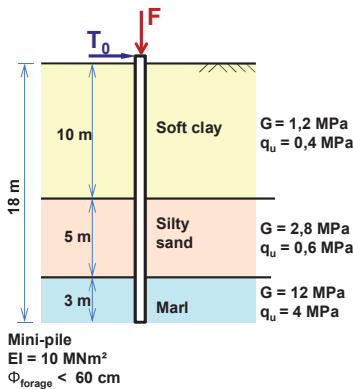


Figure 6 : Practical application – 2<sup>nd</sup> order effects

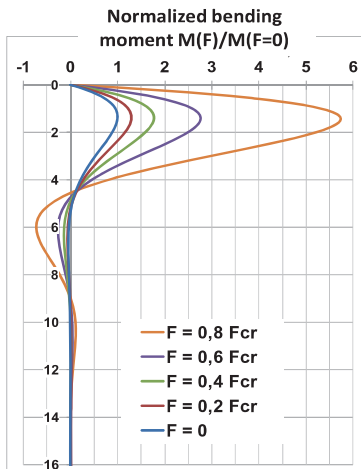


Figure 7 : Amplified bending moments due to 2<sup>nd</sup> order effects

Results show that when axial load varies from 20 to 80% of the lowest critical buckling load  $F_{cr}$ , bending moments are amplified from 1,5 to 6 times in comparison to the first order value. In particular, for  $F = 0,6 F_{cr}$ , the amplification factor is about 2,80.

This example is representative of situations where 2<sup>nd</sup> order effects may lead easily to bending failure for a loading level well below the one of the critical load.

Notice that the same results can be obtained by a complete numerical simulation in large deflection basing for example on a “step by step” routine. However, the computation time will be very much larger.

## 6 CONCLUSION

The presented method has been implemented as a calculation tool called “Piecoef+”, which proves effective in numerous design projects of deep foundations such as flexible inclusions, mini-pile, micro-pile... and where the buckling problematic had to be considered. The method avoids simplification related to the usual analytical solution and gives a rigorous estimation of the critical buckling load for complex configurations. It also allows evaluating easily the 2<sup>nd</sup> order effects for the case of a flexible pile with a form flaw or which is subject to a first lateral loading.

## REFERENCES

- [1] MANDEL M. – Buckling in homogenous elastic medium. Annales des Ponts et Chaussées, N° 20, 1936.
- [2] HETENYI M. – Beams on elastic foundation and related problems. University of Michigan Press, Ann Arbor vol 16, 1946
- [3] DAVISSON M.T. - Estimating buckling loads for piles. 2<sup>nd</sup> Pan-American CSMFE, Brazil, vol 1, 1963.
- [4] SOUCHE P. – Buckling of partially embedded piles. Annales de l'ITBTP, N° 238, 1984.
- [5] ZIENKIEWICZ O. C. & TAYLOR R. L. – The Finite Element Method. McGraw-Hill book Company (1991)
- [6] GAZETAS G. & al. – Dynamic interaction factors for floating pile groups – Journal of Geotechnical Engineering ASCE, vol 117 (1991), 1531-1548.
- [7] COIN A. & ALBIGES M. – Buckling and elastic instability, EYROLLES (1978).

# Basic study of the numerical analysis of jet grouting using smoothed particle hydrodynamics

B.Stefanova

*Hamburg University of Technology, Institute of Geotechnical Engineering and Construction Management, Harburger Schloßstraße 20, 21079 Hamburg, [bozhana.stefanova@tu-harburg.de](mailto:bozhana.stefanova@tu-harburg.de)*

## ABSTRACT

Jet grouting is a method of grouting that uses very high pressure streams and cement suspensions. The diameter of a jet grouting column depends on a series of factors, such as the soil and suspension properties as well as the processing parameters. The purpose of this paper is to outline an innovative way of modeling the jet grouting process using the Smoothed Particle Hydrodynamics (SPH) on the example of a fluid jet penetrating into sand. The SPH is a meshless particle method that has not only been established for physical and hydrodynamic modeling during the last few decades but has also proven to have a great potential in handling soil behavior. The results are supposed to provide information about the diameter of jet grouting columns, its relation to the soil and construction properties and also contribute to the economic feasibility and the quality control of the jet grouting technique.

Keywords: jet grouting, numerical analysis, smoothed particle hydrodynamics, soil-fluid interaction

## 1 INTRODUCTION

Jet grouting is a method for ground improvement and stabilization. It has been well known since the 1970's, when it was originally applied in Italy, Japan and the UK. The method uses very high pressure streams of up to 600 bar in order to break up and cement the ground. It also applies a rotating drill with small nozzles (e.g. 2mm) in order to reach the required depth. As the drill rotates and raises, columns or sections of columns are formed in the underground.

Quality management and control can be an issue during the construction of jet grouting columns. Deviations in their position and size might

occur, so that trial columns are normally required prior to the actual construction. There are also very few reference values considering the impact of soil and construction properties on the expanse of the cement suspension in the ground, that are actually applicable. Numerical analysis using conventional mesh methods such as FEM and FVM has not been successful so far, mainly due to the high pressure, turbulence and blending of different phases, that occur in the process of jet grouting.

This paper describes an innovative way of numerical analysis of soil-fluid interaction, using a meshfree method, called smoothed particle hy-

dynamics (SPH) and aims to apply this approach to represent the process of jet grouting.

## 2 SMOOTHED PARTICLE HYDRODYNAMICS

The smoothed particle hydrodynamics (SPH) is a meshfree method, that was originally used in the astrophysics in the 1970's. It has undergone a significant development since and is nowadays suitable for different physical, hydrodynamic and also geotechnical calculations.

The SPH uses particles that have the properties of the investigated materials. The values, e.g. velocity or density, for a particular particle are calculated from those of its neighbor particles using an approximation function  $W$ , called Kernel function.

For the purpose of this study a code called Gadget <sup>H2O</sup> has been employed. It is an extension of the astrophysical code Gadget 2 by Volker Springel (Springel (2001), Springel (2005)), which was developed by Christian Ulrich (Ulrich and Rung (2010), Ulrich et al. (2011)). The code of Gadget <sup>H2O</sup> was also supplemented in this study as described in chapter 2.2.2, in order to develop a code that is more suitable for geotechnical calculations.

### 2.1 Conservation equations

The equations of mass and momentum conservations are relevant for the framework of SPH. A SPH approximation needs to be applied on both equations in Cartesian coordinates.

Mass conservation is defined as follows in its Lagrangian formulation and SPH approximation:

$$\begin{aligned} \frac{D\rho}{Dt} &= -\rho \frac{\partial v^\beta}{\partial x^\beta} \\ \text{Lagrangian formulation} \\ \Rightarrow \frac{D\rho}{Dt} &= \underbrace{\sum_{j=1}^N m_j (v_i^\alpha - v_j^\alpha) \frac{\delta W_{ij}}{\partial x_i^\alpha}}_{\text{SPH approximation}} \end{aligned} \quad (1)$$

where  $\rho$  defines the density,  $v^\beta$  and  $x^\beta$  are the vectors of velocity and position in Cartesian co-

ordinates. The index  $i$  denotes the focal particle and  $j$  a neighbour particle.

The conservation of momentum is written as:

$$\begin{aligned} \frac{Dv^\alpha}{Dt} &= \frac{1}{\rho} \frac{\partial \sigma^{\alpha\beta}}{\partial x^\beta} + \frac{f^\alpha}{\rho} \\ \text{Lagrangian formulation} \\ \Rightarrow \frac{Dv_i^\alpha}{Dt} &= \underbrace{\sum_{j=1}^N \left[ m_j \left( \frac{\sigma_i^{\alpha\beta}}{\rho_i^2} + \frac{\sigma_j^{\alpha\beta}}{\rho_j^2} \right) \frac{\delta W_{ij}}{\partial x_i^\beta} \right]}_{\text{SPH approximation}} + \frac{f_i^\alpha}{\rho_i} \end{aligned} \quad (2)$$

where  $\sigma^{\alpha\beta}$  is the stress tensor and  $f^\alpha$  a volumetric force.

### 2.2 Equation of state

The pressure for fluids in the SPH is calculated by the equation of state. Soil particles are generally not included in conventional SPH formulations. Therefore, they are listed separately in section 2.2.2.

#### 2.2.1 Treatment of fluids

The pressure for fluids is calculated using pressure-density relation as in Shao and Lo (2003) and Monaghan (2004):

$$p = \left( \left( \frac{\rho}{\rho_0} \right)^\gamma - 1 \right) B \quad (3)$$

with  $p$  pressure,  $\gamma = 7$  for water,  $B$  is the reference pressure and  $\rho_0$  reference density according to Ulrich and Rung (2010).

#### 2.2.2 Treatment of soil

##### (1) Original definition according to Ulrich and Rung (2010)

The original version of Gadget <sup>H2O</sup> contains a treatment of soil particles as a fluid with variable viscosity (Ulrich and Rung (2010), Ulrich et al. (2011)). A yield criterion, similar to that of Mohr-Coulomb, is employed for the viscosity calculation as described in equation (4):



$$\mu = \frac{p \cdot \sin \varphi + c}{S^*} \quad (4)$$

with  $\varphi$  – angle of friction,  $c$  – cohesion and  $S^*$  – a parameter related to the second invariant of the strain rate tensor, as described in Ulrich and Rung (2010).

Unfortunately, this simple method has the shortcoming of not being able to calculate the stress in the soil.

### (2) Elastic behavior

A first step to separate both phases – fluid and soil – was to introduce a stress-strain relation for the soil particles. This way stress and also pressure in soil particles are calculated as a function of displacement (equation (5)) and not by the equation of state.

The application of linear elastic soil behavior was chosen as a first alternative to explore.

$$\sigma = C\varepsilon \quad (5)$$

Of course, a linear elastic modeling of soil does not describe the soil behavior during the process of jet grouting in a proper way. A more sophisticated approach is therefore required.

### (3) Elastoplastic behavior

An elastoplastic constitutive relation using Drucker-Prager yield criterion was applied. For this purpose the pattern, described by H.H. Bui in Bui et al. (2008), Bui et al. (2011a), Bui et al. (2011b) and Bui et al. (2011c), was used and implemented in the code Gadget<sup>H2O</sup>:

$$\begin{aligned} \frac{d\sigma'^{\alpha\beta}}{dt} &= \sigma'^{\alpha\gamma} \dot{\omega}^{\beta\gamma} + \\ &+ \sigma'^{\gamma\beta} \dot{\omega}^{\alpha\gamma} + 2G\dot{e}^{\alpha\beta} + K\dot{\varepsilon}^{\gamma\gamma} \delta^{\alpha\beta} - \\ &- \dot{\lambda} [3K\alpha_\psi \delta^{\alpha\beta} + \frac{G}{\sqrt{J_2}} s'^{\alpha\beta}] \end{aligned} \quad (6)$$

where  $\dot{\omega}$  is rotation rate tensor,  $G$  shear modulus,  $K$  bulk modulus,  $e$  deviator strain,  $s$  stress deviator and  $J_2 = -\frac{1}{2}(s:s)$ .  $\dot{\lambda}$  is the rate of the plastic potential:

$$\dot{\lambda} = \frac{3\alpha_\varphi K \dot{\varepsilon}^{\gamma\gamma} + \frac{G}{\sqrt{J_2}} s'^{\alpha\beta} \dot{\varepsilon}^{\alpha\beta}}{9\alpha_\varphi K \alpha_\psi + G} \quad (7)$$

with the Drucker-Prager parameters  $\alpha_\varphi = \frac{\tan \varphi}{\sqrt{9+12\tan^2 \varphi}}$  and  $\alpha_\psi$  analogue using the angle of dilatance  $\psi$ .

### 2.2.3 Boundary conditions

There are different ways to define boundaries in the framework of SPH. The use of wall particles was suitable for our calculations. These are particles, which are assigned zero acceleration at every time step.

### 2.2.4 Initial conditions for soil

The initial stress state of soil is important in order to achieve realistic stress state in the course of the calculation. Jaky's equation was implemented in SPH as the ground level was considered to be horizontal:

$$\sigma_v = \rho g z \quad (8)$$

$$\sigma_h = K_o \sigma_v \quad (9)$$

with  $z$  for the vertical distance from the top ground level and  $K_o = 1 - \sin \varphi$ .

## 3 CALCULATIONS AND RESULTS

### 3.1 Model and parameters

The simulation uses a rectangular box filled with sand particles, which is framed by sand wall particles. A water jet penetrates the box on its upper side. The jet has a velocity of 170 m/s, which equals to a pressure of 150 bar. This value corresponds to the experimental studies of Stein (2004) that were also conducted with a water jet penetrating into a sand box under a pressure of 150 bar. This way the simulation results can be compared and validated with experimental values for further studies.

The calculations were conducted in three different steps, using the formulations for soil

treatment, described in 2.2.2. The soil and simulation parameters are listed in Table 1.

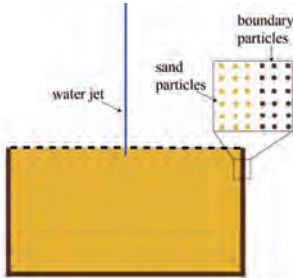


Figure 1 The model used for calculation

The time step depends on a multiple CFL condition according to Ulrich et al. (2011). It is function of the maximal pressure and velocity

Table 1 Parameters used with the different models

model parameters	acc. to Ulrich & Rung	elastic	elasto-plastic
number of particles	40037	60944	60944
wight x heigth [m]	5 x 2	5 x 2	5 x 2
pressure [bar]	150	150	150
soil density [kg/m <sup>3</sup> ]	1 00	1600	1600
angle of friction [°]	32	32	32
angle of dilatancy [°]	-	-	10
cohesion [kN/m <sup>2</sup> ]	0	0	0
Young's modulus [kN/m <sup>2</sup> ]	-	20000	20000
Poisson's ratio [-]	-	0.3	0.3
bulk modulus [kN/m <sup>2</sup> ]	-	16667	16667
shear modulus [kN/m <sup>2</sup> ]	-	7692	7692

### 3.2 Results from the first simulation

The first simulation is able to display the distribution of particles as well as their velocity, density and pressure (Figure 2).

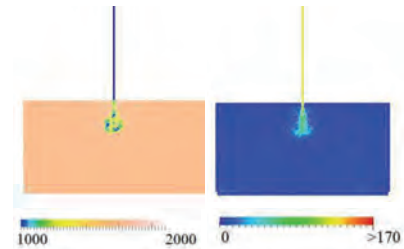


Figure 2 Results for the density distribution (left) and velocities (right) after 0.002s

However, this model has the disadvantage of not being able to display the actual stress components, as well as not including a constitutive model for soil with a yield criterion.

### 3.3 Results with elastic soil behavior

In the second simulations the stresses are calculated from the displacements using a stiffness matrix. Example results are displayed in Figure 3.

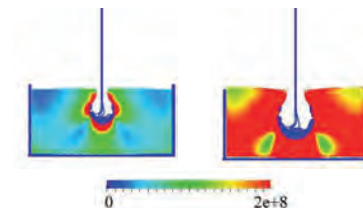


Figure 3 Stress magnitude at 0.002 and 0.005 s in [kN/m<sup>2</sup>]

Considering these results, it is obvious that the linear elastic soil behavior leads to an accumulation of large stresses. Furthermore, a remarkable increase in the volume of the soil body is to be noticed. These observations indicate that the results of this second simulation are rather exaggerated in comparison to realistic soil behavior. This calculation however presents an extended

model as a first step for a separate consideration of soil and water particles.

### 3.4 Results with elastoplastic soil behavior

The third simulation applies a more sophisticated version of the soil model as described in section 2.2.2.3. It includes an elastoplastic soil behavior and also a threshold for soil liquefaction. The latter is activated, when soil particles are exposed to large pressure impact due to the water jet, so that severe decrease in the effective stresses occurs. In this case, the sand particles are subjected to liquefaction and start to behave as a viscous fluid again.

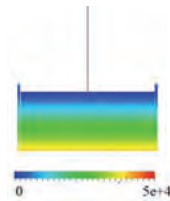


Figure 4 Initial stress magnitude in [kN/m<sup>2</sup>]

An initial stress state is employed in order to achieve a realistic stress distribution in the course of the calculation (Figure 4).

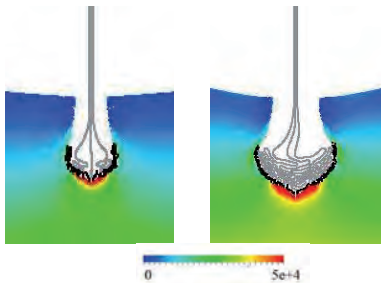


Figure 5 Stresses in the area of penetration of the water jet (zoom in) after 0.005 and 0.03s in [kN/m<sup>2</sup>]. Water jet is displayed in grey and liquefied sand in black

Example results for the magnitude of total stress in the soil are shown in Figure 5. The stress accumulation is not that striking as in the

previous simulation but still noticeable. An increase of volume is lacking and the top ground level is deformed in loading direction (Figure 6).



Figure 6 Penetration of the water jet and deformation of the sand after 0.03s

This latest improvements in the soil model provide more realistic results as previous simulations. Validation and further test are also being planned in order to confirm the accuracy of the model and to implement corrections, if necessary.

## 4 CONCLUSIONS

The smoothed particle hydrodynamics has shown a versatile potential for a wide range of calculations in physics and engineering. One aspect of growing importance for this numerical method has been geotechnical engineering.

This paper has outlined different approaches to simulate a water jet penetrating into a sand box as a simplification of the jet grouting process. It aims to study the soil-water interaction, especially when rather high pressure is applied. The SPH has the advantage of being able to deal with large deformations and different phases, which is of particular importance for this study.

Although still validation and further tests are required, the application of SPH on problems of geotechnical engineering has shown to be a promising alternative to conventional mesh based methods. In the future such simulations can be applied to problems considering fluid-soil interaction and coupling, as well as the influence of exceed pore water pressure or even soil liquefaction and erosion.

## REFERENCES

- [1] Springel, V. (2005). The cosmological simulation code GADGET-2. *Monthly Notices of the Royal Astronomical Society*, pp. 1105–1134.
- [2] Springel, V., Yoshida, N. and White, S. (2001). GADGET: a code for collisionless and gasdynamical cosmological. *New Astronomy*, pp. 79–117.
- [3] Ulrich, C. and Rung, T. (2010). SPH-Modelling of Water/Soil-Suspension Flows. Manchester, UK: 5th international SPHERIC workshop.
- [4] Ulrich, C., Bednarek, S. and Rung, T. (2011). Multiphysics SPH Simulation with Local Particle Coarsening. *Proceeding of the ASME, 30th International Conference on Ocean, Offshore and Arctic Engineering*.
- [5] Shao, S. and Lo, E. (2003). Incompressible SPH method for simulating Newtonian and non-Newtonian flows with free surface. *Advances in Water Resources*, pp. 787–800.
- [6] Monaghan, J.: Simulating free surface flows with SPH. *Journal of Computational Physics*, 2004, pp. 399-406
- [7] Bui, H., Fukagawa, R., Sako, K. and Ohno, S. (2008). Lagrangian meshfree particles method (SPH) for large deformation and failure flows of geomaterial using elastic-plastic soil constitutive model. *International Journal for Numerical and Analytical Methods in Geomechanics*, pp. 1537-1570.
- [8] Bui, H., Fukagawa, R., Sako, K. and Wells, J. (2011a). Slope stability analysis and discontinuous slope failure simulation by elasto-plastic smoothed particle hydrodynamics (SPH). *Geotechnique*, pp. 565-574.
- [9] Bui, H., Nguyen, C., Sako, K. and Fukagawa, R. (2011b). A SPH model for seepage flow through deformable porous media. *6th International SPHERIC Workshop, Hamburg*, pp. 164-171.
- [10] Bui, H.H., Sako K., Fukagawa, R. (2011c). An improved SPH method for saturated soils and its application to investigate the mechanisms of embankment failure: Case of hydrostatic pore-water pressure. *International Journal for Numerical and Analytical Methods in Geomechanics*
- [11] Stein, J. (2004) Experimentelle und numerische Untersuchungen zum Düsenstrahlverfahren, Ph.D. Thesis. Veröffentlichungen des Arbeitsbereiches Geotechnik und Baubetrieb, Band 8. Hamburg: Technische Universität Hamburg-Harburg

# 3D-interaction of structure and subsoil for a new fly ash silo, Maasvlakte Rotterdam

L.F.J. Bekken<sup>1</sup>  
*Fugro GeoServices B.V.*

W.A. Nohl  
*Fugro GeoServices B.V.*

## ABSTRACT

A new fly ash silo is built with a construction of reinforced concrete (height = 55 m, diameter = 24 m) as part of the new power plant at the E.ON site at the Maasvlakte Rotterdam, Netherlands. The total weight of the silo is 400 MN when filled with fly ash. The silo is constructed on a 2.5 m thick concrete base slab and is founded on 59 large diameter bored piles ( $\varnothing$  1.5 m) with a length of 32 m. The soil investigation revealed a mainly sand profile with a clay layer at 10 m below pile tip level, which varies in presence and thickness. The heterogeneity of the subsoil may result in differential settlements, which will lead to higher stresses in the construction depending on the stiffness of the construction. Detailed information on the heterogeneity of the subsoil, the stiffness of the structure and the pile behavior is necessary to analyze the settlement behavior and the forces in one interaction model, where all components with its properties are incorporated. A realistic interaction analysis is performed in 3D with the finite element program PLAXIS 3D. The advantage of this approach in comparison to the general accepted design approaches with a conventional elastic support model are defined.

Keywords: Foundation design, soil heterogeneity, differential settlements, structure subsoil interaction model, finite element model, PLAXIS 3D

## 1 INTRODUCTION

As part of the new power plant at the E.ON site at the Maasvlakte, a new fly ash silo is built with a construction of reinforced concrete with a total height of 55 m and a diameter of 24 m. The total weight of the silo is 400 MN when filled with fly ash. The silo is constructed on a 2.5 m thick concrete base slab with a diameter of 32 m. Figure 1 shows a cross section of the silo.

For the foundation design a grid of Cone Penetration Tests (CPT's) with depths varying from 40 to 70 m were performed. In addition, a borehole was carried out with selected undisturbed samples taken for geotechnical laboratory tests. Since deformations of the clay layers were expected to have a relatively large influence on the structure, mainly oedometer tests had been performed on the undisturbed clay samples. From the CPT's and borehole logs the soil pro-

---

<sup>1</sup> Corresponding Author: Fugro GeoServices B.V., Veurse Achterweg 10, 2260 AB Leidschendam, the Netherlands, l.bekken@fugro.nl

file had been determined. The global soil profile is presented in table 1.

The total structure is founded on 59 large diameter bored piles ( $\varnothing$  1.5 m) with pile tip level in the second sand layer (NAP -29 m). The calculated design pile bearing capacity is 11.5 MN.

The settlements of the pile group are mainly caused by compression of the 2<sup>nd</sup> clay layer below pile tip level due to an increase of stresses. This 2<sup>nd</sup> clay layer varies in presence and thickness; at some locations the thickness is 1.5 m, but the layer is not encountered at some other locations, see figure 1. The differential settlements were restricted by the Clients specifications.

The heterogeneity of the subsoil may result in differential settlements, which will lead to higher stresses in the construction depending on the stiffness of the construction. The (differential) settlements were calculated both with the analytical method and with a 3D finite element model. With the analytical method only the behavior of the subsoil can be modeled and with a finite element model both the behavior of the subsoil and the interaction with the structure can be modeled. As a consequence of the interaction also stresses and bending moments in the structure can be determined.

The advantage of the 3D finite element analysis in comparison to the general accepted design approaches with a conventional elastic support model are defined in this article.

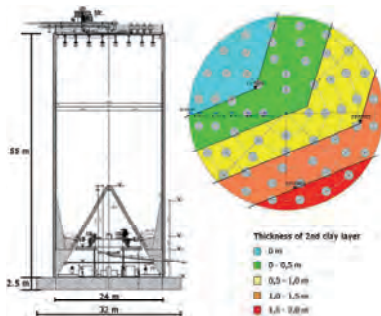


Figure 1. Cross section of the fly ash silo with top view of the pile plan and the thickness of the 2<sup>nd</sup> clay layer.

Table 1. Soil profile

Top of layer [NAP m]	Soil description	Soil layer
+5	SAND, medium dense to very dense	1 <sup>st</sup> sand layer
-20	CLAY	1 <sup>st</sup> clay layer
-21	SAND, very dense	2 <sup>nd</sup> sand layer
-40	CLAY	2 <sup>nd</sup> clay layer
-41	SAND, (medium) dense with laminations of clay	3 <sup>rd</sup> sand layer
-65	Max. investigation depth	

Note: The 2<sup>nd</sup> clay layer varies in thickness and presences.

## 2 SETTLEMENT ANALYSES WITH ANALYTICAL MODEL

### 2.1 General

The total settlement ( $s_d$ ) of the pile group was calculated according to the following relation [1]:

$$s_d = s_{1,d} + s_{2,d} \quad (1)$$

in which  $s_{1,d}$  is the settlement of the pile head, consisting of the pile tip deformation ( $s_{b,d}$ ) including the elastic pile deformation ( $s_{el,d}$ ) and  $s_{2,d}$  is the settlement caused by compression of (cohesive) layers below pile tip level.

### 2.2 Settlement $s_1$

The settlement  $s_1$  was calculated by dividing the pile force by the axial spring stiffness of a single pile. The axial spring stiffness was calculated according to the Dutch code [1]. It should be emphasized that the spring stiffness is not a constant value and depends on the actual forces.

The shaft friction only takes place effectively in the dense sand layer underneath the 1<sup>st</sup> clay layer. In reality the behavior will be stiffer on short term because the piles will also mobilize shaft friction in the top sand layers. But due to settlements in the 1<sup>st</sup> clay layer, the shaft friction in the top sand layers will be reduced considerably. Therefore the shaft friction of the top sand layers was ignored in the basic calculation of the pile bearing capacities.

### 2.3 Settlement $s_2$

The settlements of the whole pile group are mainly caused by compression of cohesive layers below the pile tip level. The settlements were calculated with the computer program DSettlement, which uses the Dutch method of Koppejan (more or less equivalent to the Bjerrum method). DSettlement calculates the settlements in the subsoil caused by an increase of stresses. Load spreading according to the Boussinesq method is hereby taken into account.

The load of the construction was modeled as a uniform distributed load at pile tip level. It is not possible to model the stiffness of the structure in detail. However it is possible to simulate a certain stress distribution depending on an estimate of stress concentration from the structure. The two extreme stress distributions are:

- Flexible plate ( $\alpha = 1$ ): uniform distributed load with value  $p$ ;
- Infinite rigid plate ( $\alpha = 0$ ): distributed load with a value  $2p$  at the perimeter and a value of 0 in the centre of the plate.

The calculated settlements for the simulated flexible plate are presented in figure 2. The maximum settlement occurs in the centre of the plate. The maximum settlement is 18 cm with the 1.5 m thick 2<sup>nd</sup> clay layer taken into account and 5 cm without the presence of this clay layer.

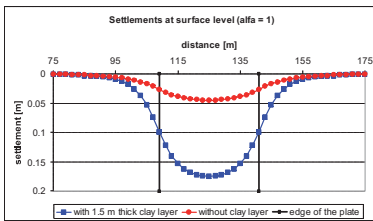


Figure 2. Settlements of the simulated flexible plate.

The calculated settlements for the simulated infinite rigid plate are presented in figure 3. The maximum settlement occurs at the perimeter of the plate. The maximum settlement is 14 cm with

the 1.5 m thick 2<sup>nd</sup> clay layer taken into account and 4 cm without the presence of this clay layer.

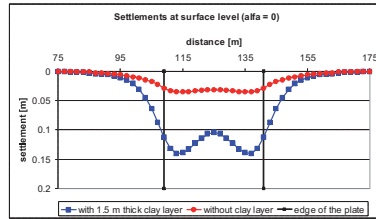


Figure 3. Settlements of the simulated infinite rigid plate.

The settlements of the base slab according to the two stress distributions were not very realistic. Due to the relative stiff base slab a uniform settlement of the base slab should be expected. Therefore the factor  $\alpha$  was varied between 0 and 1. A uniform settlement of the concrete base slab was obtained with  $\alpha = 0.6$ , see figure 4.

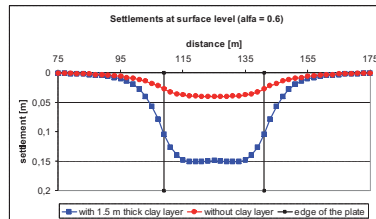


Figure 4. Settlements of the base slab.

From figure 4 it was concluded that the uniform settlement of the base slab is 15 cm with the 1.5 m thick 2<sup>nd</sup> clay layer taken into account and 4 cm without the presence of this clay layer. The differential settlement is therefore 11 cm. From these calculations it could not be concluded that the (differential) settlements meet the Clients requirements.

### 2.4 Limitations of the analytical model

A limitation of the analytical method is that no structure stiffness can be implemented. It is only possible to model a certain stress distribution.

However this stress distribution again depends on the structure stiffness.

In addition, the load redistribution in the structure as a result of the difference in soil stiffness response is also not implemented in the analytical model. The soil without the presence of the clay layer behaves stiffer than the soil with a 1.5 m thick clay layer.

The actual stress distribution is determined by the interaction of the structure and soil stiffness. A realistic interaction analysis, in which both the heterogeneity of the subsoil and the stiffness of the structure are incorporated, was performed in 3D with the finite element program PLAXIS 3D.

### 3 FINITE ELEMENT MODEL

#### 3.1 General

The main advantages of the finite element analyses are:

- Stress redistribution as a result of the structure stiffness;
- Stress redistribution as a result of the soil stiffness;
- Modeling of the pile-soil interaction;
- More advanced soil models are implemented, in which it is possible to model a strain-level dependent soil stiffness.

The main choices for a 3D model were:

- The geometry of the structure is 3D (circular plate with piles);
- Variation of the thickness and depth of the clay layer in three directions;
- 3D stress distribution in the subsoil.

The finite element analysis was performed to determine the total and differential settlements of the concrete base slab and the silo wall due to the heterogeneity of the 2<sup>nd</sup> clay layer. Furthermore the analysis should prove whether excessive load concentrations in the structure could be expected and in what degree tilting might occur. The 3D finite element model is shown in figure 5.

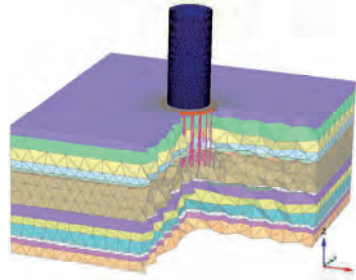


Figure 5. Input in the finite element program PLAXIS 3D.

#### 3.2 Input

The stiffness of the superstructure was modeled by the dimensions and properties of the foundation slab and the silo wall. The base slab was modeled as a volume element with a linear elastic material behavior. The silo was modeled with plate elements with linear elastic material behavior. Furthermore structural properties like the connection of the silo wall and the foundation slab were included in the finite element model.

The foundation piles were modeled by “embedded piles” which distribute the structure load to the bearing sand layer underneath the 1<sup>st</sup> clay layer. The pile-soil interaction was modeled with a representative skin resistance of 0 kN/m until the 1<sup>st</sup> clay layer and 500 kN/m below this layer and with a representative base resistance of 13 MN according to the pile bearing design. The spring characteristic of a single large diameter bored pile was checked with a calibration calculation for one foundation pile (see chapter 3.4).

#### 3.3 Soil model and parameters

The sand layers were modeled with the Hardening Soil model with small strain stiffness (HSsmall). The soil stiffness parameters of the HSsmall model were based on the CPT results.

The clay layers were modeled with the Soft Soil Creep (SSC) model. The soil parameters were based on CPT and laboratory results. The SSC model is suitable when considering creep, i.e. secondary compression. The creep was taken into account during a period of 30 years.



### 3.4 Verification

Before modeling the total structure, the pile-soil interaction was verified for a single foundation pile in the 3D finite element model. One large diameter bored pile ( $\varnothing$  1.5 m) with a length of 34 m was modeled in the subsoil.

From the finite element calculations it was concluded that the foundation pile would have a vertical displacement of 95 mm due to a representative vertical load of 9 MN. The corresponding axial pile spring stiffness was 95 MN/m. The axial spring stiffness of the pile corresponded with the calculated spring stiffness for a single pile according to the Dutch codes. Therefore, the pile-soil behavior of a single pile in the 3D finite element model was verified.

## 4 RESULTS AND DISCUSSION

The vertical (differential) settlements of the concrete base slab are shown in figure 6. Figure 7 presents a graph with the settlements of the base slab for cross sections A-A' and B-B'.

Figures 6 and 7 show an average settlement of 0.12 m for the concrete base slab. The figures also show a maximum difference in settlements of 20 mm between the centre and the perimeter of the base slab. The foundation tilts towards the positive x-axis. The settlement of the concrete base slab is 0.130 m with the 1.5 m thick 2<sup>nd</sup> clay layer taken into account and 0.113 m without the presence of this clay layer. Thus, the maximum differential settlement between the two edges of the base slab is 17 mm at a distance of 32 m, which results in a rotation of approximately 1 : 2,000.

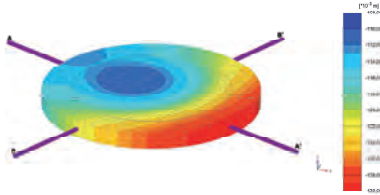


Figure 6. The vertical deformations of the base slab.

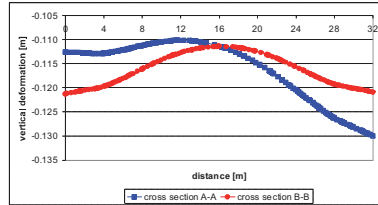


Figure 7. The vertical deformations of the base slab for cross sections A-A\* and B-B\*.

Due to stress redistributions in the finite element program the rotation is smaller compared to the analytical model. From these calculations it could be concluded that the (differential) settlements meet the Clients requirements.

The bending moments ( $M$ ) in the concrete base slab are calculated from the settlement graphs according to the following relation:

$$M = -EI \frac{d\phi}{dx} \quad (2)$$

in which  $EI$  is the bending stiffness of the concrete base slab and  $d\phi/dx$  is the curvature. The corresponding graph is presented in figure 8. The bending moment in the centre of the base slab is 3,750 kNm.

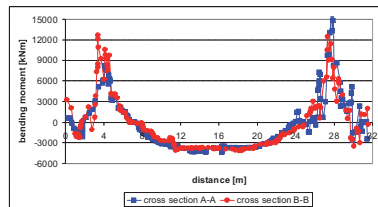


Figure 8. The bending moments in the base slab.

The bending moment in the centre of the base slab can also be determined from the normal stresses, which follow directly from the finite element calculations. Figure 9 shows the normal stresses in the concrete base slab along cross section A-A\*. The maximum normal stress in the

centre of the base slab is 3,600 kPa. The corresponding bending moment is calculated according to the following relation:

$$M = \sigma \cdot W \quad (3)$$

In which  $\sigma$  is the normal stress and  $W$  is the first moment of inertia. The corresponding maximum bending moment was 3,750 kNm.

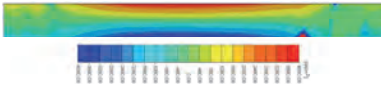


Figure 9. The normal stresses in the base slab.

The representative pile head forces, as calculated in the 3D finite element analysis, are shown in figure 10. From the analysis it was concluded that about 80% of the structure loads were directly transferred to the piles. If the load is evenly distributed over the 59 piles, the representative pile head load will be 5,450 kN/pile. However due to stress redistribution the piles in the area without the 2<sup>nd</sup> clay layer carry more load than the piles with the presence of the 1.5 m thick 2<sup>nd</sup> clay layer. The stress redistribution in the 3D finite element analyses results in a reduction of differential settlements.

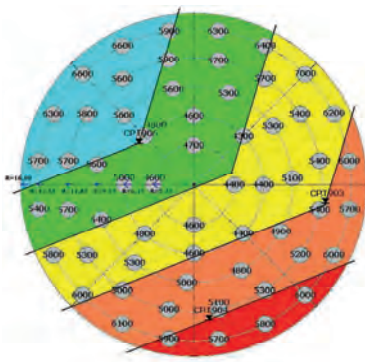


Figure 10. Representative pile head forces.

Figure 10 also shows that the pile head forces at the outer ring are larger than the pile head forces at the inner rings.

## CONCLUSIONS

The following conclusion can be drawn:

- The differential settlements obtained with the analytical method are not realistic because stress redistribution due to structure stiffness and differences in soil stiffness are not implemented.
- Due to the limitations of the analytical method, finite element analysis are performed in which the heterogeneity of the subsoil and the stiffness of the structure are incorporated in a realistic interaction calculation model. A 3D finite element model is selected since the geometry is 3D (circular base plate with foundation piles) and the heterogeneity of the subsoil varies in three directions.
- The calculated differential settlements of the base slab obtained with the 3D finite element model are considerably smaller than the differential settlements obtained with the analytical method in accordance with the usual design practice. The results obtained with the 3D finite element analysis are more realistic than the results obtained with the analytical method because the stress redistributions due to interaction is incorporated.
- The finite element analysis also provides additional information, like bending moments in the superstructure and pile forces.

## REFERENCES

- [1] NEN-EN 9997-1:2011 (NL), *Geotechnical design of structures, Part 1: General rules (Eurocode 7)*, Netherlands Normalisatie-instituut, Delft, 2011.
- [2] PLAXIS manual, *PLAXIS 3D 2010*, Plaxis bv, Delft, 2010.

# Smooth Particle Hydrodynamics (SPH) approach in simulating large penetration into soil

Andrzej Danilewicz<sup>1</sup>

*Gdańsk University of Technology, Dep. of Geotechnics, Geology and Maritime Eng.*

## ABSTRACT

A study of Smooth Particle Hydrodynamics (SPH) approach for predicting large soil deformation is presented. Theoretical basics of SPH method, including the equations governing, discussion of the importance of smoothing function length, contact formulation, boundary treatment and finally utilization in hydrocodes simulations are presented. An application of SPH to a real case of large penetrations (crater creating) into soil caused by falling mass in Dynamic Replacement Method is discussed. Limitations of Lagrangian approach, such as mesh distortion and mesh degradation are considered. Some good points as well as drawbacks of FEM, hybrid SPH+FEM approaches are presented. An examples calculated by LS-DYNA software are discussed as well.

Keywords: Smooth Particle Hydrodynamics, SPH, large deformation in soil, Dynamic Replacement Method, Impact

## 1 INTRODUCTION

The object of this paper is to propose an efficient method for large deformation (caused by penetration) soil simulation. Proposed method SPH is a discretization methodology that works without any grid or mesh, therefore it belongs to the meshfree family methods. The reason for development of SPH was limited capability of existing methods such e.g. FEM, for descriptions of problems involving fragmentation, cracks and primarily large deformations. Problems involving large deformation are important in many field of geotechnics. Three methods are usually taken under consideration of case of large de-

formation simulation: Finite Element Method with remeshing, element erosion or element deletion methodology, Discrete Element Method in which domain is represented by a set of discrete elements connected by forces, and finally Smooth Particle Hydrodynamics – mesh free Lagrangian method developed by Lucy [1], Gingold and Monaghan [2] in 1977 initially for astrophysical problems, adapted to solid mechanics by Libersky and Petschek [3] and improved over the years. The first method does not work properly in 3D cases, the second one needs a lot of computing power.

Some works relevant to large deformation into soil were made by Bojanowski and Kulak (com-

---

<sup>1</sup> Corresponding Author. Politechnika Gdańska; ul. Narutowicza 11/12; 80-233 Poland, adanilew@pg.gda.pl

parison of Lagrangian approach, SPH and Multi Material Arbitrary Lagrangian-Eulerian MM-ALE in case of bridge stability [8] and CPTU simulations [9]), but performed analysis were made for static loading. An attempt of crater creating simulations in Dynamic Compaction Method was made by Pan and Selby [10] (but in case of small deformations). An approach in simulating large penetration into soil caused by falling rigid mass in Dynamic Replacement Method was not performed before.

In this paper some basic ideas of SPH and its advantages will be exploited. An example calculated in LS-DYNA software will be presented to show advantages of mesh free SPH method in large deformation problems.

## 2 SIMULATION METHOD USING SPH

### 2.1 Basic Ideas of SPH

The foundation of Smooth Particle Hydrodynamics method is an interpolation theory. Any function at given point can be approximated by the following equation (kernel approximation <>) [4]:

$$\langle u(x, t) \rangle = \int_{R^d} u(x', t) W_h(|x - x'|) dx', \quad (1)$$

where  $W_h$  is, so called, kernel function or smoothing function and it is at least  $C^2$  class. Particle approximation uses particles within the influence domain (of radius  $\kappa h$ , where  $h$  is a smoothing length) of the smoothing function for a given particle  $i$  (Fig. 1). Each  $W$  function has to satisfy the following properties [4]:

- normalization condition: 
$$\int_{\Omega \subset R^d} W(x_i - x_j, h) d\Omega_{x_j} = 1 \quad (2)$$
- delta function property: 
$$\lim_{h \rightarrow \infty} W(x_i - x_j, h) = \delta(x_i - x_j) \quad (3)$$
- compact support:  $W(x_i - x_j) = 0$  for  $|x_i - x_j| > \kappa h, \kappa \geq 1. \quad (4)$

From many possible choices of kernel function, cubic B-spline, the one proposed by Monaghan and Lattanzio [5], is the most popular:

$$W\left(\frac{r}{h}\right) = \frac{C}{h^d} \begin{cases} 1 - 3/2q^2 + 3/4q^3 & 0 \leq q \leq 1 \\ 1/4(2-q)^3 & 1 \leq q \leq 2 \\ 0 & q > 2, \end{cases} \quad (5)$$

where  $q = r/h$ ,  $C$  is  $2/3, 10/7\pi$  or  $1/\pi$  for respectively 1, 2 or 3 dimensions. Scaling  $r = |x_i - x_j|$  guarantees one particle SPH per smoothing length  $h$ .

Dividing the continuum into  $NP$  volumes and associating with masses, each volume element with mass can be assigned to a particular SPH element, therefore discrete kernel approximation is [4]:

$$\langle u_i \rangle = \sum_{j=1}^{NP} u_j W_h(|x_i - x_j|) \frac{m_j}{\rho_j}. \quad (6)$$

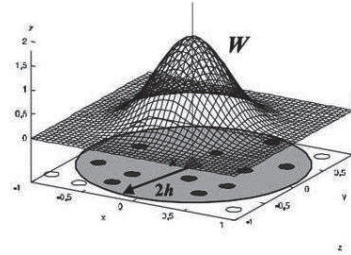


Figure 1. Kernel function  $W$ . Reprint from Hiemaier [4].

This form of approximation is directly used for approximating strong form of PDE, therefore approximating of derivatives is crucial in SPH method [4]:

$$\langle \nabla \cdot u(x, t) \rangle = - \int_{R^d} u(x', t) \cdot \nabla W_h(|x - x'|) dx', \quad (7)$$

where  $d=1, 2$  or  $3$  for respectively 1, 2 or 3 dimensions.

## 2.2 Conservation Equations

Using given SPH approximation of derivatives discrete conservation equations forms are as follows [11]:

- conservation of mass

$$\frac{d\rho_i}{dt} = \rho_i \sum_{j=1}^{NP} \frac{m_j}{\rho_j} (v_j - v_i) \cdot \frac{\partial W_{ij}}{\partial x_i} \quad (8)$$

- momentum equation

$$\frac{dv_i}{dt} = - \sum_{j=1}^{NP} m_j \left( \frac{\sigma_i}{\rho_i^2} + \frac{\sigma_j}{\rho_j^2} \right) \frac{\partial W_{ij}}{\partial x_i} \quad (9)$$

- energy equation

$$\frac{dE_i}{dt} = \frac{1}{2} \sum_{j=1}^{NP} m_j \left( \frac{\sigma_i}{\rho_i^2} + \frac{\sigma_j}{\rho_j^2} \right) v_{ij} \frac{\partial W_{ij}}{\partial x_i} \quad (10)$$

## 2.3 Artificial Viscosity

In dynamic impact simulation, loads are transmitted through the structure by shock waves. To prevent non-physical oscillations in velocity field and pressure beyond the shock wave in SPH method, some adjustments have to be done. By adding artificial viscosity equations to conservation equation it is possible to smear out shock wave over a few particle (distance bigger than the smoothing length). Proposed first by Neumann and Richtmayer [5] and adopted to SPH method by Monaghan and Gingold [2], artificial viscosity has the following form:

$$\Pi_{ij} = \begin{cases} \frac{-\alpha_{\Pi} \bar{c}_{ij} \mu_{ij} + \beta_{\Pi} \mu_{ij}^2}{\bar{\rho}_{ij}} & v_{ij} \cdot x_{ij} < 0, \\ 0 & v_{ij} \cdot x_{ij} \geq 0, \end{cases} \quad (11)$$

where:

$$\mu_{ij} = \frac{h v_{ij} \cdot x_{ij}}{x_{ij}^2 + \varepsilon_0 h_{ij}^2}; \quad (12)$$

$$h_{ij} = \frac{1}{2} (h_i + h_j); \quad (13)$$

$$\bar{c}_{ij} = \frac{1}{2} (c_i + c_j); \quad (14)$$

$$\bar{\rho}_{ij} = \frac{1}{2} (\rho_i + \rho_j); \quad (15)$$

$$v_{ij} = v_i - v_j; \quad x_{ij} = x_i - x_j; \quad (16)$$

where  $\varepsilon_0$  is usually equal 0.01 Monaghan [12],  $\alpha_{\Pi}, \beta_{\Pi}$  are viscosity terms.

Therefore, e.g. corrected momentum equation becomes the form:

$$\frac{dv_i}{dt} = - \sum_{j=1}^{NP} m_j \left( \frac{\sigma_i}{\rho_i^2} + \frac{\sigma_j}{\rho_j^2} + \Pi_{ij} \right) \frac{\partial W_{ij}}{\partial x_i}. \quad (17)$$

## 2.4 Boundary Treatment

Integration of function in SPH approximation for the given  $i$  particle has to be done inside the compact support. This requirement leads to some difficulties which can occur when inside the radius  $kh$  a sufficient number of neighbors particles does not exist. It can occur on the boundary. The solution is a so-called *ghost particle* approach (Fig.2) proposed by Libersky and Petschek [3]. For a given  $i$  SPH particle, with a distance from BC less than  $kh$ , virtual SPH particles are symmetrically placed on the opposite side of BC. The same densities and velocities with opposite sign are assigned to virtual SPH. Leonard-Jones molecular force produces repulse force to particles with position close to the boundary to prevent these particles from penetration.

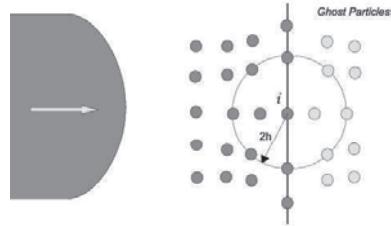


Figure 2. Ghost particle approach in SPH method.

## 2.5 Time Integration

SPH method like others hydrocodes needs explicit method for time integration. The most widely used is Störmer-Verlet algorithm well known as leap-frog (LF) method. Stability of LF method is controlled by Courant-Friedrichs-Lewy condition, one of the proposed requirements for a maximum time step is [11]:

$$\Delta t \leq C_{CFL} \frac{h}{c + s}, \quad (18)$$

where  $c$  is a sound velocity,  $h$  is a smoothing length and  $s$  is a maximum particle speed over the all particle set.

## 2.6 SPH+FEM Coupling

Four main coupling types of meshfree SPH and finite element method can be applied [4]:

- master-slave coupling (contact algorithm),
- transition elements with boundary nodes that are at the same time SPH elements,
- hybrid coupling with an extension of the kernel approximation by components from nodes inside the kernel support,
- adaptive coupling that can start with certain discretization but can also convert some parts of discretization into more adequate one upon certain criteria.

## 3 CALCULATION AND DISCUSSION

Two analysis were performed. The first one with Finite Element Method, and the second with SPH+FEM coupling method. Commercial hydrocode program LS-DYNA was used. Loop of SPH cycle has form [6]:

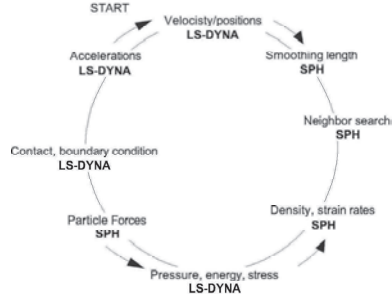


Figure 3. The calculation cycle for SPH formulation in LS-DYNA software [6].

## 3.1 Constitutive equation

Material with pressure-dependent nonlinear Drucker-Prager yield function  $\Phi$  with the following form was used:

$$\phi = \frac{1}{2} s_{ij} s_{ij} - (a_0 + a_1 p + a_2 p^2), \quad (19)$$

where  $a_0, a_1, a_2$  define the deviatoric yield function of pressure  $p$  (Tab. 1) and  $s_{ij}$  is a stress tensor. Volumetric yielding is determined by a tabulated curve of pressures versus volumetric strain. Thanks to this curve initial pressure required in SPH formulation can be easily obtained and therefore additional equation of state is not necessary.

## 3.2 Equation of State (EOS)

As mentioned in 2.3, information about the load applied on the structure is transmitted through the continuum by waves. Equation of state is a relation between pressure and volume at given temperature. It is necessary to determine the pressure in shock compressed solid. The most popular ones (for structures under crash and impact) are Mie-Grüneisen equation of state and polynomial equation of state. Relation between pressure and volumetric strain is included in chosen constitutive equation MAT\_005.

### 3.3 Model Description

Two analysis of crater creating by Dynamic Replacement Method (Fig. 4) were made: FEM and SPH+FEM, both with the same geometry, boundary and initial condition, and also material data. The falling rigid mass (modeled: 1.8m height and 0.46-0.6m width) was made from steel. The velocity at the soil surface was 7m/s.

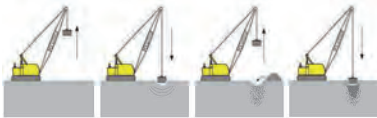


Figure 4. Dynamic Replacement Method (DRM) process (source: Keller Poland).

Soil model has a quarter cylindrical shape of radius 4.8m, height of 6.8m and it is surrounded by elastic enhancement made to represent semi-infinite soil domain. First model (FEM) was discretized by 6924 8-node quad elements. In hybrid SPH+FEM model, portion of soil expecting large deformation was modeled using 47.242 SPH elements, and the rest of the model was modeled using 5232 finite elements. The both models are shown in Figure 5.

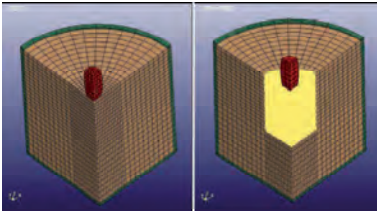


Figure 5. Numerical models for crater creating process by Dynamic Replacement Method. Left: FEM, right: SPH+FEM

Table 1. Mat\_005 material calibration (mm-s-tonne)

Parameter	Value
Mass density	2.35E-9
Shear modulus	34.474
Bulk modulus for unloading	15.024
Yield function constant a0	0
Yield function constant a1	0
Yield function constant a2	0.602
Pressure cutoff for tensile fracture	0
Volumetric crushing option	off

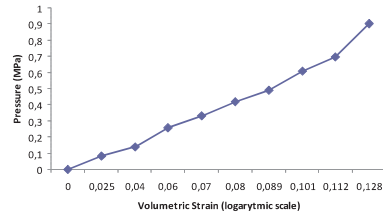


Figure 6. Volumetric strain vs. pressure curve from hydrostatic compression.

Soil constitutive parameters for material formulation MAT\_005 (soil) are listed in Table 1. Material data was adopted from paper of Bojanowski and Kulak [8]. MAT\_005 is widely using in practice, e.g. analysis of earth landing [7].

### 3.4 Results and discussion

In this study two models were analyzed. Large displacement in FEM model with Lagrange approach has caused elements distortions with negative element volume at early stage of analysis, so it is not possible to finish the analysis due to highly distorted mesh, Figure 7. Mesh degradation and hourglassing problems produce wrong energies so the FEM model was giving different results for different loading rates. Contours of effective plastic strain outputs from both models are presented in Figure 8. SPH model seems to work properly, but author was not able to perform the validation with the real test at time of writing this paper. Validation, verification and modeling of soil mixing in rock column creating process is still an author's object of study.

Finite Element Method in Lagrange formulation needs much less computational effort, but mesh distortion (and problems with hourglassing) disqualifies it from practical using in discussed problems. For a large penetration problem caused by rigid mass falling in Dynamic Replacement Method, more applicable is the SPH+FEM formulation.

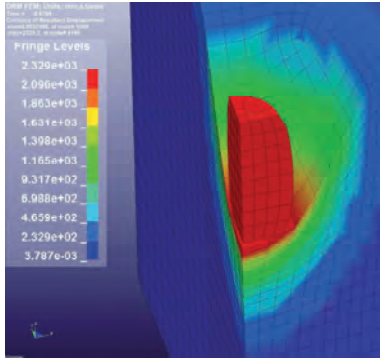


Figure 7. Contour of Displacement in FEM (Lagrange Approach) model at time 0.67s from impact.

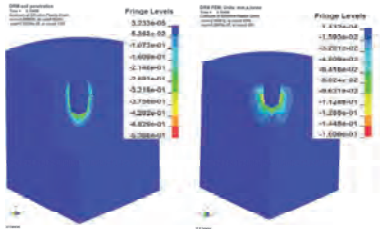


Figure 8. Contours of effective plastic strain at time 0.1s after impact. Left: SPH+FEM, Right: FEM.

## ACKNOWLEDGEMENT

The author wishes to acknowledge Polish National Science Center for its support. The discussion and correspondence with Dr. Bojanowski (Argonne National Laboratory, USA) was valuable. The support from the project DredgDikes in South Baltic Programme is also acknowledged.

## REFERENCES

- [1] L. B. Lucy, A numerical approach to the testing of the fission hypothesis, *Astronomical Journal* **82** (1977), 1013-1024.
- [2] J.J. Monaghan, R.A. Gingold, Smoothed particle hydrodynamics: Theory and applications to non-spherical stars, *Royal Astronomical Society* **181** (1977), 375-389.
- [3] L.D. Libersky, A.G. Petschek, Smooth particle hydrodynamics with strength of materials, *Proceedings of the Next Free-Lagrange Conference Held at Jackson Lake Lodge, Moran, WY, USA 3-7 June 1990* **395** (1990), 248-257.
- [4] S. Hiermaier, *Structures Under Crash and Impact*, Springer, 2008.
- [5] J. von Naumann, R.D. Richtmyer, A method for numerical calculation of hydrodynamic shocks, *Journal of Applied Physics* **21** (1950), 232-237.
- [6] *LS-DYNA theory manual*, Livermore Software Technology Corp., Livermore USA, 2006.
- [7] E.L. Fasanella, R.K.H. Lyle, K.E. Jackson, Developing soil models for dynamic impact simulations, NASA Langley Research Center.
- [8] C. Bojanowski, R. Kulak, Comparison of Lagrangian, SPH and MM-ALE approaches for modeling large deformation in soil, *11<sup>th</sup> International LS-DYNA Users Conference*, (2010).
- [9] C. Bojanowski, R. Kulak, Modeling of cone penetration test using SPH and MM-ALE approaches, *8<sup>th</sup> European LS-DYNA Users Conference*, (2011).
- [10] J.L. Pan, A.R. Selby, Simulation of dynamic compaction of loose granular soils, *Advantages in Engineering Software* **33**, (2002), 631-640.
- [11] S. Li, W.K. Liu, *Meshfree Particle Methods*, Springer, 2004.
- [12] J.J. Monaghan, *Simulating free surface flows with sph*, *Journal of Computational Physics* (1994), 399-406.



# Parallel Computational Framework for the Solution of Inverse Problems in Geotechnical Engineering

Onur Pekcan<sup>1</sup>

*Instructor Dr., Middle East Technical University*

Soner Seçkiner

*Graduate Student, Middle East Technical University*

## ABSTRACT

In this study, a software framework is developed to address the time complexity issues when mutually exclusive and computationally expensive analyses are needed in geotechnical engineering. A group of desktop computers is used as a computational platform where each computational cell is associated through network and the communication among them is achieved through regular network connections. Each cell is used to perform finite element analysis of a geotechnical problem investigated and the results are collected in a pool to be analyzed by intelligent searching schemes to further refine for better predictions of geotechnical properties. Genetic algorithm is used as a strategy to effectively the search in the space formed by alternative solutions to the backcalculation. An example problem is selected from transportation geotechnics field where the properties of geomaterials in the road infrastructure is backcalculated using the results of Falling Weight Deflectometer test. ILLI-PAVE finite element program is used in the analysis. Traditional analyses with a standard computer are compared with the one developed in this study and as a result more than 60% efficiency is achieved under normal circumstances when two desktop and more than one processing threads are used. The results indicate the potential of the proposed solution when larger high performance units become available for practicing engineers.

Keywords: parallel computing, inverse problems, finite element method, backcalculation, full-depth pavements, geotechnical engineering, transportation geotechnics, intelligent search

## 1 INTRODUCTION

In the last decade, parallel computers have become widely used in all areas of daily computing such as web browsing, standard desktop programs, small business applications etc. As the processing power in a single central processing unit (CPU) have reached its physical limits due to geometry and temperature effects, the use of multiple processors in a single computer or parallel computers have become inevitable. Natural-

ly, parallel computers have found application areas in many engineering subjects such as numerical modeling, bio-computations, nanotechnology studies, etc. Such problems require extensive computations that generally take long time when solved using single computers with limited processing power.

In geotechnical engineering, the use of parallel computing is getting popular especially due to needs induced by recent developments happened in the area of numerical modeling. Specifically

---

<sup>1</sup> Corresponding Author. Instructor Dr., Civil Engineering Department, Middle East Technical University, opekcan@metu.edu.tr

the models developed using the finite element method (FEM) including complex geometries or nonlinear material behavior needs to be relaxed in terms of computation time [1]. Nonlinear FEM based modeling studies may generally require take long time as there is a strong need for numerical iterations to converge. Therefore such algorithms are studied in detail to be implemented in parallel computers [2].

The objective of this study is to introduce the use of daily desktop computers to solve for computationally intensive and explicit tasks when they are used together as a network connected group. The solution approach is not unique [3], however, it is a recently developed one to decrease the computational effort. To illustrate the concept, an inverse problem is solved using a parallel computing implementation of an optimization scheme to solve for nondestructive evaluation of pavement layer properties. This problem is also called pavement layer backcalculation, chosen from the area of transportation geotechnics that lies in the field both geotechnical and transportation engineering. The overall aim of the backcalculation problem is that the solution needs to be obtained as quickly as possible to satisfy real time evaluation of road infrastructure.

## 2 LITERATURE SURVEY

In geotechnical engineering, inverse problems arise in many cases. For example, the backcalculation of material properties in a deep excavation given the field observation data such as monitoring the performance of deep excavations using inclinometers is a typical inverse problem [4]. This can be extended further; for example, the prediction of total resistance of piles when they are driven to the ground given the dynamic measurements [5] or the estimation of shear strength or its parameters when a slope failure occurs [6] are challenging inverse problems. Finally, the interpretation of the results of nondestructive tests used for determining material properties of transportation infrastructures is another typical inverse problem studied by many researchers [7-9]. These problems generally require many analyses depending on the difficulty

level of the inverse problem, which is a function of many parameters such as the complex material behavior, the problem geometry or the characteristics of field data, etc.

Considering the number of analyses required to obtain a reliable solution for inverse problems, intelligent searching schemes need to be used as decision makers for making auxiliary geotechnical analyses. In such situations, parallel computing is strongly needed to help solving time complexity issues.

### 2.1 Parallel Computing

Parallel computing is the idea of sharing the computing workload through computers, processors or threads available in the processors. According the characteristics of data, problem or the hardware used, it can be in various forms, the simplest version of which is the use of Message Passing Interface (MPI).

The idea of MPI was first introduced at the Supercomputing Conference in 1992 to share the workload of the computing among the others [10]. Following the experimental implementation, the first version of MPI was described in 1993 [10]. Then, together with the contribution of many researchers from around the world, continuous development of MPI started and finally the standard of MPI was released in June 1994, which was named as MPI 1.0. Since that time the MPI group of researchers met at every six months to discuss and develop the standard further [11]. The current version of MPI is 2.2 and it is the most stable and fastest version. After the development of the concept, various versions of MPI have been released as well.

MPI is a standardization of the message passing interface system for parallel computation purposes. MPI organizes the messages and send them to the responsible worker nodes. The messages can be sent by the ethernet (i.e., the local network) or by the embedded structure of the computer. The worker nodes are mapped on the virtual nodes. Afterwards MPI organizes the messages according to the importance and sequence and then the messages are sent to the virtual workers defined on the real distributed computer hardware [10]. MPI can use both data

parallelism and task parallelism. Data parallelism is called Single Instruction Multiple Data (SIMD), which is the easiest way to parallelize an algorithm. The principle behind SIMD is that the data is sent to the workers and workers started to make the same processes on different data. More complicated version of parallelism is task parallelism, also called Multiple Instruction on Multiple Data (MIMD). This version of parallelism is more complicated because both the instructions and data should be handled carefully. For general purpose computations, data parallelism is the frequently utilized method. Another parallel application program interface (API) is Open Multi-Processing (OpenMP). OpenMP uses the similar structure of MPI but it uses shared memory. Therefore, OpenMP is not appropriate for network attached multiple computer parallel computation [11]. The last one is the use of Parallel Virtual Machine (PVM), which is just another parallel programming API [12]. It is based on message passing however MPI is better and mostly utilized API than PVM because PVM is an old programming interface and its documentation is poor.

### 3 PARALLEL FRAMEWORK

In this study, a parallel implementation of a pavement layer backcalculation problem algorithm was developed using MPI. In backcalculation problem, a nondestructive Falling Weight Deflectometer (FWD) test is used for evaluating pavement structural condition. FWD provides pavement surface deflections recorded by several sensors in response to a constant load dropped from a specific distance at a certain frequency (Figure 1). These deflections are basically used for the structural capacity of pavement layers.

The parallel framework developed mainly three parts (i) Genetic Algorithms, (ii) Finite Element (FE) Analysis, and (iii) Message Passing Interface. The sections below describe how they are used together to work as a platform.

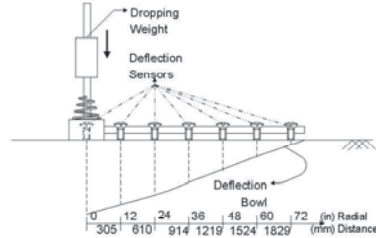


Figure 1. Falling Weight Deflectometer Test.

#### 3.1 Genetic Algorithms

Genetic Algorithms (GAs) are one of the oldest and well known meta-heuristic methods. GAs are computational models based on natural evolution [13]. They have been extremely influential in developing optimization strategies and solving search problems. In GAs, a solution to any problem may be represented by binary strings, which is the encoding of system parameters. A randomly created population with initial random parameters is used. Population members evolve such that they are getting close to satisfying the fitness criteria through number of generations. This is achieved the operators inspired by the nature such as selection, crossover, and mutation.

In the past, various forms of pavement layer backcalculation problem was solved by many researchers using GAs [14, 15]. An overview of GA algorithm used in this study is provided in Figure 2.

#### 3.2 Finite Element Analysis

FWD test simulation was performed in ILLI-PAVE program, where FWD loading was assumed to be standard 40-kN equivalent single axle loading applied as uniform pressure of 552 kPa over a circular area of 152 mm radius. The FE mesh spacing on the surface was selected uniformly such that it was chosen for the FWD sensors as follows: 0 mm (0 in.), 305 mm (12 in.), 610 mm (24 in.), 915 mm (36 in.) away from the center of the FWD plate. The surface deflections corresponding to the locations of these FWD sensors were abbreviated as  $D_0$ ,  $D_{12}$ ,  $D_{24}$  and  $D_{36}$ ,

respectively. Only four deflections were used in this study to backcalculate the layer moduli. To provide the simplicity in the analyses, a full-depth asphalt pavement (FDP) is considered where the asphalt concrete (AC) layer lies on top of the natural subgrade. The moduli values to be calculated are the modulus of asphalt ( $E_{AC}$ ) layer and resilient breakpoint modulus of natural subgrade ( $E_{R1}$ ).

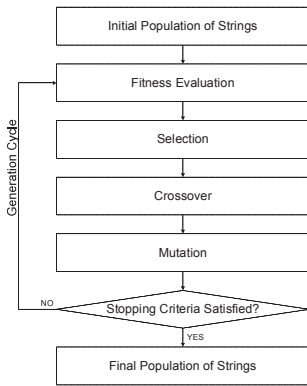


Figure 2. Genetic Algorithm Flowchart.

The fitness function used in this study is given in Equation 1, which simply measures the Euclidian distance between the FWD field deflections and those obtained from the FEM results.

$$fitness = \frac{1}{1 + \sqrt{\sum_{i=1}^4 \left( \frac{FWD_i - FEM_i}{FWD_i} \right)^2}} \quad (1)$$

### 3.3 Parallel Computing

In order to calculate the fitness function in GA based backcalculation, the deflections for each candidate in the population needs to be calculated. For this to happen ILLI-PAVE was run first and the deflections were extracted from the results of FE analysis. According to the MPI based algorithm, parallel computing analyses were carried out using three desktop computers with Intel

e8400 processor installed. Each of these computers has 1 GB of RAM and a total of 500 GB SATA hard disk. The configuration is shown in Figure 3, where the degree of parallelism measured using the number of computers in parallel. MPI 2.2 interface was used for all computations.

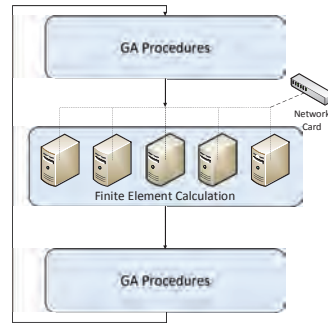


Figure 3. Fitness Evaluation of Genetic Algorithms in Parallel Computer Architecture.

The operating system used was Windows HPC 2008 (Figure 4). It distributes the tasks and data easily using the built-in functions of MPI. The framework consists of master and slave nodes. The master node does not take any computational work however it does the background operations such as the job distribution and storage management. The system uses two network interfaces: one is connected to the outer network and the other one is connected to the computers for internal communication.



Figure 4. Parallel Computers Used in this Study.

#### 4 RESULTS

In order to measure the efficiency of the parallel computational framework, a synthetic FWD station data was first created using ILLI-PAVE. This was obtained by running the FE program with random modulus values of  $E_{AC}$  and  $E_{Ri}$  and a design thickness. Then the deflections  $D_0$ ,  $D_{12}$ ,  $D_{24}$  and  $D_{36}$  that were obtained from the FE analyses and the design thickness were given to the computational framework to backcalculate the layer moduli. The GA parameters used in the analyses are provided in Table 1.

Table 1. Genetic Algorithm parameters used in this study.

Parameters	Value
Number of Generations	35
Population Size	100
Probability of Crossover	0.85
Probability of Mutation	0.01
Total String Size	22 bits

Figure 5 shows the evolution of best, maximum and average fitness through generations. For this specific FWD station, the best fitness value of 0.998 was obtained at the end of 23 generations. The analyses were carried out for 12 more generations to obtain reliable solutions. The mean absolute percentage error for the layer modulus was obtained to be 0.9% for asphalt layer and 0.09% for the breakpoint resilient modulus of natural subgrade.

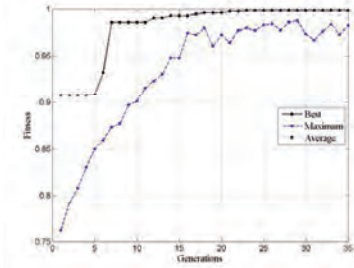


Figure 5. Evolution of Fitness Through Generations.

The analyses were repeated using different computer configurations. First a standard backcalculation analysis was performed using a single

computer and one worker (1PC-1W). Then number of workers was increased to two in a single computer (1PC-2W). Then one more computer was added to the system, each of them with two workers (2PC-2W). The run time of the analyses was decreased from 3145 seconds to 1705 seconds. Therefore the efficiency was increased by 45% compared to single computer analyses. Then number of workers was increased to 4 in a single computer (1PC-4W), which resulted in 1465 seconds of analysis time. Furthermore, with four workers in each computer, the number of computers was increased to two (2PC-4W) which provided further decrease by finishing the analysis in 1272 seconds. Finally two computers with eight workers (2PC-8W) worked on the same problem and finished the analyses in 1222 seconds. Overall 61% efficiency was achieved by using two computers and eight workers compared to using single computer and one computer. The results are provided in Figure 6.

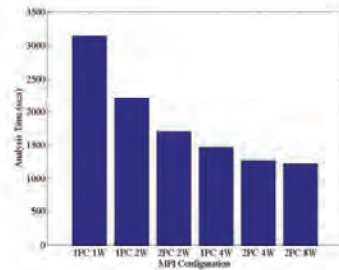


Figure 6. Comparison of Run Times with Different Message Passing Interface Configuration.

#### 5 CONCLUSION

In this study, a parallel computational framework was developed in order to solve computationally challenging problems, the solution of which may take excessive amount of time. The proof of concept was illustrated by solving pavement layer backcalculation using nondestructive testing, a well-known inverse problem chosen from the area of transportation geotechnics.

Genetic algorithm was used as an intelligent strategy to backcalculate the properties of pavement layers. The Falling Weight Deflectometer simulation was performed using ILLI-PAVE FE program. The solutions obtained through genetic algorithm required excessive amount of calculations considering the difficulty of obtaining reliable inverse solutions. To reduce the amount of time to obtain a single solution, a parallel computational framework was formed by connecting desktop computers through a network connection. Total of three computers were used, one as a head node and the others being slave ones. Message Passing Interface protocol was used for providing efficient interaction. The solutions were first obtained using a single computer and then using multiple computers. The results showed that using two computers with eight threads working simultaneously solved the backcalculation problem 61% more efficiently compared to single computer with single threads.

The major advantage of the framework is that it is scalable, i.e., as the number of computers and the number of processors in each computer increases, the efficiency of the computational solutions increases. Considering this, the developed framework brings many advantages when the solutions require mutually exclusive computations. Further work is in progress to make developed environment widely accessible for practical engineers.

## 6 ACKNOWLEDGEMENT

This work was supported in part by the BAP Coordination Office, Middle East Technical University under grant 08-11-2011-101. The authors gratefully acknowledge the contribution.

## REFERENCES

[1] Ferronato, M., C. Janna, and G. Pini, Parallel solution to ill-conditioned FE geomechanical problems. *International Journal for Numerical and Analytical Methods in Geomechanics*, 36(4), (2012), 422-437.  
 [2] Hsieh, Y.M., Parallel computation in efficient non-linear finite element analysis with applications to soft-

ground tunneling project, Massachusetts Institute of Technology: United States -Massachusetts, 2004.  
 [3] Zhang, Y., D. Gallipoli, and C.E. Augarde, Parallel hybrid particle swarm optimization and applications in geotechnical engineering, in *Advances in Computation and Intelligence*, Z. Cai, et al., Editors, Springer Berlin: Heidelberg, (2009) 466-475.  
 [4] Hashash, Y.M.A., et al., Novel approach to integration of numerical modeling and field observations for deep excavations. *Journal of Geotechnical and Geoenvironmental Engineering*, 132(8): (2006), 1019-1031.  
 [5] Likins, G. and E. March, Background of Capacity Interpretation Using Dynamic Pile Measurements, in *The Second Seminar on the Dynamics of Pile Driving*: Boulder, CO., 1981.  
 [6] Duncan, J.M. and S.G. Wright, *Soil Strength and Slope Stability*: John Wiley & Sons, 2005.  
 [7] Lytton, R.L., Backcalculation of Pavement Layer Properties, in *Nondestructive Testing of Pavements and Backcalculation of Moduli*, ASTM - STP 1026, A. J. Bush III and G. Y., Baladi, Editor, American Society for Testing and Materials: Philadelphia. (1989) 7-38.  
 [8] Bush, A.J. and G.Y. Baladi, Nondestructive Testing of Pavements and Backcalculation of Moduli, *ASTM International*, 1989.  
 [9] Von Quintus, H.L., A.J. Bush, and G.Y. Baladi, *Nondestructive Testing of Pavements and Backcalculation of Moduli*, ASTM International, 1994.  
 [10] Forum, M.P.I., *MPI: A Message-Passing Interface Standard Version 2.2*, University of Tennessee, 2009.  
 [11] Gropp, W., et al., *A High-Performance, Portable Implementation of the MPI Message Passing Interface Standard*, Argonne National Laboratory, 1996.  
 [12] Sunderam, V.S., *PVM: A Framework for Parallel Distributed Computing*, Oak Ridge National Laboratory, 1990.  
 [13] Goldberg, D.E., *Genetic Algorithms in Search, Optimization, and Machine Learning*, Reading, Mass.: Addison-Wesley Pub. Co. xiii, 1989  
 [14] Fwa, T.F., C.Y. Tan, and W.T. Chan, Backcalculation Analysis of Pavement - Layer Moduli Using Genetic Algorithms. *Transportation Research Record*, 1997, 1570: 134-142.  
 [15] Reddy, M.A., K.S. Reddy, and B.B. Pandey, Selection of Genetic Algorithm Parameters for Backcalculation of Pavement Moduli. *International Journal of Pavement Engineering*, 2004, 5(2): 81-90.

# Analyzing the displacements of a pile frame to determine its transverse load-bearing capacity

T. Tanev<sup>1</sup>, N. Kerenchev, A. Manolov, H. Dimitrov  
*University of architecture civil engineering and geodesy, Sofia*

## ABSTRACT

This paper presents a numerical study of the deformation properties of a regular pile group foundation frame, which consists of 9 piles with square cross-sections (40/40 cm) and spacing of 1,60 m (axis-to-axis). The length of the piles is 11,0 m and the thickness of the pile cap is 150 cm. Four separate analyses are carried out. Initially the pile group is calculated according to the procedure and requirements of the current Bulgarian Codes. After that a solution with elastic spring supports is presented. Spring stiffness is assumed to increase linearly with depth and stiffness-distribution coefficients are introduced. A linear-elastic plane stress analysis is performed using SAP2000 – with frame elements for the piles and membrane elements for the soil body. Finally nonlinear 2D and 3D analyses are carried out with PLAXIS 2D/3D, taking into account the plastic properties of soils. The Mohr-Coulomb failure criterion is assumed for all layers. The results are summarized and general recommendations are given for the simplified solutions, based on the more detailed nonlinear procedures. An essential observation is that load distribution differs significantly in the final stage of the plastic analysis, where the system is near a state of critical equilibrium, which corresponds to an ultimate limit state.

Keywords: pile foundations, horizontal force, bearing capacity, limit states, finite element method, soil-structure interaction

## 1 INTRODUCTION

In the case of pile foundations, “bearing capacity” often has the meaning of satisfying displacement/deformation criteria or in other words the serviceability limit states.

In terms of bearing capacity for vertical actions, there are a number of analytical solutions as well as direct analogies with results from in-situ tests. In transverse (or horizontal) direction, however, there are no clear criteria regarding ground bearing capacity. Ultimate limit states are often governed by structural failure or exces-

sive displacements greater than a certain “structural” limit [1]. Structural failure often precedes ground failure, hence making the serviceability (SLS) and structural (STR) limit states essential.

Calculating the lateral resistance (bearing capacity) of a pile is no trivial task, and often the procedures specified in building codes are inconclusive and insufficient for soil-structure interaction analyses. This paper presents a comparative study of analysis methods for determining the load-displacement relation for a pile foundation frame, subjected to significant horizontal force.

---

<sup>1</sup> Tanyo Tanev. Department of Geotechnics, University of Architecture Civil Engineering and Geodesy, Sofia, 1 Hr. Smirnenski blvd., e-mail: ttaneff@abv.bg

## 2 GEOMETRICAL AND GEOTECHNICAL PARAMETERS

The foundation frame is a regular 3x3 group of square ( $d = 40$  cm) driven piles with lengths of 11,0 m. Spacing and pile-cap thickness are shown on Figure 1. Soil above the cap base is not included in the calculations and its influence is considered as a distributed load, equivalent to the overburden pressure at depth of 1,50 m ( $q' = D_f \cdot \gamma = 28,8$  kPa).

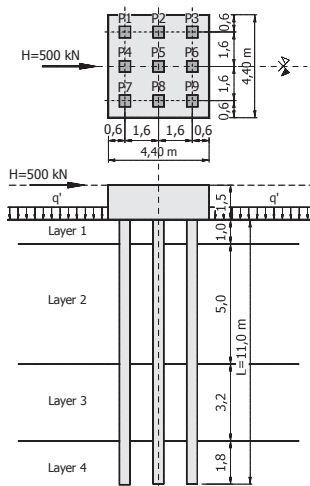


Figure 1. Pile frame geometry and soil layers

For all calculation models the center of the pile group is assumed at the origin of the global coordinate system (axis orientation differs, depending on software used).

Ground conditions are represented by four different soil layers and their geotechnical properties are given in Table 1. Layers 1-3 are cohesive clays, and Layer 4 is medium density sand.

The material for the piles and the pile cap is reinforced concrete (C25/30). Elastic isotropic behavior for the concrete is assumed with mean elastic modulus  $E = 3.10^7$  kPa and  $\nu = 0,2$ .

Table 1. Geotechnical parameters for soil layers

	$k_h$	$E$	$\nu$	$\gamma$	$\varphi'$	$c'$
Units	$kN/m^2$	$MPa$	-	$kN/m^3$	$^\circ$	$kPa$
Layer 1	2000	6,5	0,30	19,2	24 $^\circ$	7
Layer 2	2500	7,0	0,35	18,0	21 $^\circ$	25
Layer 3	3500	12,0	0,28	19,0	18 $^\circ$	30
Layer 4	8000	27,5	0,26	17,0	32 $^\circ$	3

## 3 ELASTIC SPRING MODELS

One of the first analytical solutions for piles is the analogy with beam on elastic foundation. Although this class of models is very simple and straightforward, the exact distribution of the stiffness with depth is unknown. The elastic bed gradient coefficients ( $k_h$ ), specified in Table 1, vary in a wide range, so a number of solutions are performed with different values for  $k_h$ , averaged for depth of  $8d$  (3,20 m).

### 3.1 Computational model and boundary conditions

A distinct characteristic of such models is the need to calculate equivalent spring stiffness for each node. In the case of pile frames it is common to account for group effects and force distribution between the piles. In this case it is done by introducing reduction of spring stiffness ( $k_h^* = \eta \cdot k_h$ ):

- for P1,P4,P7 -  $\eta_1 = 0,5$ ;
- for P2,P5,P8 -  $\eta_2 = 0,7$ ;
- for P3,P6,P9 -  $\eta_3 = 1,0$ ;

Nodal spring stiffness is calculated using a simplified formula:

$$k_{x,j}(z_i) = k_{y,j}(z) = k_h^* \cdot b_i \cdot z_i \cdot \bar{D}, \quad kN/m, \quad (1)$$

where:

- $k_h$  is the gradient of the lateral elastic bed coefficient,  $kN/m^4$  (see Table 1). The values are from empirical relations given in [2], based on the consistency index ( $I_C$ );
- $\bar{D}$  - the effective width of the pile:

$$\bar{D} = 1,5d + 0,5 \text{ m}; \quad (2)$$



- $d$  is the width of the pile's cross-section;
- $b_i$  are the length of the adjacent beam elements;
- $z_i$  is the depth below the surface for the current node.

The vertical spring stiffness is assumed as:

$$k_{z,i}(z_i) = 2k_{x,i}(z_i), \text{ kN/m} \quad (3)$$

Alternatively coupled spring stiffness can be obtained using (4), but the difference in the results is not significant [3].

$$[k_{eij}] = \int k(z) \cdot [\Phi]^T [\Phi] dz, \quad (4)$$

The deformed shape and discretization of the FEM model are shown on Figure 2.

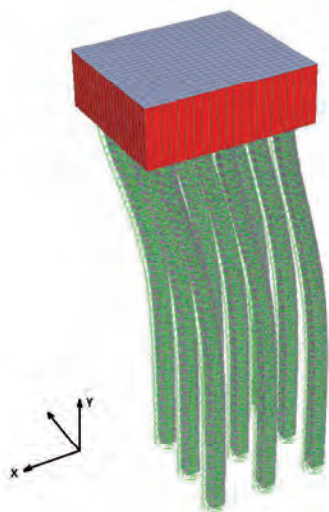


Figure 2. FEM model of the pile frame inside SAP2000

### 3.2 Results summary

The resulting deformed shape is shown on Figure 2. The data for displacements and forces is presented in Tables 2 – 4.

Table 2. Pile head displacements for different values of  $k_h$

Stiffness, kN/m <sup>3</sup>	$u_{x,exp}$ (for all piles)	$u_{y,P1}$	$u_{y,P9}$
$k_h = 1500$	0,0093 m	0,0008 m	-0,0008 m
$k_h = 2000$	0,0077 m	0,0006 m	-0,0006 m
$k_h = 2500$	0,0066 m	0,0005 m	-0,0005 m

Table 2 indicates that for a 67% increase of spring stiffness, horizontal displacements decrease by 40%

Table 3. Maximum bending moments for different  $k_h$  values

Pile row	$k_h = 1500$	$k_h = 2000$	$k_h = 2500$
P1,P4,P7	83,9 kNm	80,1 kNm	77,0 kNm
P2,P5,P8	97,9 kNm	93,1 kNm	89,4 kNm
P3,P6,P9	114,3 kNm	108,4 kNm	103,9 kNm

Maximum bending moments vary in the range of 10%, which is relatively low and is attributed to the substantial difference in stiffness of the piles and the surrounding soil.

Table 4. Maximum shear forces ( $V$ ) for different values of  $k_h$

Pile row	$k_h = 1500$	$k_h = 2000$	$k_h = 2500$
P1,P4,P7	$V_1 = 43,4$ kN	$V_1 = 43,4$ kN	$V_1 = 43,4$ kN
P2,P5,P8	$V_2 = 53,8$ kN	$V_2 = 53,8$ kN	$V_2 = 53,7$ kN
P3,P6,P9	$V_3 = 67,4$ kN	$V_3 = 67,2$ kN	$V_3 = 67,1$ kN

The results in Table 4 clearly show that load distribution ( $\eta_1 = 43,4/67,4 = 0,64$ ;  $\eta_2 = 0,80$ ) differs from the input ratios  $\eta_i$  and that forces are rather proportional to the relative stiffness.

### 3.3 Comparison with results from the simplified design procedure

Bulgarian building code provisions [2] give a simple formula for calculating the horizontal displacement of a single pile, based on stiffness increase gradient  $k_h$ . Equivalence is assumed by taking only 1/9 of the total transverse force and no group effect is considered.

Results obtained by this procedure are presented in Table 5.

Table 5. FEM results compared to Code design formula

Stiffness, $k_h$	Code (BDS-EN)	FEM model
1500	$u_x = 1,90$ cm	$u_x = 0,931$ cm
2000	$u_x = 1,60$ cm	$u_x = 0,767$ cm
2500	$u_x = 1,40$ cm	$u_x = 0,661$ cm

#### 4 2D PLANE STRESS MODELS

The two-dimensional half-space conditions are not very accurate for analyzing pile foundations. Nevertheless, this simplification is still used mainly because it can be performed using general purpose FEM software.

Two computational models are considered – linear elastic analysis in SAP2000 and an extended plastic analysis, using PLAXIS 2D.

##### 4.1 Linear elastic model

This model uses two types of elements – membrane elements with thickness of 1,0 m for the soil volume and frame elements for the piles. The decision to model the piles as beams (neglecting their thickness) is mostly because of “shear-locking” of plane stress elements in bending.

To reduce the effect of boundary fixities on global results, the soil body extends on 35 m in horizontal direction and 25 m below the pile frame. Standard boundary conditions are applied and the loading is taken as  $H_{2D} = 1/3H$ , assuming equal load distribution.

The pile cap is represented with shell elements, and a rigid body constraint is applied for the corresponding nodes.

Results obtained from this analysis are represented by displacements of the pile cap (Table 6) and maximum forces at the connection of the piles with the cap (Table 7).

Table 6. Pile head displacements (at pile-cap base)

Pile row	$u_x, m$	$u_y, m$	$\theta_y, rad$
(P1, P4, P7)	0,031	0,004	0,0019
(P2, P5, P8)	0,031	0,0	0,0019
(P3, P6, P9)	0,031	-0,004	0,0019

After analyzing the maximum shear forces  $V_i$ , alternative values for the distribution coefficients can be obtained. The factors are defined as:

$$\eta_i = \frac{V_i}{V_{i,max}}. \quad (5)$$

Table 7. Distribution of forces in the piles (at pile-cap base)

Pile row	$M_i, kNm$	$V_i, kN$	$\eta_i, -$
(P1, P4, P7)	87,4	51,3	1,00
(P2, P5, P8)	61,2	24,9	0,48
(P3, P6, P9)	87,4	51,2	1,00

##### 4.2 Nonlinear plastic model (PLAXIS 2D)

As a better approximation to real soil behavior, the Mohr-Coulomb failure criterion is assumed for all soil layers with unassociative flow rule ( $\psi = 0^\circ$ ) [4]. Geometrical data is the same as in the linear elastic model and the piles are modeled with plate (frame) elements. Interface elements are defined on both sides of each pile (positive and negative), with the same parameters as the surrounding soil.

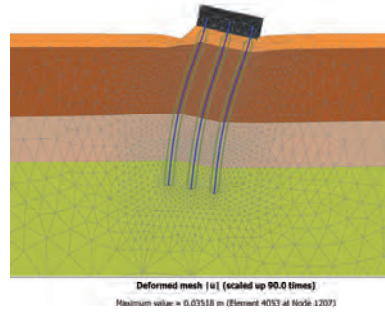


Figure 3. Deformed mesh around the frame, PLAXIS 2D

For a load of  $H = 500$  kN, the horizontal displacement of the pile-cap is  $u_x = 0,035$  m, which is close to the result obtained from the elastic solution, suggesting small plastic strains.

After the initial load step (for  $H = 500$  kN), the transverse load is increased in three increments and the corresponding load-displacement curve is obtained (Figure 4). Displacements and forces for the increased loading are structurally unacceptable, but they provide information for the bearing capacity in terms of ULS. However, such extreme loading is only theoretical and actual failure mechanisms are not considered here.

Force distribution is presented in Table 8, and corresponding distribution factors can be calculated using (5).

Table 8. Distribution of horizontal forces in piles –  $F_h$ , kN

Load, $H$	P1,P4,P7 $F_{h,1}(V_1)$	P2,P5,P8 $F_{h,2}(V_2)$	P3,P6,P9 $F_{h,3}(V_3)$
500 kN	55,4	28,5	60,8
1000 kN	98,8	61,9	139,5
2000 kN	158,8	132,0	324,4

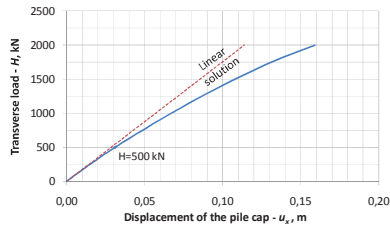


Figure 4. Load-displacement curve, PLAXIS 2D

## 5 3D MODELS

The out-of-plane effects and stiffness of the frame are essential for estimating its behavior. In order to get a better representation of the system, two three-dimensional models are evaluated.

Due to the symmetry in loading only half of the problem is analyzed using appropriate boundary conditions ( $u_z = 0$  at the plane of symmetry;  $F_{sym} = 0,5F$ ).

### 5.1 Linear elastic model (ANSYS)

In this model, piles are represented by solid (volumetric) finite elements and reduced integration is used (to avoid “shear-locking”). Elements SOLID187 are chosen (higher-order 10-noded tetrahedrons), which have quadratic displacement behavior. [5]

The deformed shape and displacement map for the pile frame are shown on Figure 5.

Forces in the piles are derived by means of differentiation of transverse displacements:

$$M_z(y) = \frac{d^2 u_z(y)}{dx^2} \cdot E_m I, \text{ kNm}, \quad (6)$$

where:

- $u_z(y)$  is the transverse displacement result, mapped on the axis of the pile;
- $E_m = 3.10^7$  kN/m<sup>2</sup> and  $I = 0,0256$  m<sup>4</sup>.

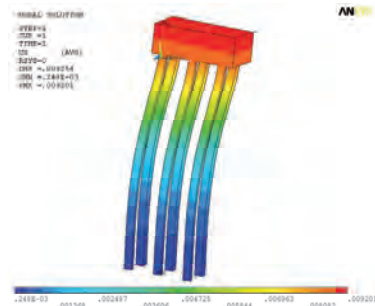


Figure 5. Displacements of the pile frame (isolated), ANSYS

### 5.2 Nonlinear plastic model (PLAXIS 3D)

Both 3D models share the same geometry, but here plastic behavior (MC failure criterion) is taken into account. The model is shown on Figure 6.

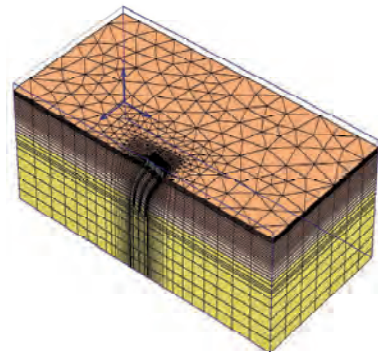


Figure 6. Computational model in PLAXIS 3D Foundation

### 5.3 Summary of results for 3D models

Displacements for the actual load of 500 kN are almost identical for the linear and nonlinear solutions, as observed in Table 9.

Table 9. Displacements of the pile-cap in the 3D models

Displacements	ANSYS 3D (Elastic)	PLAXIS 3D (Plastic)
$u_x$	0,0092 m	0,0099 m
$u_{y,min}$	-0,0009 m	-0,0011 m
$u_{y,max}$	0,0009 m	0,0011 m

Table 10. Distribution of shear forces in the piles

Pile shear forces, $F_{ki}$ ( $F_i$ ), kN	ANSYS 3D Elastic	PLAXIS 3D Plastic
P1 (=P7)	47,61 kN	48,69 kN
P2 (=P8)	38,37 kN	35,92 kN
P3 (=P9)	47,11 kN	49,30 kN
P4	34,96 kN	36,82 kN
P5	24,60 kN	27,14 kN
P6	35,00 kN	36,68 kN

Applying additional load steps ( $H = 2000$  kN) yields the load displacement curve, shown on Figure 7. No apparent limit force can be determined (without extrapolation), although the decrease in stiffness is evident.

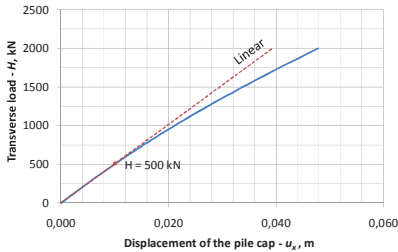


Figure 7. Load-displacement curve from PLAXIS 3D

## 6 CONCLUSIONS AND RECOMMENDATIONS

Summary of results for group effect factors ( $\eta_i$ ) and horizontal displacements ( $u_x$ ) from all analyses is presented in Table 11.

Table 11. Comparison of distribution for  $H = 500$  kN.

Model	$\eta_1$	$\eta_2$	$\eta_3$	$u_x$ , m
BG code	0,50	0,70	1,00	0,019
1D Springs	0,65	0,85	1,00	0,009
2D Elastic	1,00	0,48	1,00	0,031
2D Plastic	0,91	0,47	1,00	0,035
3D Elastic	1,00	0,78	0,99	0,009
3D Plastic	0,98	0,73	1,00	0,010

For practical cases of transversely loaded piles, linear-elastic behavior is an acceptable approximation. However plane stress solutions overestimate displacements with factors of around 3,0. From designers' point of view this is "on the safe side", but their application should be avoided.

Elastic spring models are efficient for soil-structure interaction, but only after proper spring stiffness distribution from more detailed 3D models is obtained. Equivalent elastic bed stiffness, as function over the length of each pile, can be obtained using the formula:

$$k_x(z) = \frac{d^4 u_x(z)}{dz^4} \cdot \frac{E.I}{u_x(z)}, \text{ kN} / \text{m}^2, \quad (7)$$

where:

- $u_x(z)$  is obtained from a 3D model and is numerically differentiated
- $E.I$  is the flexural stiffness of the pile.

Pile cap fixity affects results significantly and in case of soil-structure interaction, the partial restraint should be taken into account in the 3D model as an equivalent fixity.

## REFERENCES

- [1] EN1997-1: Eurocode 7 – Geotechnical design.
- [2] Б.А. Божинов, *Изчисляване на конструкции върху еластична основа*, Издателство „Техника“, София, 1982.
- [3] M. Eisenberger, D.Z. Yankelevsky, *Computers & Structures Vol. 21: Exact stiffness matrix for beams on elastic foundation*, (pp. 1355-1359), 1985
- [4] R.B.J. Brinkgreve et al., *Plaxis 2D 2010 – Scientific manual*, Plaxis bv, Netherlands, 2010
- [5] *ANSYS 13 Mechanical APDL – Theory reference*, ANSYS Inc., 2010

# Vintapperrampen: From detailed design to construction

T. V. Isgreen<sup>1</sup>  
*Ramboll Denmark A/S*

## ABSTRACT

This paper presents a young geotechnical engineers work on the project Vintapperrampen. The Geotechnical Department in Ramboll was involved in the design phase as well as with supervision in the construction phase. The main geotechnical challenges in the two phases are discussed.

Vintapperrampen is part of an access road between two highways north of Copenhagen, Denmark. Borings indicated a huge amount of organic soil in parts of the ramp. Two alternative design solutions were applied depending on the location of the ramp in relation to the ground level. When the ramp was above ground level or just below, concrete piles were driven and concrete slabs were cast above. The organic soil was excavated when the ramp was below ground level. King post walls were made in two locations, one where anchors could not be used in the sheet pile wall because of a nearby building and the one below a bridge where the construction height was the main challenge.

In the supervision phase the main challenges were to overcome the obstacles in the soil. Sheet piles and king post walls were mainly vibrated to the desired depths, except for one king post wall under the bridge which was driven by a small pile driving machine. Most elements were installed without problems where others needed more effort. A few soil anchors met resistance during boring and had to be redone with a new inclination.

Keywords: Design phase, Sheet Piling, Piles, Road, Organic soil, Settlements and Supervision.

## 1 INTRODUCTION

Vintapperrampen is part of an access road between two highways north of Copenhagen, Denmark. Up to now the access to M3 from Lyngby Omfartsvej is complicated by a roundabout and two traffic lights, cf. figure 1. The project is currently under construction and is expected to be finished August 1, 2012.

Ramboll Denmark A/S (Ramboll) acted as a consulting engineer representing the Client: The Danish Road Directorate. Different departments have worked on the design phase as well as the construction phase. The Geotechnical Department in Ramboll had a lot of challenges during the design phase for this project and some during the construction phase as well.

---

<sup>1</sup> Theis Vielsted Isgreen. Ramboll Denmark A/S. Hannemanns Allé 53, DK-2300 Copenhagen S. Denmark, thi@ramboll.dk



Figure 1. Overview of the project [1].

## 2 DESIGN PHASE

In the design phase different design challenges arose. The key challenges will be discussed.

The first part of the ramp is above ground level, where sheet piles function as a dam with the roadbed and the road on top. Tie rods connect the two sides so the sheet piles on both sides work together. The ramp is inclined downwards and the middle part of the ramp is below ground level. Sheet piles on both sides act as retaining walls with soil anchors. The ramp then levels out alongside M3, cf. figure 2. Due to the ramp, M3 had to be extended to make room for the connection between the ramp and highway. Anchored sheet piles had to replace the slope of the existing embankment along the highway.

All visible sheet piles will be covered in concrete for aesthetic reasons.

Fifteen new borings were made along the ramp alignment showing great variations of the soil. The discovered soil types included:

- Post and late glacial deposits consisting of peat, clay, silt and sand.
- Post glacial deposits of organic soil (gyt-tja).
- Tills consisting of clay, silt and sand.
- Glacial deposits of sand and gravel.



Figure 2. Overview of the ramp [1].

The deposits of organic soil in some parts of the ramp turned out to be a challenge. Slag was found in many locations in the post glacial deposits implying more corrosion of the steel than usual for these layers. The design life of the ramp is 100 years.

### 2.1 Settlement reducing measures

Calculations showed that settlements between 20 cm to 40 cm could occur in parts of the road because of organic soil layers. Measures had to be made to prevent this. Two different solutions are presented in the following.

The simplest solution was to excavate the organic soil. Because the organic soil extended to up to 6.5 m below the ground level, this solution was found only to be the most economical where the road already was some meters below ground level. The excavation of the organic soil meant that the sheet piles and ground anchors had to withstand larger forces.

An alternative to avoid the large settlements of the road from the organic soil was to drive concrete piles into the soil and cast a concrete slab on top of each pile. The slabs were placed with a distance of up to 815 mm and 200 mm distance from the sheet piles. A geotextile net was placed 200 mm above the top of the slabs. A minimum of 1.5 m of sand/gravel needs to be on top of the slabs to ensure an arch effect in the sand/gravel assisted by the geotextile net. Thereby, the entire load from the road and roadbed is transferred into the slabs, through the piles and into the soil below the organic soil deposits.

In Figure 3 a cross section of the road can be seen where the concrete piles and slabs are shown. This solution was found to be the most economically attractive where the road is above or just below the ground level.

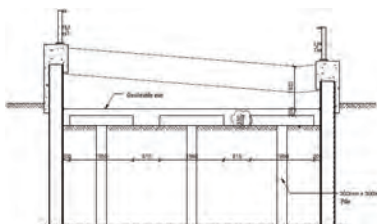


Figure 3. Cross section of the ramp where the road is above ground level with concrete piles and slabs to avoid settlements in the organic soil [1].

### 2.2 King post wall, no anchors

Close to the ramp there are several buildings. One building had to be removed because it was located in the alignment of the new ramp. Another building close to the ramp is founded on piles. A 3D model of the building and pile foundation as well as the new sheet pile wall with ground anchors was made. From visual inspection of this model it was clear that there was no room for the ground anchors between the existing piles. Thus, a solution consisting of a wall without ground anchors had to be found.

The most economically attractive solution was a King post wall with large H-profiles coupled by double sheet profiles [2]. The H-profiles have a height of 880 mm, the flange a width of 460 mm with a thickness about 23 mm. They had to withstand a large moment force, since it had to be a free wall.

### 2.3 King post wall, under bridge

The highway M3 crosses underneath the highway Lyngby Omfartsvej. This crossing proved to be a big challenge. To make room for the side extension of M3 a bicycle embankment had to be removed. The bridge is founded so that a new retaining wall is resisting the pressure from both the retained soil and the bridge foundation.

The borings showed that the soil mostly consists of clay till and glacial sand under the bridge.

The limited clearance was the main challenge. Focus had to be on what kind of machinery could be used and how a big profile could be handled under the bridge. In addition the foundation of

the bridge for Lyngby Omfartsvej had to be stable during the entire construction period as well as after the permanent construction is established, so settlements of the highway were prevented. If the bridge was exposed to deformations, the cost would be enormous and had to be avoided at all cost.

Working closely together with the contractor, Per Aarsleff A/S, to find the suitable machinery and the maximum dimensions of the profiles for the machinery, a solution was found. A king post wall with columns of HE240B profiles for every 1.0 meters with steel plates ( $t = 20$  mm) between them. Due to the small height only sections of 1.0 meters could be driven at a time, then welded together with a new section, continued driving and so on, until the required length was obtained. For the plates between the columns, the principle was the same. Sections of 1 meter at a time had to be driven. These plates were not welded together, but small plates were welded on them, to keep them aligned over each other.

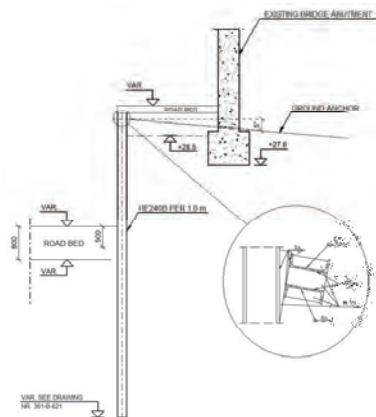


Figure 4. Cross section of king post wall under bridge [1].

Ground anchors had to be installed as well. To make sure the foundation of the bridge did not move when excavation was done, the ground anchors were designed and pre-stressed to resist the entire horizontal load from the bridge foundation



as well as some of the soil pressure. To minimize the length of the columns, the vertical forces from the anchors needed to be at a minimum because of the vertical soil resistance. So the inclination of the ground anchors was set to 5°. The low angle of the ground anchors was possible because they had a free length of 20 m and were below the bridge and road of Lyngby Omfartsvej making adequate excess pressure on the retaining zone of the ground anchors. To minimize the hole that had to be cut in the bridge foundation for the ground anchors, a bar anchor was used here, in contrast to the strand anchors used as ground anchors in the remaining project area.

To transfer the forces from the ground anchors to the HE240B columns, a steel waling was introduced. The waling needed to be on the back side of the king post wall since the concrete thickness cast on the front side was not sufficiently large to hide the waling. The waling consists of two UNP260 beams welded on the columns with triangle plates to obtain the angle of the ground anchors, cf Figure 4.

#### 2.4 Other challenges

A project like this has a lot more challenges for the geotechnical construction engineer in the design phase than have been described here. Some of them are listed below:

- Crossing of high voltage cables.
- Crossing of waterpipe.
- Sheet piles carrying small concrete bridges.
- Corners of the sheet pile walls.
- Tie rod connections due to the bending of the ramp.

### 3 CONSTRUCTION PHASE

Ramboll has undertaken supervision with the construction of Vintapperrampen. The Geotechnical Department in Ramboll has been supervising the driving of concrete piles, sheet piles and king post walls, boring of ground anchors, excavation of soil, welding and construction of the waling and anchor connections.

#### 3.1 Driving of sheet piles

The driving of the sheet piles progressed satisfactorily. The driving method depended on the accessibility at the location. The preferred method was to vibrate the sheet pile, by using a Mobil Ram, cf. Figure 5.



Figure 5. Aarsleff Mobil Ram SM 18/22 HD [3].

For the locations where this vehicle could not reach, a crane carrying a vibrator was used, cf. Figure 6.



Figure 6. Vibrating from crane [3].

A challenge with the sheet piles was recognised after the measuring of sheet pile deformations. A large section of the sheet piles had undergone lateral displacement beyond the allowable tolerance. At some locations this meant that additional concrete had to be used in the finished wall. In a large section the sheet piles were placed too close to the road. Different



departments in Ramboll had to be involved to find a solution. After going through different solution options, the best solution found was simply to move the road a little. This meant that other parts of the wall needed more concrete to make a smooth wall.

### 3.2 King post wall



Figure 7. Hammering of plate in King Post Wall under bridge [3].

The king post wall under the bridge was driven with a small ramming machine that the contractor found under the design phase. The H-profiles sometimes underwent twisting and/or lateral displacement during installation. This made it harder when ramming the plates down between the H-profiles.



Figure 8. King post wall under bridge before excavation [3].

After excavation of the soil on the front side of the king post wall it was observed that hard

clay till was between the plates and the H-profiles in most cases. So the plates were not in direct contact with the H-profiles. If the clay should fall out later on, the plates would move and settlement of the bridge might occur. It was therefore decided to weld new small steel plates between the H-profiles and the plates to keep them in place.



Figure 9. King post wall under bridge after excavation [3]

### 3.3 Driving of concrete piles

Six concrete test piles were initially driven. They had an excess length of 2 meters. To begin with they were driven to the desired design levels. Then, after about two weeks, the plan was to drive them the extra two meters. However the build-up resistance of the piles was so great that the piles would not move.

The concrete piles were ordered with an asphalt cover in the zones where organic soil was expected. The asphalt would greatly reduce the negative resistance on the piles from the organic layers. The reason for the asphalt was to keep the length of the piles down to avoid the sand/gravel layer under the clay till. The first cargo of piles after the test piles was without asphalt. From the driving log on the test piles in the area where these piles were to be placed, it was found that the piles could reach a sufficiently high bearing capacity without the asphalt. So work could continue without loss of time.

### 3.4 *Drilling and establishing ground anchors and tie rods*

The work with the ground anchors and tie rods started as soon as the sheet piles were installed and the excavation of soil or build up of road bed was done to the correct level.

A few of the drilled holes for the anchors hit some obstacles and therefore the angle of inclination of the anchors had to be changed. Due to miscommunication between the contractor and the engineers, five ground anchors in a row had the same inclination therefore the total strength was reduced because of the overlap within the anchor zone. Neither the contractor nor the engineers would risk insufficient bearing capacity. So the solution became that a new anchor replaced the middle of the five anchors. The new anchors were placed half a meter below the already installed one and with a new inclination. Then the two anchors side by side with the same inclination were tested at the same time to make sure that bearing capacity was satisfactory.



Figure 10. Boring of ground anchor [3]

### 3.5 *Excavation of organic soil*

The excavation of the organic soil was under almost full supervision from Ramboll's Geotechnical Department. The area was divided into excavation zones by the contractor. A maximum excavation depth was given to the contractor for each excavation zone. When the supervisor was satisfied that the excavation had gone beyond the organic soil, the excavation stopped in each zone. By doing it this way the contractor only

had to excavate the organic soil and save a lot of time and money than if they had to excavate the entire area to the design level made on the safe side from the borings.



Figure 11. Excavation of organic soil [3]

## 4 LESSONS LEARNT

During the project the following lessons were learnt:

- Thorough communication between all parties, external as well as internal is essential.
- Installation of king post wall with limited clearance.
- Ensure that positional tolerances for sheet pile walls as well as king post walls are kept.

## ACKNOWLEDGEMENT

This paper has been done in the framework of the project "Vintapperrampen" by Ramboll. Thanks are given to the client, The Danish Road Directorate and to the contractor Per Aarsleff A/S for good co-operation.

## REFERENCES

- [1] Ramboll Denmark A/S, Design Project Vintapperrampen, 2011.
- [2] Arcelor Mittal homepage for King Piles, <http://www.arcelormittal.com/sheetpiling/page/index/name/combined-walls>, accessed 2012-05-04.
- [3] Ramboll Denmark A/S, Supervision of construction Vintapperrampen, 2011.

# Impact of the jack-up rig installation on the jacket platform piles

## Spudcan-soil-pile interaction analyses

L. Kellezi & S. Sundararajan  
*GEO - Danish Geotechnical Institute*  
1 Maglebjergvej, DK 2800 Kgs. Lyngby, Denmark

### ABSTRACT

For the installation of a jack-up rig at an oil field offshore Mediterranean Sea an assessment of spudcan-soil-pile jacket platform interaction during rig installation is carried out. At the mudline, the nearest spudcan (edge of the spudcan) to the closest platform pile is about 15.5 m.

The piles are battered. At the location, from the seabed, the soil conditions consist of very soft to soft clay underlain by very dense to dense sand to large depth. Spudcan penetration in soft clays is associated with large soil displacements, horizontally and vertically. Depending on the relative distance between the platform and the jack-up rig this can cause considerably additional loads on the pile foundations. A spudcan penetration of about 10 m is predicted in conventional analysis. Finite element modeling of spudcan-soil-pile interaction is carried out conventionally and with Plaxis finite element program.

The finite element modeling shows that the pile location is out of the critical rupture figure developed in the soft clay during spudcan penetration. Maximum elastic pile deflections of about 10 mm are calculated. The additional bending moment induced in the pile is about 0.9 MNm. An alternative calculation based on plasticity analysis of the laterally loaded piles considering moderate soil displacements, gives 1.2 MNm. So the additional stresses induced in the pile might vary from (30 – 40) MPa. The analyses are based on the design parameters with material coefficient of 1.

The jack-up rig was installed next to the jacket platform at the considered distance. Spudcan penetrations as predicted were recorded and no impact on the pile jacket was observed during the installation.

Keywords: Jack-up Platform, conventional analysis, finite element analysis, bearing capacity, failure mechanism, bending moment, shear force,

## 1 INTRODUCTION

Large jack-up rigs are often used to perform drilling operations near to an existing jacket platform in shallow water oil and gas production.

According to [1] in several locations, depending on the soil conditions, a large volume of soil is displaced and consequently severe stresses may be induced on adjacent piles supporting the jacket platform, during spudcan installation process.

The induced loading on the pile decreases with increasing clearance between the spudcan and the pile [2]. An assessment of spudcan-soil-pile interaction is carried out during installation

of a jack-up rig at an oil field location in the Mediterranean Sea.

## 2 SPUDCAN-PLATFORM RELATIVE POSITION AND GEOMETRY

The platform-jack-up spudcans location at the mudline is shown in Figure 1. The platform base is a square of 19.31 x 19.31 m. Four leg piles are located at the corners of the platform structure.

The piles are battered 1:7.071 in both directions and are 62 m long. The diameter of the piles is 1.067 m (42 inches) and pile wall thickness is 3.81 cm (1.5 inches).

The jack-up rig has an equivalent diameter of about 18.0 m, a total height of about 6.8 m and 1.8 m height of tip to full base contact.

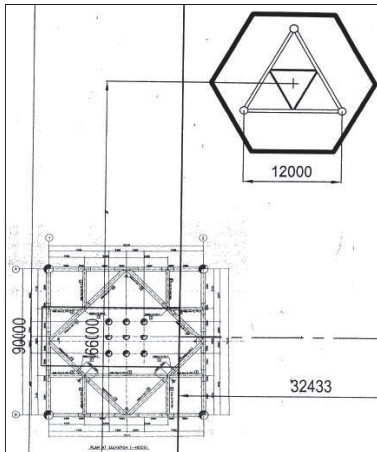


Figure 1, Platform Jack-up Spudcans Location

According to Figure 1 and considering the nearest spudcan to the platform, the spudcan edge is about 15.5 m from the closest platform pile at the mudline. As the piles are battered, the distance between the edge of the spudcan and the pile at 9.8 m depth, (depth where the sand layer starts), is about 14 m.

### 3 SOIL CONDITIONS AND PREDICTED SPUDCAN PENETRATION

The seabed soil consist of about 10 m of very soft-to-soft clay underlain by very dense to dense sand to the depth relevant for spudcan penetration analysis and the pile design.

Based on the available soil data GEO has assessed generalized design lower / upper bound soil profile applicable to 'Jack-up' rig spudcan penetration analyses at the three spudcan locations.

The upper / lower bound characteristic soil parameters are selected as cautious estimates of the value effecting the occurrence of the relevant limit state [3].

The estimated design angles of internal friction take into account the reduction for the footing size as recommended by [4]. The generalized soil profiles and the soil parameters relevant for the penetration analyses can be observed in Figure 2.

Spudcan penetrations of about 10 m are conventionally predicted for the maximum preload, (122 MN). During the penetration squeezing of the clay soil occurs while the spudcan approaches the level of the very dense sand layer at about 10 m depth below the seabed.

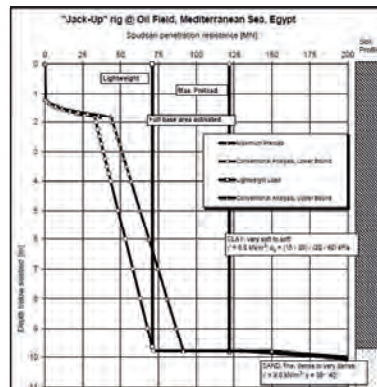


Figure 2 Conventional Penetration Predictions

### 4 SPUDCAN-SOIL-PILE INTERACTION

Spudcan penetration in soft clays is associated with large soil displacements. Depending on the relative distance between the platform and the jack-up this can cause considerably additional loads on the pile foundations.

There are different ways how to determine the magnitude and the extent of the soil movement around the spudcan and the nearby effected zone.

#### 4.1 Centrifuge Testing, Literature Survey

From the centrifuge testing of the spudcan penetration in soft clay, [5] & [6] it is observed that the soil below the spudcan is moved laterally and flown up around the spudcan edge effecting the soil displacement at an area of about one spudcan radius.

Considering the previous predicted spudcan penetration at this location, soil backflow is not likely to occur as  $d$  (penetration depth) =  $10 \text{ m} < N \cdot c_u / \gamma' = 5 \cdot 15 / 6 = 12.5 \text{ m}$ ,  $N$  (stability factor) = 5 according to [7].  $c_u$  is the undrained shear strength for the remolded soil and  $\gamma'$  the effective unit weight.

So the soil volume displaced downward during the spudcan penetration will be moving laterally-up due to squeezing of the clay (soft clay overlying sand). This can be illustrated with the below figure from the centrifuge testing of spudcan penetration on soft clay at the University of Western Australia (UWA).

In [6] centrifuge modelling of spudcan-pile interaction was carried out at Cambridge University. The soil displacements were converted into loads on the piles adjacent to the spudcan. As the spudcan penetrates, the moment distribution in each of the three considered piles was recorded.

It was observed that extensive remoulding of the soil during spudcan penetration is localised laterally, within one spudcan radius. The soil conditions considered in the test were homogeneous very soft clay of 32 m prototype scale and the piles were vertical of diameter 1.5 m.

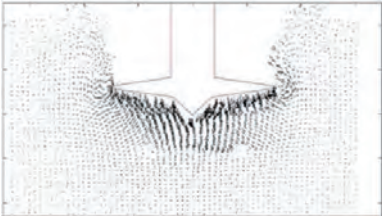


Figure 3. Centrifuge Test at UWA ([www.cofs.uwa.edu.au/Research/spudcan.html](http://www.cofs.uwa.edu.au/Research/spudcan.html)).

The four-parameter model involving p-y approach was offered as a means to determine the

impact of spudcan penetration near piles of a steel jacket structure. This can only provide an approximation of the moment developed in a pile subjected to soil movement. The influence of the relative size of the spudcan was not investigated.

#### 4.2 Two-Dimensional (2D) Finite Element Analysis

Numerical modeling, finite element large deformation analysis, can be performed to investigate the soil deformation around the spudcan during the penetration. Such a modeling has been previously carried out by the authors with finite element programs like Abaqus, Elfen, Plaxis etc. [7]-[10].

For the current analysis finite element modeling is carried out in Plaxis [11]. The program does not have strong capability to carry out large deformation analysis, neither mesh adaptivity features. However, the analysis gives an indication of the spudcan-soil-pile interaction during spudcan penetration.

The real situation is a three-dimensional (3D) one. The 2D modeling of the spudcan and the pile is carried out as an approximation. This means that the spudcan is considered acting as a continuous footing and the pile as an inclined sheet pile wall.

The geometry of the spudcan and the pile data are adapted to the 2D analysis. The spudcan is modeled as a rigid body and the pile is supposed to behave elastically modeled as a beam/plate element with the stiffness derived from the pile geometry.

Soil-spudcan interaction and pile-soil interaction are modeled implementing interface elements. As the pile is 62 m long, it is assumed to be pinned at the boundary of the finite element model.

The same soil strength parameters, as applied in the penetration analysis are implemented in the finite element analysis. Mohr-Coulomb elasto-plastic constitutive soil models, undrained conditions for the clay and drained conditions for the sand, are used considering the available data.

The deformation parameters for the clay and the sand layers are defined based on the laboratory test results. For the soft clay layer the defor-

mation modulus  $E=200*c_u$  is approximated though.

The patterns of horizontal and vertical soil deformations are shown Figure 4, which define the area around the spudcan affected mostly during spudcan penetration.

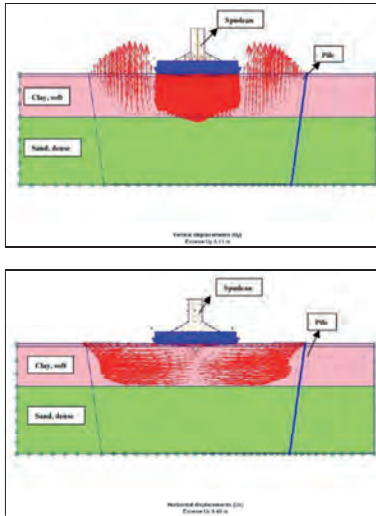


Figure 4. Vertical and Horizontal Soil Movements.

The pile is modeled as battered with the relative spudcan position as described in section 2. The top of the pile is modeled as free to rotate but fixed with regard to horizontal displacement considering the jacket structure supported by the piles. No axial pile load was considered.

As the spudcan penetration calculation starts from full base contact, the vertical soil displacement is about 8 m. This should be added up with the spudcan tip to base height of 1.8 m. It can be seen that the pile is located out of the rupture figure and not affected very much by the soil movements.

The pile deflections, additional pile bending moment and forces are shown in Figure 5.

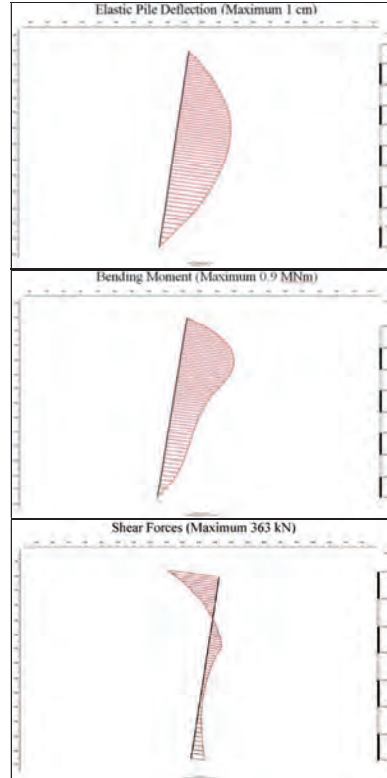


Figure 5. Additional Pile Forces and Deformations

Maximum elastic deflections of about 10 mm are recorded for the pile. The additional bending moment induced during spudcan penetration is about 0.9 MNm giving additional stresses of about 30 MPa.

However, due to very large deformations and no mesh adaptivity features implemented in Plaxis, some inaccuracies in updating the state of stress for the soil and the pile are expected. In addition, the problem is 3D and a 2D modeling

might involve uncertainties. In order to check the finite element results, alternatively a conventional approach is derived below.

#### 4.3 Ultimate Limit State Analysis

The analysis is based on Brinch Hansen ultimate resistance of rigid piles against transversal forces [12]. In the state of failure, (soil deformation is able to develop ultimate passive pressure around the pile), the pile will rotate as a rigid body around a point at a certain depth. In the current situation, a point slightly below the sand layer (about 1 m) is assumed as a rotation point.

The resultant, (passive minus active), pressure per unit length of the pile is calculated as a function of cohesion, overburden and earth pressure coefficients respectively. The soft clay is considered slightly over consolidated with  $c_u=5$  kPa at the mudline and  $c_u=30$  kPa at the bottom.

The pile is calculated as a beam with the same boundary conditions (pinned support) as in the finite element model, subjected to active and the passive forces per unit length.

A maximum ultimate bending moment at about 6 m depth is calculated to be 2.9 MNm, which gives maximum bending stresses in the pile of about 95 MPa. The soil displacements relative to the pile at the considered location will not fully develop passive earth pressure (yield), so bending moment of about 1.5 MNm is evaluated for expected soil displacements of about 4 - 5 cm. So the additional stresses induced in the pile might vary from (30 – 40) MPa.

#### 5 GENERAL CONCLUSIONS

The finite element modeling shows that the pile location is out of the critical rupture figure developed in the soft clay during spudcan penetration. Maximum elastic pile deflections are about 10 mm. The additional bending moment induced after completion of the spudcan penetration is about 0.95 MNm and the additional stresses about 30 MPa.

An alternative calculation based on plasticity analysis of the laterally loaded piles considering moderate soil displacements at the pile location,

gives 1.5 MNm. So the additional stresses induced in the pile might vary from (30 – 40) MPa. Our analyses are based on the design parameters with partial coefficient of 1.

It was recommended discussing the current assessment with the consultants who designed the platform piles. The additional stresses of the order (30–40) MPa, possibly to be induced during spudcan penetration, might or might not be critical for the pile.

#### REFERENCES

- [1] Y. Xie. & Y.K. Chow (2011), *Soil Movements and Pile Responses During Spudcan Penetration*, 13<sup>th</sup> International Conference in The Jack-Up Platform, London.
- [2] C.F. Leung. & Y.K. Chow (2012), *Experimental and Numerical Studies of Spudcan-Pile Interaction*, Offshore Technology Conference 23053, Texas, USA.
- [3] Eurocode 7: *Geotechnical Design – Part 1: General Rules*. DS/EN 1997-1. 2007.
- [4] SNAME. *Technical & Research Bulletin 5-5A. Guidelines for Site Specific Assessment of Mobile Jack-Up Units*. August 2008.
- [5] H. W. Craig. & K. Chua (1990) *Deep penetration of spudcan foundations on sand and clay*. Geotechnique 40. No. 4, page 541-556.
- [6] H. W. Craig & K. Chua (1991) *Large displacement performance of jack-up spudcans*. Centrifuge 91 page 139-144.
- [7] L. Kellezi and H. Stromann, (2003), 'FEM Analysis of Jack-up Spudcan Penetration for Multi-Layered Critical Soil Conditions'. Proceeding of BGA International Conference on Foundations, ICOF2003, Dundee, Scotland, 410-420.
- [8] L. Kellezi, G. Kudsk & P. B. Hansen, (2005), 'FE Modelling of Spudcan – Pipeline Interaction'. Proceedings, Frontiers in Offshore Geotechnics, ISFOG 2005, September, Perth, Australia, page 551 – 557.
- [9] L. Kellezi & G. Kudsk, (2009), 'Jack-up Foundation, FE Modelling of Punch Through for Sand over Clay' 12 International Conf. on Jack-up Platform. Sept. London UK, Proc. page 1-12.
- [10] L. Kellezi & H. Stadsgaard, (2012), 'Design of Gravel Banks – a Way to Avoid Jack-Up Spudcan Punch Through Type of Failure', Submitted to OTC 2012, Houston, April-May 2012.
- [11] Plaxis 2D Version 9.2. *Finite Element Code for Soil and Rock Analysis*. Delft University of Technology & Plaxis bv. The Netherlands. 2008
- [12] Hansen B. J. & Christensen N. H. (1961) *The ultimate resistance of rigid piles against transversal forces. Model tests with transversally loaded rigid piles in sand*.





# Modeling of the effect of the embankment dimensions on the mechanical behavior of railway track

Antti Kalliainen<sup>1</sup>  
*Tampere University of Technology*

## ABSTRACT

In Northern areas the railway embankments must be sized against the seasonal frost. Since practically no frost heave can be allowed on mixed corridor railway network, the embankments must be built up with relatively thick structural layers. Mutually the embankments have traditionally had narrow widths and steep slopes. Introduction of higher (25 t) axle loads is exposing the structures to increasing rate of loading. The aim of this study is to measure and model the effects of higher intensity loading of railway structures. With help of 3D Finite Element Modeling it was possible to determine a credible explanation of the embankment structure behavior when model results are interpreted on the mobilized amount of shear strains into the embankment structure. Based on the gathered data and analysis of different project rounds it was possible to create a simple guideline that determines the required embankment dimensions.

Keywords: Railway embankment, subballast layers, permanent deformation, recoverable deformation, finite element model, shear strain.

## 1 INTRODUCTION

The width and the slope angle of a railway embankment have great economical effect on the investment costs of a railway embankment. Due to the cold climate and the consequent harmful effect of seasonal frost the railway embankments are typically built up with relatively thick structural layers in Northern regions. Meantime the embankments have traditionally fairly steep slopes and narrow widths in order to cut the construction costs. Introduction of higher allowable axle loads and traffic speeds is, however, expos-

ing the embankment structures to continuously increasing intensity of repeated loading which also is increasing the rate of permanent deformations into the embankment structure. In addition, the substructure layers of railway embankment require high-quality non-frost-susceptible aggregate materials which are being more and more scarcely available in several places.

The problem described above has been studied at the Laboratory of Earth and Foundation Structures of the Tampere University of Technology. The study is divided into four main as-

---

<sup>1</sup> Antti Kalliainen, Tampere University of Technology, P.O.Box 600, FI-33101 Tampere, Finland, antti.kalliainen@tut.fi

pects: the full-scale test embankment sections located in the southwestern part of Finland, the model scale instrumented test embankments, FEM-modeling and evaluating the long term deformation behavior of railway track line based on laser scanner measurements. This paper is focusing on the observations made on the three dimensional FEM-models and a case study where the new instruction of defining the required minimum embankment width was tested at a renovation project between the towns of Tampere and Kokemäki located in the Western part of Finland. The embankment types of this study and the symbols used in this article are presented in table 1.

Table 1. Embankment types and symbols used in this study.

Embankment type	Dimensions in full scale	
	Width on top of sub-ballast (m)	Slope angle ratio (-)
Embankment A	5.4	1:1.5
Embankment B	6.0	1:1.5
Embankment C	6.8	1:1.5
Embankment D	6.0	1:2

Chapter 2 shortly describes the most significant findings observed at full-scale measurements and model scale test embankments. Chapter 3 gathers the results at the mechanical 3D-modeling and chapter 4 describes the first application of the new instruction guidelines provided from the results of this study.

## 2 FULL- AND MODEL SCALE TEST RESULTS

The two most significant findings of these tests were the essential role of subgrade stiffness on the deformation behavior of the railway embankment and the observation that recoverable vertical displacement does not vary as a function of embankment dimensions. [1,2]

Figure 1 shows the accumulated permanent lateral deformations of the embankments measured on the top of the subballast layers on tests performed on stiff and more flexible subgrade conditions. Figure 2 presents the amount of recoverable vertical displacement of the model scale test embankments at different load levels. The load level was raised after each 20 000 load

cycles in the test series. The results achieved clearly indicate that on stiff subgrade conditions the embankment does not face a notable amount of permanent deformation. On more flexible subgrade the accumulated amount of permanent deformation into the embankment structure is remarkable and the embankment dimensions have a marked effect on reducing the subsequent widening. As shown in figure 2 the recoverable deformation behavior of the track embankment structure is clearly not an explanatory factor on permanent deformation behavior of the embankment structure until collapse. [1,2]

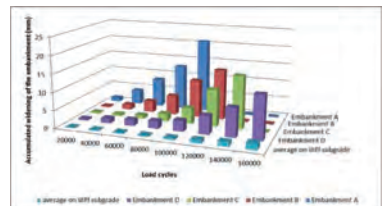


Figure 1. Subsequent widening on top of the subballast layers on the model scale test embankment series.[2]

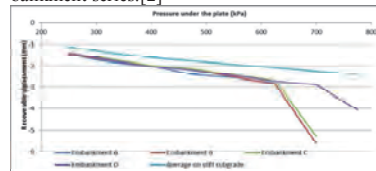


Figure 2. Recoverable vertical displacement of the model scale track structure.[2]

Similar results were gathered at monitored full-scale test embankment sections located on soft soil area (figure 3). The long term behavior of the embankment clearly shows that on flexible subgrade conditions the embankment dimensions have a great role in permanent deformation behavior of the track structure. [1]

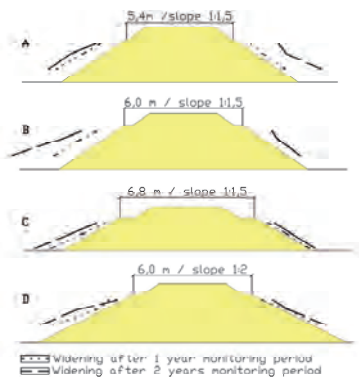


Figure 3. Average permanent lateral deformation in each of the embankment sections after one year and after two years exaggerated by 50 times. [1]

### 3 MECHANICAL MODELING OF THE RAILWAY TRACK EMBANKMENT BEHAVIOUR

Mechanical modelling of the track embankment was made with PLAXIS 3D which is a finite element program that has been developed specially for the analysis of deformation and stability in geotechnical engineering projects. [3]

PLAXIS 3D contains several different material models. Only the material model used in this study is introduced here. The Hardening-Soil model (HS) is an advanced model for the simulation of soil behaviour. Limiting states of stresses are described by means of the friction angle,  $\phi$ , the cohesion,  $c$ , and the dilatancy angle,  $\psi$ . Soil stiffness is described by using three different input stiffnesses: the triaxial loading stiffness,  $E_{50}$ , the triaxial unloading stiffness,  $E_{ur}$ , and the oedometer loading stiffness,  $E_{oed}$ . All these stiffnesses relate to a reference stress, 100 kPa in this study. In HS model all stresses increase with pressure and the yield surface is not fixed in principal stress state, but it can expand due to plastic straining. In this study, modelling was performed with linear elasticity for subgrade lay-

ers and HS model for subballast layers. HS model was chosen for the subballast layers because majority of strains caused by train load are reversible. However, a part of the strain is always permanent. With HS model the stiffness of embankment is more appropriate in both sides of the yield surface i.e. when subjected to deviatoric loading, the soil stiffness decreases simultaneously with the development of irreversible strains. [3]

Linear elasticity was considered to be suitable for the subgrade layers in this study because repeated loading should not induce a marked amount of plastic straining in the subgrade. This assumption was also checked by using Mohr-Coulomb material model for subgrade layers and practically no plastic straining was observed to appear in the calculations.

The model geometry was chosen to represent an average Finnish railway embankment and the total height of the embankment was 2.55 meters of which the subballast layers were 2 meters thick and the ballast layer was 0.55 meters. The model was constructed to profile the most critical loading stage of the embankment. The loads of two consecutive bogies were modelled as point loads. The loads were located as in load model 71 so they were at 1.6 meters interval. The magnitude of each point load was 125 kN. The model sketch is illustrated in figure 4.

#### 3.1 Model verification

The embankment material parameters used in the modelling and summarized in Table 2 have been evaluated based on extensive experience from large-scale repeated loading triaxial testing with similar type of coarse grained materials [4] and also verifications made by taking use of actual response measurements made from the track embankment on an earlier instrumentation [5].

With help of these results it was possible to compare the stiffness parameters of the model to the measured ones. Figure 5 illustrates the  $E_{ur}$  state parameters option of PLAXIS 3D. This option shows the actual stiffness of the soil at the end of calculation. At the bottom of the ballast layer the stiffness was roughly 250 MPa and at

the top parts of the subballast layer the stiffness was approximately 140-160 MPa. These achieved values were close to the measured ones, having only about 10-20 MPa difference. Based on these results, the chosen stiffness parameters were considered as suitable (table 2)

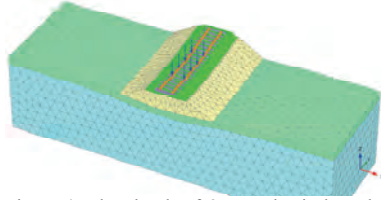


Figure 4. The sketch of 3D mechanical model used in this study.

Table 2. Material parameters used for the ballast layer and subballast layers used in final simulations.

Parameter	Value	Value	Unit	
				Ballast
Material	Identifi-cation	HS	HS	-
	Material model	HS	HS	-
	Type	Drained	Drained	-
	$\gamma_{\text{unsat}}$	20	20	kN/m <sup>3</sup>
	$\gamma_{\text{sat}}$	23	23	kN/m <sup>3</sup>
Permeability	$k_x$	1	1	m/day
	$k_y$	1	1	m/day
Stiffness	$E_{50}^{\text{ref}}$	250000	150000	kN/m <sup>2</sup>
	$E_{\text{oed}}^{\text{ref}}$	160000	120000	kN/m <sup>2</sup>
	$E_{\text{ur}}^{\text{ref}}$	500000	350000	kN/m <sup>2</sup>
	Power	0.5	0.5	m
	$\nu(\text{mu})$	0.2	0.2	-
	$p^{\text{ref}}$	100	100	kN/m <sup>2</sup>
	$K_0^{\text{nc}}$	0.2929	0.3843	-
Strength	$c_{\text{ref}}$	20	5	kN/m <sup>2</sup>
	$\Phi$	45	38	°
	$\Psi$	5	5	°
	$c_{\text{increment}}$	0	0	kN/m <sup>2</sup> /m
	$\gamma_{\text{sat}}$	0	0	m
	$R_f$	0.9	0.9	-

Since the embankment is exposed to different types of loads due to the climate condition changes, the effect of soil strength was also studied with help of a preliminary model. When the degree of saturation of the embankment material changes due to rain, wind etc. it also affects the soil strength. In this particular case, especially the friction angle  $\phi$  and the cohesion  $c$

are variables. Even though coarse grained aggregates are considered as cohesionless soils, the adequate moisture content creates suction essentially in the case of sands and this phenomenon can be modeled with help of increased cohesion. Table 3 shows the varied soil parameters. Based on the model series the strength parameters of subballast layers were chosen as relatively conservative (table 2).

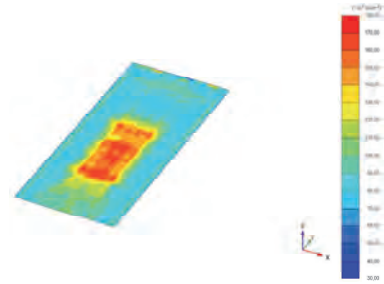


Figure 5. State parameter  $E_{\text{ur}}$  on top of the subballast layers presenting the stiffness moduli at the end of the simulation.

Table 3. Soil strength parameters in simulations defining the effects of environmental loads to the embankment structure. Dilatancy angle  $\psi$  remained at constant value of 5° at all simulations.

Simulation	$\phi$ (°)	$c$ (kPa)
1	38	1
2	38	5
3	38	10
4	41	10
5	41	15
6	45	15
7	45	20

### 3.2 Model results

After the model verification the actual simulation series was performed. As mentioned in previous publications of the study (eg. [1,2]) the accumulated level of shear strains seems to give a plausible explanation to embankment behavior under heavy train loading. Figures 6 and 7 illustrate the simulated shear strain levels into the embankment structures on soft soil area and on stiff subgrade conditions. It can clearly be indicated that on soft subgrade areas the added embankment

dimensions support the embankment structure and prevent the accumulation of harmful permanent deformations whereas on stiff subgrade conditions that spare support is not advantageous.

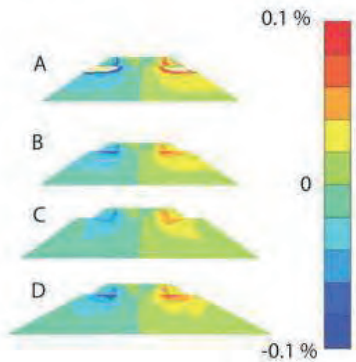


Figure 6. Accumulated shear strain levels on final simulations on soft subgrade conditions.

#### 4 A NEW METHOD IN DETERMINING THE REQUIRED MINIMUM EMBANKMENT WIDTH

The present method used in Finland only takes the desired maximum axle load and traffic speed into account in determining the required embankment width. However, the observations made during the project pointed out that the subgrade stiffness had dominant role in deformation behavior of a railway embankment. Therefore a new method was developed for the maximum axle load of 25 tonnes for freight traffic and traffic speeds between 200 and 250 kph for passenger traffic on existing railway network.

The new method is based on the measured recoverable deformation of the embankment under moving train load. The rate of loading is set to the most common locomotive type in Finland which has axle load of approximately 22 tonnes. The recoverable deformation of the embankment is measured at the centre of sleeper and the

measurement procedure is standardized as follows:

- Railway track line is first divided into sections having similar subgrade conditions.
- The recoverable vertical displacement of each section is measured from the middle of the sleeper.
- Measurement of each section is performed from a section of 25 sleepers. Five sleepers are instrumented and after each instrumented sleeper four sleepers are left without instrumentation to avoid stiffer and weaker spots of the track
- An average recoverable vertical displacement is calculated leaving the strongest and weakest measured value unnoted
- Calculated average value determines the required embankment width (figure 8)

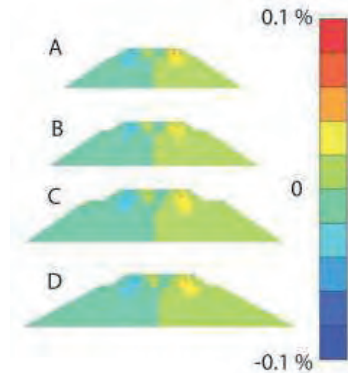


Figure 7. Accumulated shear strain levels on final simulations on soft subgrade conditions.

#### 4.1 CASE study on the new instruction guideline

The new method was tested for the first time at a track renovation project going on between towns of Tampere and Kokemäki located in the western part of Finland. Railway track line under renovation has a total length of approximately 84 km. Altogether 86 sections were measured to determine the required embankment width.

When the recoverable vertical deformation was measured, also the current embankment width was checked at most sections to verify the new method. At some of the sections the embankment width was not checked since parts of the railway track are constructed with double line railway track. In each of checked 74 sections the current embankment width was greater than the desired minimum according to the new method. Based on this information the new method and the limit values set can be considered suitable. Table 4 shows the gathered data divided into desired embankment widths.

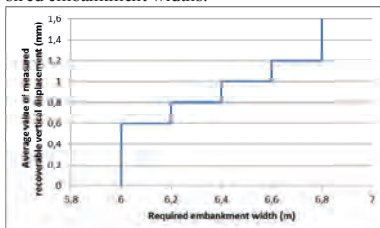


Figure 8. The limiting values of average recoverable vertical displacement according to the new guideline.

Table 4. Measured sections divided into required embankment width fragments.

Recoverable vertical displacement of the track (mm)	Required embankment width (m)	Number of sections
< 0.6	6	9
0.6..0.8	6.2	26
0.8..1.0	6.4	26
1.0..1.2	6.6	10
>1.2	6.8	15

However, the new method has some disadvantages. At almost 20 % of sections measured had a large (>0.5 mm) standard deviation in measured values. This is most likely due to the nature of the ballasted track where the condition of the track components varies a lot especially when the track is at the end of its lifecycle. On the other hand, over 40 % of sections measured the standard deviation was relatively small (<0.15 mm). This indicates that the method is relatively reliable as long as the condition of instrumented sleepers is investigated before the measurement is performed. In most cases a large standard deviation occurred the ballast layer un-

der instrumented sleepers was heavily fouled and the alignment of the sleepers were not optimal. Since the new method only describes the performance of track correctly at one point at the time, the limit values were set somewhat considerate.

## CONCLUSIONS

The finite element modeling in 3D solved several issues concerning the 2D-modelling (see e.g. [2]). With help of the results gathered it was possible to evaluate the embankment behavior more accurately based on mobilized shear strain levels.

The new guideline instruction created seems to have an advantageous approach to problems concerning the sizing of embankment dimensions. With help of the data and observations obtained during the study it is possible to point out the problematic sections of railway track line and direct the resources into correct sections during the renovation of existing railway track.

## ACKNOWLEDGEMENT

The author gratefully acknowledges the funding of Finnish Transport Agency enabling the research work presented in this paper.

## REFERENCES

- [1] Kolisoja, P & Kalliainen, A. 2009. *Modeling of the effect of embankment dimensions on the mechanical behavior of railway track*. The 17th International Conference on Soil Mechanics and Geotechnical Engineering (17th ICSMGE) Conference Proceedings. Alexandria, Egypt.
- [2] Kalliainen, A , Kolisoja, P. & Nurmikolu, A. 2010. Modeling of the effect of the embankment dimensions on the mechanical behavior of railway track. *Proceedings of the 2010 Joint Rail Conference*.
- [3] Plaxis 3D 2010. *Material models manual*. 188 pages.
- [4] Kolisoja, P. 1998. *Resilient Deformation Characteristics of Granular Materials*. Ph.D. Thesis, Tampere University of Technology, Publications 223. Tampere, Finland.
- [5] Kolisoja, P., Järvenpää, I. & Mäkelä, E. 2000. *Instrumentation and Modelling of Track Structure, 250 kN and 300 kN Axle Loads*. Finnish Rail Administration, Publication A10/2000, Helsinki, Finland

# Foundation design new Botlek lifting bridge

B. Rijnveld<sup>1</sup>

*Fugro GeoServices B.V., on secondment at A-Lanes A15 / Ballast Nedam Engineering*

J.A. Jacobse

*GEO2 Engineering B.V., on secondment at A-Lanes A15 / Ballast Nedam Engineering*

## ABSTRACT

A new lifting bridge will be constructed crossing the river Oude Maas in the Rotterdam harbour area in the Netherlands. In this paper the foundation design of the bridge piers is discussed. With respect to the bearing capacity calculations, some deviations from the Dutch code were applied. The results of recent (scientific) studies have been taken into account in the calculations for the drained situation. For the undrained situation, the influence of a relatively thin cohesive layer within the influence depth of the foundation has been investigated in more detail. For the deformation analysis deterministic 3D FEM calculations have been performed. In order to take the effect of soil heterogeneity on the deformation behaviour of the bridge piers into account, a probabilistic model was developed. This model is described in this paper.

Keywords: Foundation design, shallow foundation, soil heterogeneity, probabilistic deformation analysis

## 1 INTRODUCTION

Due to an increase in traffic load, the Dutch highway A15 in the Rotterdam harbour area will be widened. One of the main challenges in this project is the construction of a new lifting bridge crossing the river Oude Maas. Consisting of two lifting spans of about 100 m length and 60 m width, reaching more than 60 m above water level, this new bridge will be one of the largest lifting bridges in Europe. In figure 1 an artist impression of the new bridge is presented.



Figure 1. Artist impression new Botlek lifting bridge with main piers P30, P40 and P50. Source: Quist Wintermans Architecten

---

<sup>1</sup> Corresponding Author. Fugro GeoServices B.V., Archimedesbaan 13, 3439 ME Nieuwegein, Netherlands, b.rijneveld@fugro.nl

The three main bridge piers will be founded on rigid concrete blocks with footing dimensions of 15 m x 60 m, at 8 m below river bed on top of the first dense (Pleistocene) sand layer. The foundations are effectively treated as shallow foundations.

In this paper the foundation design of the new bridge will be discussed. The soil investigation, ultimate bearing capacity and deformation analyses will be described.

## 2 SOIL INVESTIGATION AND PARAMETER DETERMINATION

For the determination of the soil parameters an extensive soil investigation has been performed. A relatively dense grid of Cone Penetration Tests (CPT's) with a mutual distance of about 15 m was executed to a depth of about 3 times the foundation width. In addition, a number of boreholes were drilled with selected undisturbed samples taken at regular intervals for geotechnical laboratory tests. From the CPT's and borehole logs the soil stratigraphy has been determined, see table 1.

Table 1. Soil stratigraphy

Top of layer [m NAP]	Soil description	Soil layer
-7 à -14	SAND, clayey	cover layer
-14 à -20	SAND, (medium) dense	1 <sup>st</sup> sand layer
-33 à -39	CLAY, stiff	deep clay layer
-34 à -42	SAND, (medium) dense	2 <sup>nd</sup> sand layer
-60	Max. investigation depth	

The thickness of the deep clay layer varies strongly. At some locations the thickness is about 4 m, but the layer was not encountered at some other locations.

Classification tests, like grain size distribution (granular layers) and volumetric weight and water content (cohesive layers) were performed on samples from the different soil layers. In order to determine the strength properties of the sand layer isotropically consolidated drained triaxial tests were performed on 9 samples. The samples were prepared in the laboratory at relative den-

sities of 40%, 60% and 80%. The in situ relative density was determined from the CPT's with the correlation deduced by Baldi [1], and turned out to be about 70% for the sand layers. The characteristic strength properties were determined by statistical analyses of the results from the triaxial tests. For the friction angle of the sand below foundation level a representative value of 33° was determined, which corresponded well with correlations between friction angle and cone resistance as can be found e.g. in the Dutch Code [2].

Since deformations of the deep clay layer were expected to have a relatively large influence on the superstructure, mainly oedometer tests have been performed on samples from the deep clay layer. From experience in the area, it was known that this layer is overconsolidated, which was confirmed by the CPT results. However, the overconsolidation ratio (OCR) could not be determined from the oedometer tests, most likely due to relaxation of the samples. Therefore the OCR has been determined from the following correlation with the cone resistance [1]:

$$OCR \approx \frac{c_{u,oc}}{c_{u,nc}} \approx \frac{(q_c - \sigma_v)/17}{0.3\sigma'_v} \quad (1)$$

In which:

OCR =	overconsolidation ratio	[-]
$c_{u,oc}$ =	in situ (overconsolidated) undrained shear strength	[kPa]
$c_{u,nc}$ =	normally consolidated shear strength	[kPa]
$q_c$ =	cone resistance	[kPa]
$\sigma_v$ =	vertical total stress	[kPa]
$\sigma'_v$ =	vertical effective stress	[kPa]

The calculated OCR corresponded well with experience from other projects in the area and geological information.

The virgin stiffness and unloading/reloading stiffness was determined from the oedometer tests, which included an unloading/reloading step. The determination of these stiffness parameters from the laboratory tests was expected to be reliable, since these were determined be-



yond the preconsolidation stress, so relaxation effects are expected to be minimal.

Based on the soil investigation and laboratory tests, representative values for the soil stiffness's were determined. An representative elasticity modulus of about 40 MPa and 3.5 MPa was determined for respectively the 1<sup>st</sup> sand and deep clay layer. This is the stiffness at a reference vertical effective stress of 100 kPa. For the stress-stiffness relationship a power law was used, with a power 1.0 for sand and 0.8 for the stiff clay. For loading below the preconsolidation stress a 4 times higher value was applied.

### 3 ULTIMATE BEARING CAPACITY

As stated before the foundations are effectively treated as shallow foundations. According to the Dutch Code [2] the bearing capacity of shallow foundations should always be determined for drained and, if applicable, also for undrained conditions.

#### 3.1 Drained bearing capacity

The drained bearing capacity is determined according to the conventional bearing capacity equation developed by Buisman, Caquot, Terzaghi and Brinch Hansen, with additional factors to take the effect of the shape, load inclination and ground inclination into account [2]. Substantial research has been done regarding the different bearing capacity factors of this equation. Most discussion regards the bearing capacity factor  $N_\gamma$ . In several international codes and guidelines, like the Dutch Code [2], Eurocode 7 (EC7) [3] and American Association of State Highway and Transportation Officials (ASHTOO) [4], the factor  $N_\gamma$  is determined according to:

$$N_\gamma = 2(N_q - 1) \tan(\varphi') \quad (2)$$

In which:

$N_\gamma$  = bearing capacity factors for the influence of the self weight of the subsoil [-]  
 $N_q$  = bearing capacity factor for the influence of a surcharge load adjacent to the footing [-]  
 $\varphi'$  = effective angle of internal friction [°]

Results of recent studies indicate that the bearing capacity factor  $N_\gamma$  given in these codes may be too optimistic. From numerical studies an alternative bearing capacity factor has been determined [5]:

$$N_\gamma \approx \exp((\pi + 3\pi^2 \tan(\varphi')) / 6) \tan(\varphi')^{2\pi/5} \quad (3)$$

The calculation results obtained with this bearing capacity factor were verified with the software program LimitState:GEO. Since the results were comparable, it was decided to use equation (3) for the calculations of the bearing capacity for this project. This resulted in a +/- 15% lower ultimate bearing capacity compared to the calculation for which  $N_\gamma$  was determined according to equation (2).

For the determination of the bearing capacity a sensitivity calculation was performed. From this it could be concluded that the angle of internal friction and depth of embedment had a major impact on the calculated bearing capacity. Lowering the friction angle of the first sand layer with one degree or lowering the embedment depth with one meter reduced the bearing capacity with respectively +/- 12 and 8%. This sensitivity was considered for the determination of the characteristic parameter values.

#### 3.2 Undrained bearing capacity

According to the Dutch Code [2] for undrained situation a 'punch' mechanism should be checked. Punch may occur if a cohesive layer is present within the influence depth. For this calculation the foundation load should be placed on top of the cohesive layer, taking into account a load distribution at an angle of 8° to the vertical direction. Furthermore, the cohesive layer is assumed to be infinitely thick in [2].

For thin cohesive layers however, this approach is conservative as the slip circle cannot develop fully within the clay. This effect has been investigated by several researchers, see e.g. [6]. For a thin clay layer underlain by a much stronger sand layer this effect can be taken into account by adopting a higher bearing capacity

factor if the thickness of the cohesive layer is smaller than half the foundation width:

$$\begin{aligned} N_m &= B/2H + \pi + 1 && \text{for } H < 1/2 B \\ N_m &= \pi + 2 && \text{for } H > 1/2 B \end{aligned} \quad (4)$$

In which:

$N_m$  = bearing capacity factor [-]  
 $B$  = width of the foundation [m]  
 $H$  = thickness of the cohesive layer [m]

The calculation results obtained with this bearing capacity factor were verified with 2D FEM calculations with the software program Plaxis. Since the results were comparable, it was decided to use equation (4) for the calculations of the bearing capacity for this project. Taking the influence of the limited thickness of the deep clay layer into account, a higher ultimate bearing capacity for this mechanism of +/- 50% compared to the calculation according to the Dutch code [2].

## 4 DEFORMATION ANALYSIS

### 4.1 General

During the design process it was recognised that deformations of the foundation have a large influence on the design and construction of the superstructure, especially for the mechanical and structural design. Due to the large ratio between the height of the pylons and the width of the foundation, a small rotation of the foundation base results in a large deflection of the pylons heads. This can have a large influence on the design of the superstructure.

In order to determine safe tolerances which are taken into account by the other design disciplines, a thorough deformation analysis was performed.

### 4.2 Deterministic settlement analysis

First step in the deformation analysis was to perform 'best estimate' deformation calculations. In the early design stages analytical 2D settlement

calculations were performed. In the detail design phase additional 3D FEM calculations with the Hardening Soil Small Strain model were performed. The software program Plaxis was used for these calculations.

The foundation pressures for the main piers of the bridge are about 500 to 700 kPa. The calculated 'best estimate' settlements of the foundation footings are about 10 to 25 cm. For the rotations values in the order of magnitude of 1E-3 were calculated.

In general soil deformations are hard to predict accurately, since a lot of uncertainties are present. To get a better understanding regarding subsoil uncertainties, a sensitivity analysis was performed. The influence of variations in OCR, (virgin) stiffness and interpolation of the thickness of the deep clay layer between the soil investigation points were considered.

From the sensitivity analysis it could be concluded that the variation in calculated average settlement was about 25% for the different subsoil scenario's. Especially the uncertainty in OCR had a major impact on the calculated settlements. The calculated variation in rotation was small, compared to the variation in average settlement.

### 4.3 Probabilistic settlement analysis

Since the deformations of the foundation have a large influence on the superstructure a quantitative risk analysis was performed. Therefore the probability of exceedance of a certain design rotation which was taken into account for the superstructure had to be determined. For this a probabilistic model was made. This model is described in this paragraph and figure 2.

#### 4.3.1 Soil-structure interaction

The foundation has been modelled as an infinitely stiff foundation block, supported by linear elastic (stochastic) springs at a mutual distance of about 3 m. Since the foundation consists of a massive concrete block with a thickness of about 20 m the assumption of a stiff foundation is reasonable.

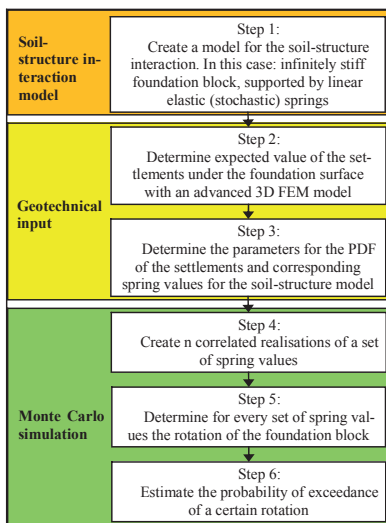


Figure 2. Flow chart probabilistic settlement model

For the PDF of the settlements a lognormal distribution was used. The standard deviation was determined on the assumption of 30% inaccuracy of the settlement calculations. That is; there is a probability of about 5% that the settlements will be 30% larger than the calculated average settlements. This a generally applied rule of thumb in the Netherlands and corresponds to a coefficient of variation of about 0.18. The expected value of the settlements were determined with an advanced 3D FEM model.

The values of the soil springs are spatially correlated. This effect was captured by the use of an exponential spatial correlation function [7]:

$$\rho = \exp(-d / L_c) \quad (6)$$

In which:

$\rho$  = correlation coefficient between the stiffness of two springs [-]  
 $d$  = distance between two springs [m]  
 $L_c$  = horizontal correlation length [m]

Since not enough data was available to determine the correlation length, a conservative estimate was made based on values known from literature. The correlation length generally ranges between 20 and 100 m [8], [9], [10]. Due to the relatively heterogenic subsoil a value of 20 m was used. This also turned out to be a governing value for the calculated rotation.

#### 4.3.2 Monte Carlo simulation

For the Monte Carlo simulation 1E6 simulations were performed. In this way probabilities as small as 1E-3 could be calculated with a relative error of about 5%, which was acceptable for this study.

For every simulation a set of spring values was generated. With the soil-structure interaction model the equilibrium rotation and (average) settlement was calculated for every set of springs. The probability of exceedance for a certain rotation can be estimated by:

$$P(\theta > \theta) \approx n_{(\theta > \theta)} / n \quad (7)$$

In which:

$P(\theta > \theta)$  = exceedance probability of rotation  $\theta$  [-]  
 $n_{(\theta > \theta)}$  = number of simulations for which the calculated rotation is larger than the reference rotation [-]  
 $n$  = total number of simulations [-]

#### 4.3.3 Results

The result of the analysis is presented in figure 2.

The results for pier 30 and 50 are almost equal because the calculated deformations with the FEM model are also almost equal for these piers. From figure 2 it can be seen that larger average settlements result in larger rotations (compare the results of pier 30 or 50 with pier 40), which is reasonable.

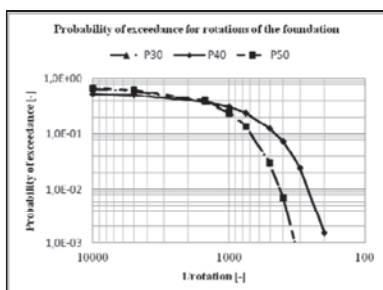


Figure 2. Results Probabilistic deformation analysis. Note that the results for P30 and P50 are almost equal

Based on the calculated probability of exceedance of a certain rotation, safe boundary conditions for the other design disciplines could be determined. During construction the deformations will be monitored and control measures can be applied if necessary. The monitoring and control measures are not discussed in this paper, since the construction of the piers is not started yet.

## CONCLUSIONS

The following conclusions for the geotechnical design of the main piers of the new Botlek bridge can be drawn:

- For this project the preconsolidation stress of the deep clay layer could not be reproduced from laboratory tests, most likely due to relaxation of the samples. Correlation with in-situ measured cone resistance however resulted in reasonable estimates for this important parameter, which corresponded well with experience in the region and geological information.
- A lot of discussion regarding the bearing capacity factor  $N_v$  has been found in literature. From the latest insights the factor presented in several international codes and guidelines may give too optimistic values for this parameter.

- According to the Dutch Code for undrained situation a ‘punch’ mechanism should be checked. In this calculation relatively thin cohesive layers below a granular top layer should be assumed to be infinitely thick. Taking into account the real thickness of the cohesive layer can be done relatively easy and results in more realistic values for the bearing capacity.
- Despite extensive soil investigation, laboratory tests and advanced soil models, prediction of soil deformation behaviour is still known to be relatively uncertain. Quantitative risk analysis can be a useful tool to deal with this uncertainty. In this case soil deformations had a major impact on a critical design aspect, that is the rotation of a large foundation footing. Use of a rather simple stochastic subsoil model made it possible to make a quantitative risk analysis in order to deal with this uncertainty.

## REFERENCES

- [1] Lunne et al., *Cone Penetration Testing in Geotechnical Practice*, Blackpool Typesetting Services Limited, UK, 1997.
- [2] NEN 6744:2007, *Geotechnics – Calculation method for shallow foundations*, Nederlands Normalisatie-instituut, Delft, 2007
- [3] NEN-EN 1997-1:2005, *Eurocode 7: Geotechnisch ontwerp Deel 1: Algemene regels*, Nederlands Normalisatie-instituut, Delft, 2005
- [4] Robert E. Kimmerling, *Geotechnical Engineering Circular No. 6 – Shallow foundations*, PanGEO Inc., Seattle, 2002
- [5] M. Hjjaj et al., *Numerical limit analysis solutions for the bearing capacity factor*, Ny, Civil, Surveying and Environmental Engineering Department, University of Newcastle, Australia, 2004.
- [6] Hans F. Winterkorn et al., *Foundation Engineering Handbook*, Van Nostrand-Reinhold, New York, 1975.
- [7] D. Breyse et al., A generic approach to soil-structure interaction considering the effects of soil heterogeneity, *Geotechnique* 54 (2004), 143–150.
- [8] Don J. DeGroot et al., Estimating Autovariance of In-Situ Soil Properties, *ASCE Journal Geotechnical Engineering* 119 (1993), 147–166.
- [9] TAW, *Technisch Rapport Waterkerende Grondconstructies*, Technische Adviescommissie voor de Waterkeringen, Den Haag, 2001.
- [10] S.H.L.L. Grijtjers, *Blijvend Vlakke Wegen*, Delft Cluster, Delft, 2009.

# Lime-treatment of sand improved by bentonite addition

Mir Amid Hashemi<sup>1</sup>, Nadia Zine, Thierry J. Massart, Jean-Claude Verbrugge and Bertrand François  
*Université Libre de Bruxelles*

## ABSTRACT

Lime treatment is an efficient way to stabilize soils. Its efficiency lies in the low quantity of lime addition and the ecological advantage related to the use of the soil already in place without requiring soil replacement. Lime mostly reacts with the clay and silt fraction of the soil while it does not stabilize a pure sand for which cement treatment is often more adapted. However, the carbon equivalent of cement is higher and stabilization requires more quantity of cement than lime. It is believed that a very low clay content can be enough to drastically increase the properties of a sandy soil by lime treatment. Hence, adding a low quantity of clayey materials in addition to lime can make sand stabilization possible. In this context, this paper presents the results of an experimental program carried out on different sand-bentonite mixtures treated with lime and then compacted under the optimum Proctor conditions. Lime-treated soils have been compressed under uniaxial conditions at different curing times. The results show that the unconfined compressive strength (UCS) of lime-treated soils is considerably increased because of a low content of bentonite added in a pure sand. Also, beyond a given bentonite content, the soil strength starts decreasing when bentonite is further added. This study shows that an optimum value of bentonite content that induces a maximum compressive strength can be obtained. However this optimum value of bentonite content seems to depend on the considered curing time.

Keywords: Lime, Stabilization, Bentonite, Mixture

## 1 INTRODUCTION

Clay soils can be stabilized by the addition of small percentages, by weight, of lime. Its efficiency lies in the low quantity of lime addition and the related ecological advantage because it uses the soil already in place without requiring

soil replacement. Lime treatment has its effect on soil at two different levels. First, lime reacts quickly with clay by modifying its structure. It allows the clay minerals to merge and form bigger aggregates (Little, 1995). The second effect is soil stabilization. Long term pozzolanic reactions take place after soil modification (Eades, 1962). CSH (Calcium Silicate Hydrate) and CAH (Calcium Aluminate Hydrate) formations

---

<sup>1</sup> *Mir Amid Hashemi, Université Libre de Bruxelles, CP 194/2, 87, Av. Buyl, 1050 Bruxelles, Belgium  
mihashem@ulb.ac.be*

from pozzolanic reactions improve the soil mechanical properties. In clayey soils treated with lime, the reaction takes place between the calcium of the lime and the silicates and aluminates of the clay minerals. However, the reaction is slow because it requires the dissolution of clay minerals into silicium and aluminium ions. The dissolution is possible only at high alkaline solutions ( $\text{pH} > 10$ ) (Keller, 1964). Research on soil stabilization was active during the last decades. (Estéoule and Perret, 1979) and (De Bel, 2008) observed an increase on the unconfined compressive strength (UCS) in phases as a function of time. Many important parameters influence soil stabilization, such as water content and dry density of soil (Locat et. al., 1990). Also, higher temperatures increase the speed of the reaction (Estéoule and Perret, 1979), (De Bel, 2008). Conversely organic matter decreases the efficiency of lime (Locat et. al., 1990). In addition, the clay mineral type is an important parameter of soil stabilization (Bell, 1996). Montmorillonite, for example, has a better efficiency for lime adsorption than kaolinite. Consequently, CEC value is an important factor to be considered. On the other hand, a major advantage of lime is that its production, compared to cement production, releases less carbon dioxide. Consequently, it becomes more ecologically-efficient to use lime for soil stabilization if time is not an important factor. However, sandy soils cannot be treated in the same way. These are usually treated with cement (NRS, 1969).

The idea of the present study is to make lime stabilization possible with sand by adding clay minerals. This paper contributes to the understanding of the effect of a small amount of bentonite on the efficiency of sandy soils treated with lime. In the present work, different proportions of sand-bentonite mixtures have been studied. Therefore, two series of tests have been carried out. The first series consist of investigating the properties of sand-bentonite mixtures at high bentonite content (HBC). Three different compositions have been chosen for unconfined compression tests: 30%, 45% and 60% bentonite mixed with 70%, 55% and 40% sand respectively. A second series of tests have been carried out at lower bentonite contents (LBC): 5%, 10%,

15% and 20% in weight of bentonite and respectively 95%, 90%, 85%, 80% in weight of sand.

## 2 METHODOLOGY

### 2.1 Soil materials

The sand used in the experience is homometric with a  $D_{50}$  of  $260\mu\text{m}$  (i.e. the particles have all more or less the same size). The reason for taking homometric sand is to have the simplest sand possible and the easiest to consider in subsequent theoretical and numerical modeling. It corresponds to the skeleton of the mixture. The second part of the mixture is bentonite. This part stands for the clayey cohesive matrix that reacts with lime. Bentonite is taken because of its high reactivity with lime (principally montmorillonite), its cheapness and its availability in the market. Since sodium bentonite is known to have a very high swelling index, calcium bentonite is thus chosen to avoid any excessive swelling upon wetting ( $7\text{ml}/2\text{g}$ ). It has 65% of fine particles ( $< 2\mu\text{m}$ ), 28% silt ( $2\mu\text{m} < D < 67\mu\text{m}$ ) and 7% sand ( $> 67\mu\text{m}$ ).

### 2.2 Proctor Compaction (ASTM D-3668)

In order to match in situ field conditions, tested samples should be prepared at 98.5% of the Normal Proctor Optimum (OPN) density. Consequently, a preliminary step before sample preparation is the determination of the Optimum Proctor Curve. The soil is mixed by hand with a precise lime quantity. The lime quantity has been calculated according to the Eades & Grim procedure (ASTM D-6276) (Eades and Grim, 1966). It has been decided to add 1% lime for the LBC soils; 2% for the HBC soils and 3% for the pure bentonite. Distilled water is poured at different moisture contents. Finally, the wet soil is put in a plastic bag to mellow for 24 hours at  $20^\circ\text{C}$ . After 24h, compaction takes place. The results give the Normal Proctor Optimum density and the Optimum moisture content to use for the samples preparation.

### 2.3 Unconfined compression test (ASTM D-5102)

Unconfined compression test allows measuring both compression resistance and stiffness of the mixtures. Five samples of each composition and for each curing time have been prepared at 98.5% OPN according to the same procedure as Proctor. Their dimensions are of 70mm length and 36mm diameter. In order to avoid any exchange with the outside, the sample is protected by a plastic film, an aluminum film and a layer of paraffin. The samples are then put at 20°C and stay for curing. Afterward, unconfined compression tests are performed to determine the force displacement curve and obtain the UCS.

## 3 RESULTS

### 3.1 Proctor Optima

Based on (Kenney et. al., 1992), (Ferber, 2005), the studied mixtures of sand and bentonite have all a maximum optimum dry density at a known composition which is higher than the optimum dry density of sand and bentonite taken separately. Proctor tests for our compositions have also been carried out to point out this property for the lime treated mixtures. Results in Figure 1 shows that there exists a mixture with the highest Normal Proctor Optimum: the mixture with 10% bentonite. It reaches a density of 17.3kN/m<sup>3</sup>. Dry density reached from Proctor compaction of pure sand is of course higher than in the case of pure bentonite. However, the addition of a small amount of bentonite in pure sand enhances the obtained optimum dry density, because fine particles fill the macro voids between sand particles.

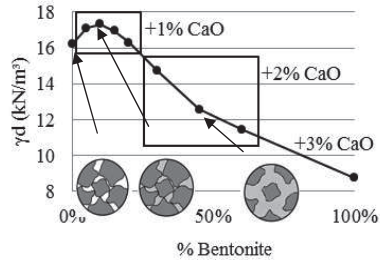


Figure 1. Normal Proctor Optimum of mixtures in function of their bentonite content

However, if too much bentonite is added, clay starts to separate the sand particles from each other which progressively reduces the resulting dry density (cf. Figure 1). For similar sand-bentonite mixtures, (Kenney et. al., 1992), (Sivapullaiah et. al., 1998) and (Ferber, 2005) obtained a maximum dry density at around 20% of bentonite. In our case, the optimal bentonite content seems a bit lower. It may be explained by the fact that the soil is treated. So the treated clay aggregates fill more rapidly the voids hence they are larger.

### 3.2 Unconfined compression tests for high bentonite content mixtures

The UCS of HBC mixtures all treated with 2% of lime has been evaluated at different curing times: 7, 14, 28, 56 days. An untreated mixture (referred as curing time 0) has also been tested for each composition. Figure 2 shows the UCS for HBC mixtures, in function of the curing time. The symbols show the exact value of each sample and the lines represent their mean value for each curing time. As expected, UCS increases with time. More striking is the fact that the mixture at 30% bentonite is more resistant than the others. After 56 days, its UCS is 350% higher.

### 3.3 Unconfined compression tests for low bentonite content mixtures

Mixtures at LBC are also investigated. Fig. 3 shows the evolution of the UCS of LBC mixtures. The composition with the highest UCS depends on the curing time. At the beginning (i.e. 7 to 14 days), the mixture with 20% of bentonite gives the best UCS but at 28 and 56 days, the mixture at 15% has the maximum value. Finally, after 112 days, the mixture of 10% overtakes all the previous mixtures and has the maximum UCS. All the LBC mixtures have been treated equally at 1% of lime as specified in the Eades & Grim test. As time goes by, the optimal composition goes further and further on the lower bentonite content mixtures. Figure 4 shows another view of this phenomenon. The optimum mixture at 7 days is at 20% but at 56 days, the optimum at 1% lime is at 15%. It is also shown in Figure 4 that after 7 days (short period of curing time), both 1% lime and 2% lime curves are linked to one continuous curve. Thus, at short time period, the UCS values for all 6 mixtures follow one curve because the lime content added has been calculated following the Eades & Grim procedure which is consequently sufficient to stabilize the soil at short term. However, this continuity is broken at longer curing times (cf. Figure 4). A discontinuity is observed between the curves at 1% and 2% of lime, which could indicate that the Eades & Grim procedure does not necessarily give the best results for soil stabilization.

### 3.4 Lime consumption

A complementary test, the Leduc Method (Perret, 1979), has also been carried out. The goal is to determine the lime consumption of the samples in function of curing time. The Fig. 5 shows the amount of lime still left in the soil samples in function of curing time. The HBC mixtures have a higher value of lime availability because they have been treated with 2% lime as opposed to the LBC mixtures treated at 1% lime. These results show two different conclusions.

First, in each two series (HBC & LBC), the lime consumption of the highest bentonite content decreases more rapidly than the two others. The mixture at 60% bentonite has reacted more

quickly with lime than the mixture at 45% and 30%. For the LBC the results show the same property. The mixture at 20% bentonite consumes the lime faster than the mixtures at 15% and 10%. The lime reacts faster in an environment containing more bentonite.

Second, for LBC, the UCS of the mixture at 10% continues to increase at long curing time whereas the other mixtures reach a constant value (Fig. 3). This is consistent with the lime consumption (Fig. 5). The decrease of lime content is important for the 10% bentonite mixture between 28 and 112 days. On the other hand, for the two other mixtures, the lime consumption seems to have stabilized after 56 days. The quantity of lime has thus not been sufficient for mixtures at 15% and 20% bentonite. Both UCS stabilization for mixtures at 15% and 20% of bentonite after 56 days and UCS increase at HBC at 56 days show that if the 15% and 20% bentonite mixtures have been treated with more lime, their UCS would be increased.

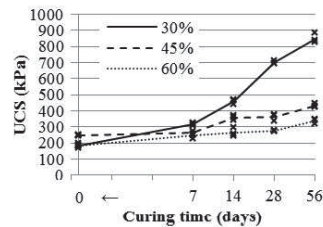


Figure 2. Compression resistance of the mixtures at 30%, 45% and 60% cured with 2% lime

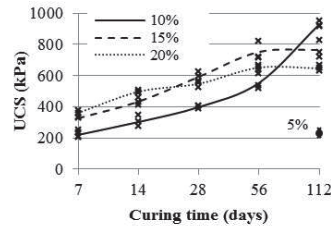


Figure 3. Compression resistance of the mixtures at 5%, 10%, 15% and 20% cured with 1% lime



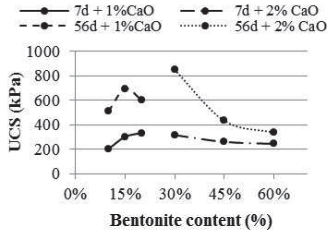


Figure 4. UCS in function of the bentonite content for two curing times

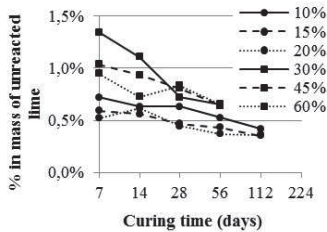


Figure 5. Lime consumption of all the mixtures in function of curing time

### 3.5 Temperature effect

Unconfined compression tests for lower bentonite contents (such as 5%, 10%, 15% and 20% bentonite) show interesting results of optimum displacement in terms of bentonite contents as a function of the curing time. However, to have a more rapid and quicker result, and also to investigate temperature effects, unconfined compression tests have also been carried out for low bentonite contents at 50°C for 7 days and 14 days curing time as shown in Figure 6.

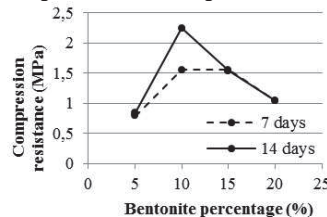


Figure 6. UCS of low bentonite mixtures at 50°C

Apart from the one at 10% bentonite, the mixtures treated at 50°C have already reached their maximal compression resistance after 7 days. At 14 days curing time, the compression resistance for these mixtures still stays the same. However, the mixture at 10% bentonite still evolves after 7 days. Consequently, for the mixtures at 15% and 20% bentonite, all the lime reacted with the soil before 7 days. On the other hand, in the mixture at 10% bentonite, the lime still has an ongoing reaction. Finally, Figure 6 shows a maximum value of compression resistance after 14 days at 50°C for the mixture at 10% bentonite. Further studies and investigations are being done to examine curing time periods at high temperatures shorter than 7 days. One of the advantages with high temperature is that the results come much quicker than the tests done in common room temperature curing times but the results should be taken with extreme caution if comparison has to be done with soil treatment at 20°C since reaction types may change between such different temperatures. ASTM 5102 indeed notes that temperatures higher than 49°C should normally be avoided and the use of a curing temperature of 40°C does not cause any significant additional pozzolanic reactions. Consequently, in order to obtain quicker results, accelerated curing times at a temperature of 38°C recommended in (Mooney and Toohy, 2010) can be considered.

## 4 DISCUSSION & FURTHER STUDY

Reaction between lime and bentonite depends on both quantities in the mixture. If too few quantity of lime is added the reaction prematurely stops. For example, the reaction of 1% lime with 20% bentonite and 80% sand gives a final UCS of approx. 600kPa but a treatment with 2% lime on the 30% bentonite – 70% sand mixture presents an UCS of 850kPa after 56 days and continues to higher values. This leads us to ask which optimal quantity of lime is then needed to fully react with the bentonite in the mixture. This answer needs to first measure the maximum UCS value that can reach the lime treated mixture at “infinite time”. The idea is then to use accele-

rated curing times at 38°C so the maximum value is reached much faster than 20°C treatment.

## 5 CONCLUSION

Sand takes an important part in the process of soil stabilization even if it does not directly react with lime. A soil having an important part of clay does not necessarily behave better than a more sandy soil when treated with lime. This interesting phenomenon gives us a reason to investigate further in detail the interaction between lime treatment and sand. This paper shows that lime treated bentonite behaves like a binder between sand particles. In the first step, three compositions have been studied showing that the one with the lowest bentonite content is the most resistant. This observation led us to investigate lower bentonite contents to find at which mixture composition this UCS is optimal. The results show that the optimal mixture is not the same in function of curing time. At shorter curing times, the mixture at 20% bentonite has the highest UCS, but as curing gets longer, the optimum appears for lower bentonite contents until it arrives at 10% bentonite after 112 days. There are two reasons for this to happen. First, it appeared that the mixture with the highest bentonite content reacts the most rapidly. And second, the amount of lime added in the soil has been taken as the same for the LBC mixtures and is insufficient for an optimal UCS increase in the case of higher bentonite contents. The evolution of this UCS increase is consequently stabilized too prematurely for mixtures at 15% and 20% bentonite. The next step of this research is to calculate the maximum UCS at "infinite" curing time (when no reactives are anymore present). For this, accelerated curing times at the temperature of 38°C are being taken into account.

## 6 REFERENCES

Bell F.G. (1996). Lime stabilization of clay minerals and soils. *Engineering Geology* n°42: 223-237.  
De Bel R., Gomes A.C. and Verbrugge J.C. (2009). Contribution of loamy soil treatment to

improve embankments performance. *Geotechnical Special Publication n°189 ASCE*: 186-191.

Eades J.L. and Grim R.E. (1966). A quick test to determine lime requirements for lime stabilization. *Highway Research Record n°139*: 61-72.

Eades J.L., Nichols F.P. and Grim R.E. (1962). Formation of new minerals with lime stabilization as proven by field experiments in Virginia. *Highway Research Board Bulletin n°335*: 31-39.

Estéoule J. and Perret P. (1979). Etude expérimentale des phénomènes de stabilisation des sols fins par la chaux. *Bull. Liaison Labo. P. et Ch. n°99, janv.-févr.*: 99-109.

Ferber V. (2005). Sensibilité des sols fins compactés à l'humidification : apport d'un modèle de microstructure. *PhD* pp. 283.

Keller W.D. (1964). Process of origin and alteration of clay mineral, *Soil Clay Mineralogy. C.I. Rich, G.W.Kunze (ed.), University of North Carolina*.

Kenney T.C., Van Veen W.A., Swallow M.A. and Sungaila M.A. (1992). Hydraulic conductivity of compacted bentonite-sand mixtures. *Canadian Geotechnical Journal* 29-3, June 1992: 364-374.

Little D.N. (1995). Handbook for stabilization of pavement subgrades and base courses with lime, *Kendall/Hunt Pub. Co. pp. 219*.

Locat J., Bérubé M.A. and Choquette M. (1990). Laboratory investigations on the lime stabilization of sensitive clays: shear strength development, *Can. Geotech. J.* 27: 294-304.

Mooney M.A. and Toohey N.M. (2010). Accelerated curing and strength-modulus correlation for lime-stabilized soils, *Colorado Department of Transportation, Report N° CDOT-2010-1*.

NRS, National Research Council (U.S.), Building Research Advisory Board (1969). Chemical Soil Stabilization, *National Academies, pp. 49*.

Perret P. (1979). Application pratique des nouvelles données expérimentales relatives à la stabilisation des sols fins par la chaux, *Bulletin de Liaison des Laboratoires des Ponts et Chaussées (LCPC) n°99*: 110-118.

# Experimental study of fibre reinforced fly ash behaviour

T. Čiháková<sup>1</sup>

*Czech Technical University in Prague*

## ABSTRACT

The fly ash is a secondary raw material that is produced by the thermal power plants as a by-product of the energy production. Storing the fly ash in the landfills or tailing dams is a large environmental burden. Therefore, we try to reuse the fly ash in the environmental friendly ways. Nowadays, this material is used e.g. as a construction material in earth structures of transport infrastructure. The need for the maximum utilization of the fly ash leads to the efforts to improve geotechnical properties of this material. This paper presents one of the fly ash improvements, which is called "microreinforcement". Small randomly oriented fibres are mixed into the fly ash in microreinforcement method. The paper deals with laboratory testing of this composite material. The consolidation tests and the unconfined compression tests were carried out to identify the deformation properties and the stress-strain behavior. The results from the laboratory testing showed that the inclusion of the fibres in the fly ash changes its behavior and leads to the improvement of geotechnical properties.

Fly ash, Soil reinforcement, Microreinforcement, Fibres, Consolidation test, Unconfined compression test,

## 1 INTRODUCTION

Fly ash is a by-product, which is produced by the thermal power plants. If there is no possibility for reuse of this material, it is necessary to store the fly ash in the landfills that are a large environmental burden. A great emphasis is put on the environmental protection nowadays. Therefore, the reuse of these waste materials is a very topical theme.

This waste material can be used as a building material, e.g. in the construction of the earth structures. This brings not only environmental, but also economical benefits due to the low cost of this material. The need for the maximum utilization of the waste materials in the earth structures leads to the efforts to improve the geotechnical properties of this material. For example, cement or lime stabilization is very often used in the road structures nowadays.

Another possibility how to improve the mechanical and physical properties of the fly ash is the inclusion of randomly oriented small fibers of the synthetic or natural origin. This process is

---

<sup>1</sup> Tereza Čiháková . Czech Technical University in Prague, Thákurova 7, Praha 6, 160 29, tereza.cihakova@fsv.cvut.cz

called "microreinforcement". This method was mainly employed for the reinforcement of the sandy and the fine-grained soils in the past, while the fly ash reinforcement stood in the background. But the present research shows that the fly ash is a very suitable material for this method, mainly due to the fine grains and an easier incorporation of fibers.

The fibre reinforcement method has been known for approximately 30 years. It is obvious that it was inspired by the observations of the vegetation. The penetration of the root system in the soil leads to the improvement of the soil properties. The research has so far concentrated on the laboratory testing of the composite material and the method is not widely used in practice.

## 2 FLY ASH

Fly ash is generated by burning brown coal. It is a non-combustible organic part of the coal, which used to be a part of the plant or used to be floated in to the coal by the groundwater. It should be noted at the beginning that in this paper the term "fly ash" means only the ash produced by the conventional coal combustion. It is not fluidized ash or ash produced by the combustion of solid waste. These materials have different physical and chemical properties.

Fly ash without the addition of the additives is most commonly used in structures in the form of the agglomerate. The agglomerate is a mixture of the fly ash with the water content specified by the compaction test. In this way, the modified fly ash is used e.g. in the construction of the embankments or the dykes, backfills for retaining walls and the recultivation of the landscape which was affected by mining in the past.

## 3 FIBRE REINFORCEMENT

The idea of the soil reinforcement comes from the fact that soils have a relatively good compression strength, while their tensile strength is practically zero [1]. It led to the idea of the addition of another element into the soil, the rein-

forcement, which has good tensile properties. This treatment improves the geotechnical properties that determine the design. Analogy can be certainly found in the reinforcement of the plain concrete by the steel bars.

Mostly steel elements were used as the reinforcement in the past. However, with the great development of the plastics in the sixties of the last century, the steel was fully replaced by the synthetic materials.

The soil reinforcement can be divided into two main directions. The first direction can be described as "macro-reinforcement". In this method, the geosynthetic reinforcement, such as the plastic strips, the geotextiles or the geogrids, is embedded among layers of the natural soil. This method is currently widely used in the construction of the earth structures of the transport structures, dams, retaining structures, etc.

This paper is focused on the second direction, i.e. "micro-reinforcement", in which a small amount (0.5 - 4% by weight of the soil) of the short fibres is mixed with the soil. Again, an analogy can be found with the concrete structures, in which various wires or synthetic fibres are added to the plain concrete and thereby improve its properties.

The material of the fibres is of an either artificial or a natural origin. The fibres of the natural origin can be e.g. of coconut shells, sisal, hemp or jute. As man-made fibres were initially used geogrid or geotextile, which were cut into small pieces. Although with the later development, short fibres, which are the same as for the fibre concrete, began to be used. The material of the used fibres is for example, polypropylene, polyester, polyamide or nylon.

Sandy and fine-grained soils are much more suitable for the reinforcement than the gravel soils, because their average grain size is not significantly larger than the fibre length. The reinforcing of the gravel soil has no effect. On the other hand, clay is not suitable for reinforcing too, because clay tends to make clods. Therefore, the preparation of homogenous mixture is difficult.

#### 4 LABORATORY TESTING

In this paper, the results of laboratory testing are presented. The first test was meant to identify important properties of the unreinforced fly ash such as the grain size distribution and the compaction curve. Then, the fibre reinforced material was tested. The consolidation tests and the unconfined compression tests were carried out at the beginning of the research.

##### 4.1 Materials

The lignite fly ash from the thermal power plant Melnik was chosen. This fly ash is generated by the conventional coal combustion. The specific gravity is  $2040 \text{ kg}\cdot\text{m}^{-3}$ . The grain size distribution can be seen in the figure 1, from which it is obvious that we can talk about the sandy silt as regards the soil classification. Particle size is  $0.01 - 0.5 \text{ mm}$ .

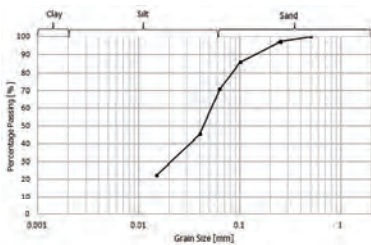


Figure 1. Grain size distribution

It was necessary to determine the compaction curve of the fly ash. Proctor standard tests were performed. The results of the test are in the figure 2. For the optimum moisture content  $w_{\text{opt}} = 22\%$  maximal dry density of fly ash  $\rho_d = 1252 \text{ kg}\cdot\text{m}^{-3}$  was achieved. It was proved that the fly ash is not very sensitive to the changes in the water content.

The polypropylene fibres Forta Ferro were selected, which are originally used for fibre reinforced concrete. The tensile strength is  $620 - 758 \text{ MPa}$ . The fibres were delivered in the length of  $38 \text{ mm}$ . This length was then adjusted to a final

$12 \text{ mm}$ , so that the fibre size matches the size of the prepared samples.

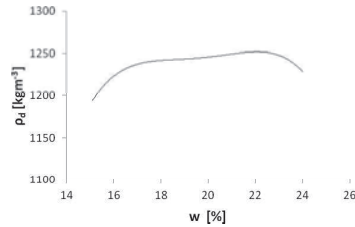


Figure 2. Dry density vs. water content relation

##### 4.2 Sample preparation

The methodology of the mixture preparation is very important. It must be guaranteed that the final material is homogenous, i.e. that the fibres are oriented in different directions. The method of the preparation has to be practicable not only in the laboratory, but also in-situ.

The preparation of a homogeneous mixture of the dry fly ash and the synthetic fibres is very difficult, because the fibres tend to cluster and electrify. Moreover, the fly ash in the dry state is a very dusty material. Therefore, it is advantageous to mix the fly ash with the fibres in wet state and especially in the optimum moisture content. This fact has been confirmed by several research [2], [3].

The preparation of the material is less difficult in the laboratory than in-situ. Fly ash- fibre mixture can be mixed by hand or some common mixing equipment in the laboratory. However, during the construction on the site, the addition of the fibres is more difficult and attention has to be paid to this process.

Laboratory tests were carried out on three different mixtures. In the first mixture fly ash was without the addition of fibres. Thus, it was moisturized on the optimal moisture content  $w_{\text{opt}}=22\%$ . The second mixture consists of the fly ash and 1 % of the fibres Forta Ferro (percentage content is related to the dry weight of the fly ash). It was

proved in several past researches [4], that the inclusion of the fibres does not affect the compaction. Therefore, 22 % of water was added as in the previous mixture. The third tested material consists of fly ash and 2 % of the fibres and the same water content as 1% fibre mixture.



Figure 3. Fly ash – fibre mixture

#### 4.3 Consolidation test

A consolidation test was performed first. The consolidation test examines the deformation behavior of the tested material. The deformation characteristics are important properties which are used in designing earth structures. A moisturized material was compacted in an compaction mould. Samples of cylindrical shape were then cut from the compacted material and were trimmed to the height of an oedometer ring, which is 20 mm high and its area is 40 cm<sup>2</sup>. The sample was set in the oedometer device and a loading started. The loading was applied continuously and after reaching 800 kPa, the test was stopped. The chosen loading speed was 3 kPa /min.

The test results are shown in the picture 4. The strains corresponding pressures 400kPa and 800kPa are given in the table 1. The results from the consolidation tests show that the inclusion increases the settlement, i.e. it worsens the compressibility. The compressibility increased by 13 – 17%. Nevertheless, later unconfined compression tests indicated that, although the defor-

mation is larger, the sample is able to resist greater stress.

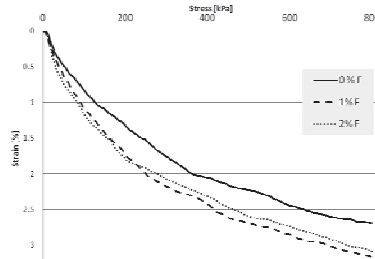


Figure 4. Consolidation curves

Table 1. Results from consolidation tests

	Strain [%]	
	$\sigma = 400 \text{ kPa}$	$\sigma = 800 \text{ kPa}$
Fly ash + 0 % fibres	2.05	2.69
Fly ash + 1 % fibres	2.40 (117%)	3.16 (117%)
Fly ash + 2 % fibres	2.32 (113%)	3.09 (115%)

#### 4.4 Unconfined compression test

The unconfined compression strength (UCS) is also a very important characteristic that is primarily used in the earth structures design. The unconfined compression test is a laboratory test in which a cylindrical sample is stressed by the axial force until failure. UCS is the stress at which failure occurs. Not only stress is recorded, but also the deformation of the sample and therefore the sample strain.

In these tests, cylindrical samples with the diameter of 38 mm and the height of 76 mm were prepared. All the samples were compacted using the hand tamping to the mould of given dimensions. This sample was placed in the press and tested. Three samples at the minimum were always tested for each mixture.

The graphical representation of the test results is in the picture 5. There are 3 curves – for the unreinforced fly ash, the reinforced fly ash by 1% and 2% content of fibres. The graph shows the dependence between the axial stress and the vertical strain.

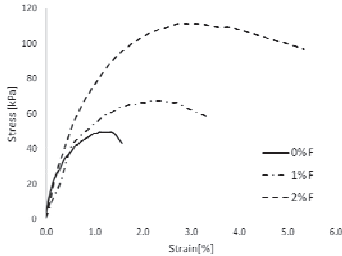


Figure 5. Stress-strain curves from UCS tests

The unreinforced sample reached the maximum axial stress 49.5 kPa at 1% strain. After that slip surface created very quickly and the sample collapsed. The slip surface is shown in the picture 6.

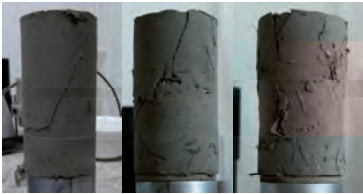


Figure 6. Samples after UCS tests (from left: without fibres, 1% of fibres and 2 % of fibres)

The fly ash reinforced by 1 % of the fibres reached maximum stress 67 kPa at 2.2 % strain. After this stage, the axial stress was decreasing gradually. When the relative deformation reached 3%, a less noticeable slip surface appeared at the top of the sample (figure 6).

The fly ash reinforced by 2 % of fibres reached the maximum value of the stress 111 kPa at 2.72 % strain. The sample was further deforming, but a significant slip surface was not created and the sample didn't fail (figure 6).

The unconfined compression tests proved that the reinforcement has an essential and positive impact on the stress-strain behaviour of the fly ash. The fibre reinforcement leads to increasing UCS (in some cases up to twice as much). However, this tension is achieved at the expense of the larger relative deformation. The main differ-

ence in the behavior of the unreinforced and the reinforced fly ash occurs after reaching the maximum axial stress. While the unreinforced fly ash fails very early after reaching the peak stress, the reinforced specimens are very ductile. Laboratory testing also demonstrated that there is no significant development of the slip surface as in the fly ash without the fibres. This property was observed especially in fly ash with the 2 % of fibres.

## 5 CONCLUSION

The need to maximize the utilization of the thermal power plant waste in the earth structures leads to the need to improve the geotechnical properties of this material. In this paper, the method of the fly ash reinforcement by randomly oriented fibres was presented. The laboratory tests proved that the addition of the short fibres contributes positively to the geotechnical properties of fly ash. Although the consolidation tests have shown that the fibre reinforced fly ash is more compressible than the unreinforced fly ash, the results of the unconfined compression tests demonstrate that the inclusion of the fibres has a positive effect on the stress-strain behaviour. Fibres in the fly ash contribute to the higher unconfined compression strength, the ductile behaviour of this material and the limitation of the slip surface development. This research is at the beginning and the most important tests (such as the triaxial tests) have not been performed yet. Further laboratory test should be also conducted on larger sample (e.g. with 38 mm long fibres), because they characterize the in-situ conditions better. However, it is already apparent that this treatment leads to the improvement of the geotechnical properties of fly ash. In order to start using this material in practice, further research must be also focused on the technology of the preparation of the material in-situ, not only in the laboratory.

#### ACKNOWLEDGEMENT

This work was supported by the Grant Agency of the Czech Technical University in Prague, grant No.SGS12/036/OHK1/1T/11.

#### REFERENCES

- [1] I. Vanicek, M. Vanicek, *Earth Structures in Transport, Water and Environmental Engineering*, Springer-Verlag, New York, 2008.
- [2] H. Rubisarova, F. Kresta, Experimental study of random reinforcement by polymeric fibres, EuroGeo4, available on-line:  
[http://www.arcadisgt.cz/\\_public/upload/datastorage/102010/d5740/rubisarova-kresta-eurogeo4-0302.pdf](http://www.arcadisgt.cz/_public/upload/datastorage/102010/d5740/rubisarova-kresta-eurogeo4-0302.pdf)
- [3] S. R. Kaniraj, V. Gayathri, Geotechnical behavior of fly ash mixed with randomly oriented fiber inclusions, *Geotextiles and Geomembranes* **21** (2003), 123-149.
- [4] R. Kumar, V.K. Kanaujia, D. Chandra, Engineering behavior of fibre-reinforced pond ash and silty sand, *Geosynthetics International* **6** (1999)



# Improvement solutions for very compressible soils

## Case study: Tulcea wastewater treatment plant

C. Burlacu<sup>1</sup>

*Technical University of Civil Engineering Bucharest*

### ABSTRACT

This paper presents the improvement solutions for very compressible soils for the wastewater treatment plant of Tulcea city, Romania. The common settlement calculations on unimproved natural soil, which were performed using the oedometric moduli  $E_{oed}$  between 200 and 300 kPa, indicated that the settlements for the analyzed wastewater treatment plant components were between 15 and 25 cm. On account of the high compressibility of the foundation soil for the analyzed site, methods of improvement by compacted granular material cushions or columns have been proposed, depending on the dimensions, the transmitted loads and the technological role of the wastewater treatment plant components.

Experimental polygons were performed on the site. These consisted in the measurement of the foundation soil settlement under a rigid slab (2x3 m), loaded up to a pressure of about 84kPa in case of polygons 1, 2 and 3 and of 143 kPa in case of polygons 4 and 5. Polygons 2 and 4 were performed on the natural soil in excavations of 1m depth, while polygons 1, 3 and 5 were performed on compacted granular material cushions of 1m thickness, the cushions' base being at 1m depth.

Due to the considerable settlements foreseen and to possible differential settlements, in case of two of the wastewater treatment plant's components, compacted granular material columns were proposed as improvement method and in case of the other components the compacted granular material cushions were chosen for the improvement.

Keywords: Compacted cushions, settlement experimental polygons, very compressible soils.

### 1 INTRODUCTION

Wastewater treatment plant of Tulcea city is going to be situated in the eastern part of the city (Figure 1), on the Sf. Gheorghe arm of Danube river. The site is polygonal shaped and it has a total surface of about 2.9 ha. From the geomorphological point of view, the researched area is situated within Tulcea hills that are part of Do-

brogea de Nord plateau. Tulcea city was formed following the contact between Danube Meadow and the extension of Tulcea hills that dominate the Danube in the south.

The region is characterized by a hilly relief with gentle slopes, crossed by valleys that are quite parallel to the opening towards Danube Meadow.

---

<sup>1</sup> Catalin Burlacu. Technical University of Civil Engineering Bucharest, Lacul Tei Bvd. no. 122-124 sector 2 Bucharest, [cataburlacu@gmail.com](mailto:cataburlacu@gmail.com)



Figure 1. The positioning of the city of Tulcea (image taken from Google Earth).

## 2 GEOTECHNICAL CHARACTERISTICS OF THE FOUNDATION SOIL

Within the limits of the site, there were performed 5 geotechnical boreholes and for each of them medium dynamic penetration tests were conducted. Although at the beginning all the boreholes were scheduled to be carried out up to 20 m depth, F3 borehole was extended in order to reach a high bearing capacity layer. Given the fact that from 23.70 m depth a grey clay layer with plant debris (high content of organic matter) was found, the borehole was limited at 27m depth.

The researched area has a rich hydrographic network, including the Danube River in the north part. The studies carried out by direct observation showed that the field is quite horizontal and that it is bordered by three draining channels. The underground water stabilization level could be observed in a few existing excavation pits (Figure 2).

Following the field and laboratory tests conducted, it was established that, under the 30 cm thick vegetal layer, up to the depth of 2 - 3,5 m, the foundation soil consists of a package of cohesive materials (brown clay – silty clay) having stiff consistency above ground water level and medium – soft consistency under this level. The works also indicated the existence of a layer of silty sand – clayey sand, which has very soft

consistency, up to the maximum depth of 8 m, followed by a package of very uniform brown sand. At the base of the borehole soft consistency brown silty clay was found. Underground water level was found at a depth of 1,4 - 2,3 m, this level stabilizing at 0,7 - 1,8 m depth because of its rising character [2]. Given the soil characteristics (sandy, permeable) and the presence of Danube River near the site, the underground water level is directly influenced by the level of the Danube.



Figure 2. Existing excavation pit.

## 3 FOUNDATION SOLUTIONS

Given the high compressibility of the foundation soil, geotechnical studies carried out on the site recommended, as foundation solutions, the improvement of the soil by compacted granular material columns or cushions.

Depending on the actual ground pressures, and on the dimensions of the objects of the wastewater treatment plant, for some of them the direct foundation on granular material columns was proposed. In case of objects with smaller dimensions and loads, and whose settlement does not influence the technological process of the wastewater treatment plant, a calculation regarding the direct foundation on compacted granular material (crushed stone) cushion was made.

The foundation soil stratification revealed by the geotechnical study was synthesized in two calculation boreholes (FC1 corresponding to geotechnical borehole F4 and F5 and FC2 corresponding to geotechnical borehole F1, F2 and F3) (Figure 4). This stratification (tables 1 and 2) was used for calculations regarding soil improvement.

Table 1. FC 1 log

Layer	Thickness (m)	$\gamma$ (kN/m <sup>3</sup> )	E (MPa)	$\phi$ (°)	c (kPa)
Clayey silt – silty clay	2.35	18.4	6.5	12	25
Sand – silty sand	5.65	17.4	8.0	25	5
Fine sand	9.70	18.0	11.0	30	0
Silty clay	6.00	18.1	4.5	8	17
Clay with plant debris	3.30	15.6	5.0	8	20

Groundwater table: -2.40 m

Table 2. FC 2 log

Layer	Thickness (m)	$\gamma$ (kN/m <sup>3</sup> )	E (MPa)	$\phi$ (°)	c (kPa)
Silty-clay	3.00	18.0	6.5	12	25
Silty (clayey) sand	5.00	17.4	5.0	25	5
Fine sand	10.00	18.0	11.0	30	0
Silty clay	5.70	18.1	4.5	8	17
Clay with plant debris	3.30	15.6	5.0	8	20

Groundwater table: -2.00 m

In the predimensioning stage, in order to determine the thickness of the compacted granular material cushion, settlement calculations were made after the previous determination of the pressures at the cushion inferior limit level. Cushion thickness dimensioning is made by different formulas that take into account the reduction of the pressure exerted on the inferior part of the cushion (Figure 3), up to an acceptable pressure value for the soil under the cushion, taking into account a uniform pressure repartition ( $\alpha$  was considered to be 45°) [1].

At the inferior level, cushions thickness is limited by the ground water level, and the superior level is determined by the technological flow.

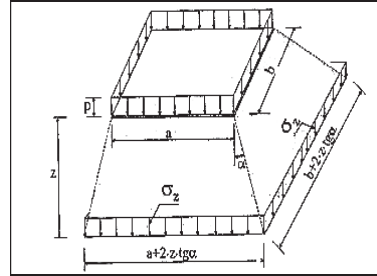


Figure 3. Pressure distribution under a compacted cushion.

Table 3 presents the results of the settlement calculations for the considered cushion thickness.

Table 3. Summarizing table of cushion thickness and estimated settlement

Obj. no.	Object name	Cushion thickness (m)	Estimated settlement (mm)
1	Overflow chamber	1.00	16.2
2	Inlet flow measurement	1.00	
3	Blower station	2.00	90.3
4	Outlet chamber	1.00	15.3
5	Sludge mixing chamber	1.00	38.1
6	Gas flare	1.00	17.8
7	Gas holder	1.50	72.8
8	Sludge storage tank	1.00	55.1
9	Sludge storage area	2.00	199.9
10	Office building	1.50	55.5
11	Gatehouse	1.00	20.6
12	Liquid gas tank	2.50	56.0
13	Biofilter	2.50	126.8

#### 4 EXPERIMENTAL POLYGONS

Experimental polygons (Figure 4) consisted in the measurement of the foundation soil settlement under a rigid slab (2x3 m), loaded up to a pressure of about 84 kPa in case of polygons 1, 2 and 3 and of 143 kPa in case of polygons 4 and 5.

Polygons 1, 3 and 5 were performed on compacted granular material cushions of 1 m thick, the cushions' base being at 1m depth, and the superior level of the cushion being at the natural soil level. Polygons 2 and 4 were performed on the natural soil in excavations of 1m depth.

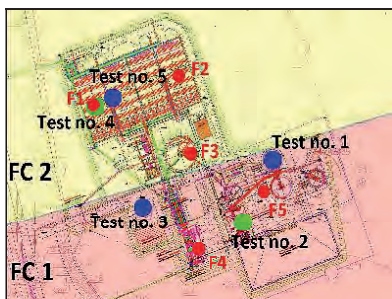


Figure 4. Experimental polygons positioning.

The foundation soil was loaded with concrete slabs having different thicknesses and dimensions (Figure 6). After laying the first concrete slab, the initial level measurements („zero” level) were carried out. After laying each prefabricated element, four level measurements were carried out again at three marks located in three corners of the base slab (Figure 5). After finalizing the loading, readings were made at different time intervals until settlement stabilization. The laying in the most symmetrical manner of the prefabricated elements provided a centric load of the base slab.

In what concerns polygon no. 1 (FC1 area), the settlement measurements indicated final settlements of 11 mm at mark no. 1, 9 mm at mark no. 2 and 11 mm at mark no. 3, with a medium settlement of 10 mm. The value of 11,9 mm obtained following the settlement calculation is very close to the value measured within the experimental polygon.



Figure 5. Settlement measurement mark.



Figure 6. Loading with concrete slabs.

The experimental polygon no. 2 (FC1 area) was conducted at 1 m depth and on natural ground. The medium measured settlement was of 36 mm, while the settlement calculations indicated an estimated settlement of only 10 mm. Given this difference between the measured settlement and the estimated one, it results that the deformation moduli estimated for the layers of the foundation soil were overestimated, the material being actually more compressible. In order to obtain by calculation a settlement comparable to the one measured, deformation moduli obtained between the loads 50-100 kPa were considered.

Experimental polygon no. 3 was located on the administrative building parking lot, on 1 m thick compacted granular material cushion. During excavation, local moistening of the ground was observed, while during the execution of the compacted granular material cushion, waving of the cushion under the compactor cylinder was observed. The relative settlement calculated between points 2 and 3 is 0,0148[-], while the Romanian standard 3300/2-85 allows maximum values of 0,006[-] for buildings whose structure does not bear supplementary efforts caused by uneven settlements.

The experimental polygon no. 4 (FC2 area) was conducted at 1 m depth on natural ground. Settlement measurements were performed until the completion of the loading, and shortly after that the concrete slabs collapsed (Figure 7).



Figure 7. Collapse of the concrete slabs.

The collapse of the structure can be motivated only by an exceeding bearing capacity of the foundation soil. According to the calculation borehole FC2 for the medium-soft- stiff consistency silty clay layer located at -1 m,  $\phi$  was estimated to be  $12^\circ$  and  $c$  was estimated to be 25 kPa. Given the values mentioned above and taking into account a  $2 \times 3$  m foundation, the bearing capacity obtained ( $p_{cr} = 310$  kPa) is much higher than the applied pressure which is 143 kPa. Therefore, these parameters have also been overestimated. Figure 8 presents the correlation between the friction angle and cohesion for which the obtained bearing capacity value is 143 kPa.

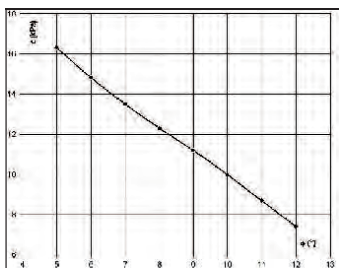


Figure 8.  $\phi - c$  correlation for  $p_{cr} = 143$  kPa.

As in case of polygon no. 2, the settlement estimated by calculation was much smaller than the settlements measured during the test, because of the overestimation of the deformation modulus.

Polygon no. 5 was located nearby the experimental polygon no. 4, on 1 m thick compacted granular material cushion. The settlement estimated by calculation (taking into account the moduli obtained between the loads 50-100 kPa) was of 57 mm, value which is very close to the experimental results.

## 5 CONCLUSIONS

After the 5 experimental polygons were conducted, the values obtained by direct measurement of the settlement were compared with the ones estimated after the settlement calculation.

Given that the measured settlements were higher than the ones initially estimated by calculation, it resulted that deformation moduli of the foundation soil layers were overestimated.

Even under centric load conditions, differential settlements have been recorded.

The cushion effect was significant in case of polygons no. 1 and no. 3, the resulted settlements being of 8-10 mm. On the other hand, on natural ground the settlement resulted was of 36 mm.

In what concerns polygon no. 5, unlike polygon no. 4, due to the cushion, the settlements are significantly reduced and the bearing capacity is no longer exceeded. Nevertheless, significant settlements are obtained under 140 kPa loads.

Due to the significant settlements estimated and to the possibility of differential settlements, in case of two of the wastewater treatment plant objects, compacted granular material columns were proposed as improvement method, while for all the other objects the compacted granular material cushions were recommended.

The settlement of all the technological objects in the wastewater treatment plant will be monitored.

## REFERENCES

- [1] A. Stanciu, *Foundations*, Editura Tehnica, Bucharest, 2006.
- [2] Geotechnical study for the wastewater treatment plant of Tulcea city.
- [3] Technical project for foundation solutions of the wastewater treatment plant of Tulcea city.



# Influence of gravel density in clay reinforced with stone columns. Laboratory study

M. Miranda<sup>1</sup>

*University of Cantabria (Spain)*

## ABSTRACT

Small scale tests were performed in the laboratory to study the influence of the density of columns in the deformation and radial consolidation around end-bearing columns installed in soft soils. For this purpose, the behavior of a horizontal slice of a representative unit cell formed by the column and the surrounding soil was analyzed. Two column densities were tested, with a relative density of  $D_r=100\%$  [1] and  $D_r=30\%$ . Gravel was used for the central column and kaolin clay for the natural soil. Some interesting results are the vertical strain reduction of approximately 15% for columns with  $D_r=30\%$  and 25% for columns with 100%, and the stress concentration factor between 4 and 15 for  $D_r=100\%$  and 3-7 for  $D_r=30\%$ . The experimental results have been compared with some of the theoretical solutions more used in the study of stone columns behavior.

Keywords: Stone column, settlement reduction, unit cell, stress concentration factor, area replacement ratio

## 1 INTRODUCTION

Stone columns are one of the most employed techniques for reinforcing soft soils under structures foundations or embankments. Vertical drains, pre-loading and injections are also frequently used in Spain. The stone columns are cylindrical gravel inclusions in the natural soft soils, usually installed in a uniform grid pattern by vibro-replacement or vibro-displacement. Their main effects are: improvement of soil strength, reduction of settlements, acceleration of consolidation, reduction of potential of liquefaction, and increase of embankments stability.

The behavior of soft soils reinforced with stone columns can be analyzed by some developed solutions, [2,3,4,5]. The semi-empirical-method in

[6] is one of the most used methods in the study of settlements reduction.

This paper presents a laboratory study of deformation and radial consolidation around end-bearing stone columns under distributed vertical load. Under these conditions the unit cell simplification is widely employed, considering a cylinder of soil with a single stone column. Regarding the consolidation decoupling method proposed in [7], may permit the study of only radial drainage. Therefore, the study can be reduced to a horizontal slice that is representative of the unit cell at any depth.

The small scale tests were carried out in a Rowe-Barden cell, instrumented to measure pore pressures and vertical stresses at different distances from the center. The main focus is the

---

<sup>1</sup> University of Cantabria, Avda. de Los Castros, s/n, 39005, Santander, Spain. e-mail: mirandama@unican.es



study of radial consolidation, settlements and stress distribution between columns and soil.

## 2 TESTING PROGRAMME

In practice, column diameters ( $d_c$ ) are between 0.8 and 1.2 m and the effective diameter of the zone influenced by a column ( $d_e$ ) is in the range of 1.5 to 4.5 m. Therefore, the typical diameter ratios  $N = d_e/d_c$  vary between 1.5 and 5.

The tests carried out in this research project are similar to those performed before by the same research group, and presented in [1]. Therefore the test procedure, materials and the equipment are nearly identical, however with the addition of some improvements.

As described above, the model represents one horizontal slice of a unit cell with pure radial drainage and with rigid vertical load applied. The boundary conditions are as follows: i) impervious and rigid base and outer wall, ii) impervious and rigid top surface, iii) free draining column and iv) impervious and rigid top plate.

### 2.1 Equipment

Model tests were performed in a Rowe-Barden cell 254 mm in diameter and 146 mm in height, which provides the previously described conditions. Therefore the effective diameter of the sample is fixed to  $d_e = 254$  mm. Considering the above range values of spacing in real treatments, the horizontal scale factor in the tests is approximately 1/10. The study has been done for two different geometries, diameter ratios of  $N=3$  ( $d_c=63.5$  mm) and  $N=4$  ( $d_c=84.65$  mm), which correspond to area replacement ratios ( $a_r$ ) of 11.11% and 6.25% respectively.

The Rowe-Barden cell was instrumented to measure pore pressure and total vertical stresses at different points under the soil, and total vertical stresses under the column. The distribution of the transducers in the base of the Rowe-Barden was designed according to both test geometries  $N=3$  and  $N=4$ .

Pore pressure is recorded by transducers (PPT) located at the base of the cell at different distances from the center  $r=37, 41, 46, 58, 76$

and 115 mm for  $N=4$  tests and  $r=49, 53, 58, 69, 84.5$  and 115 mm for  $N=3$  tests. Porous bronze discs were settled at the points of measurements and connected to a hole in the base that ends in its lateral wall where the PPT with a de-airing box was installed.

Total stress transducers were installed in the base at the points of measurement. Both, column and soil transducers are 8 mm diameter but their measurement range is different: soil's transducers are in the range 0 to 10 bars whereas those for the column are in 0 to 50 bars. Three total stress transducers were placed under the column at 22.5 mm of the center of the cell. All this instrumentation can be seen in Figure 1.

Vertical displacement was measured using a LVDT (linear variable differential transformer) located on the top of the rigid plate.

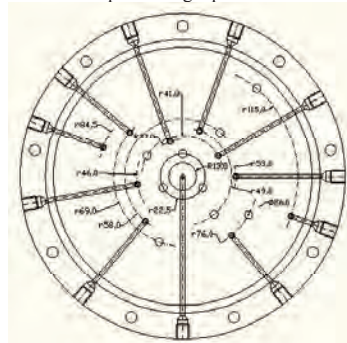


Figure 1. Instrumentation on the base of the Rowe-Barden cell.

### 2.2 Materials

Kaolin was used to represent the soft clayed soil. The properties obtained from an oedometric test and various consolidated-undrained triaxial tests are presented in Table 1.

Table 1. Properties of Kaolin

Parameter	Value
Liquid Limit (%)	73
Plastic Limit (%)	38
$c_v$ ( $\text{cm}^2/\text{s}$ )	$2.5 \cdot 10^{-3}$
Compression index, $C_c$	0.53
Swelling index, $C_s$	0.10
Angle of internal friction, $\phi$ ( $^\circ$ )	26.5



Gravel with a uniform particle size distribution between 4 and 5 mm was used for the stone column. Two different gravel densities were employed in order to study its influence in the treatment of soft soils. In a previous research [1] a first set of trials was performed with a density of  $\gamma = 16.5 \text{ kN/m}^3$  that is similar to that employed in a real treatment. In the present research the maximum and minimum density of the gravel were obtained following the ASTM normative and giving  $\gamma = 16.5 \text{ kN/m}^3$  and  $\gamma = 11.11 \text{ kN/m}^3$  respectively. Finally, a density of  $\gamma = 14 \text{ kN/m}^3$  was chosen for this new analysis in order to compare the results with those obtained in the previous research with  $\gamma = 16.5 \text{ kN/m}^3$ . This new density corresponds to a relative density of  $D_r = 30\%$  whereas the previous one was nearly 100%. Conventional drained triaxial tests were performed to obtain gravel properties in samples with  $\gamma = 14 \text{ kN/m}^3$ , as well as it was done for  $\gamma = 16.5 \text{ kN/m}^3$ . These tests are not considered appropriate for defining the Young modulus of the gravel because the condition of constant horizontal pressure is not representative of the real situation in the column. So that, two tests with zero lateral strain  $K_0$  were performed to obtain the gravel's oedometric modulus. The gravel's angle of internal friction, angle of dilatancy and oedometric modulus are shown in Table 2.

Table 2. Properties of the gravel

	$\phi$ (°)	$\psi$ (°)	$E_m$ (kPa)
$D_r = 100\%$	46	10	39000
$D_r = 30\%$	42	0	16000

### 2.3 Sample preparation

Sample preparation consists of obtaining kaolin consolidated at 100 kPa. This process begins with the mixture of kaolin powder with a content of water of 1.5 times its liquid limit to ensure a homogeneous structure. This slurry is poured into the Rowe-Barden cell, whose lateral contour was previously smeared with grease to reduce the friction between the soil and the cell. The first step of consolidation, up to 50 kPa with large volume changes, is given by means of dead weights with no precise control of vertical strain. After this initial consolidation, the cell is connected to a hydraulic pressure system and the soil

is consolidated under a vertical pressure of 100kPa.

### 2.4 Column installation

Frozen stone columns were used in the tests. This method of column installation does not represent the field column installation; nevertheless it allows the control of the gravel density.

First, the gravel is merely poured into the mould to achieve the density  $\gamma = 14 \text{ kN/m}^3$ , and then it is frozen at  $-20^\circ\text{C}$ . Once the Kaolin is consolidated under 100 kPa, an open-ended steel tube is inserted into the middle of the kaolin sample, assisted with a vertical metallic jack. The soil inside the tube is extracted, and the hole is carefully cleaned. Once the tube is removed a sand layer of 4 mm and a perforated steel plate are placed to avoid direct contact between the gravel and the transducers. The frozen column is placed in the pre-bored whole and left to thaw for 3 hours. An impervious rigid plate is placed on the top of the sample surface. The sample is reconnected to the hydraulic pressure system and consolidated under a load of 100 kPa. Once the sample is consolidated its length is comprised between 65 and 75 mm.

### 2.5 Testing procedure

The tests consist of five steps of equal stress increments of 100 kPa. In each step, the load is applied and drainage is not allowed until the increment of pore pressure reaches the same value as the load increment applied. Then, the drainage is allowed and radial consolidation occurs for 24 hours. This proceeding is employed to capture the initial stages of the consolidation. To avoid problems with the air inside the sample a back pressure of 300 kPa is applied in the whole process. This pressure has been subtracted from all the results presented in this paper.

A total of 7 tests were performed with  $D_r = 30\%$ : three of them with  $N=4$  (numbered 6N4 to 8N4) and four with  $N=3$  (numbered 5N3 to 8N3). The results of these tests are compared with the previous tests with  $D_r = 100\%$  [1], numbered 1N4 to 5N4 and 1N3 to 4N3.

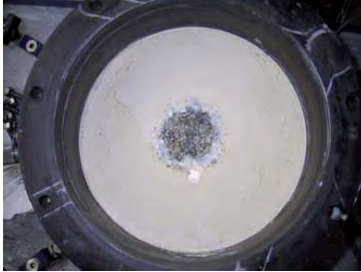


Figure 2. Column-soil sample after being tested

### 3 RESULTS

Pore pressure, vertical stresses and vertical strain were recorded during the five load steps of each test. Results has been obtained in terms of: i) pore pressure dissipation, ii) vertical stresses on the soil and column, and iii) vertical strain reduction. Nevertheless, in this paper results in vertical stresses for geometry  $N=4$  and vertical strains for both geometries will be exclusively presented.

#### 3.1 Vertical stresses

Vertical stresses on the soil and the column are given in Figure 3 and Figure 4 for the 200 to 300 kPa step of test 7N4. Upon application of the undrained load increment, there is an instantaneous increase of stresses on the soil and column. With the drainage closed there is a slight progressive increase in the soil load. This behavior of the soil is accomplished with a decrease in the stresses on the column, consistent with the condition of equilibrium under constant load. After opening the drainage, the stresses near the column decrease, reach a minimum, and then increase towards the final value. At greater distances from the column, the stresses show a monotonic decrease with time, reaching the same final value. Those behaviors are consistent with the consolidation theory where the closest points consolidated faster, and also, a decrease of vertical stress is required to maintain the condition of equal vertical strain. The stresses measured close to the

outer wall are clearly influenced by wall friction with a lower final value (Figure 3).

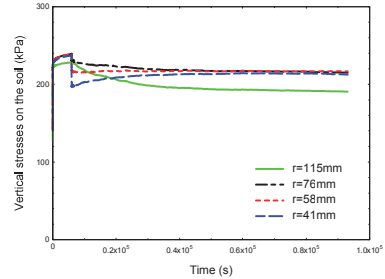


Figure 3. Vertical stresses on the soil at 200-300 kPa load step in 7N4 test

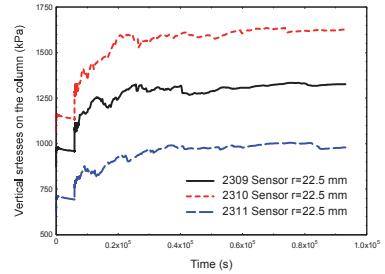


Figure 4. Vertical stresses on the column 200-300 kPa in 7N4 test.

Vertical stresses at the end of each load step in  $N=4$  tests are shown in Table 3 for  $D_r=30\%$  and in Table 4 for  $D_r=100\%$ . Vertical stresses on the column ( $\sigma_{vs}$ ) are smaller for  $D_r=30\%$  tests, which is in agreement with the lower column stiffness. Therefore, the stresses on the soil ( $\sigma_{vc}$ ) are greater in these tests as the soil has to support a higher portion of the load increment.

Table 3. Colum/soil stiffness ratio for different stresses reached on the soil. Test with  $D_r=30\%$ .

Stress (kPa)	$\sigma_{vc}$ (kPa)	$\sigma_{vs}$ (kPa)	$E_s$ (kPa)	$E_{mc}/E_s$
100-200	640-921	69-170	825	20
200-300	921-1415	170-254	1329	12
300-400	1415-1938	245-315	1799	9
400-500	1938-2145	315-387	2277	7
500-600	2145-2403	387-461	2743	6

Table 4. Colum/soil stiffness ratio for different stresses reached on the soil. Test with  $D_r=100\%$

Stress (kPa)	$\sigma_{vc}$ (kPa)	$\sigma_{vs}$ (kPa)	$E_c$ (kPa)	$E_c / E_s$
100-200	1180-218	32-140	633	47
200-300	1640-2775	115-210	1190	25
300-400	1950-3140	185-280	1712	14
400-500	2250-3500	255-350	2256	13
500-600	2490-3865	320-420	2760	11

The stress concentration factor ( $SCF = \Delta\sigma_{vc} / \Delta\sigma_{vs}$ ) at the end of each load step has been calculated. The vertical stress under the column is considered the direct average of measurement in the three transducers under the column, and the vertical stress on the soil as the weighted average of the transducers considering the influence area of each one. The  $SCF$  values are presented in Table 5 for both densities and only for the geometry  $N=4$ .

Table 5. Incremental  $SCF$  at the end of each load step.

Stress (kPa)	$\gamma=16.5\text{kN/m}^3$	
	N4 SCF	N4 SCF
100-200	14.80	6.59
200-300	8.00	6.99
300-400	6.83	5.76
400-500	5.82	3.50
500-600	4.25	3.90

The range of  $SCF$  values is 4-15 for  $D_r = 100\%$  tests and 4-7 for  $D_r = 30\%$  tests. Neglecting the results for the first step, when the soil is overconsolidated, it can be observed that  $SCF$  decreases with the applied vertical stress in both densities. This tendency can be attributed to the decrease in the stiffness ratio between the column and the soil due to the increase of kaolin modulus with pressure (Table 3 for  $D_r=30\%$  and Table 4 for  $D_r=100\%$ ). Moreover, results for the first step show a  $SCF$  value about two times greater for dense column tests than for the loose column ones. Nevertheless, this difference tends to decrease with the applied vertical stress, reaching a similar value in the last load step. This could be attributed to the similar variation in the stiffness ratio between column and soil for each density (Table 3 and Table 4).

In both cases,  $SCF$  values are below those predicted by the simple oedometric approach, where they are equal to the ratio of oedometric modulus of column relative to that of the soil (10-25 in  $D_r=100\%$  and 12 to 6 in  $D_r=30\%$ ).

The values of  $SCF$  are also lower than those predicted in [2] with an elastic solution, what shows that column yielding occurs.

### 3.2 Settlements

Vertical strains were obtained from the LVDT readings. In the results presented next, these strains were calculated in reference to the height of the sample once it is consolidated under 100kPa.

The reduction in vertical strain of the clay reinforced with stone columns is usually expressed as the ratio of vertical strains in test with columns ( $\epsilon_{v,c}$ ) to vertical strain with non-columns ( $\epsilon_{v,\theta}$ ), under the same load, named strain reduction factor ( $\beta = \epsilon_{v,c} / \epsilon_{v,\theta}$ ). This reduction exists because columns are stiffer than soil, which leads to a reduction of vertical strains. Results for both geometries and  $D_r=100\%$  are presented in Table 6 and results for tests with  $D_r=30\%$  are given in Table 7. They show that the strain reduction in tests with geometry  $N=4$  and with  $D_r = 100\%$  is about 30% and for those with  $D_r = 30\%$  is reduced to 15%. These results are in concordance with the column stiffness.

In the same way tests with the dense column and geometry  $N=3$  shown a reduction close to 35% and those with loose gravel column gives a reduction about 30%.

Table 6. Reduction in vertical strain in  $\gamma=16.5\text{kN/m}^3$  tests.

	1N4	2N4	3N4	4N4	1N3	2N3	3N3
$\beta$	0.71	0.74	0.72	0.78	0.66	0.64	0.65

Table 7. Reduction in vertical strain in  $\gamma=14\text{kN/m}^3$  tests.

	6N4	7N4	8N4	5N3	6N3	7N3	8N3
$\beta$	-----	0.84	0.84	-----	0.73	-----	0.71

The reduction of vertical strain is compared in Figure 5 with the semi-empirical method in [6] and with the elastic solution given in [2]. A friction angle of  $42^\circ$  was chosen for the gravel according to triaxial test carried out on loose gravel samples. The strain reduction obtained with the elastic solution is related to a column-soil stiffness ratio of 5, 10 and 20 covering the ranges obtained in the tests.

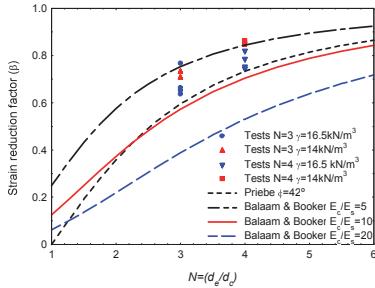


Figure 5. Comparison of the strain reduction factor obtained in the tests with Priebe and Balaam and Booker solution.

A significant difference between the elastic solution and the test results is observed. This is due to the fact that the column's plasticity is not taken into account in the theoretical solutions. Therefore an overestimation is obtained.

#### 4 CONCLUSION

This paper provides an analysis of the behaviour of one soft clay sample reinforced with a stone column. Two different relative densities of the gravel and two different column diameters have been analyzed. Tests were performed in a Rowe-Barden oedometric cell.

Vertical stresses on the soil are higher for  $D_r=30\%$  tests than for  $D_r=100\%$  ones, which is in agreement with the stiffness ratio between the column and soil in each density. The opposite result was obtained for vertical stresses on the column. The stress concentration factor obtained is in the range of 15 to 4, which is far from those predicted by elastic solutions. Plastic strains of the column could be responsible for these differences [3].

The vertical strain results show that vertical compressibility is reduced to approximately 85% for  $D_r=30\%$  and 75% for  $D_r=100\%$  in tests with geometry  $N=4$ . These results show a reduction

of settlements around 10% when the column relative density increases from 30% to 100%. In tests with geometry  $N=3$  the reduction is about 70% and 65% for  $D_r=30\%$  and  $D_r=100\%$  respectively. This reduction results in a decrease of the vertical strain of approximately 10% more when the replacement area increases from 6.25 to 11.11%.

#### ACKNOWLEDGEMENT

This work is part of a research project on "An integrated calculation procedure for stone columns, considering the influence of the method of installation", for the Spanish Ministry of Science and Innovation (Ref: BIA2009-13602)

#### REFERENCES

- [1] Cimentada, A., da Costa, A., Cañizal, J. & Sagaseta, C. Laboratory study on radial consolidation and deformation in clay reinforced with Stone columns. *Canadian Geotechnical Journal* **48** (2011), 1:36-52.
- [2] Balaam, N.P. & Booker, J.R. Analysis of rigid rafts supported by granular piles. *Int. Journal for Numerical and Analytical Methods in Geomechanics* **5** (1981), 379-403.
- [3] Castro, J. & Sagaseta, C. Consolidation around stone columns. Influence of columns deformation. *Int. Journal for Numerical and Analytical Methods in Geomechanics* **33** (2009), 851-877.
- [4] Han, J. & Ye, S.L. A simplified solution for the consolidation rate of stone column reinforced foundations. *Journal of Geotechnical and Geoenvironmental Engineering* **127** (2001), 597-603.
- [5] Pulko, B. and Majes, B. Simple and accurate predictions of settlements of stone column reinforced with soil. In proceedings of the 16<sup>th</sup> International conference on soils Mechanic and Geotechnical Engineering, Osaka, Japan, 12-16 September 2005. Millpress, Amsterdam, the Netherlands. pp. 1401-1404.
- [6] Priebe, H.J. Design of vibro replacement. *Ground engineering* **28** (1995), 31-37.
- [7] Carrillo, N. Simple two and three dimensional cases in the theory of consolidation of soils. *Journal of Mathematical Physics* **21** (1942), 1-5.

# Chemically enhanced drainage of clayey soils by means of guanidinium solutions: Experimental testing and numerical modeling

P. Minder<sup>1</sup>, M. Plötze, A.M. Puzrin  
*Institute for Geotechnical Engineering, ETH Zurich*

## ABSTRACT

Seepage of groundwater in creeping landslides is a key parameter for the creep velocity. Drainage is one of the measures to increase the stability. The in-situ creation of zones of higher permeability as part of a drainage system with increased operating life has a high potential in commercial application.

Permeability tests were performed to investigate the effect of an environmentally compatible organic salt on the hydraulic conductivity of water through smectite bearing clays. The modification by the chemical was found to be persistent due to a strong ion-exchange reaction. Oedometer test and pore size measurements have shown that the newly formed soil structure was stable also under high compressive stresses.

The evolution of the permeable zone during injection of the modified pore fluid was modeled by coupling the chemical processes with the hydro-mechanical behavior of the soil on a micromechanical level. Boundary value problems of the evolving permeable zone during chemical treatment of the soil were solved with a commercial numerical code (COMSOL). The obtained results were compared with available solutions for special cases, such as the non-reactive radial dispersion problem.

Keywords: ground improvement, permeability, chemical-hydraulic coupling.

## 1 INTRODUCTION

Seepage of groundwater in creeping landslides is a key parameter for the creep velocity. A reduction of the water table by means of drainage could increase the overall safety critical slopes. Conventional drainages systems based on drainage pipes are prone to failure due to the ongoing deformation in such unstable slopes. Additionally, the installation of such systems includes temporarily destabilizing interventions and can become critical when the slopes are close to failure. The development of alternative drainage techniques with increased operating life in creeping

landslides has therefore a high potential in commercial application.

The hydraulic conductivity is one of the soil properties highly influenced by chemicals in the pore solution. Large increase can be observed, when fine grained soil is permeated with organic liquids or salt solutions [1]. This has so far been encountered as a negative effect on the performance of hydraulic barriers but has not been adopted in a positive sense to transform soil locally into high permeable zones acting as drainage conduits.

The hydration of cations in the interlayer of smectites causes inner-crystalline swelling. The

---

<sup>1</sup> Corresponding Author. IGT, ETH Zurich, Wolfgang-Pauli-Str. 15, CH-8093 Zürich, pascal.minder@igt.baug.ethz.ch

formation of water shells around these cations depends on the cation itself and on the water content of the clay [2]. The intercalation of organic molecules in the interlayer as well as the exchange with very strong bonding cations can make these modified clay minerals hydrophobic and decreases or even inhibits the water uptake in the interlayer [3].

For fine grained soils, both theoretical and experimental studies have pointed out a high dependency of permeability on the pore fluid. Major influence factors are the type of liquid (mainly via its dielectric constant), type of dissolved salts and ionic strength of the solutes (e.g. [4], [1]). These studies were often carried out in the context of hydraulic barrier design and containment of nuclear wastes, where the reduction was an unintended and dangerous effect caused by contaminants and leachates.

Mineralogical investigations indicated that guanidinium cations affect directly the interlayer distance of the stacked sheet-silicate structure of montmorillonite [5]. This strongly binding cation is therefore chosen as a possible chemical agent to increase permeability by inhibition of interlayer swelling.

Modeling of advective flow with a dynamic permeability field was initially performed with discrete interface penetration models [6]. Constitutive modeling of the reasons for the increase of permeability on a micro structural level of the pore system was proposed by [7] and implemented in a coupled one-dimensional transport equation of the chemical [8]. Numerical solutions were obtained using finite difference formulations.

With the goal of purposely creating zones of higher permeability in-situ as part of a drainage system, this paper focuses on the fundamental aspects required in the development of this soil improvement technique. Enhancing soil permeability with chemicals may be accompanied with unexpected side effects such as a deterioration of stiffness and strength. In field applications such mechanical consequences could result in large deformation or failure. The effects on other geotechnical parameters than hydraulic conductivity therefore need to be addressed as well.

In order to upscale the laboratory findings to field conditions numerical modeling of the observed phenomena will play a significant role. In this study preliminary simulations are performed with a commercial FEM-code to tests its suitability of modeling the observed phenomena.

## 2 MATERIALS AND METHODS

In order to assess the mechanisms behind the increase in permeability caused by guanidinium, experiments on three different scales were performed. Mineralogical analyses were carried out to quantify the reaction of the chemical with the clay phase. A closer look on the resulting changes on particle and aggregate scale was taken, to understand the changes in soil fabric and structure. The macroscopic stability of the new features was determined in standard geotechnical tests with the aim of retrieving proper input parameters for the subsequent numerical modeling.

### 2.1 Material

The laboratory tests were carried out on soil samples reconstituted with commercially available, standardized constituents. A commercial Ca-bentonite (Calcigel®, Südchemie, Germany) with a total montmorillonite content of 65% was used as fine grained component. Other occurring mineral phases in this bentonite were quartz, feldspar, kaolinite and mica. During the mineralogical analyses a well-studied Na-Bentonite (MX-80, Amcol, USA) was used for comparison as well. Where appropriate the bentonites were stretched with rounded inert quartz grains (washed Perth sand,  $d_{50} = 0.24$  mm, Cook Industrial Minerals, Australia).

The pore water of the reconstituted samples was prepared with a 0.01 mol/L  $\text{CaCl}_2$  solution as standardized groundwater equivalent.

Guanidine solutions were prepared from analytical grade guanidinium hydrochloride salt ( $\text{C}(\text{NH}_2)_3\text{Cl}$ ,  $\geq 99\%$ , Fluka Analytical) and demineralized water.

## 2.2 Adsorption measurements

Sorption of guanidinium ions on clay surfaces was determined by batch adsorption measurements. Soil samples were suspended in guanidine solutions with different initial concentrations. Guanidine concentrations were measured in the supernatant after the reaction with the clay and compared with the initial concentration. The concentrations were determined with a fluorescent spectrometric method after [9]. The total adsorbed amount of guanidine ions was compared with the cation exchange capacity of the clay measured with Copper-complex method by [10].

The hydration of the inner and outer crystalline clay surfaces was investigated based on the characteristic water vapor adsorption from atmospheres with constant relative humidity ranging from 11% to 85% RH. Dry clay powder was thereby stored above saturated salt solutions at constant temperature until the sample weight was stationary. Both adsorption and desorption paths were measured. All adsorption data is expressed relative to dry weight of the soil at 120 °C.

## 2.3 Investigations on particle scale

Mercury intrusion porosimetry (MIP, PASCAL 240/440, Porotec, Germany) on dry bentonite samples was used to quantify the alterations of the pores system due to guanidine treatment. Homo-ionic bentonites were produced by saturation with 1.0 mol/L calcium and guanidinium solutions, respectively. The resulting soils were washed with demineralized water to remove excess ions and to avoid their precipitation in the inter-particle pore space. Images of the particles and aggregates in this suspension were taken with a scanning electron microscope. Compacted soil samples were then reconstituted from the washed material at a water content slightly above to their liquid limit. Crack-free pieces of the slowly dried samples were subjected to vacuum evacuation for 2 h prior to mercury intrusion.

## 2.4 Macroscopic tests

Oedometric tests on compacted mixtures of bentonite (40%) and quartz sand (60%) were carried out to assess both the increase in permeability

and the effects on stiffness due to the chemical treatment. Samples were reconstituted with different chemical composition of the pore water - either artificial groundwater or guanidine solutions - and subsequently tested according to the procedure given in ASTM D2435-04.

The same mixtures were used in constant head permeameter tests, where the permeability was tested on both modified and unmodified soil. Additionally the temporal evolution of the average permeability was registered during flow-through treatment starting with unmodified soil.

## 2.5 Numerical modeling

Two modules of the commercial finite element code COMSOL Multiphysics V. 4.2 were used to simulate the propagation of guanidinium and its permeability improvement in soil.

The built in features for saturated flow in porous media (“Darcy’s law”) and advective-diffusive transport (“Species transport in porous media”) were coupled via a concentration dependent hydraulic conductivity. One dimensional and radial symmetric transport of the chemical was considered.

# 3 RESULTS AND DISCUSSION

## 3.1 Mineralogical indications for the underlying chemical process

Guanidine is adsorbed up to a certain saturation concentration (Figure 1). The well-fitting Langmuir sorption isotherm ( $R^2=0.94$ ) indicates a limited amount of adsorption sites with a saturation constant of 6.1 mg/g. Based on the cation exchange capacity of equivalently 7.4 mg/g it can be concluded, that more than 80% of the cations in the clay phase are readily exchanged by simple suspension in guanidine solutions.

Smectite clays are generally capable of adsorbing large amount of water from humid air due to interlayer hydration and capillary condensation. The measured curves for the unmodified bentonites (Figure 2) are in good agreement with published data [11] and show the typical features such as the hysteresis upon desorption and step-

wise dehydration of sodium cations. Modified bentonites however are much less sensitive to air moisture and have reduced hysteresis during desorption.

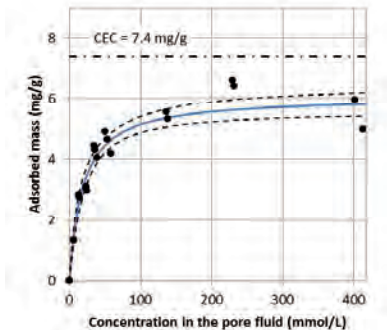


Figure 1. Sorption of guanidinium ions. The dash dotted line indicates the theoretical maximum adsorption based on the cation exchange capacity. The Langmuir sorption isotherm (full line) with 95% confidence bands is shown for the best fit parameter.

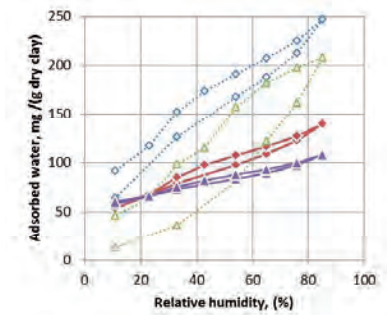


Figure 2. Influence of guanidine modification on water adsorption of Ca-bentonite (square) and Na-bentonite (triangle). Natural clays (dotted lines) show a high sensitivity against relative humidity and a pronounced hysteresis. Both phenomena are strongly reduced for the modified forms (full lines).

### 3.2 Particles and pores

During sample preparation of modified bentonites, a granular, non-plastic behaviour was ob-

served. Microscopic images (Figure 3) revealed that in suspension the clay fraction aggregated upon addition of guanidinium.

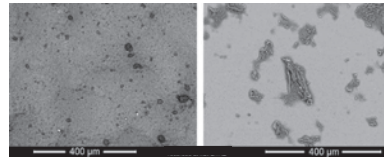


Figure 3. SEM-Images of dried bentonite suspensions after washing with demineralized water. The exposure to guanidinium ions (right) lead to the formation aggregates, whereas the calcium form remains finely dispersed (left).

Compacted samples were analysed with MIP in order to check whether these aggregates are capable of maintaining an open pore structure. Considerable changes in the pore system were detected. Even though the unmodified soil was prepared at a higher water content ( $w_{L,Ca} = 102\%$ ) the modified bentonite ( $w_{L,Gnd} = 64\%$ ) features a larger accessible pore volume (Figure 4). The largest contribution to the additional pore volume stems from pores with average radii of  $1 \mu\text{m}$ . The total pore volume of these larger pores increases from  $42 \text{ mm}^3/\text{g}$  to  $234 \text{ mm}^3/\text{g}$ . The volume in the smaller pore fraction (radius  $< 0.1 \mu\text{m}$ ) however is reduced from  $62 \text{ mm}^3/\text{g}$  to  $56 \text{ mm}^3/\text{g}$ .

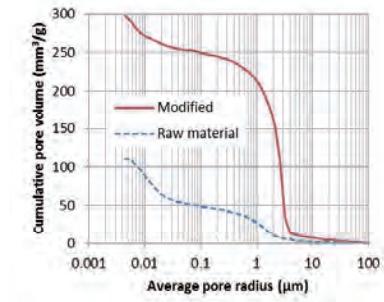


Figure 4. Cumulative pore size distribution of two bentonite samples measured with mercury intrusion porosimetry.



### 3.3 Geotechnical parameters

Oedometer tests on a triplicates series were analysed with respect to changes in stiffness. The difference between unmodified and natural soil was in the order of the standard deviation for initial loading as well as for unloading/reloading (Table 1). Additionally, the evaluation of the time-settlement curve based on the Terzaghi theory for one dimensional consolidation provided hydraulic conductivities at different stress levels. Figure 5 clearly shows, that despite vertical stresses of up to 800 kPa, the increased permeability is maintained also after compaction.

Table 1. Stiffness parameters averaged over three samples and three load steps each. Standard deviation is given in parenthesis.

	Raw material	Modified
Compression index $C_c$	0.38 (0.04)	0.35 (0.02)
Swelling index $C_s$	0.09 (0.03)	0.11 (0.03)

By means of permeameter tests the magnitude of possible improvement in smectite soil was determined. By mixing soils with guanidinium solutions an increase of permeability by the factor 30 was achieved (Figure 6). Even when unmodified samples were simply permeated with guanidinium solutions, the average hydraulic conductivity increased one order of magnitude.

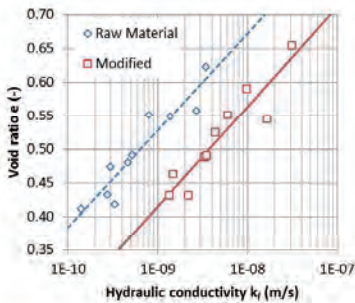


Figure 5. Decrease of hydraulic conductivity during sample compaction (including log-linear regression). For identical void ratio the modified soil is constantly one order of magnitude more permeable.

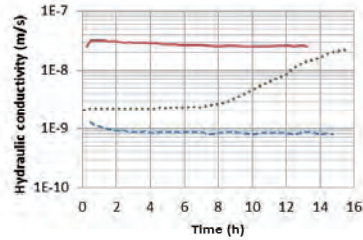


Figure 6. Evolution of hydraulic conductivity during flow through treatment (dotted line). For comparison the data for raw material (dashed line) and reconstituted modified soil samples (full line) are given.

### 3.4 Numerical modeling

For practical application, we should be able to assess consequences of the installation of such drainage and its effectiveness. This requires analytical or numerical tools to simulate the chemical drainage phenomenon in real scale problems. Analytical solutions are only available for simple cases of stationary flow fields [12]. In order to simulate non-stationary flow fields during creation of the drain, the numerical code COMSOL was implemented. For stationary flow, numerical solutions are similar to those obtained with the analytical solution (Fig. 7). As is seen, for non-stationary fields the difference in the results cannot be ignored (circles vs. dashed line in Fig. 7).

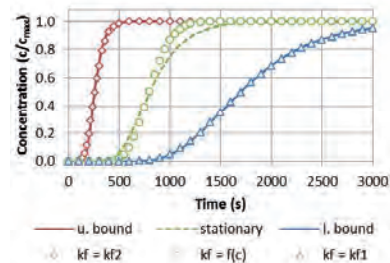


Figure 7. Break-through curves in a radial flow field with variable permeability. Lines are calculated with an analytical solution assuming constant permeability. Symbols represent the numerical data.

In particular, when the analytical tools are used to predict the time required to form a drainage pipe of a certain size, this difference becomes significant. Figure 8 shows that the analytical solutions lead to severe overestimation of this time, i.e. non-stationary flow improves the chemical drainage efficiency.

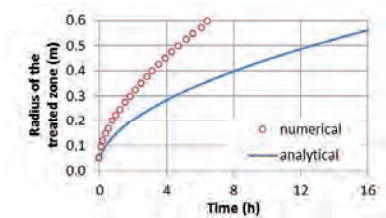


Figure 8. Propagation of the chemical front around a cylindrical injection well. The numerical solution accounts for the accelerated flow due to improved permeability and provides a more accurate prediction than the analytical solutions with stationary flow.

#### 4 CONCLUSION

Based on the experimental work on different scales the following conclusions could be drawn:

The origin of the increase in permeability due to guanidinium ions lies in its fixation to the inner and outer clay surfaces due to a cation exchange reaction. This fixation results in a strong inhibition of the water uptake into the interlayer space and an aggregation of the clay minerals.

The aggregated, non-swelling particles provide an open pores system with pores of about 1  $\mu\text{m}$ . Upon wetting these pores are no longer filled with an expanding clay phase but kept open. The pore water remains available for circulation and is not bound as immobile interlayer water. The compression tests have shown that the structure is stable also under stresses up to 800 kPa.

Despite these drastic changes on the micro-structural level, the stiffness is not significantly affected by chemical treatment. A negative influence on this particular mechanical property can therefore be excluded.

A simple numerical implementation of concentration dependent permeability into a com-

mercial FEM-code showed that the obtained results lie within limits given by analytical solutions. Additional physical features such as the adsorption kinetics or coupled hydro-mechanics are readily available within this code and can be included for future extension of the model.

#### ACKNOWLEDGEMENT

This work has been supported by a grant Nr. 200021-137689 from the Swiss National Science Foundation, Switzerland.

#### REFERENCES

- [1] F.T. Madsen, J.K. Mitchell, Chemical effects on clay hydraulic conductivity and their determination, *Mitteilungen des IGBM*, ETH Zürich, **135** (1989), 67.
- [2] F.T. Madsen, M. Müller-Vonmoos, The swelling behaviour of clays. *App. Clay Sci.*, **4**(2) (1989), 143-156.
- [3] G. Lagaly, M. Ogawa, I. Dékány, Clay Mineral Organic Interactions. In: F. Bergaya, B.K.G. Theng, G. Lagaly, (eds.) *Handbook of Clay Science*. Elsevier, (2006), 309-377.
- [4] F. Fernandez, R.M. Quigley, Hydraulic conductivity of natural clays permeated with simple liquid hydrocarbons. *Can. Geotech. J.*, **22**(2) (1985), 205-214.
- [5] M. Plötze, G. Kahr, Diagnostic intercalation in clay minerals - use of guanidine carbonate. *Proc. of the 4th MECC, Mineralogia*, **33**(2008) 132.
- [6] V. Ravi, A.A. Jennings, Penetration model parameter-estimation from dynamic permeability measurements. *Soil Sci. Soc. Am. J.*, **54**(1) (1990), 13-19.
- [7] T. Hueckel, M. Kaczmarek, P. Caramuscio, P. Theoretical assessment of fabric and permeability changes in clays affected by organic contaminants. *Can. Geotech. J.*, **34**(4) (1997), 588-603.
- [8] M. Kaczmarek, T. Hueckel, V. Chawla, P. Imperiali, Transport through a clay barrier with the contaminant concentration dependent permeability. *Transport Porous Med.*, **29**(2) (1997), 159-178.
- [9] R.B. Conn, R.B. Davis, Green Fluorescence of Guanidinium Compounds with Ninhydrin, *Nature*. **183** (1959), 1053-1055.
- [10] L.P. Meier, G. Kahr, Determination of the cation exchange capacity (CEC) of clay minerals using the complexes of copper(II) ion with triethylenetetramine, *Clays Clay Miner.*, **47** (1999), 386-388.
- [11] R. Keren, I. Shainberg, Water vapor isotherms and heat of immersion. Na/Ca-montmorillonite systems I: Homioionic clay, *Clays Clay Miner.* **23** (1975), 193-200.
- [12] P. Hsieh, A new formula for the analytical solution of the radial dispersion problem, *Water Resour. Res.* **22**(11) (1986), 1597-1605.

# The investigations and the monitoring of three landslides along Durres-Morine motorway

*A. Kosho*<sup>1</sup>

*1)Geotechnical Engineer at "A.L.T.E.A. & GEOSTUDIO 2000" Laboratory, Tirane, Albania*

## ABSTRACT

This paper aims to deal with the investigations and monitoring of three landslides along Durres-Morin Motorway, in Albania. The objective of this investigation is to determine the causes of landslide, stability analysis of the slopes, physical and mechanical characteristics of soils and rock mass and stabilization of the slope. This investigation includes accurate studies and works (field and laboratory works) to elaborate the geological maps 1:500 of the sliding areas. Based on works done we will explain the geological conditions based upon pre-existing investigations and new investigations made by us (A.L.T.E.A. & Geostudio 2000, Laboratory Testing for Construction Materials and Geotechnical Study). We will give information about: geology of the sliding areas, hydrogeology condition of the sliding areas and discontinuities in the direction of the slant and in the other directions. At the end of this paper we will give the conclusions and the recommendations for these slopes stability.

## Key words

investigation, landslide, sliding area, geomorphology, hydrogeology, discontinuities, inclinometer, displacement

## 1.INTRODUCTION

The landslides we have investigated are located in Durres-Morin Motorway. The first one is met near the bridge no.5, section 2 road Rreshen - Kolsh. The second one is met at km 10 + 500, section 2 and the third one at km 15 + 500, section 1, both of them also part of road Rreshen

– Kolsh. Durres- Morin Motorway is one of the largest projects of Albanian infrastructure. For the first time in Albania we are monitoring the stability of the landslides and the zones where they are located. This is a long process, and we will keep monitoring until the zone and the landslide will reach its equilibrium.

### 1.1 Purpose

The objective of these investigations is to determine the causes of landslide, stability analysis of the slopes, physical and mechanical characteristics of soils and rock mass, stabilization of the slopes and the monitoring until the landslides reach their equilibrium.

## 2 CAUSES OF LANDSLIDES AND THE MORPHOLOGY OF DISCONTINUITIES

### 2.1 Causes of landslides

The main causes of these landslides with big dimensions are a lot but we have noticed as more important the following:

1. The most remarkable geological and geodynamic features identified in the zones where the landslides are met are: erosion, weathering and movement of soil masses down the ground slopes, tectonic fault, which have a direct and negative influence on the slope stability.
2. The shakings created from the explosions with mine has broken the equilibrium and the block to be reactivated towards the river.
3. The presence of the natural sources of the water.

### 2.2 The morphology of the discontinuities

From the measurements made the inclination angle is  $30-50^\circ$  and helps a lot the movement. The faces of discontinuities are a little rough and do not create a lot of resistance on the cut

### 2.3 The investigation of the landslides

The investigations of the landslides pass through the steps below:

1. Geological survey.
2. Boreholes and trial pits
3. Laboratory testing
4. Interpretation results of reading inclinometers of landslide area and periodical monitoring
5. Conclusions

### 2.4 The investigations near bridge no.5

#### 2.4.1 Geological survey

During the geological survey we have noticed that the sliding area near bridge no.5 passes near the valley of the river Fani i Vogel. There is an intensive development of geodynamic phenomenon. At the slide area near bridge no.5 are visible the erosion and weathering phenomenon, the movement of soil mass down the slope and the tectonic faults. In this region the intrusive basic rocks are present. There have been studied all joint and discontinuities, their density, direction, nature and the filling material. Based on this results this is a landslide in the rock masses and is classified in class I (first) Slope with active landslide. The material is continually moving, is fresh formed and very well defined. From the measurements made the inclination is  $40-45^\circ$  and helps a lot the movement, they are filled with clay material. The faces of discontinuities are a little rough and do not create a lot of resistance on the cut. The shear strength along a joint is low.



Figure 1. Photo from the landslide.

#### 2.4.2 Boreholes and trial pits

In the area where is located the landslide near bridge no.5 are made 8 drills to install the inclinometers. The drills start from 0.00 to 50 mW we can obtain better results and can be more secure during the investigation and the monitoring of the landslide.



Figure 2. Photo at the place where is done the borehole



Figure 3. Photo of the borehole

#### 2.4.3 Laboratory testing

We have done lots of laboratory works to determine the physical and mechanical characteristics of soils and rocks in the area of the landslide. We have divided the laboratory test into two groups: laboratory works for rocks and for soils.

#### 2.4.5 Interpretation results of reading inclinometers of landslide area and periodical monitoring

On the landslide area near Bridge no.5 are installed 8 inclinometers. The main direction of the movement is East and North. During the process of construction of the piles of the bridge the inclinometers gave no measurements, because they are blocked in the depth at which the embankment of the road begins. This happened because of the pressures created from the compression of the material of the embankment. During the measures of BH-7 the readings taken at the moment of the rock block from the inclinometer BH-7 shows the movement of some sliding rock masses which is still occurring with intensity. These elements prove that an active movement of the upper part of the road escarpment is taking place on the North and West directions. It is im-

possible to take measurements in the depth of 14.50 m because of a large displacement which doesn't allow us to determine the shift magnitude.

The same thing was noticed also during the measures of BH-8.



Figure 4. Photo of the inclinometer



Figure 5. Photo of cone protection of inclinometer tube

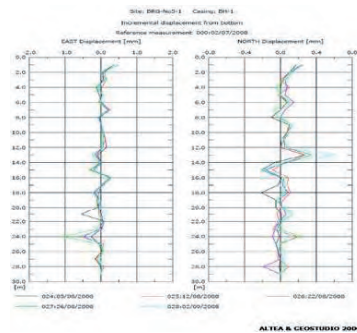


Figure 6. Inclinometer displacement from bottom

We make a periodical monitoring using the inclinometers installed in the slide area, so we can be sure that there isn't any present risk for the slope stability and the area of landslide is in equilibrium.

#### 2.4.6 Conclusions

1. The studied zone is composed of quaternary rock deposits composed by gabbros, micro gabbros, gabbros diorite and basalts with good physical and mechanical characteristics.
2. The sliding area is an old sliding rock mass which has been reactivated in the moment of the start of the works for building the body of the new road.
3. The main reasons of this sliding are geomorphologic, geologic and artificial reasons.
4. Sliding area is classified in class I (first) slope with active landslide. The material is continually moving.

### 2.5 The investigations of the landslide at km 10 + 500, section 2, road Rreshen-Kolsh

#### 2.5.1 Geological survey

In the region where this landslide passes there is an intensive development of geodynamic phenomenon. In the region where is the wall RW-05 area are present the deposits of the intrusive ultra basic rocks such as peridotite, olivinite and serpentinite. This kind of formation is very strong. These rocks have grey to white color and are composed of pyroxenes and olivine. The superficial part of these rocks has very cracks filled with clay materials with different widths and very dense. There have been studied all joint and discontinuities. From the measurements made the inclination is  $45-50^\circ$  and helps a lot the movement. The faces of discontinuities and the shear strength have the same characteristics as mentioned in the first landslide. The main discontinuities are in direction of slant.



Figure 7. Photo of the rocks geology

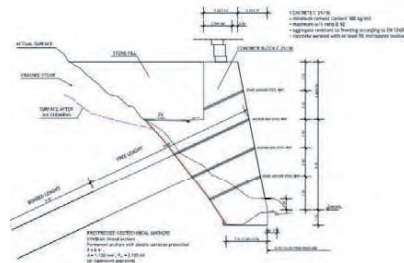
#### 2.5.2 Boreholes and trial pits

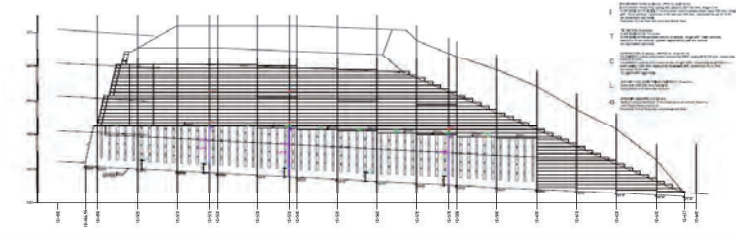
In the area where is located the landslide at km 10+500 are made some drills to install the inclinometers, tiltmeters and the load cells.

#### 2.5.3 Laboratory testing

We have done lots of laboratory works to determine the physical and mechanical characteristics of rocks in the area of the landslide such as bulk density, point load test, RCK, etc.

#### 2.5.4 Periodical monitoring





The monitoring that we have done in this area of landslide is new in Albania. We are proud of being the first company using such professional and secure methods of monitoring. We have applied three types of monitoring in this area using:

1. Inclinometers to measure the inclination with respect to the vertical at specific elevations. From the inclinations measurement it is possible, through the use of numerical integration methods, to evaluate the displacement.



Figure 8. Photo during the inclinometer's reading

2. Tiltmeters, which provides a direct measure of the effect on the structure of complex process as for example the soil consolidation with related differential settlement, sand liquefaction, water table variation, etc. Reading the inclination values we obtain information on construction stability and soil foundation behavior. The most meaningful measurements are the differences among the readings in the time. For monitoring purpose they can provide very useful information to understand the behavior or more simply they can provide an early warning of dangerous situation to activate civil defense actions program.

3. Anchor load cells used in cable anchor tendon and rock bolts monitoring for tunnel, diaphragm or retaining wall. Other possible applications are: load measurement on pile during testing and operation; load distribution below the steel lining of

tunnel and under the supports of bridge or viaducts.



Figure 14. Anchor load cells

### 2.5.5 Conclusions

1. The studied zone is composed of Quaternary and rock deposits composed by peridotite, dunite, olivinite and pyroxenes.

2. The main discontinuities are in direction of the slant and the faces of discontinuities are a little rough and do not create a lot of resistance on the cut. The shear strength along a joint is low.

3. According the characteristics of rock we recommend the foundations of the wall or the bridges with piles because the excavation created possibility to activate the sliding of the slopes.

## 2.6 The investigations of the landslide at km 15+500, section 1, road Rreshen – Kolsh.

### 2.6.1 Geological survey

In the region where this landslide passes there is an intensive development of geodynamic phenomenon. There are present deposits of volcanic and sedimentary rocks such as basalt and shale. Volcanic and sedimentary rocks are very strong have grey to green color are composed pyroxenes olivine and plagioclase. The superficial part of these rocks has very cracks. From the measurements made the inclination of the slop slid-



ing area is 30-35° at the sliding area is present more crack of the surface and helps a lot the movement, they are filled with clay material.

### 2.6.2 Boreholes and trial pits

In the area where is located the landslide at km 15+ 500 are made 13 drills to instalate 13 piezometers.The drills start from 0.00 to 40 m.



Figure 15.Place in done boreholes

### 2.6.3 Laboratory testing

We have done lots of laboratory works to determine the physical and mechanical characteristics of soils and rocks in the area of the landslide.

### 2.6.4 Periodical monitoring

To make a good monitoring of this landslide we have used piezometers.The piezometers are used to measure the water pressure a very important data for the stability of slopes and structures.



Figure 17.The cover of piezometers

### 2.6.5 Conclusions

1. The studied zone is composed of Quaternary and rock deposits composed by shale and basalts with good physical and mechanical characteristics.

2. The sliding area is an old sliding rock mass which has been reactivated in the moment of the

start of the works for building the body of the new road.

3. Sliding area is classified in class I (first) Slope with active landslide. The material is continually moving; it is fresh formed and very well defined.

4. Definitive precautions will be taken after the monitoring for a certain time has finished and the geotechnical analyses of the stabilization.

## CONCLUSIONS

1.The area where Rreshen- Kolsh Motorway passes is a valley with problematic geodynamic features.There are many landslides in this zone and we can categorize them into two big groups: rock slides and soil slides.

2.The rocks lanslides are near the biggest tectonic faults.

3.The soil lanslides are located in the colluvium deposits and it is present the underground water level.

4.The geotechnical study of these regions with a low stability and the engineering protection are effective .This conclusion is reached by the continuous monitoring

5.Albania has a broken relief and the slopes of our contry are unstable.After doing the study and stabilisation works it is recommendated to have a continuous monitoring process to have a better assessment for the effectivity of the stabilisation precautions taken

## ACKNOWLEDGEMENT

I would like to thank Mr.Skender ALLKJA and ALTEA& Geostudio 2000, for the perfect work that has made.

## REFERENCES

- [1] ALTEA & GEOSTUDIO 2000, Geological report Rreshen-Kolsh Motorway
- [2] Taylor & Francis, London 2005, The stability of slopes, 2nd edition, E.N. Bromhead
- [3] Taylor & Francis 2006, Debris Flow Mechanics, Prediction and Countermeasures Author Tamotsu Takahashi Consulting Geotechnical Engineer
- [4] Kiyoo Mogi Professor of university of Tokyo 2009, Experimental Rock Mechanics



# Influence of non-local strain regularization on the evolution of shear bands

B. Schädlich & H.F. Schweiger

*Institute for Soil Mechanics and Foundation Engineering, Graz University of Technology, Austria*

## ABSTRACT

The numerical analysis of strain softening problems by means of the conventional finite element method is well known to suffer from severe mesh dependency, and various approaches have been proposed to overcome this deficiency. Among these, the non-local approach has received increasing attention over the last two decades due to its relatively simple implementation and mechanically plausible assumptions. In this study the consequences of different assumptions for the non-local strain regularization are investigated with regard to the evolution of shear bands. A partially non-local approach has been implemented into a multilaminate constitutive model. The constitutive model employs a Hvorslev surface to describe peak shear strength and dilatancy in the heavily overconsolidated range. It is shown that the numerical shear band in biaxial test simulations rotates in softening and settles at  $\sim 45^\circ$  if softening is allowed to spread to stress points outside the initial shear band. This contradicts experimental findings, which show much steeper and virtually constant shear bands. Limiting strain regularization to stress points at or close to failure provides significantly better match with the experimental data.

Keywords: Non-local approach, Hvorslev surface, multilaminate model, strain softening

## 1 INTRODUCTION

Strain softening, i.e. reduction of shear strength with accumulating deformations, is a commonly observed phenomenon in geomaterials like rocks, dense sands and stiff, overconsolidated clays. Due to loosening of the material and destruction of the initial soil fabric, the load bearing capacity of the soil reduces after the maximum shear strength is mobilized, and approaches a critical state at sufficiently large deformations. Post-peak deformations concentrate in narrow shear bands, whose size is governed by the average grain size of the material.

While these effects are well known from experimental investigations, numerical simulation of strain softening e.g. with the finite element method is hampered by severe mesh dependency. The size of the finite elements provides an internal length scale, which governs the rate of post-peak strain softening and the size of the numerical shear band. Consequently, the numerical softening behavior is heavily influenced by the coarseness of the finite element mesh.

In this study non-local strain regularization is employed to obtain mesh independent results. This approach is based on averaging the plastic strains in the vicinity of the current stress point.

The non-local approach is implemented into a multilaminate constitutive model which can account for the shear strength and dilatancy of heavily overconsolidated clays.

The major objective of this paper is to show the impact of different assumptions for the non-local approach on the evolution of shear bands. Two versions of the non-local approach are compared: The first version employs strain regularization only in the post-peak region, and strain averaging is confined to stress points which are already in softening. In the second version, regularization is carried out also before peak strength is mobilized, and softening can spread to stress points which have not fully mobilized their peak shear strength yet. Numerical results of biaxial test simulations employing both models are compared with experimental results and analytical solutions.

## 2 MULTILAMINATE HVORSLEV SURFACE MODEL

The multilaminate constitutive model employed in this study is described in detail in [1]. Therefore only the features relevant for this study are reported here.

### 2.1 Multilaminate framework

Multilaminate constitutive models are based on the idea that the material behavior can be formulated on a distinct number of so-called integration planes with varying orientation. Each plane  $i$  represents a sector of a virtual sphere of unit radius around the stress point and is assigned a weight factor  $w_i$  according to the proportion of its sector with regard to the volume of the unit sphere. The global plastic strain increment  $d\boldsymbol{\varepsilon}_{gl}^{pl}$  to a prescribed load increment is obtained by summation of the contributions of all planes.

$$\boldsymbol{\sigma}_{i,loc} = (\sigma_{n,i} \quad \tau_{s,i} \quad \tau_{t,i})^T = (\mathbf{T}_i)^T \cdot \boldsymbol{\sigma}_{gl} \quad (1)$$

$$\mathbf{T}_i = \frac{\partial \boldsymbol{\sigma}_{i,loc}}{\partial \boldsymbol{\sigma}_{gl}} \quad (2)$$

$$d\boldsymbol{\varepsilon}_{gl}^{pl} = 3 \cdot \sum_i \mathbf{T}_i \cdot d\boldsymbol{\varepsilon}_{i,loc}^{pl} \cdot w_i \quad (3)$$

$$d\boldsymbol{\varepsilon}_{i,loc}^{pl} = (\varepsilon_{n,pl} \quad \gamma_{s,pl} \quad \gamma_{t,pl})^T \quad (4)$$

### 2.2 Yield and plastic potentials functions

Local plastic strain increments  $d\boldsymbol{\varepsilon}_{gl}^{pl}$  are calculated according to plasticity theory on integration plane level. Yield and plastic potential functions are formulated in local shear and normal stresses,  $\tau = (\tau_s^2 + \tau_t^2)^{0.5}$  and  $\sigma'_n$ , and local plastic shear and normal strains,  $\gamma_{pl} = (\gamma_{s,pl}^2 + \gamma_{t,pl}^2)^{0.5}$  and  $\varepsilon_{n,pl}$ , respectively. Yield surfaces are mobilized separately on all integration planes in anisotropic loading, thus accounting for anisotropy induced by plastic strains.

Three yield surfaces are defined in the model (Figure 1). The elliptical, fully associated cap yield surface  $f_{cap}$  controls the behavior in compression and is defined by the pre-consolidation pressure  $\sigma'_{nc}$ . In deviatoric loading the shear yield surface  $f_{cone}$  gets activated, which is controlled by the mobilized friction angle  $\phi'_m$ . Non-associated plasticity is employed for the cone yield surface, with the direction of the plastic strain increment given by the angle of dilatancy,  $\psi$ . Mobilization of dilatancy is defined by a cubical function in dependency on  $\phi'_m$  [2].

The Hvorslev yield surface  $f_{HV}$  is connected to  $f_{cap}$  at the critical state line and can be considered as the shear strength envelope on integration plane level.

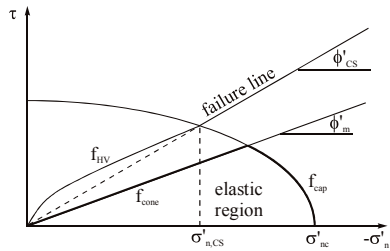


Figure 1: Local yield surfaces

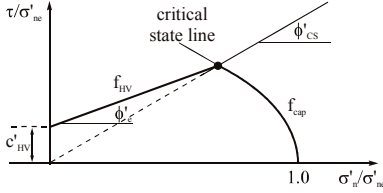


Figure 2: Local normalized shear strength envelope

$$f_{HV} = \tau + \sigma'_n \cdot \tan \phi'_e - c'_{HV} \quad (5)$$

$$c'_{HV} = B \cdot \left( \frac{\tan \phi'_e}{\tan \phi'_{CS}} - 1 \right) \cdot \sigma'_{nc} \quad (6)$$

The Hvorslev surface plots as a straight line in a normalized  $\tau/\sigma'_{nc}$  vs.  $\sigma'_n/\sigma'_{nc}$  diagram (with  $\sigma'_{nc}$  being the equivalent pressure on the local normal compression line), defined by the angle  $\phi'_e$  (Figure 2). The position of the Hvorslev surface changes with the size of the cap yield surface and vice versa. Positive plastic normal strains, caused by dilatancy at the Hvorslev yield surface, reduce  $\sigma'_{nc}$ , whereas negative (compressive) plastic normal strains from the cap yield surface enlarge  $\sigma'_{nc}$ . Hardening rules of the cap and cone yield surface are described in detail in [1].

In the heavily overconsolidated range (left of the critical state line in Figure 2), dilatancy is governed by the distance of the current stress state to the critical state line (Figure 3).

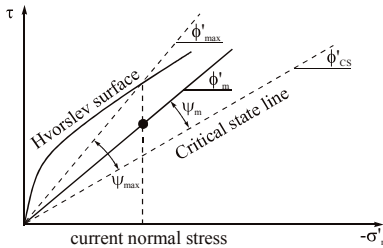


Figure 3: Mobilized and maximum angle of dilatancy

The maximum angle of dilatancy,  $\psi_{max}$ , is obtained from the difference between Hvorslev surface and the critical state friction angle  $\phi'_{CS}$ . As the Hvorslev surface reduces in size after the peak shear strength is mobilized, strain softening is initiated and the soil approaches the critical state with  $\psi_m = \psi_{max} = 0$ .

### 2.3 Strain softening

Strain softening is induced by the evolution of dilatant plastic strains, which result in contraction of the cap and Hvorslev yield surface. The plastic strains of the cone and Hvorslev surface are summed up and multiplied with the softening parameter  $h_{soft}$  to obtain the damage strain  $\epsilon_{di}$  (equation 9). In a first version of the model (labeled 'reference' further on), reduction of  $\sigma'_{nc}$  in softening is only calculated from the damage strain accumulated after peak strength has been mobilized (equation 8). Therefore, only plastic strains from the Hvorslev yield surface contribute to strain softening. In the 'modified' version of the model,  $\sigma'_{nc}$  is already reduced before the initial peak strength is reached due to dilatancy at the cone yield surface above the critical state line (equation 7). Consequently, failure in the modified model occurs slightly below the peak strength of the reference model (Figure 4).

Reference:

$$\sigma'_{nc,soft} = \left[ |\sigma'_{nc}|^{1-m} + K \cdot \frac{(m-1)}{p_{ref}^{m-1}} \cdot (\epsilon_{di}^* - \epsilon_{di,peak}^*) \right]^{\frac{1}{1-m}} \quad (7)$$

Modified:

$$\sigma'_{nc,soft} = \left[ |\sigma'_{nc}|^{1-m} + K \cdot \frac{(m-1)}{p_{ref}^{m-1}} \cdot \epsilon_{di}^* \right]^{\frac{1}{1-m}} \quad (8)$$

$$\epsilon_{di} = h_{soft} \cdot (\epsilon_{n,cone}^p + \epsilon_{n,HV}^p) \quad (9)$$

Averaged, non-local quantities are marked by '\*' and obtained as explained in the next section.  $K$  is the volumetric hardening parameter,  $m$  and  $p_{ref}$  are the exponent and the reference stress of the stress dependent stiffness [1].

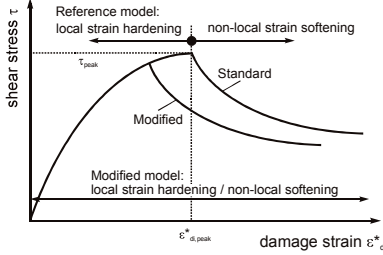


Figure 4: Schematic stress-strain curves of reference and modified strain softening model

### 3 NON-LOCAL STRAIN REGULARIZATION

A partially non-local approach has been employed in this study, in which only the damage strain  $\varepsilon_d$  is treated as a non-local quantity. Local plastic strains  $\varepsilon_{d,k}$  in the neighboring stress points  $k$  are averaged to obtain the non-local damage strain  $\varepsilon_d^*$  of the current stress point.

$$\varepsilon_d^* = \frac{1}{V_w} \cdot \sum_{k=1}^{k_{SP}} \varepsilon_{d,k} \cdot \omega'_k \cdot V_k \quad (10)$$

$$V_w = \sum_{k=1}^{k_{SP}} \omega'_k \cdot V_k \quad (11)$$

$$\omega'(r) = \frac{r}{l_{cal}^2} \cdot e^{-\left(\frac{r}{l_{cal}}\right)^2} \quad (12)$$

$k_{SP}$  is the number of stress points in the averaging area,  $V_k$  is the soil volume assigned to stress point  $k$ , and  $\omega'_k$  is the value of the weight function  $\omega'$  at the stress point  $k$ . The weighting function  $\omega'$  proposed by Galavi [2] is utilized (equation 12), which assigns zero weight to the current stress point. The internal length  $l_{cal}$  determines the averaging area, and  $r$  is the distance of stress point  $k$  to the current stress point.

## 4 BIAXIAL TEST SIMULATIONS

### 4.1 Numerical model and material parameters

Evolution of shear bands is studied in biaxial test simulations. The test specimen is 1.0 m high and 0.5 m wide, with very stiff and fully rough end-plates at the top and the bottom of the specimen. Drained plane strain conditions are applied. After applying initial stresses of  $\sigma'_v = \sigma'_h = -100$  kPa, vertical displacement of the top end plate is gradually increased. A slight geometric shift of the top plate of 1 mm to the right has been applied to enforce the formation of a single shear band. Four different meshes with 84, 158, 334 and 646 15-noded triangular finite elements are used (Figure 5).

Material parameters are derived from undrained triaxial tests on reconstituted, overconsolidated Pietrafitta clay [3]. Derivation of the model parameters and the comparison of model predictions and experimental results is shown in [1]. Parameters relevant for the current study are listed in Table 1.

Table 1. Material parameters of Pietrafitta clay

parameter	value
$E_{oed,ref}$	1020 kPa
$E_{ur,ref}$	8140 kPa
$p_{ref}$	100 kPa
$m$	1.0
$\phi'_{cs}$	30.0°
$\phi'_e$	23.8°
$\sigma'_{nc}$ (initial)	-2000 kPa
$h_{sof}$	40
$l_{cal}$	5 cm

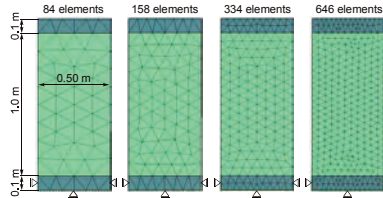


Figure 5: Numerical biaxial model and FE-meshes

#### 4.2 Reference model

Load-displacement curves obtained with the reference model for the different FE meshes show sufficient regularization (Figure 6). Shear bands develop shortly after peak, starting from the shear strain concentration at the edges of the end plates, and maintain the same inclination throughout the simulation (Figure 7). Frictional strength and dilatancy predicted by the Hvorslev surface model can be back calculated from the stress ratio at failure as  $\phi'_{max} = 45.3^\circ$  and  $\psi_{max} = 15.3^\circ$ . The inclination of the numerical shear bands to the horizontal is  $\approx 63^\circ$  for all the FE meshes. This value is close to the Coulomb solution ( $\Theta_C \approx 68^\circ$ , equation 13), which is governed by frictional strength. The Roscoe solution [4] (equation 14), which is based on kinematic considerations, delivers  $\Theta_R \approx 53^\circ$ , which is significantly below the value obtained in the numerical simulations.

$$\theta_C = 45^\circ + \phi'_{max} / 2 \quad (13)$$

$$\theta_R = 45^\circ + \psi'_{max} / 2 \quad (14)$$

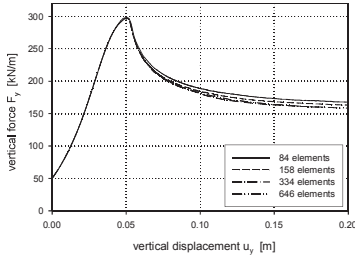


Figure 6: Load displacement curves with reference model

#### 4.3 Modified model

Applying the modified model with non-local strain regularization in the pre-peak range also delivers virtually mesh-independent load-displacement curves. Shear band inclinations at

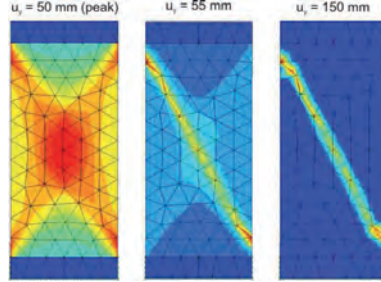


Figure 7: Shear band evolution with reference model (158 elements)

residual load level, however, differ notably from the results of the reference model (Figure 8) for all FE meshes. While the shear band also starts to develop from the strain concentrations at the end plates at peak, the shear band starts to rotate in subsequent loading and approaches  $\Theta \approx 45^\circ$  at residual load level. That value coincides with the Roscoe solution for  $\psi = 0$ . Varying the shear strength parameters of the material ( $\phi'_{CS}$ ,  $\phi'_e$ ) had no notable influence on the final shear band inclinations. Only when a very small internal length  $l_{cal}$  was adopted (and the softening parameter  $h_{soft}$  scaled down accordingly), the numerical shear band maintained its position in softening (Figure 9). A much finer FE-mesh had to be used in this case to ensure sufficient regularization.

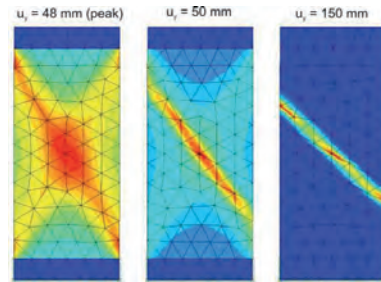


Figure 8: Shear band evolution with modified model (158 elements)

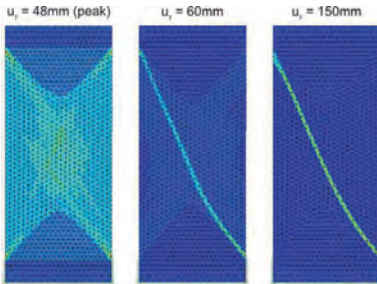


Figure 9: Shear band evolution with modified model for  $l_{cut} = 1$  cm,  $h_{soft} = 3$  (2440 elements)

## 5 CONCLUSIONS

The assumptions made in non-local strain regularization may strongly influence the evolution of shear bands obtained from the numerical model. If regularization is carried out only at the stress points which are already at failure (reference model), the shear band maintains its initial position and does not rotate notably with further loading. If regularization is extended to stress points which have not yet mobilized peak strength (modified model), softening is induced in the material adjacent to the shear band. Consequently, the shear band can easily change its position within the sample. In this case, shear bands settle at  $\Theta \approx 45^\circ$  at residual load level, which equals the Roscoe solution for  $\psi = 0$  (critical state).

The tendency of FE simulations to predict the Roscoe solution in biaxial test simulations has been noted previously by other authors [5], and may be related to the rather large thickness of the numerical shear band compared to the outer dimensions of the numerical model. As shown analytically by Vermeer [6], kinematic boundary conditions become more influential with increasing thickness of the shear band, and hence shear bands will evolve along lines of zero extension, as predicted by the Roscoe solution. For very thin shear bands, static boundary conditions govern the orientation of the shear band, as predicted by the Coulomb solution. Experimental results support these considerations. The real shear band

thickness is known to increase with the average grain size. Accordingly, fine sands and clays yield shear band orientations close to the Coulomb solution, while coarse grained gravel tends to yield the Roscoe solution [7]. In any case, however, rotation of shear bands – as obtained with the modified model - is not observed experimentally. Reducing shear strength in stress points outside the initial shear band therefore seems to be not appropriate to model the strain softening behavior of geomaterials.

Despite the distinct differences in the simulation of biaxial tests, the impact of these assumptions in the simulation of practical geotechnical problems remains to be investigated. In many practical cases, the geometry of the shear band is governed by geometrical constraints (external loads and structures), rather than by material properties. In this case it can be expected that both versions of the model will predict a very similar behavior.

## ACKNOWLEDGEMENT

The financial support for the first author by FWF Austria (grant no. P21225-N13) is gratefully acknowledged.

## REFERENCES

- [1] Schädlich, B. 2012. A multilaminar constitutive model for stiff soils, Ph.D. thesis, Graz University of Technology.
- [2] Schweiger, H.F., Wiltafsky, C., Scharinger, F. & Galavi, V. 2009. A multilaminar framework for modelling induced and inherent anisotropy of soils. *Geotechnique* **59** (2), 87-101.
- [3] Burland, J.B., Rampello, S., Georgiannou, V.N. & Calabresi, G. 1996. A laboratory study of the strength of four stiff clays. *Geotechnique* **46** (3), 491-514.
- [4] Roscoe, K. H. 1970. The influence of strains in soil mechanics. *Geotechnique* **20** (2), 129-170.
- [5] Brinkgreve, R.B.J. 1994. Geomaterial models and numerical analysis of softening. Ph.D. thesis, Delft university press.
- [6] Vermeer, P.A. 1990. The orientation of shear bands in biaxial tests. *Geotechnique* **40** (2), 223-236.
- [7] Arthur, J.R.F. & Dunstan, T. 1982. Rupture layers in granular materials. Proc. IUTAM Conference on Deformation and Failure of Granular Materials, Vermeer & Luger (eds.), Delft, Netherlands, 453-459.

# Measuring of the horizontal stress in overconsolidated soils

R. Malát<sup>1</sup>

*Department of Engineering Geology, Institute of Hydrogeology, Engineering Geology and Applied Geophysics, Faculty of Science, Charles University, Albertov 6, Prague 120 00, Czech Republic, richardmalat@gmail.com*

## ABSTRACT

Assessment of horizontal stress in overconsolidated soils causes considerable problems. All currently used methods involve imperfections. The conventional in-situ techniques using empirical formulae based on laboratory measurements are inappropriate due to ageing and other effects invalidating all laboratory measurements of  $K_0$ . The present study consists of two parts. First it focuses on the definition of coefficient of earth pressure at rest. Secondly it analyses in-situ measuring by Marchetti's flat dilatometer (FDM) in Miocene overconsolidated clay strata called "Tegeł" at the town of Bmo, Czech Rep. The measured data are compared to a numerical analysis of the FDM using hypoplastic constitutive model.

Keywords: Earth pressure at rest coefficient, overconsolidation, clay, Marchetti's dilatometer, in-situ soil testing, hypoplastic constitutive model, overconsolidation ratio

## 1 INTRODUCTION

Knowledge of the horizontal stress in the massif is essential for analyses of various geotechnical constructions (tunnels, pile foundations, etc.). The coefficient of the at rest earth pressure  $K_0$  is defined as the ratio of horizontal and vertical effective stresses.

$$(\sigma'_h / \sigma'_v) = K_0 \quad (1)$$

Effective vertical stress can be evaluated directly by formula (2)

$$\Sigma \gamma \cdot h - u = \sigma'_v \quad (2)$$

The horizontal stress is dependent on the stress history, and therefore it is difficult – or even impossible - to assess its value in overconsolidated soils.

## 2 ASSESSMENT OF HORIZONTAL STRESS IN NORMALLY CONSOLIDATED SOILS

In the normally consolidated soils the  $K_0$  and the horizontal stress  $\sigma'_h$  can be calculated by Jáky's formula [4], later simplified by the author [5] to the form

$$1 - \sin \phi' = K_{0,NC} \quad (3)$$

---

<sup>1</sup> Corresponding Author. Affiliation, Contact address, e-mail

Jáky's formula was based on a theoretical analysis of the symmetrical wedge of normally consolidated sand. The analysis involved some simplifications, and the orientation of normal stresses was incorrect (for example [9], [11] or [12]). However, further analyses using more realistic orientation of normal stresses led to differences of several percent only (see the correction of the original Jáky's formula published by Piatpongsa et al. [11])

$$1.02(1 - \sin\phi') = K_{0,NC} \quad (4)$$

### 3 ASSESSMENT OF HORIZONTAL STRESS IN OVERCONSOLIDATED SOILS

For overconsolidated soils no theoretically founded expression has been put forward for  $K_{0,OC}$ , i.e. for calculating horizontal stress  $\sigma'_h$ . All published formulae are empirical and imprecise.

It is generally accepted that  $K_{0,OC}$  is a function of the overconsolidated ratio OCR ([1], [7], [8]), where OCR is defined as the ratio of maximal vertical effective stress and the present vertical effective stress

$$(\sigma'_{v,max.} / \sigma'_v) = OCR \quad (5)$$

Brooker and Ireland [1] published a relation between  $K_{0,OC}$  and OCR in a form of a graph, based on laboratory data from a soft oedometer. Schmidt [13] suggested a power law expression for  $K_{0,OC}$ ,  $K_{0,NC}$  and OCR conforming to their data, which was later utilised in the widely used expression by Mayne and Kulhawy [7]

$$K_{0,OC} = K_{0,NC} OCR^{sin\phi'} \quad (6)$$

The relation (6), which is a result of statistical analysis of laboratory data of a diverse origin, seems extremely easy to be used in practice. However the correct determination of real OCR, which is by a rule influenced by all kinds of ageing effects (e.g., creep), makes the use of (6) questionable.

### 3.1 Laboratory tests to evaluate OCR

Creep, which may be particularly significant in clays, moves the position of the real maximal vertical stress  $\sigma'_{v,max.}$  to the position of an apparent maximal vertical stress  $\sigma^{*'}_{v,max.}$  (see Fig. 1).

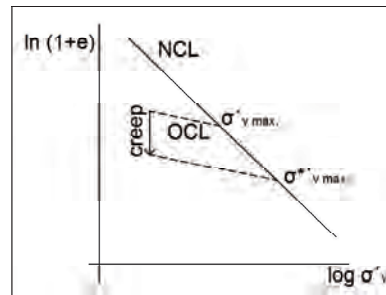


Figure 1. An influence of creep on  $\sigma'_{v,max.}$  position.

The oedometer test is a common technique for evaluating  $\sigma'_{v,max.}$ . Due to creep however the test produces a pseudo-overconsolidation value of  $\sigma^{*'}_{v,max.}$  instead of the present overconsolidation pressure  $\sigma'_{v,max.}$ . Hence, both the OCR and  $K_{0,OC}$  values determined by (6) not considering creep (ageing) are inappropriate and false.

### 3.2 Direct evaluation of $K_{0,OC}$ by laboratory tests

In principle, in the laboratory it is relatively easy to maintain zero radial strain of a cylindrical specimens, and to measure the required radial and axial stresses (triaxial cell, 'soft' oedometer, e.g. [8]). The main problem in any direct determination of  $K_{0,OC}$  in the laboratory is the stress state of the undisturbed specimens at the beginning of the test, which does not correspond to the stresses in-situ. No satisfactory solution of the problem has been found, despite several methods being proposed ([2],[14]). Therefore direct measurement of the  $K_{0,OC}$  in the laboratory is not a good option.



### 3.3 Assessment of the $K_0$ and OCR by flat dilatometer (Marchetti)

Flat dilatometer is a device for in-situ measurements (Fig. 2). The position of the membrane is given by the gas pressure, which is measured at two positions and is designated  $p_0$  and  $p_1$ , respectively.

Data pressure  $p_0$  are used to calculate  $K_0$  and OCR. When measuring  $p_0$  the membrane of the dilatometer remains levelled with the spade (Fig. 2).

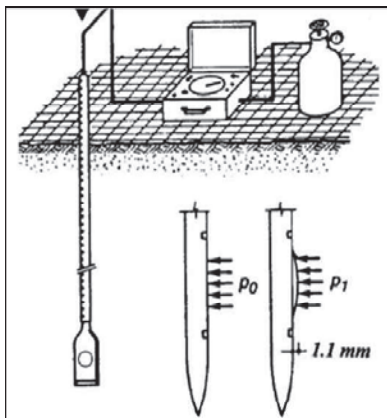


Figure 2. Flat dilatometer [6].

The width of the dilatometer is 14 mm. When the instrumented is installed into the ground an expansion of the soil is formed. Hence, the pressure measured is higher than the earth pressure at rest. A coefficient of the earth pressure  $K_D$  corresponding to the measured data is introduced

$$K_D = (p_0 - u_0) / \sigma'_v \quad (7)$$

and the coefficient of the earth pressure at rest  $K_0$  is calculated

$$K_0 = (K_D / 1.5)^{0.47} - 0.6 \quad (8)$$

The overconsolidation ratio OCR is

$$OCR = (0.5K_D)^{1.5} \quad (9)$$

Marchetti's [6] equations (8) and (9) are based on the laboratory data by Brooker and Ireland [1] and Mayne and Kulhawy [7].

## 4 IN-SITU MEASUREMENTS

### 4.1 Geotechnical condition at the tested field

Investigated site lies at the town of Brno in the eastern part of Czech Republic. The phreatic water table is 4.7 metres under the surface. At the site, about 5.5 metres were excavated 30 years ago, which still generates negative pore pressures. At the depth of 11.7 metres the pore pressure of -32 kPa was measured (after dissipation of excess pore pressures caused by the sounding) by a Push-in pressure spade cell (Fig. 3).

The value of present vertical effective stress  $\sigma'_{v \text{ initial}}$  was estimated to be 185 kPa. At the particular site the "Tegel" strata were found from the depth of 5.3 metres.

### 4.2 Dilatometer sounding

During December 2011 and January 2012 two dilatometer soundings were carried out. The data from the depth of 11.7 metres are compared with a numerical model in this paper. The pore pressure was measured by the Push-in spade pressure cell, as the flat dilatometer is not capable of measuring pore pressures.

### 4.3 Results from flat dilatometer

Table 1 shows the values of the  $K_D$  and  $K_0$  coefficients calculated by the formulae (7) and (8), respectively.

Table 1. Data measured by flat dilatometer at the depth of 11.7 metres.

Parameter	Value
$K_D$ probe1	8.0
$K_0$ probe1	1.6
$K_D$ probe2	8.0
$K_0$ probe2	1.6



Figure 3. Push-in pressure spade cell.

## 5 NUMERICAL MODEL

For the numerical analysis the hypoplastic model [15] was used. The advantage of the hypoplastic model is a nonlinear stiffness, depending on strain. The  $K_0$  value used for comparisons is taken from a current parametric study [10], which fits a numerical model to in-situ measurements of convergence profiles of an exploratory edit near the investigated site. The study yielded  $K_0 \sim 1.2$ . Both the calibration and the parameters for the hypoplastic model are taken from [15].

The numerical analysis was carried out using the Plaxis software. The model is built as a two dimensional plane strain analysis which involved six phases:

- Generation of the initial stress condition with  $K_0 = 1.2$ .

- Excavation of the 5.5 metres thick layer in order to reach the pore pressure -32 kPa at the depth of 11.7 metres. This phase was done via consolidation analysis.
- The displacement caused by installing a dilatometer 200 millimetres high and 7 millimetres wide at the depth of 11.6 – 11.8 metres on the left boundary of the model. The prescribed displacement simulated a half of the dilatometer, symmetrical along the vertical axis. The displacement was gradually applied at four steps, each being 50 millimetres high. For simplicity a continuous loading by the dilatometer was simulated in this way. All phases employed a plastic undrained analysis.

### 5.1 The results of the numerical analysis

The results are shown in Table 2. Horizontal pressure  $\sigma'_h$  denotes the pressure generated on a surface of the prescribed displacement from the phase no. 6 of the numerical model (see Fig. 4 and 5). The value of the horizontal stress corresponding to the measured value by the dilatometer is considered to be in the middle of the prescribed displacement (at the depth 11.7 metres). The coefficient „ $K_{model}$ “ given by the ratio of horizontal and vertical stress from the numerical model corresponds to Marchetti’s coefficient  $K_D$ .

Table 2. Data from numerical model from depth of 11,7 metres after application of the prescribed displacement.

Parameter	Value
$\sigma'_{v \text{ initial}}$	185kPa
$\sigma'_h$	298kPa
$K_{model}$	1.61

## 6 COMPARISON

If the coefficient  $K$  from Table 2 is used in the formula (8) instead of  $K_D$ , the resulting value of the coefficient of earth pressure at rest becomes  $K_0 = 0.43$ . The difference between both value is significant (flat dilatometer gives  $K_0 = 1.6$ ). The reasons are probably following:

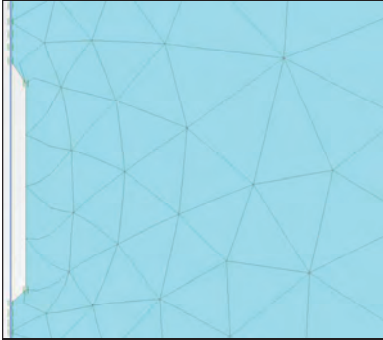


Figure 4. Prescribed displacement on the left boundary of the model.



Figure 5. Distribution of the horizontal stress on the prescribed displacement.

- The hypoplastic constitutive model used in the analysis was isotropic. An anisotropic modification is currently being developed.
- Marchetti's formulae for calculation of the  $K_0$  ( $K_{0,OC}$ ) and OCR are constructed in-

correctly due to fitting to the laboratory tests which are not relevant (ageing, pseudo-overconsolidation etc).

- The presented numerical model was simplified in comparison with the real in-situ conditions, and was two dimensional only.
- The "Tegel" strata are affected by tectonic processes and therefore it should be considered as a discontinuum. However, it is idealized as a continuum in the numerical analysis.

## 7 CONCLUSIONS

The present analysis of the Marchetti's formulae shows that they can hardly give correct solution for overconsolidated clay. Problems are caused by fitting to the inappropriate laboratory result, which cannot take account of the ageing effects.

The difference between  $K_0$  calculated from in-situ data and from the data given by the numerical model is significant.

## ACKNOWLEDGEMENT

The work was supported by the grant P105/11/1884 and P105/12/1705 of the Czech Science Foundation.

## REFERENCES

- [1] E.W. Brooker, H.O. Ireland, Earth pressures at rest related to stress history, *Canadian Geotechnical Journal* **2** (1965), 1–15.
- [2] V.K. Garga, M.A. Khan, Laboratory evaluation of  $K_0$  for overconsolidated clays, *Canadian geotechnical journal* **28** (5) (1991), 650-659
- [3] K.K. Hamouche, S. Leroueil, M. Roy, and A.J. Lutenegeger, In situ evaluation of  $K_0$  in eastern Canada clays, *Canadian Geotechnical Journal* **32** (4) (1995), 677–688
- [4] J. Jáky, A nyugalmi nyomás tenyezője (The coefficient of earth pressure at rest), *Magyar Mernok es Epitesz-Egyulet Kozlonye* (1944), 355–358.
- [5] J. Jáky, Pressure in silos, *Proceedings of the 2nd International Conference on Soil Mechanics and Foundation Engineering* **1** (1948), 103–107.

- [6] S. Marchetti, In Situ Tests by Flat Dilatometer, *Journal of the Geotechnical Engineering Division, ASCE* **106** (1980), 299–321.
- [7] P.W. Mayne, F.H. Kulhawy, (1982) K<sub>0</sub>-OCR relationships in soil. *Journal of Geotechnical Engineering Div. ASCE* **6** (1982), 851–872.
- [8] G. Mesri, T.M. Hayat, The coefficient of earth pressure at rest, *Canadian Geotechnical Journal* **30** (4) (1993), 647–666.
- [9] R.L. Michalowski, Coefficient of earth pressure at rest, *Journal of Geotechnical and Geoenvironmental Engineering ASCE* **131**(11) (2005), 1429–1433.
- [10] V. Novák, MSc thesis under preparation
- [11] T. Pipatpongsa, S. Heng, A. Iizuka, H. Ohta, Rationale for coefficient of earth pressure derived from prismatic sand heap. *JSCCE Journal of Applied Mechanics* **12** (2009), 383–394.
- [12] T. Pipatpongsa, B. Vardhanabhuti, Analyses of coefficient of lateral earth pressure in wedge-shaped granular mound based on Jaky's (1944) hypothesis, *The 14th National Convention on Civil Engineering of Thailand* (2009), 147–152.
- [13] B. Schmidt, discussion of "Earth pressures at rest related to stress history", *Canadian Geotechnical Journal* **1**(3) (1966), 239-242.
- [14] V. Sivakumar, T. Navaneethan, D. Hughes, G. Gallagher, An assessment of the earth pressure coefficient in overconsolidated clays, *Geotechnique* **59** (2009), 825-838.
- [15] T. Svoboda, D. Mašín, J. Boháč, Hypoplastic and Mohr-Coulomb models in simulations of a tunnel in clay, *Tunnel* **18** (4) (2009), 59–68.

# Centrifuge tests to evaluate the Po river embankment seismic response

*D. Giretti*<sup>1</sup>

*University of Ferrara, Italy*

## ABSTRACT

On the behalf of the Italian Department for the Civil Protection, the Po River Basin Authority carried out a research project to evaluate the seismic hazard of about 90 km of the right embankment of the Po river, from Boretto (Reggio Emilia Province) to Ro (Ferrara Province). The project aim is the assessment of 1) the regional seismic risk of the areas under study, 2) the soil properties of the embankment and the foundation ground via site investigation and laboratory tests, 3) the local seismic response of the foundation soil, 4) the liquefaction potential of the foundation soil and 5) the stability of the bank under static and dynamic conditions.

In order to investigate the seismic response of the embankment, a series of dynamic centrifuge tests on model banks were performed using a single degree of freedom shaking table. The models were reconstructed using silty and sandy soils retrieved in situ. Two soil profiles and two geometries were tested. Four time histories were applied to each model; the accelerograms were deduced from a local seismic response analysis carried out referring to one of the investigated site.

The tests showed a significant tendency of the embankments to amplify the input motions. The amplification is significant in a wide range of frequencies and increases from the base towards the top. No signs of local instability were observed during tests. The experimental results are compared with the preliminary results of a numerical 2D response analyses of the embankments.

Keywords: Centrifuge, shaking table, embankment, ground response

## 1 INTRODUCTION

The embankments of the Po river have strategic importance for the purpose of civil protection. Thus the Po River Basin Authority (AdBPo) was financed by the Italian Department for the Civil Protection to carry out a research project ("SIS-MAPO") to evaluate the seismic behaviour of about 90 km of the right bank of the Po river, belonging to municipalities with the highest seismic hazard from Boretto (Reggio Emilia Province) to Ro (Ferrara Province).

The research project has been carried out through several steps: (i) analysis of the regional

seismic hazard; (ii) site characterization of the 90 km of right bank of the Po river under study via a large series of in situ tests (including CPTUs, soundings, down hole and cross hole tests, MASW, ReMi, seismic refraction wave tests, monitoring of the environmental vibrations, installation of piezometers in boreholes [1]) and laboratory tests on undisturbed samples; (iii) local seismic response analysis; (iv) evaluation of the liquefaction potential; (v) evaluation of seismic response and seismic stability of the banks via numerical simulations and dynamic centrifuge tests. This paper presents the results of the centrifuge tests.

---

<sup>1</sup> Engineering Department, via Saragat 1 - 44122 Ferrara - Italy, daniela.giretti@unife.it

The model embankments were reconstructed using silty and sandy soils retrieved in situ during soundings. Two soil profiles and two geometries were tested. For each model, four tests were carried out, using four different earthquakes, applied at the bottom of the bank. The input motions were defined through a mono-dimensional seismic ground response analysis carried out referring to one of the site investigated for the project.

In order to investigate the experimental behavior of the models, two-dimensional response analyses of the banks have been carried out using a finite element code. The experimental and numerical results are compared in this paper.

## 2 GEOLOGICAL AND GEOTECHNICAL SETTINGS

The 90 km of the Po river embankment from Boretto to Ro, included in the SISMAPO research project, are located in the last third of the river (Central and Eastern Sector of the Po Valley). The main tectonic structure of the whole area is a buried ridge known as the Ferrara Folds, which reaches its maximum height NW the city of Ferrara under the Po river, near the site of Casaglia, which was assumed as the reference site for the centrifuge tests.

The subsoil of the whole area is characterized by alluvial deposits of different depositional environments, which consist in an alternating sequence of silty-clayey layers of alluvial plain and sandy horizons of channel and levee, sometimes with fine conglomerates. These deposits are more than 500 m thick near Boretto, reach their minimum depth (110-120 m) near Ferrara, due to the buried structural high of the Ferrara folds, then their thickness increases towards the delta mouth. The depth of the seismic bedrock (shear wave velocity,  $V_s > 800$  m/s) is about 80 m in the western area (Reggio Emilia) and about 110-120 m in the eastern region (Ferrara).

The regional seismic hazard study included in the SISMAPO project indicates relatively low levels of ground shaking. The seismic risk increases from west to east: in the eastern sector the greater contribution to seismic hazard is giv-

en by relatively small local earthquakes (magnitude around 5 within few tens of km) while in the western sector strong distant earthquakes (magnitude  $> 6$  and distances of the order of hundred kilometers or more) are expected.

Table 1 summarizes the Casaglia site soil profile as resulted from a couple of 150 m deep soundings and reports the profile of the shear wave velocity,  $V_s$  measured by a 150 m deep cross-hole test realized in the boreholes; the tests were performed from the ground surface. The foundation soil is characterized by alternation of silty and clayey soils and sandy soils. The substratum of the alluvial succession, made by sandy marine sediments Lower Pleistocene in age, was drilled at the depth of 110 m and the Miocene marl, top of the pre-Quaternary succession of the Ferrara Folds, was drilled at the depth of 130 m. The shear wave velocity increases as the depth increases and reaches higher values than 800 m/s in the Quaternary marine substratum and 1200 m/s at the marl roof.

The small-strain shear stiffness of the foundation soils was measured in the laboratory by resonant column (RC) and triaxial Bender elements (BE) tests on undisturbed samples. Figure 1 shows the dependency of the shear modulus and the damping ratio on the strain level, as observed in RC tests (dots). In Figure 1 the curves adopted for the ground response analyses are also reported as continuous lines.

As to the embankment, it mainly consists of overconsolidated sandy silt and silty sand, as deduced from piezocone penetration tests and soundings performed from the top of the bank in the neighborhoods of the reference site.

## 3 GROUND RESPONSE ANALYSIS OF THE FOUNDATION SOIL

For evaluating the input motions to be applied at the base of the model embankments during the seismic centrifuge tests, a ground response analysis was performed for the site of Casaglia, using the code Proshake [1], that performs 1D dynamic analysis in the frequency domain. The non-linear soil behavior and the strain dependent damping are accounted for through the equivalent linear

method, that gives a reasonable estimate of soil response for moderate levels of shearing intensity and provided that no significant pore water pressure develops during seismic excitation. The analysis was performed under free field conditions; the soil profile and properties given in Table 1 and the stiffness and damping curves reported in Figure 1 were adopted. The seismic bedrock was placed at the depth of 120 m, intermediate value between the depth of the sandy marine sediments and the marl roof.

As input motions, six rock outcrop natural records selected via the seismic hazard study for the Ferrara region were adopted. The input accelerograms were assumed to be applied to a rock outcropping and deconvoluted to the seismic bedrock.

The main characteristics of the earthquakes obtained at the ground surface are given in Table 2, where PGA, PGD and PGV are the peak ground acceleration, velocity and displacement,  $d_{90}$  is the significant duration,  $I_a$  is the Arias intensity and  $s_i$  is the Housner Spectrum Intensity evaluated on the pseudo-acceleration spectrum

Table 1. Casaglia site: soil profile, shear wave velocity and natural unit weight.

Depth from m to m	soil type	$V_s$ m/s	$\gamma_n$ kN/m <sup>3</sup>
0 – 15	clay – silty clay	170	18
15 – 31	sand – silty sand	220	18
31 – 39	sand – silty sand	270	18
39 – 65	clay-silty clay	300	18
65 – 80	sand – silty sand	400	18
80 – 110	clay – silty clay	500	19
110-130	clay – silty clay and silty sand	900	22
> 130	Miocene marl	>1200	22

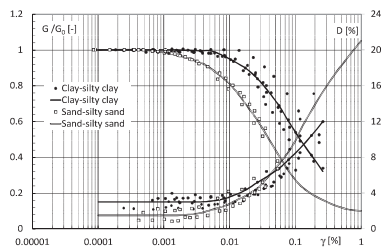


Figure 1. Non dimensional shear modulus,  $G/G_0$  and damping ratio,  $D$  against shear strain,  $\gamma$  from RC tests.

PSA. Four of the six accelerograms computed at the ground surface (base of the bank) were employed as input motions of the dynamic centrifuge tests: N. 1\*, 2\*, 3\*, 6\*.

Table 2. Characteristic of the accelerograms computed at the ground surface.

N.	PGA g	PGV m/s	PGD m	$d_{90}$ s	$I_a$ m/s	$s_i$ m/s
1*	0.228	0.176	0.029	13.245	0.876	0.863
2*	0.281	0.184	0.026	3.000	0.292	0.464
3*	0.218	0.175	0.026	3.900	0.323	0.646
4*	0.214	0.148	0.014	3.630	0.400	0.453
5*	0.215	0.193	0.028	1.305	0.170	0.495
6*	0.297	0.229	0.039	4.170	1.023	0.668

## 4 CENTRIFUGE TESTS

### 4.1 The ISMGEO centrifuge

The model tests were performed using the ISMGEO (Istituto Sperimentale Modelli Geotecnici, Seriate – BG – Italy) Geotechnical Centrifuge, IGC, which is a beam centrifuge made up of a symmetrical rotating arm with a diameter of 6 m, a height of 2 m and a width of 1 m. The arm holds two swinging platforms, one used to carry the model container and the other the counterweight. During the test, the platforms lock horizontally to the arm to prevent transmitting the working loads to the basket suspensions. An outer fairing rotates concurrently to the arm to reduce air resistance and perturbation during flight. Further details can be found in [2]. The IGC houses a single degree of freedom shaking table, which is able to reproduce real strong motions at the model scale. The shaker is connected to the rigid arm. Its axis of motion is parallel to the centrifuge rotational axis, thus problems related to Corioli's acceleration are avoided. The shake table works under an acceleration field up to 100g ( $g$  = gravity acceleration) and can provide excitations at frequencies up to 1000 Hz and acceleration up to 50g.

As to the similarity relationships between a centrifuge model and the prototype, in a model geometrically scaled  $N$  (i.e. the model length is  $N$  times smaller than in the prototype) and subjected to a centrifuge acceleration of  $Ng$ , both

stresses and strains are scaled at 1:1, the time in dynamic processes is reduced by factor of N and the acceleration is enhanced by factor of N.

#### 4.2 Test set-up

The adopted geometrical scaling factor of the models is  $N=50$ . All the models were tested under an acceleration field of  $a = 50g$ , which was reached in correspondence of the bottom of the embankments. A simplified trapezoidal cross section was adopted for the tests; four models were tested, as represented in Figure 2, where the middle cross-sections are shown. The model dimensions are listed in Table 3.

The sand and the silt used to reconstitute the models were retrieved in situ during the soundings realized from the top of the bank near the reference site. The sand has a mean grain size  $D_{50} = 0.69$  mm and a uniformity coefficient  $U_c=3.16$ . The silt has a clay content lower than 15%. The models were reconstituted within a rigid container under plain strain conditions and were free to slide in direction of the seismic excitation (x direction, see Fig. 2). They were prepared in 2 cm thick horizontal layers by tamping, then they were cut to form the slopes. The sand was reconstituted at a moisture content  $w = 5\%$  and a natural unit weight of  $\gamma_n = 16$  kN/m<sup>3</sup>; the silt at  $w = 10\%$  and  $\gamma_n = 15.4$  kN/m<sup>3</sup>.

Six miniaturized accelerometers were fixed to each model (Fig. 2) to measure the accelerations in the direction of the excitation; one was installed at the container bottom (ACCX B) and five were embedded within the embankment (along the middle cross-section, ACCX 1-5). Two displacement transducers were placed on the top of the embankment to measure the vertical settlements. The instrumentation measures were recorded at a frequency of 5000 Hz.

After model preparation, the container was placed into the centrifuge, whose speed was slowly increased to reach the acceleration target value of 50g. After the model consolidated under its weight, the input accelerogram was triggered.

Sixteen dynamic tests were performed: each model was tested under the accelerograms N. 1\*, 2\*, 3\*, 6\* obtained from the ground response analysis (Tab. 2). In the tests, the time histories

of acceleration were properly scaled, i.e.  $a_{mod}=50 \cdot a_{prot}$ ,  $t_{d,mod}=t_{d,prot}/50$ ,  $f_{mod}=50 \cdot f_{prot}$ .

Since in site the embankment is generally not saturated (except during exceptional flood events) seepage was not modeled in the tests. The suction was not accounted for.

Table 3. Model and prototype dimensions.

Model	Soil	B	b	H	$\alpha$
		mod/prot mm/m	mod/prot mm/m	mod/prot mm/m	°
M1-1	silt	750/37.5	140/7	150/7.5	26
M1-2	silt/sand				
M2-1	silt	750/37.5	140/7	200/10	33
M2-2	silt/sand				

B= base of the embankment    b= top of the embankment  
H= height of the embankment     $\alpha$ = slope

#### 4.3 Some results

In the following section the results of the tests on the models M2-1, subjected to the four earthquakes 1\*, 2\*, 3\* and 6\* are reported; all the results are plotted at the prototype scale.

Figure 3 shows the Fourier amplitude spectra (FAS) of the accelerations measured during the tests. ACCX B is the acceleration measured at the base of the embankment (time history of the acceleration performed by the shaking table); ACCX 1-5 are the accelerations measured within the models. These results show that amplification effects takes place within the embankment. The maximum acceleration increases from the base towards the top. For all the input motions applied, amplification is significant in the range of frequency of 2.5 – 20 Hz. The amplification phenomena observed are quantified by the amplification factors defined by Equations. 1 and 2:

$$FA_{0.1-0.5} = \frac{s_{i,0.1-0.5}(PSA_{top})}{s_{i,0.1-0.5}(PSA_{base})} \quad (1)$$

$$FA_{0.5-1.5} = \frac{s_{i,0.5-1.5}(PSA_{top})}{s_{i,0.5-1.5}(PSA_{base})} \quad (2)$$

where:  $s_{i,0.1-0.5}$  and  $s_{i,0.5-1.5}$  are the Housner intensity of the pseudo-acceleration spectrum between the periods 0.1–0.5 s and 0.5–1.5 s, respectively;  $PSA_{top}$  and  $PSA_{base}$  are the spectra of the pseudo-accelerations measured at the top and the base of the models, respectively.



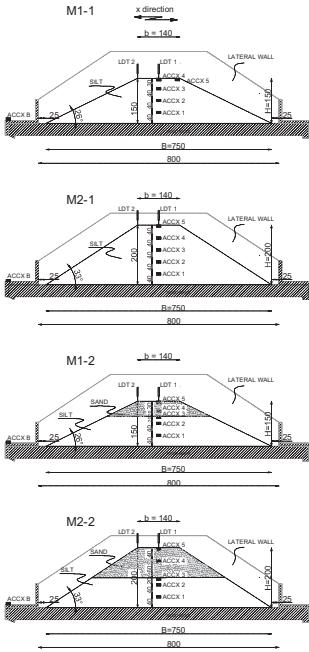


Figure 2. Model schemes and dimensions (measures in mm).

The computed values of the amplification factors are listed in Table 4, where the peak acceleration values measured at the model base and top are also reported. Despite of the significant accelerations measured within the models, very small settlements of the top of the embankments were measured during all tests and no sign of local instability phenomena were observed during the applied earthquakes.

Table 4. Amplification factors.

Model	input	PGA <sub>base</sub> [g]	PGA <sub>top</sub> [g]	FA <sub>0.1-0.5</sub> [-]	FA <sub>0.5-1.5</sub> [-]
M2-1	1*	0.28	0.61	2.2	1.2
M2-1	2*	0.39	0.98	2.8	1.4
M2-1	3*	0.35	1.10	3.0	1.2
M2-1	6*	0.39	1.08	2.8	1.4

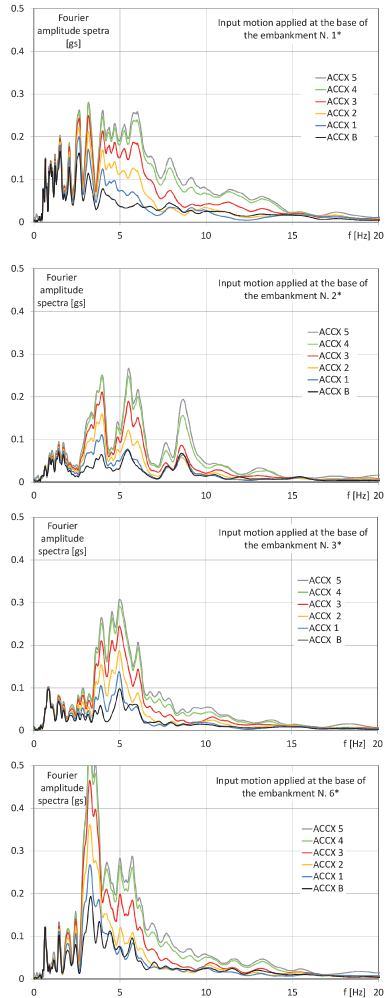


Figure 3. Fourier amplitude spectra of the accelerations measured within the models M2-1 subjected to the input motions N. 1\*, 2\*, 3\* and 6\*.

## 5 NUMERICAL ANALYSIS

Preliminary 2D response analysis of the models tested in centrifuge have been carried out using the finite element code QUAD4M [3], which performs seismic ground response analysis in the time domain and accounts for non-linear stress-strain soil behavior and strain dependent damping through the linear-equivalent procedure. The simulations have been performed referring to the prototype scale.

The mesh representing each embankment consists of quadrilateral and triangular elements and is fixed at the base, modeled as a rigid boundary in order to reproduce the rigid bottom of the centrifuge container. The measured accelerograms performed by the shake table have been applied at the base of each numerical model as input motions. A shear modulus,  $G_0$  constant with the height of the embankment has been assumed for the elements of the mesh. The  $G_0$  values attributed to the models have been estimated back-analyzing the results of the centrifuge tests. For the model M2-1, a value  $G_0 = 48$  MPa have been estimated and assumed in the 2D response analyses. The shear modulus degradation curves and the damping curves measured via RC tests on silt and sand samples retrieved from the centrifuge models at the end of tests were used.

The accelerograms resulting from the seismic wave propagation analysis have been obtained for the nodes of the mesh corresponding to the location of the accelerometers in the centrifuge models. In Figure 4, the PSA of the accelerations computed at the top of the model M2-1 are compared to those measured in centrifuge for the input motion N. 6\*. The PSA of the input motion is also reported. The Figures show quite a good agreement between the results of the numerical analysis and centrifuge measures.

## 6 CONSIDERATIONS

This paper presents the results of dynamic centrifuge tests performed to investigate the seismic behavior of the Po river embankments subjected to the earthquakes expected in the Ferrara Province. The experimentation involved the perfor-

mance of tests on four different models, subjected to four different accelerograms. The main aim of the tests is to create an experimental database on the base of which calibrating and validating numerical models for advanced parametric analysis. As an example, this paper presents some preliminary results of the numerical simulations of the experiments, to reproduce the seismic response of the embankments.

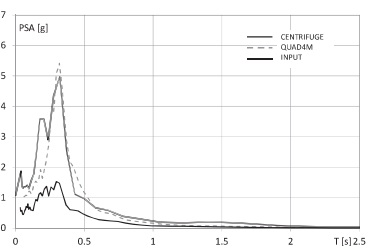


Figure 4. Model M2-1, input motion N. 6\*: computed (QUAD4M) and measured (centrifuge) pseudo acceleration spectra.

## ACKNOWLEDGEMENT

The research reported herein was financed by the Po River Basin Authority, whose support is gratefully acknowledged. The ISMGEO staff and Mr. Sergio Airoidi are acknowledged for assistance in centrifuge works.

## REFERENCES

- [1] Idriss, I.M. & Sun, J.I. (1992). "SHAKE91: A computer program for conducting equivalent linear seismic response analyses of horizontally layered soil deposits," User's Guide, University of California, Davis, California, 13 pp.
- [2] Baldi, G., Belloni, G., Maggioni, W. (1988). The ISMES Geotechnical Centrifuge. In Centrifuge 88, Paris, Corté J. F. Ed., Balkema, Rotterdam, pp. 45-48.
- [3] Hudson M, Idriss IM, Beikae M. QUAD4M. A computer program to evaluate the seismic response of soil structures using finite element procedures and incorporating a compliant base. Davis: Center for Geotechnical Modeling, Department of Civil and Environmental Engineering, University of California; 1994.

# Comprehensive geotechnical monitoring of the landslide processes and the retaining structures in the city of Sochi

A. Ryabukhin<sup>1</sup>

*“STC GeoProekt”, Russia, Krasnodar*

## ABSTRACT

When constructing the important structures in the landslide hazardous areas, it is necessary to carry out geotechnical monitoring. A program of comprehensive geotechnical monitoring of the landslide plots at “Agura” interchange in the city of Sochi is given in the present article. The development project observation results being obtained have been analyzed. The data being obtained prove an acceptable operation of the structures.

Keywords: Landslides, geotechnical monitoring, road interchange

## 1 INTRODUCTION

The natural climatic conditions, the lithologic-and-structural features of the rocks, which form the slopes, and an anthropogenic influence promote the development of many landslide phenomena on the Black Sea coast of Krasnodar Territory. A landslide displacement of soils is a result of a multiple influence of the natural and technogenic factors and can be prepared during many years or can take place in the process of an initial mastering of the slope [1]. The engineering-geological process of a formation and development of the landslide displacements is far more complicated than the mathematical models, the design diagrams and the graphs. In reality, there always exist the unsuspected uncertainties, which

are connected with an inconstancy of the soil features and an imperfection of the design methods, which give only a mechanical solution of the natural task [2]. It results in the frequent accidents both at the stage of construction and the operation of the landslide protection structures. Carrying out of geotechnical monitoring is one of the most effective methods of the landslide risk management.

## 2 OBSERVATION OBJECT

Within the framework of the wide-ranging preparation for the Sochi 2014 Olympic Games, an alternate route of Kurortny Prospect is being constructed; it will decrease an intensity of the

---

<sup>1</sup> A. Ryabukhin “STC GeoProekt”, Russia, Krasnodar, ryabukhin@geoproekt.net

traffic infrastructure of the city. The highway is situated along the sea coast slope with an exit to a ridge, which separates the seaside and a valley of the river Agura. One of its main points is situated at an interstream area of Agura-Bzugu where Obkhod (the Bypass) of the city of Sochi and A-147 highway Dzhubga-Sochi are met. This area is in the low mountain part of the sea coast under the complicated engineering-geological conditions where there are according to the list of state monitoring service two ancient landslides No. 214 and No. 215.

The landslide No. 214 has a slightly knobby surface, forested parts; its area is nearly 9000 m<sup>2</sup>, its approximate thickness is 14 to 16 m. Small erosion insets with the deepness of 0.5 m in the clay soils are observed; they are caused by temporary waterways. The surface morphology of the landslide No. 215 is a small stepped one as well; the breakaway brows have the dimensions up to 1 m; the area is nearly 14000 m<sup>2</sup>, its thickness is 8 to 10 m. The landslide bodies consist of the deposits with an insignificant capture of the bedrock. They are at the stage of a long-term stabilization, which has resulted in a formation of the powerful landslide strata in the floor of the valley. But in the course of construction, a large scale level of a microblock displacement activation hazard remains at the points of a coincidence of the surface inclines and the bedrock stratification. A construction of a pile anchor landslide protection structure is envisaged in order to protect from an influence of the hazardous geological processes (Figure 1).



Figure 1. Pile anchor landslide protection structure at the interchange in the area of the city of Sochi

### 3 GEOTECHNICAL MONITORING PROGRAM

At the design stage of the protection measures, a comprehensive geotechnical monitoring system was worked out; its implementation began in June, 2009, together with the geotechnical survey. Its main task is a prevention of the emergency situation development at the interchange being considered as well as an assessment of sufficiency and effectiveness of the protection solutions being adopted (Figure 2 & 3).

Within the framework of the program, the scheduled route observations of the site are carried out monthly. They are aimed at an ascertainment of the changes in geomorphology and the landscape geobotanical conditions as well as a check of the design solution fulfilment quality. The total extension of the route is more than 1 km; 30 station points are situated here. In order to measure the construction displacements, 63 marks are put; they are plugs with the washers. The geodetic base stations are arranged. The marks are situated at the borders of the deformation sections in pares at the same vertical. Their position in plan and from top to bottom is determined with the help of an electronic tachometer monthly. The landslide accumulations are mapped with the help of the methods of seismic profiling and electric profiling as well. A complex use of various methods makes it possible to obtain more complete and detailed information concerning the processes, which take place at the site. A position of the geophysical profiles for various cycles remains unchanged. The surveys are carried out quarterly.

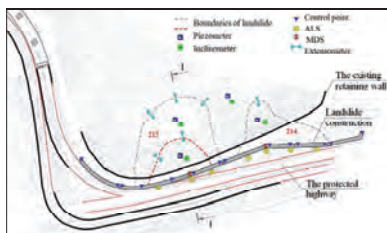


Figure 2. Layout of geotechnical equipment at "Agura" interchange

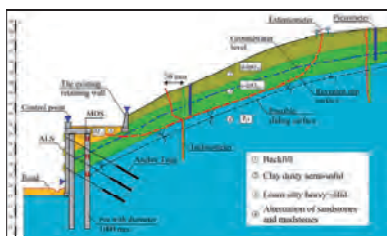


Figure 3. Layout of equipment in section 1-1 at "Agura" interchange

The depth displacements of soil are observed with the help of five deviation recording wells, which have the depth of 14 to 18 m. They are arranged at the borders of the existing landslide systems as well as at the places of their possible development. In order to observe the ground water level, the pressure observation wells with the depth of 10 m are arranged nearby. As vegetation is dense, it is impossible to arrange a network of the monuments in order to trace the surface displacements at this part. For this purpose, a system of 6 surface extensometers is used; they are embedded in concrete at the depth of 0.4 m. A landslide pressure influence on the structure is assessed with the help of the mechanical deformation sensors (MDS), which are arranged in two most loaded piles. The sensors are placed in pares in the sections, which are arranged with spacing of 4 m (Figure 4).



Figure 4. MDS installation in the body of a cast-in-place pile

The anchor load sensors (ALS) were mounted using bolted connections. When they were arranged, the anchors were tightened up to the design stress of 200 kN. Equipment was installed mutually by the specialists of the manufactures: the open joint-stock company "Avangard" (city of St.-Petersburg) and "SisGeo" (city of Milan). Total quantity of the equipment being installed and the interval of the readings are given in Table 1.

Table 1. Quantity of the geotechnical equipment being installed

Name	Quantity	Interval of readings
Inclinometer	5 wells, total length of 80 m	fortnightly
Piezometer	5 wells, total length of 50 m	half-weekly
Extensometer	6 pieces	fortnightly
Anchor load sensors	21 pieces	fortnightly
Mechanical deformation sensor	12 pieces	fortnightly

#### 4 ANALYSIS OF FINDINGS

The results, which were obtained during the geophysical investigations, made it possible to specify the borders of the landslide parts and to define the area of filtration and increased fissuring. The seismic exploration data demonstrated the presence of irregularities and an increase of longitudinal wave velocity at the depth of 5.5 to 7 m in the area of the landslide No. 215; it

proved instability and watering of the present zone.

According to the meteorological data, the precipitation was 126.9 mm in March, 2011; it exceeds the norm by more than 20%. It resulted in a significant rise of the ground water level and an activation of the tongue part of the landslide No. 215 along the border of bedding of loams and argillites. It was proved by the data, which were obtained from inclinometer I-4, which total displacement was more than 60 mm, as well as the readings of piezometer P-4 situated at the depth of 8 m (Figure 5). At that period, a small increase of load (within the limits of 25 kN) was registered at the anchor load sensors ALS-4, 5 and 6, which were arranged at an axis of the displacement being supposed (Figure 5). It is a bit more than 2.5% from the carrying capacity of the anchor and exerts practically no influence on the operation of the whole structure. No significant changes in the stressed state of the piles being observed were detected.

The analysis of the geodetic measurements showed that small deformations at that part of the wall were registered from March 16 till April 2, 2011. Maximal values of the vectors of the planned displacements did not exceed 9 mm. At other parts, the readings remained within the limits of the device accuracy. During the visual investigations, the landslide activity signs were registered, i.e. the deformations of the existing retaining rubblestone wall and the fresh soil stripping brow with the height of 0.3 to 0.5 m. In order to track them, additional extensometric ranges were installed. It is necessary to note that the visual manifestations of the landslide activity took place only this day month after the inclinometric pipe displacement beginning. After spring, intensive precipitation stopped; it resulted in a gradual stabilization of the situation

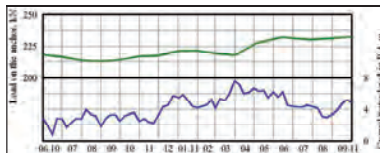


Figure 5. Load change at ALS-4 and position of ground water level in piezometric well P-4

## 5 CONCLUSIONS

The data being obtained prove that the landslide protection structure has an adequate carrying capacity margin. No additional measures are required; it is more expedient to evacuate the soil, which droops from the upper part, because the upper road will not be used when the construction is over. Further observations will make it possible to provide the long-term forecasts of the state of the landslide hazardous masses and the engineering structures in order to prevent the possible emergency situations.

Thus, it is possible to make a conclusion that the elaborated comprehensive geotechnical monitoring system provides a completely trouble-free operation of the interchange being considered. The instrumental observations make it possible to register the changes, which take place in the landslide mass body, much earlier than their visual signs appear. In some cases, it can become a decisive factor when an emergency situation occurrence should be prevented and a significant material damage can be caused.

## REFERENCES

- [1] S. I. Matsiy, *Landslide protection*, AIVI-design, Krasnodar, 2010.
- [2] S. I. Matsiy, E. V. Bezuglova *Landslide risk management*, AIVI-design, Krasnodar, 2010

# The impact of seismic events to the intensity of 6 points or higher on the stress-strain state landslide dangerous slopes in clay neogenic age Carpathian region of Ukraine

Khavkin K.<sup>1</sup>

*Young researcher, State Research Institute of Building Constructions, Kyiv, Ukraine*

## ABSTRACT

The report covers regional properties of stress-strain state of landslides with a plane of sliding lying in Neogene clays. Three main patterns and models of landslide process development (lateral spreads, earthflows and slides) for the Carpathian region of Poland and Ukraine are determined. As a result of numeral design of the tensely-deformed state of changes of cut taking into account actual accelerogram of the Chernivtsi region on the basis of complex PLAXIS it is found out a direct dynamic method: seismic events by intensity to 6 points can considerably worsen descriptions of soils in the zone of shute, to influence on firmness of slope and size of pressure of change. The further increase of seismic of building( to 7-8 points) ground results in the substantial decline of coefficient of firmness. A slope at first proof ( $K_{st} > 1$ ) goes across ( $K_{st} = 1$ ) in a century ( $K_{st} < 1$ ).

Keywords: Computational mechanics, landslides, stress analysis

## 1 INTRODUCTION

Neogene clays are widespread in the Carpathian region of Poland and Ukraine and together with slope processes play a determinative role in the selection of construction sites. As construction sites with the favorable engineer and geological conditions have been already developed, in recent decade buildings and facilities are constructed more often on landslide-prone slopes with sagging, high-yield and peat-muddy soils. The correct determination of landslide danger levels for construction sites makes possible to develop such territories efficiently and on the rims.

Landslide problem is utterly actual for the Carpathian region of Poland and Ukraine and for the Chernivtsi region particularly where landslides affect more than 9 per cent of the territory [1]. It is the highest indicator throughout

Ukraine. So, the problem is acute, what is underlined by the development and approval by the Cabinet of Ministers of Ukraine of the comprehensive program of landslide protection measures on the territory of Chernivtsi region for the period from 2005 to 2014 [1].

In the city of Chernivtsi and its region there are numerous occurrences of landslides in the Neogene argillaceous deposits. Such slopes feature the complex spatial stress-strain state caused by the processes of the Neogene clays deconsolidation and seismic activities. Lateral spreads, earthflows and slides are widespread. Analysis of design works and in-situ implementation of landslide protection measures in the city of Chernivtsi and its region has shown that in the Chernivtsi region the landslide protection facilities have been constructed only for the railway system. As little as five landslide-prone sites are

---

<sup>1</sup> Solgar@ukr.net

protected in the city of Chernivtsi although the total number of such sites exceeds 60. As a rule, the landslide protection activities were conducted by non-domestic design and building companies and had a sporadic character.

As is known, the Ministry of Regional Development, Construction, and Housing and Communal Services of Ukraine develops diligently the new construction standards of Ukraine (State Construction Norms - DBN) that would be harmonized with European construction standards, as the USSR construction standards were too averaged out throughout the territory of the former Soviet Union. The developed DBN V 1.1-3-97 [2] defines only the main principles of landslide protection and does not distinguish between landslide slopes with sagging soils, the Neogene clay landslides and others. That's why it is necessary to refine regional features of landslide soil base and landslide-prone slopes of the Chernivtsi region as well as peculiarities of the landslide pressure onto supporting buildings.

## 2 THEORETICAL BASES OF LANDSLIDE DEVELOPMENT MODELING

Ukrainian scientists G.Rudko and V.Salomatyn [3] have dealt with the problem of landslide development modeling for the Chernivtsi region. They found three main patterns and models of landslide development such as lateral spread, earthflow and slide on the territory of the Chernivtsi region.

The known greatest Chernivtsi landslides are lateral spreads with sliding surfaces lying in the Neogene clays. The lateral spreads occur on the slopes with rocks underlying fast horizontally. E.Yemeljanova has studied the engineer and geological features of such landslides in her works. For the landslide slopes that are prone to lateral spreads the following section and form of sliding plane are specific:

- Height exceeds 30m;
- Length in a plan is not less than 70 m;
- Front width exceeds 50 m; and
- Sliding surface inclination  $\alpha$  does not exceed 15°.

The specific section of the landslide com-

bined with the regional features of a soil base therefore leads to some peculiar properties of landslide pressure distribution diagram and development of technical solutions on design of supporting landslide-protective buildings. The thicknesses of engineer and geological elements are not given purposely. It should be noted that the thickness of the Neogene clay in the vertical direction may reach more than 200.0 m in the lateral spreads.

According to S.Ter-Martirosyan [4], these rocks are over-consolidated, as they were subjected to pressure of approximately 40 kg/cm<sup>2</sup> in the course of their historical development [5]. Besides, the Neogene clays have very high values of physical and mechanical properties. In some cases specific cohesion may reach approximately 240 kPa in consolidated drained spread [5].

As M.Demchyshyn outlines in his works, a characteristic feature of landslides and landslide slopes of the Chernivtsi region is a long preparation period before the stage of a main displacement due to a long period of a gravitation equilibrium disturbance that is more than 80 years in some cases. Naturally, this may be connected with the high values of physical and mechanical properties of the Neogene clays.

We have obtained a typical diagram of landslide pressure (E) distribution using simplified Landslip software and numerical modeling.

Its peculiarities are directly connected with the regional features of soil base of landslide slopes damaged by lateral spreads. The consideration of the characteristic segments of the distribution diagram of landslide pressure shows the following:

- OA segment. Landslide pressure may not exist in this segment (or may have a positive value). This is caused by that fact that here sliding surface inclination may be too rapid, even exceeding 70°. The value of  $E_{min}$  may reach 200-400 kN/m.

- AC segment. The landslide pressure abruptly increases and remains constant along the main length of the AC segment, and then uniformly decreases to the segment end. The value  $E_{max}$  changes within the range from 700 kN/m to 2500 kN/m. The uniform character of the



landslide pressure decreasing can be explained by the sliding surface configuration (practically, by its horizontal nature).

- CD segment. Here the landslide pressure does not always exist and can reach the values of 200-400 kN/m.

Correspondingly, in these segments the landslide thickness varies by the height within the following limits:

- OA segment. The landslide thickness changes from 0 up to 10 m;

- AC segment. The landslide thickness changes, firstly increasing from 10 up to 25 m and then decreasing up to 5 or 0 m;

- CD segment. The landslide pressure is not always present. The landslide thickness changes from 5 up to 0 m.

However, the Landslip software and computational methods of Maslov-Berer, Shakhunians, Bishop and Spencer put some restrictions, namely, like the most of computational methods of assessment, they are based on the application of the granular solids limit stress state theory used as mathematical model of cohesive and cohesionless soils, as well as of fissured rock. But when determining the stability coefficients and landslide pressure, the landslides science state-of-the-art allows using the following simplifying provisions not only in the mentioned computational methods:

- \* the slopes stability is determined by means of two-dimensional problem solution, that is, the narrow strip of the slope is considered and its operation conditions are extended over the neighboring areas;

- \* the hypothesis of consolidated body may be accepted, that is the sliding prism is considered either as entirely stiff and undeformed or as composed of a few butt-jointed, but also stiff undeformed blocks. This allows replacing the stresses with the forces, when calculating their ultimate equilibrium;

- \* The previously defined sliding surface, which a priori should correspond to the ultimate equilibrium conditions and the design sliding coefficient minimum (the landslide pressure maximum), may be accepted;

- \* the undeclared theories of the limit stress state of the granular media and the additional in-

fluences of underground waters and seismic forces on the sliding prism may be taken into account;

- \* in some calculation methods a single equation of statics is accepted, and the forces of interactions between the blocks, which the sliding prism may be divided into, are not considered;

- \* in many cases the limit stress state theory is applied to the calculations of states of the soil massifs, which are in a prelimit or out-of-limit states (the stability factor is greater or less than 1) not taken into account by this theory.

The further calculations are performed with the application of the Plaxis software. For the description of landslide slopes, the Plaxis software mostly uses the [Mohr-Coulomb model](#). The comprehensive [Mohr-Coulomb model](#) is composed of the six functions  $f_{i(a,b)}$ , which are formulated in the conditions of the main stresses  $\sigma'_i$  and appear as follows [9]. Two model parameters in the formulas from 1 to 6 are well known as an internal friction angle  $\varphi$  and soil unit cohesion  $c$ .

### 3 LANDSLIDES DEFORMATION FOR THE CHERNIVTSI REGION

Therefore, the Mohr-Coulomb model contains five main parameters: Young's modulus (E); Poisson's ratio ( $\nu$ ); soil unit cohesion (c); internal friction angle ( $\varphi$ ) and dilatancy angle ( $\psi$ ).

The discretization of the slope computed by means of the Plaxis software is shown in Fig. 1.

For modeling a landslide massif by the finite element method taking into account the disturbed soil interlayer in accordance with the sliding line position, the selection of the given interlayer physical-mechanical characteristics can be performed on the basis of computations by LANDSLIP software and laboratory tests by slip-by-slip method.

Mathematical modeling was performed for the following physical-mechanical characteristics of soils:

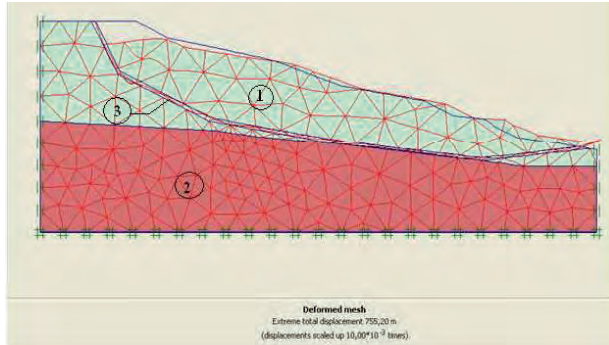


Fig. 1. The deformed mesh of the sliding massif finite elements with the seismic actions being ignored, where 1-loam, 2- firm clay, 3- soil interlayer corresponding to the sliding line

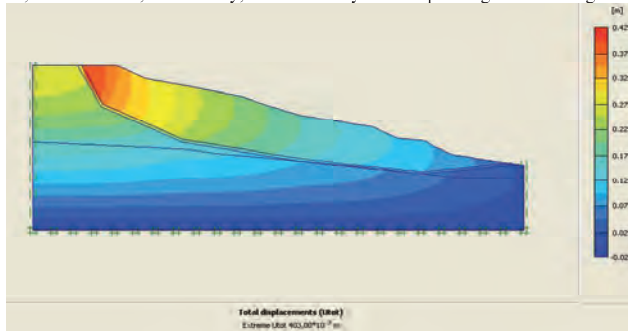


Fig. 2. Total displacements in a landslide because of its dead weight

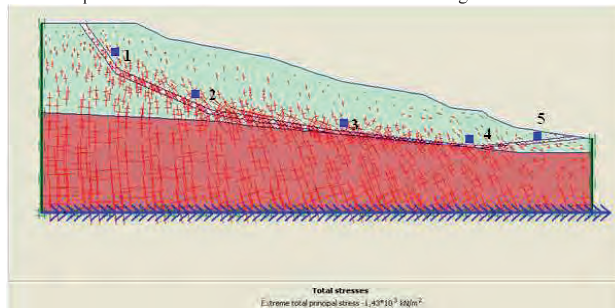


Fig. 3. Total stresses in a landslide due to its dead weight at dynamic loading

- 1) Loam  $\gamma_{\text{unsat}}=18 \text{ kH/M}^3$ ;  $\gamma_{\text{sat}}=20 \text{ kH/M}^3$ ;  
 $E_{\text{ref}}=6 \cdot 10^4 \text{ kH/M}^2$ ;  $\nu=0.35$ ;  $c=20 \text{ kH/M}^2$ ;  $\varphi=25^\circ$ ;  
 2) Clay  $\gamma_{\text{unsat}}=21 \text{ kH/M}^3$ ;  $\gamma_{\text{sat}}=25 \text{ kH/M}^3$ ;  
 $E_{\text{ref}}=9 \cdot 10^4 \text{ kH/M}^2$ ;  $\nu=0.4$ ;  $c=22 \text{ kH/M}^2$ ;  $\varphi=21^\circ$ ;  
 3) Interlayer  $\gamma_{\text{unsat}}=11 \text{ kH/M}^3$ ;  $\gamma_{\text{sat}}=11 \text{ kH/M}^3$ ;  
 $E_{\text{ref}}=1 \cdot 10^4 \text{ kH/M}^2$ ;  $\nu=0.3$ ;  $c=4 \text{ kH/M}^2$ ;  $\varphi=14^\circ$ .

The following computations were performed:

- 1 – Computations without dynamic loading.
- 2 – Computations with dynamic loading of 7-points seismicity.

In Fig. 2 there are total displacements, which occur in the same landslide due to its dead weight. In these cases the coefficient of stability is equal to  $K_{\text{st}}=1.169$ . If the same computations are performed on the given landslide without any interlayer,  $K_{\text{st}}=2.068$ . In Fig. 3 there are total stresses which occur in the Chernivtsi landslide because of its dead weight at dynamic loading. And also there are the locations, in which the comparative analysis was performed.

The comparative analysis of stresses was performed in the main locations with the dynamic loading of 7 points and without dynamic loading. For this purpose five most typical locations were taken in the landslide base. The comparative analysis was performed in three directions in order to determine the direction where the stress variations were the most intense. The analysis showed that with the seismicity increase the loss of structure stability was approximately 10% (table 1).

Table 1

		Location №	1	2	3	4	5
$\sigma$ kN/m <sup>2</sup>	Without dynamic loading		38,6	79,3	122,4	65,9	6,0
	7 points loading		30,4	71,2	108,5	62,9	5,5

#### 4 CONCLUSIONS

The calculations showed that seismic events of intensity up to 6 points can degrade significantly the characteristics of soil along the sliding surface and influence the slope stability and the value of landslide pressure on supporting buildings. The

further increase of the site seismicity (up to 7-8 points) results in the significant decrease of the stability coefficient. The slope, which firstly is stable ( $K_{\text{st}} > 1$ ), turns into a limit equilibrium state ( $K_{\text{st}} = 1$ ) and then its state becomes unstable ( $K_{\text{st}} < 1$ ).

Based on the computations results, it is possible to follow step-by-step the process of the stresses redistribution in the landslide slope with its seismicity increase, which eventually causes the slope motion (unloading of accumulated stresses).

The Plaxis software use ensured the simplification of the landslide-prone slopes computations, the increase of their accuracy and the elimination of errors which were inherent in the simplified methods of Spencer, Bishop, Maslov-Berer and Shakhunians

#### REFERENCES

- [1] Comprehensive program of landslide-prevention measures for 2005 – 2014 / Kyiv, Cabinet of Ministers of Ukraine (2004). - Mode of access: <http://zakon.rada.gov.ua/cgi-bin/laws/main.cgi?nreg=1256-2004-%EF>
- [2] DBN B.1.1-3-97. Engineering protection of territories, buildings and facilities from landslides and landslips. The main provisions. – Kyiv: the Ukrainian State Committee for Construction, Architectural and Housing Policy, 1998. - 40 p
- [3] Rudko G. I., Salomatin V. N. Temporary methodological recommendations on the organization of the geological environment monitoring in Ukraine (The USSR Western regions are taken as example). – Kiev: Naukova dumka, 1987. - 185 p.
- [4] Ter-Martirosyan Z. G. Mechanics of soils: Study guide. – Moscow: Construction HEI Association Publisher, 2005. - 488 p.
- [5] Nature in Chernivtsi region / Ed. K. I. Gerenchuk. – Lviv: “Vyshecha shkola”, 1978. - 160 p.